Interface and multifunctional device spintronics : studies with synchrotron radiation

Michal Studniarek

To cite this version:

Michal Studniarek. Interface and multifunctional device spintronics : studies with synchrotron radiation. Condensed Matter [cond-mat]. Université de Strasbourg, 2016. English. NNT : 2016STRAE028 . tel-01469309

HAL Id: tel-01469309
https://theses.hal.science/tel-01469309

Submitted on 16 Feb 2017

THÈSE de DOCTORAT

pour obtenir le titre de
Docteur de l'université de Strasbourg
Discipline/Spécialité: Physique

Interface and Multifunctional Device Spintronics. Studies with Synchrotron Radiation.

Université de Strasbourg
École Doctorale de Physique et Chimie-Physique
Institut de Physique et Chimie des Matériaux de Strasbourg

présentée par
Michał Studniarek
soutenue le 10 Novembre 2016

Jury :

Directeur de thèse:	Dr. Samy Boukari
Rapporteurs externes:	Prof. Luis Hueso Prof. Jan Vogel
Examinateurs:	Prof. Wolfgang Weber Dr. Philippe Ohresser Dr. Martin Bowen

Acknowledgments

When I came to Strasbourg in 2010 for a short scientific trip organized by my Polish university, I never would have guessed that this city will become a witness of one of the greatest adventures of my life. This PhD manuscript you are holding in your hands, dear reader, is the culmination point of my journey. The impact of this experience on my life, however, reaches far beyond what is written in it, and this is due to exceptional people who I had a pleasure and an honor to be surrounded with during this way.

I would like to start with acknowledgments of my scientific mentors at the IPCMS: Prof. Eric Beaurepaire, Dr. Samy Boukari, and Dr. Martin Bowen. I am immensely grateful for giving me possibility to perform the PhD studies at your side. You were my guides and tutors in a great variety of research domains. You shaped me and opened for me the world of science for what I remain truly indebted.

I would like to specially thank Mr. Jacek Arabski, without who I would never have come this way. You were unprecedentedly supportive for me during this time and you taught me how the selfless guidance in a scientific community should look like. Thank you for your involvement in my arrival to the IPCMS and for your care during this whole time.

Among all the scientists of the IPMCS, I would like to acknowledge especially some of them who had the biggest impact on me. Great thanks to Prof. Wolfgang Weber, for his continuous availability and willingness to answer any scientific question any time. I enjoyed every discussion with you whether scientific or more philosophical. You remain for me as an example to follow of a professor truly devoted to his students. Thanks to Dr. Victor Da Costa for being my internship supervisor, teaching me everything I know about vacuum technologies or scanning probe microscopy, and for the common work we did at the Multi-Probe set-up. Thanks to Dr. Loïc Joly, for sharing your knowledge about the synchrotrons, especially from the electrical management and programming point of view. I appreciate all your advice and help in deciding about the next step of my scientific career. Thanks also to Dr. Fabrice Scheurer, from who I experienced an unusually kind and open attitude towards me as a PhD student. I would also like to thank Dr. Guy Schmerber for very active scientific collaboration, a lot of positive energy, and nice talks in the corridors of the IPCMS. I would like to thank Bernard Muller for his absolutely positive temperament and for our common trips to the SOLEIL synchrotron for assembling the new insert at the DEIMOS beamline. Thanks to Christophe Kieber and Emmanuel Sternitzky for a technical support and electronic skills without which we would not have performed many of the experiments presented in this manuscript. I would like to thank Dr. Benoît Heinrich for help with x-ray diffraction data analysis. Also, an important person in the IPCMS who I want to acknowledge is Madame Véronique Wernher, our group administrator. Thank you for your outstanding skills and kindness during the organization of my numerous scientific trips.

My PhD studies were carried out in collaboration with the DEIMOS beamline of the synchrotron SOLEIL, and therefore I would like to express my gratitude to some people I met there. In the first place, I want to greatly thank the principal beamline scientist Dr. Philippe Ohresser. You initiated my fascination with the synchrotron facilities and, as we know now, in this way you determined my next carrier step. All my present knowledge about the light sources and spectroscopic techniques in the soft x-ray range I owe to you. Thank you for your support, supervision, and help throughout these years. During my stays at the DEIMOS beamline I was always very kindly received. For this also I would like to thank Dr. Edwige Otero, Dr. Fadi Choueikani, Dr. Jean-Paul Kappler, Dr. Kai Chen (former post-doc), Florian Leduc, and Dr. Niéli Daffe. You made my visits at the beamline always a very pleasant time such that I could feel really comfortable among you. I regret that the framework of my studies did not allow me to spend more time with you, yet I am very grateful for the time I had. Special thanks to Florian Leduc, whose strong motivation and involvement in solving technical issues, during our long scientific missions, were in my opinion extraordinary.

Separately, I want to thank the staff of the other beamlines at the SOLEIL synchrotron where I had pleasure to carry out the experiments. These people include Dr. Fausto Sirotti, Dr. Mathieu Sillly, Gilles Le Marchang from the TEMPO beamline, and Dr. François Bertran, Dr. Patrick Le Fevre, and Françoise Deschamps from the CASSIOPÉE beamline. Thank you for providing us with a top-class experimental stations and your constant readiness to help during our measurements.

During my studies I realized that the overall result of one's PhD thesis does not only depend on the subject or technical possibilities, but equally on the teamwork and the atmosphere in the group. Now, I can proudly say that I had enormous luck to work in a very friendly and stimulating environment. This I solely owe to my dear friends and colleagues from the institute. Thanks to my officemate Beata Taudul, for your friendship, tons of talks, going outs, and that you were always a decent distraction factor, in all its positive meanings. I want to thank Dr. Filip Schleicher, for showing me the charm of Alsacian castles at night, for uncountable trips and beers drunk together. Thanks also to Dr. Wojciech Szewc, for your selfless help every time I needed it, mountain trips, and tons of positive stories. I would also like to thank Etienne Urbain for our common time spend in the lab and outside, for movie meetings, and talks. Thanks to Dr. Adam Brandstetter-Kunc for our fruitful coffee breaks, discussions, and reciprocal help on the way towards the end of this studies. Also thanks to the new PhD student Kostia Katcko, for help and adding a new positive energy to the group. I would like to distinguish a peculiar group of people, that is Dr. Ufuk Halisdemir, Dr. Marie Hervé, and Dr. Charles-Henri Lambert, with whom we formed a team for a few strongly demanding scientific missions at the DEIMOS beamline. You showed me the level of teamwork I never saw before and proved that among such strongly taking care of each other people the limits are shifted. The anthems of our trips will remain in my heart. There are also other students or post-docs I would like to mention and who made my stay at the IPCMS feel like at home. These include: Mathilde Menard, Ziyad Chaker, Dr. Senthil Kuppusamy, Dr. Staz Makarchuk, Dr. Burak Ozdamar, Jérôme Hurst, Dr. Julien Fierling, Dr. Nicolas Bachellier, Dr. Guillaume Froehlicher,

Mathias Dolci, and Andra Craciun. The other students I would like to thank and who are former members of the IPCMS working now in other research groups all over the world are: Dr. Anant Dixit, Dr. Dimitra Xenioti, Dr. Vincent Davesne, Dr. Saber Gueddida, and Dr. Hashim Jabbar. Special thanks also to Dr. Manuel Gruber for our common experiments, your kindness, and great willingness to discuss science.

Except this remarkable community I met at the IPCMS and DEIMOS beamline, there are some people from ”outside” I would like to mention. In the first place, I want to thank Arek Mika, for our long talks: scientific, but most of all, the ones not connected with physics, for infinite understanding, our memorable trips, and the everlasting friendship since our graduate studies. In addition, I want to thank: Guillaume Urbain, Marcin Lindner, Dr. Marek Twardoch, Ola Czmiel, Daria Dziewit, and Justyna Skuza for endless meetings, overnight mountain trips, and all the activities when we could enjoy the social life together.

At the very end I would like to express my most personal words of gratitude to whom I eventually owe where I am presently. This manuscript could not have been written if not my beloved fiancée, and soon wife, Tosia. You were my eternal motivation and the best support of all times. You made the time when I was formulating this manuscript the best summer of my life. I would like to thank my parents, and grand-parents, who since my very childhood have been always encouraging me to look for the answers. This is you who affected me with the desire to explore the nuances of science, what is manifested by this manuscript. My thanks go also to my brother Kuba for the best level brotherhood ever and a great relationship despite large distances. I could not forget about our beloved family member Bernese mountain dog Bary (also known as the hiker or mountain swimmer), from whom we could all learn how to be a human.

My family, dear friends, colleagues: this manuscript is for you.

Contents

Résumé in French

Nous sommes tous témoins d'une évolution remarquable de la technologie électronique. Il ne faut pas être un spécialiste du domaine pour remarquer la croissance de la puissance et la diminution de la taille des appareils électroniques qu'on utilise au quotidien. Cette évolution exponentielle qui était prédite Gordon Moore[1] est à la fois fascinante et stimulante. L'électronique inorganique employant uniquement la charge des électrons est appelle électronique classique et possède une histoire remarquablement intrigante. Elle a donnée naissance à des composants qui sont au cœur de tous les téléphones cellulaires ou ordinateurs contemporains. Son début peut être arbitrairement fixée en 1959, date de la commercialisation du premier transistor planaire. Ce simple dispositif semi-conducteur est à l'origine des processeurs d'aujourd'hui comprenant des milliards de transistors. Cette tendance envisagée par Gordon Moore[1] en 1965 est devenue l'une des plus grandes prévisions des temps modernes[2] et une prophétie auto-réalisatrice.[3] Cependant, les limitations de l'électronique classique se multiplient de plus en plus, que ce soit des contraintes liées à la miniaturisation ou des questions fondamentales.[4,5] Cela pousse à développer des technologies alternatives.

C'est de cette manière qu'a émergé le domaine de *l'électronique de spin*, aussi nommé *spintronique*, qui exploite une propriété auparavant inutilisée, le spin de l'électron.[6] Cela a donné naissance à de nouveaux concepts et nouvelles perspectives qui ont rapidement trouvé leur chemin vers des applications comme les têtes de lecture de disques durs magnétiques par exemple.[7] Récemment des dispositifs spintroniques hybrides inorganique/organique ont pu être fabriqué, ce qui a conduit au développement d'un nouveau domaine de recherche appelé *spintronique-organiques*.[8] Une recherche intensive est menée pour fabriquer avec des produits organiques des composants allant au-delà des limites de l'électronique traditionnelle.[9] Cela a permis de développe des injecteurs de spin, des redresseurs organiques, des capteurs, des éléments de mémoire à une seule molécule et bien plus.

Nous croyons que l'approche multifonctionnelle est l'une des directions qui permettra de maintenir une croissance conforme à la loi de Moore. De manière générale il s'agit de fabriquer des matériaux ou dispositifs qui sont sensibles a plusieurs stimuli externes et / ou possèdent des signaux de réponse multiples. Ces stimuli externes peuvent inclure le champ magnétique ou électrique, le courant, la température, la pression, la lumière, et autres. La réponse peut être une modification des propriétés physiques du matériau/dispositif, une variation des propriétés du transport électronique, ou encore de l'émission de lumière. D'une manière générale un matériau/dispositif multifonctionnel peut être représenté par un élément logique avec plusieurs canaux d'entrée et de sortie. De cette façon, un dispositif présentant de telles caractéristiques fournit plusieurs états disponibles ainsi que des multiples degrés de liberté. Ceci peut être effectivement réalisé dans les domaines de la spintronique classique et organique.

Un excellent exemple de la multifonctionnalité dans la spintronique inorganique est fourni par les jonctions tunnel magnétiques étudiées en profondeur par Schleicher *et al.*[10,11] Une sensibilité de l'effet tunnel à des facteurs externes tels que la température,[12] et à des facteurs intrinsèque tel que les changements électroniques ou structuraux fournissent un vaste terrain pour la multifonctionnalité. L'introduction de la matière organique dans les dispositifs spintroniques pousse encore plus loin les propriétés multifonctionnelles des dispositifs.

Contrairement aux composantes inorganiques ou les propriétés physiques et chimiques du matériau sont fixées et déterminées par les éléments constitutifs, les composantes organiques ont une structure plutôt complexe avec des propriétés qui dépendent fortement de facteurs aussi subtils que le type des liaisons ou encore la conformation moléculaire. Par conséquent, des aspects tels que la structure électronique et les niveaux d'énergie des orbitales, peuvent être relativement facilement ajustés de manière à obtenir des caractéristiques souhaitées. En outre, la multifonctionnalité peut permettre d'altérer via des stimuli externes ces attributs établis par la structure chimique (type des liaisons, conformation, etc.). Un bon exemple de multifonctionnalité au sein de la spintronique organique est fourni par les matériaux conducteurs et semi-conducteurs moléculaires magnétiques[9,13]), qui combinent des sels organiques avec des couches magnétiques inorganiques et montrent une coexistence spécifique du ferromagnétisme, de la conductivité, et de la magnétorésistante géante en fonction des espèces donneuses organiques sélectionnées.[14] Un travail remarquable était présenté par Castellano *et al.*[15] Les auteurs ont utilisé une approche métallo-supramoléculaire pour fabriquer un dispositif spintronique.

Une sous-classe distincte de matériaux organiques à multifonctionnalité intrinsèque est la famille des composés à transition de spin (SCO).[16] D'une manière générale, les complexes SCO sont constitués d'un ion métallique de transition entouré par des ligands organiques de telle manière que la structure électronique de l'ion présente une bistabilité de l'état de spin avec au moins deux configurations possibles: bas spin (BS) et un haut spin (HS). La transition entre les deux états est nommée transition de spin (SCO en anglais), et peut être déclenché par la température, la lumière, la pression, un champ magnétique, la tension ou par le courant. Ces possibilités expliquent pourquoi une recherche intense est menée dans ce domaine.

Le but de ce travail est d'exploiter cette approche multifonctionnelle et d'ouvrir la voie vers des dispositifs électroniques à plusieurs degrés de liberté en travaillant à la frontière entre la physique et la chimie, et en associant divers domaines, habituellement développés séparément, tels que l'électronique classique et la spintronique, les systèmes multiferroïques ou encore les matériaux à transition de spin. Le travail présenté dans le manuscrit a été réalisée dans le cadre d'une collaboration entre l'Institut de Physique et Chimie des Matériaux De Strasbourg (IPCMS) et la ligne de lumière DEIMOS du synchrotron SOLEIL.

Nous commencerons par présenter les études sur les interfaces hybrides entre molécules organiques et matériaux ferromagnétiques. Ce type d'interfaces est présent dans presque tous les dispositifs spintroniques organiques. Nous montrerons que l'hybridation et le couplage des orbitales électroniques aux interfaces fait apparaître une polarisation magnétique appelé spinterface hybride. Ensuite, nous étudierons les propriétés de ce système lorsque le couplage se transmet de manière indirecte à travers un espacer non-magnétique. Le prochain niveau de complexité que nous proposerons est le contrôle des propriétés d'une telle spinterface directe/ indirecte en recourant à un substrat multiferroïque. Enfin, nous explorerons les avantages de l'utilisation de matériaux SCO pour des applications nécessitant des ouches organiques et interfaces intrinsèquement multifonctionnelles. Et enfin, nous présenterons une nouvelle méthodologie de mesure de jonctions qui a pu être mise en œuvre grâce à l'utilisation d'un nouvel insert électrique mis en place sur la ligne de lumière DEIMOS (Versatile Variable Temperature Insert). L'assemblage de ce dispositif était l'un des objectifs de cette thèse. Nous montrerons que cet insert permet de sonder dans un dispositif microélectronique la contribution des atomes participant aux transport.

Spinterface ferromagnétique/organique hybride

L'interface inorganique/organique est un élément clef de presque tous les dispositifs spintronique organique. Indépendamment de l'architecture du dispositif, il est toujours nécessaire d'employer, au mieux, les contacts métalliques ou bien faire recours à la technologie des semi-conducteurs. Pleinement saisir la nature de cette interface est d'un intérêt particulier pour la spintronique organique. Cette région de contact a été reconnue comme étant d'une grande importance,[18] mais aussi elle reste souvent source de graves obstacles.[18] Un exemple d'un tel obstacle est la difficulté de prédire le mécanisme de l'hybridation dépendante du spin à l'interface FM/molécule. L'adsorption induit une hybridation entre la molécule organique et le ferromagnétique qui peut conduire à un couplage magnétique et une polarisation de spin à l'interface,[19] c'est-à-dire à formation d'une spinterface. Nous avons consacré des expériences à explorer ces effets dans le système Co/manganèse-phtalocyanine (MnPc). Il a été étudié en détail du point de vue de la polarisation spin par Djeghloul *et al.*[20] qui a démontré

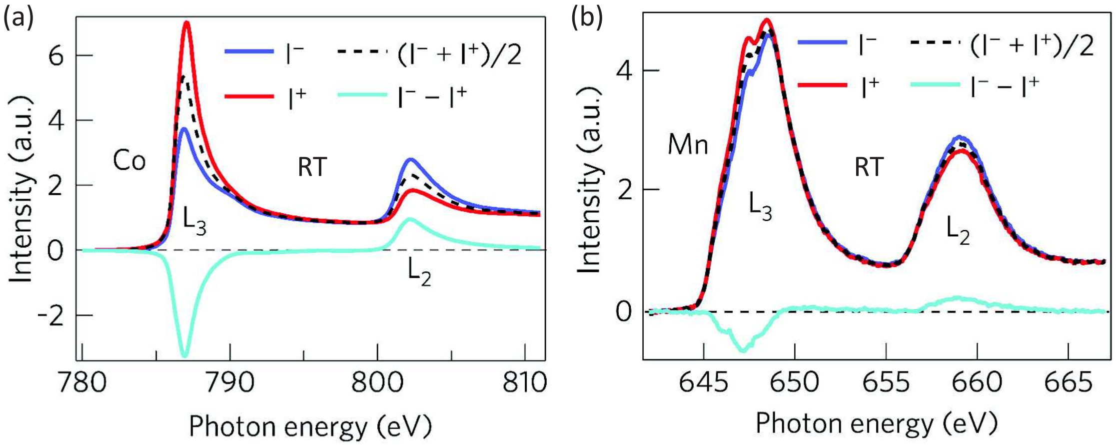

Figure 1: Couplage magnétique dans des hétérostructures Co/MnPc. Absorption X et dichroïsme au seuil $L_{3,2}$ du Co (a) et du Mn (b) montrant le couplage ferromagnétique à température ambiante entre la première couche moléculaire et le substrat de cobalt (mesure effectuées avec 0.1 T). Les courbes sont normalisées par l'intégrale de la raie. Figure prise de la réf. 17.

que l'interface Co/MnPc est fortement polarisée positivement à température ambiante. Nous avons utilisé la spectroscopie d'absorption des rayons X (XAS) et le dichroïsme circulaire magnétique de rayons X (XMCD) de la ligne DEIMOS pour déterminer la structure magnétique de l'hétérostructure Co/MnPc.

Les échantillons ont été fabriqués in situ et les mesures XAS et XMCD réalisées au seuil $L_{3,2}$ du Co et du Mn à température ambiante. Les résultats sont présentés Fig. 1. Le signal XMCD du substrat Co et du Mn des molécules déposées ont le même signe, ce qui indique un couplage ferromagnétique entre le Co et le Mn à température ambiante. De plus, des études réalisées sur un échantillon dont l'épaisseur de MnPc varie ont révélées que le couplage FM observé à l'interface conduit à un ordre antiferromagnétique (AFM) entre les couches moléculaires consécutives. Cette structure magnétique est responsable de l'anisotropie d'échange exercée par la couche moléculaire sur le Co.[21] Ce type de structure peut permettre dans des applications, à température ambiante, de stabiliser l'aimantation de molécules ou de maintenir la polarisation d'un courant. Suite à ces résultats, on peut se demander s'il est possible de former une spinterface hybride en utilisant un couplage d'échange indirect à travers un espacer non-magnétique. L'avantage serait de pouvoir contrôler le transfert de charge et l'hybridation entre les molécules et le ferromagnétique, notamment dans le cas de molécule fragiles comme les complexes à transition de spins.[22]

Nous avons également étudié l'ordre magnétique de la couche moléculaire lorsqu'elle est séparée du Co par un espaceur non magnétique de Cu. Des échantillons en forme de coin du type Cu(100)//Co/Cu/MnPc ont été étudiés par XMCD au seuil $L_{3,2}$ du Co et du Mn. Les moments magnétiques du Mn de la première couche de MnPc sont couplés au Co par une interaction d'échange indirecte (IEC) du type RKKY. Le couplage est oscillant. Il peut être traité comme un champ d'échange tendant à aligner les moments du Mn soit parallèlement soit anti-parallèlement au Co en fonction de l'épaisseur de Cu. Ce système, où la couche ferromagnétique est protégée par un métal noble peut être considéré comme une spinterface protégée. Des molécules non-sublimables pourraient ainsi être déposées par voie humide sans altérer le ferromagnétique, tout en étant couplées avec lui.[22]

Spinterface couplée par échange indirecte

Nous avons étudié le système Cu(100)//Co(14 ML)/Cu(d_{Cu})/MnPc dans lequel on pouvait s'attendre à un couplage oscillant (FM/AFM) entre le Mn et le Co à travers l'espaceur de Cu. Il y a plusieurs approches pour expliquer ce mécanisme dont l'un est l'interaction de Ruderman-Kittel-Kasuya-Yosida (RKKY) : les électrons s du Cu sont polarisés par la présence du Co. Alternativement, le couplage d'échange indirect peut être traité comme une interaction médié par des états de puits quantiques polarisés dans le Cu. Bien que de tels couplages indirects aient été largement étudiés dans des systèmes inorganiques[23] ils n'ont jamais été démontrés avec l'utilisation de centres paramagnétiques de molécules organiques. Pour combler cette lacune, nous avons effectué des expériences à la ligne de lumière DEIMOS. Un échantillon en forme de coin d'épaisseur d_{Cu} de Cu variable a été fabriquée in situ dans l'environnement de préparation de la ligne DEIMOS (Fig. 2 (a)). L'échantillon a été divisé en deux parties : (i) Co/Cu/Co/MnPc contenant la référence Co/Cu/Co bien connue et (ii) la partie

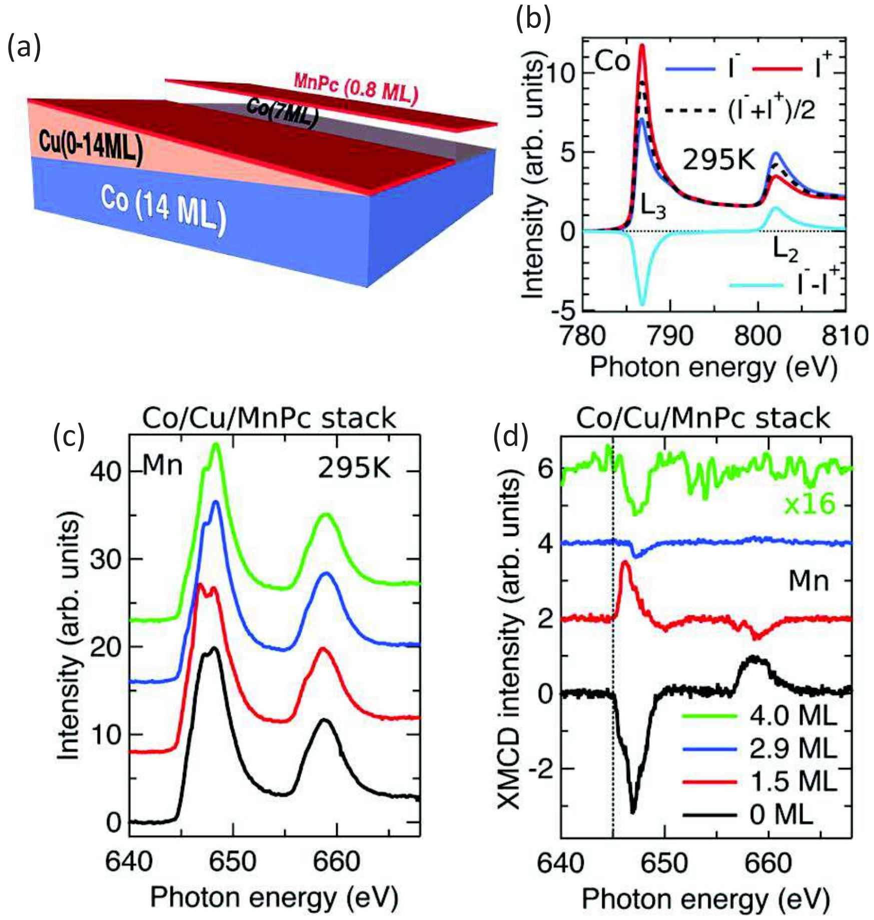

Figure 2: Couplage d'échange indirect entre les centres Mn dans les MnPc et le Co, médié par l'espaceur de Cu. (a) Illustration de l'échantillon étudié. (b) Exemples de XAS et de XMCD aux seuils $L_{3,2}$ de la couche de Co inférieure. (c) XAS et (d) XMCD aux seuils Mn $L_{3,2}$ de MnPc en fonction de l'épaisseur d_{Cu} de l'espaceur de Cu. La modification de la forme des seuils du Mn est due au changement de la composition du substrat (Co à Cu). L'oscillation du signe de l'XMCD du Mn révèle un couplage FM/AFM. Les mesures étaient effectuées à température ambiante avec un champ de $H = 0.1\,\mathrm{T}$. Figure prise de la réf. 21.

d'intérêt Co/Cu/MnPc.

Nous avons effectué des mesures XAS et XMCD au seuil $L_{3,2}$ du Co et Mn. Dans un premier temps nous comparons les spectres XMCD au seuil $L_{3,2}$du Mn dans le MnPc, acquis à différents endroits de l'échantillon, c'est à dire pour des épaisseurs d_{Cu}différentes de l'espaceur, à ceux du Co (Fig. 2 (d)). Comme on pouvait s'y attendre, lorsque l'épaisseur $d_{\mathrm{Cu}} = 0$ le signe de l'XMCD du Mn et Co est le même impliquant le couplage FM déjà observé à l'interface Co/MnPc. Pour une épaisseur $d_{\mathrm{Cu}} = 1.5\,\mathrm{ML}$ (monocouches), le XMCD de Mn est opposée à celui de Co, ce qui signifie que maintenant l'aimantation de Co et Mn sont antiparallèles. Pour une épaisseur $d_{\mathrm{Cu}} = 3\,\mathrm{ML}$ le couplage redevient ferromagnétique. Ainsi nous prétendons d'observer les oscillations du couplage avec une amplitude décroissante compatible avec la relation $J_{\mathrm{IEC}} \sim 1/d_{\mathrm{Cu}}^2$ prédite par la théorie.[24]

Pour avoir un meilleur aperçu du caractère des oscillations, nous avons mesuré l'absorption au maximum du seuil L_3 de Co et Mn pour les deux hélicités des rayons X et les deux sens du champ magnétique ($|H| = 0.1\,\mathrm{T}$) en fonction de la position le long du coin de Cu. Ensuite, pour soustraire le bruit du fond le balayage a été répété à l'énergie du préseuil. La procédure a été refaite sur les deux parties de l'échantillon. Le résultat est présenté à la Fig. 3. Par la suite, nous discutons de l'évolution de l'intensité de la courbe avec l'épaisseur du Cu pour l'empilement de référence (Fig. 3, partie supérieure). Dans un premier temps, nous observons un signe négatif au seuil L_3-edge de Co. À une épaisseur $d_{\mathrm{Cu}} = 6.9\,\mathrm{ML}$ nous observons une inversion de signe du signal XMCD montrant un alignement AFM entre la couche supérieure et inférieure de Co. Ensuite, nous observons une oscillation du signal avec deux pics à $d_{\mathrm{Cu}} = 9.5\,\mathrm{ML}$ et 12.2 ML, mais l'amplitude des changements diminue et le signal n'atteint pas les valeurs positives. Ceci s'explique par l'influence du champ magnétique extérieur qui est en compétition avec le couplage indirect et/ou la taille du faisceau de rayon-x qui intègre le signal de régions dont l'aimantation peut être opposée. La courbe théorique donnant le couplage en fonction de l'épaisseur (Fig. 3, ligne continue grise) est en très bon accord avec la périodicité des oscillations enregistrées pendant l'expérience. Enfin, on observe que la courbe obtenue pour Mn dans le MnPc sur l'empilement de référence suit celle de Co en raison du couplage ferromagnétique (FM) à l'interface Co/MnPc qui était mentionnée auparavant. De cette manière, on déduit que l'empilement de référence Co/Cu/Co/MnPc présente le couplage d'échange intercouche attendu pour Co/Cu/Co, ce qui prouve que l'épaisseur de Cu est bien calibrée. Notez que nous ne voyons pas les oscillations pour $d_{\mathrm{Cu}} < 6.9\,\mathrm{ML}$ ce que nous attribuons aux problèmes de rugosité à l'interface Cu/Co.[25]

Par la suite nous comparons les résultats de la partie de référence avec ceux obtenus sur l'autre moitié de l'échantillon, c'est-à-dire Co/Cu/MnPc (Fig. 3, panneau inférieur). Rappelez-vous que l'épaisseur de Cu sur cette partie de l'échantillon est la même que sur la partie de référence. Premièrement, on note que les oscillations commencent pour d_{Cu} beaucoup plus faible que sur la partie de référence. Nous observons au moins deux maxima additionnels à $d_{\mathrm{Cu}} = 1.7\,\mathrm{ML}$ et 4.1 ML. Ceci provient d'une interface Cu/MnPc plus nette, dépourvue de problème d'inter-diffusions (grande taille des molécules de MnPc). Les oscillations suivent la même périodicité que celles de la partie de référence. En diminuant la température de RT à 4.8 K l'amplitude des oscillations augmente. Cela peut être compris si nous considérons couplage d'échange intercouche comme une contribution au champ magnétique effectif H_{eff} agissant sur le Mn, avec $H_{\mathrm{eff}} = H_{\mathrm{IEC}} + H_{\mathrm{ext}}$, où $|H_{\mathrm{ext}}| = 0.1\,\mathrm{T}$ désigne le champ extérieur. Notez que dans cette approche simple, H_{eff} peut être de signe opposé à H_{ext} en raison de la contribution du couplage. L'aimantation des moments paramagnétiques de Mn dans le champ H_{eff} est donnée par la fonction Brillouin, ce qui implique que plus de moments magnétiques de Mn sont alignés à basse température ce qui à son tour augmente l'amplitude des oscillations. D'autre part, l'augmentation du champ magnétique externe à 6.5 T à basse température conduit à un décalage de la courbe entière vers des valeurs inférieures ce qui provient de l'alignement des molécules non couplées à l'intérieur du système (c'est-à-dire celles soumises uniquement à H_{ext} et non à H_{IEC}). Cela souligne l'interaction subtile de la température, du champ magnétique externe et l'ordre induit par le couplage intercouche. Les résultats obtenus à la Fig. 3 prouvent sans ambiguïté que l'existence d'un couplage d'échange entre les centres Mn des MnPc

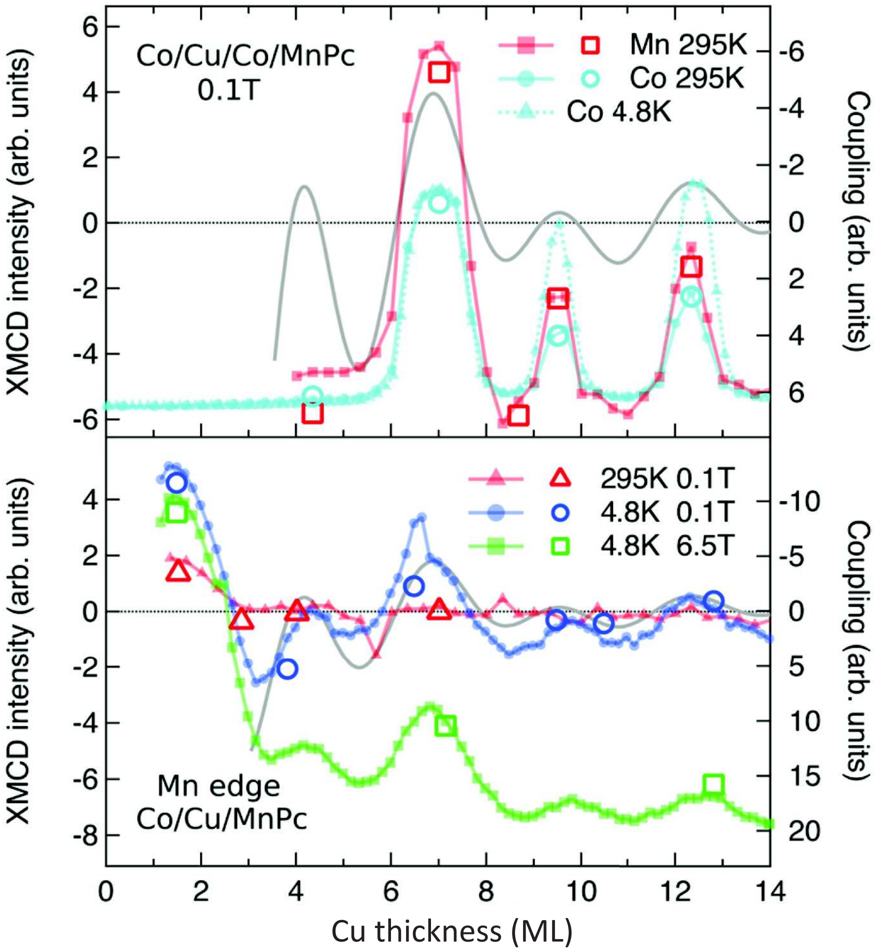

Figure 3: Oscillations du couplage magnétique. XMCD au seuil L_3 de Co (786 eV) et Mn (646.8 eV) dans MnPc en fonction de l'épaisseur du Cu dans l'empilement de référence Co/Cu/Co/MnPc (panneau supérieur), et l'empilement d'intérêt Co/Cu/MnPc (panneau inférieur). Le signal XMCD de Mn est normalisé pour pouvoir être comparé à celui du Co. La ligne grise est la courbe théorique de l'équation Eq. 5.1 (Voir texte principal). Figure prise de la réf. 21.

et Co à travers l'espacer non magnétique de Cu.

De cette manière, nous avons démontré que le couplage de la spinterface hybride peut également être réalisé de manière indirecte. Ensuite, la question qui se pose naturellement est de savoir si l'interface Cu/MnPc dans le système Co/Cu/MnPc est également polarisée en spin? Pour résoudre à ce problème, nous avons mis en place une expérience à la ligne de faisceau CASSIOPÉE du synchrotron SOLEIL.

Les échantillons ont été préparés in situ. La procédure de fabrication était similaire à celle utilisée à la ligne DEIMOS, mais avec une épaisseur uniforme de couches sur toute la zone de l'échantillon. Nous avons utilisé la photoémission résolu en spin pour étudier la structure électronique à l'interface Cu/MnPc. Les photons UV avec une énergie de 20 eV et une polarisation linéaire horizontale de la lumière a frappé l'échantillon à 45°. Les photoélectrons émis ont été recueillis perpendiculairement à la surface avec un analyseur Scienta SES2002 couplé à un détecteur de spin. Un électroaimant situé au-dessous du dispositif expérimental a été utilisé pour aimanter la couche Co de manière rémanente. Toutes les mesures ont été effectuées à température ambiante.

Pour extraire le signal de photoémission résolu par spin qui provient à la fois de l'interface Cu/MnPc et des couches moléculaires au-dessus de l'interface, nous avons utilisé une procédure de soustraction qui tient compte de l'atténuation induite par les molécules du signal de photoémission du Co. Le raisonnement présenté ci-après est similaire à ce qui a déjà été présenté en détail dans la réf. 20 and 26 pour les systèmes phtalocyanine sur du Co(100) et carbone amorphe sur Co(100), respectivement. Nous avons enregistré des spectres provenant de couches Cu(100)//Co/Cu/MnPc et soustrait de ces spectres ceux obtenus avant le dépôt moléculaire, c'est-à-dire sur l'empilement Cu(100)//Co/Cu. De cette manière, nous obtenons la polarisation de spin à l'interface Cu/MnPc. Le résultat de cette procédure, c'est-à-dire des spectres correspondant à l'interface Cu(2 ML)/MnPc(1.6 ML) sont présentés sur la Fig. 4. On peut voir clairement une forte polarisation de spin au niveau de Fermi, dominée par les spins positifs avec un maximum à une énergie de liaison de 0.3 eV. Cela signifie que la polarisation de spin à l'interface au niveau de Fermi est opposée en signe à celle du cobalt. L'augmentation de l'intensité vers des énergies de liaison plus élevées provient des états moléculaires du MnPc.[27]

Nous avons effectué les mêmes mesures pour une couverture différente de MnPc et pour plusieurs épaisseurs de Cu ($d_{\mathrm{Cu}} = 1.5\,\mathrm{ML}, 2\,\mathrm{ML}, 3\,\mathrm{ML}$). Pour toutes ces épaisseurs, nous trouvons une polarisation de spin positive forte et persistante à l'interface Cu/MnPc au niveau de Fermi et à température ambiante. Pour s'assurer que la polarisation ne découle pas des molécules qui sont en contact direct avec la couche FM, dues par exemple à une couche incomplète de Cu, des mesures de spectroscopie

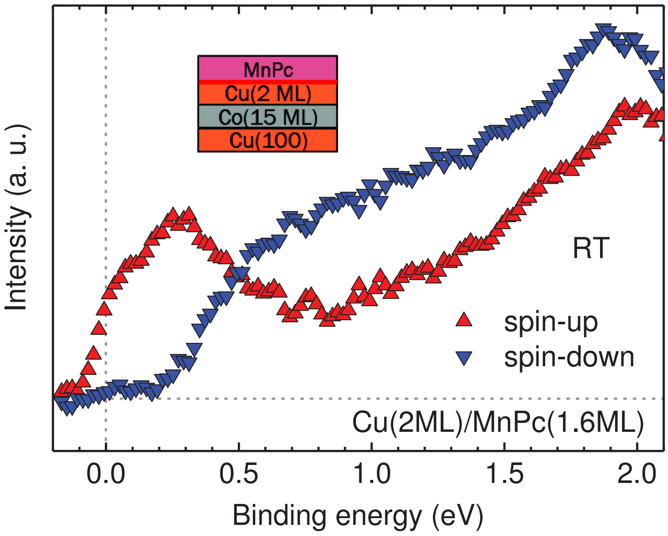

Figure 4: Spectroscopie résolue en spin à l'interface Cu(2 ML)/MnPc(1.6 ML). Intensité de photoémission pour chaque canal de spin provenant de l'interface Co/Cu(2 ML)/MnPc(1.6 ML)) après soustraction des courbes de références acquises sur l'empilement Co/Cu(2 ML). Notez une forte polarisation en spin positive au niveau de Fermi. L'encart présente la composition de l'échantillon avec l'interface d'intérêt Cu/MnPc marquée en rouge.

de diffusion d'ions ont été effectuées à l'IS2M (Mulhouse). Ces mesures ont confirmés qu'une épaisseur de 1.3 ML de Cu couvre complètement le substrat de Co, de sorte que l'on peut, approximativement, affirmer qu'aucune molécule de MnPc n'est en contact avec le Co pour une épaisseur de Cu de 1.5 ML.

En plus de la stabilisation du moment magnétique de Mn dans les MnPc précédemment observé, nous avons montré la formation d'une spinterface à l'interface Cu/MnPc dans le système Co/Cu/MnPc. Il est important de souligner que les effets observés se produisent à température ambiante.

Nous proposons comme application de ce concept de spinterface indirecte la notion de spinterface protégée. Par rapport à la spinterface se développant à l'interface Co/MnPc, le système Co/Cu/MnPc permet la réduction du transfert de charge et l'hybridation en passant d'un substrat FM fortement réactif à une surface de métal noble. Le système permet de conserver les propriétés intéressantes d'une spinterface hybride directe, c'est-à-dire (i) la stabilisation du moment magnétique des MnPc et (ii) la forte polarisation de spin à E_F, ces deux effets se produisant à température ambiante. Ceci en perspective devrait permettre la formation de spinterfaces hybrides actives avec l'utilisation par exemple de molécules SCO dont les propriétés peuvent se dégrader lors de l'adsorption.[22] Notons que ce système permet une ingénierie du couplage en changeant son signe (FM vs. AFM) et son intensité en ajustant l'épaisseur de l'espaceur. En outre, la protection d'une couche FM, sensible à l'atmosphère, par un métal noble permettrait de déposer toutes les molécules, et pas uniquement celles sublimables sous vide, en utilisant une voie humide.

Contrôle ferroélectrique d'une spinterface hybride

Les propriétés des spinterfaces hybrides discutées auparavant, qu'elles soient directes ou indirectes, mettent en avance leur grand potentiel pour des applications spintroniques. Cependant, une fois formé, ce système a des caractéristiques fixées. Nous proposons une extension de ce concept par une fonctionnalité sous forme de contrôle externe à partir d'un substrat multiferroïque. C'est pourquoi nous avons conçu le dispositif spintronique magnétique-organique représenté Fig. 5 (a).

Sur un substrat commercialise texturé de PZT ($\mathrm{Pb(Zr,Ti)O_3}$), muni d'un électrode du bas en Pt, nous avons déposé à travers un masque circulaire 9 ML de Co et 1 ML de FePc. L'empilement a été recouvert par une couche de Pt et au-dessus nous avons évaporé un contact en or. Le dispositif contient donc deux interfaces couplées : (i) couplage magnétoélectrique à l'interface (MEC) PZT/Co,[28] et (ii) une interface hybride Co/FePc. Le dispositif présente deux états de polarisation que nous désignons par $\mathrm{P}\uparrow$ ($\mathrm{P}\downarrow$) pour le vecteur de polarisation pointant hors du plan et vers l'électrode supérieure (inférieure).

La structure électronique aux interfaces PZT/Co et Co/FePc a été déterminée par absorption X à la ligne de faisceau DEIMOS du synchrotron SOLEIL. Le nouvel insert de cette ligne, dont l'assemblage faisait partie de cette thèse, a été utilisé pour l'accès électrique in situ et pour l'inversion de la polarisation du PZT. Nous avons effectué le cycle suivant pour la polarisation du $\mathrm{P}\downarrow \rightarrow \mathrm{P}\uparrow \rightarrow \mathrm{P}_2\downarrow$ et nous avons mesuré l'absorption aux seuils $L_{3,2}$ de Ti dans le substrat de PZT, Co et Fe de molécules de FePc dans un état ferroélectrique rémanent. Tous les résultats présentés ont été acquis au centre de l'empilement avec une incidence de 45° d'incidence et à température ambiante en rendement total d'électrons et en fluorescence.

Il a été démontré dans des expériences ex situ que la commutation de l'état du PZT doit être accompagnée d'altérations réversibles visibles sur les spectres XAS aux seuils $L_{3,2}$ du Ti.[29] Nous avons employé ce fait et utilisé le XAS et le dichroïsme linéaire (XLD) pour fournir une preuve de l'inversion de la polarisation du PZT.[29] Pour cela, nous avons comparé les spectres-moyennées obtenus pour les états de polarisation consécutifs du PZT (Fig. 6). En comparant la différence entre les courbes après la première et la deuxième séquence de polarisation (Fig. 6 (b) et (d)) on observe les changements réversibles à la fois sur le seuil L_3 et L_2. Nous suggérons que ces résultats proviennent des modifications du champ cristallin dans la maille élémentaire de PZT qui est due au déplacement d'ions Ti pendant la commutation. Les changements réversibles observés valident le bon fonctionnement du dispositif et une commutation électronique de l'état du substrat.

L'étude récente de l'hétérostructure PZT/Co par Vlašín *et al.*[28] montre que les altérations du moment magnétique du spin en fonction du renversement de polarisation ferroélectrique provient des effets de proximités. Pour pouvoir observer ces changements, nous nous sommes concentrés sur le spectre XMCD aux seuils $L_{3,2}$ du Co. Les spectres XAS et XMCD dans l'état initial P$\downarrow$ sont représentés Fig. 7 (a) et Fig. 7 (b).

Par la suite, nous avons examiné comment l'inversion de la polarisation du PZT influence à la fois l'absorption des rayons X (Fig. 7 (c)) et le XMCD (Fig. 7 (d)). Les spectre XAS moyennés, aux seuils L_3 et L_2, du Co ont une forme du type spectre dérivé dont le signe s'inverse entre les deux états de polarisation. Il en est de même lorsque l'on

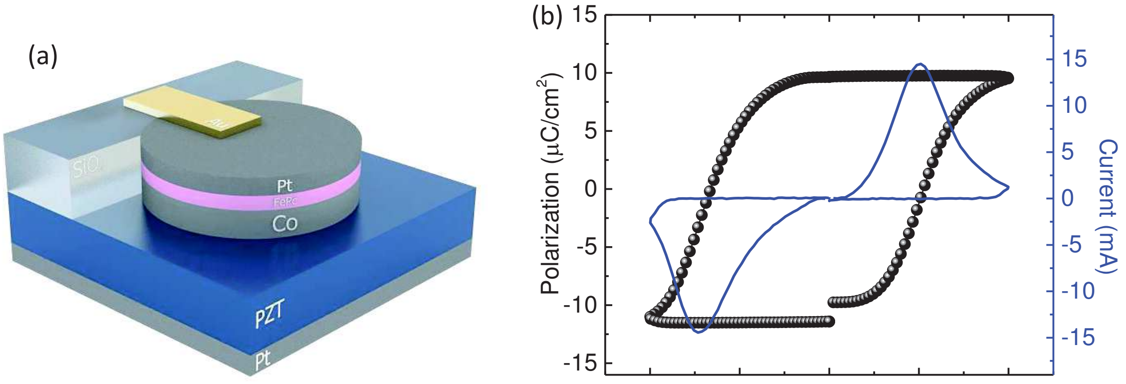

Figure 5: Un dispositif spintronique organique magnétoélectrique. (a) Model 3D du dispositif vertical combinant l'interface MEC PZT/Co, et la spinterface magnétique/organique de Co/FePc. L'empilement est composée de : Pt(150 nm)/PZT//Co(9 ML)/FePc(1 ML)/Pt(9 ML). L'échantillon dont la surface est $4 \times 4\,\mathrm{mm}^2$ contient le dispositif dont la surface est approximativement de $\sim 3\,\mathrm{mm}^2$. (b) Mesure de la polarisation du dispositif. Les pics dans les courbes $I(V)$ révèlent deux états ferroélectriques du dispositif avec une polarisation de $\sim \pm 12\,\mu\mathrm{C/cm}^2$.

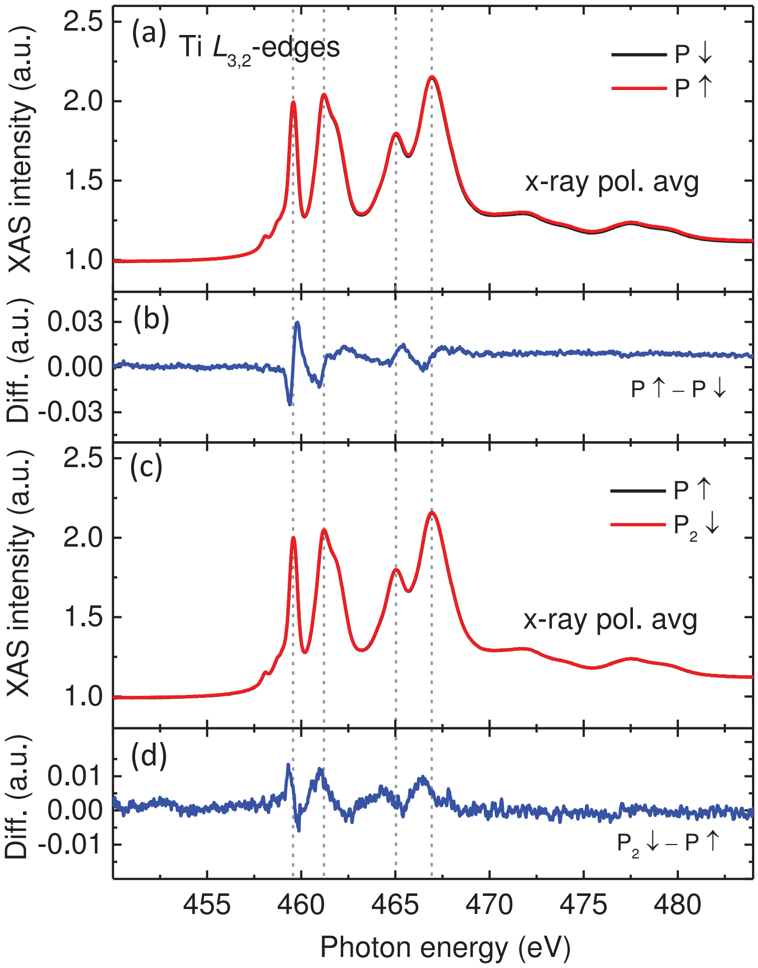

Figure 6: Modification de la structure électronique de Ti lors de la commutation ferroélectrique du dispositif. Spectres XAS moyennés acquis en polarisation linéaire aux seuils $L_{3,2}$ du Ti pour les états de polarisation ferroélectrique P ↓, P ↑, et P_2 ↓ Les graphs (a) et (c) montrent l'absorption des rayons X moyenne qui est utilisée pour calculer les différences (b) et (d). Les caractéristiques apparaissant dans les spectres de signe opposé montrent que les changements de la structure électronique du Ti sont réversibles. Les spectres ont été acquise en fluorescence avec un champ magnétique appliqué de $H = 0.1\,\mathrm{T}$.

considère les changements des spectres XMCD, qui atteignent une amplitude maximale de $\sim 0.5\%$ au bord seuil L_3 (Fig. 7 (d)). Nous suggérons que les altérations illustrées dans la Fig. 7 (c) et (d) proviennent des changements provoqués par la polarisation ferroélectrique influençant le Co en raison du couplage magnétoélectrique à l'interface PZT/Co.[28] De cette façon, nous validons le fonctionnement de la première interface PZT/Co dans le dispositif.

Enfin, nous nous concentrons sur la deuxième interface dans le dispositif, qui est une spinterface hybride Co/FePc. Le couplage FM des centres Fe entre FePc et Co, résultant de l'hybridation dépendante du spin à l'interface, a d'abord été confirmée par le spectre XMCD de Fe et du Co aux bords $L_{3,2}$ et à température ambiante. Ensuite, nous avons étudié comment la structure électronique du Fe est modifiée lors du changement de la polarisation du PZT. La Fig. 8 présente les spectres XMCD aux

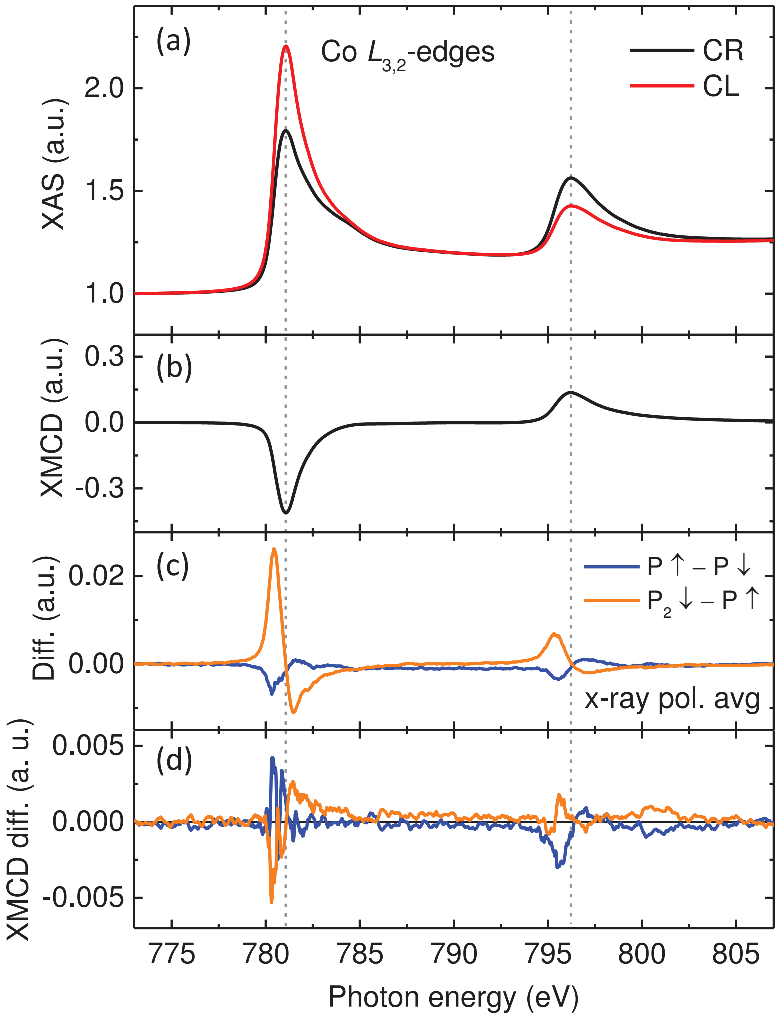

Figure 7: Modifications des propriétés électroniques et magnétiques du Co sur la commutation ferroélectrique du dispositif. (a) Exemples de spectres XAS acquis au bord $L_{3,2}$ de Co pour l'état initial P↓ avec (b) le XMCD résultant. La différence des (c) (c) deux spectres XAS de polarisation radiale des rayons X moyens, et (d) le spectre XMCD, ont été calculés pour le premier (P↑ − P↓) et la seconde (P_2↓ − P↑) renversement de la polarisation du PZT. Les spectres ont été acquis en mode de rendement électronique (*electron yield*) total dans les deux directions du domaine magnétique $|H| = 0.1\,\mathrm{T}$.

seuils $L_{3,2}$ de Fe à l'interface FePc. Le large seuil L_3 est dépourvu de mutiplets, ce qui est typique lors de l'hybridation entre des molécules de Pc et le Co.[30] On peut observer des caractéristiques du spectre XMCD au seuil L_3 du Fe qui sont réversibles avec la commutation de la polarisation du PZT (Fig. 8). Nous nous concentrons sur les zones des courbes marquées A, B et C. (i) Le spectre XMCD du pré-seuil (la zone A, marquée par la flèche rouge) est présente pour P↑ mais pas pour l'état P↓ state. (ii) Le maximum du spectre XMCD au seuil L_3 (zone B) est décalé de 0.1 eV lors de la commutation de la polarisation du PZT. (iii) La zone C est un maximum local pour P↓ mais pas pour l'état P↑. Ceci souligne les fortes similitudes dans le spectre XMCD au seuil du dans les zones A, B et C entre les états P↓ et P_2↓.

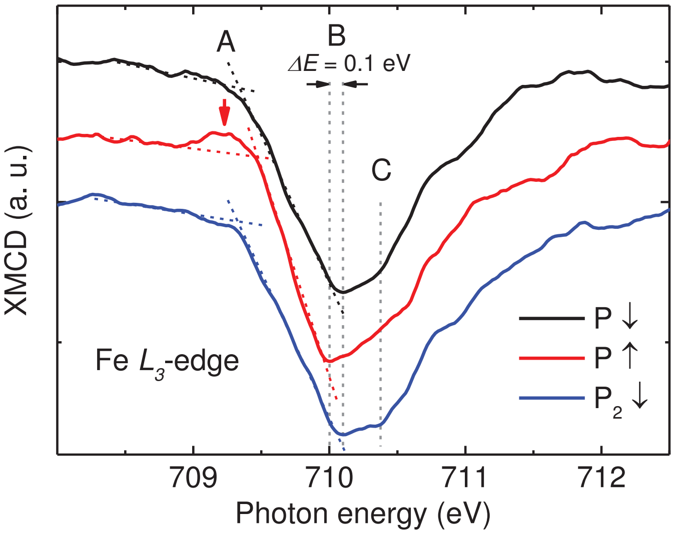

Figure 8: Modifications du spectre XMCD du seuil L_3 du Fe pendant la commutation ferroélectrique du dispositif. Spectres XMCD au seuil L_3 du Fe des FePc, acquis pour des polarisations consécutives du PZT : P ↓, P ↑, et P_2 ↓. Les zones A, B et C, révélant les changement en fonction de polarisation, sont identiques pour P ↓ et P_2 ↓. Les spectres ont été acquis en rendement total d'électron dans les deux sens du champ magnétique $|H| = 0.1\,\mathrm{T}$.

Ainsi on voit que les modifications du spectre XMCD au seuil L3 du Fe des FePc déposées sur Co sont modestes mais entièrement réversibles. Ceci indique que l'état magnétique de la couche moléculaire de FePc, qui est représentatif des propriétés de la spinterface hybride, est modifié à travers la fine couche de Co due à la commutation de la polarisation ferroélectrique du PZT. Cela ouvre des perspectives pour des dispositifs où des spinterfaces hybrides peuvent être contrôlées ferroélectriquement.

De plus, ces résultats suggèrent que les changements des propriétés magnéto-électriques à l'interface PZT/Co altèrent le magnétisme de la couche de Co(9 ML). Nous supposons que les altérations induites sur le substrat FE se propagent à travers toute la structure doublement couplée, c'est-à-dire linterface PZT/Co couplée magnétoélectriquement et l'interface hybride Co/FePc.

Vers un dispositif multifonctionnel à base de complexes à transition de spin

Dans les études précédemment discutées sur l'interface hybride métal/organique et les dispositifs prototypiques magnétoélectrique-organique, le choix des matières organiques a été limité pour des raisons de simplicité aux phtalocyanines métalliques. Celles-ci, malgré leurs excellentes propriétés du point de vue des applications spintroniques mentionnées ci-dessus, sont des couches "passives" dont les propriétés sont plutôt constantes sur une large gamme des conditions externes, par exemple, température, pression, champ magnétique, etc. A un niveau supérieur de complexité nous proposons des couches "actives" ou des interfaces composées de complexes à transition de spin.

Nous imposons deux conditions sur les propriétés du matériau pour la fabrication des dispositifs organiques verticaux : (i) sublimabilité du matériau qui assure une bonne pureté et le contrôle de l'épaisseur des couches fabriquées, et (ii) continuité des couches sublimées permettant à la couche après dépôt d'être encapsulée de manière adéquate entre deux électrodes et participer au transport.

Nous commençons par la démonstration de la multifonctionnalité intrinsèque des couches SCO avec un nouveau matériau sublimable $Fe\{[3,5\text{-dimethylopyrazolyl}]_3BH_2\}_2$, que nous appelons Fe-pyrz. Le matériau a été fourni par le Dr Ana Gaspar du groupe du Professeur José Antonio Real of the Institut de Ciencia Molecukar Departament de Quimica Inorganica (Universitat de Valencia). Dans la première étape nous avons vérifié la sublimabilité du nouveau composé et utilisé un magnétomètre à SQUID pour valider la transition de spin en enregistrant la susceptibilité magnétique en fonction de la température de l'échantillon en poudre et du film épais (Fig. 9). Les mesures ont révélé une transition de spin complète dans le film sublimé. De plus, ce composé a permis de produire les premiers exemples de films présentant une transition de spin hystérétique.

Dans l'étape suivante, nous avons effectué des expériences à la ligne TEMPO du synchrotron SOLEIL dédié au piégeage d'état de spin excité induit par la lumière (LIESST) dans le film de Fe-pyrz. En effectuant le spectre XAS aux seuils $L_{3,2}$ du Fe, nous avons montré qu'en l'utilisation un laser à 400 nm ou un LED blanche, nous pouvons modifier de manière réversible la proportion HS des molécules (Fig. 10) à basse température. Nous avons ainsi démontré la multifonctionnalité intrinsèque de ces couches de SCO Fe-pyrz par sa sensibilité à la température et l'irradiation lumineuse. Ceci peut être utilisé pour des couches actives dans les dispositifs.

Nous avons dédié des études à la morphologie de la surface pour vérifier la condition (ii) de continuité des films mince de Fe-pyrz. Elles ont montré que le dépôt du matériau

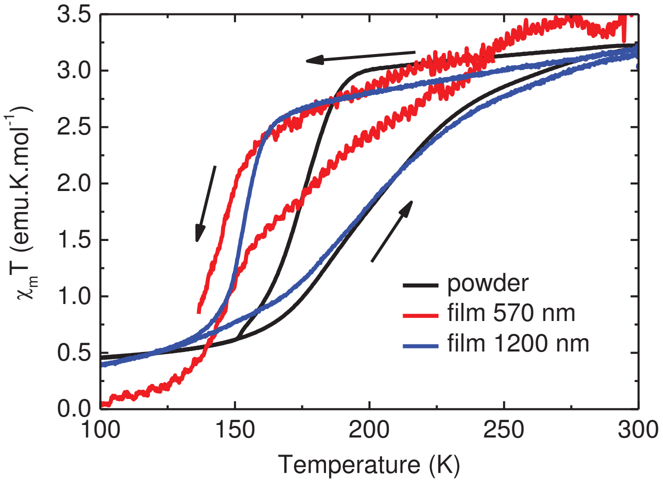

Figure 9: Transition de spin de molécules de Fe-pyrz en poudre et sublimées. Susceptibilité magnétique en fonction de la température pour de la poudre de Fe-pyrz et deux films épais sublimés sur SiO_x. La transition est conservée dans les films. La mesure a été effectuée avec un SQUID et champ magnétique $H = 4\,T$. Les flèches indiquent direction de balayage. Figure tirée de la réf. 31.

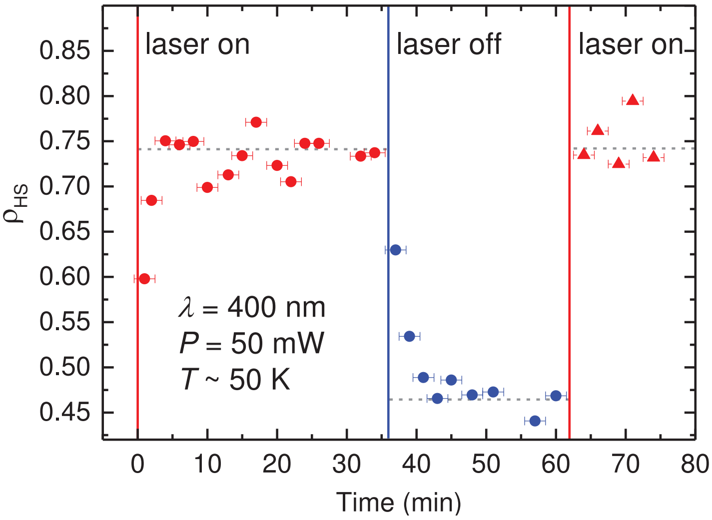

Figure 10: Commutation réversible de la proportion HS dans un film de Fe-pyrz provoquée par laser. Evolution de la proportion haut spin (ρ_{HS}) en fonction de l'éclairage par un laser à 400 nm.

sur du Cu (100) se fait suivant le mécanisme de Frank-van der Merwe, c.-à.-d. couche par couche. Cependant, le même matériau sublimé sur des substrats SiO_x moins réactifs forme des microcristallites. Ceci correspond à une croissance de type Volmer-Weber. Pour résumer, le Fe-pyrz présente une croissance fortement dépendante du substrat ce qui ne remplit que partiellement l'exigence (ii) pour la fabrication de dispositifs organiques verticaux.

Au cours des études menées, nous avons réalisé qu'il pouvait être très difficile de trouver des matériaux qui rempliraient les exigences imposées. C'est pourquoi allons proposer une approche visant à obtenir les propriétés souhaitées pour un matériau en fonctionnalisant des complexes par voie chimique.

Fonctionnalisation de matériaux à transition de spin

Dans cette section nous introduisons une nouvelle approche dans le domaine des matériaux à transition de spin : la fonctionnalisation chimique de composés sublimables. Ce concept, étant plutôt évité pour ne pas altérer les capacités de transition d'un complexe, est pourtant l'un des plus grands intérêts de la spintronique organique qui est la possibilité d'ingénierie chimique. Nous démontrons cette approche en partant de deux complexes parents : $Fe(bpz)_2(phen)$ (bpz = dihydrobis(pyrazolyl)borate, phen = 1,10-phenanthroline) et $Fe(bpz)_2(bpy)$ (bpy = 2,2'-bipyridine). Les travaux présentés dans la section suivante ont été réalisés en étroite collaboration avec le groupe du Professeur Mario Ruben dans le Département des Matériaux Organiques (DMO) à l'IPCMS. La synthèse des matériaux a été réalisée par le Dr Senthil Kuppusamy.

Notre nouvelle approche d'ingénierie chimique permet une modification de l'organisation moléculaire après, donc aussi indirectement des interactions intermoléculaires. Or celles-ci sont connues pour influencer fortement la performance de transition du composé. En outre, la fonctionnalisation ouvre des possibilités plus exotiques telles que l'ajout de groupes permettant l'ancrage sur une surface ou des propriétés de photoluminescence. Dans notre approche nous avons l'intention de fonctionnaliser le matériau de sorte qu'il conserve sa sublimabilité et la transition de spin.

Pour commencer, nous introduisons un Fe(bpz)$_2$(phen) comprenant un groupe NH$_2$, que nous appelons un complexe polyvalent, ceci parce qu'il est facile de remplacer le groupe NH$_2$ par un autre groupe fonctionnel. Nous avons vérifié que le matériau nouvellement présente une transition de spin à l'état de poudre. Ensuite, nous avons confirmé sa sublimabilité et en utilisant des spectres XAS à différentes températures nous avons déterminé la proportion HS. Nous avons observé que seulement $\sim$ 25% des molécules dans le film subissent une transition HS$\rightarrow$BS. Nous avons montré que la raison pour cela se trouve dans la modification de l'empilement moléculaire après sublimation. Les mesures des diffractions de rayons X (XRD) sur la poudre de référence et le film sublimé ont révélé que les molécules sublimées sont partiellement cristallisées dans une structure qui ne correspond pas celle la poudre. C'est à notre avis la raison pour laquelle seuls 25% du film transite.

Dans un deuxième exemple de fonctionnalisation, nous avons utilisé le complexe parent Fe(bpz)$_2$(bpy). La croissance ce complexe lorsqu'il est sublimé sur un oxyde est de type de Volmer-Weber.[32] Notre motivation était de fonctionnaliser le complexe afin de modifier sa croissance sur la surface et former des films plus uniformes. Nous avons commencé avec la dérivée du complexe polyvalent : Fe(bpz)$_2$C$_1$-bpy, et étendu sa structure par une longue chaîne linéaire alkyl C$_{12}$. Nous nous attendons à ce que l'ajout d'une chaîne impose une direction préférentielle lors de la croissance. Le Fe(bpz)$_2$C$_{12}$-bpy nouvellement synthétisé est facilement sublimable et présente une transition de spin complète sous forme de poudre et presque complète dans des films sublimés épais. Pour avoir un aperçu de l'organisation moléculaire, nous avons d'abord effectué des

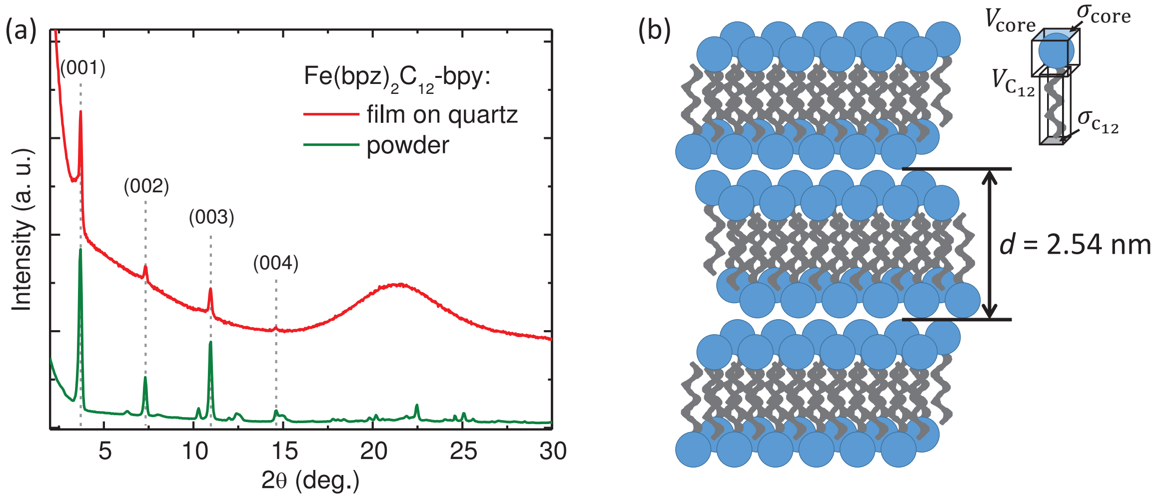

Figure 11: Organisation dans le film épais de Fe(bpz)$_2$C$_{12}$-bpy. (a) Diffraction des rayons X d'un film sublimé de Fe(bpz)$_2$C$_{12}$-bpy sur un substrat en quartz comparé à la poudre de référence. Les pics équidistants (001) – (004) et le large pic à $2\theta = 17° - 25°$ révèlent une phase cristal liquide smectique A dans le film épais. Les diffractogrammes ont été acquis à la température ambiante dans le mode $\theta - 2\theta$, avec une longueur d'onde monochromatique de $\lambda_{\mathrm{CuK}\alpha 1} = 1.54056$ Å. (b) Modèle en bicouches du film de Fe(bpz)$_2$C$_{12}$-bpy avec des chaines C$_{12}$ interdigitées déduit à partir des mesures effectuées.

mesures de diffraction de rayons X (Fig. 11 (a)). Le diffractogramme acquis sur un film épais présente une série des pics étroits aux petits angles et un pic plus large centrée à $2\theta \sim 22°$.Cela ressemble à un diffractogramme typique d'un cristal liquide. Les pics aux petits angles sont équidistants, révélant une organisation lamellaire à longue portée typique d'une phase smectique. A partir de la loi de Bragg, on trouve un espacement lamellaire de $d = 2.43\,\text{nm}$. On en déduit donc la formation d'une mésophase smectique A dans l'épaisseur du film de Fe(bpz)$_2$C$_{12}$-bpy. Le pic entre $2\theta = 17 - 25°$ provient de l'arrangement latéral que nous attribuons à la présence des chaînes alkyle linéaires avec une petite contribution des ligands Fe(bpz)$_2$(bpy). L'élargissement du pic suggère un caractère fondu des chaînes, l'absence de ce caractère dans le cas de la poudre implique une cristallisation des noyaux et des chaînes moléculaires.

Pour déduire l'arrangement moléculaire, nous avons utilisé un raisonnement géométrique. Nous avons calculé le volume théorique d'une seule molécule ainsi que ses sections efficaces que nous avons ensuite lié à un espacement lamellaire de 2.43 nm. Les relations obtenues impliquent une organisation en bicouche avec des chaînes alkyles interdigitées et fortement repliées. Donc, nous supposons que le seul agencement d'empilement moléculaire possible dans ce cas est celui présenté à la Fig. 11 (b).

Pour confirmer cette hypothèse, nous avons effectué des mesures en AFM à température ambiante sur les films fabriqués (Fig. 12). Nous avons découvert que les molécules s'empilement en terrasses. En mesurant le profil des marches on observés deux hauteurs caractéristiques de $d \sim 1.1 - 1.3\,\text{nm}$ ou $d \sim 2.2 - 2.6\,\text{nm}$. Celles-ci sont compatibles avec l'espacement dans le spectre XRD et correspondent à l'espacement d'une couche ou bicouche. En se basant sur les mesures d'AFM nous confirmons la présence d'une mésophase smectique au sein des films sublimés.

Nous avons ainsi démontré la fonctionnalisation du complexe modifie les propriétés

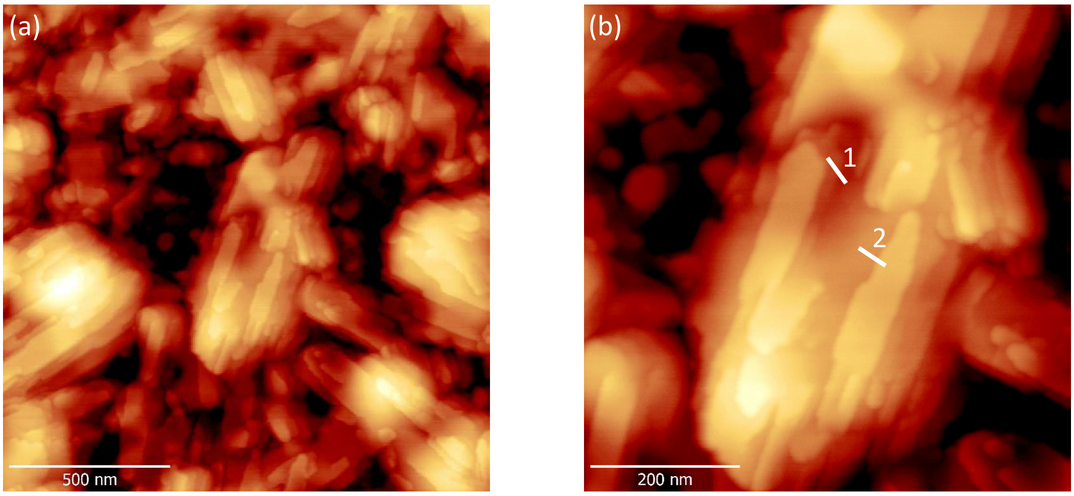

Figure 12: Morphologie de la surface d'un film de Fe(bpz)$_2$C$_{12}$-bpy sublimé. Topographie de la surface réalisée par AFM (à température ambiante) sur du Si/SiO$_x$(400 nm)/Fe(bpz)$_2$C$_{12}$-bpy(10 nm). (a) Image à grande échelle montrant l'existence de terrasses plates. (b) Détail de l'image (a) soulignant les couches consécutives avec une hauteur de marche de $d = 1.26\,\text{nm}$ et $d = 2.44\,\text{nm}$ le long des profils 1 et 2 respectivement, que nous identifions comme les monocouches et les bicouches de l'empilement moléculaire lamellaire.

du matériau en changeant l'empilement moléculaire, tout en préservant la transition de spin et la sublimabilité. A notre connaissance, c'est la première tentative réussie d'une telle modification des propriétés d'un complexe à de transition de spin. Nous pensons que cela ouvrira la voie à une approche orientée vers l'ingénierie des complexes à transition de spin et permettra l'ajustement des propriétés chimiques de ces composés en vue d'applications. Dans cette perspective, nous travaillons sur des complexes combinant transitions de spin avec un groupe permettant l'ancrage sur une surface et des ligands photoluminescents.

Sondage des atomes actifs dans un dispositif en utilisant le rayonnement synchrotron

Une des tâches dans le cadre de cette thèse et de la collaboration avec la ligne DEIMOS du synchrotron SOLEIL était de développer un insert permettant d'effectuer des mesures d'absorption X simultanément avec un accès électrique à l'échantillon. Ce nouvel insert nommé Versatile Variable Temperature Insert (V^2TI, Fig. 13) est le résultat d'une coopération fructueuse entre l'équipe de la ligne DEIMOS et l'équipe d'ingénieurs et les personnels De l'IPCMS. Nous avons ensuite utilisé l'insert nouvellement développé pour mettre en œuvre une nouvelle méthodologie permettant de sonder *in operando* les atomes actifs d'un dispositif.

Dans nos études, nous avons examiné le cas des jonctions tunnel magnétiques CoFeB/MgO/CoFeB[7] dont le fonctionnement est connu comme ne faisant intervenir

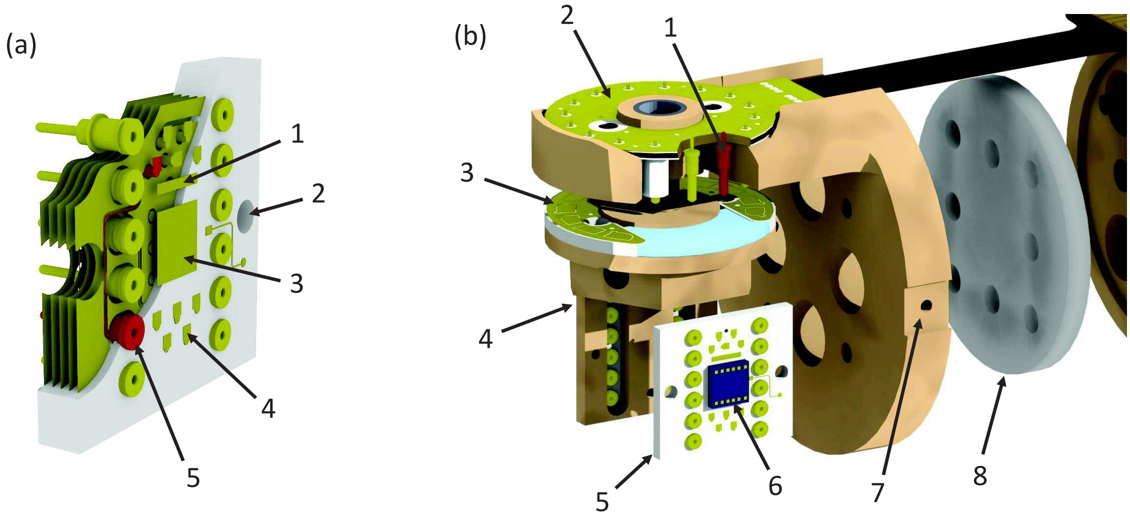

Figure 13: Tête du V^2TI head et puce dédiée. (a) Coupe transversale du support porte échantillon avec : 1 - le pavé de la bande de rendement électronique total, 2 - trous pour la fixation de la vis, 3 - bloc assurant le contact thermique, 4 - l'une des pattes de connexion, 5 - l'un des douze tulipes. (b) Vue d'ensemble du V^2TI avec : 1 - contact entre la tête et le port échantillon du PCB, 2 - PCB du tête, 3 - PCB du port-échantillon, 4 - porte-échantillon, 5 - puce dédiée, 6 - échantillon, 7 - position du capteur de température, 8 - disque saphir. Les figures sont prises de la réf. 33.

qu'un très petit sous-ensemble des atomes constituant les jonctions.[34] Nous proposons une méthodologie mettant l'accent uniquement sur les atomes impliqués dans le fonctionnement des dispositifs. Ceci est possible en mesurant leurs propriétés de magnétotransport lorsqu'ils absorbent les rayons X lors du scénario suivants. Lorsque les photons X frappent l'échantillon, ils excitent toutes les espèces atomiques ayant un seuil d'absorption inférieur à l'énergie des photons (Fig. 14 (a)). Toutefois, lorsque le courant passe à travers le dispositif, il est connu que seulement un petit sous-ensemble des atomes participe au transport, nommée points chauds (Fig. 14 (e)). En combinant simultanément les mesures d'absorption X et de transport électronique nous obtenons une double sélectivité permettant d'évaluer seulement la contribution des espèces atomiques qui sont actifs dans le transport.

Nous avons enregistré une mesure XAS de référence référentielle aux seuils K de l'oxygène sur la structure CoFeB/MgO avant et après recuit (Fig. 15 (a)). Nous avons identifié des pics du préseuil associée à des états d'oxydes à l'interface.[35–37] Ceux-ci sont atténuées lors d'un recuit connu pour améliorer pour augmenter la magnétorésistance tunnel (TMR) des jonctions. Maintenant, nous nous concentrons uniquement sur ces états d'oxyde et le fonctionnement du dispositif d'étude lors de leur excitation.

Nous avons enregistré la résistance du dispositif recuit dans les états parallèle (R_P) et antiparallèle (R_AP) tout en balayant l'énergie des photons à travers le seuil K de l'oxygène (Fig. 15 (b) et (c)). Nous avons noté une diminution de la résistance du

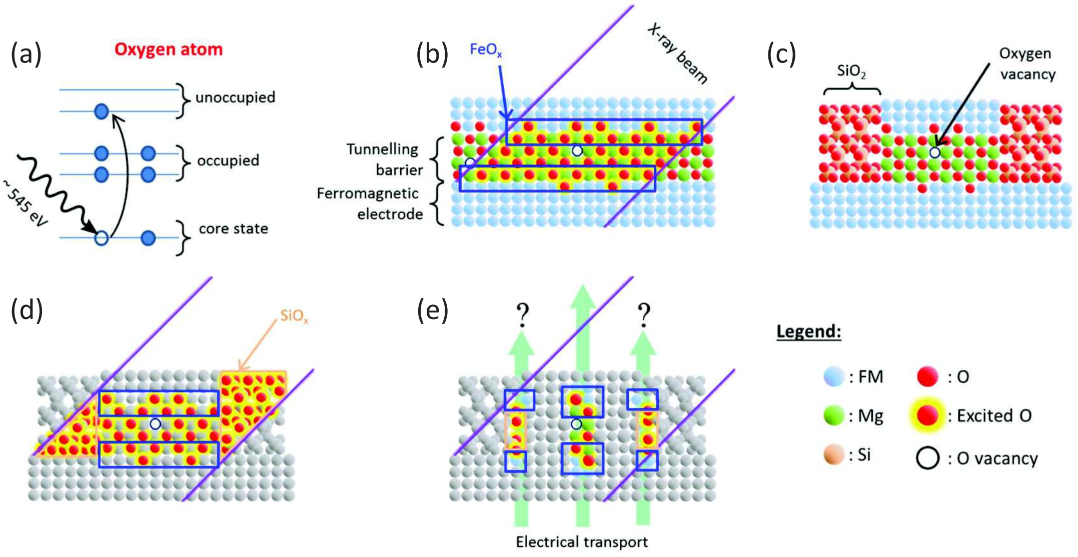

Figure 14: Sondage des atomes actifs dans le dispositif, en combinant les mesures de XAS et magnetotransport. (a) Photons dont l'énergie permet de sonder (exciter) les espèces atomiques d'intérêt (ici seuil K de l'oxygène). (b) Illustration de la barrière tunnel en MgO encapsulée par deux électrodes FM. Les rayons X excitent tous les sites d'oxygène dans le système. Les rectangles bleus indiquent les régions où il y a potentiellement des oxydes. (c) Le pilier d'une seule MTJ encapsulée par SiO_2. Les défauts de structure localisés, par exemple, les lacunes d'oxygène, peuvent canaliser tout le courant tunnel. (d) Schéma de la mesure XAS sondant l'ensemble des atomes d'oxygène du système. (e) Mesure simultané d'absorption et mesure électrique révélant les informations concernant uniquement les sites oxygénés qui contribuent au transport.

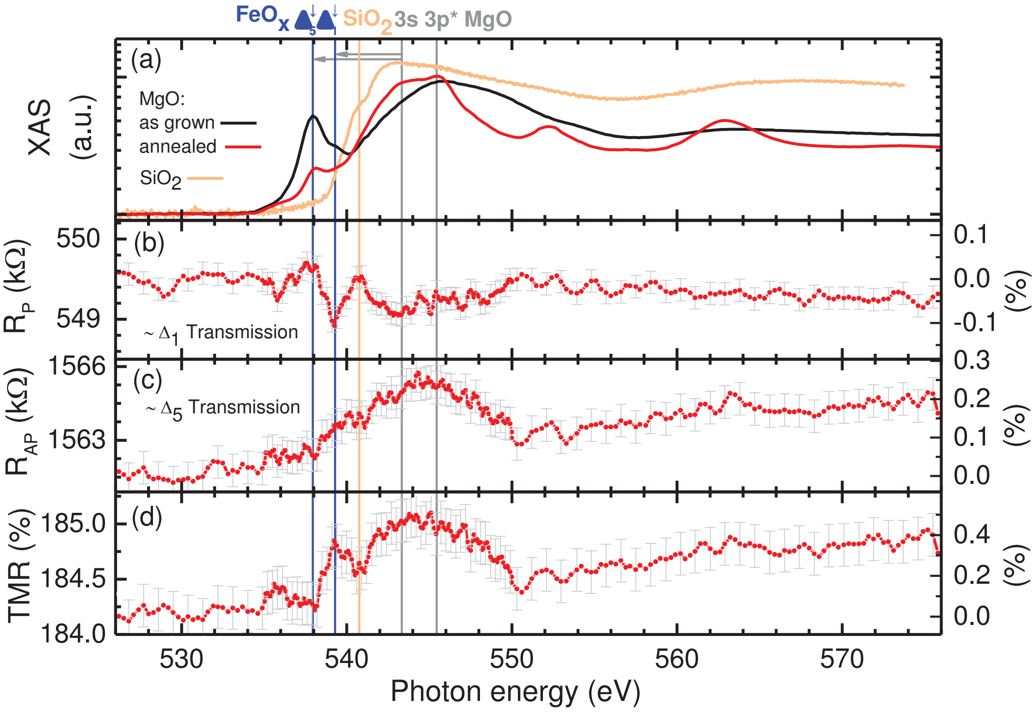

Figure 15: Combinaison des mesures XAS et de magnétorésistance de jonctions tunnel magnétiques. (a) Spectres XAS acquis avec une polarisation linéaire verticale des photons sur les jonctions en MgO recuit et non recuit et encapsulées avec du SiO_2. On remarque une diminution de l'intensité des pics d'oxyde de Fe lors du recuit. Résistance des jonctions dans les états P (b), AP (c), et TMR (d) en fonction de l'énergie des photons, enregistrée à $T = 20\,K$ et une faible tension de polarisation $V = \pm 10\,mV$. L'échelle de droite représente l'écart par rapport à la ligne de base établie au préseuil.

dispositif lors de l'excitation des états d'oxyde en configuration parallèle. Ceci suggère que malgré le recuit les oxydes sont encore présents dans le système et participent activement au transport. Notez que cette information serait inaccessible si on utilisait que l'absorption X. De cette façon, nous avons démontré comment la spectroscopie des rayons X peut être combinée avec les mesures de transport électronique pour obtenir une sélectivité atomique d'un petit sous-ensemble d'atomes contribuant aux performances d'un dispositif microélectronique. Nous pensons que par le développement du V^2TI et la mise en place d'une nouvelle méthodologie nous avons fourni un outil à une large communauté scientifique, qui permettra de mieux comprendre comment fonctionnent les dispositifs microélectroniques et quelles sont les contributions de certaines espèces atomiques à leurs performances.

Conclusions

Cette thèse est dédiée aux *multifunctionality* qui peuvent émerger aux confluents de plusieurs domaines comme la spintronique, l'électronique organique, la multiferroicité et les matériaux à transition de spin. Nous avons étudié les interfaces ferromagnétiques/organiques hybrides comme un élément essentiel de chaque dispositif spintronique organique. Nous avons mis l'accent sur le potentiel de ces structures et de plus nous avons montré comment elles peuvent être utilisées pour des systèmes fonctionnels plus complexes. Nous avons conçu un dispositif magnétoélectrique-organique fournissant un contrôle externe d'une spinterface hybride par un substrat multiferroïque. Nous avons exploré le caractère multifonctionnel intrinsèque des matériaux SCO pour des couches actives dans des dispositifs organiques. Nous avons obtenu un nouveau composé à transition de spin sublimable avec un comportement hystérétique. Nous avons développé une nouvelle approche de fonctionnalisation des molécules SCO afin d'ajuster les propriétés du matériau aux applications souhaitées. Nous l'avons démontré en modifiant la structure chimique du dispositif tout en préservant sa sublimabilité et la transition de spin. Enfin, nous avons développé une nouvelle méthodologie avec l'utilisation d'un nouvel insert V^2TI à la ligne DEIMOS, permettant d'évaluer la contribution des atomes actifs dans le transport d'un dispositif microélectronique fonctionnel. Cela a été démontré grâce à la double sélectivité de l'énergie des photons de rayons X et du fonctionnement de l'appareil.

Motivation and manuscript organization

We are all the witnesses of an outstanding evolution of the electronics technology. One does not have to be a specialist in the field to experience an increasing computational power and decreasing size of the electronic devices of everyday use. This well predicted by Gordon Moore[1] advancement is equally fascinating as challenging to keep the pace of the development for the upcoming years.

The *classical electronic* encoding the information solely by the charge of the electrons is the mainstream technology still dictating the trends in the field. However, its limitations rise recently more and more concerns such as the constraints of a miniaturization, or fundamental questions of the smallest achievable electronic element.[4,5] That gives a push for alternative technologies to develop. In that way emerged *spin-electronics*, or *spintronics*, exploiting a previously unused attribute of the electron - spin.[6] That opened new perspectives and enabled the concepts which rapidly found their way towards a widespread applications in, *e.g.*, hard disks read heads.[7] Independently, an idea of employing carbon-based materials in a hybrid inorganic/organic devices initiated a domain called *organic spintronics*.[8] This propelled an intensive research over the organics as an alternative and exotic from electronic structure point of view materials promising for applications far beyond the limits of the mainstream electronics.[9] These unique possibilities include the highly efficient spin injectors, organic rectifiers, sensors, single molecule memory elements and more.

In addition to that, organic materials may manifest a high degree of a *multifunctional potential*. That means a perspective for the devices being sensitive to more than one stimulus and/or having a multiresponse signal what illustratively may be schematized as a logic gate with numerous input and output channels. Further, relatively uncomplicated, chemical engineering allows a subtle tuning of such devices' operation.[15] The emergent field of *multifunctional spintronics* opens a way for sophisticated multipurpose devices with a multitude of degrees of freedom.

The aim of this work is to investigate this multifunctional character emerging when organic and inorganic materials are combined towards a future spintronic device. One of the obstacles in this task is the not fully understood nature of the interfaces, electronic structure and correlations within such formed, rather complex, hybrid systems. In this scope, our main experimental method was the soft x-ray spectroscopy[38] which provides a very sensitive and chemically selective tool to resolve these electronic and magnetic properties of a material or an interface. The work presented in this manuscript was performed in a collaboration between the Institut de Physique et Chimie des Matériaux de Strasbourg (IPCMS) and the DEIMOS beamline of the synchrotron SOLEIL. The next paragraphs briefly explain to the reader the organization of the manuscript.

Part I is devoted to an introduction which starts with reviewing of the nowadays electronics. We explain the milestones and the main concepts of the spintronics and emphasize on the assets and liabilities of realizing it with use of organic materials. A special stress is put on the explanation of the notion of multifunctionality. The first part also introduces the domain of intrinsically multifunctional spin transition complexes and the fundamentals of a spin crossover phenomenon.

In the second part, we introduce the experimental techniques and the sample preparation methods. These include the introduction to the ultra high vacuum environment and the description of the set-ups used in this thesis for the fabrication of inorganic/organic multilayered structures. Then, we discuss the merits of the synchrotron-grade experiments and provide the fundamentals of the x-ray absorption spectroscopy (XAS), x-ray magnetic circular dichroism (XMCD), and spin-resolved photoemission spectroscopy (SR-PES). Finally, we describe the capabilities of the DEIMOS and CASSIOPÉE beamlines of the SOLEIL synchrotron, where the aforementioned techniques were used. We stress on the development of the new Versatile Variable Temperature Insert (V^2TI) at the DEIMOS beamline, whose design and assembling was in the framework of this PhD studies. We demonstrate the first *in operando* experiment on multifunctional MgO-based magnetic tunnel junctions that allowed us to develop a novel methodology to probe the impact of a device's active atoms on its spintronic performance.

Part III contains the results and discussion. In Chapter 3 we begin with the experimental studies of the smallest building block of nearly every organic spintronic device, namely the ferromagnetic/organic interface. By employing XAS and XMCD we evidenced a room temperature ferromagnetic (FM) coupling of prototypical manganese-phthalocyanine (MnPc) molecules to the underlying cobalt substrate and the formation of a spinterface (spin-polarized interface). Further studies revealed the coupling to be at the origin of the antiferromagnetic (AFM) order that appears within the MnPc molecular layers. This led to the observation of an exchange bias (EB) exerted by the organic layer on the ferromagnet, up to a blocking temperature $T_\mathrm{B} = 100\,\mathrm{K}$. In the next step, we demonstrated by XAS/XMCD techniques that the observed magnetic ordering may also occur when mediated by an interlayer exchange coupling (IEC) through a Cu spacer. By means of the SR-PES we proved that the Cu/MnPc interface in the IEC system Co/Cu/MnPc exhibits a strong spin-polarization near the Fermi level. All of these, reveal a great potential of the generic FM/organic interfaces for spintronic applications such as the pinning layers, or hybrid spin injectors.

In Chapter 4, we increase the complexity of the previously studied system by resorting to the artificial multiferroics. By adding a ferroelectric Pb(Zr,Ti)O_3 (PZT) substrate we created a multifunctional doubly coupled interface PZT/Co/FePc such that it contained a magnetoelectric system PZT/Co and the spinterface Co/FePc. These formed a prototypical magnetoelectric-organic device with a perspective for a ferroelectric control over an organic spinterface. We performed *in situ* experiments, employing the V^2TI electrical access and the soft x-ray spectroscopy techniques, and proved the proper switching of the PZT. By means of XMCD we observed the Co magnetization variation arising from the consequent magnetoelectric coupling at the PZT/Co interface, and this change of Co magnetization occurred to have an impact on the FePc layer, as can be seen through reversible features in the Fe L_3-edge XMCD signal. In that way we demonstrated a synergy between the artificial multiferroic systems and an organic spinterface towards a multifunctional device.

In the last chapter, we present a study over intrinsically multifunctional materials, namely the spin crossover (SCO) complexes, as potential materials for an active layer in a spintronic device. We first report on a new sublimable compound, Fe-pyrz, and its characteristics in a sublimed film form. Then, we propose a novel approach in the SCO field based on the functionalization of the materials with preservation of their spin transition and sublimability. We demonstrate that by designing the molecular structure we can control the material properties such as the stacking arrangement in a sublimed film. That, we anticipate, may initiate a new trend in the chemical designing of the SCO compounds.

At the end, we present the outcomes of the performed experiments and point out their implications and perspectives for further studies.

Part I

Introduction and background

1

Introduction to multifunctional spintronics

The profound impact of nowadays electronics technology on our lives does not have to be explained anymore. Its prevalence makes rather challenging to point out domains where it could not find its application by making life easier, safer, or just more comfortable. This implausible development within the past decades we owe to myriads of researchers who relentlessly pursued the new directions of advancement. The aim of this introduction is to review the milestones of this progress, introduce the present challenges in the field, and based on that justify a motivation behind the work carried out in this thesis.

1.1 Classical electronics

The inorganic electronics employing solely the charge of the electrons, as we know it from every contemporary cellphone or computer, and which we will refer to as classical electronics, has remarkably intriguing history. Its beginning can be arbitrarily dated back to 1959 when the first planar transistor was commercially released. This crude semiconducting device was about to pave the way towards today's multi-billion-transistor processors with a progress rate following the unprecedented exponential dynamics. This trend envisioned by Gordon Moore[1] as far back as 1965 became considered as one of the greatest previsions of the modern times[2] and self-fulfilling prophecy.[3]

Doubling the number of transitions per unit area every 12 – 18 month became a pursued Moore's Law standard for the International Technology Roadmap for Semiconductors (ITRS 2.0).[39] This miniaturization measured by a minimum feature size or a minimum half-pitch of a semiconducting integrated circuit has improved from 10 µm in 1971 to 14 nm available in modern processors. Improvement to the technological 10 nm node is foreseen for the beginning of 2017.

To have an idea about the extend of this technological progress one can consider the evolution of the global electronic market revenue reaching level of $\sim$ 180 billion U.S. dollars for year 2015 with as much as 500 million users worldwide. It is observed to grow by $\sim 10\%$ each year and is expected to hit nearly 300 billion U.S. dollars revenue in 2020.[40] To keep the pace of the expansion requires a substantial investment in the exploratory research.

Although 7 nm transistors have been demonstrated, 5 nm is considered by the ITRS as presumably the last technological node in the semiconducting silicon-based domain. Further miniaturization inevitably leads to critical technological issues such as the power limits, ”soft” errors, or wiring problems, and more fundamental as the contribution of the surface effects, or eventually the charge tunneling when the element size is comparable with a thermal de Broglie wavelength of the electron.[4,5] These challenges do not only concern the electronic transport. The data storage technology based on recording the information with oriented magnetic domains, *e.g.*, traditional HDDs, suffers from the supraparamagnetic limit which leads to a thermal self-erasure for the memory cells of size below ~ 10 nm.[41]

All of these together form obstacles and threats for the Moore’s Law to collapse. This is why new development directions are needed. A promising field in this respect is organic spintronics, *i.e.*, spin-electronics realized with use of the carbon-based materials, to which this thesis is dedicated. In the following we describe the main concepts of spintronics and then explain the advantages and challenges arising from realizing it with use of organic materials.

1.2 Spintronics

Spin-electronics,[6,42] contrary to its classical counterpart, attempts to exploit not only the charge of the electron but also its intrinsic angular momentum - spin. This provides an additional degree of freedom and leads to emergence of the new magnetic field driven effects.

It is commonly accepted to associate the birth of spintronics to the discovery of giant magnetoresistance (GMR) in 1988 by the groups of Albert Fert[43] and Peter Grünberg.[44] They demonstrated that transport across the Fe ferromagnetic (FM) layers separated by a non-magnetic Cr spacer depends on the relative parallel (P) or antiparallel (AP) orientation of these FM layers’ magnetization (Fig. 1.1 (a)). This concept was predicted as early as 1936 by Nevill Mott[45] who considered the conduction of $3d$ electrons of a transition metal with the exchange splitted majority and minority subbands. He provided the so-called ”two current model” describing a diffusive transport across the FM layer. The two conduction channels were associated with distinct transport properties, such that the electrons with consistent (opposite) spin direction with respect to the electrode magnetization had lower (greater) probability of being scattered (Fig. 1.1 (b), (c)). This simple picture eventually leads to a general relation $R_{\mathrm{P}} < R_{\mathrm{AP}}$, defining the giant magnetoresistance ratio as:

$$GMR = \frac{R_{\mathrm{AP}} - R_{\mathrm{P}}}{R_{\mathrm{P}}} \tag{1.1}$$

The GMR-based junction, or so-called a spin valve, may be realized in two architectures: CIP (current in-plane) or CPP (current perpendicular-to-plane). The discovery of the GMR opened a way for magnetic field controlled transport devices which in 1993 found an application as sensors for the automotive industry, and later in 1997 as

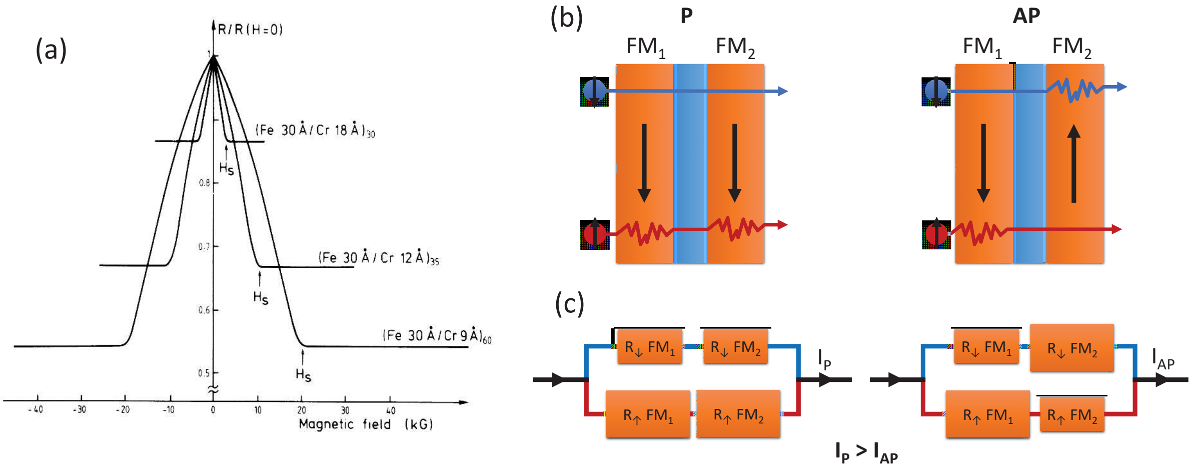

Figure 1.1: Giant magnetoresistance (GMR). (a) Transport across three Fe/Cr superlattices at 4.2 K with current and magnetic field applied along (110) direction in sample plane revealing a giant magnetoresistance (figure taken from ref. 43). (b) Schematic illustration of the two current model across the FM layers separated by a non-magnetic spacer in the parallel (P) and antiparallel (AP) configuration of the electrodes' magnetization. Majority (minority) electrons, marked in blue (red), traversing the FM layer with magnetization parallel (antiparallel) to the spin direction have lower (greater) probability of being scattered. This results in larger device resistance for the AP configuration than for P (in general). (c) Equivalent schematic circuits explaining the occurrence of GMR. The size of the resistors reflects the scattering probability.

the hard disks read heads leading to the increase of stored information density from 1 Gbit/in^2 to 600 Gbit/in^2.[46] Finally, both Albert Fert and Peter Grünberg received the Nobel Prize for the GMR in 2007.[47]

The next breakthrough in spintronics came with the concept of tunneling magnetoresistence (TMR).[7] It was first proposed by Michel Jullière[48] in 1975 and was based on the idea of replacing a non-magnetic metal separating the FM electrodes by a thin isolating layer. In that way a diffusive regime of conduction was replaced by tunneling. This led to advantages such as larger magnetoresistance and a possibility of a down-scaling. In 1995 Moodera[49] and Miyazaki[50] demonstrated a room temperature operating magnetic tunnel junctions (MTJ) with amorphous Al_2O_3 barrier exhibiting a TMR over $\sim 10\%$. Almost a decade later Wang and coworkers[51] improved this result to nearly 70% on a similar device. In 2001 Mathon and Umerski[52] theoretically predicted TMR as high as 1000% for a device where the amorphous layers were replaced by the epitaxial ones. Further development of the nanofabrication methods led to the verification of this hypothesis and the reports on a single-crystal Fe/MgO/Fe systems of a $\sim 200\%$ TMR by teams of Yuasa[53] and Parkin.[54]

The first step towards understanding of the mechanism behind the tunnel magnetoresistance was the work of Meservey and Tedrow[55] in 1971. They pointed out a spin-dependent tunneling (SDT) between the FM layers as occurring across two separate channels in the absence of the spin-flip events. The concept was further developed by Jullière[48] and now is widely known as the Jullière's model for the tunneling mag-

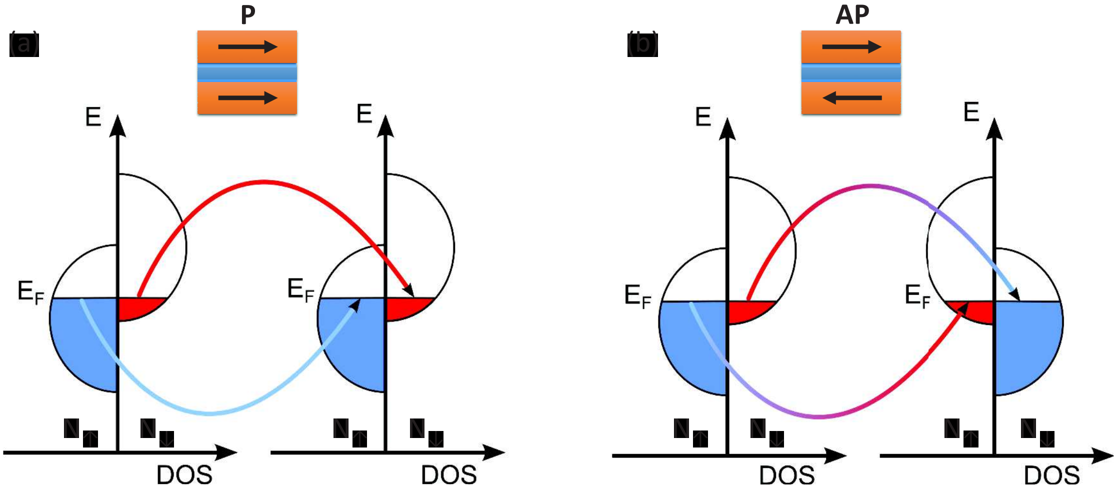

Figure 1.2: Spin-dependent tunneling between two ferromagnetic layers. Schematic illustration of tunneling between the spin-splitted $3d$ bands of two FM electrodes separated by an insulator for (a) parallel (P), and (b) antiparallel (AP) configuration of the electrodes' magnetization. $N_{\uparrow(\downarrow)}$ denotes the density of states of the spin-up (spin-down) electrons.

netoresistance. In the following part we briefly describe this approach.

The exchange splitting of the $3d$ electrons in a ferromagnetic material leads to formation of the majority and minority subbands (Fig. 1.2). The unequal density of states (DOS) at the Fermi energy (E_F) defines the spin polarization as:[56]

$$P = \frac{N_\uparrow v_\uparrow - N_\downarrow v_\downarrow}{N_\uparrow v_\uparrow + N_\downarrow v_\downarrow} \tag{1.2}$$

where $N_{\uparrow(\downarrow)}$ is the density of states, and $v_{\uparrow(\downarrow)}$ the Fermi velocity for majority (minority) electrons at E_F. Depending on the material's magnetization and its band structure the arising polarization can be positive, negative, or zero. A handful of materials exhibit non-zero DOS for only one spin channel at Fermi level, thus the polarization $P = 100\%$. Those are referred to as half-metals,[57] *e.g.*, $\mathrm{CrO_2}$[58] with only $N_\uparrow$ channel at E_F. Typical $3d$ transition metals exhibit a positive polarization of $P \sim 40\%$.[59–61] As the reader will see later, a spin polarization can also arise at the interfaces due to the proximity effects. We will later refer to such region as a spinterface.

The schematic illustration of SDT according to the Jullière's model for the parallel and antiparallel configurations of the FM electrodes magnetization is presented in Fig. 1.2. Considering the parallel case (Fig. 1.2 (a)) one sees that both electrodes have positive spin polarization ($P_{1,2} > 0$) such that the majority channel is defined by the spin-up ($N_\uparrow$) electrons. The Jullière's model assumes that SDT is an elastic process, *i.e.*, spin-flip is forbidden, and that it involves only the conduction electrons occupying levels close to the Fermi energy (valid for small values of applied bias voltage). Therefore, the overall tunneling probability depends entirely on the spin polarization of the FM layers and thus on available states in the counter electrode. This leads to conductance in parallel configuration expressed as:

$$G \sim N_\uparrow^1 N_\uparrow^2 + N_\downarrow^1 N_\downarrow^2 \tag{1.3}$$

where $N_{\uparrow/\downarrow}^{1(2)}$ denotes the spin-dependent density of states for the first (second) FM electrode. Therefore, in parallel situation the electrons in both majority and minority channels have approximately an equal number of the available states in the counter electrode. The situation is changed for AP. The minority (majority) electrons are tunneling to majority (minority) subbands in the second FM layer. In that way the minority electrons in the first electrode will tunnel with the same probability as in parallel configuration, meanwile the abundant majority electrons would find a reduced number of available states in the counter electrode. Therefore, the tunneling probability is reduced. In this picture one finds a general relation $G_\mathrm{P} > G_\mathrm{AP}$ ($R_\mathrm{P} < R_\mathrm{AP}$), leading eventually to the well known definition of TMR ratio:[7]

$$TMR = \frac{G_\mathrm{P} - G_\mathrm{AP}}{G_\mathrm{AP}} = \frac{R_\mathrm{AP} - R_\mathrm{P}}{R_\mathrm{P}} = \frac{2P_1P_2}{1 - P_1P_2} \tag{1.4}$$

where $R_{\mathrm{P(AP)}}$ and $G_{\mathrm{P(AP)}}$ stand for the resistance and conductance in P (AP) configurations, and $P_{1(2)}$ is the spin polarization at E_F of the first (second) FM electrode.

Note that this simple, yet powerful model predicts the TMR to be solely determined by the properties of the FM electrodes. This however is an approximation. The SDT was shown to be strongly dependent also on a tunnel barrier and particularly the nature of the chemical bonds and localized states at the FM/barrier interface.[62,63] This was highlighted by the work of De Teresa *et al.*[64] who demonstrated that the TMR can be switched from positive to negative just by changing the barrier material and keeping the same set of the FM layers. This emphasized an additional spin polarization arising at the interface as a relevant factor determining the SDT probability. Furthermore, Butler *et al.*[65] revealed a distinct symmetry dependent decay rates of the electrons wave function within the MgO barrier in Fe/MgO/Fe system. They showed that the particular Bloch states in $3d$ metal along (100) direction denoted as Δ_1 (s, p_z, $d_{3z^2-r^2}$), Δ_2 ($d_{x^2-y^2}$), and Δ_5 (p_x, p_y, d_{xz}, d_{yz}), have different decay rates depending on a complex band structure of MgO. In the cases of Fe, Co, and CoFe electrodes, only Δ_1 electrons govern a device P state and Δ_5 its AP counterpart. Due to this so-called symmetry filtering, the TMR value for the MgO-based MTJs is notably increased.[54] Finally, in the recent work Schleicher *et al.*[10] stressed on the influence of the localized defect states within MgO on the device TMR.

The magnetic tunnel junctions, which are probably the most prominent realization of a spintronics concept, found a wide industrial application in the hard disk read heads. In September 2004, Seagate Technology shipped the first HDD (120 GB, 2.5” drive) with $\mathrm{TiO_x}$-based MTJ read head.[66] In 2008, Western Digital announced that ”the industry has made the transition to tunnel-junction magnetoresistive technology for the head reader function”.[67] Since then, the read heads of manufactured HDDs have been made of MgO-based MTJs what led to a five-fold increase in the data storage capacity (179 GB/in^2 vs. 1 TB/in^2). This flawless example of a pathway from the GMR discovery by Fert and Grünberg in 1988 to present widespread application of the TMR in nowadays computers demonstrates the enormous potential of spin-electronics and a strong demand of the market for new solutions.

1.3 Organic spintronics

The first concept to employ an organic material in electronic device emerged in 1974 with the classical work of Arieh Aviram and Mark Ratner entitled ”Molecular Rectifiers”.[68] It raised the idea that a system as small as a single molecule can act as an efficient functional circuit element. The organics offered rather distinct transport mechanism than known from the inorganic solids. The band picture of the quasi-free conduction electrons and holes was replaced by a hopping transport across the atomic sites of the molecule. Due to its semiconducting behavior these materials, referred to as organic semiconductors (OSCs), were successfully applied especially in the field of optoelectronics as, *e.g.*, presently commercially available organic light emitting diodes (OLED).[69]

The OSCs appeared to exhibit also the unique advantages from spintronics perspective. Firstly, OSCs manifest an improved spin coherence with time ($> 10\,\mu s$)[70,71] and distance ($10^2 - 10^3$ nm)[72,73] with respect to conventional inorganic semiconductors. That means that a spin current in diffusive regime may be transferred across organic layer on much larger distances than through the inorganic counterparts.[74] This is due to a low spin-orbit coupling in carbon-based materials which scales with the atomic number as Z^4.[75] Secondly, potentially low cost production of the OSCs and a wide tuning possibilities of its physical and chemical properties provide a significant versatility. Finally, the OCSs allow fabrication of flexible electronics.[8] On the other hand, employing an OCS in spintronics does not devoid of the obstacles. One of the major problems is a low charge mobility within the organics. To have a general idea, a typical p-doped silicon has mobility of $450\,\mathrm{cm^2\,V^{-1}\,s^{-1}}$ meanwhile rubrene, one of the most conducting OCS, only $10\,\mathrm{cm^2\,V^{-1}\,s^{-1}}$.[76] This leads to resistance mismatch and integrability problems at inorganic/organic contact.[77] Despite that, the organic spintronics is a dynamically expanding field emerging as a promising alternative for conventional spintronics. Comprehensive reviews of recent progresses in this domain can be found in ref. 75, 77, 78.

The first who fabricated a spintronic device comprising an organic material as diffusive barrier was Dediu *et al.*[72] in 2002. They established a long spin diffusion length of about 200 nm and relaxation time of 1 µs in sexithienyl (6T) placed between $La_{0.7}Sr_{0.3}MnO_3$ (LSMO) electrodes (Fig. 1.3 (a)). They observed a magnetoresistance of $\sim 30\%$, yet it probably emerged from the so-called organic magentoresistance (OMAR)[77] originating from the interaction between the spins of injected electrons with the holes in organic barrier. The authors did not evidence directly a device P and AP states because of the limitations of their experimental set-up.

Note that such use of the organics between the metallic electrodes forms rather a hybrid inorganic/organic junction. Nevertheless, in the following we use a term *organic spintronic device* for the one with at least some element(s) made of a carbon-based material. The first organic spin valve demonstration was attributed to Xiong *et al.*[79] in 2004. They used 8-hydroxy-quinoline aluminum (Alq_3) sandwiched in a vertical architecture between LSMO and Co electrodes (Fig. 1.3 (b)). Their work evidenced a proper GMR of 40% at 11 K disappearing at temperature 200 K, yet with the AP state less resistive than P, thus so-called inverse spin valve effect. Interestingly, this behavior with use of Alq_3 is one of the most widely reproduced results in the field of organic spintronics and was shown to be independent on the top electrode material.[81,82] It is even more astonishing since both Co and LSMO were proved to be majority spin injectors ($P_{1,2} > 0$),[64,83] thus one should find $R_{\mathrm{P}} < R_{\mathrm{AP}}$ for LSMO/Alq$_3$/Co device. A new light on this discrepancy was shed by the eminent work of Barraud and coworkers.[80] They fabricated the vertical LSMO/Alq$_3$/Co junctions by nanoindentation with an AFM tip (Fig. 1.3 (c)) and found a positive TMR of nearly 300% at 2 K. They developed a spin hybridization transport model and proposed the introduction of an effective spin polarization P^* which combines the FM originating spin imbalance, as considered in Eq. 1.2, and a new contribution arising from a spin-dependent hybridization at metal/organic interface. The latter may invert or lever P^* with respect to a generic FM contribution depending on a metal/molecule coupling. This implied $P^*_{\mathrm{Co/Alq_3}} > 0$ and $P^*_{\mathrm{LSMO/Alq_3}} < 0$ as the origin of inverted spin valve effect. Additionally, they pointed out the effect of an inversion to be strongly localized with disordered contribution in space and energy. This, in turn, was identified as the cause of the observed positive TMR on small junctions and rather negative for the large area ones where the averaged inversion effect dominates. This work highlighted a compelling role of the interfacial

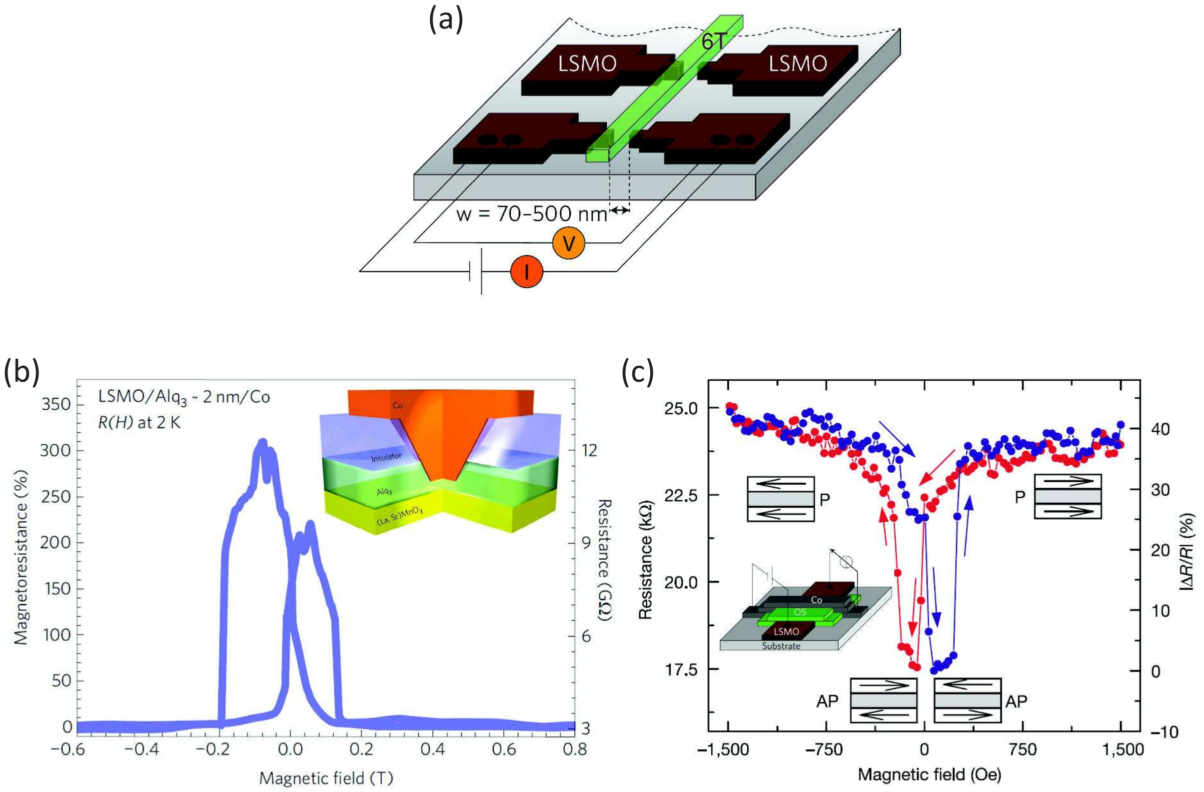

Figure 1.3: Organic spintronic device. (a) First reported organic spintronic device comprising a diffusive barrier of sexithienyl (6T) between La$_{0.7}$Sr$_{0.3}$MnO$_3$ (LSMO) electrodes in lateral configuration. (b) Large area vertical spin-valve device with 8-hydroxy-quinoline aluminium (Alq$_3$) sandwiched between LSMO and Co electrodes revealing negative $\sim$ 40% GMR at 11 K. (c) LSMO/Alq$_3$/Co device made by nanoindentation with a TMR of $\sim$ 300% at 2 K explained in terms of the spin-dependent hybridization at the metal/molecule interface. Figures taken from ref. 72, 79, 80.

metal/organic hybridization as determining a device performance. In the next section, we focus on a more detailed description of this hybridization mechanism and resulting spin polarization at the interface.

1.3.1 Hybridization at a metal/organic contact

The inorganic/organic interface is an inevitable element of nearly every organic spintronic device. Independently of a device architecture there is always necessity to employ, at best, the metallic contacts or resort to the semiconductors technology. To fully grasp the nature of this interface is of a special interest for organic spintronics. As demonstrated in the previous section, this particular contact region was recognized as of great importance,[18] yet it often remains also as a source of serious obstacles.[18]

In case of the fully inorganic systems the interfacial region appears as rather conceived and described by the overlapping surface states or relative work functions of the materials. In contrary, the effects appearing at the inorganic/organic contact seem to be more complex and dependent on such factors as the contact area, molecular conformation, its end-groups, or the nature of the molecule itself. That makes the transport picture not yet fully understood.[84] It is further complicated by rather complex molecular orbitals structure as well as great variety of available materials with strongly diverse chemical and physical properties. The metal/organic interfaces were intensively studied, mainly due to arising problem of a resistance mismatch. A comprehensive review of this issue can be found in ref. 77 (and references therein). In this brief section, we survey the present knowledge about a metal/organic hybridization in general and then discuss, a particularly important from a perspective of this thesis, the case of metal-phthalocyanine molecules on a ferromagnetic surface.

The challenging description of a metal/organic contact originates from very distinctive electronic structure of the two materials. For sake of simplicity we will refer here to a simple case of any ferromagnetic bulk and a single organic molecule. The electronic structure of the former can be described in terms of its $3d$ bands with $P \neq 0$ at the Fermi energy arising from the exchange splitting, meanwhile of the latter by the highest occupied molecular orbital (HOMO) and the lowest unoccupied molecular orbital (LUMO). In case of absence of the metal-molecule interaction (Fig. 1.4 (a)) the electronic structure at the interface is simply a superposition of the two constituting sides. Yet, this is hardly ever the case. Rather, a coupling between the metal and the molecule leads to broadening of the HOMO (Fig. 1.4 (b)) and its spin-dependent shift in energy (Fig. 1.4 (c)). The former results from an increase of the orbital lifetime which is a consequence of a metal-molecule hybridization. Thus, the broadening is proportional to a degree of hybridization, which in turn strongly depends on the geometry and spatial extend of the molecular orbitals. Note that the effect can be spin-dependent, *i.e.*, unequally broadening the majority and minority subbands. Eventually, the energy shift of these subbands can occur again in a spin-dependent manner. Within this picture one observes an interfacial electronic structure which strongly depends on such factors as the metal-molecule interaction (unique for each pair of materials), configuration of the molecular orbitals, geometrical arrangement of the molecule, its end-groups etc.[84,85]

A considerable effort was devoted to studies over the metal/organic interfaces. These include the work of Zhan *et al.*[86] over Co/Alq$_3$ revealing the interface associated dipole moment shifting the energy bands of the molecule by 1.5 eV towards the higher energies. On the other hand, the HOMO of Alq_3 for LSMO/Alq_3 was reported to be subjected to a downward shift by 0.9 eV.[87] An interesting study was carried out by Schmaus *et al.*[88] who observed a spin-selective LUMO broadening of a metal-free phthalocyanine in contact with the Co clusters leading to 60% of GMR across a single molecule. A comprehensive theoretical work was conducted by Atodiresei and coworkers[89] who systematically performed *ab initio* calculations for the different types of planar molecules adsorbed on the Fe surface. They identified the major role of a Zener-type exchange mechanism[90] in the molecule/transition metal hybridization. This, involving the mixing of out-of-plane p_z orbitals of the molecule and d_{z^2}, d_{xz}, d_{yz} bands of the metal leads to p band broadening and its spin-dependent shift above E_F.

One easily sees that these ferromagnetic/organic interfaces give plenty of room for tailoring. It is therefore unsurprising that the interface engineering has drawn a considerable attention.[85,91–94] The aforementioned complexity of the system allows the crafting of potentially desired characteristics such as the spin injection. The contribution of the spin-dependent broadening and the shift of the molecular HOMO can be subtly controlled and result in emergence of a positive or negative spin polarization at the interface, thus formation of a spinterface (compare Fig. 1.4 (b) and (c)). This was stressed by Atodiresei *et al.*[89] and Barraud *et al.*[80] who additionally inferred that the spin injection efficiency can be tailored from inversion to amplification by selection of the appropriate molecular species.

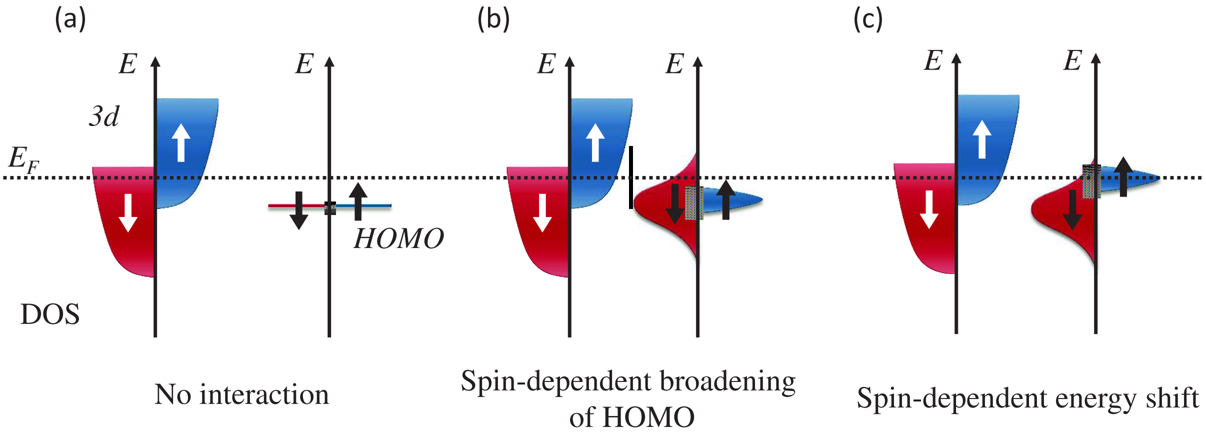

Figure 1.4: Formation of a hybrid FM/organic spinterface. A schematic illustration of the spin-splitted $3d$ subbands of a ferromagnet and the HOMO of a molecule. In the absence of the interaction (a) the interface electronic structure is a superposition of the two sides. When the molecule is brought closer to the surface the HOMO can be (b) broadened due to the metal-molecule hybridization, and/or (c) shifted in energy. Both effects can be spin-dependent leading to the unequal majority and minority electrons populations at E_F thus to formation of a spinterface. Figure reproduced from ref. 85.

1.3.2 Spin polarization at the interface

In this section, we invoke the study carried out by Djeghloul *et al.*[20] to discuss in detail how the spin-polarized interface may emerge at the metal/molecule contact. The theoretical prediction of a hybridization between the molecule and the metal and resulting spin polarization can be carried out by means of the local density of states (l-DOS) as provided by *ab initio* methods. Figure 1.5 presents a result of such calculation for the manganese-phthalocyanine (MnPc) molecule atop of the Co(100) surface with varying a metal-molecule distance. In other words, the calculation simulates a molecule approaching the metallic surface and monitors the DOS of both.

For a large distance $\Delta z = 6.6\,\text{Å}$ (Fig. 1.5 (a)) ensuring the absence of interaction, Co exhibits an out-of-plane z-DOS at the Fermi level corresponding to the unbalanced spin-down subband of the $3d$ states. The molecule, in turn, manifests the sharp orbitals with exclusively spin-down channel at E_F. When the molecule-Co distance is reduced to $3.5\,\text{Å}$ (Fig. 1.5 (b)) the π orbitals of the molecular rings overlap with the surface sites of Co causing a shift of the E_F from $-2.4\,\text{eV}$ to $-2.2\,\text{eV}$. The Co states are barely affected, meanwhile the initially sharp spin-down states of the molecule are now dispersed on the energy scale. Note that the in-plane molecular states remain unaltered. Finally, when the molecule is brought into contact with the surface at $\Delta z = 2.1\,\text{Å}$ (Fig. 1.5 (c)) the hybridization may occur. During this process an average of 3.5 electron is transferred from Co to the MnPc molecule leading to the orbitals reconfiguration what gives rise to a new set of the hybrid interface states. As a consequence, we observe the altered, yet still dominant, out-of-plane spin-down d subband of Co and new spin-up states of

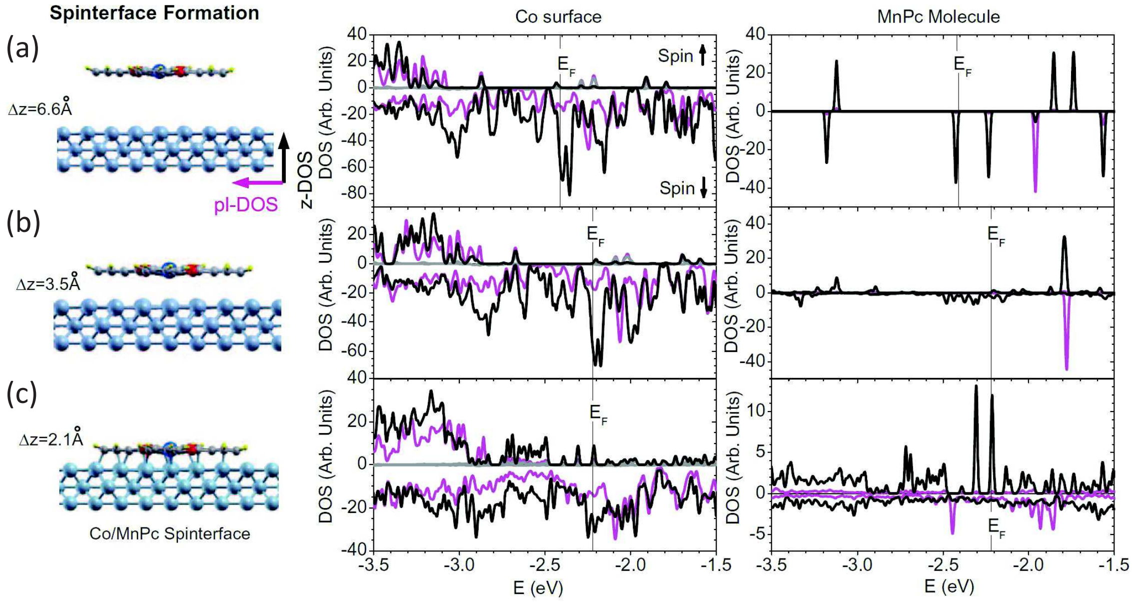

Figure 1.5: Spinterface formation between manganese-phthalocyanine (MnPc) and cobalt. Results of the *ab initio* calculations performed for a single MnPc molecule on the *fcc* Co surface for a molecule-metal distance $\Delta z =$ (a) $6.6\,\text{Å}$, (b) $3.5\,\text{Å}$, and (c) $2.1\,\text{Å}$. Both Co and MnPc states are presented with in-plane (pl-DOS) and out-of-plane (z-DOS) contributions of the spin-up and spin-down channels. The Co/MnPc hybridization leads to spin polarization P $\sim +80\%$ at the interface. Figure taken from ref. 20.

the molecule at the Fermi level. The out-of-plane orientation of emergent molecular states points to the p_z-d hybridization mechanism[89] as invoked in the previous section. A further insight into the site-projected DOS (Fig. 1.6 (a)) reveals a major contribution of the carbon and nitrogen atoms (out-of-plane $2p$ π states) and a small of the Mn site (d_z states). Eventually, the hybridization at the Co/MnPc interface results in a polarization of $P = +80\%$ at E_F. Note that it is of opposite sign to that of Co.

This was confirmed by the direct and inverse photoemission spectroscopy measurement (Fig. 1.6 (b)). It is noteworthy that identical result was found for the metal free H_2Pc on Co, what further supports the hypothesis of a secondary role of the Mn site in the spinterface formation.

In this way we explained how a metal/organic contact may have a highly effective spin filtering properties at room temperature as predicted by Barraud *et al.*[80] It is noteworthy, that the spin polarization at the interface is strongly dependent on the molecular geometry and constituting atomic sites.[89] Some recent remarkable studies over a spinterface include such systems as Co/CuPc,[95] Fe/C_{60},[96] or NiFe/Alq_3.[97] An excellent summary of the achievements in this field up to year 2014 can be found in ref. 94. Perhaps one of the most conclusive study was carried out by Djeghloul *et al.*[26] who substituted the organic molecules with an amorphous carbon directly deposited atop the Co layer and performed the spin-resolved photoemission spectroscopy experiment. It revealed an equally strong (and with the same sign) polarization at the interface as for Co/MnPc or Co/H_2Pc.[20] They concluded that a dominant contribution to the spinterface formation arises from the π electrons of the sp^2-hybridized carbon atoms and the $3d$ electrons of Co. This shed light onto the generic group of the interfaces with organic materials and the way they may promote a spin-polarized current.[98]

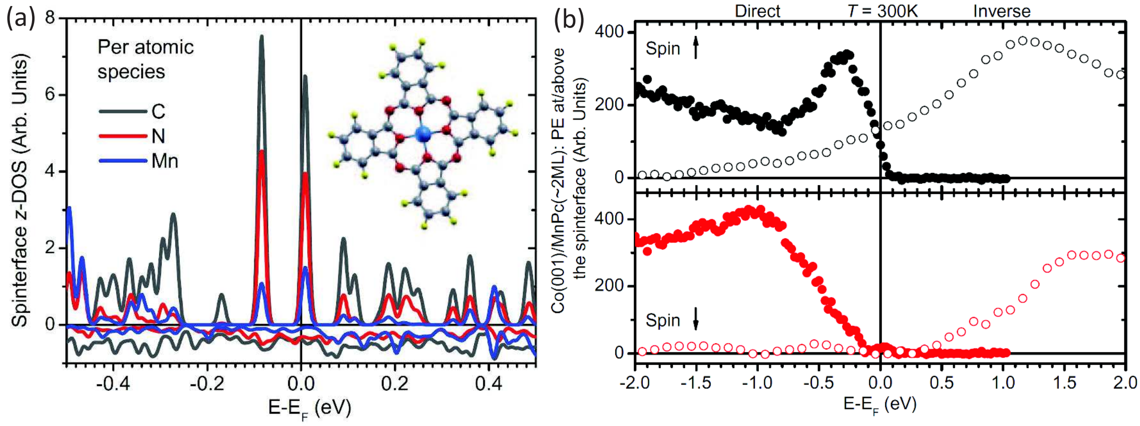

Figure 1.6: Highly spin-polarized Co/MnPc spinterface. (a) Site-projected density of states of a single MnPc molecule on the Co surface revealing a major (minor) role of the carbon and nitrogen $2p$ (manganese d_z) states in a spinterface formation. (b) Spin-resolved electron distribution curves for the direct (closed circles) and inverse (open circles) photoemission (PE) spectroscopy on Co/MnPc(2.6 (2.0) ML for direct (inverse) PE) confirming the spin polarization $P \sim +80\%$ at the Fermi level. Measurement was performed at RT and the photon energy 100 eV. Figure taken from ref. 20.

1.3.3 Multifunctionality

The organic materials can exhibit a high degree of multifunctionality. That is to say, its properties can be altered with use of several stimuli or/and these alterations may be accompanied with numerous responses. The stimuli may include the magnetic or electric field, current, temperature, pressure, light, etc. Generally speaking, a multifunctional material or device can be illustratively considered as a logic element with more than one input channel and/or multiple output signals. In that way, a device with such characteristics provides a multitude of available states thus many degrees of freedom. Multifunctionality is exhaustively pursued in both domains of classical and organic spintronics. Here, we revoke and briefly describe some prominent examples in these fields to generalize the notion of multifunctionality and justify its appearance in this thesis title.

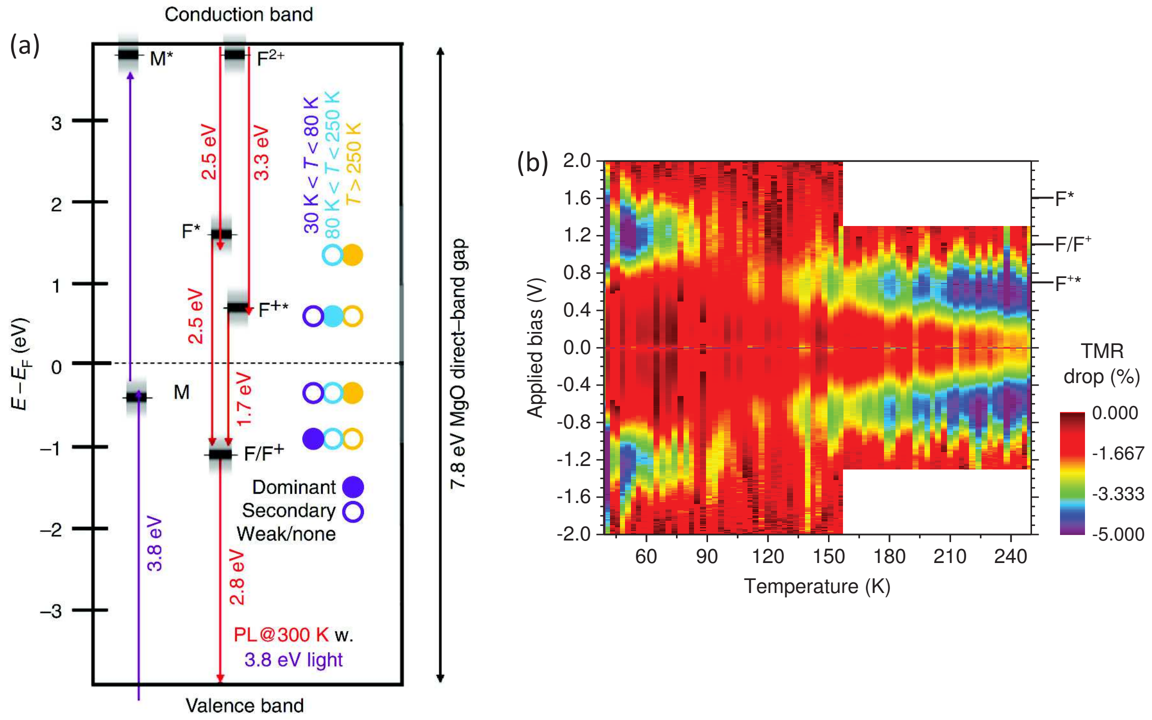

Figure 1.7: Multifunctionality of MgO-based MTJs. (a) Energy diagram of the oxygen defect states in MgO barrier where F denotes a single oxygen vacancy which can be ionized (F^+), excited (F^*) or both (F^{+*}). A colour code of the dots reflects a thermal addressing of a specific defect state in the transport. (b) Voltage-temperature map of TMR revealing an impact of the localized states F^* (F^{+*}) at low (high) temperatures. Figures taken from ref. 10.

An excellent example of a multifunctionality in inorganic spintronics is provided by the magnetic tunnel junctions (MTJs) referred to in the previous section. A sensitivity of the tunneling effect to external factors like temperature,[12] and intrinsic as electronic or structural changes provides a playground for the multifunctionality to occur. We will now survey the possible triggers altering a magnetoresistive response of MTJ. In 2004, Huai *et al.*[99] demonstrated that applying a high density current across the junction leads to magnetization precession in a free layer, namely a spin transfer torque (STT), which eventually may cause the magnetization reversal. That provides an electrical functionality of basically magnetic field controlled spintronic response of MTJ. The STT was also demonstrated to be potentially provoked via optical excitations,[100] therefore adding a functional stimulant in form of light. A distinct effect, called thermagnonic process, can generate the STT by a heat flow across an FM layer.[101, 102] That means the change of a spintronic response may be provoked also by a temperature gradient. On the other hand, the STT can open a new output channel by triggering a microwave emission.[103] All of that together drives an interest on MTJs to form a basis for a spin transfer torque random access memory (STT-MRAM).[104] An interesting study underscoring the multifunctional character of MgO-based MTJs was carried out by Schleicher *et al.*[10] They showed a defect-mediated tunneling across the localized oxygen defect states within the MgO barrier such that a transport through the specific states can be activated by temperature or bias voltage. A potential landscape of this defect states with an impact of the defects addressing on the device's TMR are illustrated in Fig. 1.7. This highlights how multiple stimuli (inputs) may affect a spintronic response (outputs) of the MTJs. Other multifunctional systems studied within the scope of classical spintronics include semiconducting oxides,[105–107] perovskites heterostructures,[108, 109] or polymorphic nanostructures.[110]

The introduction of organic materials into spintronics pushed even further the multifunctional perspectives. In contrast to the inorganic counterpart where both physical and chemical properties of the material are ”fixed” and determined by the constituent elements, the organic compounds have rather complex structure with emergent properties that strongly dependent on such subtle factors as the type of atomic bonds or the molecular conformation. Therefore, such crucial aspects as the electronic structure

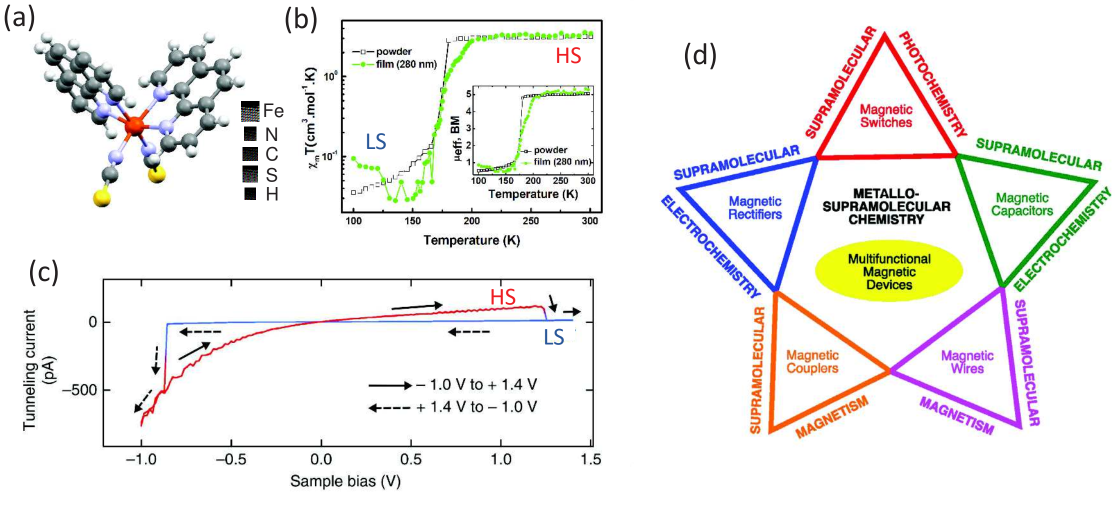

Figure 1.8: Multifunctionality in organic spintronics. (a) Model of Fe(phen)NCS_2 (phen - 1,10-phenanthroline). Multifunctionality of spin crossover is demonstrated by a thermal transition (b) and an electric field induced switching (c) of of Fe(phen)NCS_2 revealing two resistive states assigned to a high spin (HS) and a low spin (LS) state of Fe ion. (d) Diagram of the relations between various areas of supramolecular chemistry used to design new multifunctional devices for the molecular spintronics. Figures taken from ref. 15, 22.

and orbitals energy positions determining, *e.g.*, spin-dependent broadening and energy shift during hybridization with metal, can be relatively easily adjusted so as to attain a desired characteristics. Moreover, multifunctionality possibly allows the alteration of these attributes established by the chemical structure (bond types, conformation, etc.) by providing the external stimuli. A good example of multifunctionality within organic spintronics is provided by the magnetic molecular conductors or semiconductors[9,13] which combine organic salts with inorganic magnetic layers and exhibit a specific coexistence of ferromagnetism, conductivity, and GMR depending on the selected organic donor species.[14] In another case, Prezioso *et al.*[111] demonstrated the LSMO/Alq$_3$/Co junctions manifesting a multilevel magnetoresistance tunable by electric field. A truly remarkable work by Castellano *et al.*[15] presented a metallosupramolecular approach towards multifunctional compounds for spintronic applications. They demonstrated a strategy for tailoring a chemical structure of dinuclear Cu(II) metallocyclophanes with aromatic polyoxalamide ligands, to obtain an exchange-coupled (FM or AFM), photo- and/or electroactive molecules. The authors proposed a ligand engineering to control a vulnerability of the molecule to the specific stimuli, and therefore functionalizing a complex such that it may be used as molecular magnetic coupler, wire, capacitor, rectifier, or a switch.

A distinct subclass of organic materials with intrinsic multifunctionality is the family of so-called spin crossover (SCO) complexes.[16] These are also in focus of this thesis and will described in detail in Section 2. Generally speaking, the SCO materials consist of a transition metal ion surrounded by organic ligands in such a way that the electronic structure of the ion exhibits a bistability of the spin state with at least two configurations possible: a low spin (LS) and a high spin (HS). The transition between

Figure 1.9: Multifunctional spintronics. The cloud of words illustrating a diversity of the multifunctional approach in spintronics. Red color marks the families of the materials, orange - the potential sources or phenomena generating multifunctionality, blue - the stimuli (inputs), and grey - possible responses (outputs) after stimulation. The list is non-exhaustive.

the two, namely a spin crossover, can be triggered by, *e.g.*, temperature, light, pressure, magnetic field, bias voltage, or current. This corroborates a great multifunctional potential of these complexes explaining an intensive research of their properties over the last decades.

To sum up this survey of a multifunctionality in spintronics, we stress that it can emerge in numerous ways within a plentiful of materials. They includes both the organics and inorganics, hybrid systems, conductors, oxides and semiconductors. We invoked the examples where multifunctionality is an intrinsic material property, appears as a result of the interfacial effects, or defects states within a bulk. These may be a consequence of, *e.g.*, hybridization, charge transfer, spin transfer torque, or exchange interaction. A large variety of available stimuli like the electric and magnetic field, pressure, temperature or current can provoke a response in a form of a change in material conductivity, spin state, electric polarization, magnetoresistance, magnetic state, etc. This non-exhaustive list, artistically presented in Fig. 1.9, illustrates a great diversity of the multifunctional approach in spintronics underscoring its application for the versatile devices such as the multipurpose sensors or non-volatile memory elements.

2

Spin crossover

In general notion, a spin crossover (SCO) refers to an effect of a spin state bistability in some coordination complexes, which can be provoked upon delivering an external stimulation. In this section, we explain the origin of SCO and provide its thermodynamical description. We emphasize on the multifunctional character of the SCO complexes by reviewing its response to various external stimuli.

2.1 Ligand field theory

A vast majority of the SCO complexes are coordination compounds which encapsulate a transition metal ion by a cage of organic ligands. In the following we employ a ligand

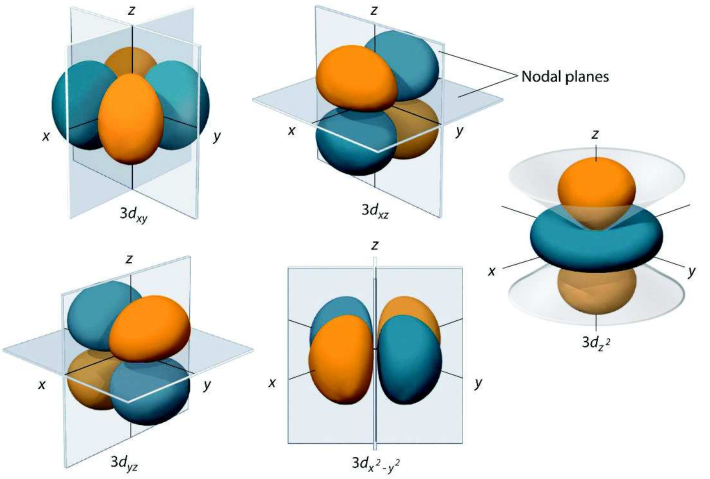

Figure 2.1: Symmetry of the 3*d* orbitals of a transition metal. All five orbitals are degenerate for a free atom. Figure taken from ref. 112.

field theory (LFT) to describe the electronic structure of such complex and emergent spin state bistability. Since our later work will be focused on the most numerous family of the octahedral systems we will provide a description for this particular subgroup.

Let us consider a case of a free transition metal atom. Its valence band is formed out of five degenerate d orbitals denoted as d_{xy}, d_{xz}, d_{yz}, d_{z^2}, and $d_{x^2-y^2}$ (Fig. 2.1). When incorporating such atom into an octahedral system the degeneracy is lifted. Description of this effect was initially proposed by Bethe *et al.*[113] and then referred to as crystal-field theory. The concept explained how a symmetry-dependent crystal field, *i.e.*, an electrostatic interaction from the anions in the crystal, provokes an orbital energy splitting. This approach based on the interaction between point charges was similar to the case of a ligand generated field, yet it did not take into account the nature of the chemical bonds. That was later included by Van Vleck giving rise to so-called ligand field theory.

Now, we consider a metal ion with its initially degenerated d orbitals in coordination complex as subjected to a ligand field. In case of a spherical electrostatic field all the d orbitals would be raised by the same energy. However, if we assume a perfectly octahedral system where the ligands are lying symmetrically on both sides of the x, y, z axes, the electrons on the metal orbitals which are pointing in between the axes, *i.e.*, d_{xy}, d_{xz}, d_{yz}, would feel less repulsion than the one on the orbitals pointing directly towards the ligands, *i.e.*, $d_{x^2-y^2}$. Therefore, these two groups would feel a different strength of the electrostatic field leading to the energy split as illustrated in Fig. 2.2. Within this picture, the three orbitals d_{xy}, d_{xz}, d_{yz} form a basis to the irreducible representation t_{2g}, meanwhile d_{z^2} and $d_{x^2-y^2}$ to e_g in the O_h system.

The energy difference between these groups is referred to as ligand/crystal field splitting and is denoted as Δ_o or $10Dq$ with Dq being an energy unit for a given compound. An octahedral splitting raises the e_g group by $3/5\ \Delta_o$ ($6\ Dq$) and lowers the t_{2g} by $2/5\ \Delta_o$ ($4\ Dq$). The strength of this splitting strongly depends on the nature of both metal and ligands and on the symmetry of the system. One can list the types of ligands in a spectrochemical series according to the ligand field strength they exert: $CO > CN^- > NO_2^- > NCS^- > H_2O > OH^- > F^- > Cl^- > SCN^- > Br^- > I^-$.

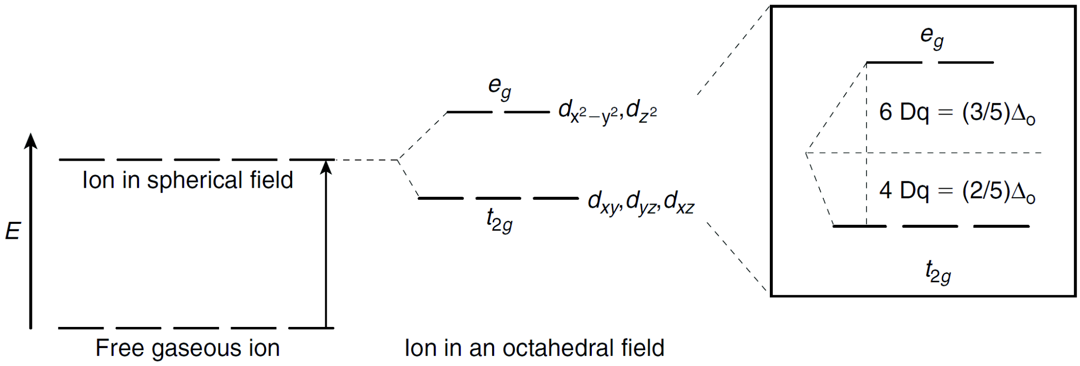

Figure 2.2: Splitting of a transition metal 3*d* orbitals in an octahedral environment. The ligand field theory predicts an equal energy rise for all the orbitals in a spherical field. The octahedral environment unequally acts on the distinct 3*d* orbitals giving rise to its splitting into the t_{2g} and e_g symmetry groups. Figure taken from ref. 112.

A similar ranking for the metals can be listed as: $Pt^{4+} > Ir^{3+} > Pd^{4+} > Ru^{3+} > Rh^{3+} > Mo^{3+} > Mn^{3+} > Co^{3+} > Fe^{3+} > V^{2+} > Fe^{2+} > Co^{2+} > Ni^{2+}$. A distortion from an ideally symmetric system can cause a further lifting of the t_{2g} and e_g degeneracy what is referred to as Jahn-Teller effect.[114]

In a more complex picture we can consider a hybridization between the metal and ligand orbitals. This can be performed within a molecular orbitals approach which predicts a formation of the bonding, non-bonding, and anti-bonding molecular orbitals described, in a good approximation, as a linear combination of the constituents with appropriate weighting parameters. The resulting orbitals would have a bonding character if one finds a consistency in sign of an atomic wave function associated with the overlapping region. An exemplary case of a hybridization between a $3d$ metal and a ligand forming the σ bonds by donating a pair of the electrons (*e.g.*, H_2O, NH_3) is illustrated in Fig. 2.3. The electrons on a ligand side occupy the $2p$ or the hybrid sp, sp^2, or sp^3 orbitals. By recalling the spatial orientation of the $3d$ orbitals (Fig. 2.1) it is clear that only d_{z^2} and $d_{x^2-y^2}$ can form the bonding molecular orbitals by their direct overlap. In contrary, $3d_{xy}$, $3d_{xz}$, and $3d_{yz}$ forming the t_{2g} group do not interact with the ligand orbitals. The other contributing valence shell orbitals of the metal including $4s$ and $4p$ form an octahedral system with a total of 6 bonding and 6 anti-bonding molecular orbitals. Note that usually the ligand orbitals $a_{1g} + e_g + t_{2g}$ lie lower in energy than the metal $3d$ orbitals.

Now, we discuss the molecular occupancy leading eventually to a spin crossover. Let us consider the case from Fig. 2.3. If a transition metal has three $3d$ electrons or less, the t_{2g} orbitals are occupied according to Hund's rules such that each orbital

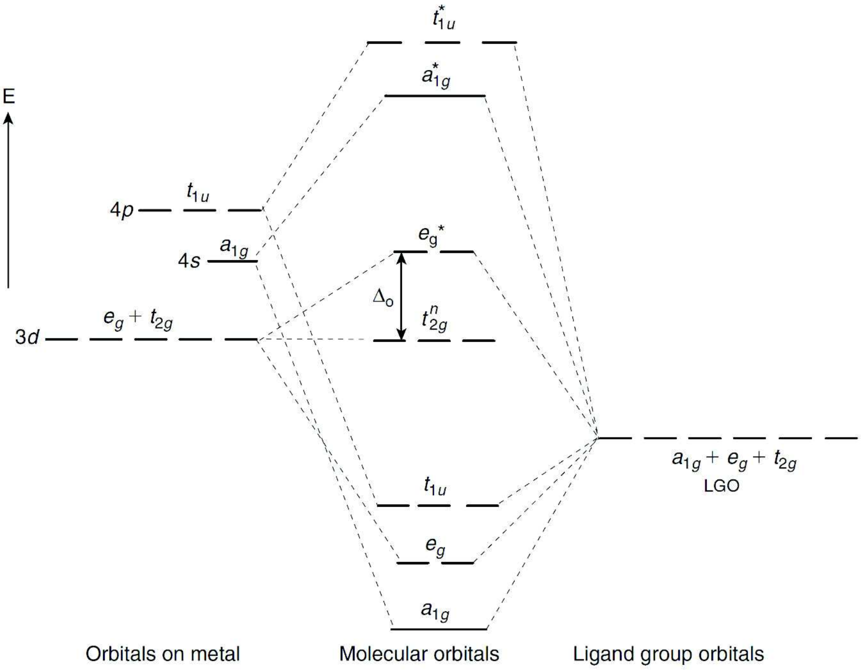

Figure 2.3: Hybridization of a 3*d* metal with a ligand in an octahedral system. A concerned ligand forms a σ bond with the metal by donating a pair of the electrons. The metal and ligand atomic orbitals hybridize to a set of 6 bonding and 6 anti-bonding molecular orbitals. Figure taken from ref. 112.

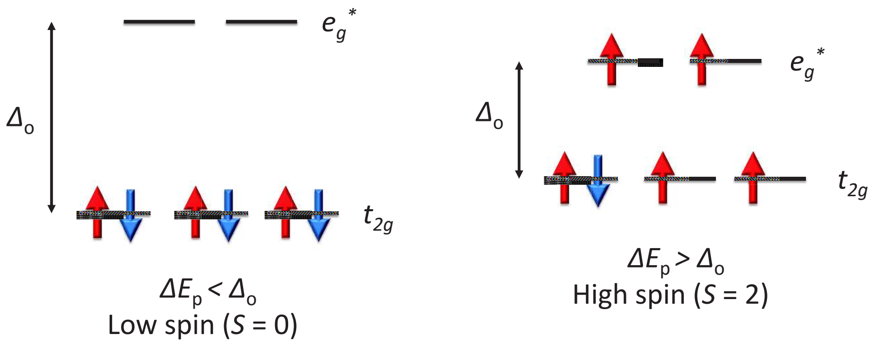

Figure 2.4: Occupancy of the e_g^* and t_{2g} orbitals of a d^6 metal in octahedral environment. Depending on a relative strength of the ligand field Δ_o and the electron pairing energy ΔE_p the occupancy scheme may lead to zero (four) uncompensated electrons, thus low spin (high spin) state with a net spin $S = 0$ ($S = 2$).

carries one electron. For a metal with four $3d$ electrons and more the occupancy can follow one of the two scenarios depending on a relation between the ligand field strength and an electron pairing energy ΔE_p. The latter is a measure of the energy cost for the two electrons to occupy the same orbital and results from the exchange interaction and Coulomb repulsion. Fig. 2.4 presents the two occupancy schemes for a metal with d^6 configuration, *e.g.*, Fe^{2+}. In the case where the ligand field strength is greater than the pairing energy ($\Delta E_p < \Delta_o$) all six charges occupy the t_{2g} orbitals such that there are no unpaired electrons thus the net spin is equal zero. This case we refer to as a low spin state (LS). In contrary, when the ligand field strength is reduced such that it is lower than the pairing energy ($\Delta E_p > \Delta_o$) the electrons occupy the orbitals of e_g^* symmetry group before pairing the uncompensated electrons in t_{2g} orbitals. This

Table 2.1: Number of unpaired electrons and a ground state configuration for the d^n metals in octahedral environment. Note that the d^3 to d^7 metals can have two possible configurations.

d^n	Number of unpaired electrons	Configuration
d^1 (Ti^{3+})	1	$t_{2g}^{(1)}$
d^2 (V^{3+})	2	$t_{2g}^{(2)}$
d^3 (Cr^{3+}, V^{2+})	3	$t_{2g}^{(3)}$
d^4 (Cr^{2+}, Mn^{3+})	2 (4)	$t_{2g}^{(4)}$ ($t_{2g}^{(3)}e_g^{(1)}$)
d^5 (Mn^{2+}, Fe^{3+})	1 (5)	$t_{2g}^{(5)}$ ($t_{2g}^{(3)}e_g^{(2)}$)
d^6 (Fe^{2+}, Co^{3+})	0 (4)	$t_{2g}^{(6)}$ ($t_{2g}^{(4)}e_g^{(2)}$)
d^7 (Co^{2+})	1 (3)	$t_{2g}^{(6)}e_g^1$ ($t_{2g}^{(5)}e_g^{(2)}$)
d^8 (Ni^{2+})	2	$t_{2g}^{(6)}e_g^2$
d^9 (Cu^{2+})	1	$t_{2g}^{(6)}e_g^3$
d^{10} (Cu^+, Zn^{2+})	0	$t_{2g}^{(6)}e_g^4$

leads to a net spin $S = 2$, *i.e.*, so-called high spin state (HS). In Tab. 2.1 we list the possible configurations and a number of unpaired electrons for a series of the d^n metals. We see that only for d^4 to d^7 metals one can have the two electronic configurations resulting in a different spin states. A more detailed picture for a given d^n configuration can be obtained by presenting a Tanabe-Sugano diagram[115] which plots all the Russel-Saunders multiplet terms as a function of ligand field strength Δ_o. This is presented for a d^6 configuration in Fig. 2.5.

We showed how the metal 3d bands splitting in an octahedral coordination complex can result in two possible spin states depending on a ligand field strength. We also mentioned that a ligand field exerted on a metal ion is proportional to a metal-ligand distance. Therefore, one can expect that at certain conditions when $\Delta E_p \approx \Delta_o$ a manipulation of the metal-ligand bond length would cause a conversion of the metal electronic configuration, hence a change of the spin state. That is illustrated as a $^1A_1$,$\leftrightarrow$$^5T_2$ transition on Tanabe-Sugano diagram (Fig. 2.5) where $^1A_1$ ($^5T_2$) denotes a multiplet term for the LS (HS) state. This transition is referred to as spin crossover and can be triggered by various external factors, *e.g.*, temperature, pressure, light, electric field, etc. It was observed in nature for some minerals[116] and hemoproteins.[117] The first artificial SCO material was synthesized by Cambi *et al.*[118] in 1931. Till now, we know a few hundreds of the coordination spin transition compounds including single, double, and polynuclear complexes in solutions, crystals, liquid crystals or polymers.[119–123]

There are numerous experimental techniques suitable to detect the SCO and to probe the spin state of the metal ion. The most frequently used can be subdivided into detection of the magnetic/electronic properties modification such as the magnetic

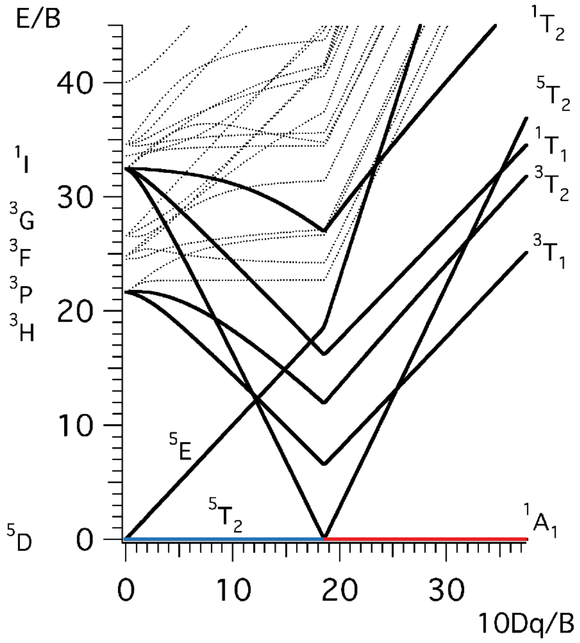

Figure 2.5: Tanabe-Sugano diagram for a d^6 metal ion in octahedral field. The Russel-Saunders multiplet terms plotted as a function of ligand field strength $10\,Dq$ (Δ_o). The ground states corresponding to the low spin ($^1A_1$) and the high spin ($^5T_2$) states are marked in red and blue, respectively. Figure taken from ref. 124.

susceptibility measurement (SQUID, magnetometry),[125,126] optical absorption,[127] reflectivity,[128] XAS,[129,130] Mössbauer spectroscopy,[131] scanning tunneling spectroscopy,[22] and the ones exploiting the volume or thermodynamical parameters variation: x-ray diffraction,[132] scanning probe microscopy,[22,133] calorimetric measurements.[125,134] In the framework of this thesis we particularly employed the SQUID and x-ray absorption spectroscopy.

In the next section we provide a thermodynamical description of the SCO phenomenon.

2.2 Thermodynamical description

From a thermodynamical standpoint a spin crossover can be regarded as a phase transition similarly to many other phenomena in a solid state. Fig. 2.6 illustrates schematically the two potential wells attributed to the HS and LS states in a metal-ligand distance (r_{HL}) coordinate system. A vertical gap between the lowest vibrational states of the LS and HS wells is called the zero-point energy separation $\Delta E^{\mathrm{o}}_{\mathrm{HL}} = E^{\mathrm{o}}_{\mathrm{HS}} - E^{\mathrm{o}}_{\mathrm{LS}}$. Let us consider now a difference of the Gibbs free energy associated with the HS and LS phases:

$$\Delta G(T,p) = G_{\mathrm{HS}}(T,p) - G_{\mathrm{LS}}(T,P) = \Delta H - T\Delta S \tag{2.1}$$

ΔH and ΔS denote a variation of the molar enthalpy and entropy. At low temperatures where $T\Delta S$ is negligible the more stable state is that of a lower energy (typically LS). By increasing the temperature the ΔH term is being decreased eventually leading to $G = 0$. That defines the transition temperature $T_{1/2} = \Delta H/\Delta S$ at which both HS and LS are equally populated. The information about such thermodynamical quantities as the enthalpy and entropy can be obtained by calorimetric measurements.[125,134]

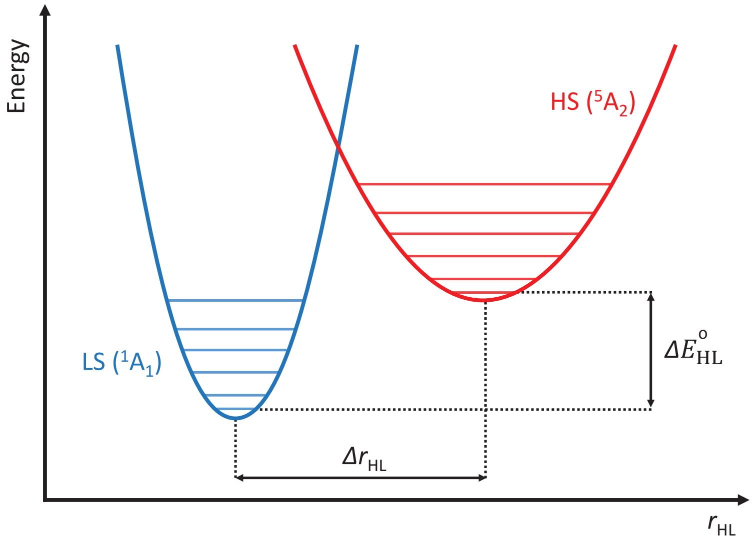

Figure 2.6: Potential wells associated with the HS and LS states of a d^6 metal in an octahedral environment. A vertical gap between the lowest vibrational states of the HS and LS states is referred to as zero-point energy separation $\Delta E^{\mathrm{o}}_{\mathrm{HL}}$. The x axis is defined as a metal-ligand distance r_{HL}.

We now describe the meaning of the two ΔH and ΔS terms and its role for a spin crossover. Note that this description has macroscopic character and does not include any cooperative effects between the molecules (discussed later). The molar enthalpy difference $\Delta H = H_{\mathrm{HS}} - H_{\mathrm{LS}}$ typically of order $10 - 20\,\mathrm{kJ\,mol^{-1}}$ is directly related to a zero-point energy separation $\Delta E^{\mathrm{o}}_{\mathrm{HL}}$.[135] The entropy change $\Delta S = S_{\mathrm{HS}} - S_{\mathrm{LS}}$ takes values $50 - 80\,\mathrm{J\,mol^{-1}\,K^{-1}}$[135] and can be separated into the electronic and vibrational contributions. A pioneer work of Sorai and Seki[136] over a heat capacity of $\mathrm{Fe(phen)_2(NCS)_2}$ and $\mathrm{Fe(phen)_2(NCSe)_2}$ revealed that an electronic contribution of the entropy amounts to $\sim 30\%$ of its total variation for the octahedral systems. If the system symmetry is reduced this contribution can be more significant. The rest 70% is attributed to a vibrational term resulting from the intramolecular stretching and deformation modes. The intermolecular effects are supposed to play a minor role.[137] Therefore, thermodynamically speaking a spin crossover is an entropy driven process arising from coupling between the electronic molecular states and the phonons.[138]

Now, we derive an expression for a high spin proportion evolution with temperature denoted as $\rho_{\mathrm{HS}}(T)$ (sometimes in literature also $\gamma_{\mathrm{HS}}(T)$). A fraction of the high spin at the equilibrium condition for a given temperature and pressure can be obtained from the minimization of the Gibbs free energy, that is for condition:

$$\left(\frac{\partial G(\rho_{\mathrm{HS}}, p, T)}{\partial \rho_{\mathrm{HS}}}\right)_{T,p} = 0 \tag{2.2}$$

Then, the expansion of the free energy G per single molecule limited to a quadratic ρ^2_{HS} term takes the form:[139]

$$G/N = (1-\rho_{\mathrm{HS}})G_{\mathrm{LS}} + \rho_{\mathrm{HS}}G_{\mathrm{HS}} + \Gamma\rho_{\mathrm{HS}}(1-\rho_{\mathrm{HS}}) - TS_{mix} \tag{2.3}$$

where N is a number of the molecules in an ensemble, $G_{\mathrm{LS}} = G(\rho_{\mathrm{HS}} = 0)/N$ and $G_{\mathrm{LS}} = G(\rho_{\mathrm{HS}} = 1)/N$ is the Gibbs free energy per molecule in the LS and HS state respectively, and $S_{\mathrm{mix}} = -k_{\mathrm{B}}[\rho_{\mathrm{HS}} \ln \rho_{\mathrm{HS}} + (1-\rho_{\mathrm{HS}}) \ln(1-\rho_{\mathrm{HS}})]$ corresponds to an entropy of mixing of the LS and HS phases. The quadratic term Γ is an interaction constant resulting from a coupling between the coexisting phases. This term attracted a notable attention and was recognized by Slichter and Drickamer[140] as responsible for elastic interactions between the phases which can substantially modify the high spin fraction evolution with temperature and pressure. Since then, the Γ term has been referred to as cooperativity. The larger its contribution the more abrupt the spin transition curve. It may also lead to hysteretic behavior of transition curve or its two-step evolution. The cooperativity was commonly accepted to be emerging from the electron-phonon coupling between the molecules, thus a long-range elastic interactions.[137] That is why a diluted SCO systems, *e.g.*, in solution, manifest a more gradual spin transition[139] than solids.[137] There are also other possible sources of the cooperative effects including the exchange[141] or electrostatic interactions[142] between the molecules.

By combining Eq. 2.1 and 2.3 and including the equilibrium condition from Eq. 2.2 one obtains an expression relating the high spin fraction to the temperature as:

$$T(\rho_{\mathrm{HS}}) = \frac{\Delta H + \Gamma(1-2\rho_{\mathrm{HS}})}{R \ln\left(\frac{1-\rho_{\mathrm{HS}}}{\rho_{\mathrm{HS}}}\right) + \Delta S} \tag{2.4}$$

where R is the gas constant. We illustratively represent this relation in Fig. 2.7 for exemplary thermodynamical parameters $\Delta H = 15\,\mathrm{kJ\,mol^{-1}}$, $\Delta S = 65\,\mathrm{J\,mol^{-1}\,K^{-1}}$ and three different values of the cooperative term Γ. In absence of the cooperativity ($\Gamma = 0$) the transition is gradual. It becomes more abrupt when the cooperativity is increased to $\Gamma = 300\,\mathrm{J\,mol^{-1}}$, and beyond the extreme case for $\Gamma = 2RT_{1/2}$ transition manifests a hysteresis. This is visualised in Fig. 2.7 for $\Gamma = 1000\,\mathrm{J\,mol^{-1}}$. Note that the transition temperature $T_{1/2}$ is independent of cooperativity.

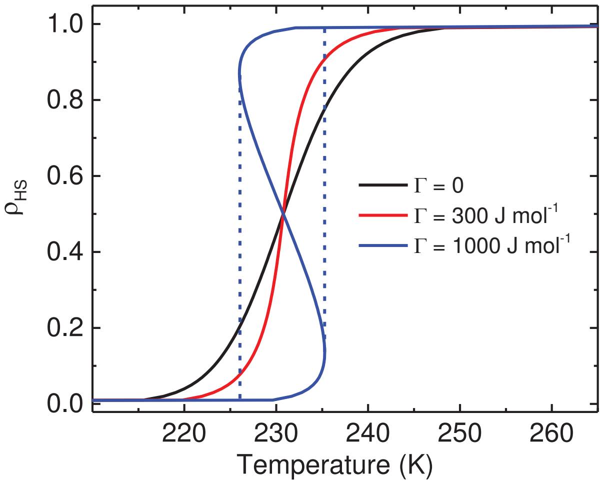

Figure 2.7: Influence of the cooperativity on a spin transition. A high spin proportion evolution with temperature as calculated with Eq. 2.4 for three different values of cooperative term $\Gamma = 0$, 300, and $1000\,\mathrm{J\,mol^{-1}}$ and with exemplary thermodynamical parameters $\Delta H = 15\,\mathrm{kJ\,mol^{-1}}$, $\Delta S = 65\,\mathrm{J\,mol^{-1}\,K^{-1}}$.

2.3 Multifunctionality of SCO: response to external stimuli

In the previous section we employed the ligand field theory and the thermodynamics to describe the spin transition phenomenon occurring in the vicinity of a bistability region where $\Delta E_{\mathrm{P}} \approx \Delta_{\mathrm{o}}$. In this section, we will review the possible triggers of the SCO and discuss the material response to it. Fig. 2.8 presents a comprehensive list of the available stimuli with the temperature, pressure, magnetic field, light, and x-rays discussed in detail further in this section with a special emphasis on the SCO in Fe(II)-based complexes which will be a subject of the study later in this thesis.

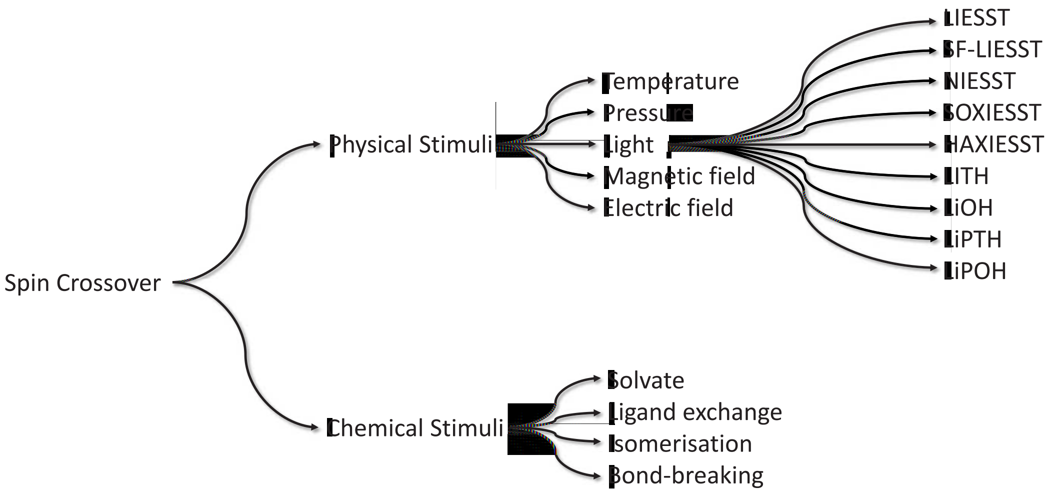

Figure 2.8: Multifunctionality of the spin crossover materials. A comprehensive list of available stimuli which may be used to provoke a spin crossover. The light irradiation can be followed by light- (LI-), strong-field- (SF-), nuclear- (N-), soft x-ray- (SOX-), and hard x-ray- (HAX-) induced excited spin state trapping (-IESST), light induced- (LI-) or light perturbed (LiP-) thermal hysteresis (-TH) or optical hysteresis (-OH). Graph reproduced from ref. 143.

2.3.1 Temperature

Temperature change is so far the most common perturbation used to provoke the SCO. Spin transition occurs when vibrational energy attributed to the zero-point energy separation is reached, that is for $\Delta E^\circ_{\mathrm{HL}} = k_{\mathrm{B}}T$. This can be explained in an intuitive picture by the metal-ligand bonds expansion (contraction) upon the temperature increase (decrease) and thus the modification of the ligand field strength which eventually reverses the favorable configuration. Fig. 2.9 illustrates the main types of the temperature induced transition curve. The transition temperature $T_{1/2}$ may strongly differ between various SCO complexes from above room temperature[145,146] to as low as 100 K.[147]

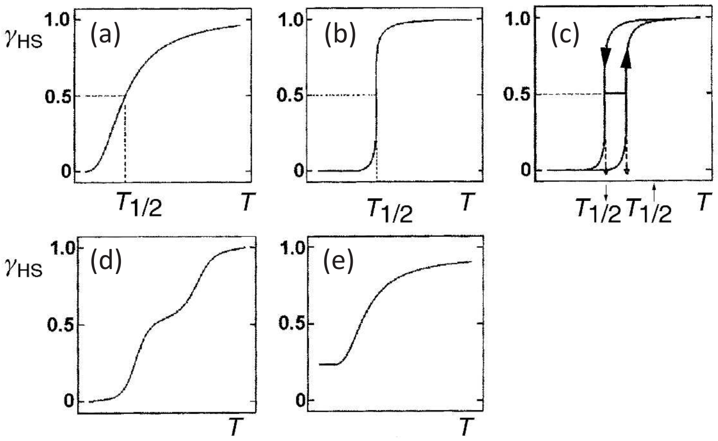

Figure 2.9: Thermally provoked spin transition. The main types of the thermally provoked transition curves: (a) gradual, (b) abrupt, (c) hysteretic, (d) with steps, and (e) incomplete. Figure reprinted from ref. 144.

2.3.2 Pressure

The external pressure can be both trigger and modifier of a spin transition. The pioneer work in this field belongs to Drickamer *et al.*[148] who studied Fe(phen)$_2$(NCS)$_2$ under pressure by means of Mössbauer spectroscopy. This along with the work of Usha *et al.*[149] revealed an increase of transition temperature $T_{1/2}$ and more gradual character of transition with increasing pressure. This can be explained in terms of the enthalpy variation denoted as:

$$\Delta H = \Delta U + p\Delta V \tag{2.5}$$

where ΔU is a change of the internal energy, p the external pressure, and ΔV change of a unit cell volume. This relation points to the enthalpy variation ΔH as directly proportional to pressure with both ΔV and the ligand field strength (reflected in ΔU) proved to be pressure independent.[151] The effect of external pressure can be regarded as an effective increase of the zero-point energy separation by $p\Delta V$. Therefore, the increase of external pressure leads to a favoring of the low spin state thus to an increase of $T_{1/2}$. In the mean field approximation of the free Gibbs energy, transition temperature dependence on pressure can be expressed as:[150]

$$\frac{\partial T_{1/2}}{\partial p} = \frac{\delta v}{\Delta S} \tag{2.6}$$

with $\delta v > 0$ as a volume change of the crystal per one molecule and $\Delta S > 0$ change of the entropy at $T_{1/2}$. The same approach predicts a change of a transition hysteresis width and a critical pressure at which the hysteresis disappears completely. The example of a transition temperature evolution with pressure for [Fe(phy)$_2$](ClO$_4$)$_2$ is presented in Fig. 2.10. A variation of the external pressure can also result in less intuitive behavior than discussed above. For instance, it can induce a spin transition in compounds which do not exhibit a thermal switching (*e.g.*, Fe(phen)$_2$Cl$_2$[152]), or induce the phase transition leading to formation of a high spin fraction at low temperature.[153]

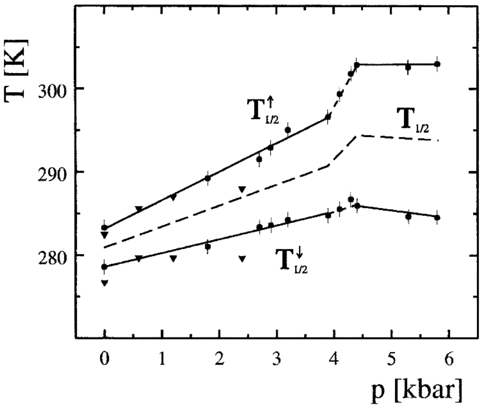

Figure 2.10: Transition temperature dependence on the external pressure for [Fe(phy)$_2$](ClO$_4$)$_2$. The circles represent the theoretical values and the triangles an experimental result from the Mössbauer spectroscopy. Figure taken from ref. 150.

2.3.3 Magnetic field

In the previous section we invoked a low spin stabilizing effect of the external pressure. Contrary to that, the magnetic field favors a high spin state and therefore shifts $T_{1/2}$ towards the lower temperatures. This can be rationalized by a stronger interaction with the field of the HS state with the magnetic susceptibility χ^{HS} which is nearly two orders of magnitude greater than χ^{LS}. Modification of $T_{1/2}$ is then proportional to the square of the field intensity. Different effects are obtained by applying static or pulsed magnetic fields.

Studies of Gütlich *et al.*[155] on Fe-phen revealed a shift of $\Delta T_{1/2} = -0.11 \pm 0.04\,\mathrm{K}$ under the applied field of $H = 5.5\,\mathrm{T}$. Lejay *et al.*[156] demonstrated a variation of $\Delta T_{1/2} = -0.6\,\mathrm{K}$ for Co(III) complex under a static field $H = 20\,\mathrm{T}$. The work of Garcia *et al.*[154] on $\mathrm{Mn^{III}[(pyrol)_3tren]}$ revealed a quadratic relation $T_{1/2} = 43.7 - 0.003H^2$ with the field value expressed in Tesla units and the transition temperature in Kelvins. One easily sees that the effect is weak and requires high magnetic fields. Since high continuous fields are difficult to achieve, a notable attention was paid to studies over an impact of the pulsed magnetic field on the spin transition. It is worth mentioning that such investigations require a fast detection system of the spin state what was predominantly realized by a reflectivity measurements.

The first report on the SCO response to a pulsed magnetic field is a work of Negre *et al.*[157] with Fe-phen. It revealed a persisting 15% increase of the HS proportion after applying a 1.5 s long pulse with a maximum of 32 T achieved after 70 ms. Undoubtedly, this implies that a pulsed magnetic field can trigger the SCO. Further investigations of Bousseksou *et al.*[158] revealed that depending on the initial state (ascending or descending branch of the thermal hysteresis loop), the magnetic field induced perturbative effect can be reversible or irreversible (Fig. 2.12).

There are certain theoretical approaches describing how a magnetic field interacts with the spin crossover compound. Within the framework of thermodynamics, the magnetic field dependence of a spin transition temperature can be derived from the

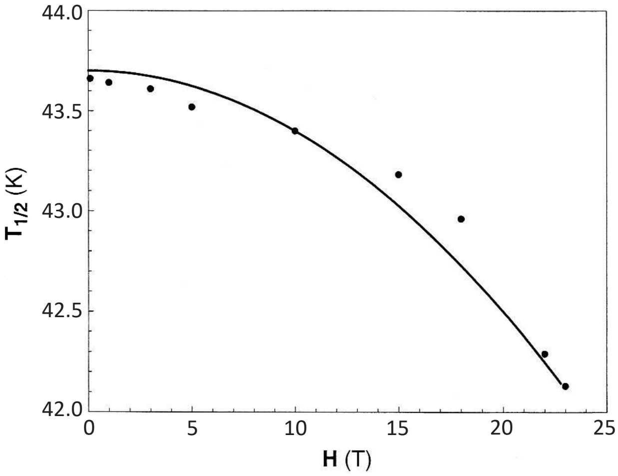

Figure 2.11: Transition temperature dependence on a static magnetic field. The solid circles represent the experimental values of transition temperature $T_{1/2}$ for $\mathrm{Mn^{III}[(pyrol)_3tren]}$ and the solid line is a least square fit of relation $T_{1/2} = 43.7 - 0.003H^2$. Figure taken from ref. 154.

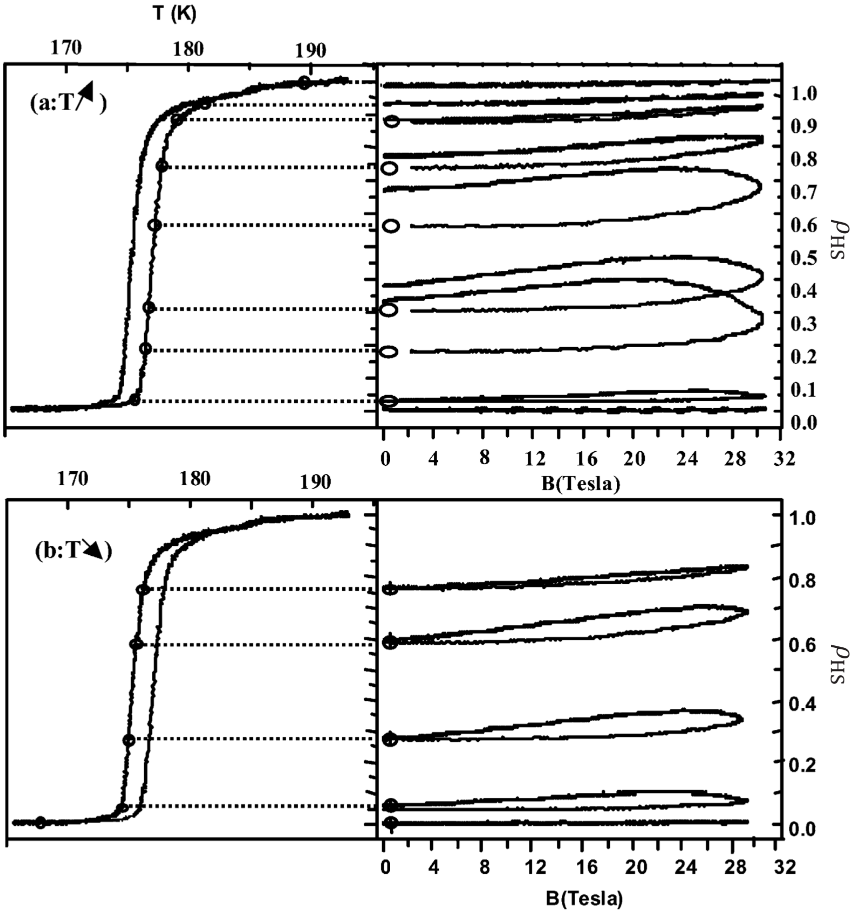

Figure 2.12: Variation of HS proportion in Fe-phen stimulated by a pulsed magnetic field. The reversible or irreversible character of a perturbation appears as the closed or open loop respectively. Figure taken from ref. 158.

magnetic free-energy in the following form:

$$\Delta T_{1/2} = T_{1/2}(B) - T_{1/2}(0) = \frac{-4(\mu_B B)^2}{k_B \Delta(0)} \tag{2.7}$$

where μ_B is the Bohr magneton, B the magnetic field in Tesla units, k_B the Boltzmann constant, and $\Delta(0)$ the energy gap between the HS and LS states at zero magnetic field. The minus sign is in agreement with a downward shift implying a HS stabilizing effect. The better understanding of the dynamic processes following the strong field pulses requires a more sophisticated theory predominantly provided by Ising-like models with dynamical extension.

2.3.4 Light

The discovery of a spin transition induced by light was one of the milestones in the field of spin crossover. In 1982, McGarvey *et al.*[159] observed a perturbation of the spin state equilibrium and the excitation from the LS to metastable HS of $Fe(biz)_3^{2+}$, $Fe(ppa)_2^{2+}$, and $Fe(pyimH)_3^{2+}$ in solutions when irradiated by a 530 nm laser. Two years later, Decurtins *et al.*[160] confirmed the effect to exist also in solids and referred to it as light induced excited spin state trapping (LIESST). Finally, Hauser *et al.*[161] discovered the reverse-LIESST intensifying henceforth the interest on SCO as potential optical switches or sensing elements.

The same general mechanism of a (reverse-)LIESST applies to all SCO complexes. It is schematically illustrated in Fig. 2.13. Below a certain material specific threshold denoted as T_{LIESST} (usually below 100 K) the molecule initially in $^1\mathrm{A}_1$ (LS) state can be promoted by a green light to $^1\mathrm{T}_1$. The lifetime of this state is typically of the nanoseconds and then the cascade relaxation $^1\mathrm{T}_1 \rightarrow {}^3\mathrm{T}_1$ occurs. After that, two paths are possible with one of them populating a metastable $^5\mathrm{T}_2$ (HS) state. The only relaxation process between $^5\mathrm{T}_2$ and $^1\mathrm{A}_1$ is a thermal tunneling (radiative relaxation forbidden) thus the lifetime of a metastable HS is relatively long at low temperatures. Above T_{LIESST} the relaxation to $^1\mathrm{A}_1$ is thermally activated and trapping is no longer possible. Alternatively, the LIESST was reported to be possible by red light illumination (980 nm) along the path $^1\mathrm{A}_1 \rightarrow {}^3\mathrm{T}_1 \rightarrow {}^5\mathrm{T}_2$. It is worth mentioning that the compounds with the ligands extended π-systems exhibit a metal to ligand charge transfer state (MLCT). The ligand-field bands can be submerged in these states and the LIESST may be therefore mediated by the ^{1}MLCT and ^{3}MLTC states. This case applies to the compounds with, *e.g.*, pyridyl type ligands.[124] The reverse-LIESST can be provoked by a red light which stimulates the $^5\mathrm{T}_2 \rightarrow {}^5\mathrm{E}$ transition, which through an intermediate $^5\mathrm{E} \rightarrow {}^3\mathrm{T}_1$ state, leads finally to $^1\mathrm{A}_1$ (LS). Interestingly, there are reports on the systems where LIESST can occur also from the HS to metastable LS state.[162]

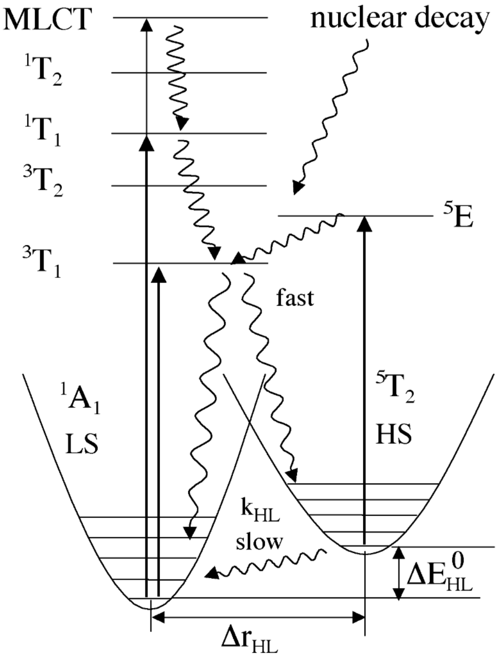

Figure 2.13: LIESST and reverse-LIESST in Fe(II) complex. Schematic illustration of the SCO complex electronic structure in a bistability region with the allowed *d*-*d* transitions represented by the straight lines and the radiationless relaxation processes by the curvy ones. The metal-ligand charge transfer state (MLCT) appears for the compounds with π electron extended ligands. Figure taken from ref. 124.

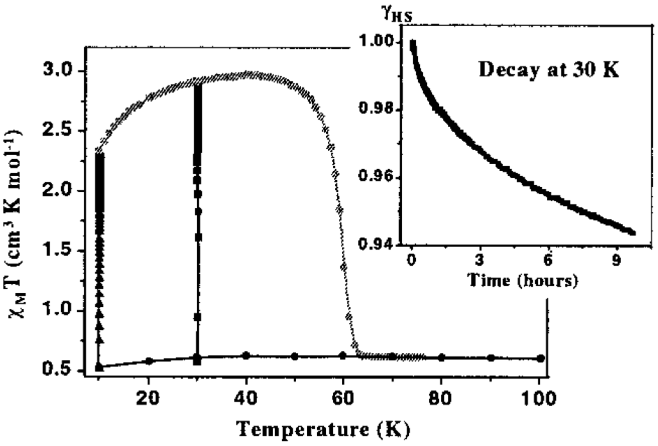

Figure 2.14: LIESST in Fe-phen. The magnetic susceptibility measurement as a function of temperature with the LIESST effect at $T = 10\,\mathrm{K}$ (solid black triangles) and $T = 30\,\mathrm{K}$ (black solid squares). The gray circles correspond to transition curve in the dark. The inset plots the relaxation of the HS proportion in time revealing persisting 94% after 9 hours. Figure taken from ref. 168.

The LIESST was first observed for the complexes in solution and later also confirmed in solids, diluted crystal systems, Langmuir-Blodget layers, molecules embedded in polymer matrices, or UHV sublimed films.[163] The rule of the thumb states that T_{LIESST} decreases with increasing $T_{1/2}$.[164] The highest reported T_{LIESST} threshold was 132 K for $[\mathrm{Fe(L)(CN)_2}]{\cdot}\mathrm{H_2O}$ with L as a Schiff-base macrocyclic ligand.[165] The intensive studies over the LIESST brought to light also other interesting, light related phenomena in SCO compounds. These include the light-induced thermal-hysteresis (LITH),[166] light-induced perturbation of a thermal hysteresis (LIPTH),[143] or ligand-driven light-induced spin change (LD-LISC).[167] In the next paragraph we describe the mechanism of relaxation following the LIESST.

The studies of a metastable HS → LS relaxation are as old as the LIESST itself. One of the models describing this process is the theory of Buhks *et al.*[169] developed in 1980 for the spin transition compounds in solutions. It presumes a quantum mechanical tunneling as the relaxation mechanism at sufficiently low temperatures, what later was experimentally confirmed by Xie *et al.*[170] for the SCO complex embedded in a polymer matrix. We will base our further considerations on this particular theory.

Two potential wells of the HS and LS state are separated by $\Delta Q_{\mathrm{HL}} = \sqrt{6}\Delta r_{\mathrm{HL}}$ (Fig. 2.15 (a)). The average value of $r_{\mathrm{HL}} \sim 0.2$ Å corresponds to $\Delta Q_{\mathrm{HL}} \sim 0.5$ Å. Classically, a transition between the two wells is possible only if the system has enough energy to overcome the barrier. In quantum mechanical case, a probability of a non-radiative transition from any vibration level m of the HS to m' of the LS can be expressed by the Fermi's Golden Rule as:

$$w_{mm'} = \frac{2\pi}{\hbar^2\omega}\beta_{\mathrm{HL}}^2|\langle\chi_{m'}|\chi_m\rangle|^2\delta(E_{m'}, E_m) \tag{2.8}$$

where $\hbar\omega$ denotes the vibrational energy, $\beta_{\mathrm{HL}} = \langle\Phi_{\mathrm{LS}}|H_{\mathrm{SO}}|\Phi_{\mathrm{HS}}\rangle$ is the matrix element given by second order spin-orbit coupling and $|\langle\chi_{m'}|\chi_m\rangle|^2$ represents the Franck-Condon factor reflecting an overlap of the vibrational functions of the HS and LS states.

The Dirac delta function keeps the energy conservation valid. Now, we introduce the zero-point energy separation in vibrational quanta units as $n = \frac{\Delta E^{\circ}_{\mathrm{HL}}}{\hbar\omega}$. Including the energy conservation condition: $m' = m + n$, we can express the relaxation rate constant in form:

$$k_{\mathrm{HL}}(T \to 0) = \frac{2\pi}{\hbar^2\omega}\beta^2_{\mathrm{HL}}|\langle\chi_n|\chi_{\mathrm{o}}\rangle|^2 \tag{2.9}$$

where:

$$|\langle\chi_n|\chi_{\mathrm{o}}\rangle|^2 = \frac{S^n e^{-S}}{n!} \tag{2.10}$$

and:

$$S = \frac{\frac{1}{2}f\Delta Q^2_{\mathrm{HL}}}{\hbar\omega} \tag{2.11}$$

This approach assumes a non-zero population only of the ground vibrational state of HS. The Eg. 2.10 imposes the harmonic approximation with S as the Huang-Rhys factor (Eq. 2.11) reflecting a horizontal separation of the HS and LS potential wells. Expression 2.9 is valid only at the limit $T \to 0$ where the rate is temperature independent. To obtain the expression for the non-zero temperatures one has to average Eg. 2.9 over all the vibrational levels of the HS state, that is:

$$k_{\mathrm{HL}}(T) = \frac{2\pi}{\hbar^2\omega}\beta^2_{\mathrm{HL}}F(T) \tag{2.12}$$

where the temperature dependent Franck-Condon factor takes form:

$$F_n(T) = \frac{\sum_m |\langle\chi_{m+n}|\chi_m\rangle|^2 e^{\frac{-m\hbar\omega}{k_{\mathrm{B}}T}}}{\sum_m e^{\frac{-m\hbar\omega}{k_{\mathrm{B}}T}}} \tag{2.13}$$

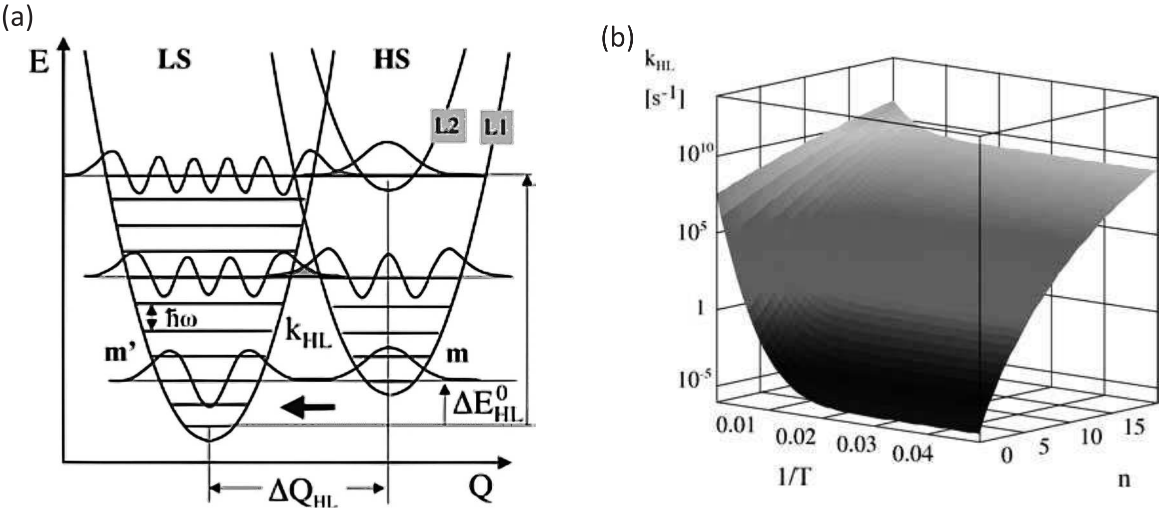

Figure 2.15: LIESST relaxation. (a) The LS and HS potential wells along a totally symmetric normal coordinate ($\Delta Q_{\mathrm{HL}} = \sqrt{6}\Delta r_{\mathrm{HL}}$) illustrating the LIESST relaxation from the metastable high spin state m to the low spin state m'. (b) The dependence of the relaxation rate k_{HL} on T^{-1} and reduced energy gap n, calculated from Eq. 2.12 for parameters $S = 45$, $\hbar\omega = 250$ cm^{-1}, $\beta_{\mathrm{HL}} = 150$ cm^{-1}. Figures reprinted from ref. 124.

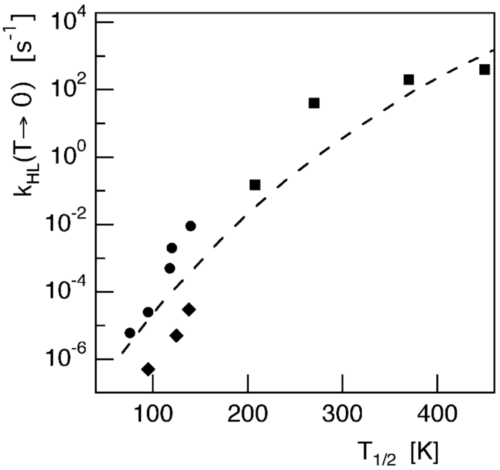

Figure 2.16: HS → LS relaxation constant as a function of transition temperature. A theoretical rate constant calculated for the low temperature tunneling limit and the standard parameters (dashed line) along with the experimental data obtained for picolylamine (circles), tetrazoles (diamonds), $(\mathrm{mepy})_{3-x}(\mathrm{py})_x$ (squares). Figure taken from ref. 154.

The dependence of the relaxation rate k_{HL} as a function of inverse temperature $1/T$ and a reduced energy gap n for a standard set of parameters is plotted in Fig. 2.15 (b). One can easily notice that below $T \sim 50\,\mathrm{K}$ the rate is temperature independent. This points to a pure tunneling regime. For this region the rate increases exponentially with n. Once the temperature is increased the relaxation is thermally activated and the process is considered as the tunneling from thermally populated high spin states.

It is worth mentioning, that the relaxation rate k_{HL} covers a very broad range of values for various Fe(II) compounds. This is visually represented in Fig. 2.15 (b) by varying the reduced energy gap n value while keeping $1/T$ constant. One can relate the reduced energy gap n to transition temperature $T_{1/2}$ by approximating:

$$n = \frac{\Delta E^{\circ}_{\mathrm{HL}}}{\hbar\omega} \approx \frac{\Delta H^{\circ}_{\mathrm{HL}}}{\hbar\omega} = \frac{T_{1/2}\Delta S^{\circ}_{\mathrm{HL}}}{\hbar\omega} \approx 0.02 \cdot T_{1/2} \tag{2.14}$$

This relation assumes the temperature independent $\Delta H^{\circ}_{\mathrm{HL}}$ and a standard value of the $\Delta S^{\circ}_{\mathrm{HL}}$ term.

Finally, by combining Eg. 2.14 with Eq. 2.10 and then substituting it to the low temperature tunneling limit (Eq. 2.9) one obtains the relaxation parameter k_{HL} evolution with transition temperature $T_{1/2}$ as plotted in Fig. 2.16. It highlights the notable range of relaxation constant value which can be as low as $10^{-6}\,\mathrm{s}^{-1}$ ($\tau > 10$ days) for $[\mathrm{Fe(ptz)_6}]^{2+}$ with $T_{1/2} = 96\,\mathrm{K}$ and up to $1 \times 10^4\,\mathrm{s}^{-1}$ ($\tau < 1$ ms) for $[\mathrm{Fe(py)_3tren}]^{2+}$ with $T_{1/2} > 400\,\mathrm{K}$. The relation from Eq. 2.14 can be used for approximating the energy gap based on a measured value of k_{HL} at low temperature.

There are multiple factors which may modify the LIESST relaxation dynamics. One of the most important is a cooperativity which leads to a non-linear kinetics and self-acceleration of the process.[171] In simple words, during the relaxation, a fraction of the molecules being already in the LS state, by having a greater volume then the HS, start to exert the pressure on the system. In a denser lattice the internal pressure increases leading to a rise of $\Delta E^{\circ}_{\mathrm{HL}}$, what accelerates the consequent relaxations. The scheme

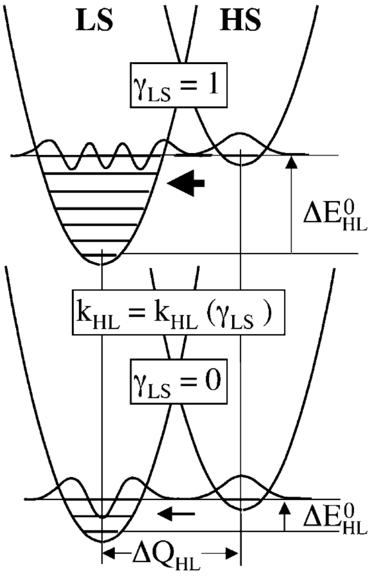

Figure 2.17: HS → LS relaxation in a cooperative environment. The LS and HS state potential wells representing the case of the self-accelerating LIESST relaxation. The cooperative effects lead to a pressure induced increase of the zero-point energy separation $\Delta E^{\mathrm{o}}_{\mathrm{HL}}$ and thus to LS proportion dependent relaxation rate constant. Figure taken from ref. 124.

of the process is depicted in Fig. 2.17. In the mean-field approximation this effect can be expressed as the LS fraction (ρ_{LS}) dependent zero-point energy separation: $\Delta E^{\mathrm{o}}_{\mathrm{HL}} = \Delta E^{\mathrm{o}}_{\mathrm{HL}}(\rho_{\mathrm{LS}} = 0) + 2\Gamma\rho_{\mathrm{LS}}$. Unsurprisingly, the external pressure itself was also reported to modify the LIESST relaxation dynamics.[151,172]

2.3.5 X-ray radiation

The x-ray absorption is a common and very efficient method for probing the spin state of the metal ion in the SCO compounds. On the other hand, the x-ray radiation can also provoke the transition in a way analogous to visible light. However, its intentional use as a trigger is rather seldom mainly because of a non-practical applicability. Furthermore, the photons within the soft x-ray range have already sufficient energy to break the molecular bonds and thus irreversibly shatter the SCO. The x-ray induced spin transition is an inevitable side effect of a synchrotron-grade experiments and that is why one needs to carefully take it under considerations during, *e.g.*, x-ray absorption measurements.

The x-rays were reported to trigger SCO in 1997 by work of Collison *et al.*[173] on Fe-phen. This concerned the radiation in soft range of x-rays and thus was consequently referred to as soft x-ray induced excited spin state trapping (SOXIESST). The later studies of Vankó *et al.*[174] provided the evidence of a similar effect with a use of the hard x-rays, *i.e.*, HAXIESST. Fig. 2.18 illustrates the proposed pathways for the spin transition when compound is subjected to x-rays. The irradiation at low temperature leads from the LS to the metastable high spin state denoted as HS*. The side effect called the SOXPC (soft x-ray photochemistry) which is dependent on the radiation intensity and an exposure time may cause the molecular bonds rupture and irreversible blocking of the molecule in the low spin state (denoted LS'). Meanwhile the SOXIESST is fully reversible the SOXPC leads to an irreparable material damage. Our group performed the first SOXIESST combined with the LIESST studies on a sublimed film of Fe-phen.[163] Fig. 2.19 shows the dynamics of trapping when the molecules are photoexcited with the white LED and the soft x-rays. Note the timescale, saturation level and radiation intensity dependence of both effects (Fig. 2.19 (a)). The SOXIESST effect was proved to be non-resonant.

Despite few promising theories, to date there is no direct explanation for either SOXIESST or SOXPC mechanism. The aforementioned study over Fe-phen (Fig. 2.14) provided a valuable information regarding the precautions which one needs to take so as to reduce the impact of these side effects. These include: (i) reduction of the x-ray beam intensity, (ii) minimization of the exposure time, and if needed (iii) occasional change of the beam spot position.

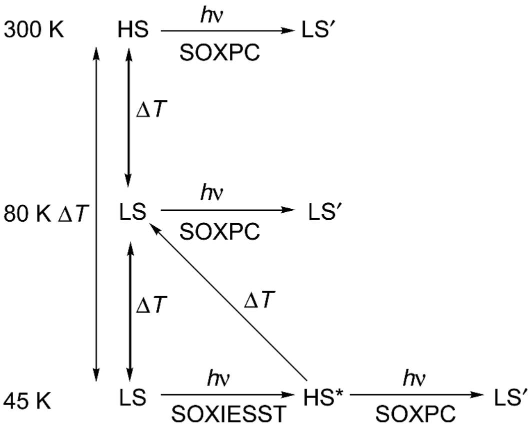

Figure 2.18: Possible pathways for a spin transition under the soft x-ray beam. The soft x-ray induced excited spin state trapping (SOXIESST) triggers the LS to HS* (metastable) transition at low temperature. Concurrently, the soft x-ray photochemistry (SOXPC) may lead to the molecular bonds rupture and blocking in the irreversible LS'. Figure reprinted from ref. 173.

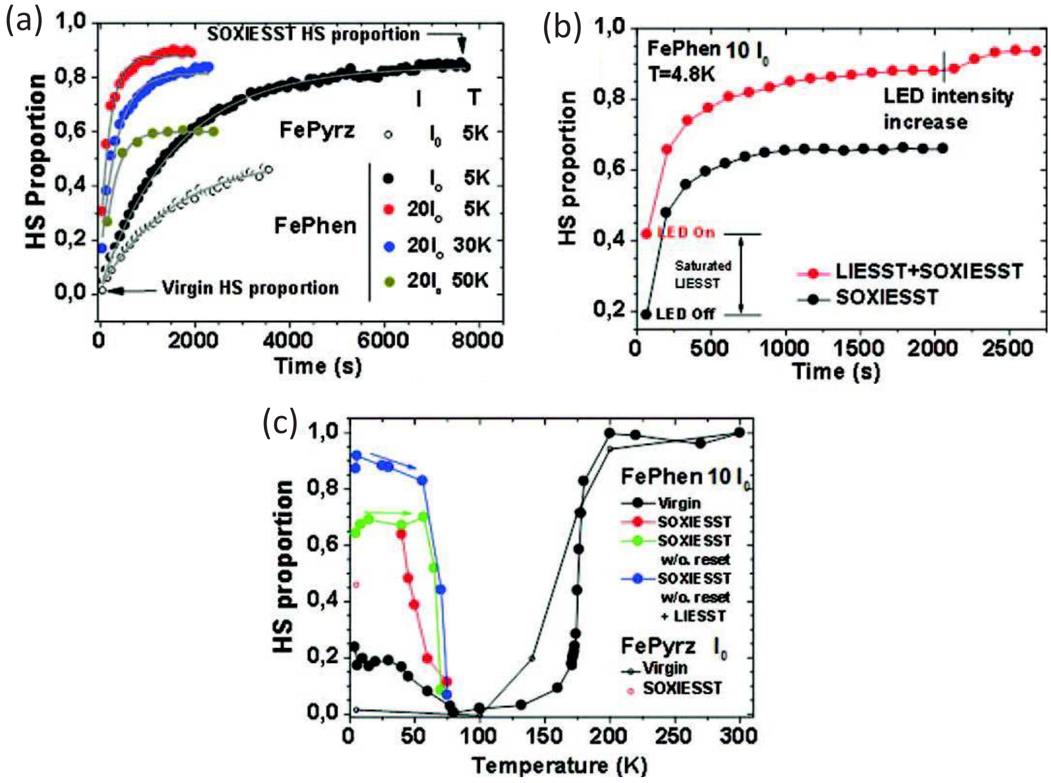

Figure 2.19: SOXIESST and LIESST effects dynamics in a sublimed Fephen film. (a) The evolution of the HS proportion upon the soft x-ray irradiation of the film. Note the dynamics dependence on the radiation intensity. (b) Comparison of the HS evolution dynamics of the SOXIESST, and combined SOXIESST and LIESST. (c) Temperature dependence of the two effects revealing a similar T_{SOXIESST} and T_{LIESST} critical temperatures. Figures taken from ref. 163.

Part II

Experimental methods

3

Ultra-high vacuum environment

In this part, we focus on the description of the experimental techniques used within the framework of this thesis both from its physical fundamentals and technical realization point of view. We start with an introduction to the ultra-high vacuum environment needed for a vast majority of the sample preparation and analysis presented in this manuscript as well as required by the experimental techniques described in the next chapters.

3.1 Introduction to vacuum technologies

The vacuum technology broadly understood as providing the environment of lowered pressure with respect to the atmosphere plays an indispensable role in nearly every nanotechnology laboratory. The main objective of the vacuum environment is to minimize the number of the particles in a given operational volume and therefore limit the amount of potential contaminants. That is necessary when one cares about the purity and cleanliness of the fabricated materials, structures, or interfaces. On the other hand, it is required for some technological processes and the surface sensitive studies. The scientific community working with the vacuum technologies use interchangeably the three units of pressure: $1\,\mathrm{mbar} = 100\,\mathrm{Pa} = 0.76\,\mathrm{Torr}$. Within this thesis, the millibar will be adopted.

To have a notion about the vacuum influence on the surface contamination one can use a measure of the time required for the formation of a single monolayer of adsorbed gas particles on a surface approximated as:[175]

$$t = \frac{3 \times 10^{-6}}{p} \tag{3.1}$$

where pressure p is expressed in millibars. At the atmospheric pressure ($p \sim 1013\,\mathrm{mbar}$) and at RT a surface is covered by a monolayer of contaminants after $\sim 3\,\mathrm{ns}$. That time is increased to $\sim 3\,\mathrm{ms}$ for $p = 10^{-3}\,\mathrm{mbar}$ and to $\sim 8\,\mathrm{h}$ for $p = 10^{-10}\,\mathrm{mbar}$. That underscores an absolute need of a vacuum environment for all the surface sensitive techniques such as scanning tunneling (electron) microscopy, electron diffraction, Auger electron spectroscopy, or photoelectron spectroscopy. That is also crucial for the studies of interfacial effects since an appearance of any contaminant in between the two materials during the fabrication process would shatter the emergence of desired phenomena. The reader will see later that vacuum is also necessary for the experiments involving the use of the soft x-ray photons.

The monolayer formation time from Eq. 3.1 is used to subdivide the vacuum into the commonly distinguished regimes listed in Tab. 3.1. Note that the indicated pressure ranges may differ between the sources and research domains. Sometimes additionally to the listed ones an extreme high vacuum is distinguished for pressures lower than $10^{-12}\,\mathrm{mbar}$.

The *in situ* sample preparations, surface morphology studies with STM, and the soft x-ray spectroscopy experiments described in this manuscript were conducted under the ultra-high vacuum conditions ($P = 10^{-8} - 10^{-10}\,\mathrm{mbar}$).

Table 3.1: Vacuum regimes. The list has arbitrary character and the pressure ranges can differ between the sources or research domains.

	Pressure [mbar]	Mean free path [cm]	ML formation [s]
Low vacuum (LV)	1013 – 1	$< 10^{-2}$	$< 10^{-5}$
Medium vacuum (MV)	1 – 10^{-3}	10^{-2} – 10	10^{-5} – 10^{-2}
High vacuum (HV)	10 – 10^{-5}	10^{3} – 10^{7}	10^{-2} – 100
Ultra-high vacuum (UHV)	$< 10^{-7}$	$> 10^{5}$	> 100

The standard laboratory-grade vacuum system is composed of a set of stainless steel chambers equipped with the vacuum pumps. The comprehensive list of the various available pumping systems can be found in ref. 176. Usually, the UHV conditions are obtained by a combination of primary, molecular, and ionic pumps. The first ones are commonly rotary pumps which provide a primary vacuum required for an operation of the turbo molecular pumps (TMP). These are kinetic pumps consisting of the alternating stator and rotor blades whose task is to transfer the gas particles from the inlet to the outlet. Alternatively, the ionic pumps (IP) based on a getter mechanism use a high voltage to ionize the gas particles and then accelerate them towards the getter material which traps the ions. The IPs are especially useful in the set-ups requiring a high mechanical stability, *e.g.*, STM systems, as these pumps are devoid of the rotating elements therefore they do not generate mechanical noise. On the other hand, the IP can not start operation at the atmospheric pressure and this is why it is complementarily used with a TMP.

We mentioned that some specific experimental techniques require a vacuum environment. These include the soft x-ray spectroscopy which will be described in detail in the next chapter. Let us now assume a monochromatic beam of the x-ray photons with energy $1\,\mathrm{keV}$ propagating in a dry air. The attenuation of the x-ray intensity due to the absorption and scattering events in medium can be expressed as: $I/I_\text{o} = \exp(-(\mu_\text{x}/\rho)d)$, where I_o is the initial intensity of the beam, μ_x the linear x-ray absorption coefficient, and ρ density of matter traversed by x-rays over a distance d. Now, by using a mass attenuation coefficient of $-3606 \times 10^3\,\text{g/cm}$ for 1 keV photons in dry air[177] of density $\rho = 1.2 \times 10^{-3}\,\text{g/cm}^3$ one finds a 90% intensity drop already after a distance of 5 mm. To increase it to 10 m one needs to reduce the pressure to 10^{-1} mbar. The vacuum has to be further improved if one wants to use the lower energy photons. In practice, to obtain a maximum signal intensity and provide a low-level contamination environment, the soft x-ray beamlines operate in the UHV regime.

3.2 Multi-Probe system

In this section we briefly describe the Multi-Probe (MP) system located at the IPCMS devoted to the fabrication of metal/organic nanostructures and their characterization by scanning probe microscopy. The set-up was used for the sample fabrication for exchange bias studies (Sec. 5.3), growth morphology investigations of the SCO materials (Sec. 7.2.4), and a casual surface characterizations.

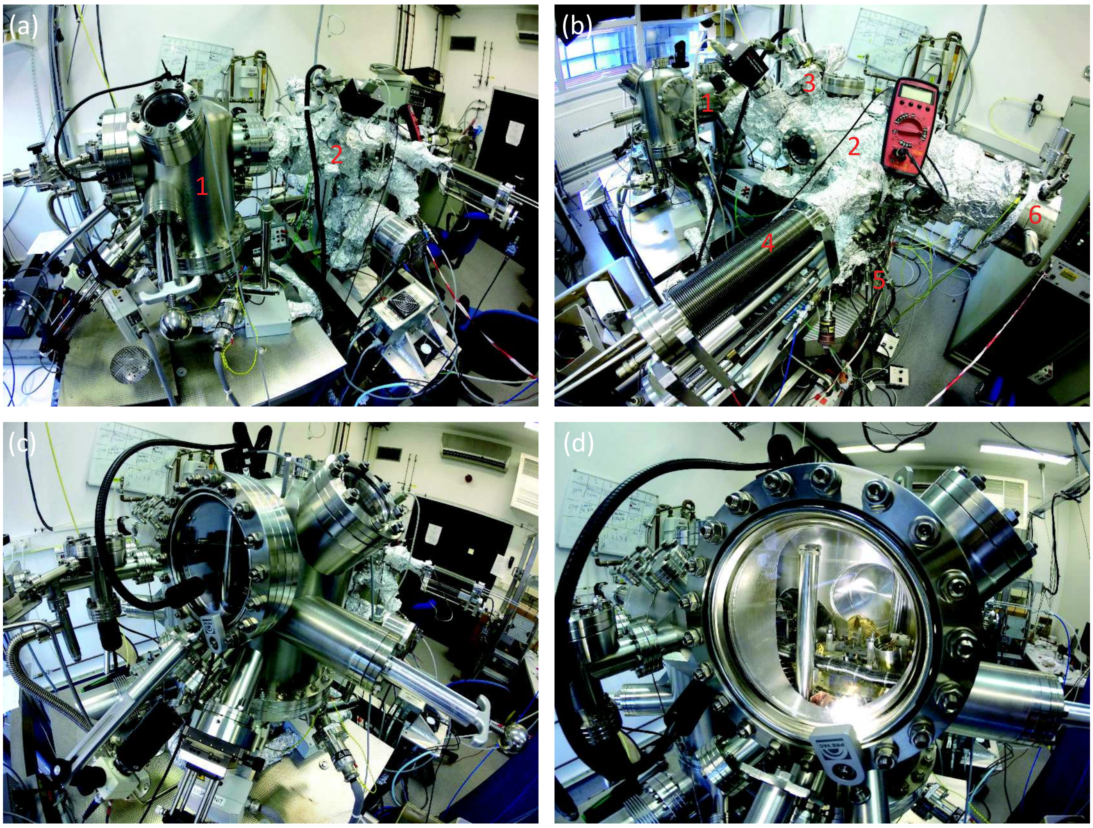

Figure 3.1: Multi-Probe system. (a)-(b) The Multi-Probe system consisting of (1) scanning probe microscopy chamber, and (2) preparation chamber. (c)-(d) The Omicron UHV variable temperature AFM XA station. 3 - Ar^+-ion sputtering gun, 4 - quartz microbalance, 5 - Tectra double e-beam evaporator, 6 - AES and LEED analyzer.

The Mutli-Probe is composed of two main vacuum segments: (1) scanning probe microscopy chamber, and (2) preparation chamber. Both are equipped with a separate set of primary pump, TMP, and IP generating a base pressure of $\sim 2 \times 10^{-10}$ mbar. The chamber (2) is dedicated to the surface/tip preparation and the fabrication of the samples. It is equipped with an Ar^+-ion sputtering gun, a substrate and tip annealing stage, mass spectrometer, Auger electron spectroscopy (AES) analyzer and a low energy electron diffraction (LEED) apparatus allowing the preparation of a clean atomically flat substrate and the later characterization of the fabricated structures. The organic materials can be thermally sublimated from two Knudsen cells, and metals deposited from Tectra double e-beam evaporator. The Omicron-based transfer system enables the relocation of the fabricated sample to the scanning probe microscopy chamber (Fig. 3.1 (a)(b), $(1) \leftrightarrow (2)$). It contains a commercial Omicron UHV variable temperature AFM XA microscope (Fig. 3.1 (c)(d)) for a surface morphology and spectroscopic studies in a temperature range $T = 50\,\mathrm{K} - 650\,\mathrm{K}$ in one of the following modes: (conductive) atomic force microscopy ((c)AFM), scanning tunneling microscopy (STM), piezoresponse force microscopy (PFM), Kelvin probe force microscopy (KPFM), QPlus. The switching between the operation modes is done by *in situ* replacement of the sensor and reconfiguration of the software.

The stage of the scanning probe microscope is suspended on the springs with the eddy current dumping system to minimize vibrations. In addition, both chambers of MP are equipped with pneumatic legs whose task is to lift the whole set-up during the measurement and decouple it from the environmental mechanical noise. During the measurement, the turbo molecular pumps are switched off and the vacuum is maintained by the ionic pumps. Within the framework of this thesis the STM and AFM modes of the microscope were used.

3.3 Hybrid system

The Hybrid system is a set-up located at the IPCMS and dedicated to fabrication and processing of the multilayered nanostructures. Its name stands behind a reach variety of available deposition techniques of organic and inorganic materials, which the system interconnects in an expanded UHV environment. We used the Hybrid set-up to fabricate the samples for studies of the magnetoelectric organic device (Sec. 6.2) and vertical spin crossover junctions (Sec. 7.3.2.3).

The Hybrid system consists of 5 connected vacuum chambers, each with a separate pumping system (Figure 3.2). The samples are introduced by a load-lock chamber (Fig. 3.2 (a)(2)) or alternatively through the glove box (Fig. 3.2 (a)(1)). The latter provides the neutral argon environment and allows such manipulations as sample annealing or spin-coating. Once the sample is introduced to vacuum, the robot arm is used for a transfer between four functional chambers.

The sputtering chamber (Fig. 3.2 (4)) is dedicated to deposition of metallic and isolating layers from three preselected magnetron targets. These include cobalt, iron, platinum, copper, chromium, magnesium oxide, and more. Manipulating the values of the argon flux and magnetrons' power allows precise control over the deposition rate and enables alloying of materials. Additionally, the chamber is equipped with the shadow mask arm for deposition of defined motifs. The advantage of the sputtering

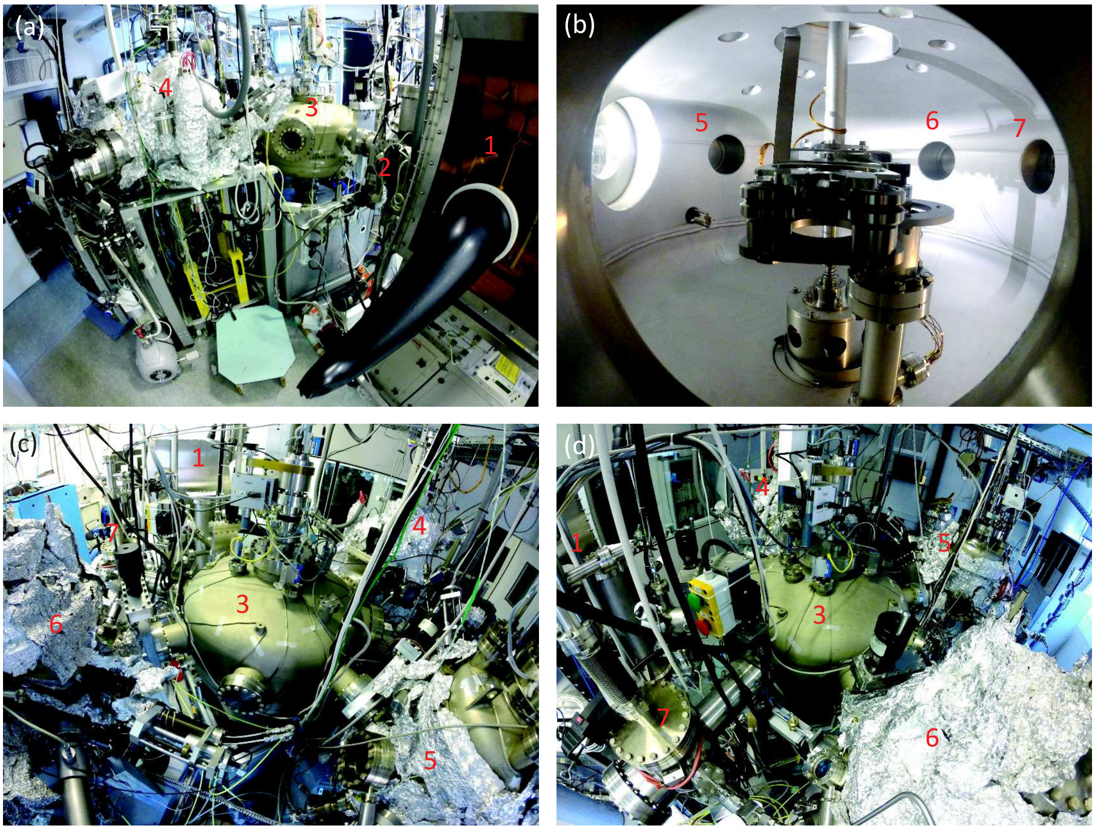

Figure 3.2: Hybrid system. (a) Side, and (c)-(d) top view pictures of the Hybrid system. (b) Inside of the robot chamber with a transfer arm and visible valve gates to the functional chambers. 1 - glove box, 2 - load-lock, 3 - robot, 4 - sputtering, 5 - evaporation, 6 - organic molecular beam epitaxy, and 7 - annealing chambers.

technique is a short preparation time of the process.

The evaporation chamber (Fig. 3.2 (5)) is equipped with effusion cells for thermal evaporation of metals. It can hold up to 3 independent cells. During the period of this thesis it was used for deposition of gold, iron, and cobalt. In addition, the sample cooling system allows reduction of the temperature down to $\sim 100\,\mathrm{K}$ by liquid nitrogen what is especially useful if one intends to avoid the interdiffusion of deposited metal into the previously prepared layers. The chamber is also provided with the shadow mask arm. In contrary to sputtering, the thermal evaporation requires a notable amount of time for gradual warming up of the cells before deposition but offers an excellent quality (smoothness) of fabricated films.

The organic molecular beam epitaxy chamber (OMBE) (Fig. 3.2 (6)) is dedicated solely to sublimation of the organic materials. It allows mounting of four independent Knudsen cells. The additional surface characterization technique is provided by RHEED (reflection high-energy electron diffraction) analyzer.

The annealing chamber (Fig. 3.2 (7)) is used as a sample preparation stage and a storing position. Independently, annealing is also possible in each of discussed above chambers by use of resistive ovens.

The Hybrid system is maintained under the high vacuum (load-lock, sputtering chamber) and ultra-high vacuum (OMBE, evaporation chamber, robot chamber). Each functional chamber allows a live control over deposited material thickness by dedicated quartz microbalance. All these together make the Hybrid set-up a versatile platform for fabrication of a complex inorganic/organic multilayered structures. The major advantage of the system is that the sample remains in at least high vacuum conditions between the consecutive deposition steps, what ensures the minimum contamination level and thus the excellent quality of the interfaces.

4

Synchrotron-based experiments

The following chapter is devoted to an introduction to synchrotron radiation and synchrotron-based techniques used in this thesis. We invoke the physical fundamentals of the x-ray absorption spectroscopy (XAS), x-ray magnetic circular dichroism (XMCD), and spin-resolved photoemission spectroscopy (SR-PES). We provide the technical specification of the DEIMOS and CASSIOPÉE beamlines of the French SOLEIL synchrotron on which these experiments were carried out. Finally, we describe the new electrical insert of the DEIMOS beamline developed during this thesis and the first combined *in operando* XAS and magnetotransport experiment on the MgO-based MTJs.

4.1 Introduction to synchrotron radiation

When a charged particle is accelerated along a circular trajectory it emits electromagnetic waves referred to as the synchrotron radiation. This statement being nowadays a common knowledge has its origin in a discovery of Wilhelm Röntgen who in 1895 demonstrated the generation of radiation by an electron-discharge tube.[178] In 1897 Joseph Larmor and Alfred Lienard showed that the total power of such emitted radiation by an accelerated electron is proportional to $(E/m_o c^2)^4/R^2$, where E is the electron kinetic energy, m_o its rest mass, and R the radius of the circular trajectory. Nearly 50 years later radiation from circulating electrons was accidentally observed in a betatron at the General Electric Research Laboratory in Schenectady.[179] This synchrotron radiation initially perceived as unwanted effect was rapidly recognized as of great potential for material science.[180]

The first synchrotron facility for outside users was open in 1961 in Washington, D.C.[181] Today, there are 47 facilities worldwide[182] providing a high brilliance radiation for a broad range of research domains and scientific activities. A synchrotron consists of the source of the electrons and the linear accelerator which supply the so called booster (Fig. 4.1 (a)(1)-(2)). A booster's task is to increase the electrons velocity to a nominal energy and inject them into a storage ring (Fig. 4.1 (a)(3)). The usual storage ring energy ranges from 0.18 GeV for the SURF synchrotron in Maryland (U.S.) to 12 GeV for the PETRA II in Hamburg (Germany). The electrons generate synchrotron radiation while traversing bending magnets or insertion devices (wigglers, undulators) located in the straight sections of the ring. This radiation directed into particular measurement stations, called the beamlines, is used as a probe of matter in various experimental techniques.

The relativistic velocity is a key feature of the circulating electrons and stands behind the predominance of the synchrotron-based techniques over the laboratory-grate experiments. Let us assume a fine beam of electrons traveling with a velocity close to the speed of light across an undulator which consists of an array of evenly spaced permanent magnets with alternating magnetization orientation (Fig. 4.1 (b)). The Lorentz force exerted on the electrons by the magnetic field bends their trajectory changing therefore the electrons' acceleration vector. This, in turn, leads to emission of the synchrotron radiation with a wavelength proportional to the undulator period λ_u. In the frame of reference associated with the relativistic electrons, λ_u is subjected to the Lorentz contraction such that $\lambda'_\mathrm{u} = \lambda_\mathrm{u}/\gamma(v)$, with $\gamma(v)$ as the Lorentz factor. Furthermore, the relativistic Doppler effect shifts the wavelength of the emitted light seen by a static observer as $\lambda' \sim \lambda/2\gamma(v)$. Eventually, the two effects lead to the emitted wavelength dependence on the undulator period as $\lambda \sim \lambda_\mathrm{u}/2\gamma(v)^2$. The Lorentz factor $\gamma_v = E/E_\mathrm{ro}$, where E is the storage ring energy and E_ro the electron rest energy, amounts to a level of thousands for the modern synchrotrons ($\gamma \sim 5380$ for SOLEIL). That makes a typical undulator with a period of a few centimeters to generate a radiation in the x-ray range. In addition, the relativistic electrons velocity causes the emission cone elongation to a fine directional shape of the aperture proportional to $1/\gamma(v)$.

All these effects result in a remarkably high brilliance defined as a flux of photons per unit solid angle corresponding to 0.1% of the bandwidth and reflecting the photons con-

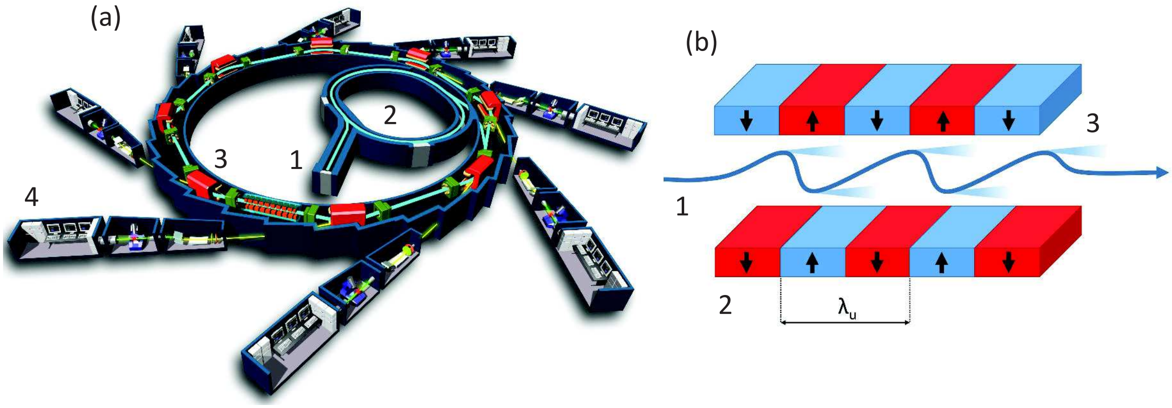

Figure 4.1: Synchrotron radiation. (a) Schematic illustration of a synchrotron facility with (1) the electron gun and linear accelerator, (2) the booster and (3) storage ring, (4) a beamline.[183] (b) A beam of electrons (1) traversing an array of magnets (2) in the undulator/wiggler of the period λ_u, generating the synchrotron radiation (3). The electrons oscillate in a horizontal plane.

centration. The third generation synchrotrons, *i.e.*, exploiting undulators as insertion devices, are characterized by brilliance of $10^{15} - 10^{21}$ photons/(s·mrad^2·mm^2·0.1%BW), what is far beyond the possibilities of any laboratory-grade source. In addition, a control over the magnetic field strength and the geometry of the array of magnets in the insertion device allows a precise tuning of the emitted radiation energy (Fig. 4.2), ranging from the infrared (0.01 eV) to the very hard x-rays (500 keV), as well as controlling the photons polarization state (both circular and linear).

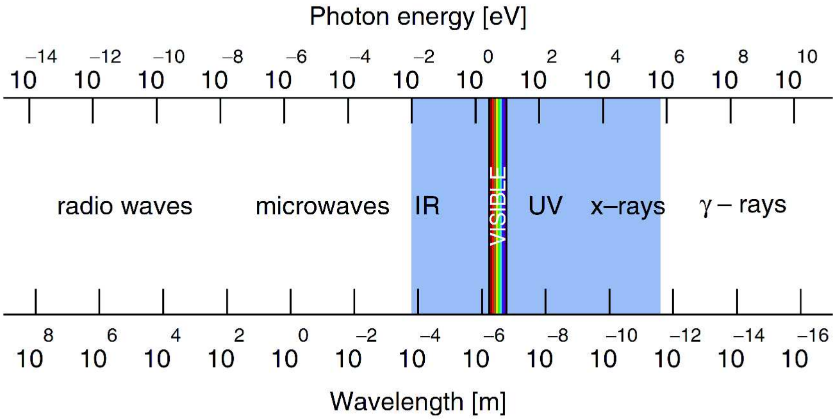

Figure 4.2: Tunability of the synchrotron radiation. The electromagnetic spectrum and the range of available radiation energies covered by the modern synchrotron sources (in grey). Figure taken from ref. 181.

To sum up, the synchrotron facilities offer an unprecedented light intensity with a widely tunable photon energy and a control over the light polarization. These along with a good source stability, possible small beam dimensions and a time-resolution stands behind the versatility of the synchrotrons for myriads of research domains. The synchrotron-based experiments presented in this manuscript were carried out at the French SOLEIL synchrotron located in Saint-Aubin. It is a 3rd generation source with a storage ring energy of 3 GeV. The experiments were conducted particularly on the DEIMOS and CASSIOPÉE beamlines.

4.2 X-ray absorption spectroscopy

When photons impinge the material they can be refracted, absorbed, or transmitted and depending on their energy the interaction with matter can be very different. Figure 4.3 presents a dependence of various processes' cross section, *i.e.*, a likelihood of a process to occur, as a function of the photon energy for the exemplary case of barium atom.

When the photon energy is greater than 1 MeV the most probable effect is the electron-positron pair generation or absorption by a nucleus.[184] While decreasing the photon energy one observes a rising probability for the Compton scattering, *i.e.*, inelastic scattering where part of the photon energy is transferred to an electron, and for Thomson scattering which is an elastic counterpart of the previous process. For even lower energies the dominant effect is the photoelectric absorption. This is essentially

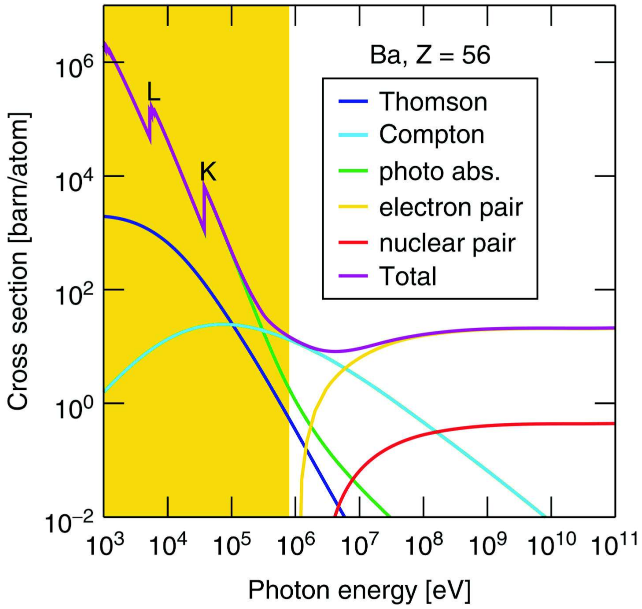

Figure 4.3: Interaction of photon with matter. The cross section dependence on the photon energy of various photon-matter interaction processes for an atom of barium. The yellow region corresponds to the energies covered by modern synchrotron facilities. Figure taken from ref. 181.

an absorption by the bound electrons of the atom and their removal from the shell. It is the most likely interaction between 350 eV and 100 keV,[184] that is for the photons in the x-ray range which are conventionally recognized as of energy from 100 eV to 100 keV. In the following we discuss in detail this particular process.

4.2.1 Photoelectric absorption cross section

The photoelectric absorption occurs if the photon energy is comparable to binding energy of the electron in an atomic shell. The energy of the photon is then transferred to the electron which is either ejected from the atom or placed in an empty state near the Fermi level. Therefore, the effect has a resonant character and results in a typical sawtooth absorption edges which are named as K, L_1, L_2, L_3, M_1, M_2, etc., and correspond to absorption of the electrons in the $1s$, $2s$, $2p_{1/2}$, $2p_{3/2}$, $3s$, $3p_{1/2}$ shell of the atom.

The probability of the photoelectric process can be expressed by corresponding cross section. This important quantity is a meeting point of the experiment and the theory of photon-matter interaction. Within the phenomenological picture it is straightforward to define the absorption cross section as the number of the absorption events per second (W) normalized by the photon flux (Φ_o):[185]

$$\sigma_\mathrm{a} = \frac{W}{\Phi_\mathrm{o}} \tag{4.1}$$

By employing the quantum mechanical treatment the number of absorption events W per unit time is given by the Fermi's Golden Rule:[186,187]

$$W = \int \frac{2\pi}{\hbar} |M_{if}|^2 \rho(E_f) \delta(E_f - E_i - \hbar\omega) \mathrm{d}E_f \tag{4.2}$$

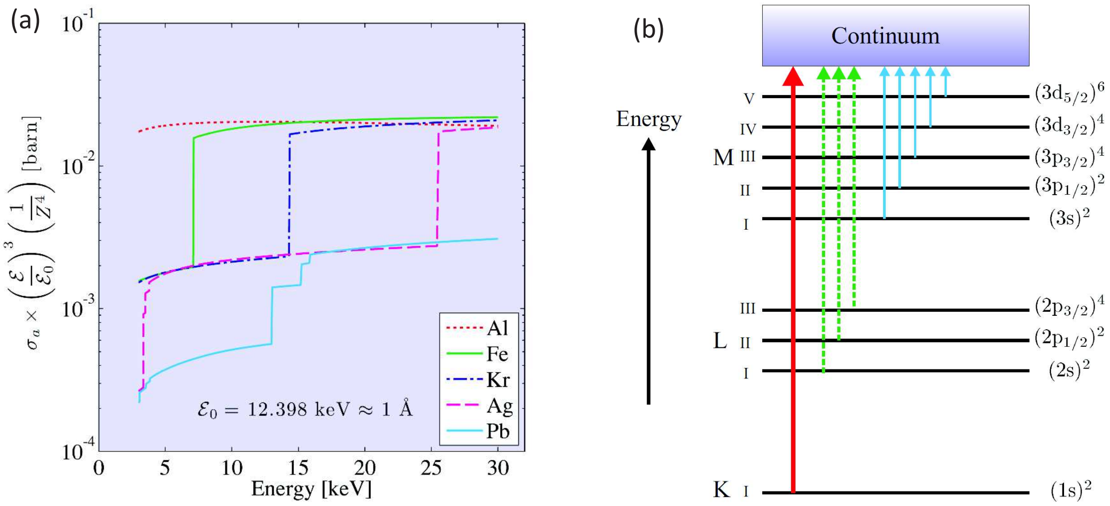

Figure 4.4: Photoelectric absorption of x-ray photons. (a) The scaled photoelectric absorption cross section dependence on the incident photon energy. The discontinuities correspond to the resonance with the electrons binding energy. (b) A schematic illustration of the photoelectric absorption on a given atomic shell giving rise to K, L, M absorption edges in the x-ray absorption spectra. The shells are labeled as $(nl_j)^{2j+1}$ where n, l, and j are the principal, orbital and total angular momentum quantum numbers respectively. Figure taken from ref. 181.

where $|M_{if}| = \langle f| H_{\mathrm{I}} |i\rangle$ is the matrix element describing a transition from the initial i to the final f state with the interaction Hamiltonian H_{I}, $\hbar\omega$ is the photon energy, $\rho(E_f)$ the density of the final states, and the Dirac delta function δ keeps the energy conservation valid. The interaction Hamiltonian can be expressed as a sum of two terms:[185]

$$H_{\mathrm{I}} = H_{\mathrm{I1}} + H_{\mathrm{I2}} = \frac{e}{m_{\mathrm{e}}}\boldsymbol{p} \cdot \boldsymbol{A} + \frac{e^2}{2m_{\mathrm{e}}}\boldsymbol{A^2} \tag{4.3}$$

with e and m_{e} as the electron charge and mass, $\boldsymbol{p}$ the electron momentum operator, and $\boldsymbol{A}$ the vector potential of the incident photon field. The linear term H_{I1} corresponds to a first-order transition such as the x-ray absorption or photoemission process, meanwhile H_{I2} describes the scattering and diffraction. Since we will employ only XAS and PES techniques we focus exclusively on the first-order perturbation with the interaction Hamiltonian described as H_{I1} in Eq. 4.3. We can expand the term H_{I1} as:

$$H_{\mathrm{I1}} = \frac{e}{m_{\mathrm{e}}}\boldsymbol{p} \cdot \boldsymbol{A} = \boldsymbol{p} \cdot \boldsymbol{e}_\lambda (1 + i\boldsymbol{k} \cdot \boldsymbol{r} - \frac{1}{2}(\boldsymbol{k} \cdot \boldsymbol{r})^2 + ...)e^{-i\omega t} \tag{4.4}$$

where $\boldsymbol{e_\lambda}$ is the polarization vector of the photon and $\boldsymbol{r}$ the position operator. By using the commutation relation:

$$\boldsymbol{p} \cdot \boldsymbol{e_\lambda} = \frac{m_{\mathrm{e}}}{ih}[\boldsymbol{e}_\lambda \cdot \boldsymbol{r}, H_i] \tag{4.5}$$

and limiting ourselves to the first order of the expansion 4.4 we obtain the expression for the dipolar cross section in the following form:

$$\sigma_{\mathrm{a}}(\omega) = 2\pi^2 \alpha\hbar\omega \langle i| \boldsymbol{e_\lambda} \cdot \boldsymbol{r} |f\rangle^2 \delta(\hbar\omega - E_f + E_i)\rho_f(E_f) \tag{4.6}$$

where $\alpha = \frac{e^2}{4\pi\epsilon_o\hbar c}$ is a fine structure constant. The derived equation reflects the photoabsorption probability per unit time and unit area as a function of the photon energy. The SI unit of the cross section is area (m^2) sometimes expressed in barns ($10^{-28}\,m^2$).

In Figure 4.4 (a) we show the scaled cross section dependence on the incident photon energy for selected elements. The curves discontinuities at certain element-specific thresholds reflect the particular absorption edges and result from a unique set of the binding energies for the electron shells in a given element. Until the photon energy is lower than a binding energy of the electron, the absorption probability stays low. Once this binding energy is reached the cross section discretely increases implying thus the enlarged probability of the transition. This cross section dependence on both photon energy and atomic number stays behind the principal advantage of the x-ray absorption, namely its chemical selectivity.

The photoelectric absorption cross section scales with the photon energy as $1/E^3$ what on a linear plot is reflected as a characteristic decrease of the intensity in the post-edge region (Fig. 4.5 (b)). In turn, the cross section increases rapidly with the atomic number, that is as Z^4. These two dependencies together are visualized in Fig. 4.4 (a) where the cross section normalized by factor $\sim Z^4/E^3$ appears as nearly constant. Note that for the photon energies below 5 keV one observes a deviation from this behavior: the cross sections evolves as $\sim Z^5/E$.[181, 188]

The sharp absorption edges as they appear on log-log scale (Fig. 4.5 (a)) are typical for isolated atoms in, *e.g.*, gas phase. When the atoms are interacting (liquids, molecules, solids) the edges manifest a more complicated structure often accompanied by many closely appearing peaks, so-called multiplet structure. The example is provided in Fig. 4.6 where the same krypton atoms exhibit a K-edge with more features in the monocrystal than in the gas phase. These features result from the local electronic structure of absorbing atoms, their symmetry and the interaction with the environment. The region of the edge proximity extending over about 50 eV is referred

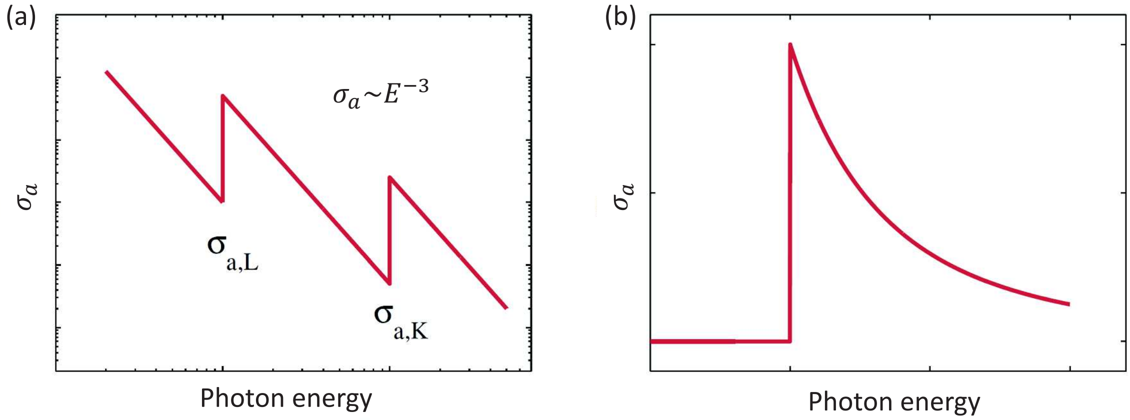

Figure 4.5: Photoelectric absorption cross section dependence on photon energy. (a) Double logarithmic plot of the photoelectric absorption cross section as a function of the photon energy emphasizing the appearance of a sharp L and K edges and an inverse cube dependence on the energy between the edges. (b) Linear plot of the same dependence showing a characteristic decrease after the absorption edge. Figure taken from ref. 181.

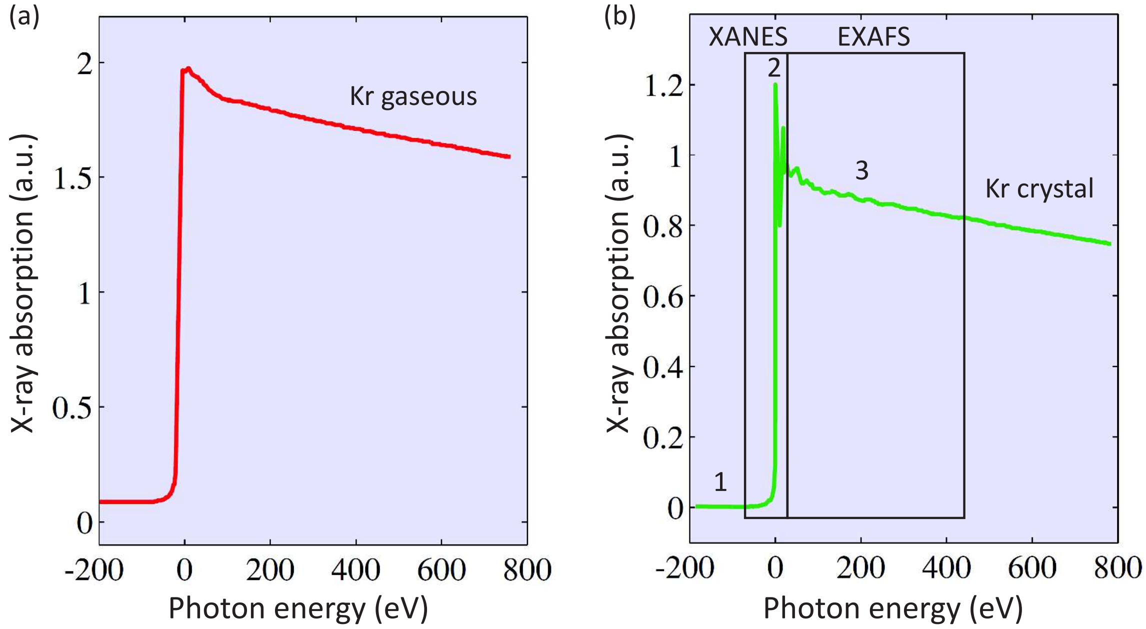

Figure 4.6: X-ray *K*-edge absorption spectra of krypton. The absorption at *K*-edge of Kr in (a) gas phase, and (b) crystalline form. Three regions of the edge correspond to situation where (1) the photons energy is below the electrons ionization potential, (2) the electrons are resonantly excited to unoccupied states near the Fermi level, and (3) the photon energy is large enough to eject the electrons away from the atom. The *K* absorption edge of the crystal exhibits the multiplet features in the x-ray absorption near edge structure (XANES) region and the oscillations in the extended x-ray absorption fine structure (EXAFS) region. Figure taken from ref. 181.

to as x-ray absorption near edge structure (XANES) or near edge x-ray absorption fine structure (NEXAFS). It may provide a useful information in studies of a different oxidation states or symmetry system of an element.[189, 190] In turn, the region of 50 eV – 1000 eV above the edge is called the extended x-ray absorption fine structure (EXAFS) and reflects the long-range ordering in the material. The oscillations present in this energy range are related to the interatomic distances and the coordination number.[191]

Now, based on the example of a crystalline krypton from Fig. 4.6 (b) we can distinguish three regions of every absorption edge. At the pre-edge region (1), the photons energy is too low to excite the electrons. At certain threshold (2), the energy is sufficient to promote core electrons to the unoccupied states near the Fermi level. This is reflected by the rapid increase of the absorption often accompanied by an ”overshot” resonance from the standard step-like behavior. The particular edge shape in this region provides the information about the electronic structure of the material. At greater photons energies the electrons are ejected from the atom to the continuum of states (3) and the interfering wave functions of the escaping electrons reflected in the EXAFS oscillations give the information about the long-range ordering in the material.

The x-ray absorption spectroscopy (XAS), by recording the absorption as a function of the photon energy at a given edge, is a powerful tool providing an insight into material’s electronic structure and its environment. The energy positions of the absorption edges which are unique for each element stand behind the chemical selectivity of XAS and allow the studies of the correlations in the complex systems. Finally, the great brilliance of the modern synchrotron sources gives a remarkably high signal to noise ratio enabling recording the absorption spectra of a very small amount of matter (submonolayers) or strongly diluted systems.

4.2.2 X-ray attenuation

The x-ray photons while crossing the material can be absorbed what leads to beam intensity attenuation as depicted in Figure 4.7. This intensity attenuation can be expressed as:

$$I(d) = I_{\mathrm{o}} e^{-\mu_{\mathrm{x}} d} \tag{4.7}$$

where I_{o} is the initial intensity of the incident photon beam, d the distance traveled in the material, and μ_{x} the linear absorption coefficient. The latter can be related to the absorption cross section in a following way:

$$\mu_{\mathrm{x}} = \rho_{\mathrm{a}} \sigma_{\mathrm{a}} = \frac{N_{\mathrm{A}}}{A} \rho_{\mathrm{m}} \sigma_{\mathrm{a}} \tag{4.8}$$

with ρ_{a} as the atomic number density (atoms/volume), ρ_{m} the atomic mass density (mass/volume), N_{A} the Avogadro's number, and A the atomic mass number (mass/mol). It is convenient to use the so-called mass attenuation coefficient $\mu = \mu_{\mathrm{x}}/\rho$ which by definition is independent of material density thus of its phase. The experimental values of the mass coefficient for various materials as provided by the National Institute of Standard Technology can be found in ref. 177 and elsewhere.[192,193]

The x-ray attenuation length, defined as the inverse of the linear absorption coefficient, $\lambda_{\mathrm{x}} = 1/\mu$, is one of the limiting factors in the synchrotron-grade experiments especially for a strongly attenuated soft x-rays photons. One therefore needs to carefully design the architecture of the studied sample so as to ascertain a sufficiently large

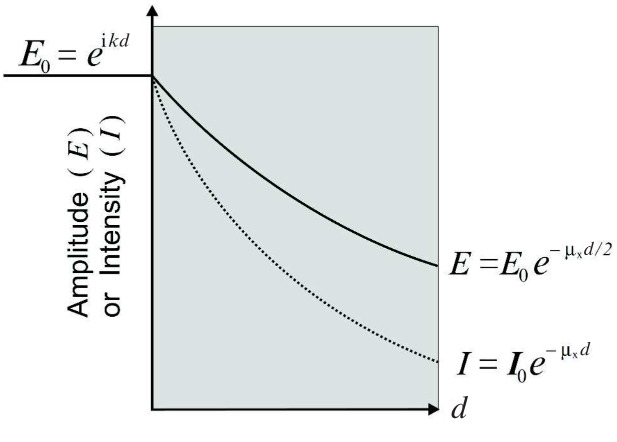

Figure 4.7: Attenuation of x-ray photons. The x-ray beam with the initial amplitude E_{o} (intensity I_{o}) when traversing the matter exponentially attenuates as $E = E_{\mathrm{o}} e^{-\mu_{\mathrm{x}} d/2}$ ($I = I_{\mathrm{o}} e^{-\mu_{\mathrm{x}} d}$) due to the absorption events, where μ_{x} is the linear absorption coefficient and d the distance traveled in material. Figure taken from ref. 194.

signal intensity at buried layers. Very helpful in this respect are available x-ray attenuation calculators providing information about the attenuation length for the specific materials within a given photon energy range.[195,196]

The reader will see in the next section that in the soft x-ray range the attenuation of the x-ray photons is usually overshadowed by the probing depth associated with adopted absorption detection method.

4.2.3 Detection methods of the x-ray absorption

We referred to an absorption event by its cross section reflecting the transition probability. Since it is often impossible to experimentally measure its value one needs to resort to indirect methods. We can distinguish three main x-ray absorption detection techniques: (1) transmission, (2) total electron yield (TEY), and (3) total fluorescence yield (TFY). In the following we discuss these methods by limiting ourselves exclusively to the absorption of photons in the soft x-ray energy range.

The most direct method to record the x-ray absorption as a function of the incident photon energy is to measure the initial intensity of the beam and relate it to the intensity after it passes across the material. That is referred to as transmission mode which may provide the information about the cross section according to Eq. 4.7. The transmission detection requires at least partially transparent samples what is in general hard to achieve due to the strongly attenuated soft x-ray photons. That is why this technique is rather seldom used in the soft x-ray spectroscopy, yet was employed in numerous pioneer works.[197]

The indirect detection methods (2) and (3) are interchangeably employed according to, as the reader will see later, its associated limits and assets. For the further discussion, we need to introduce the two main scenario following the atom excitation by the soft x-ray photon. We stated before that when the photon has sufficient energy it may promote the core electron to the empty state near the Fermi level (Fig. 4.8 (a)) or eject the electron out of the atom. This absorption process occurs usually in a timescale shorter than 10^{-20} s. The atom remains with the core hole of a typical lifetime $10^{-15} - 10^{-16}$ s which eventually needs to be filled. The relaxation can follow along two main pathways. The first scenario is a radiative recombination onto the empty inner state accompanied by the emission of a photon (Fig. 4.8 (b)). The second process is a non-radiative relaxation with emission of a so-called Auger electron (Fig. 4.8 (c)) which causes the cascade emission of secondary electrons. These when located sufficiently close to the surface may leave the sample.

Therefore, the first relaxation channel is associated with the emission of photons and the second of electrons. The number of those photons/electrons is indirectly proportional to the amount of the absorption events thus to cross section. By placing a photodiode in the vicinity of the studied sample one can collect the emitted photons and obtain the so-called total fluorescence yield signal (TFY). On the other hand, the photoelectrons emitted from the sample can be collected either by a detector, yet this limits the acceptance to a narrow solid angle, or in more universal approach by measuring the current from the ground to the sample. The latter neutralizes the system after the photoemission thus takes into account all the charges which left the sample. This is referred to as total electron yield mode (TEY).

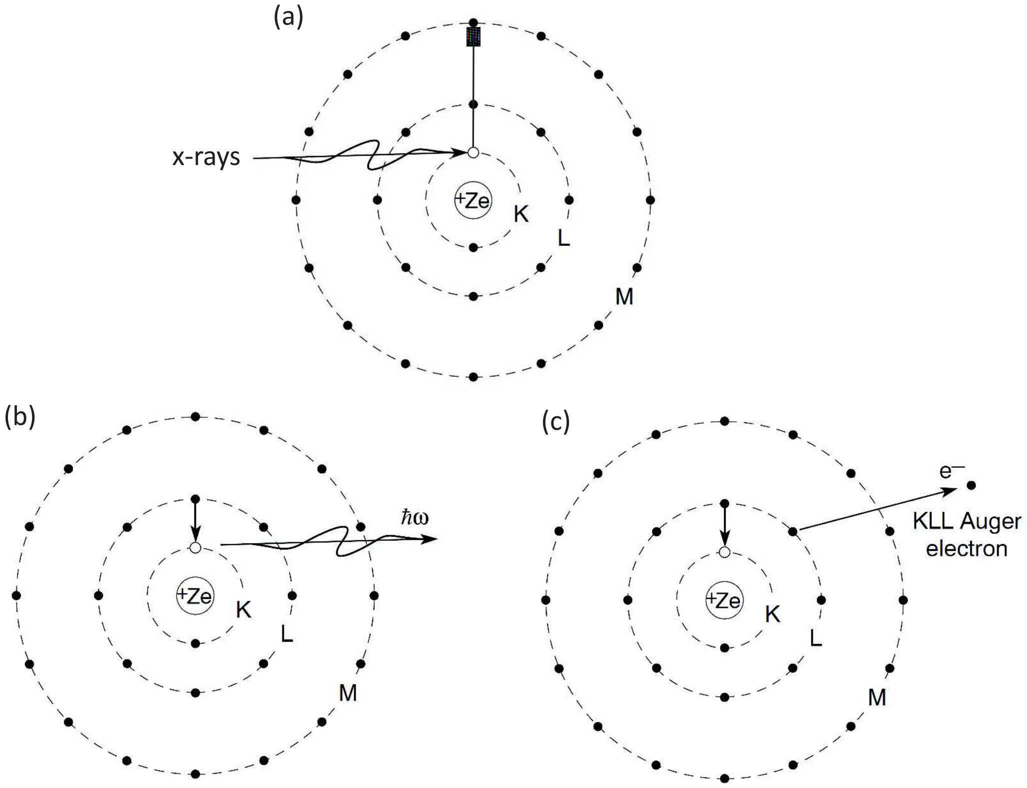

Figure 4.8: Excitation and relaxation channels of an atom interacting with the x-ray photon. (a) X-ray photon of sufficient energy promotes the core electron to an empty state near the Fermi level. The resulting core hole with a lifetime of $10^{-15} - 10^{-16}$ s can be filled via (b) a radiative recombination with emission of a photon, or (c) an Auger process accompanied by emission of a photoelectron. Figure taken from ref. 198.

The TEY method is very practical since it requires only a sensitive amperemeter connected between the ground and the sample. Note however that the TEY signal can be detected only if the electrons leave the sample. This is fulfilled when the electron inelastic mean free path is shorter than its distance to the surface and if its kinetic energy is large enough to overcome the solid/vacuum interface potential. Otherwise, the excited electron is scattered and eventually loses its energy required to escape from the sample. In practice, this limits the effective probing depth with TEY to only a few nanometers what is much shorter than the x-ray penetration depth resulting from previously discussed beam attenuation. This is highlighted in Figure 4.9 presenting the inelastic mean free path of the electron as a function of its energy. Although strictly speaking one should consider rather the escape depth which accounts only for those charges which have sufficient energy to overcome the surface potential, the mean free path may be used to give an idea about the probing depth, which for the soft x-ray photons (100 eV – 10 keV) is in the range of several nanometers. That is why TEY is considered as a surface sensitive detection. However, in extreme cases of thick samples and grazing incidence measurements, the TEY probing depth can be comparable or larger than the x-ray attenuation length. This leads to so-called saturation effects

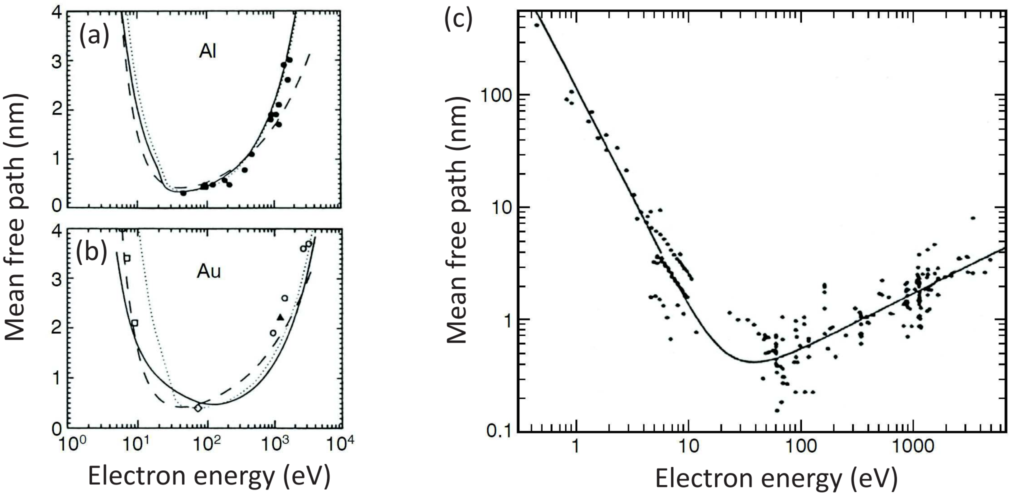

Figure 4.9: Mean free path of electrons in solid. Inelastic mean free path in (a) Al, or (b) Au as a function of electron energy, and (c) universal curve highlighting a limited probing depth of the total electron yield detection for the x-ray absorption in the soft x-ray range (100 eV – 10 keV). Figure taken from ref. 198.

which cause in general the underestimation of the edge intensities and can be a serious obstacle in quantitative analysis of the XAS spectra.[199, 200]

The TFY detection is often employed in-parallel and complementarily to TEY. Contrary to electron detection, the emitted photons are not scattered on their way toward the surface and this is why the effective probing depth of TFY is much greater than of TEY. The fluorescence detection is thus often considered as bulk sensitive. However, it is limited by the self-absorption process which occurs when the photon emitted in radiative relaxation is reabsorbed by another atom.[201–203] This, similarly to the saturation effect for TEY, underestimates the intensity of the recorded spectra.

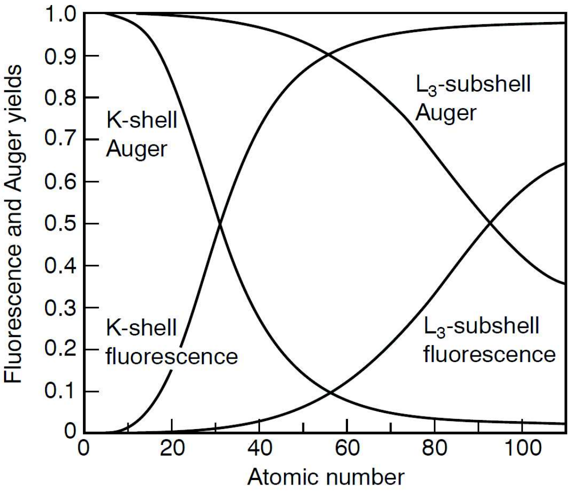

Figure 4.10: TEY and TFY dependence on the atomic number. The yields of the fluorescent and Auger relaxation as a function of the atomic number Z for the K- and L_3-edge. Figure taken from ref. 198.

Therefore, one easily sees that both TEY and TFY have advantages and drawbacks and in certain conditions one of the two modes can be more efficient than the other. Despite discussed experimental issues the effectiveness of the two relaxation channels is also dependent on the atomic number Z and the absorption edge.[204] This is illustrated in Fig. 4.10 as the TFY and TEY contributions at K-edge and L_3-edge with varying Z. For the light elements ($Z < 20$) the K-edge gives much stronger signal in TEY channel than in TFY, what is reversed for the heavier atoms ($Z > 20$). The TEY and TFY contributions at L_3-edge show a similar dependence, yet with the dominating TEY up to atomic number $Z = 87$.

4.3 X-ray magnetic circular dichroism

We described in the previous sections how XAS can be employed to probe the electronic structure of materials. Now, we focus on magnetic properties which can be extracted from the x-ray magnetic circular dichroism (XMCD). The term dichroism originates from the classical optics and refers to a peculiar ability of the matter to differently interact (absorb, scatter, reflect, etc.) with light of different characteristics (wavelength, polarization, etc.). The dichroism in the x-ray energy spectrum means essentially a distinct absorption cross section for the photons of different polarization state.

The x-ray magnetic circular dichroism employs the fact that the magnetic materials may differently absorb the x-ray photons with the opposite circular polarization. We define the right (left) circular polarization as the one associated with helical clockwise (anticlockwise) rotating electric field vector around the propagation direction $\boldsymbol{k}$, by looking into the oncoming wave (towards the source).[205] We will refer to these polarization states as CL and CR associated with the absorption coefficients μ^+ and μ^-. The XMCD is conventionally defined as the difference of the XAS spectra acquired with the CL and CR polarized photons.

To properly understand the mechanism behind XMCD one has to consider a two step process: (i) the absorption of the oppositely CL/CR polarized photons by the core electrons, and (ii) transition of these electrons to the unoccupied valence states near the Fermi level. In the following section, we provide an intuitive explanation of these processes.

4.3.1 Dipole selection rules

By equation 4.6 we expressed the photoelectric absorption cross section with a matrix element $\langle i | \boldsymbol{e_\lambda} \cdot \boldsymbol{r} | f \rangle$ for the transition from initial i to final f state. The $\boldsymbol{e_\lambda} \cdot \boldsymbol{r}$ is the electric dipole operator which imposes the so-called selection rules giving a non-zero transition probability only if:

$$\Delta l = \pm 1 \qquad \Delta j = 0, \pm 1 \qquad \Delta m_j = \pm 1, 0 \qquad \Delta s = 0 \tag{4.9}$$

These are referred to as dipolar selection rules. The orbital quantum number rule $\Delta l = \pm 1$ emerges from the spherical harmonics parity and forbids the transition within the same subshell of the atom, *e.g.*, $2s \rightarrow 2p$. The spin flip during the transition is forbidden by $\Delta s = 0$. These yield the total angular quantum number selection rule

$\Delta j = \Delta(s+l) = 0, \pm 1$. Finally, the incident photon angular momentum conservation is reflected by $\Delta m_j = \pm 1, 0$. It arises from the fact that the circular photons carry the angular momentum of $-\hbar$ ($+\hbar$) for CL (CR) polarization as the eigenvalue of the angular momentum operator J_z which has to be conserved. This means that the momentum of the electron must increase (decrease) by $\hbar$ ($-\hbar$) upon absorption of the photon with the CR (CL) polarization or remain constant ($\Delta m_j = 0$) if the photon polarization is linear.[198] The electric dipole selection rules listed in Eq. 4.9 are denoted for the states in spin-orbit basis functions as $|R_{n,l}(r); l, s, j, m_j\rangle$ where $R_{n,l}$ is the radial part of a spherical harmonic. A complete derivation of the dipole selection rules can be found in ref. 190.

In the following, we provide an illustrative explanation on how the rules from Eq. 4.9 lead to the different absorption of the CL and CR polarized x-ray photons. Figure 4.11 presents the results of the calculations for case of a transition metal and the absorption at its $L_{3,2}$-edges, *i.e.*, $2p \rightarrow 3d$ transitions. The one-electron picture was employed with the wave functions of hydrogen atoms and the quantization axis along the z direction. The $3d$ orbitals of a transition metal in cubic symmetry were considered with the inclusion of the exchange splitting, the fully occupied spin-down ($m_\mathrm{s} = -1/2$), and partially occupied spin-up states ($m_\mathrm{s} = +1/2$). The $2p$ orbitals degeneracy is lifted by the spin-orbit coupling into $2p_{j=3/2}$ and $2p_{j=1/2}$ giving rise to the L_3 and L_2 edges respectively. The quantization axis z is parallel to the $\boldsymbol{k}$ vector of light.[206] The photon angular momentum is denoted as $q = +1$ ($q = -1$) in $\hbar$ units for

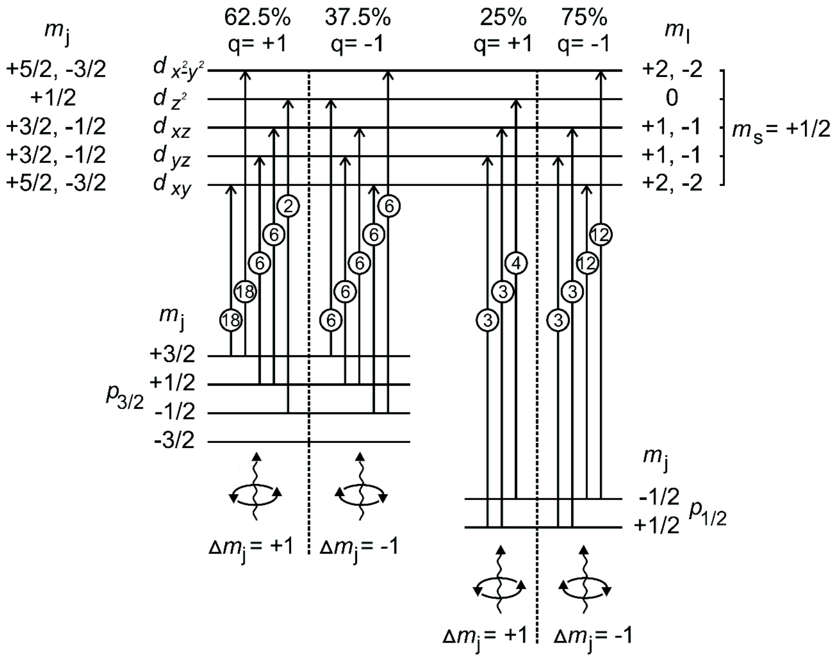

Figure 4.11: Origin of XMCD at the $L_{3,2}$-edges of a transition metal. Calculation of the transition probability from a $3d$ metal spin-orbit splitted $2p$ states to the exchange splitted $3d$ valence states with completely filled spin-down ($m_\mathrm{s} = -1/2$) and partially filled spin-up states ($m_\mathrm{s} = +1/2$). The absorption of the CR (CL) photons promote 62.5% (37.5%) of the spin-up electrons at L_3-edge and 25% (75%) of the spin-up electrons at L_2-edge. Figure taken from ref. 206.

the CL (CR) polarization.

In the first phase of the absorption process, the photons partially transfer its angular momentum to the electrons' spin through the spin-orbit coupling. This generates the spin-polarization of the excited photoelectrons correspondingly with the opposite sign for the CL and CR polarized photons. Due to the opposite spin-orbit coupling at the L_3 $(l + s)$ and the L_2 $(l - s)$ edges the arising spin polarization is also opposite in sign. The spin polarization axis stays along the direction of the photon propagation direction $\boldsymbol{k}$.

In the second phase, the exchange splitted valence bands act as the detector of the spin-polarized photoelectrons obeying the selection rules. That is why the signal is further proportional to number of the empty states in the $3d$ orbitals. Therefore, as illustrated in Fig. 4.11 the CR (CL) photons excite 62.5% (37.5%) of the spin-up photoelectrons at L_3-edge and 25% (75%) at L_2-edge. By generalizing this case to the partially filled both spin-up and spin-down channels one obtains the imbalance between the number of the absorption events provoked by CR and CL polarized x-ray photons, which reflects in turn the unequal population of the spin-up and spin-down electrons in the $3d$ states at the Fermi level. This finally provides the information about the magnetic properties of the material. Note that if absorption of CL and CR photons is equal, the XMCD vanishes. It is important to notice that the photon angular momentum $\pm\hbar$ is not purely converted into electron spin. Part of it may be transferred to the electron orbital momentum. This can be also an important quantity detected by the valence shells if one finds the non-zero orbital magnetic moment of the latter (unequal density of states for m_l and $-m_l$ quantum numbers). Eventually, the XMCD signal is proportional to the magnetization $\langle M \rangle$ along the propagation $\boldsymbol{k}$ vector. That makes the XMCD technique suitable for studying ferro- or ferrimagnets and paramagnetic materials. Note that the antiferromagnetism can not be resolved by XMCD ($\langle M \rangle = 0$).

In Fig. 4.12 we present the exemplary XAS and XMCD spectra acquired at the $L_{3,2}$-edges of iron. The two circular light polarizations, denoted as μ^+ and μ^-, give rise to x-ray absorption intensity higher (lower) for μ^- (μ^+) at the L_3-edge and inversely at the L_2-edge (Fig. 4.12 (a)). That results in a typical XMCD signal for a transition metal with negative (positive) sign at the L_3-edge (L_2-edge) (Fig. 4.12 (b)). Note that in the previous discussion we considered XMCD as calculated from two XAS spectra acquired with the opposite x-ray photon helicities and fixed magnetic field. In practice, we sequentially reverse both the photons polarization and direction of the field, such that $\mu^+(+H) = \mu^-(-H)$, so as to reduce the impact of instrumental errors.

In the next section, we introduce the so-called sum rules which allow to extract the orbital and spin magnetic moment of the probed element from the XMCD spectra.

4.3.2 Sum rules

We use the example from Fig. 4.12 to introduce the sum rules for a $3d$ metal relating the integrals of the dichroism at the $L_{3,2}$-edges to the magnetic spin and orbital moments. Since there are many equivalent notations of the sum rules we employ the one proposed by Chen *et al.*[197] The complete derivation can be found in ref. 207, 208. We will denote the absorption coefficients μ^+ and μ^- as corresponding to the CL and CR polarized photons respectively, and assume the x-ray propagation vector $\boldsymbol{k}$ parallel to the magnetization direction. As the state of the art, the sum rules require three spectra to be recorded: μ^+, μ^-, and μ^o, where the latter corresponds to the linear x-ray polarization. Then, one can define the so called white line, *i.e.*, the overall XAS intensity across the edge as $(\mu^+ + \mu^- + \mu^{\text{o}})$. The μ^{o} is usually approximated as $\mu^{\text{o}} = (\mu^+ + \mu^-)/2$ allowing to express the white line as $3/2(\mu^+ + \mu^-)$. Within this picture the sum rules for the $L_{3,2}$-edges can be formulated as the following:

$$m_{\text{orb}} = -\frac{4\int_{L_3+L_2}(\mu^+ - \mu^-)\mathrm{d}E}{3\int_{L_3+L_2}(\mu^+ + \mu^-)\mathrm{d}E}(10 - n_{3d}) \tag{4.10}$$

$$m_{\text{spin}} = \frac{6\int_{L_3}(\mu^+ - \mu^-)\mathrm{d}E - 4\int_{L_3+L_2}(\mu^+ - \mu^-)\mathrm{d}E}{\int_{L_3+L_2}(\mu^+ + \mu^-)\mathrm{d}E}(10 - n_{3d})\left(1 + \frac{7\langle T_z\rangle}{2\langle S_z\rangle}\right)^{-1} \tag{4.11}$$

where m_{orb} and m_{spin} stand for the orbital and spin magnetic moment respectively (in units of μ_{B} per atom), n_{3d} is the number of electrons in the $3d$ shells, $\langle T_z\rangle$ the expectation value of the magnetic dipole operator, and $\langle S_z\rangle$ the expectation value of the z-component of the spin equal half of m_{spin} in Hartree units. The term $\langle T_z\rangle/\langle S_z\rangle$ was shown by first-principle calculations to be in general negligible in case of $3d$ metals (-0.38% for *bcc* Fe, -0.26% for *hcp* Co).[209,210] This was later reported to be non-valid for $3d$ metals in symmetry other than cubic and close to the surface or interface region where strongly distorted sites may rise a significant contribution to $\langle T_z\rangle$[211] due to anisotropy of charge distribution. Stöhr and König proposed a method for canceling the term $\langle T_z\rangle$ in non-cubic $3d$ systems by performing three XMCD measurements along orthogonal directions with assumption that the magnetic anisotropy of the material is small.[212]

The integrals from Eq. 4.10 and 4.11 over the corresponding $L_{3,2}$-edges can be denoted as presented in Fig. 4.12 (b) and (c):

$$p = \int_{L_3}(\mu^+ - \mu^-)\mathrm{d}E \tag{4.12}$$

$$q = \int_{L_3+L_2}(\mu^+ - \mu^-)\mathrm{d}E \tag{4.13}$$

$$r = \int_{L_3+L_2}(\mu^+ + \mu^-)\mathrm{d}E \tag{4.14}$$

In that way, one obtains a simplified form of the sum rules for the $L_{3,2}$-edges of a transition metal in form:

$$m_{\text{orb}} = -\frac{4q(10 - n_{3d})}{r} \quad [\mu_{\text{B}}/atom] \tag{4.15}$$

$$m_{\text{spin}} = \frac{(6p - 4q)(10 - n_{3d})}{r} \quad [\mu_{\text{B}}/atom] \tag{4.16}$$

The above expressions assume the saturation of the material's magnetization, completely circular polarization of the x-ray photons, and magnetization vector parallel to

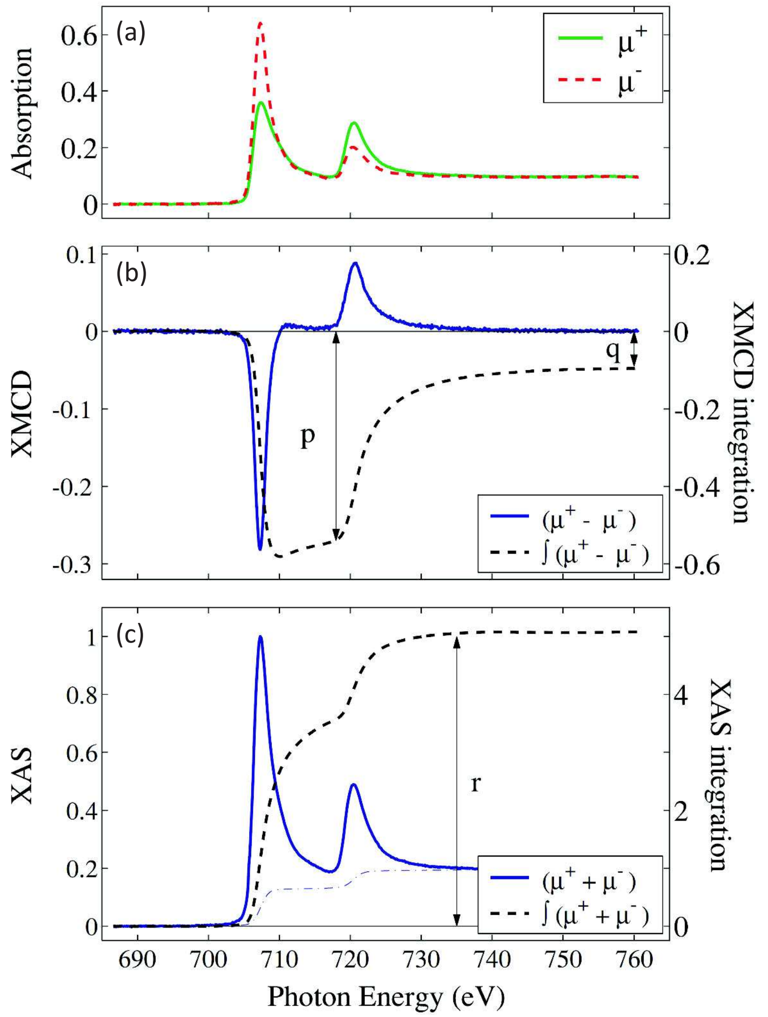

Figure 4.12: XMCD at $L_{3,2}$-edges of Fe. (a) The XAS spectra at the $L_{3,2}$-edges of Fe for two x-ray helicities μ^+ and μ^- at the fixed magnetic field, with (b) resulting XMCD spectrum, and (c) the summed XAS for both x-ray polarizations. The integrals p, q, and r are employed in the sum rules allowing to extract the orbital m_{orb} and spin m_{spin} magnetic moments (see Eq. 4.15 and 4.16). Figure taken from ref. 197.

the photon propagation direction $\boldsymbol{k}$. In some cases one needs to normalize the obtained values by $P_{\mathrm{circ}} \cos\theta$, with θ as the angle between the propagation vector and magnetization, and P_{circ} the degree of circular polarization of photons. In the case of the normal incidence measurements presented in this manuscript and performed at the DEIMOS beamline this correction factor is negligible since magnetic field was kept parallel to the x-ray propagation direction ($\boldsymbol{k} \parallel \boldsymbol{H}$) and the degree of circular x-ray polarization was close to unity.[213] For the grazing incident measurements one has to account for the projection of the magnetization vector on the x-ray propagation direction $\boldsymbol{k}$.

Note that a good accuracy in establishing the spin magnetic moment (Eq. 4.16) is possible only if the L_3 and L_2 edges are sufficiently energy-separated (see integrals p and q). This is why the spin sum rule can not be applied to the K-edge spectra, and the elements whose small spin-orbit coupling causes the $L_{3,2}$-edges overlap.[214]

Chen *et al.*[197] proved that the sum rules for the Fe $L_{3,2}$-edges are in a good agreement with other experimental methods (within 7%). Piamonteze *et al.*[214] carried out a comprehensive study over the possible sources of the spin sum rule inaccuracy for metals with configuration $3d^4$ – $3d^9$ accounting for the crystal field effects and the $3d$ spin-orbit coupling. It revealed a decreasing error with an increasing d^n occupancy, such that a negligible error was found for Cu^{+2} ($3d^9$), 5–10% for Ni^2 ($3d^8$), 5–20% for Co^{2+} ($3d^7$) or Fe^{2+} ($3d^6$), and as much as $\sim$ 50% for Mn^{3+} ($3d^4$). The experimental work of O'Brien *et al.*[215] emphasized that when applied to transition metals the sum rules can yield an accurate result within the error as low as 5%.

One has to keep in mind that the XMCD sum rules are very sensitive to the aforementioned saturation or self-absorption effects, which are strongly pronounced in the soft x-ray range. The sum rules are in general inapplicable to the XAS spectra recorded in TFY mode.[216]

4.4 Spin-resolved photoemission spectroscopy

In the previous sections, we explained the process of the photoelectric absorption leading to either the excitation of a core electron to the empty states near the Fermi level or the electron ejection from the atom. In the latter case the kinetic energy of the emitted electrons may provide a useful information about the material's electronic structure. This is exploited in the photoemission spectroscopy which is discussed in the present section.

The photoemission spectroscopy (PES), also referred to as photoelectron spectroscopy, uses preferably monochromatic photons to irradiate the sample, and employs an electron-energy analyzer to collect the excited photoelectrons (Fig. 4.13 (a)). The analyzer determines the kinetic energy of the electrons and their direction of emission. The energy distribution of the photoelectrons reflects the ground state electron distribution in the solid, liquid or gas providing thus the information about the occupancy, bonding character, chemical composition, etc. (Fig. 4.13 (b)).

The use of photoelectrons as a probe of the electronic structure of materials has notable advantages. First of all, the inelastic mean free path of the electrons can be tuned such that only a very limited material thickness is probed (see Fig. 4.9 (c)). That makes the PES an excellent tool for surface studies of thin films or interfaces. Secondly, the electrons can be easily counted and their energy precisely determined by electrostatic field-based detectors giving an overall high energy resolution. Note that the PES technique particularly requires a high vacuum environment because of both surface sensitivity and detection principle.

The kinetic energy of the photoelectrons is related to the incident photon energy and the binding energy of the electron by the energy conservation law:[217]

$$E_{\mathrm{pe}} = \hbar\omega - E_{\mathrm{b}} - \Phi \tag{4.17}$$

where $E_{\mathrm{pe}} = \frac{p^2}{2m_{\mathrm{e}}}$ stands for the kinetic energy of the photoelectron, E_{b} is binding energy, and Φ the work function of the spectrometer. The binding energy E_{b} is generally measured with respect to the Fermi level in solids and to the vacuum level in free atoms or molecules. The kinetic (binding) energy distribution of the photoelectrons is

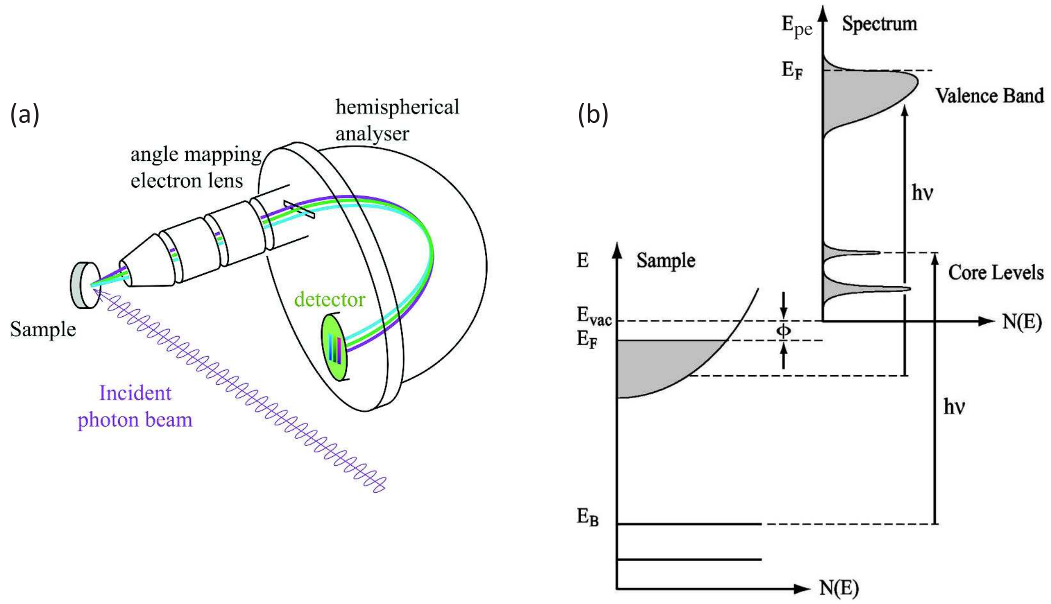

Figure 4.13: Photoemission spectroscopy (PES). (a) Experimental geometry of a photoemission experiment. (b) Scheme illustrating the material's electronic structure reflected in the kinetic energy distribution E_{pe} of the photoelectrons. Figures taken from ref. 185 and 217.

in general a replica of the electron distribution in the material (Fig. 4.13 (b)).[217] Aside of E_{pe}, the direction of the photoelectron momentum with respect to the impinging light and the surface is sometimes measured, what is referred to as angle-resolved PES (ARPES). Since our experiments did not require angular resolution we will omit here the details of this technique. In the following, we present the three-step model of the photoemission process. During this considerations we limit ourselves exclusively to PES in solids.

4.4.1 Three-step model

To understand the physical mechanisms behind the PES one can employ the so called three-step model[217,218] (Fig. 4.14) which decomposes the photoemission process into three independent stages: (1) photoionization of the electron, (2) diffusion toward surface, and (3) escape from the material.

In step (1), the photon energy is transferred to the electron which is promoted to the excited state. This process described in terms of the Fermi's Golden Rule (Eq. 4.2), defining the probability of transition from the initial to final state upon the photoelectric absorption, was described in Section 4.2.1. For the following discussion, we use the nearly free electron model in the extended zone scheme. The latter, shown as physically relevant to describe the PES process,[219] denotes a "vertical" direct transition in which the electron momentum is conserved ($\boldsymbol{k_f} = \boldsymbol{k_i}$ in reduced zone scheme) as:[217]

$$\boldsymbol{k_f} = \boldsymbol{k_i} + \boldsymbol{G} \tag{4.18}$$

where $\boldsymbol{G}$ is a reciprocal lattice vector. Apparently, in the soft x-ray and ultraviolet range the transfer of photon momentum to electron is negligible. That is to say, the

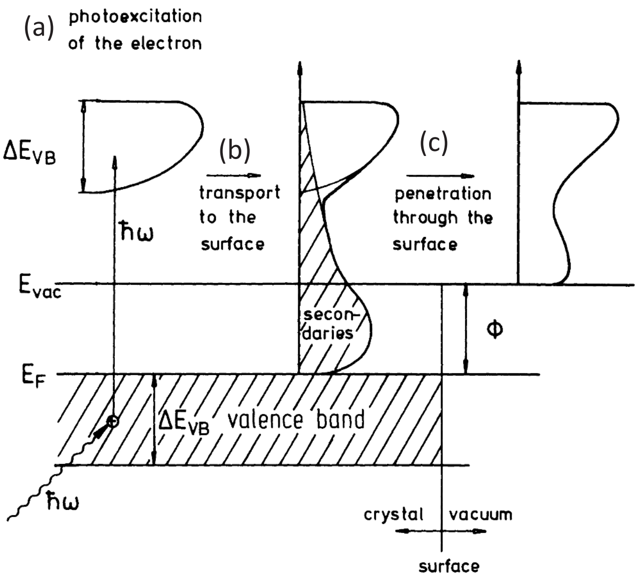

Figure 4.14: Three-step model of the photoemission process. The incident photon is absorbed by the electron which transits to the excited state (a). The electron propagates in the solid generating secondary electrons in scattering processes (b). If the electron has sufficient kinetic energy it may escape from the material (c), and can be detected in PES measurement. Figure taken from ref. 217.

electron momentum is unaltered upon photoexcitation, thus only "vertical" transitions are possible. By assuming the parabolic free electron energy dispersion, the final states for such transition can only emerge as a result of the bands folded into the first Brilouin zone for $\boldsymbol{G} \neq 0$. This is why the photoemission may occur only with involvement of a non-zero reciprocal lattice vector $\boldsymbol{G}$.[217] In materials where there is no translational symmetry, therefore no direct $\boldsymbol{k}$-conserving transition is possible, the momentum required for the excitation can be provided by the surface due to a strong variation of the potential along the z axis. This is referred to as surface photoelectric effect and requires a more sophisticated model to be described.[220]

After photoionization, the electron propagates in the solid (step 2) and undergoes the scattering processes which can be elastic or inelastic accompanied by generation of secondary electrons, phonons, or plasmons. The scattering in solids is rather dominated by electron-electron interactions.[217] That limits the inelastic mean free path of the electrons which determines the probing depth of PES. The intensity of the photoelectrons found with the same energy after propagation over a distance d can be expressed as:

$$I(d) = I_o e^{-d/\lambda(E)} \tag{4.19}$$

where I_o is the initial intensity of the primary electrons and $\lambda(E)$ stands for the inelastic mean free path. The evolution of the latter with energy, the so-called "universal curve" (Fig. 4.9), underscores the surface sensitivity of the PES in the ultraviolet and soft x-ray range.

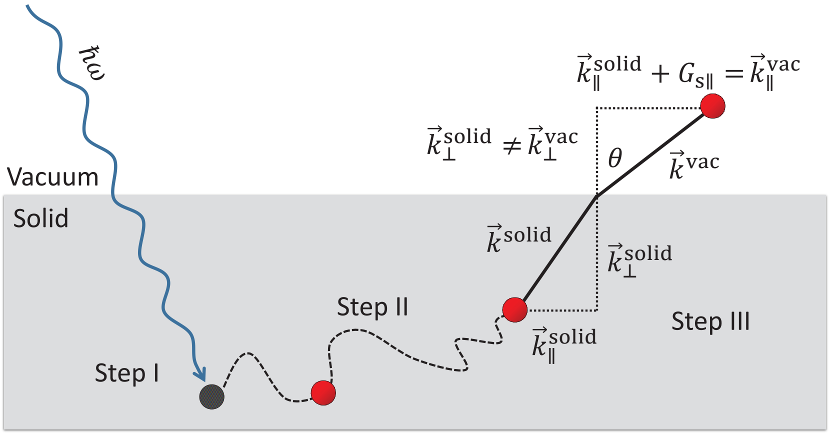

Figure 4.15: Emission of photoelectron. Schematic illustration of the photoelectron emission following the three-step model: the photoelectric absorption (step I), diffusion towards the surface (step II), and the escape from the material (step III). The electron crossing of the solid/vacuum interface is conserving the parallel component of the electron wave vector (Eq. 4.22).

Eventually, the electron may reach the surface and escape from the material (step 3). Only those electrons which have sufficient kinetic energy to overcome the surface potential barrier may escape, otherwise they are reflected back into the bulk. This condition can be expressed as:[217]

$$\frac{\hbar^2}{2m_\text{e}}\boldsymbol{k}_\perp^2 \geq E_\text{vac} - E_\text{vb} \tag{4.20}$$

where $\boldsymbol{k}_\perp$ is component of the electron wave vector normal to the surface, E_vac the vacuum level, and $E_\text{vb}(< 0)$ top of valence band. Essentially, Eq. 4.20 means the overpassing of material's work function.

The electron transfer across the solid/vacuum interface conserves the parallel component of the electron wave vector expressed in the extended Brillouin zone scheme as:

$$\boldsymbol{k}_\parallel^\text{vac} = \boldsymbol{k}_\parallel^\text{solid} + \boldsymbol{G}_{\text{s}\parallel} = \boldsymbol{p}_\parallel/\hbar \tag{4.21}$$

where $\boldsymbol{k}_\parallel^{\text{solid (vac)}}$ denotes the parallel component of the electron wave vector in the solid (vacuum), $\boldsymbol{G}_{\text{s}\parallel}$ is a reciprocal lattice vector of the surface Brillouin zone, and $\boldsymbol{p}_\parallel$ the photoelectron momentum in vacuum. In the nearly free electron model for the excited electrons $\boldsymbol{k}_\parallel$ obeys the Snell's law (neglecting the umklapp process):

$$\boldsymbol{k}_\parallel^\text{solid} = \sin\theta\left(\frac{2m_\text{e}}{\hbar^2}E_\text{pe}\right)^{1/2} \tag{4.22}$$

where θ is the angle between the trajectory of the photoelectron and the surface normal outside the material. This is schematically illustrated in Figure 4.15. Finally, we can express the kinetic energy of the photoelectron outside the material as:

$$E_\text{pe} = \frac{\hbar^2}{2m_\text{e}}\left[(\boldsymbol{k}_\parallel^\text{solid} + \boldsymbol{G}_{\text{s}\parallel})^2 + \left(\frac{\boldsymbol{p}_\perp}{\hbar}\right)^2\right] = E_f(k) - E_\text{vb} \tag{4.23}$$

where $\boldsymbol{p}_\perp/\hbar$ stays for the perpendicular component of the electron wave vector in vacuum and $E_f(k)$ is the energy of the final state.

In that way, we introduced the main ingredients of the three-step model of the photoemission and explained the mechanism behind PES. This approach, whose complete derivation can be found in ref. 217, was claimed to incorrectly neglect the energy loss of the electrons due to inelastic scattering events and to violate the uncertainty principle. However, numerous verifications of the model with the experiment proved the three-step approach to be a good approximation.[221–224]

4.4.2 Cross section

Independently of the three-step model we can formulate the expression for a photoelectric cross section (see Eq. 4.2) in a particular case where the final state is a continuum, that is if the electron is ejected from the atom. The transition probability with the photoelectron emission can be expressed as:

$$W = \int \frac{2\pi}{\hbar} |M_{if}|^2 \rho(E_{\mathrm{pe}}) \delta(E_{\mathrm{pe}} - \hbar\omega + E_{\mathrm{b}}) \mathrm{d}E_{\mathrm{pe}} \tag{4.24}$$

where again $|M_{if}|^2$ is the transition matrix element. The density of final states $\rho(E_{\mathrm{pe}})$ can be evaluated by considering a volume V with a uniform density of states in reciprocal space of $V/(2\pi)^3$. Therefore, by definition $\rho(E_{\mathrm{pe}})\mathrm{d}E_{\mathrm{pe}}$ corresponds to the number of states with energy between E_{pe} and $E_{\mathrm{pe}} + \mathrm{d}E_{\mathrm{pe}}$ equal to the number of states with wave vectors $\boldsymbol{k}_{\mathrm{pe}}$ to $\boldsymbol{k}_{pe} + \mathrm{d}\boldsymbol{k}_{\mathrm{pe}}$. That allows to write:

$$\rho(E_{\mathrm{pe}}) = 2 \left(\frac{V}{8\pi^3} \right) \left(\frac{\mathrm{d}\boldsymbol{q}}{\mathrm{d}E_{\mathrm{pe}}} \right) \tag{4.25}$$

where $\mathrm{d}\boldsymbol{q}$ is the volume element in reciprocal space and 2 stays for the two possible spin states of the electron. Now, we can replace the volume element $\mathrm{d}\boldsymbol{q}$ by integration over the entire solid angle $q^2 \sin\theta \mathrm{d}q \mathrm{d}\theta \mathrm{d}\phi$ and express the cross section of the photoemission process in analogous way as in Eq. 4.6:

$$\sigma_{\mathrm{a}} = \frac{2\pi}{\hbar c} \frac{V^2}{4\pi^2} \int |M_{if}|^2 \delta(E_{\mathrm{pe}} - \hbar\omega + E_{\mathrm{b}}) q^2 \sin\theta \mathrm{d}q \mathrm{d}\theta \mathrm{d}\phi \tag{4.26}$$

In that way, we obtained the probability per unit time and unit area of the photoelectric absorption process with emission of the photoelectron.

4.4.3 Spin resolution

While discussing the dipole selection rules in Section 4.3.1 we inferred that the electric dipole transition provoked by photoelastic absorption forbids the spin-flip process, that is $\Delta s = 0$. This also applies to the photoemission meaning that the photoelectron should conserve its spin from the initial state. Therefore, one could detect the electron spin polarization (ESP) of arriving photoelectrons. A comprehensive theoretical description of ESP photoelectrons can be found in ref. 225–227. The spin conservation of dipolar transition is employed in the spin-resolved photoemission spectroscopy (SR-PES) which is a suitable technique to resolve the spin-dependent electronic structure of magnetic materials.

In the following considerations, we assume a completely spin-conserving photoemission process, yet this is not always the case. The spin-flip transition may occur in materials with a strong spin-orbit coupling or be provoked by the high energy photons, however the ratio of the latter to the spin-conserving transitions in the ultraviolet and soft x-ray region was estimated as $\sim 2 \times 10^{-2}$.[226] A complete review of the effects in the origin of a non-spin-conserving photoemission as well as induced spin asymmetry in non-magnetic materials can be found in ref. 225.

In order to detect the ESP one needs a spin detector, that is a tool which would separate and count the electron with two spin directions. This is experimentally realized in two ways exploiting either the exchange interaction or the spin-orbit coupling mechanism. The most common spin detectors rely on the latter effect and are referred to as Mott polarimeters after Nevill Mott who provided the concept of spin-dependent inelastic scattering.[228] Since for the experiments presented in this thesis we used the Mott detector, we will omit the description of the exchange interaction-based polarimeters.

The Mott detectors take advantage of the asymmetry resulting from the scattering of spin polarized electrons by heavy atom nucleus. Let us invoke the classical picture of a free electron moving in the field $\boldsymbol{E}$ of the atomic nucleus generating the magnetic field $\boldsymbol{B}$ in the rest frame of the electron as:[229]

$$\boldsymbol{B} = -\frac{1}{c}\boldsymbol{v} \times \boldsymbol{E} \tag{4.27}$$

where $\boldsymbol{v}$ is the electron velocity. Now, we can introduce the distance $\boldsymbol{r}$ between the electron and the nucleus and express the electric field as $\boldsymbol{E} = (Zq/r^3)\boldsymbol{r}$ where Z is the

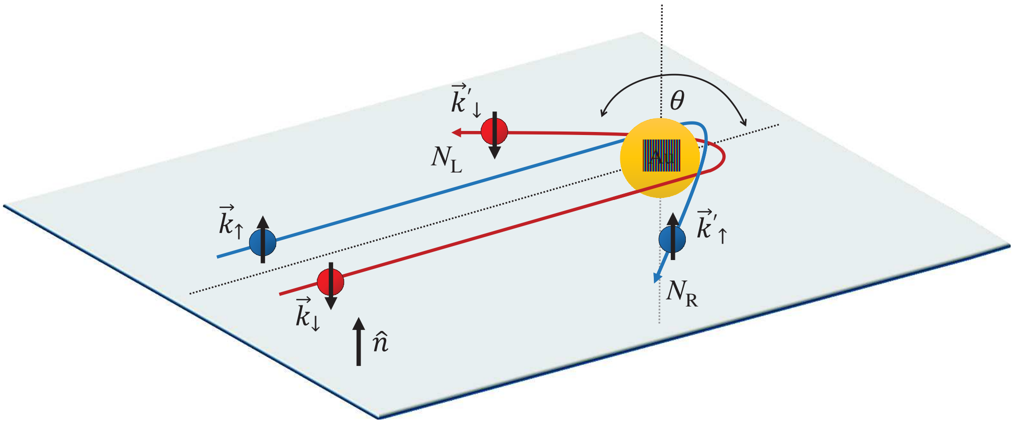

Figure 4.16: Spin-dependent scattering of the electron. Schematic illustration of the spin-dependent scattering of the spin-up and spin-down electrons by the nucleus of gold atom. The spin-orbit interaction results in the spin-dependent scattering and thus left-right asymmetry.

atomic number of the nucleus. This leads to expression:

$$\boldsymbol{B} = \frac{Ze}{cr^3}\boldsymbol{r} \times \boldsymbol{v} = \frac{Ze}{m_{\mathrm{e}}cr^3}\boldsymbol{L} \tag{4.28}$$

with $\boldsymbol{L} = m_{\mathrm{e}}\boldsymbol{r} \times \boldsymbol{v}$ as the electron orbital angular momentum. The electron magnetic moment $\boldsymbol{\mu}_{\mathbf{s}}$ interacts with this field giving rise to the spin-orbit term: $V_{\mathrm{SO}} = -\boldsymbol{\mu}_{\mathbf{s}} \cdot \boldsymbol{B}$ with the electron spin related to the electron magnetic moment as: $\boldsymbol{\mu}_{\mathbf{s}} = -(e/2m_{\mathrm{e}}c)\boldsymbol{S}$, where g is the gyromagnetic factor ($g \sim 2$ for free electron). Therefore, we can now rewrite the spin-orbit coupling as:

$$V_{\mathrm{SO}} = \frac{Ze^2}{2m_{\mathrm{e}}^2c^2r^3}\boldsymbol{L} \cdot \boldsymbol{S} \tag{4.29}$$

This spin-orbit term contributes to the scattering potential and thus introduces the spin dependence. One can easily see that this effect should be the strongest for heavy nuclei atoms which maximize the spin-orbit coupling. We can express the scattering cross section as:[230]

$$\sigma_{\mathrm{s}}(\theta) = I(\theta)(1 + S(\theta)\boldsymbol{P} \cdot \hat{\boldsymbol{n}}) \tag{4.30}$$

where θ is the scattering angle (see Fig. 4.16), $S(\theta)$ the asymmetry function, $I(\theta)$ the isotropic spin-averaged scattered intensity, $\boldsymbol{P}$ the polarization of the scattered electron, and $\hat{\boldsymbol{n}}$ a unit vector normal to the scattering plane relating the wave vectors of the incident $\boldsymbol{k}$ and scattered $\boldsymbol{k'}$ electrons as $\hat{\boldsymbol{n}} = \frac{\boldsymbol{k} \times \boldsymbol{k'}}{|\boldsymbol{k} \times \boldsymbol{k'}|}$.

Let us now consider the incident electron beam with non-zero spin polarization. The scattering of such beam on a high-Z nucleus would lead to left-right asymmetry defined as:

$$A(\theta) = \frac{N_{\mathrm{L}} - N_{\mathrm{R}}}{N_{\mathrm{L}} + N_{\mathrm{R}}} = \frac{\sigma_{\mathrm{a}\uparrow}(\theta) - \sigma_{\mathrm{a}\downarrow}(\theta)}{\sigma_{\mathrm{a}\uparrow}(\theta) + \sigma_{\mathrm{a}\downarrow}(\theta)} = PS(\theta) \tag{4.31}$$

where $N_{L(R)}$ denotes the number of electrons scattered to the left (right) direction with respect to incident beam (Fig. 4.16). This equation relating the scattering asymmetry

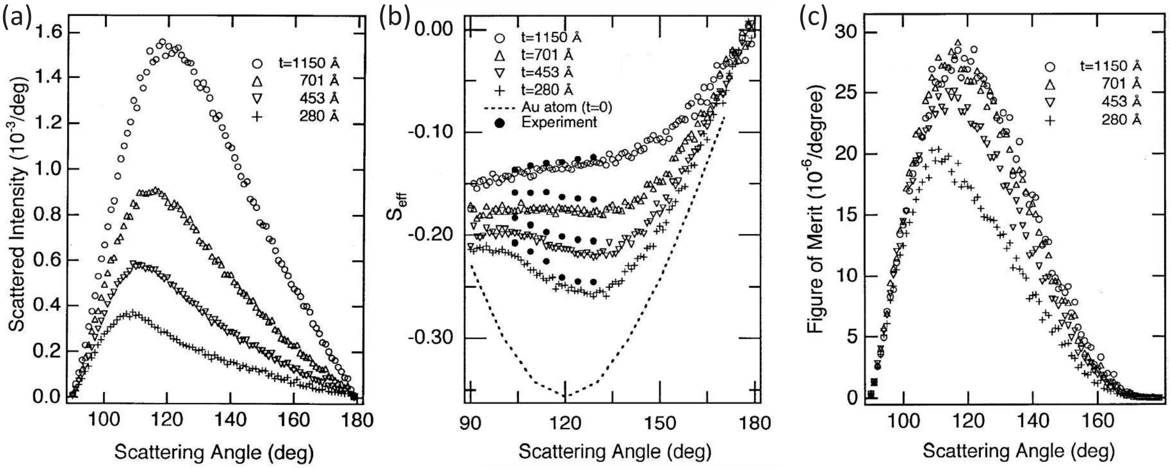

Figure 4.17: Mott scattering of the electrons on gold foil. Results of Monte Carlo calculations for (a) the scattered intensity, (b) effective Sherman function S_{eff}, and (c) Figure of Merit as a function of the scattering angle for 50 keV electrons and a gold foil of thickness 280 Å – 1150 Å. Figures taken from ref. 231.

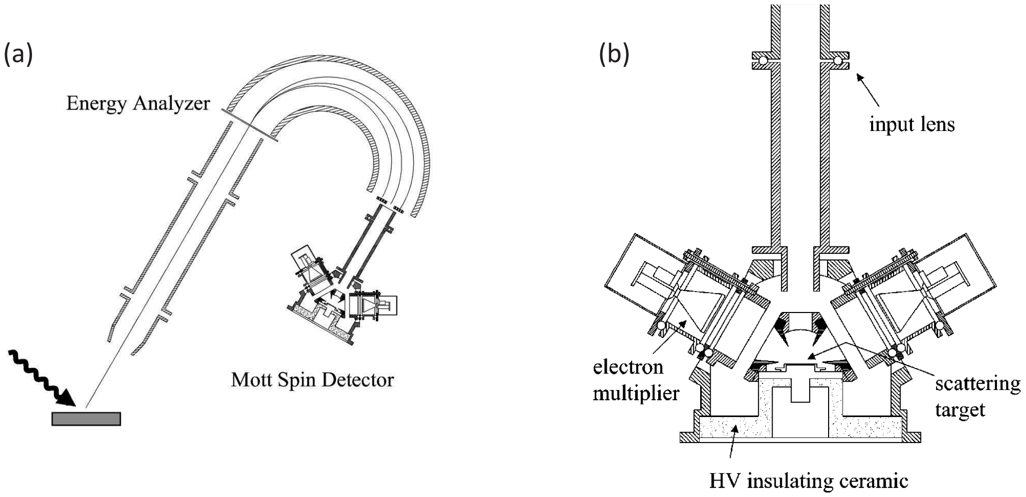

Figure 4.18: Mott detector. (a) Cross section of the Mott polarimeter coupled to the electron-energy analyzer. (b) Cross section of the Mott detector. The photoelectrons are accelerated by the input lens and hit the scattering target (typically Au mesh). The asymmetry (see Eq. 4.31) is established by the difference of scattered electrons collected on two symmetric detectors at $\theta = \pm 120°$. Figures taken from ref. 233.

$A(\theta)$ to the spin polarization P is basis of the Mott polarimetry. The proportionality factor $S(\theta)$ is referred to as Sherman function.[232] It plays a significant role and has to be known to obtain the spin-polarization P from the measurement of the asymmetry. Therefore, in order to make the asymmetry detectable one should look for experimental conditions which maximize $S(\theta)$. On the other hand, the intensity of scattered electrons corresponding to a maximum of $S(\theta)$ has to be large enough so as to ascertain a good signal to noise ratio. These two conditions are combined in the quantity called the figure of merit or polarimeter efficiency:[230]

$$FOM = \epsilon = \frac{I}{I_o} S^2_{\mathrm{eff}}(\theta) \tag{4.32}$$

where I_o is the initial intensity of the photoelectrons, I the summed intensity of the scattered electrons, and S_{eff} the effective Sherman function taking into account the solid scatterer (not a single nucleus). The inverse square of the FOM is the statistical error of the experiment. The highest signal to noise ratio and maximum spin resolution is obtained for the maximum of FOM. Figure 4.17 presents the result of calculations for the scattered intensity, S_{eff}, and FOM for a gold target.[231] One clearly sees that the maximum of FOM is obtained for a scattering angle $\sim 120°$. That is why in general the polarimeters are realized in backscattering geometry with two symmetrically positioned detectors at $\theta = \pm 120°$. The modern Mott detectors are characterized with an efficiency of order $1 - 5 \times 10^{-4}$, what is typically three orders of magnitude lower than non-spin-resolved photoemission.[233,234] This implies relatively long acquisition times for SR-PES.

Typical Mott detectors use gold foil as a scatterer due to aforementioned strong spin-orbit coupling, non-oxidizing surface, and low reactivity.[229] Figure 4.18 presents a scheme of a Mott detector coupled to hemispherical electron-energy analyzer. In the SR-PES experiment the photons impinge the sample and generate the photoelectrons

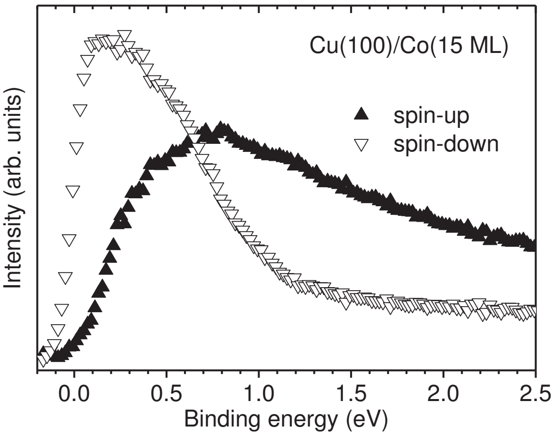

Figure 4.19: Spin-resolved PES of Cu(100)//Co(15 ML). Spin-resolved electron distribution curves for cobalt revealing a strong asymmetry near the Fermi level resulting from the exchange splitting of the Co 3*d* bands.

which due to spin-conserving photoabsorption process may exhibit non-zero ESP. The electrons are collected by the energy analyzer which filters only carriers with the desired energy. Then, usually the electrons are either directed onto a 2D detector for a non-spin-resolved PES measurement, or deflected towards the Mott detector. The latter, depicted in Fig. 4.18 (b), first accelerates the electrons usually to $\sim 100\,\mathrm{keV}$ – 150 keV towards the scattering foil. The foil is typically made of a gold thin film deposited on a low-Z material in order to minimize the multi-scattering processes. The photoelectrons after being scattered are collected by two electron multipliers and finally counted by detectors placed symmetrically at ±120° (maximum of efficiency). The asymmetry is then calculated as the difference of summarized counts between the two detectors. Often, the Mott polarimeters are equipped with two pairs of detectors used to discriminate the transverse and longitudinal scattering planes and measure two components of the incident electron polarization.[229] Figure 4.19 presents the exemplary spin-resolved electron distribution curves for cobalt demonstrating a strong asymmetry near the Fermi level resulting from the exchange splitting of the 3*d* bands.

In this section, we introduced the fundamentals of the spin-resolved photoemission spectroscopy and explained how this technique can be used to determine the spin-dependent electronic structures of the material. As the reader will see later, this makes the SR-PES a powerful tool to investigate the spin-polarization at the interfaces. In the next section, we describe the technical capabilities of the CASSIOPÉE and DEIMOS beamlines of the SOLEIL synchrotron where the SR-PES, XAS, and XMCD experiments presented in this thesis were carried out.

4.5 CASSIOPÉE beamline (SR-PES)

CASSIOPÉE is an acronym of Combined Angular- and Spin-resolved SpectroscopIes Of PhotoEmitted Electrons and the name of the beamline at the synchrotron SOLEIL. The beamline is optimized for large angles and a high energy resolution to studies of the electronic and magnetic properties of solids in low-dimensional systems. These include

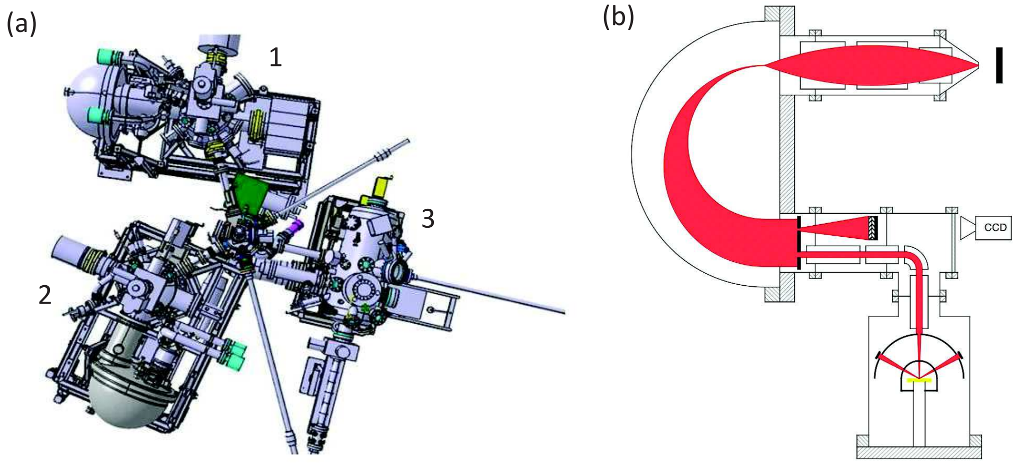

Figure 4.20: Measurement endstations of the CASSIOPÉE beamline. (a) Top view of the spin-resolved (1) and angle-resolved (2) photoemission spectroscopy dedicated endstations along with the preparation MBE chamber (3) at the CASSIOPÉE beamline. (b) Cross section of a Scienta SES 2002 hemispherical electron-energy analyzer coupled to a custom made Mott detector installed at the SR-PES endstation of the beamline.

strongly correlated complex oxides, topological insulators, or materials for spintronics. The high surface sensitivity of the exploited techniques puts the emphasis on the interfacial structures and surface effects.

CASSIOPÉE is an ultraviolet to soft x-ray beamline offering a photon energy range 8 eV – 1500 eV, an energy resolution of $E/\Delta E \sim 20000 - 70000$, and a flux of 2×10^{13} phot./s/0.1%BW (at the sample). The linear and circular polarized photons are provided by one of the two undulators: Apple II HU60 (100 eV – 1500 eV) or HU256 (8 eV – 155 eV). The beamline is equipped with two endstations dedicated to the spin-resolved or angle-resolved photoemission spectroscopy respectively.

The top view of the two beamline endstations is depicted in Fig. 4.20 (a). Since for the experiments performed within the framework of this thesis we used only the SR-PES endstation we will not describe here the ARPES branch of the beamline.

The measurement chamber of the SR-PES endstation is equipped with a Scienta SES 2002 analyzer coupled to a Mott detector (Fig 4.20 (b)). The latter is a custom made detector with four channelplates and a gold scattering foil. The electromagnet for magnetizing the sample is located below the measurement stage. Because of the principle of a photoemission detection the magnetic field can not be applied during the acquisition. The measurement chamber allows cooling the sample down to 40 K. The photon beam spot at the sample is approximately of size 720 µm × 350 µm. The measurement chamber base pressure is kept at $\sim 10^{-10}$ mbar.

Both endstations of the CASSIOPÉE beamline are connected to the preparation chamber which allows *in situ* sample fabrication. This includes surface preparation and characterization tools: Ar^{+}-ion sputtering gun, sample annealing stage, LEED, RHEED, and AES analyzer. The metals can be deposited from Thermionics custom made evaporator or Omicron EFM-3 device. The additional flanks allow the installation of molecular cells for the deposition of organic materials.

Within the framework of this thesis we employed the SR-PES endstation of the

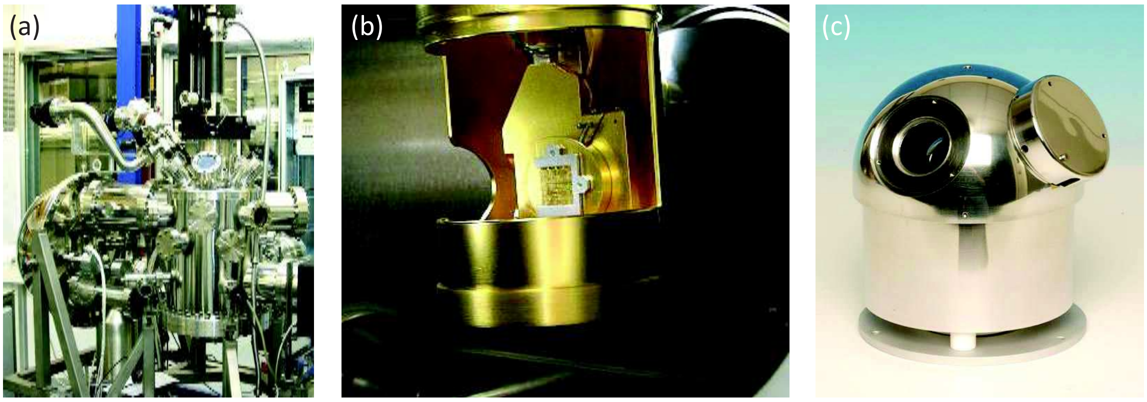

Figure 4.21: SR-PES endstation of the CASSIOPÉE beamline. Picture of (a) the SR-PES-dedicated endstation, (b) the sample inside the SR-PES measurement chamber (in the back visible input of the energy-analyzer), and (c) the Mott detector with one of the channelplates removed. Pictures taken from ref. 235 and 236.

CASSIOPÉE beamline to resolve the spin polarization at the Cu/MnPc interface of the interlayer exchange coupled system Cu(100)//Co/Cu/MnPc (Sec. 5.5).

4.6 DEIMOS beamline (XAS, XMCD)

DEIMOS[213] stands for the Dichroism Experimental Installation for Magneto-Optical Spectroscopy and is the name of the soft x-ray beamline at the SOLEIL synchrotron dedicated to the soft x-ray spectroscopy and dichroic techniques. The beamline is optimized for high energy and photon flux stability so as to generate highly reproducible spectra with very high sensitivity. The main interest domains of the beamline include the magnetism of organic/inorganic materials at the nanoscale, on the surface/interface, or in the liquid phase, magnetic correlations in hybrid systems, magnetocrystalline anisotropy, single molecule magnets, superparamagnetic nanoparticles, etc. The work presented in this PhD thesis was carried out in a collaboration between the DEIMOS beamline and the IPCMS.

The beamline provides photons in the soft x-ray energy range 350 eV – 2500 eV (with resolution $E/\Delta E \sim 6000 - 10000$) delivered by two alternatively operating undulators: Apple II HU52 and EMPU65.[238] The latter has a hybrid electromagnet/permanent magnet design allowing a fast 5 Hz switching rate of the circular photons polarization for the XMCD measurements. The high density variable groove depth (VGD) grating of the monochromator ascertains as good energy stability as ~ 1 meV/h. The photon flux on the sample was established as $\sim 6 \times 10^{12}$ phot./s/0.1%BW with predefined beam spot size of 80 µm × 80 µm or 800 µm × 800 µm. It is worth mentioning that a special care was taken at the DEIMOS beamline to obtain a controllable ratio of the resolving power to photon flux such that it can be adjusted depending on the requirement of the experiment and robustness of the studied material. It is of significant importance for studies of the organic materials which can undergo an x-ray induced decomposition (see. Sec. 2.3.5). The controllable photon flux allows to minimize this effect.

The photons energy range of the DEIMOS beamline covers the L-edges of $3d$ and $4f$ metals, M-edges of rare earth, and K-edges of carbon, nitrogen, oxygen, sulfur. This provides a powerful tool for element-specific studies of the magnetic and electronic properties of many molecular spintronic materials by means of the x-ray absorption spectroscopy (XAS) or x-ray magnetic (natural) circular (linear) dichroism (XMCD, XMLD, XNLD) with a notable sensitivity.

Presently, the DEIMOS beamline is equipped with two endstations called later the cryo-magnet and MK2T. The former (Fig. 4.22 (c)) consists of the Air Liquid custom made cryomagnet with two superconducting coils. It allows the application of a magnetic field up to $\pm 7\,\mathrm{T}$ parallel and $\pm 2\,\mathrm{T}$ perpendicular to the x-ray propagation direction. The sample temperature can be controlled in the range $1.5\,\mathrm{K} - 370\,\mathrm{K}$. The second endstation called MK2T was designed to meet the needs of the research domains requiring an elevated sample temperature far beyond room temperature. This is not possible in the cryo-magnet due to the vicinity of the cryogenic liquids. The MK2T is equipped with the water-cooled $\pm 2\,\mathrm{T}$ electromagnet and allows to control the sample temperature in the range $30\,\mathrm{K} - 1000\,\mathrm{K}$. Both endstations enable x-ray absorption detection in total fluorescence and electron yield modes. In both, the currents are measured by Novelec MCCE-2 high-sensitivity low-current electrometers coupled to NI-6602 counting cards.

The beamline provides an *in situ* preparation and surface characterization environment (Fig. 4.22 (d)). It allows the thermal evaporation of metals as well as sublimation of organic materials. The characterization can be performed by a LEED apparatus or an AES spectrometer. A notable convenience is provided by an integrated Omicron VT SPM for a direct insight into the morphology of *in situ* fabricated structures. All the preparation, transfer, and the measurement chambers are kept at a base pressure

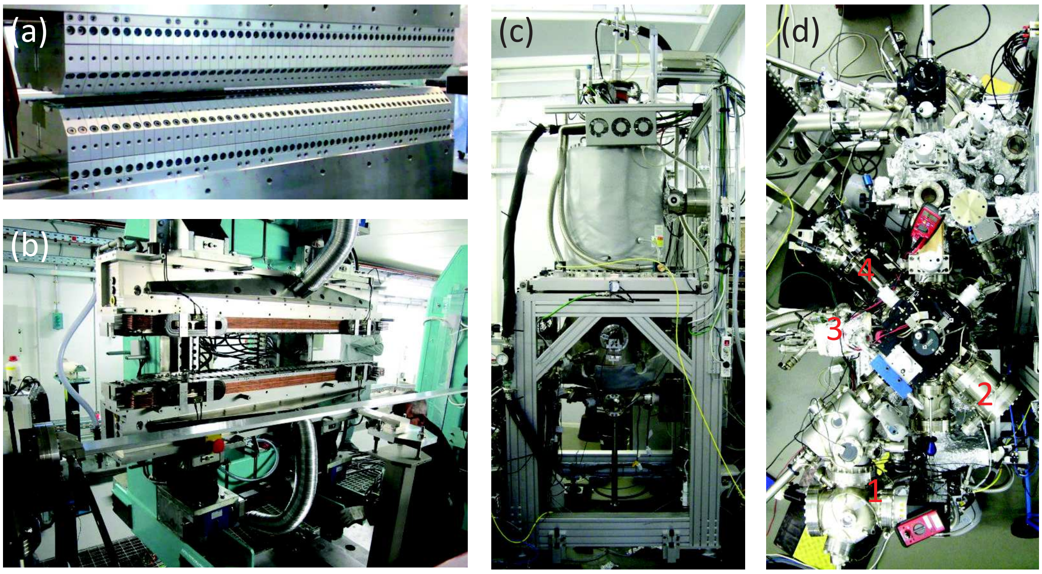

Figure 4.22: DEIMOS beamline. (a) Apple II HU52, and (b) EMPHU65 undulators, (c) cryo-magnet endstation, and (d) sample preparation environment of the DEIMOS beamline. 1 - variable temperature Omicron STM, 2 - LEED apparatus, 3 - EFM-3 metal evaporator, 4 - AES analyzer.[237]

of $\sim 10^{-10}$ mbar.

It is worth mentioning, that the DEIMOS beamline was also optimized from the point of view of the data acquisition time. The standard x-ray absorption measurements in a step-by-step procedure proceeds by the following algorithm to obtain a single energy point measurement: (1) set the gap and phase of the undulator, (2) move the monochromator grating and mirrors, (3) record the absorption signal from the detectors. These steps are repeated along the mesh of defined photon energies. This approach is highly time consuming due to acceleration and deceleration of the undulator and monochromator motors. A typical 100 eV-wide scan takes approximately 40 minutes in this procedure with almost 90% of a dead-time. This has been improved by a factor of ten by the in-house developed *Turboscan* procedure at the DEIMOS beamline.[239] The new scan procedure dynamically couples the motors of the undulator and monochromator such that during the continuous motors movement the data are recorded on-the-fly as a function of time which is later translated into photon energy scale. A single XAS curve over 100 eV performed with *Turboscan* takes only $\sim 2-4$ min. This is a notable improvement allowing faster data recording thus reduction of the potential drift and impact of environment.

In the framework of this thesis, we carried out the XAS, XMCD experiments with use of the cryo-magnet endstation (Sections 5.2, 5.3, 5.4, 6.2.2, 7.3.2.2) as well as combined XAS and electrical studies with the use of the MK2T branch (Section 4.8). The later was realized with the Versatile Variable Temperature Insert (V^2TI), that is an alternative insert of the DEIMOS beamline, whose development was part of this thesis. We describe the technical aspects of the insert and its capabilities in the next section.

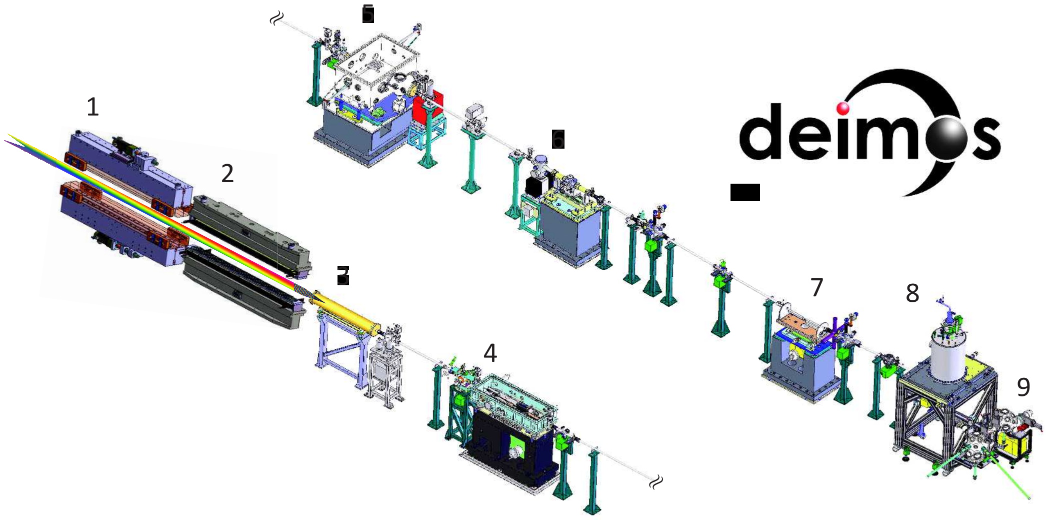

Figure 4.23: DEIMOS beamline elements. 1 - EMPU65, and 2 - APPLE II HU52 undulators, 3 - buffer chamber, 4 - optics chamber, 5 - monochromator, 6 - exit slits, 7 - refocusing chamber, 8 - cryo-magnet endstation, 9 - sample preparation environment. The MK2T endstation which is installed behind the cryo-magnet is not present on the drawing.[237]

4.7 Versatile Variable Temperature Insert at the DEIMOS beamline

In the past decade one can observe a growing interest on material studies as not exclusively from the perspective of its intrinsic characteristics but rather its operation within the complete device.[240,241] These so-called *in operando* investigations can give a direct link between the material properties and its real impact on the performance of a manufactured functional device. This perspective was at the origin of the idea to develop an alternative insert for the DEIMOS beamline combining the virtues of the soft x-ray spectroscopy and *in situ* electrical access to the sample. The new insert was named the Versatile Variable Temperature Insert (V^2TI) and its development was one of the objectives of this thesis.

The electrical access to the sample enables a range of possibilities such as measuring the transport properties, electrically polarizing the sample, operating the piezo-elements, providing the electrical stimulation, etc. When combined with the x-ray beam one can distinguish the two main scenarios: (i) where the x-ray photons are used to probe the material changes due to electrical stimulation, or (ii) where the current or voltage is monitored to detect the alterations in the material structure provoked by the x-ray photoexcitation. A straightforward example of materials suitable for such studies are artificial magnetoelectrics[242,243] which interconnect two ferroic orders and thus may be probed in a combined XAS and electric approach.

The V^2TI emerged as a result of a fruitful collaboration between the DEIMOS beamline's scientists and the engineering team of the IPCMS. The insert design is based

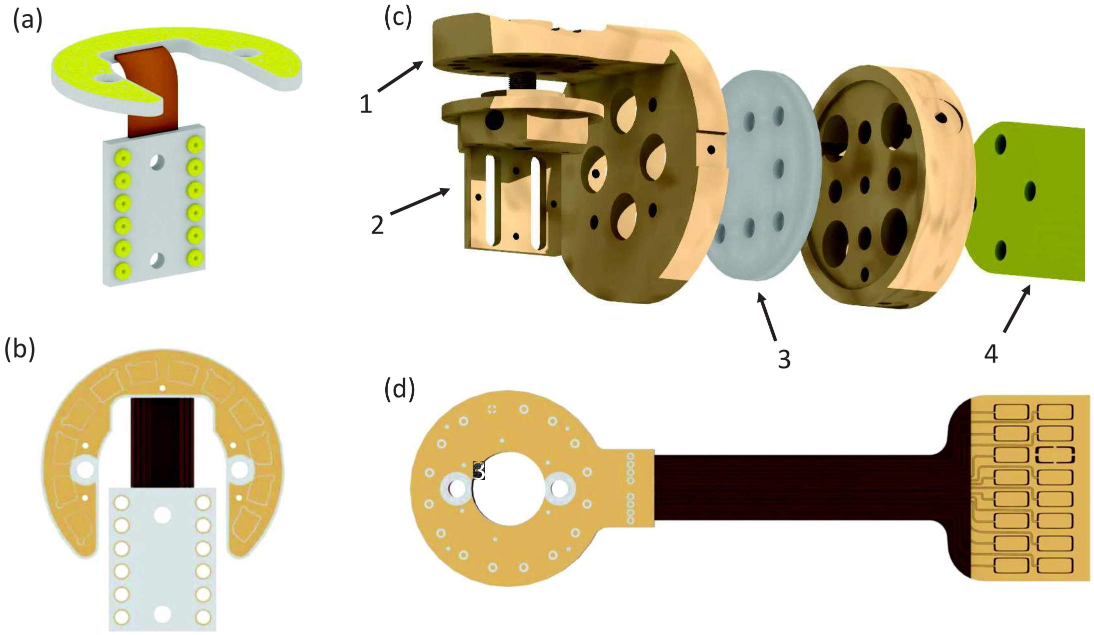

Figure 4.24: Versatile Variable Temperature Insert (V^2TI). (a) Sample holder PCB and (b) its top view. (c) Exploded view of the insert with: 1 - head, 2 - sample holder, 3 - sapphire disk, and 4 - cold finger. (d) The top PCB of the insert's head. Figures taken from ref. 33.

on a UHV cryostat fabricated by Janis (ref. ST-402) and operating in temperature range 1.8 K – 420 K. The head of the insert made of a copper block was designed and manufactures at the IPCMS. The exploded view of the head is illustrated in Fig. 4.24 (c). One of the biggest challenges in the project was to ascertain a good thermal conductivity between the cold finger and the head, with simultaneously a good electric isolation (required resistance greater than 200 GΩ) for TEY detection. This was realized with a separating disk made of sapphire (Fig. 4.25 (c) (3)) which is well known for its good (poor) thermal (electric) conductivity. The electrical contacts were provided with the printed circuit boards (PCB), depicted in Fig. 4.24 (b) and (d), made of copper tracks on a hydrocarbon/ceramic insulator. The top PCB (Fig. 4.24 (d)) connects the outside wires to the insert head bypassing the sapphire disk. When assembling the sample holder (Fig. 4.24 (c)(2)) with the insert's head, the sample holder PCB (Fig. 4.24 (a),(b)) provides further contact to the the sample through the dedicated chip (Fig. 4.25 (a)).

Now, we explain the methodology of introducing the sample to the measurement stage. Prior to the beamtime, the users are provided with the dedicated V^{2}TI chips illustrated in Fig. 4.25 (a). The sample is glued to the central pad (Fig. 4.25 (a)(4)) which ensures a good thermal contact. The sample is bonded to the selected contacting pads (Fig. 4.25 (a)(1)) and the TEY detection is possible by connecting the sample with a bar pad (Fig. 4.25 (a)(2)). After the users' arrival to the beamline, the chip containing the sample is fixed with molybdenum screws to the sample holder (Fig. 4.25(b)(4)) which is then introduced to the beamline's UHV environment via the load-lock chamber. After reaching a proper vacuum level the holder with the sample is *in situ* transferred and assembled with the V^{2}TI head by screwing in from below.

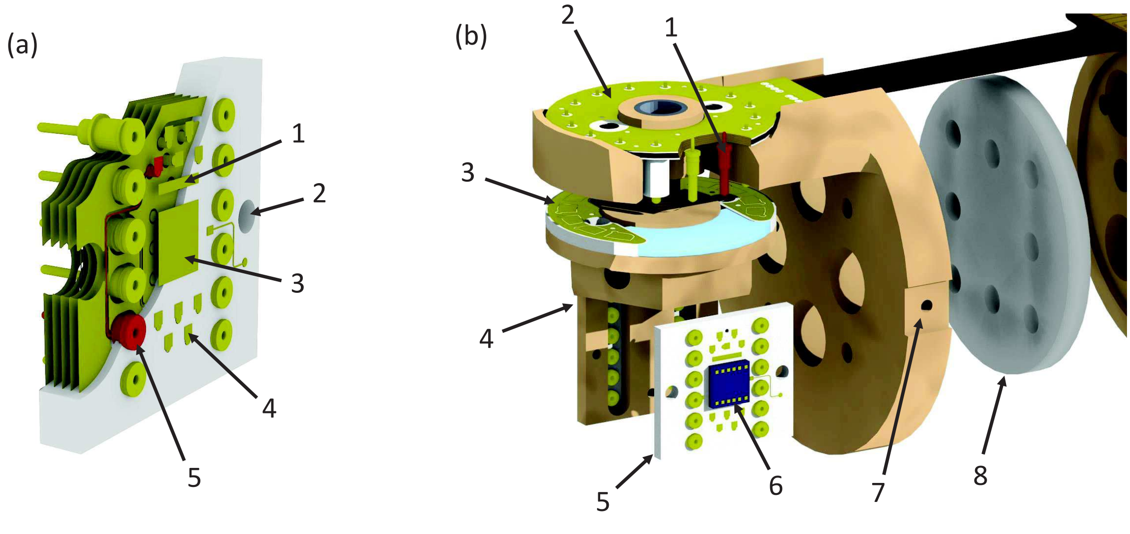

Figure 4.25: V^{2}TI head and dedicated chip. (a) Cross section of the V^{2}TI chip with: 1 - total electron yield bar pad, 2 - hole for fixing the screw, 3 - central pad for the thermal contact, 4 - one of the connection pads, 5 - one of the twelve tulips. (b) Exploded view of the V^{2}TI head with: 1 - pin contacting the head and sample holder PCBs, 2 - head PCB, 3 - sample holder PCB, 4 - sample holder, 5 - dedicated chip, 6 - the sample, 7 - temperature sensor position, 8 - sapphire disk. Figures taken from ref. 33.

This establishes a contact between the sample holder and the head PCB via the pins (Fig. 4.25(b)(2)) forming thus an electrical link between the sample and the outside of the vacuum. Note that it is crucial to properly screw the sample holder such that appropriate PCB pads are connected. Eventually, after these steps one obtains the sample in the UHV environment of the beamline, under the x-ray beam, and with *in situ* electrical access.

From sixteen wires provided by the head (Fig. 4.25(d)) twelve are connected through the holder to the chip, such that there are always four leads blind (technical limitation of the chip design). Two alternative sample holders were manufactured providing two measurement geometries with normal and 45° x-ray incidence. In both configurations the magnetic field is applied along the x-ray beam propagation direction. For test measurements the V^2TI was mounted at the side port of the cryo-magnet endstation and afterwards moved permanently to the newly developed MK2T.

We performed the preliminary tests of the insert from the point of view of its electrical isolation and the cooling performance. The TEY measured as a neutralizing current flowing from the ground to the insert head was established to be affected by a leakage current as low as $(50 \pm 10)\,\mathrm{fA}$ without any sample mounted. To verify the influence of the current flow through the investigated device on the leakage current we mounted a test sample containing MgO-based magnetic tunnel junctions (Fig. 4.26 (d)). We passed $20\,\mu\mathrm{A}$ through an exemplary device and noticed a leakage current increase to $(70 \pm 10)\,\mathrm{fA}$ which is still an excellent result. Since a typical TEY signal is in the pico – nanoampere range, we infer that both TEY detection of XAS and electrical transport measurements can be effectively performed simultaneously. Note that the

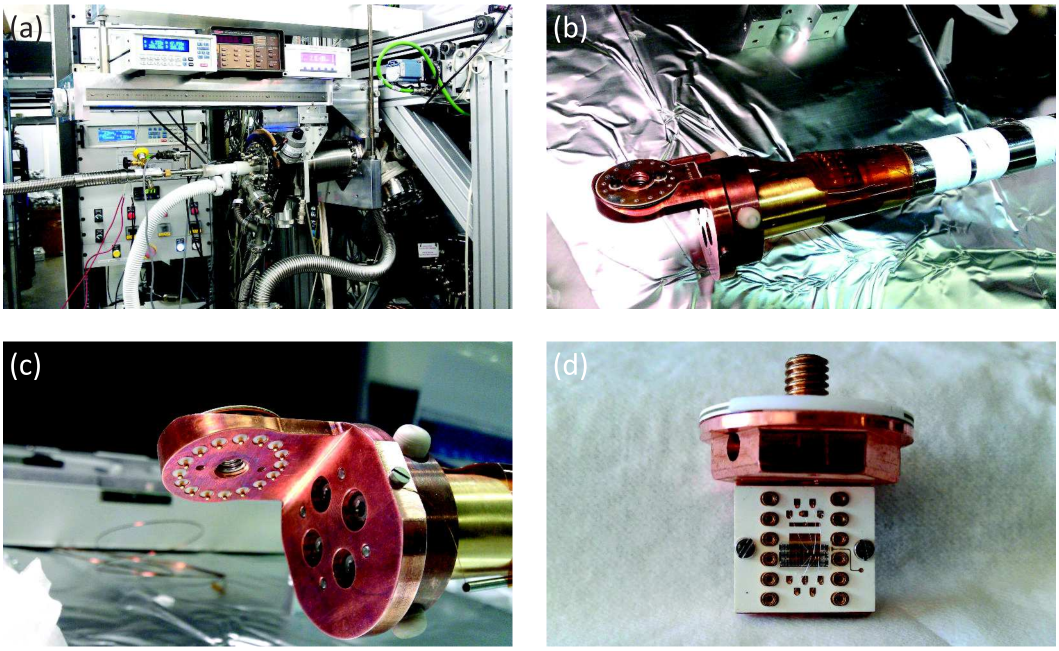

Figure 4.26: Test measurements of V^2TI. (a) V^2TI mounted at the side port of the cryo-magnet endstation of the DEIMOS beamline. (b)-(c) Outside picture of the insert's head. (d) Sample holder with mounted chip and the sample containing MgO-based MTJs.

insert design does not preclude the TFY detection by a photodiode.

The temperature of the sample mounted on the V^2TI is measured by a diode sensor (ref. Scientific Instruments Si410C) located at the side of the insert's head (Fig. 4.25 (b)(7)). The cooling down is done by introducing liquid helium from the external container (Fig. 4.26 (a)) and then the temperature is stabilized by the heaters of the cryostat operated by a Lakeshore controller. The lowest achievable temperature was established as 12 K (on the sample) with a helium consumption rate of 0.6 l/h. We verified that the difference between the head sensor indication and the real sample temperature does not exceed 10 K.

The full operation of the insert was announced in May 2014 and since then it is available for the external users. In that way the DEIMOS beamline provided a powerful tool combining usually separately carried out electrical measurements and material studies with the use of the soft x-ray spectroscopy. The V^2TI was described in detail in a technical publication (see ref. 33).

In June 2014 we performed the first scientific experiments with the use of the insert demonstrating how the joint XAS and electronic transport measurements can resolve the contribution of the specific active atomic species in the operation of a microelectronic device. We present the methodology of the experiments and its outcome in the following section.

4.8 Probing a device's active atoms using synchrotron radiation

Last years brought an intensification of the combined material and device studies in the so-called *in operando* approach for applications ranging from gas sensing to information or energy technologies.[240,241,244–247] The aim of those studies is to create a link between usually separately investigated device's material properties and its performance. The newly developed V^2TI insert at the DEIMOS beamline allows such joint studies. We exploited these possibilities on the MgO-based magnetic tunnel junctions and developed the methodology allowing to asses a contribution of given, active in transport, atomic sites on the device performance. We believe that this opens a way for directly probing how buried atomic species, whether abundant or as a dopant or contaminant, may impact the device operation. This approach, described in the following part, deserved a separate publication submitted at the time of writing of this manuscript.[248]

We explained before how the x-ray absorption spectroscopy by tuning the energy of the x-ray photons drive the core level excitations of specific atomic species within the sample. The obtained absorption spectra yield the information about the quantity of atoms, their charge state, chemical environment and the resulting electronic/magnetic properties. This combined with a high brilliance of a synchrotron facility allows to resolve a minute populations of the atoms, even if they are buried within the complex multilayer structure of a device. Now, operating this device so as to alter its state, meanwhile photoexciting the specific species by x-rays, can provide an insight on the proportion of the atoms which actually contribute to define the device state. While *in operando* studies are easily done for, *e.g.*, batteries,[245] this is more tenuous for the microelectronic devices ranging from memristors[244] to photovoltaic cells.[246]

In our studies we considered the case of magnetic tunnel junctions[7] where the picture of operation involving the spin and electronic symmetry is known to be mediated by a very small subset of the atoms.[34,52,65] We propose a methodology focusing the XAS studies only on those atoms involved in the operation by measuring their magnetotransport properties as they absorb the x-rays.

The stacks with composition glass//Ta(5)/Co(10)/IrMn(7.5)/FeCoB(4)/MgO(2.5)/FeCoB(2.5)/Ta(1)/Pt(1) (with all numbers in nanometers) were fabricated as described in ref. 249 and post-annealed in an in-plane magnetic field of $H = 200\,\text{Oe}$ for 1 h at 300 °C. This both crystallizes the MTJ interfaces and increases the lower electrode's coercive field thanks to the IrMn antiferromagnetic pinning layer. The FeCoB layers exhibit in-plane magnetization. The optical lithography was then used to define the MTJs[250] with optical access atop the junction pillar.[251] The SiO_2 was used to insulate the bottom and top electrodes of the device.

4.8.1 Experimental set-up

The samples containing MTJs were mounted on the V^2TI insert assembled to the MK2T endstation of the DEIMOS beamline. The x-rays impinged on the sample at 45°. To set the junction in the parallel (P) and antiparallel (AP) states, a magnetic field of the same amplitude ($|H| = 0.03\,\text{T}$) but opposite sign was applied along the direction of the x-ray photon propagation.

To perform the magnetotransport measurements we employed the electrical set-up developed at the IPCMS and called the mobile Fert bench (mFert). It consists of a Keithley sourcemeter working in a voltage source mode, dual analog/digital input/output board (DAQ), a dedicated electrical multiplexor designed to electrostati-

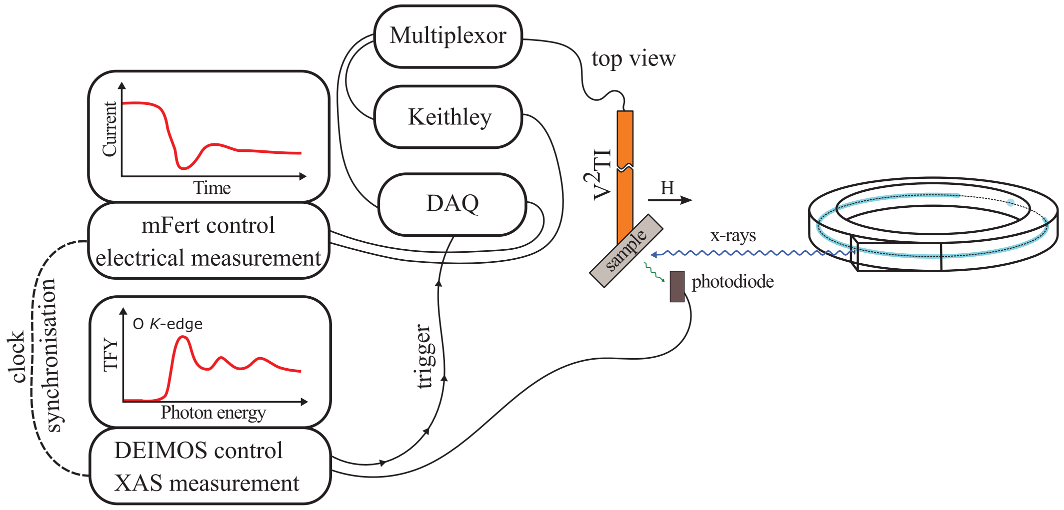

Figure 4.27: Integrated XAS and electrical measurement with use of the V^2TI. The mFert bench was employed to record the device current (resistance) vs. time and the DEIMOS control station to acquire the XAS spectra. The time-stamp synchronization between the two measurement lines allowed a simultaneous measurement in the current - photon energy space.

cally protect the devices, and a laptop with a Labview-based software to control the bench. The x-ray beam characteristics, magnetic field and the sample temperature were regulated from the DEIMOS control station. In order to integrate the mFert measurement within the beamline's Python programming environment, the DEIMOS station was programmed to trigger the mFert DAQ. To obtain the magnetotransport data as a function of the photon energy, the clocks of both mFert and DEIMOS station computers were synchronized to the external SOLEIL synchrotron counter. The timestamps were saved to the output files of current versus time (mFert) and XAS versus photon energy (DEIMOS), such that one may simultaneously express both the current and XAS as a function of photon energy. The scheme of the two integrated measurement lines (mFert and DEIMOS) is depicted in Fig. 4.27.

The x-ray absorption spectra were recorded in total electron yield mode systematically normalized to the current measured on a gold plated grid located before the endstation. The electrical measurements were performed in the four-point protocol in the voltage source mode of Keithley 2636 with the MTJ lower electrode grounded.

4.8.2 Device positioning against the x-ray beam

Combined XAS and electrical studies require a proper alignment such that the x-ray beam impinges exactly on the probed junction. To do so, we acquired the x-ray intensity maps over the sample area of interest (Fig. 4.28). This was performed by recording the x-ray absorption intensity in TEY mode with fixed photon energy (here Co L_3-edge) along the x, y mesh, where both coordinates lie in a sample plane and z points in the x-ray propagation direction. Then, plotting the intensity as a function of the endstation positions allows to distinguish between lithographically processed oxide and metallic surface features.

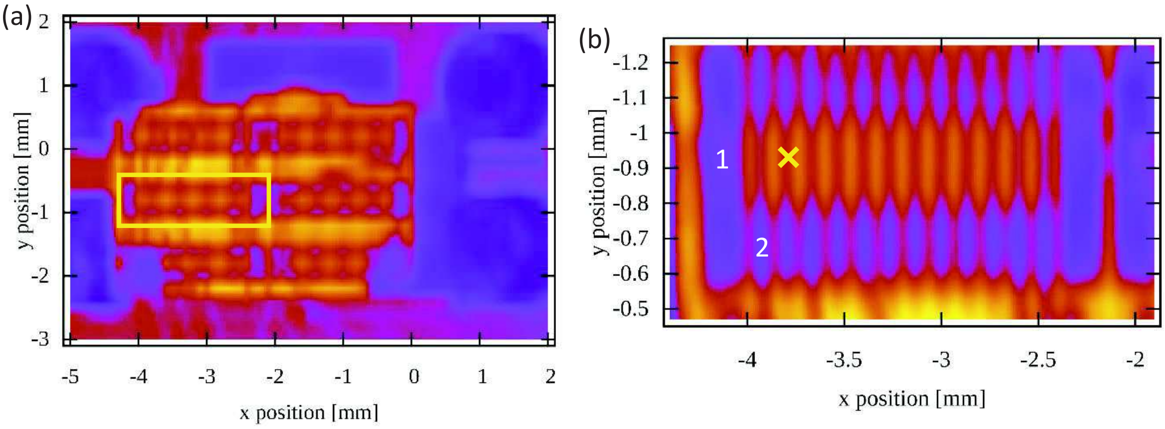

Figure 4.28: Device alignment with the x-ray beam. X-ray intensity maps acquired at photon energy 788 eV (Co L_3-edge). The bright orange areas (large absorption) emerge from the top FeCoB electrode, and the dark violet (negligible absorption) to where FeCoB is covered by the metallic contacts. (a) Large-scale map showing the sample on the chip. The yellow square marks the region of interest, *i.e.*, a single row of 20 identical MTJs. (b) Fine alignment revealing the position of the bottom (1), top (2) electrode pads and the junction of interest marked with "x".

4.8.3 Combined XAS and magnetotransport measurement

Although the atoms of the FM electrodes of the MTJ define the macroscopic magnetization thus the state of the device, the key role for the performance is played by the spin- and symmetry-polarized density of electronic states created at the interface between the FM electron and the tunnel barrier. The XAS characterization studies have before focused on these interfaces in full stacks, thin FM layers at these interfaces,[252,253] or by examining the bonds between the electrode atoms and the barrier.[37,254–258]

In Fig. 4.29 we show the XAS spectra at the O K-edge of the referential stacks for our MTJs, *i.e.*, non-processed FeCoB FM electrodes and the MgO tunnel barrier that are either as-grown or annealed. The energy range $537 < E(eV) < 541$, that is the pre-edge region, which precedes the O K-edge maximum absorption at 543.5 eV reveals the oxygen sites chemical environment. The observed pre-peaks in the XAS on the non-annealed samples were qualitatively identified[35–37] as the spin- and symmetry-polarized bands of Fe oxides, with a 1.4 eV crystal field splitting (between Δ_1 and Δ_5 states) and a 3.6 eV spin-splitting (between spin ↑ and ↓ states). We use the notation of the electron symmetry ($\Delta_{1,5}$) after analyzing the orbital geometries (e_g, t_{2g}) and corresponding electron wave function symmetries.[11,34] Annealing the sample causes a strong decrease of the Fe oxide peaks spectral intensity. The reduction of these interfacial Fe oxides inferred from the XAS studies[37] is at the origin of the microscopic explanation on why annealing increases the TMR. Notably, the disappearance of the FeO_x $\Delta_1^{\downarrow}$ peak, which indicates reduced Fe-O bonds across the interface, implies the closing of a tunneling transmission channel that would otherwise decrease TMR.[260]

Note that the oxygen was present not exclusively within the pillar of the MTJ barrier, but also in a glass substrate and the SiO_2 layer that isolated the top from the bottom electrodes. Since the x-ray beam size exceeded the 20 µm diameter of the junction the XAS spectra acquired during the combined transport measurements reflect

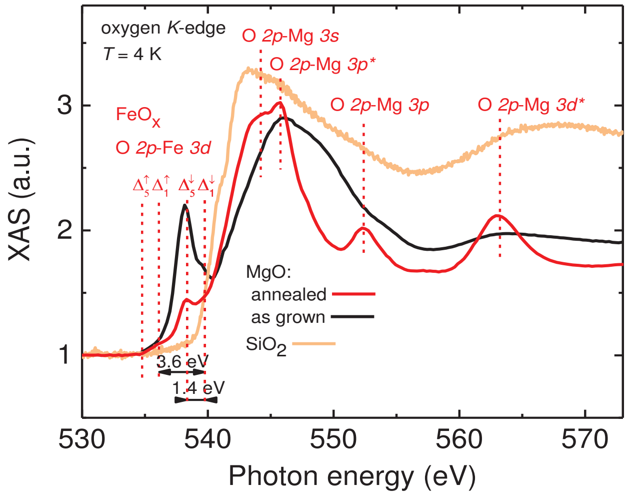

Figure 4.29: The referential XAS spectra of MgO and SiO_2. X-ray absorption acquired on the annealed and non-annealed CoFeB/MgO, and glass/SiO_2 non-processed stacks. The peak assignment is based on the literature[37,259] and reflects the allowed transitions from oxygen 1s core to the final state indicated in red.

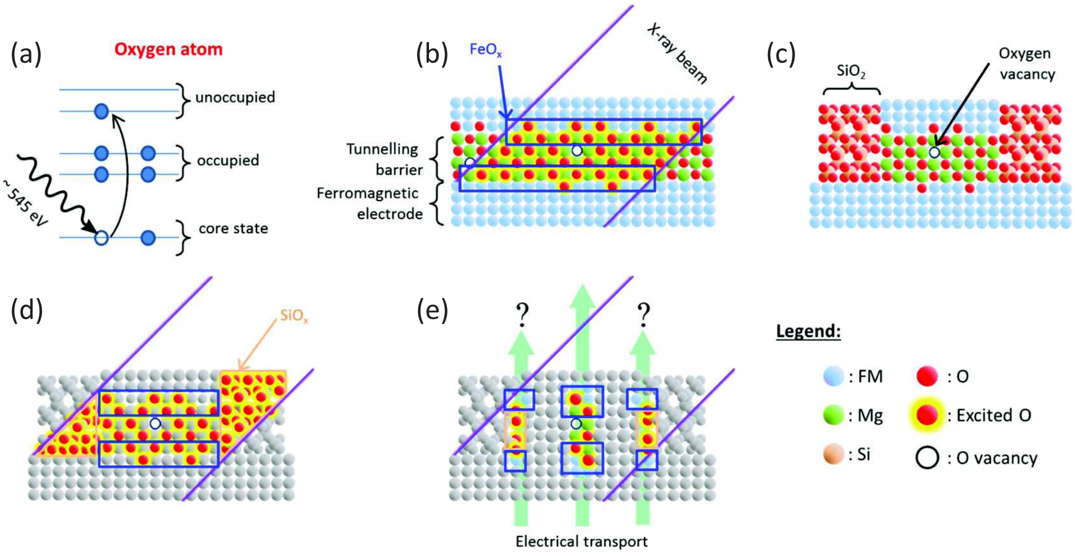

Figure 4.30: Probing a device's active atoms with combined XAS and magnetotransport measurements. (a) The photons with tuned energy (here to O K-edge) allow to probe (excite) the selected atomic species. (b) Illustration of the MgO tunnel barrier encapsulated by two FM electrodes. The x-rays excite all the oxygen sites in the system. Blue rectangles emphasize the regions of potential appearance of the interfacial oxides. (c) The pillar of a single MTJ encapsulated by SiO_2. The localized structural defects, *e.g.*, oxygen vacancy, may funnel all the tunneling current. (d) Schematic of the XAS measurement probing all the oxygen sites within the system. (e) Principle of combined XAS and electric measurement revealing the information about only those oxygen sites which contribute to the transport.

all the mentioned contributions. This is why the spectra presented in Fig. 4.29 were recorded separately on the referential stacks.

The direct linking of the spectroscopic studies discussed above to magnetotransport is rather tenuous. Firstly, the XAS data do not resolve whether the witnessed Fe oxides may nevertheless participate in magnetotransport and we can only state that they are reduced upon annealing. Secondly, as we mentioned the magnetotransport involves only a subset of these interfacial atoms. It is commonly accepted that the nanoscale structural defects in the tunnel barrier lead to an effective reduction of the barrier spatial extent and energy height.[10, 261–264] These form the so-called "hotspots" which funnel almost all the tunneling current[262, 265] and therefore their combined electronic properties shall drive the overall MTJ performance. This is illustratively depicted in Fig. 4.30 (c). Note that the MTJ encapsulation in a form of dielectric SiO_2 layer (see Fig. 4.30 (d)) can in principle alter the MTJ pillar periphery chemistry and thus impact also TMR, yet the understanding of this impact is rather unknown.

Now, we discuss the combined XAS and electric measurement. We recorded the electronic transport across the MTJ while sweeping the photon energy. As mentioned before, we used a synchronization protocol on the basis of a common timestamp for the two output datasets to obtain the MTJ current flow as a function of the photon energy ($I(t) + XAS(E) \rightarrow I(E)$). In Fig. 4.31 we present an exemplary $I(E)$ curve for the energy range corresponding to the O K-edge. The large signal variation at

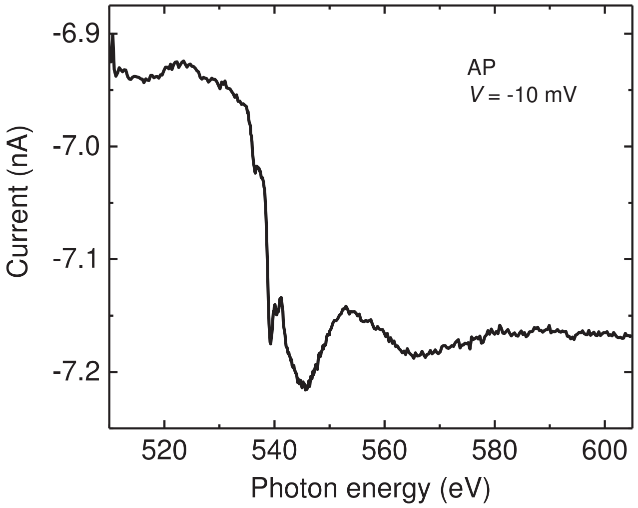

Figure 4.31: Synchronized XAS and magnetotransport measurement. The exemplary raw transport curve as a function of the photon energy resulting from the synchronized measurement of $I(t)$ and $XAS(E)$. The large signal variation around 537 eV arises from the contribution of the photocurrent.

$\sim$ 537 eV results mainly from the x-ray-generated secondary electrons, that is the photocurrent (PC), which contribute to the magnetotransport. In order to witness the subtle alterations of the device transport properties upon x-ray absorption one has to subtract the contribution of PC. It is important to notice, that in our case the PC flows always in the same direction, therefore by approximating a low bias junction transport as symmetric we can perform the subtraction in the following way:

$$R(E) = \frac{2V}{I_+(E) - I_-(E)} \tag{4.33}$$

where V is the absolute value of the bias voltage and $I_{+\ (-)}(E)$ stands for the MTJ current as a function of the photon energy for positive (negative) voltage. In this way, we separate the PC generation from the effects arising from the electronic modifications of the junction matter.

Figure 4.32 (b) and (c) show the resulting $R(E)$ dependence at $T = 20\,\mathrm{K}$ upon reaching the O K-edge for a 10 mV applied voltage in the parallel (R_P) and antiparallel (R_AP) configurations of the electrode magnetization. These MTJ P and AP magnetic states are governed by the dominant transmission channel of the electrons with Δ_1 and Δ_5 symmetries respectively.[34, 52, 65] We present the data obtained for the x-ray photons with linear vertical polarization, that is in the plane of the MTJ interfaces, as the representative dataset.

We focus first on the pre-edge energy region and find that R_P exhibits a large minimum at 539.3 eV when addressing the $\Delta_1^\downarrow$ state of the interfacial Fe oxide. This may be explained by an additional electron in the "excited" state which enhances the electrical transport across the otherwise insulating Fe oxide, causing the resistance to decrease. The appearance of this effect only in R_P upon addressing the $\Delta_1^\downarrow$ is not surprising since the Δ_1 transmission channel dominates the solid-state tunneling across MgO in the P state. On the contrary, R_AP is not affected by the photoexcitation of

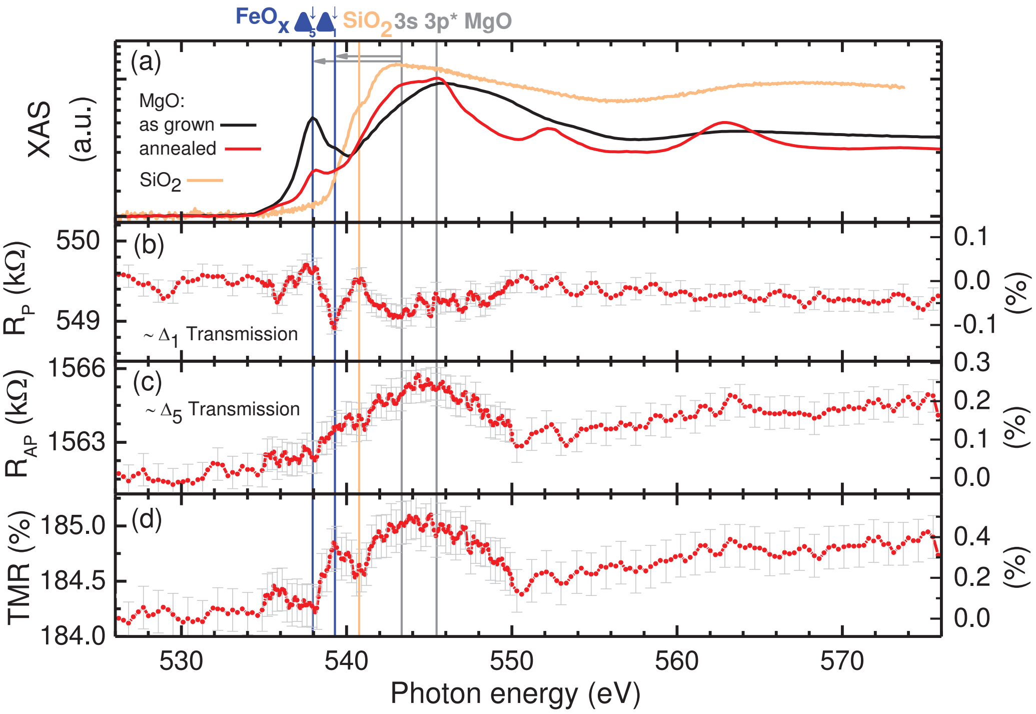

Figure 4.32: Combined XAS and magnetoresistance measurements of MgO-based MTJ. (a) The XAS spectra acquired with linear vertical polarized photons at the reference stacks of annealed and non-annealed MgO, and encapsulating SiO_2. Note a decreasing intensity of the Fe oxide peaks upon annealing. The photon energy dependence of the MTJ resistance in P (b) and AP (c) states with resulting TMR ratio (d) were recorded at $T = 20\,\mathrm{K}$ and low bias voltage $V = \pm 10\,\mathrm{mV}$. The right hand scale reflects the deviation from the baseline established at the pre-edge region.

the Fe oxide spin-down states ($\Delta_5^{\downarrow}$) since the corresponding spin-up states are fully occupied, that is there are no available states in the counter electrode. This leads to the modification of the MTJ TMR at 10 mV (Fig. 4.32 (d)) within the O K pre-edge at 539.3 eV due to altering the electronic structure of the Fe oxides at the MTJ interfaces. This implies that despite the disappearance of the interfacial oxides upon annealing as witnessed by spectroscopic studies, the combined XAS and electric measurement reveal that the FeO_x states are still present at the interface and that they limit the TMR of the device. In addition, one observes no strong correlation between the XAS of the encapsulating SiO_2 and the magnetotransport for R_P and R_{AP}. This means that the excitation of the Si-O states do not influence the device performance, what implies that the MTJ pillar periphery plays a secondary role in the device's operation. Note, that this technique opens a new perspectives for evaluating the influence of the interfacial mixed states on the performance of a complete device.

Now, we discuss the junction's performance alteration upon reaching the maximum of the oxygen K-edge. While sweeping the photon energy across the K-edge region (535 eV – 545 eV) R_P stays mostly unaffected, that is decreases by 0.1%. In contrary, R_{AP} increases by 0.25%. The resulting TMR ratio, reaching $\sim 180\%$ in our MTJs at $T = 20\,\mathrm{K}$, increases by $\sim 0.5\%$.

In order to understand this behavior, we calculated the complex band structure

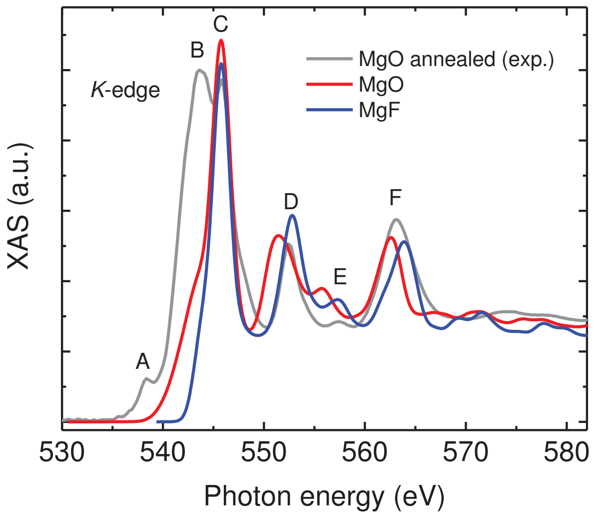

Figure 4.33: Theoretical XAS spectra of MgO and MgF. The result of calculation for the K-edge shape of the oxygen (fluorine) within MgO (MgF). The spectra are energy-shifted and compared to the experimental data acquired on annealed CoFeB/MgO stack. The peaks C, D, E, and F well reproduce the experimental result. The substitution of the oxygen sites with fluorine preserves the same set of allowed dipolar transitions.

(CBS) of an MgO under the x-ray excitation. The theoretical simulations presented in the following part were carried out by Beata Taudul from Mebarek Alouani's group at the IPCMS. The CBS was calculated by using the so-called $Z+1$ approach. This widely used approximation for simulating the electronic structure of an atom upon absorption of the x-ray photon[266–268] places an additional electron in the conduction band which mimics the x-ray excited state. This in practice means the replacement of the oxygen in MgO by fluorine.

To validate this approach, the theoretical XAS of MgO and MgF were calculated using the VASP package.[269] Details about the implementation of the XAS code can be found in ref. 270. The cell contained MgO and MgF in the *bcc* structure and two atoms per unit cell. Calculations were performed using GGA(PBE)[271] for the exchange correlation energy within the PAW[272] basis set. The k-point 9×9×9 points was G-centered. The plane wave cut-off for the ground state was set to 500 eV with the convergence criteria 1×10^{-5} eV. The results are presented in Fig. 4.33. To match the experimental XAS spectra the theoretical curves were energy-shifted and a step function was added. Note that these calculations do not include the core hole in MgF. For the calculated XAS spectra we find a good agreement regarding the energy separation between the peaks C, D, E, and F. The edge shapes imply that replacing the oxygen sites with fluorine keeps a similar set of allowed dipolar transitions. Therefore, this suggest that the assumed approximation gives a reasonable outcome.

To further validate the use of $Z+1$ method the ground state calculations were conducted for MgF and MgO with and without taking into account the core hole (denoted later as "Oh"). That was performed with the Quantum Espresso package.[273] In Fig. 4.34 (a) we first compare the total DOS of MgOh and MgF conduction bands and acknowledge their similar shapes. This is further confirmed by the p-projected DOS (Fig. 4.34 (b)) for fluorine and oxygen atoms including the core hole. This

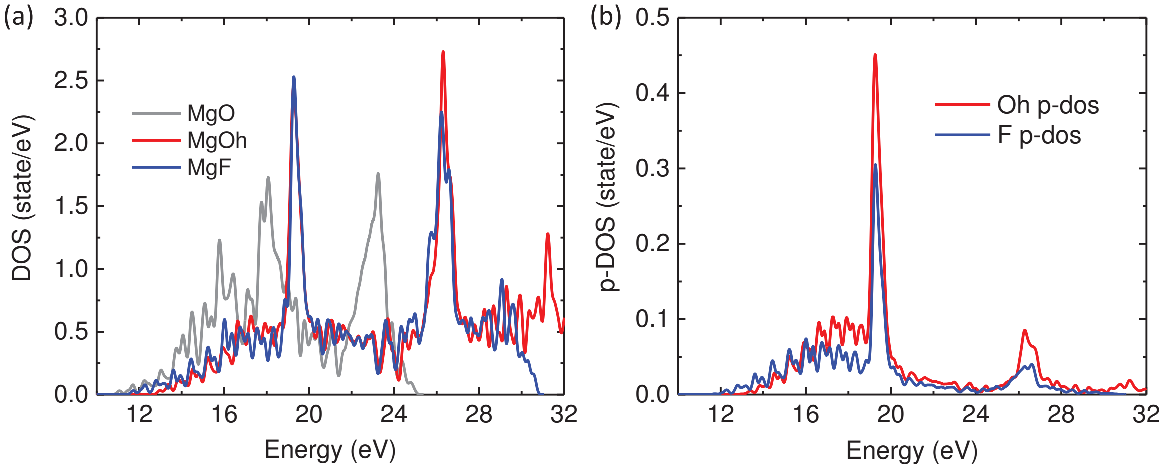

Figure 4.34: Calculation of the MgO and MgF ground state density of states. The total (a) and *p*-projected (b) conduction band DOS of MgF, MgO, and MgOh with "Oh" denoting the inclusion of the core hole.

implies that MgF can be used as the approximation of the x-ray photoexcited MgO with a core hole, thus that the $Z + 1$ approach can be employed to calculated CBS. Note that the DOS of MgF and MgO without the core hole are substantially different.

Finally, the CBS calculations were carried out with the PWcond[274, 275] module of the Quantum Espresso package.[273] Because of the limitations of the method used to analyse the CBS we assumed the case where all of the oxygen atoms are excited. Within the more realistic picture one would consider the calculations of a supercell containing only one "excited" atom. However, the use of supercells inevitably leads to the so-called band folding that makes impossible to extract the information about the Δ_5 complex loop. Furthermore, one excited atom in a supercell (64 MgO atoms with one oxygen atom replaced by fluorine) results only in minor changes in the resulting CBS (not shown here). That is why we assumed the limiting case with the maximum possible impact of the x-ray absorption on the Δ_1 and Δ_5 transmission channels. Note that this picture is closer to the scenario where the tunneling current is funneled through the "hotspots". We used a tetragonal cell with 4 atoms. The CBS loops were evaluated along $\Gamma - X$ high symmetry direction of the Brillouin zone. We extracted only the data corresponding to the Δ_1 and Δ_5 symmetry channels. The Fermi level was set to the mid gap of MgO. The result of CBS calculation is presented in Fig. 4.35 where the MgF core hole loops are denoted as the "excited MgO".

The calculated loops lengths are directly related to the tunneling current attenuation coefficients κ_1 and κ_5 of the electrons with symmetry Δ_1 and Δ_5 respectively.[11] Now, we focus on the variation of these two attenuation coefficients when the MgO becomes excited. We see that around the Fermi level the κ_1 coefficient, governing the transmission in the P state, increases very moderately. In contrary, we witness a notable increase of the κ_5 rate, which dominates the transmission in the MTJ AP state. Now, if we simply assume R (R_o) to be the MTJ resistance with (without) the x-ray photoelectron the attenuation can be expressed as $R = R_o e^{-\kappa d}$, where d is the barrier thickness. Then, the absolute changes $d\kappa_1 = -0.05$ and $d\kappa_5 = -0.15$ in the tunneling attenuation lead to a three times smaller impact on R_P compared to R_{AP}. This supports our experimental observations of a sizeable increase in R_{AP} and a much lower impact on R_{P} (within the noise level). Note that the CBS calculations were to simulate the extreme case and the direction of the experimentally observed phenomena and not to model the real system. This is why one should consider it as giving a qualitative trend comparable with the experiment.

In that way, we demonstrated how the soft x-ray spectroscopy can be combined with the electric transport measurement to obtain a device-driven atomic selectivity. This double selectivity can provide the information about a small subset of atoms contributing to performance of a microelectronic device such as the MgO-based magnetic tunnel junction. This technique enabled by the development of the $\mathrm{V^2TI}$ may promote a more comprehensive understanding of how a complete device operate. The application of this method can give an insight into the next-generation materials,[276,277] photophysics of the perovskite solar cells,[278–280] and more generally promote the synergy in material and spectroscopic studies towards a better understanding of the mostly phenomenological picture of the device operation.

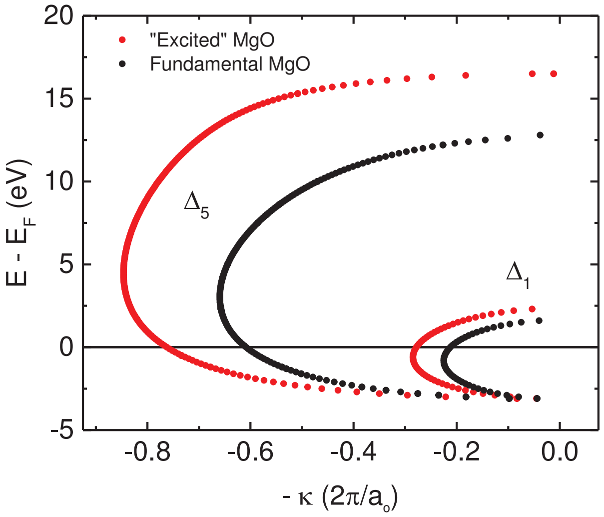

Figure 4.35: Complex band structure calculation of MgO. Result of the Z+1 simulation described in text. The complex loops length for the Δ_1 and Δ_5 electronic symmetry reflects the alteration of the tunneling current attenuation coefficients κ_1 and κ_5 upon absorption of the x-ray photon by the oxygen site. This confirms the minor (sizeable) variation of the R_{P} (R_{AP}), governed by Δ_1 (Δ_5) transmission channel, upon reaching the oxygen K-edge witnessed in the experiment.

Part III

Results and discussion

5

Metal/organic interface: magnetic ordering and spin polarization

We mentioned that one of the advantages of employing the organic materials in spintronics lies in a great potential from perspective of chemical engineering. The advancement of modern chemistry gives almost unlimited possibilities allowing creative designing of structure and properties of the compounds. Whatsoever, the broad range of possible characteristics also impose a requirement of its careful selection in order to maximize the potential usefulness in the field of spintronics. There are few notably important issues to be regarded in this respect. (i) One has to consider a chemical compatibility of the compound to desired molecular deposition technique. The non-neutral complexes will not undergo a UHV thermal sublimation, in some cases molecular bonds may break before the sublimation occurs, for wet deposition methods the compound has to be compatible with a solvent, etc. (ii) The choice of the elements comprising the molecule determines not only its general physical properties, but as well such subtle characteristics as the molecular magnetic moment or electronegativity, essential from the spintronic perspective. (iii) A molecular geometry is also an important factor governing the adsorption and stacking arrangement when a complex is deposited on a surface. This dictates the orbitals overlap, hybridization with the substrate and intermolecular interactions. (iv) Finally, the complexity and cost of synthesis often determine whether material is applicable for a large scale production. The optimization of all those criteria at the same time is often impossible and one has to find a compromise while choosing appropriate complex. This is why organic spintronics in a particular way requires a good synergy between the material science and organic chemistry.

5.1 Metal-phthalocyanine complexes

For studying the hybrid metal/organic interfaces we chose the archetypal phthalocyanine (Pc) molecules. Their early history dates back to 1907 when the first metal-free H_2Pc was accidentally synthesized by Braun and Tchemiac.[281] Although the term "phthalocyanine" was introduced as late as in 1933 by Linstead,[282] the discovery of Braun and Tchemiac is considered as the birth of this molecular family. The Pcs include already mentioned metal-free phthalocyanine and several thousand of derivatives including over 40 metal-phthalocyanine (MPc) complexes. The latter drew a particular attention in the field of electronics/spintronics and will be discussed in detail in this section.

Copper phthalocyanine (CuPc) was the first metal-Pc to be synthesized in 1927 by de Diesbach and von der Weid.[283] They pointed out the remarkable stability of the complex to alkalis, heat, light or acids, insolubility in water and organic solvents. Thanks to these properties and a deep blue color it was very fast recognized as a valuable coloring matter and loudly called the first blue pigment discovery in 100 years. Mass produced since 1934 under the name Monastral or phthalo blue till this day finds its main application in dying industry. The next metal-Pc discovered was FePc in 1928 followed later by many others.[284] Popularization of the phthalocyanines stimulated the scientific community to study its structure and properties. This gave rise to application of Pcs in such fields as the petroleum industry or medicine. Finally, phthalocyanines occurred to be relevant also for the field of organic electronics and applications in the photovoltaics,[285,286] light emitters,[287,288] field-effect transistors,[289] gas sensors,[290] or even data storage technology.[291]

There are numerous arguments for metal-phthalocynanines to be also promising candidates for spintronic applications. Referring to the criteria mentioned on the beginning of this chapter: (i) MPcs are characterized with a very good thermal stability and robustness in sublimation. This allows fabrication of the pure UHV sublimed thin

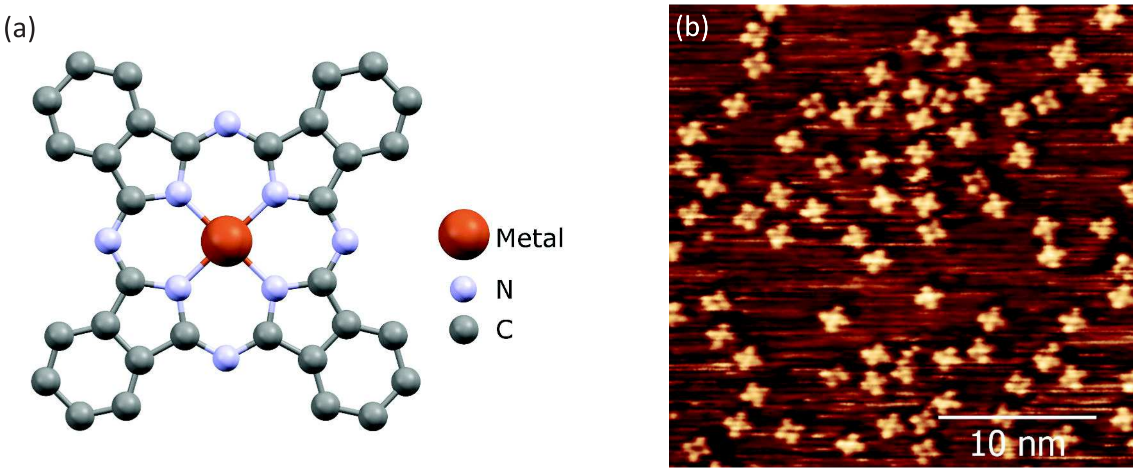

Figure 5.1: Metal-phthalocyanine (MPc). (a) Model of metal-phthalocyanine molecule. (b) I-const. room temperature STM image of MnPc on Cu(100) surface revealing planar adsorption of molecules on the surface. Area: $29 \times 29\,\mathrm{nm}^2$, $I = 500\,\mathrm{pA}$, $V = -0.8\,\mathrm{V}$.

films; (ii) there is a wide range of available MPcs differing with the metal ion and the ones with a transition metal center may possess a localized magnetic moment; (iii) majority of metal-phthalocyanine molecules have planar symmetry what imposes a flat adsorption on a surface exposing many atomic sites for potential hybridization; (iv) due to the commonness of this complexes in industry it is easy and cheap to obtain them in a pure form. The next section provides a detailed description of the molecular structure and electronic/magnetic properties of metal-phthalocyanines with an emphasis on Mn- and FePc which were used in this thesis.

5.1.1 Structural properties

Phthalocyanines are macrocyclic compounds of formula $C_{32}H_{18}N_8$ (metal free molecule). In metal-Pc two central hydrogen atoms are replaced with a divalent metal (Fig. 5.1 (a)). Two of the nitrogens share the electrons with a metal forming thus the covalent bonds meanwhile the other two the coordinate covalent. In that way, the 4 isoindol units form an organic cage for a central ion. The character of the chemical bonds explains the unusual stability and robustness of the MPc molecules.

A metal-free Pc has a D_{2h} symmetry and adding a central metal cation increases the symmetry to D_{4h}.[292] Raman spectroscopy studies revealed the N-metal-N cage size to be dependent on the ion and ranging from 3.66 Å for NiPc to 3.96 Å for PtPc.[293] Vast majority of the MPcs have a planar symmetry with a few exceptions (ZnPc, SnPc, PbPc), where the central ion protrudes from the molecular plane reducing the symmetry to C_{4v}.

The x-ray diffraction studies revealed that all MPcs crystallize in the monoclinic system with 2 molecules per unit cell.[295] The phthalocyanines exhibit a polymorphism of a stacking arrangement differing with a tilt of the molecular plane with respect to the growth direction.[296] Since our studies are limited to the molecular thin films we omit here details of the structural properties within the monocrystals. At least 3 polymorphic forms of phthalocyanine films were discovered with two: α and β, considered

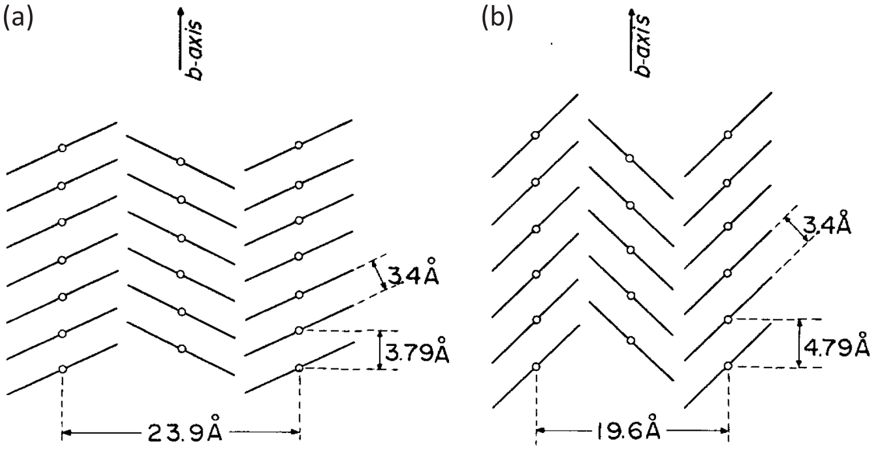

Figure 5.2: Polymorphism of CuPc. Two polymorphic (a) α, and (b) β forms of CuPc stacking arrangement with a 65° and 45° angle of molecular plate to b-axis respectively. Figure taken from ref. 294.

as metastable (Fig. 5.2). They crystallize in $C2/c$ and $P2_1/a$ space groups respectively. Both can be obtained in UHV by a thermal sublimation. A crystallization of a given polymorph strongly depends on such factors as the substrate type[297] or deposition temperature.[295] Roughly speaking, the thin films of MnPc sublimed at room temperature tend to form the α structure, meanwhile the β form can be achieved in a high-temperature deposition process or a postgrowth annealing of the α film at 200 °C. On the other hand, the α polymorph of FePc is metastable and can be formed in a cold deposition. The stable β one is obtained in both room temperature sublimation and annealing of the α film to 350 °C.[298] The preferential stacking within the phthalocyanine films was reported to be strongly dependent on a material thickness. For example, the thin films of H_2Pc up to $\sim 55\,\mathrm{nm}$ tend towards the α form, within thickness range $\sim 55\,\mathrm{nm}$ to $95\,\mathrm{nm}$ one finds a coexistence of both forms, and for thick films of more than $\sim 100\,\mathrm{nm}$ the β-phase is a stable one.[296]

5.1.2 Electronic structure and magnetic properties

The geometrical aspects of both molecular symmetry and stacking arrangement discussed in the previous section determine the electronic properties of Pc. A considerable effort was devoted to conceive and experimentally verify the electronic structure of metal-phthalocyanines.[299,300]

Liao *et al.*[299] theoretically predicted, by means of density functional theory, that the central metal cation is strongly bound by as much as 10 eV to the Pc ring. Otherwise degenerated $3d$ bands of the free metal atom are subjected to a strong ligand field in MPc which splits them into $a_{1g}(d_{z^2})$, $b_{1g}(d_{x^2-y^2})$, $e_g(d_{zx}$ and $d_{yz})$, $b_{2g}(d_{xy})$ with xy in the molecular plane. The orbitals d_{xz} and d_{yz} have a π character meanwhile the rest are of σ type. The electronic configuration of the MPc ground state strongly depends on the metal ion and other factors such as temperature. These dependencies are on one hand a source of a complication for resolving the structure, on the other hand add a tunability to the system (*e.g.*, manipulation of magnetic anisotropy direction[301]).

Many comprehensive studies were dedicated to resolve the electronic structure of MPcs with various metal cations. The most important for us, MnPc and FePc, have similar configuration and therefore can be discussed collectively. Figure 5.3 presents the result of DFT calculation of the molecular orbital levels for several MPcs. One can deduce that in the case of FePc (similar to MnPc) the HOMO constitutes of the Fe-d_π orbitals (e_g symmetry). The configuration of its ground state seems to be still an open debate. Evangelisti *et al.*[298] suggested that both α and β polymorphs of FePc exhibit $(b_{2g})^2(e_g)^3(a_{1g})^1$ configuration what is in agreement with observed strong Fe-Fe direct exchange coupling along the molecular chains. The HOMO of MnPc has been calculated as one of the three configurations with $(b_{2g})^1(e_g)^3(a_{1g})^1(b_{1g})^0$ as the lowest in energy,[301] what was supported experimentally for MnPc in Ar matrix.[302] Note that with increasing the atomic number of the metal ion the HOMO of MPc becomes more and more Pc determined (decrease of d character, Fig. 5.3 Cu-, Zn-, MgPc)).

Fig. 5.4 shows the spin-resolved density of states (SR-DOS) for Fe- and MnPc free molecule. In case of FePc, it is clear that the states present at the Fermi level are of Fe d orbitals origin (with main component $d_{x^2-y^2}$).[303] The second order spin-orbit coupling in a tetragonal field leads to the $(d\uparrow)^4(d\downarrow)^2$ configuration ($S = 1$).[304]

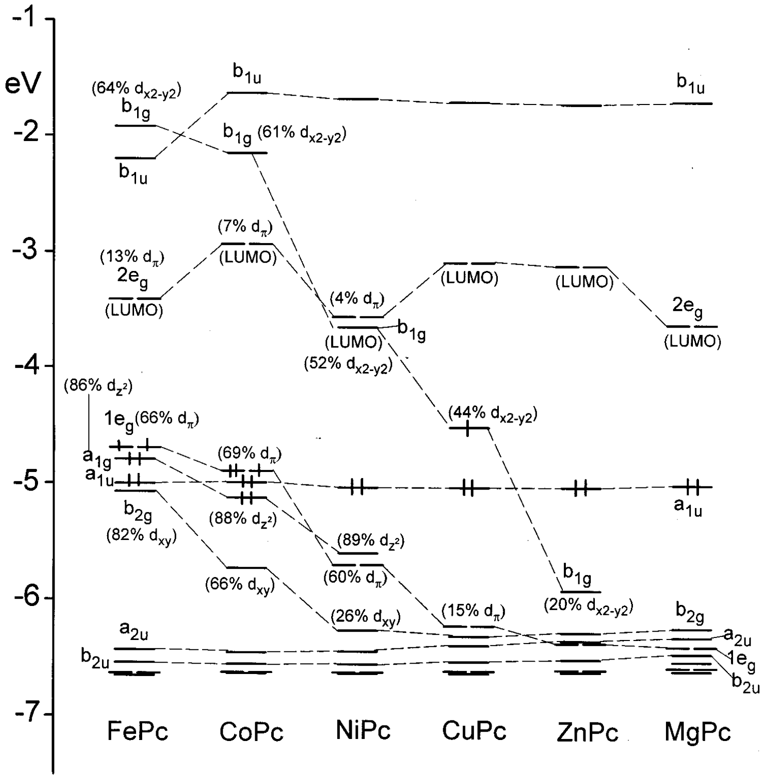

Figure 5.3: The outer orbitals energy levels of MPcs. The result of DFT calculation revealing the HOMO of FePc to have a high degree of Fe-*d* character. By increasing the atomic number of a metal ion the HOMO of MPc becomes more Pc determined. The orbital occupancy in percentage is indicated in parentheses. The figure taken from ref. 299.

This unbalanced populations of the Fe 3*d* spin-up/spin-down electrons result in a net magnetic moment of 2.0 μ_B per FePc molecule. The SR-DOS of MnPc (Fig. 5.4 (b)) reveals a high degree of spin polarization of Mn orbitals (pink coloured area) as well as the orbitals of the Pc ring (a_{1g}, b_{2g}, e_{1g}). The resulting net magnetic moment is 3.0 μ_B per MnPc molecule. Table 5.1 collects the magnetic moments with distinction to the spin and orbital contributions and the magnetocrystalline anisotropy energies for Fe- and MnPc free molecules. Note that the magnetocrystalline anisotropy for MnPc has an out-of-plane orientation meanwhile in case of FePc it lies in the molecular plane.

As mentioned before, the character of the magnetic correlations in MPcs columnar chain depends on the electronic configuration of the metal cation, intermolecular distance, and the tilt of the molecular plane. Accordingly, one should therefore expect unequal magnetic properties for the α and β polymorphs.

In order to understand the magnetic properties of the MPcs one has to consider its intrinsic and intermolecular contribution. We mentioned before that a non-zero spin of the metal cation of MPc can be a source of a localized magnetic moment. This intrinsic feature is responsible for a paramagnetism of a free MPc molecule. When deposited on a surface the molecules can form the aforementioned columnar structure leading to the molecular orbitals overlap and thus to exchange interactions. This in turn, depending on a stacking arrangement and the tilt of the molecular plane, can result in ferro/antiferromagnetism of the structure and a spontaneous magnetization in the

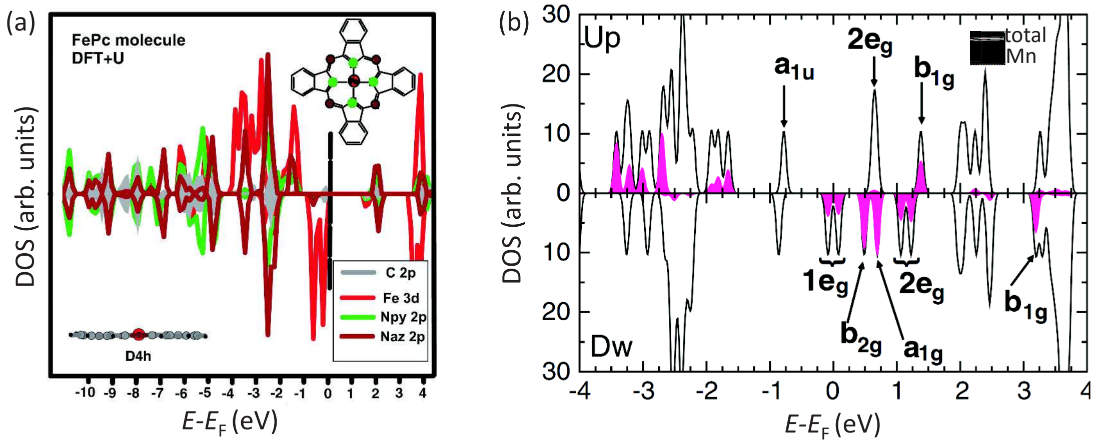

Figure 5.4: Spin-resolved density of states of Fe- and MnPc. The result of calculation for (a) FePc and (b) MnPc free molecules. The majority and minority channels are drawn respectively on the opposite sides of the horizontal axis. Figures taken from ref. 305 and 306.

absence of the external magnetic field. There is also possible an interesting scenario in double-decker MPc complexes (*e.g.*, Pc_2Ln, Ln - traivalen lanthanide ion) where spontaneous magnetization occurs without a long-range magnetic ordering. The latter case referred to as single-molecule magnet (SMM) is not the object of this study and will be omitted. In the next paragraph, we discuss the magnetism of Fe- and MnPc molecules.

The FePc molecules in the metastable α stacking (Fig. 5.5 (e)) exhibit a strong exchange coupling of the Fe centers along the vertical axis of the chain and a weak intercolumnar antiferromagnetic coupling with moments canting leading to a soft ferromagnetism below 10 K.[298] The energy of magnetic coupling between the Fe atoms along the chain was established as $J/\mathrm{k_B} \sim 15\,\mathrm{K}$ with an effective spin of $S = 1$ per metal atom. One the other hand, the β form of FePc exhibits no magnetic ordering due to the reduced exchange coupling along the chain, hence it remains paramagnetic at all temperatures.

Conversely, the α (β) form of MnPc exhibits the antiferromagnetic (ferromagnetic) ordering within the molecular chain. The schematic arrangement of the two neighboring molecular columns of the β MnPc is depicted in Fig 5.5 (f). A short 3.4 Å distance

Table 5.1: The result of *ab initio* calculations for the nearest metal-nitrogen distance (d_{MN}), total spin (M_{S}) and orbital (M_{L}) magnetic moments, and magnetocrystalline anisotropy energies (E_{MCA}) in Mn- and FePc free molecule. The positive (negative) sign of E_{MCA} corresponds to out of (in) molecular plane orientation of the easy axis. Data taken from ref. 307.

	d_{MN} (Å)	M_{s} (μ_{B})	M_{L} (μ_{B})	E_{MCA} (meV)
MnPc	1.95	3.0	0.19	2.72
FePc	1.94	2.0	0.15	-1.18

and 90° Mn-N-Mn configuration allows the superexchange interaction resulting in ferromagnetism below $T_\mathrm{C} \sim 9\,\mathrm{K}$ with an exchange energy $J = 7.7\,\mathrm{cm} - 1$ and the total spin $S = 3/2$ per molecule.[308] The β polymorph of MnPc exhibits a stacking angle of 65° promoting the AFM ordering.

More precisely, the magnetism of MPcs can be explained by considering the overlap of particular molecular orbitals (Fig. 5.5 (a) – (d)). The only path for a ferromagnetic coupling is formed between the E_g orbital of Pc ring and a_{1g} of the metal cation (Fig. 5.5 (a)). The AFM interaction is established by the overlap of the e_g orbital of the metal and E_g of Pc (Fig. 5.5 (b)). Within this picture, the change of the molecular plane tilt (compare Fig. 5.5 (a),(b) and (c),(d)) eventually leads to the competing FM/AFM couplings and particularly different magnetic ordering in the α and β phases. One has to keep in mind the key importance for the magnetic coupling of the ground state configuration which is responsible for unequal behavior of Fe- and MnPc in these considerations.

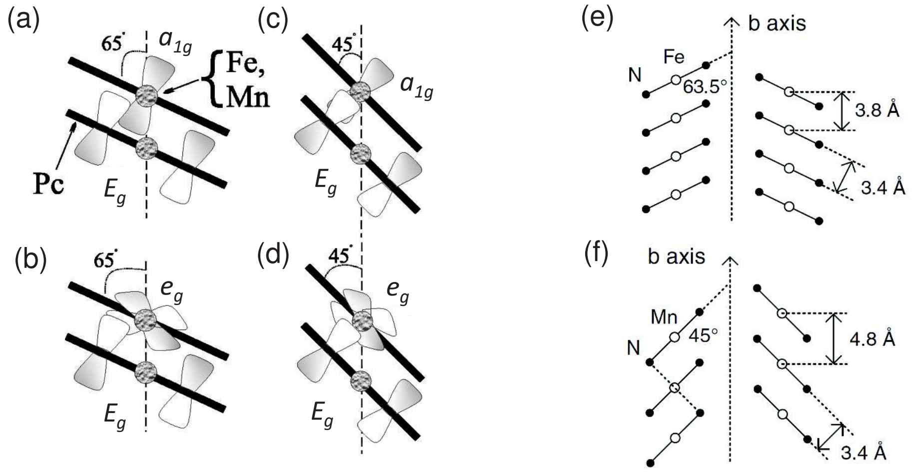

Figure 5.5: Magnetic ordering within the Fe- and MnPc molecular chain. The orbitals overlap between the adjacent Fe- and MnPc molecules in (a)-(b) α, and (c)-(d) β form. The stacking arrangement of the molecular chain along b axis for (e) FePc in the α polymorph, and (f) MnPc in the β polymorph. Figures taken from ref. 298 and 309.

The invoked information about the metal-phthalocyanine complexes are essential for further understanding of the effects arising at the hybrid FM/organic interface. In the next sections, we present the results of the studies dedicated to particular ferromagnetic/organometallic heterostructure.

5.2 Magnetic ordering in a Co/MnPc heterostructure

In the theoretical introduction (Sec. 1.3.2) we discussed how a spinterface between an organic molecule and a ferromagnet can be formed in a particular case of Co/MnPc. The p_z-d hybridization[89] accompanied by the electron transfer towards the molecule eventually leads to the orbitals reconfiguration and appearance of the new interface states. This in turn may induce a magnetic moment stabilization within the molecule or appearance of the spin polarization at the Fermi level. One has to keep in mind that the nature of emerging spinterface strongly depends on a particular molecule-substrate pair. This was emphasized by a work of Rizzini *et al.*[310] who performed a comprehensive study over a coupling of the single, double, and triple-decker metal-phthalocyanines to various metallic substrates. They stressed on the adsorption induced charge transfer from the substrate to π orbitals of the molecular macrocycles and to d orbitals of the metal ion, leading to a suppression or enhancement of the molecular magnetic moment depending on the d-π exchange coupling and the symmetry of d states. The magnetic moment coupling to an FM surface was found to be ferromagnetic for all cases of the planar MPcs due to a direct exchange path formed between the metal ion and the underlying substrate atoms. Particularly manganese-phthalocyanine FM coupling to Co substrate at room temperature was also reported.[311,312]

I want to stress that despite my considerable involvement and personal participation in the experiments presented in the following sections (5.2 – 5.4), the main contribution belongs to my predecessor.[17] These studies were continued within the framework of this thesis and extended by a spin-resolved photoemission experiments (Sec. 5.5). The outcomes of those investigations were used to design a concept of more complex multiferroic system presented in Sec. 6.2.

In this part, we present a study on the magnetic coupling of the Mn paramagnetic centers of MnPc molecules to ferromagnetic Co at the interface and a consequent magnetic order stabilization within the organic layer. For this purpose, we devoted an experiment at the DEIMOS beamline. The wedge-shaped sample was *in situ* fabricated according to the following procedure. A Cu(100) monocrystal was cleaned by Ar^+-ion sputtering and annealed at 500 °C. Then, 7 ML of cobalt was deposited uniformly onto Cu(100). In order to flatten the Co layer the stack was annealed at 100 °C for 10 min. Finally, the MnPc molecular layers were deposited from Knudsen cell heated up to 380 °C. During the sublimation a shutter was moved in front of the sample such that a wedge varying the MnPc thickness was obtained (0 – 3.6 ML along 4.5 mm distance). The nominal thickness value was established by using the STM, XAS, AES and a quartz microbalance. Note that the spatial extend of the x-ray beam limited the thickness resolution to ±0.5 ML. The XAS/XMCD measurements were performed in the total electron yield mode. Since the easy axis of Co was oriented in the sample plane the x-rays were impinging at 40° to the surface in order to probe the in-plane component of the magnetization.

The measurements were performed under two specific external conditions: (1) at room temperature ($T = 295\,\mathrm{K}$) and low magnetic field ($H = 0.1\,\mathrm{T}$), and (2) at low temperature ($T = 4.8\,\mathrm{K}$) and strong magnetic field ($H = 6.5\,\mathrm{T}$). Since the paramagnetic Mn centers obey the Brillouin function, the situation (1) leads only to negligible

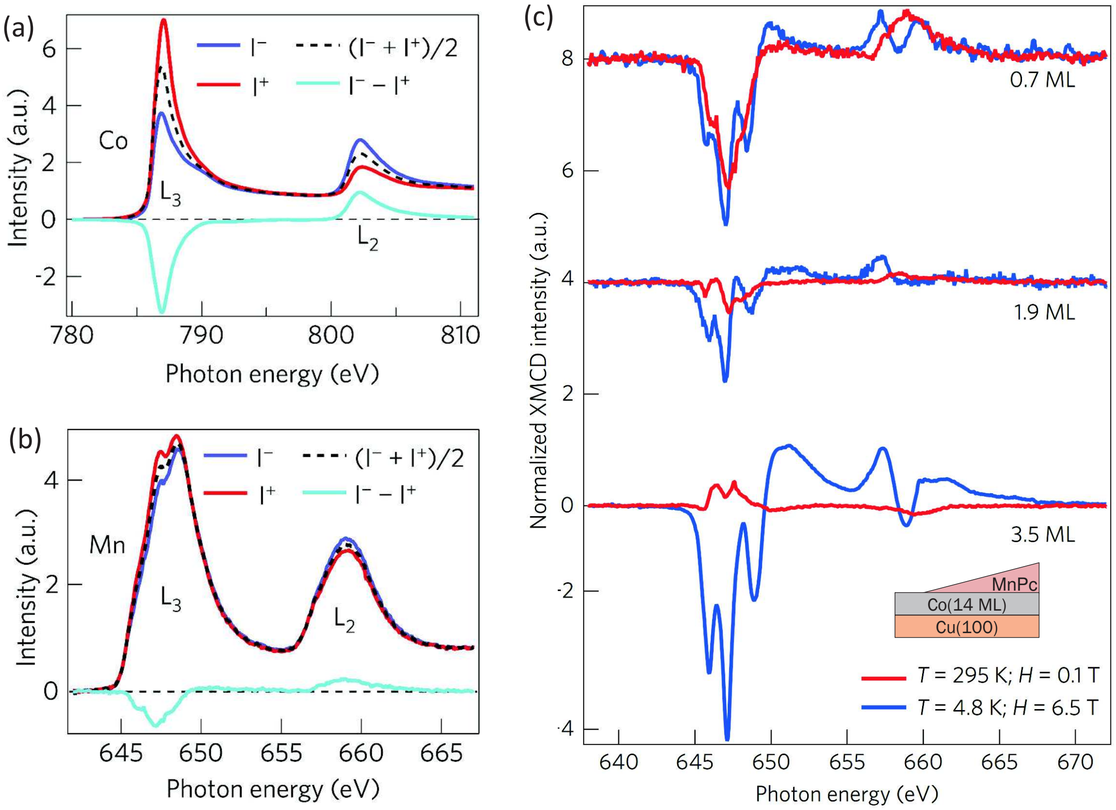

Figure 5.6: Magnetic coupling in Co/MnPc heterostructure. XAS and corresponding XMCD signal at $L_{3,2}$-edges of Co (a), and Mn (b) revealing the FM coupling of the first molecular layer to underlying ferrommagnet at RT ($H = 0.1\,\mathrm{T}$). (c) XMCD at Mn $L_{3,2}$-edges recorded along the molecular wedge for 0.7 ML, 1.9 ML, and 3.5 ML thickness. The difference between blue and red curve represents the non-coupled paramagnetic Mn centers in the system. All curves are normalized to white line integral thus to amount of probed matter. Inset depicts the sample composition. Figures reprinted from ref. 17.

amount of Mn moments to be oriented along H, whereas the field is sufficient to saturate the Co layer magnetization. The case (2), in turn, ensures the sufficient conditions (low T, large H) to align a considerable amount of the Mn magnetic moments along the field direction.

In Fig. 5.6 (a) and (b) we present the XMCD at $L_{3,2}$-edges of Co and Mn measured in conditions corresponding to the case (1). One clearly sees the non-zero XMCD of Mn, with the same sign as that of Co. Considering the applied conditions, such a signal can not arise from the alignment of the paramagnetic Mn centers, thus it must be a consequence of the interfacial coupling. We infer that the first ML of MnPc is FM coupled to Co at room temperature.

In the next step, we studied how the XMCD evolves when increasing the molecular thickness (Fig. 5.6 (c)). The measurement was repeated in conditions (1) and (2) and related to the XMCD at Co $L_{3,2}$-edges as shown in Fig. 5.6 (a). The comparison of recorded signals measured in case (1) and (2) allows to deduce the amount of the paramagnetic, non-coupled Mn moments in the system. The curves recorded for 0.7 ML in case (1) and (2) reveal almost equal intensity suggesting that nearly all the Mn sites are FM aligned to Co. For 1.9 ML of MnPc the XMCD recorded in conditions (1) decreases 4 times with respect to the one at 0.7 ML. Since XMCD is sensitive to the mean magnetic moment, this can be explained only by a contribution of the AFM ordering within the system. We rule out a possibility of decoupled molecules since these would lead to only twofold decrease of the intensity and at least a similar amplitude of the curve for case (2). Finally, for 3.5 ML we observe a sign reversal of the Mn XMCD such that it is in opposition to that of Co. This proves the mean magnetic moment of Mn centers to be AFM oriented with respect to Co. This result was additionally supported by the opposite switching of Mn and Co magnetic moment while reversing the external magnetic field. To comment on the curves obtained in conditions (2), for 1.9 ML and 3.5 ML we observe an overall substantially larger amplitude than for case (1). This we relate to an increasing number of the paramagnetic molecules with increasing layer thickness. We suggest that the thicker the organic layer the greater amount of the molecules which are disordered and do not form the columnar structures to allow the exchange interaction, thus coupling. Therefore, they contribute to the paramagnetic signal.

The discussed results reveal that the first ML of MnPc is FM coupled to the underlying Co at room temperature what further drives the AFM order stabilization between the consequent MnPc layers away from the interface. To support this outcome, a theoretical *ab initio* calculations were carried out by the group of Mebarek Alouani at the IPCMS. The result is illustrated in Fig. 5.7. The adsorption geometry was chosen as the most energetically favorable and corresponding to the one experimentally witnessed by Chen *et al.*[313] First, we comment on the resulting Mn magnetic moment dependence on where the molecule is situated. The MnPc of the first ML being in a direct contact with Co exhibits a reduced magnetic moment ($2.51\,\mu_\mathrm{B}$) with respect to the free molecule what is a consequence of a strong hybridization with the substrate accompanied by a charge transfer. The further the molecule is from the substrate the closer its magnetic moment to the one of the free molecule. Concerning the character of the coupling, the simulation confirms a strong FM coupling at the interface followed by the AFM ordering within further MnPc layers. Therefore, it supports our experimental results. In addition, an opposite sign of the XMCD at the Mn $L_{3,2}$-edges for 3.5 ML with respect to that of Co can be rationalized by the reduced magnetic moment of the first ML of MnPc. More details about the simulations can be found in the Supplementary Information to ref. 21.

To summarize, we showed the interfacial coupling between Co and Mn in MnPc at RT and the resulting AFM order stabilization within the organic layers. Note that this is opposite to the ferromagnetic interactions that exist between adjacent molecules in MnPc crystals.[308] We emphasize on the importance of a geometrical stacking and a key role of a columnar growth within the organic layer. The efficient magnetic coupling as illustrated in Fig. 5.6 is possible only when MnPcs are adsorbed such that the molecular planes are parallel to each other. This is difficult to fulfil utterly due to an imperfect molecular growth. Our XMCD studies (Fig. 5.6) along with the x-ray natural linear dichroism (XNLD) at nitrogen *K*-edge of MnPc and a low temperature STM (data included in the Supplementary Information to ref. 21) revealed that the molecules within the first and second ML are adsorbed almost completely flat on the Co surface meanwhile this is the case for only about one third of MnPcs within the third

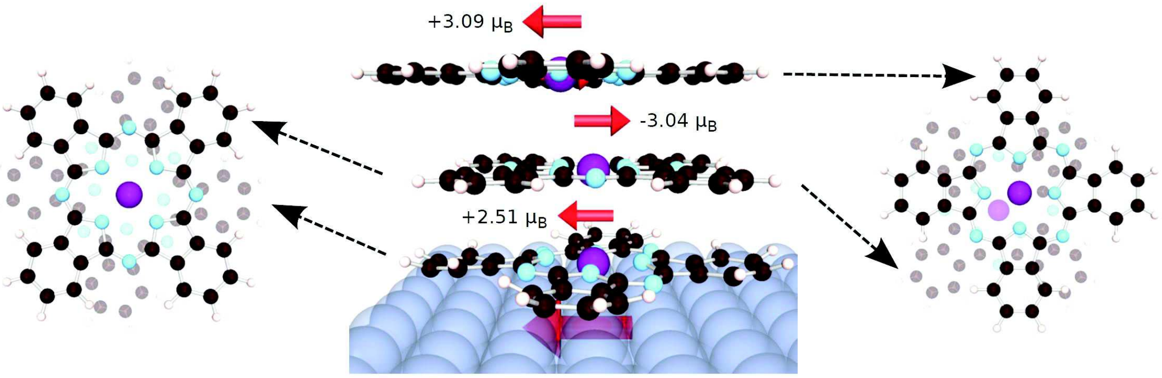

Figure 5.7: Stacking geometry and magnetic moment alignment of the MnPc molecules on Co surface. The result of *ab initio* calculations carried out for a column of 3 MnPc molecules adsorbed on the Co surface. The stacking geometry was chosen as the most energetically favorable one. The FM coupling at Co/MnPc interface and the AFM ordering of magnetic moments in the first, second, and third ML of MnPc support experimental result. Note the reduced magnetic moment of the first ML of MnPc resulting from a spinterface formation with Co. Figure taken from ref. 17.

and fourth ML.

The magnetic ordering of the ferromagnetic/organometallic system presented above resembles a well known case for inorganic system of a ferromagnet pinned by an antiferromagnet. This scenario usually leads to a phenomenon called the exchange bias (EB). In the next section we will briefly explain the origin of this effect and investigate its occurrence within the studied Co/MnPc heterostructure.

5.3 Exchange bias of Co induced by MnPc

The exchange bias, or briefly EB, can emerge whenever a ferromagnetic material is subjected to a source of unidirectional anisotropy. This can occur when a ferromagnet is exchanged coupled to an antiferromagnet. In that case the spins of the AFM at the interface exert an additional torque on the FM layer, such that the magnetic field required to reverse the FM magnetization is enlarged in one direction. Within this simplified picture, the EB eventually leads to an alteration of the FM hysteresis loop in two possible scenario. First, when an AFM material has a large magnetic anisotropy it may generate a shift of the FM associated hysteresis loop such that it is centered around a non-zero magnetic field. Second, when the AFM anisotropy is small, it eventually leads to a coercive field increase. In majority of cases the two manifestations appear simultaneously. This behavior, especially when controlled in a desired manner, finds an important application in the field of a data storage technology.[314,315] In simple words, the EB allows a particular tuning of a magnetic properties of the FM so as to adjust the material characteristics to meet the criteria of industrial applications. A prominent example in this respect is the use of the EB to reduce a saturating field required for an FM electrode switching within a GMR device,[316] what nowadays is a widely exploited technology in hard disks read heads. That underscores the relevance of EB for industrial applications. One has to keep in mind that since the origin of EB is accepted to be arising from the interfacial effects, its exact physical nature remains rather elusive.[317] This extensively studied effect was a subject of many comprehensive reviews[315,318,319] including at the nanometric scale.[320]

Exchange bias in inorganic systems was widely investigated starting from a fine particles ensemble,[321,322] thin film bilayer,[315,318,323] to lithographically fabricated nanostructures,[324,325] AFM-FM matrices[326,327] or core-shell nanoparticles.[328] In 2012, Lodi Rizzini *et al.*[329] demonstrated that a single molecule of $\mathrm{TbPc_2}$ can be subjected to EB when deposited on the Mn surface. Since Co/MnPc heterostructure discussed in the previous section resembles an inorganic FM/AFM bilayers we dedicated particular studies to check whether EB can be present in these structures. The results are discussed in the following.

The samples of composition Cu(100)//Co(20 ML)/MnPc(25 ML)/Au(15 ML) were grown in UHV environment of the Multi-Probe system. The fabrication procedure was done according to the recipe adopted from the *in situ* preparation at the DEIMOS beamline. In addition, a gold capping layer was used to prevent both organic MnPc and ferromagnetic Co layers from deteriorating in atmosphere. To study the hysteresis associated to Co/MnPc system we used a magneto-optical Kerr effect (MOKE).

The sample was subjected to a field cooling (FC) along the easy axis of Co at $H = +0.2\,\mathrm{T}$ which is sufficient to saturate Co magnetization. Then, the hysteresis loops were acquired by sweeping the magnetic field and recording an ellipticity of the reflected 670 nm laser. In Fig. 5.8 we present the hysteresis loops obtained at temperatures $T = 300\,\mathrm{K}$, 58 K, and 14 K. One clearly sees the at RT the curve is symmetric and exhibits a small coercivity. After the field cooling to $T = 58\,\mathrm{K}$ the hysteresis becomes broader and shifts towards negative fields. The effect becomes more prominent when temperature is further decreased. The hysteresis shift measured as a function of temperature revealed a blocking temperature $T_\mathrm{B} \sim 100\,\mathrm{K}$. Therefore, we claim that the hysteresis broadening and its shift in opposite to the FC direction occurring below characteristic blocking temperature T_B is a proof of the EB induced by the AFM MnPc layer on the FM Co.

The appearance of EB as observed in Fig. 5.8 suggests that the first ML of MnPc is a source of additional magnetic anisotropy imposed on Co. This was confirmed by DFT calculation supporting the experiment. In addition, the shift of the hysteresis loops implies that the AFM ordering within MnPc does not flip along with Co below T_B, otherwise EB would appear merely as increase of coercivity. The XMCD studies revealed that this is not the case for 2 ML of MnPc. Therefore, this implies that eventually at least 3 ML thick molecular columns are responsible for the observed EB. The presence of such structures within the stack was confirmed by the low temperature STM measurements.

To provide an additional evidence for the effect to originate from the EB mechanism the MOKE measurement was redone for both FC directions resulting each time with the hysteresis loop shift of the opposite sign. In addition, the measurement acquired with FC applied out-of-plane revealed the absence of EB. The study was repeated over the several MnPc layer thicknesses and showed a decreasing amplitude of EB with reducing the thickness. This dependence is observed commonly for the inorganic systems.[318] The minimum MnPc thickness at which we witnessed EB was established

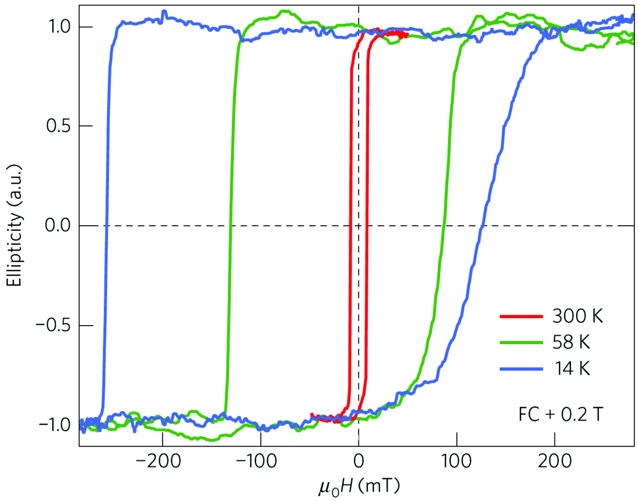

Figure 5.8: Exchange bias of Co induced by organic MnPc layer. Magnetic hysteresis loops as determined by MOKE experiment on stack Cu(100)//Co(20 ML)/MnPc(25 ML)/Au(20 ML) for $T = 300\,\mathrm{K}$, 58 K, and 14 K. The curves acquired at $T = 58\,\mathrm{K}$ and 14 K were subjected to field cooling with $H = +0.2\,\mathrm{T}$. Figure taken from ref. 21.

as 10 ML, suggesting that the effect shows up between 0 and 10 ML of the molecules. To emphasize on the key role of the molecular layer for EB the MOKE was performed also on a stack without MnPc, *i.e.*, Cu(100)//Co(20 ML)/Au(20 ML). It resulted in centered hysteresis loop, thus no EB.

To sum up, the experimental results implied that the FM coupling at Co/MnPc interface stabilizes the AFM ordering between the consecutive molecular layers and induces EB on the ferromagnetic Co below T_B ~100 K. This effect, manifesting all the hallmarks of unidirectional anisotropy as observed in inorganic systems, is a notable step towards functional organic spintronics. It does not only allow the substitution of inorganic material by organic counterpart in applications exploiting EB, but also opens the additional perspectives for, *e.g.*, spin-polarized transport through organic layer stabilized by FM.

5.4 MnPc magnetism stabilization by interlayer exchange coupling

In the previous sections we investigated the magnetic ordering and its consequences within a system where the MnPc molecules are in a direct contact with cobalt. One has to keep in mind that the fabrication of such heterostructure and the requirement on the excellent quality of a metal/organic interface imposes a fabrication in UHV conditions. This, however, is rather expensive and not suitable for a large scale production. One of the approaches to overcome this problem without risking the oxidation of the FM layer is to employ a noble metal spacer as the mediator of the interaction. This concept, referred to as interlayer exchange coupling (IEC), was extensively studied for inorganic systems[43, 330–332] what eventually led to the discovery of giant magnetoresistance.

In the next paragraphs we briefly describe the fundamentals of IEC.

There are numerous models attempting to explain how a magnetic interaction can be moderated by conduction electrons of the non-magnetic metal. One of the earliest was the Ruderman-Kittel-Kasuya-Yosida (RKKY)[333–335] approach describing coupling between the magnetic moment of the *d* shell electrons to the conduction electrons through the exchange interaction. In this localized model the perturbative calculations of the *s*-*d* or *s*-*f* interaction Hamiltonian[336] predicts a spin polarization of conduction electrons around the magnetic impurity. If we now assume the two FM layers separated by a non-magnetic spacer, the emergent spin polarization in a non-magnetic material may serve as a mediator of the magnetism between the side layers. Although the RKKY interaction model gives an intuitive explanation for IEC, the proper description should have a delocalized character to account for a strong hybridization of $3d$ states.

This can be provided by the quantum-size-effect model regarding a spacer as of reduced dimensionality, *i.e.*, quantum well (QW). The conduction electrons in a spacer are reflected by two interfaces which in a free electron model can be represented as the spin-dependent potential steps. The multiply reflected charges interfere with its wave functions giving rise to confined electronic states whenever the reflection probability is close to unity.[337] The positions of those energy levels, thus DOS at the Fermi level, depend on the spacer thickness. This was evidenced in numerous systems by the photoemission experiments along the wedge-shaped spacer,[338,339] which revealed the oscillator DOS at E_{F} with increasing material thickness. One can expect a coupling through such separator to be occurring at certain thicknesses associated with the electronic states crossing the Fermi level.[340] The inclusion of the spin-dependent reflectance of the electrons makes the quantum well states also spin-dependent, promoting therefore a coupling of either majority or minority electrons.[341] This finally results in the oscillatory FM/AFM coupling with varying the non-magnetic spacer thickness. The QW approach to IEC was accepted to be more relevant than the RKKY interaction due to the delocalized electron treatment.[337]

The origin of the IEC oscillation period was for a long time unclear and later proved to be emerging from the particular bulk Fermi surface of the spacer material.[332,342] In a simplified picture if one assumes a coherent reflection at the QW's interfaces, each parallel to the interface electron wave vector is associated with the Fermi vector of the Fermi surface which gives rise to the oscillations as a function of the spacer thickness. The integration over the entire interface Brillouin zone results in canceling out of those oscillations everywhere, except of the regions of a sharp cut-offs, *i.e.*, where two sheets of the Fermi surface are parallel in direction perpendicular to the interface. The vectors connecting these sheets are referred to as critical spanning vectors. The electrons around these vectors contribute in phase to the oscillations amplitude. Therefore, the periodicity and the number of contributing terms depend strongly on the spacer material. It was shown that the number of oscillating periods is proportional to the parallel to interface density of atoms in spacer.[342]

The character of the IEC coupling can be determined by the calculation of the total energy difference between the parallel and antiparallel alignment of the FM layers, *i.e.*, $2J \sim E_{\mathrm{AP}} - E_{\mathrm{P}}$.[338] This can be performed in the local-spin-density approximation (LSDA)[343] or by tight-binding models.[344] Each time a QW state crosses the Fermi level it increases the E_{P} term favoring therefore the AFM coupling. Note that this energy calculation remains challenging due to a several orders of magnitude smaller value of the energy difference than the total energy itself.[337, 342]

A theoretical description of the IEC can be alternatively provided by many other models including the first-principles, tight-binding calculations, free-electron, or *s*-*d* mixing approach (Anderson model). The comprehensive reviews on those can be found in ref. 345 and 346.

To work with the experimental data one can employ a frequently used analytical expression for the IEC strength as proposed by Qiu and Smith:[24]

$$J_{\mathrm{IEC}} = \frac{A_1}{d^2} \sin\left(\frac{2\pi d}{\Lambda_1} + \Phi_1\right) + \frac{A_2}{d^2} \sin\left(\frac{2\pi d}{\Lambda_2} + \Phi_2\right) \tag{5.1}$$

where d stays for the spacer thickness, Λ_1, Λ_2 are the long and short periodicities deduced from the Fermi surface of the spacer, and Φ_1, Φ_2 are the phase shifts. A_1 and A_2 stand for the amplitudes which were shown to be related to roughness at the interfaces.[23] The sign of J determines the coupling character such that $J > 0$ ($J < 0$) corresponds to the FM (AFM) alignment. The two contributing periodicities for a Cu spacer were attributed to the critical spanning vectors at the belly and neck region of the Fermi surface.[338]

The IEC was extensively studied in inorganic systems but never observed directly for the metal/organic structures. Thus, we devoted a particular effort to fill this gap. The experiment devoted to IEC within Co/Cu/MnPc was carried out at the DEIMOS beamline of the SOLEIL synchrotron.

The sample was fabricated *in situ* within the DEIMOS preparation environment. On clean Cu(100) monocrystal, 14 ML of Co were deposited and annealed in a procedure analogous to the one described in the previous experiments (Sec. 5.2, 5.3). Then, the entire sample was covered with a Cu wedge varying d_{Cu} thickness in the range 0 − 14 ML. During this process the substrate was cooled to −140 °C so as to minimize the Co-Cu interdiffusion at the interface. Then, on one half of the sample we deposited 7 ML of Co to obtain a referential Co/Cu/Co system. The whole sample area was covered with 0.7 ML of MnPc. In that way, the investigated sample contained (i) a Co/Cu/Cu/MnPc referential stack, and (ii) the Co/Cu/MnPc system of interest. Fig. 5.9 (a) presents the scheme of the fabricated structure.

All the XAS and XMCD results presented in the following part were obtained with an x-ray beam oriented at 40° with respect to the sample plane in TEY detection. Fig. 5.9 (b) presents the XAS and XMCD signal at the $L_{3,2}$-edges of the bottom Co layer to which we later qualitatively compared the spectra obtained at Mn $L_{3,2}$-edges of MnPc.

Now, we compare the XMCD spectra at Mn $L_{3,2}$-edges of MnPc, acquired at different wedge position thus for different spacer thickness d_{Cu}, to that of bottom Co (Fig. 5.9 (d)). Unsurprisingly, for $d_{\mathrm{Cu}} = 0$ the sign of Mn and Co XMCD is the same implying the already observed FM coupling at Co/MnPc interface. At $d_{\mathrm{Cu}} = 1.5$ ML the XMCD of Mn is opposite to that of Co, which means that now the Co and Mn magnetization are antiparallel. For $d_{\mathrm{Cu}} = 3$ ML coupling turns back to the FM character. Note that the decreasing coupling amplitude is consistent with $J_{\mathrm{IEC}} \sim 1/d_{\mathrm{Cu}}^2$ predicted by theory[24] (Eq. 5.1).

Meanwhile the edge shape of Co remains unaltered along the Cu wedge, the Mn

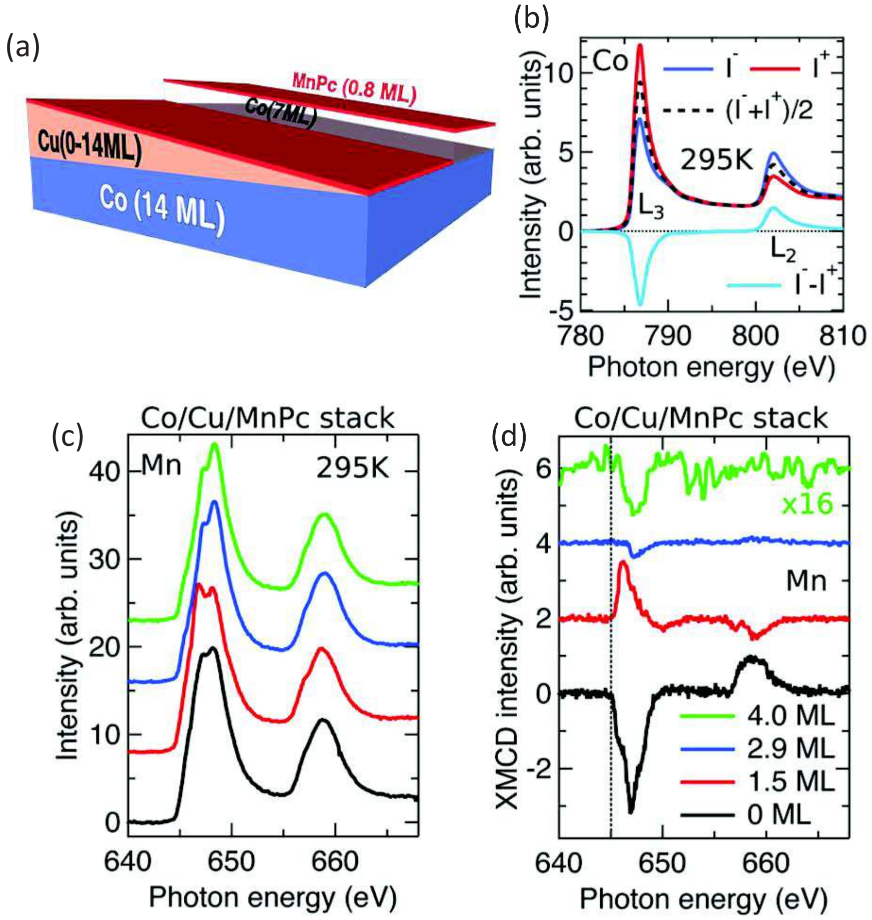

Figure 5.9: Interlayer exchange coupling of Mn centers in MnPc to Co mediated by Cu spacer. (a) Illustration of investigated sample for IEC studies. (b) Exemplary XAS and XMCD at $L_{3,2}$-edges of bottom Co layer. (c) XAS and (d) XMCD at the Mn $L_{3,2}$-edges of MnPc as a function of Cu spacer thickness (d_{Cu}). Note the edge shape modification due to varying substrate material (Co to Cu) and sign of XMCD revealing an oscillatory FM/AFM coupling character. Measurement performed at RT and $H = 0.1\,\mathrm{T}$. Figure taken from ref. 21.

$L_{3,2}$-edges spectra varies with increasing the spacer thickness (5.9 (c)). This can be rationalized by modification of the molecular electronic structure in response to variation of the substrate material (Co to Cu).

To have a better insight into the character of the oscillations we traced the changes along the Cu wedge by performing a position dependent scan and recording the absorption at the maximum of Co and Mn L_3-edge for both x-ray helicities and magnetic field directions ($|H| = 0.1\,\mathrm{T}$). Then, the scan was repeated at the pre-edge energy for the background subtraction. The procedure was redone on both sides of the sample. The result is presented in Fig. 5.10. We now discuss the curve intensity evolution with the Cu spacer thickness for the reference stack (Fig. 5.10, top panel). Initially, we observe a negative sign at L_3-edge of Co. At $d_{\mathrm{Cu}} = 6.9\,\mathrm{ML}$ we see the variation of a signal and its sign reversal to positive values suggesting therefore the AFM alignment between the top and bottom Co layers. Then, we observe the oscillations with two peaks at $d_{\mathrm{Cu}} = 9.5\,\mathrm{ML}$ and $12.2\,\mathrm{ML}$, yet the amplitude of the changes is decreased and it does not reach the positive values. The latter we explain as arising from the influence of the external magnetic field concurrent to IEC and/or the x-ray spot size probing and thus averaging the region extended over the oppositely oriented moments. The theoretical curve expressed by Eq. (5.1) was fitted to the data using the following parameters: $\Lambda_1 = 2.7\,\mathrm{ML}$ and $\Lambda_2 = 5.6\,\mathrm{ML}$,[23,347] $A_1/A_2 = 1.2$.[347] The associated phase values were found as $\Phi_1 = 1.15\,\mathrm{rad}$ and $\Phi_2 = -3.34\,\mathrm{rad}$. The theoretical curve (Fig. 5.10, grey solid line) was found to well reproduce the periodicity of oscillations recorded by experiment. The amplitude in turn should not be compared as the two values of coupling strength and the changes observed at maximum of L_3-edge are different. Finally, we observe that the curve obtained for Mn within MnPc on the referential stack follows the one of Co due to the aforementioned FM coupling at Co/MnPc interface. In this way, we infer that the referential stack Co/Cu/Co/MnPc exhibits the well known interlayer exchange coupling proving that the Cu thickness is well calibrated. Note that we do not witness the oscillations below $d_{\mathrm{Cu}} = 6.9\,\mathrm{ML}$ what we attribute to the roughness issues at the Cu/Co interface.[25]

Now, we focus on the results obtained on the other half of the sample, *i.e.*, Co/Cu/MnPc (Fig. 5.10 (bottom panel)). Remember that the Cu thickness on this part of the sample is the same as on the referential part. At first, we notice that the oscillations start for much lower d_{Cu} than in case of referential stack. We observe at least two additional maxima at $d_{\mathrm{Cu}} = 1.7\,\mathrm{ML}$ and $4.1\,\mathrm{ML}$. This comes from a sharper Cu/MnPc interface devoid of an interdiffusion issue (large size of the MnPc molecules). The oscillations follow the same periodicity as the one on the reference part. By decreasing the temperature from RT to 4.8 K the amplitude of the oscillations increases. This can be understood if we consider IEC as a contribution to the effective magnetic field as $H_{\mathrm{eff}} = H_{\mathrm{IEC}} + H_{\mathrm{ext}}$ where $|H_{\mathrm{ext}}| = 0.1\,\mathrm{T}$ denotes the external field. Note that in this simple approach H_{eff} can be of opposite sign to H_{ext} due to IEC contribution. The coupled Mn paramagnetic moments obey the Brillouin function with H_{eff} as a magnetic field, what implies that more Mn magnetic moments are aligned at low temperature what in turn enhances the aforementioned oscillations amplitude. On the other hand, the increase of the external magnetic field at low temperature to 6.5 T leads to a shift of the whole curve towards lower values what originates from the alignment of the non-coupled molecules within the system (*i.e.*, the ones subjected only to H_{ext} and not to H_{IEC}). This underscores the subtle interplay of the temperature, external magnetic field, and IEC induced ordering. The results collected in Fig. 5.10 unambiguously prove the interlayer exchange coupling of the paramagnetic Mn centers within MnPc to Co through the Cu non-magnetic spacer.

To sum up this part, we demonstrated for the first time that the paramagnetic centers of the organometallic molecules can be coupled to an FM through a non-magnetic spacer of thickness up to $\sim 2\,\mathrm{nm}$. This creates a next pathway in organic spintronics linking the virtues of the ferromagnetic materials, noble metal layers, and paramagnetic centers in organic molecular cage. Such system may offer notable advantages over similar, fully inorganic, counterparts. The use of organometallic molecules may solve some growth related problems, *e.g.*, interdiffusion, which deteriorate IEC. Moreover, the organic cage within the molecules prevents the paramagnetic ions to interact between each other and potentially give rise to unwanted competitive effects. Secondly, this study leads to the concept of a "protected spinterface", *i.e.*, a ferromagnetic substrate

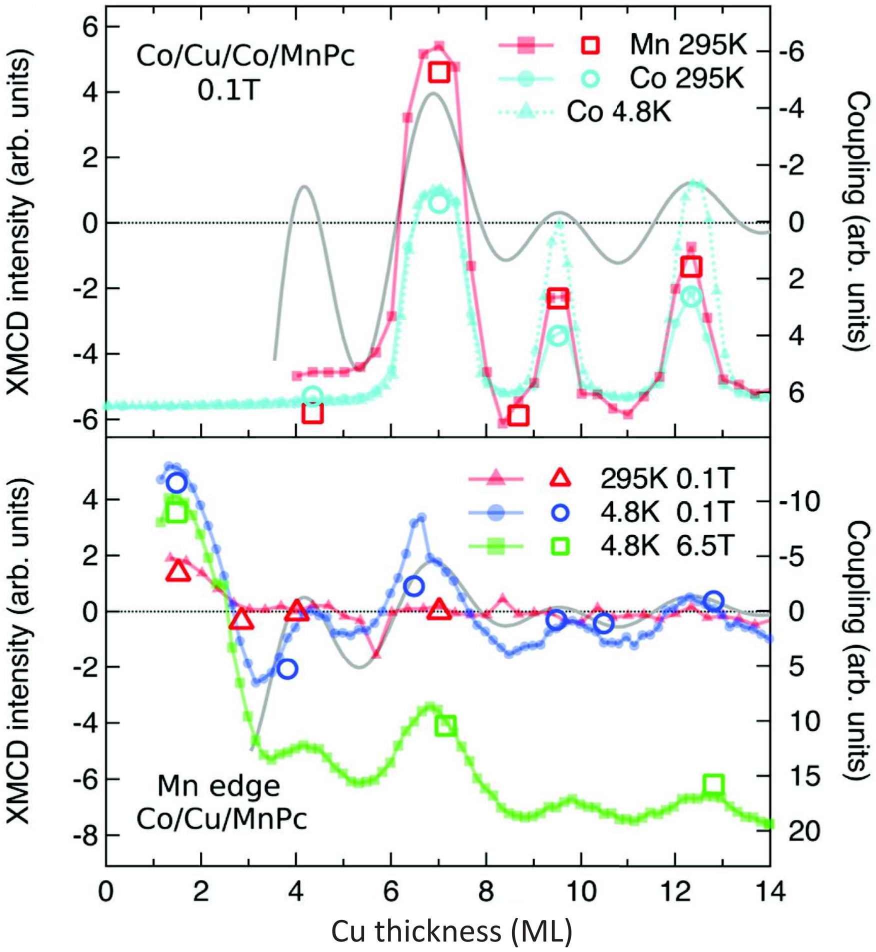

Figure 5.10: IEC induced oscillations of the magnetic coupling. XMCD amplitude at L_3-edge of Co (786 eV) and Mn (646.8 eV) within MnPc as a function of Cu spacer thickness within referential stack Co/Cu/Co/MnPc (top panel), and stack of interest Co/Cu/MnPc (bottom panel). The markers represent the extracted XMCD intensity used for fixing the position of solid lines. XMCD of Mn is renormalized to be comparable to that of Co. Grey line is a theoretical curve fitted from Eq. (5.1). Figure taken from ref. 21.

covered by a noble metal which prevents its degradation caused by the environment (*e.g.*, oxidation). One can further deposit on such heterostructure any kind of a non-UHV-compatible organic material by, *e.g.*, wet deposition techniques, and in this way obtain the IEC mediated coupling. Moreover, such system can serve to reduce a direct molecule-substrate interaction which may play a key role in some subtle molecular phenomena such as spin crossover.[22] Note that by controlling the spacer thickness one can also tune the nature and character (FM/AFM) of a magnetic coupling.

Before, we stated that the molecular magnetic moment alignment with an FM is a consequence of a spin dependent-hybridization and formation of a spinterface. Motivated by the results presented in this sections we devoted an effort to experimentally investigate whether the interface Cu/MnPc within such interlayer exchange coupled system also exhibits a spin polarization. In the next part, we present the results of these studies.

5.5 Spin polarization at Cu/MnPc interface in the interlayer exchange coupled system

In the theoretical introduction (Sec. 1.3.2) we explained how the molecular electronic structure is altered when MnPc is adsorbed on a ferromagnetic surface. We stated that the adsorption induced hybridization leads on average to a transfer of 3.5 electrons from Co to the molecule what may eventually be accompanied by a strong spin-dependent hybridization between C p_z and Co d orbitals and thus by the formation of a spinterface. We emphasized the importance of the latter for the spin-injection applications and discussed the examples of the systems Co/MnPc[20] and Co/C[26] for which strong spin polarization values are found close to the Fermi level. Since we showed in the previous section that the magnetic ordering can equally occur when the MnPc molecules and Co are separated by a Cu layer, *i.e.*, without a direct Co-MnPc contact, the evident question arises whether the interface Cu/MnPc in the interlayer exchange coupled system Co/Cu/MnPc is also spin-polarized? In this section, we provide the results of a study trying to answer this question.

5.5.1 Experimental set-up and sample fabrication

The experiments presented in this section have been performed at the CASSIOPÉE beamline of the SOLEIL synchrotron. Both the technical aspects of the beamline and fundamentals of spin-resolved photoemission spectroscopy (SR-PES) were described in sections 4.4 and 4.5. The main goal of the project was to employ SR-PES to study the spin-polarized electronic structure at the Cu/MnPc interface within the Cu(100)//Co/Cu/MnPc system.

The samples were *in situ* grown in the beamline's preparation environment. The fabrication procedure was similar to the one used at the DEIMOS beamline during the experiments presented in the previous sections. However, the wedges of either Cu or MnPc could not be realized, so that the sample contained always a uniform material thickness across the whole area. A monocrystalline Cu(100) substrate was cleaned in a standard way by Ar^+-ion sputtering followed by an annealing at 550 °C. Since the experiment required reusing of the same single crystals, the cleanliness of the substrate was ascertained by Auger electron spectroscopy. In each case, the basis of the sample consisted of a 15 ML thick Co film on Cu(100), which was annealed at 100 °C for 10 min in order to reduce the surface roughness of the Co film. A non-magnetic Cu spacer layer (1.5 ML, 2 ML, or 3 ML) was then deposited onto the Co film. The determination of the Cu thickness was based on the observation of clear RHEED oscillations during the deposition of Cu directly onto the Cu(100) crystal (Fig. 5.11 (b)). Finally, the MnPc molecules were sublimed from the same Knudsen cell as used during the experiments at the DEIMOS beamline.

For the photoemission experiments we used the spin-resolved branch of the CASSIOPÉE beamline. The experimental geometry is depicted in Fig. 5.11 (a). The UV photons with 20 eV energy and horizontal linear light polarization impinged the sample at 45°. The emitted photoelectrons were collected in normal-emission geometry with a Scienta SES2002 analyzer which was coupled to a spin detector. An electromagnet situated below the experimental stage was used to remanently magnetize the Co layer.

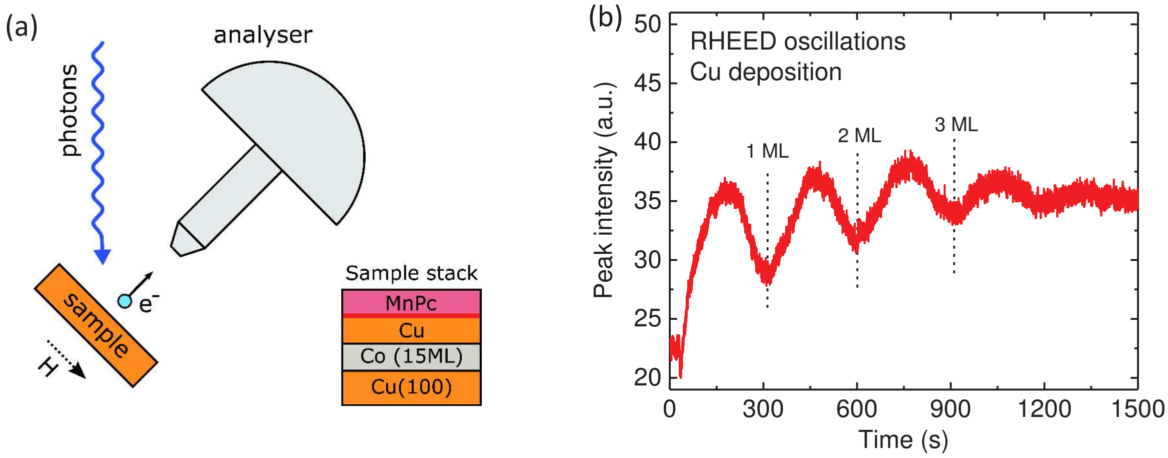

Figure 5.11: Investigation of the spin polarization at the Cu/MnPc interface. (a) The experimental geometry of the spin-resolved photoemission spectroscopy measurement on the CASSIOPÉE beamline (top view). The UV photons with an energy of 20 eV and linear horizontal polarization were used. Detection was performed by a Scienta SES2002 analyzer coupled to a spin detector. The magnetic field direction is marked with dotted line as the measurement is performed in remanent magnetization state. The sample stack illustrates the composition of the studied system with the interface of interest marked in red. (b) RHEED oscillations recorded during the deposition of Cu onto the Cu(100) substrate and used for the determination of the Cu evaporation rate. The minima correspond to the completion of individual Cu layers.

We emphasized that the magnetic field cannot be applied during the measurements as this would make any photoemission experiment impossible. Therefore, the experiments could only be performed with the ferromagnetic substrate in its remanent magnetization state. To get rid of the artifacts in the determination of the spin polarization the measurements were performed with frequently reversed direction of the ferromagnet magnetization. All measurements were performed at room temperature.

Before we discuss the results obtained in the spin-resolved photoemission experiments, we want to emphasize on the key role of the growth of Cu on Cu(100)//Co at least for the first layers. In fact, as the reader will see later, this issue is of extreme importance for a correct interpretation of the photoemission data. In addition to the RHEED oscillations which served us only to determine the rate of the Cu evaporator, the ion scattering spectroscopy (ISS) experiments were carried out at the IS2M at Mulhouse. This very surface sensitive method provided us with the information about the Co concentration at the sample surface as a function of the Cu coverage (Fig. 5.12). It revealed that a Cu film of more than 1.3 ML covers completely the Co surface. In other words, the subsequently deposited MnPc molecules on Cu(100)//Co/Cu stack with a top Cu thickness above 1.3 ML can definitely not be in direct contact with the ferromagnetic Co layer.

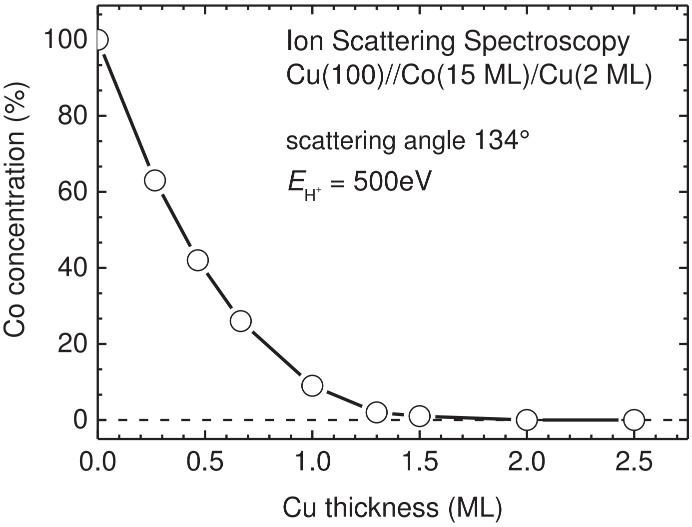

Figure 5.12: Ion scattering spectroscopy measurement of Cu(100)//Co(15 ML)/Cu(2 ML). The Co concentration reaches 10% for 1 ML of Cu coverage and becomes zero for thicknesses above 1.3 ML. The measurement was performed with H^+ ions with an energy of 500 eV and a scattering angle of 134°.

5.5.2 Spin polarization of Cu(100)//Co/Cu/MnPc

Figure 5.13 shows the spin-resolved electron distribution curves as a function of the binding energy acquired after each of the three consecutive steps of the stack fabrication. Figure 5.13 (a) reveals a strong imbalance of the spin-up and spin-down channels of the Co film resulting in a strong negative spin polarization P close to the Fermi level (Fig. 5.14). When the Co film is covered by 2 ML of Cu (Fig. 5.13 (b)) one observes the features of the Co valence band close to the Fermi level to be attenuated what is explained by the finite mean free path of the electrons, and the appearance of a new structure above 2 eV binding energy, which arises from the 3*d* valence band of Cu. Figure 5.14 shows that the deposition of Cu leads to an overall decrease of the spin polarization which is particularly prominent for the Cu 3*d* feature. This is not astonishing since the latter feature contributes with a significant intensity while it does not possess any spin polarization. Figure 5.13 (c) presents the spin-resolved spectra after the additional coverage of the stack with 0.8 ML of MnPc. Despite a further attenuation of the Co induced valence band structures at lower binding energies, the additional features are observed at about 0.3 eV in the spin-up channel and at about 0.8 eV in the spin-down channel (both indicated by an arrow). The corresponding spin polarization spectrum (Fig. 5.14) indicates the clear features at the same binding energies. The particular form of the feature at 0.3 eV suggests that it is not simply due to an additional attenuation of the Co signal but the result of an additional positively spin-polarized MnPc induced intensity. Concerning the feature at 0.8 eV in the spin-down channel, we remark a sign change of the spin polarization in the energy range between 0.8 eV and 1 eV. This can only be explained if the additional feature at 0.8 eV is predominantly negatively spin-polarized.

To extract the spin-resolved photoemission signal (difference spectrum) that comes both from the Cu/MnPc interface and from the molecular layers atop the interface, we used a subtraction procedure that takes into account the molecule-induced attenuation of the Co photoemission signal.

The reasoning which is presented in the following is similar to what has already

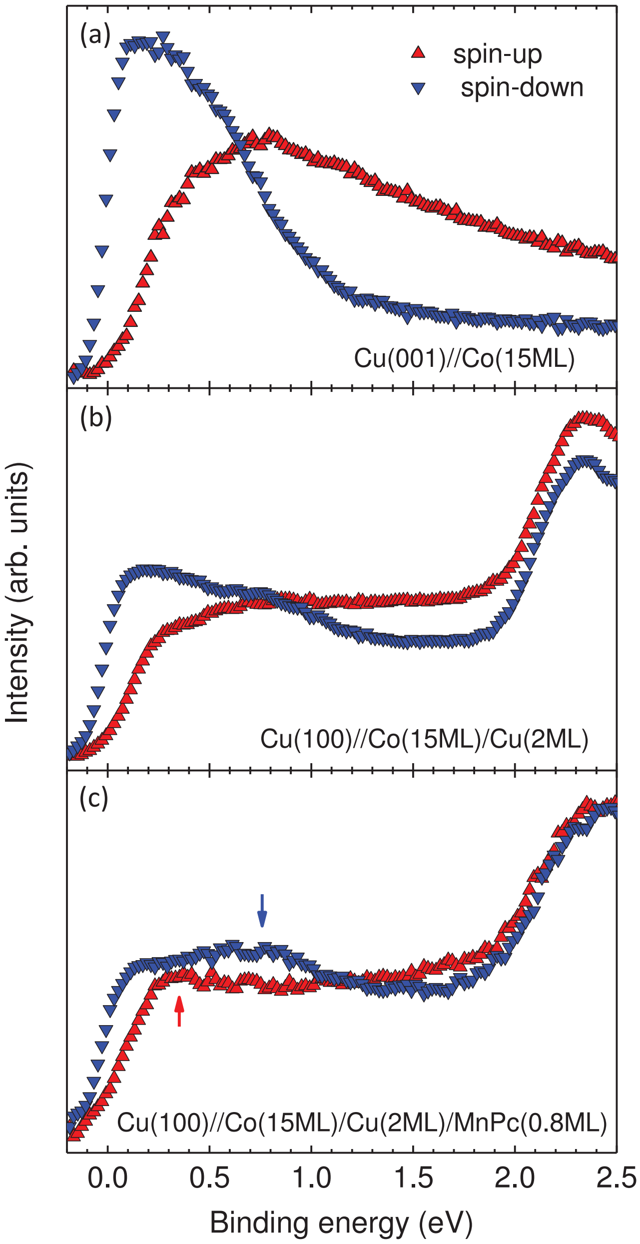

Figure 5.13: Spin-resolved electron distribution curves as a function of a binding energy for the consecutive steps of the stack fabrication. The electron distribution curves obtained on (a) Cu(100)//Co(15 ML), (b) Cu(100)//Co(15 ML)/Cu(2 ML), and (c) Cu(100)//Co(15 ML)/Cu(2 ML)/MnPc(0.8 ML) stacks. The structure at binding energies above 2 eV results from the 3*d* valence band of Cu. The deposition of MnPc on Cu results in the appearance of the characteristic features at 0.3 eV and 0.8 eV (marked with arrows on panel (c)).

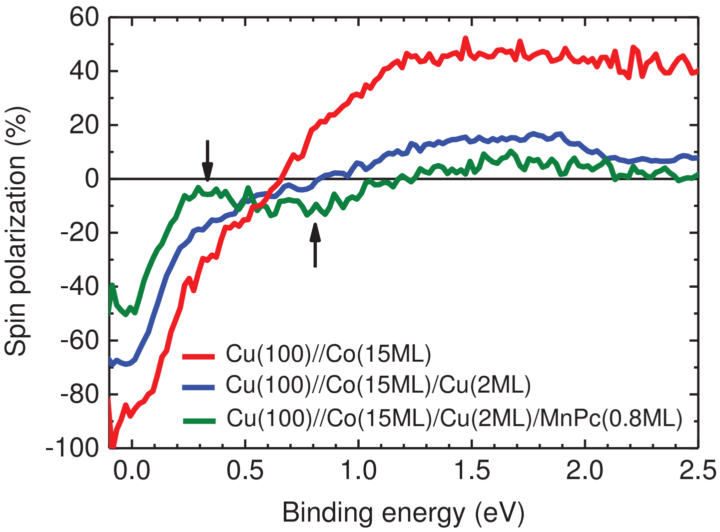

Figure 5.14: Spin polarization for the consecutive steps of the stack fabrication. Spin polarization calculated from data in Fig. 5.13 according to Equation 1.2. Note the attenuation of the signal after deposition of Cu and MnPc. The features marked by the arrows originate from the deposition of the MnPc molecules and cannot be explained by a simple attenuation of the Co induced valence band structures.

been presented in great detail in ref. 20 and 26 for the systems phthalocyanine on Co(100) and amorphous carbon on Co(100), respectively.

We only stress here that our procedure supposes that the energy-dependent structure of the spin-resolved photoemission signal arising from the Co/Cu stack does not change significantly when it is covered by a molecular layer. Several aspects support this supposition: (i) a change of the magnetization of the ferromagnetic Co layer due to the MnPc molecules can be excluded as the molecules are separated from the Co surface by a Cu spacer layer. (ii) Since a realistic inelastic mean free path in the Co/Cu stack is of ~ 0.8 nm, only 20% of the Co/Cu photoemission signal originates from the topmost layer while the rest arises from the lower uninfluenced layers. Consequently, the structures appearing in the photoemission signal coming from the buried Co/Cu are not significantly different from those of the uncovered by MnPc stack.

5.5.3 Spin polarization at the Cu/MnPc interface

Figure 5.15 (a) shows the spin-resolved difference spectra, *i.e.*, the spin-resolved spectra of Co/Cu(2 ML)/MnPc(0.8 ML) after subtraction of the suitably normalized referential curves acquired on Co/Cu(2 ML) stack. One clearly sees a strong positive spin polarization at the Fermi level dominated by the spin-up channel with a maximum at a binding energy of 0.3 eV. At ~ 0.5 eV the spin polarization reverses to negative. That means the spin polarization of the interface at the Fermi level is opposite in sign to that of cobalt. The increase of the intensity towards higher binding energies arises from the MnPc molecular states.[27,348] Most surprisingly, the witnessed result is very similar to that obtained in experiments whereas the MnPc molecules were directly deposited onto the ferromagnetic Co layer.[20]

To ensure the Cu surface to be properly covered with the molecules we deposited an additional amount of MnPc and repeated the measurements on Cu/MnPc(1.6 ML). The result is presented in Fig. 5.15 (b). Note the reduced noise level which is due to a much longer acquisition time. The spin polarization at the interface remains unchanged with respect to 0.8 ML of MnPc. It is noteworthy, that the overall intensity increase is now more prominent with a clear peak at the binding energy at ~ 2 eV. This results from a stronger contribution of the molecular states due to the thicker MnPc layer. In this way we confirm that the MnPc molecules form a spinterface with Cu giving rise to a positive spin polarization $P_{\mathrm{Cu/MnPc}} > 0$, that is opposite to the one arising on cobalt ($P_{\mathrm{Co}} < 0$). Surprisingly, the observed effect is similar to the case when the molecules are in a direct contact with Co. However, the presence of a significant number of MnPc molecules in contact with Co can be excluded, as we have already shown in Section 5.5.1 by ISS measurement. In the next step we studied the evolution of the spin-resolved photoemission spectra with the Cu layer thickness.

We performed the measurements for three different Cu thicknesses d_{Cu}= 1.5 ML, 2 ML, and 3 ML and the MnPc coverage of 1 ML. The results are presented in Fig. 5.16. Note a much greater scattering of the data points compared to the previous measurements (Fig. 5.15) due to a more limited acquisition time. It is strikingly clear that the strong positive spin polarization at the Fermi level persists up to at least 3 ML of Cu coverage. The difference spectra (Fig. 5.16 (left)) reveal the presence of a dominant spin-up feature close to the Fermi level for all investigated Cu thicknesses. In addition to these interfacial features one observes a systematic overall increase in intensity at higher binding energies due to the Cu 3*d* valence band which becomes more prominent with increasing Cu thickness. Note that the two characteristic features in the spin polarization spectrum of Fig. 5.14 appear also in the spin polarization spectra in Fig. 5.16 (right). Most importantly, one could also find the situation where the spin po-

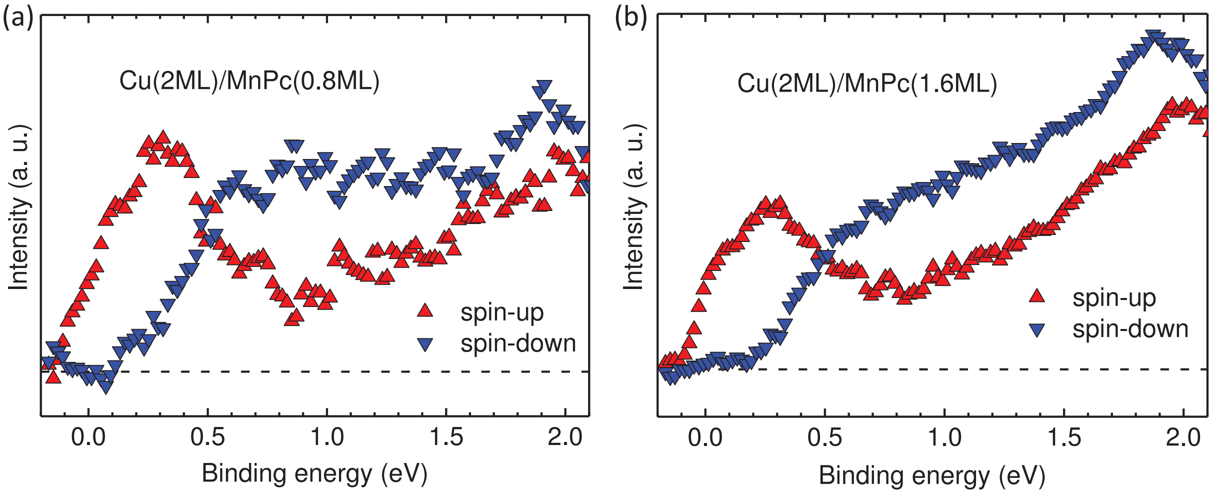

Figure 5.15: Spin-resolved electron distribution curves for Cu(2 ML)/MnPc interface. Spin-resolved difference spectra, *i.e.*, the spin-resolved spectra of Co/Cu(2 ML)/MnPc after subtraction of the suitably normalized referential curves acquired on Co/Cu(2 ML) stack, for (a) 0.8 ML and (b) 1.6 ML of MnPc thickness. Note a strong positive spin polarization at the Fermi level and its reversal at ~ 0.5 eV.

larization is even reversed in sign (at 0.3 eV binding energy), *i.e.*, positive, with respect to the spin polarization spectrum of the Co/Cu stack. This confirms thus the presence of a positively spin-polarized feature at 0.3 eV as seen in the difference spectra.

To summarize, we have shown that the Cu/MnPc interface within the Cu(100)//Co/Cu/MnPc stack is strongly spin-polarized. We observed a feature in the spin-up channel yielding a positive P at E_F for 3 different non-magnetic Cu spacer thicknesses (1.5 ML, 2 ML, and 3 ML). Most surprisingly, the amplitude of the structure, its energy position as well as its line width essentially resemble those of MnPc molecules directly deposited onto Co[20] which is a rather unexpected result.

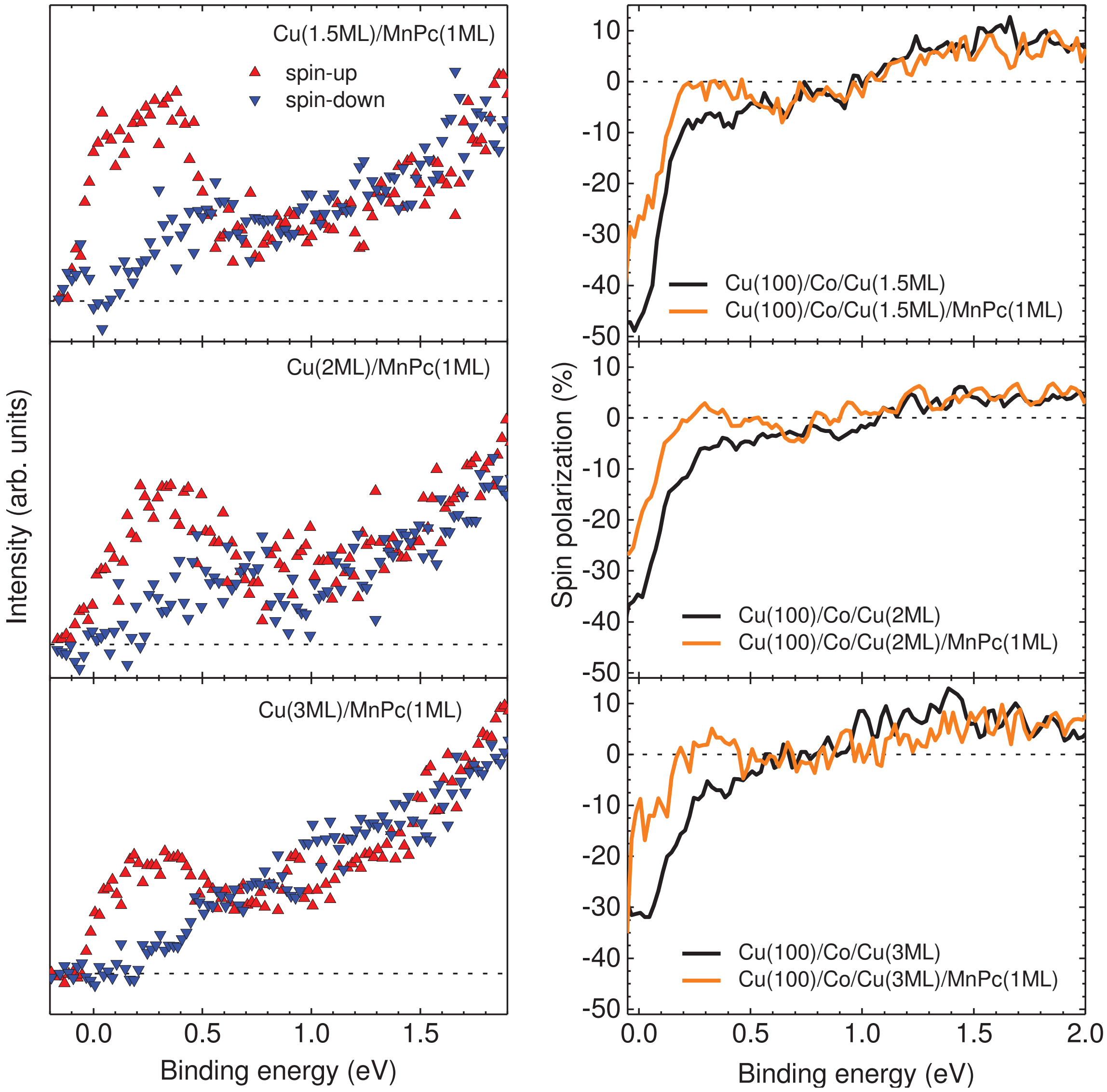

Figure 5.16: Spin polarization of Cu(d_Cu)/MnPc(1 ML) for different Cu thicknesses. Difference spectra of the Cu/MnPc(1 ML) interface (left) and spin polarization of the untreated (*i.e.*, before subtraction) spin-resolved spectra (right) for $d_\mathrm{Cu} = 1.5$ ML (top panels), 2 ML (middle panels) and 3 ML (bottom panels).

5.5.4 Theoretical predictions

The *ab initio* calculations were carried out by the group of Mebarek Alouani at the IPCMS to support the experiment. The aim was to predict both magnetic coupling of the Mn centers to Co and the spin polarization at the Cu/MnPc interface within the Co/Cu/MnPc system with varying a non-magnetic Cu spacer thickness. The results of the calculations presented in this section are included in the Supplementary Information to ref. 349. Since one of the applications of the spinterface is spin-injection, the calculations were performed within the ±25 meV region around the Fermi level so as to consider exclusively the levels contributing to the electronic transport at room temperature. The results presented in Table 5.2 were obtained by using the VASP package[269] and the generalized gradient approximation for the exchange-correlation potential as parametrized by Perdew, Burke, and Ernzerhof.[271] Projector augmented wave (PAW) pseudopotentials were used as provided by the VASP package.[272] The Cu and Co layers were modeled in *fcc* lattice (lattice constant of 0.36 nm) with the supercell approach (3 ML, 8×8 atoms each separated by vacuum). The energy cutoff for a plane wave basis was set as 450 eV. The data for $d_{\mathrm{Cu}} = 0$ ML was taken from

Table 5.2: *Ab initio* calculation of the DOS and the electronic/magnetic properties of Co(100)/Cu(d_{Cu})/MnPc stack. The magnetic moment of the FM Co layer is positive with the negative spin polarization at the Fermi energy. The N_{nn} denotes the nitrogen atoms which are closer to the central manganese atom and N_{fn} the ones which are more distant. The spin polarization has been calculated for Co/MnPc (d_{Cu} = 0ML) or Cu/MnPc (d_{Cu} = 1, 2, 3 ML) interfaces. Data taken from Supplementary Information of ref. 349.

	d_{Cu} (ML)			
	0[20]	1	2	3
Magnetic moment (μ_{B})				
Mn	+2.54	-2.78	+2.79	+2.8
N_{nn}	+0.01	+0.1	-0.1	-0.1
N_{fn}	+0.1	-0.04	+0.05	+0.01
C	-0.22	+0.08	-0.18	-0.21
Exchange energy				
ΔE (eV)	-0.438	+0.116	-0.035	-0.003
$\mu_{\mathrm{o}} H_{\mathrm{ex}}$ (T)	+1490	-360	+110	+12
Density of states				
z-DOS (a.u.)	0.25456	0.0423	0.15732	0.20961
pl-DOS (a.u.)	0.03322	0.0044	0.0096	0.00675
z-DOS/pl-DOS (a.u.)	7.66	9.72	16.39	31.05
z-P ($E_{\mathrm{F}} \pm 25$ meV) (%)	+65.8	-98.3	+30	+74
pl-P ($E_{\mathrm{F}} \pm 25$ meV) (%)	-69	-99.2	+17	+51.1
Total P ($E_{\mathrm{F}} \pm 25$ meV) (%)	+50.2	-98.4	+29.3	+73.3

ref. 20. The molecular structure of MnPc adsorbed on the surface was optimized by including the van-der-Waals interaction as described in ref. 350.

To begin with, we comment on the calculated DOS and resulting spin polarization at the Cu/MnPc interface. By comparing the planar (pl-DOS) and perpendicular (z-DOS) density-of-states one can easily notice a dominating out-of-plane orientation. That becomes even more notable when the thickness of the Cu spacer increases (compare z-DOS/pl-DOS for different d_{Cu}). This unsurprisingly points towards the main path for the spinterface formation essentially along the growth direction. The linear horizontal polarization of the photons used in our experiment probes equally the perpendicular and planar states, yet the contribution of the latter is negligible accord-

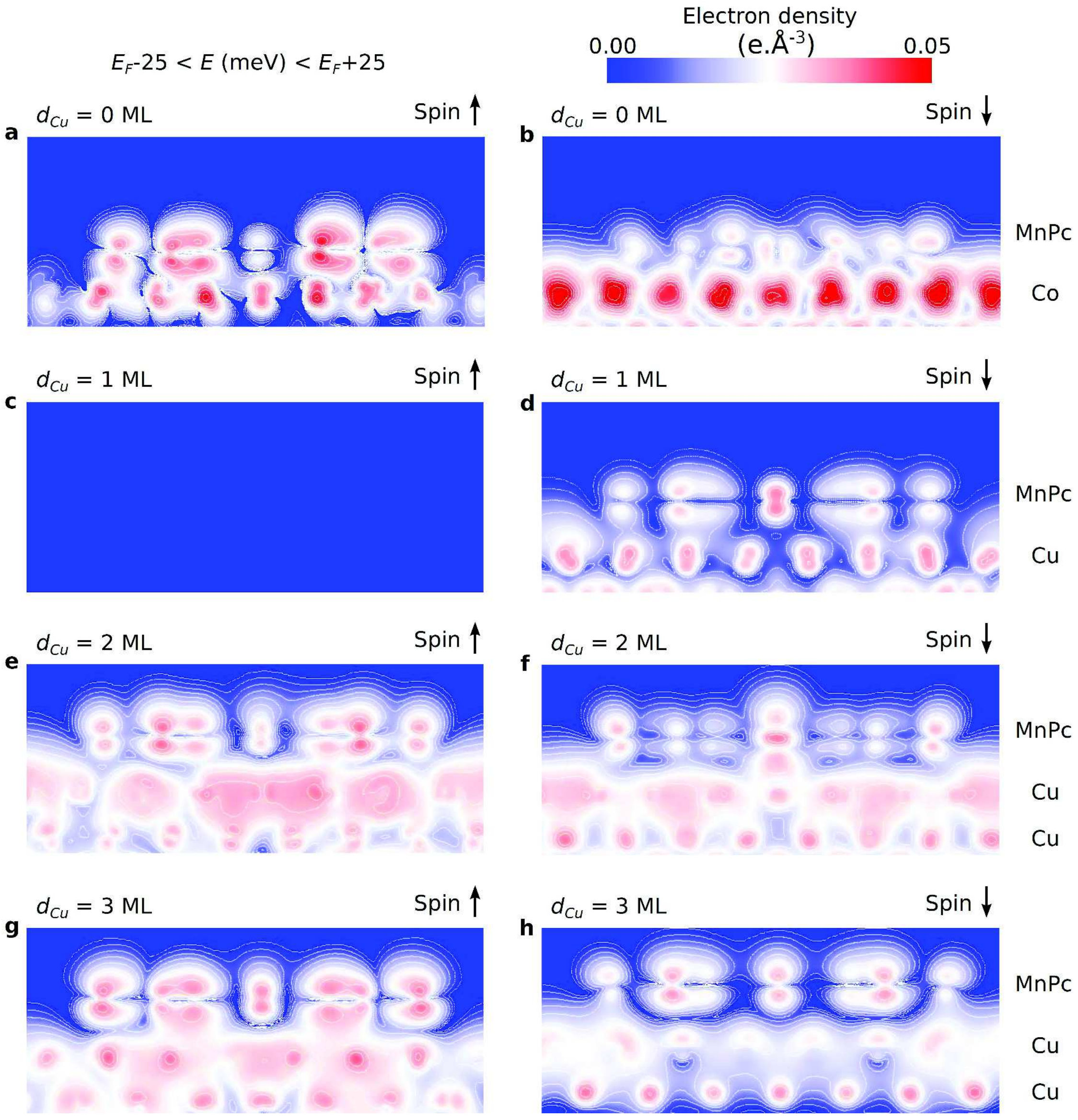

Figure 5.17: Spin-polarized spatial DOS maps of Co/Cu/MnPc for various Cu spacer thicknesses d_{Cu}. The calculations were performed within the ±25 meV around the Fermi energy for (a),(b) $d_{\mathrm{Cu}} = 0\,\mathrm{ML}$, (c),(d) $d_{\mathrm{Cu}} = 1\,\mathrm{ML}$, (e),(f) $d_{\mathrm{Cu}} = 2\,\mathrm{ML}$, and (g),(h) $d_{\mathrm{Cu}} = 3\,\mathrm{ML}$. Figure taken from the Supplementary Information to ref. 349.

ing to the reasoning above. The direct Co/MnPc interface exhibits a polarization of $P = +50.2\%$ at the Fermi energy. Introducing 1 ML of Cu leads to a reversal of the polarization such that it is nearly completely negative $P = -100\%$. The spin polarization sign again turns to positive when the Cu thickness is increased to 2 ML and 3 ML. This is in qualitative agreement with our experiment if we assume a rapid polarization sign reversal to positive between $d_{\mathrm{Cu}} = 1\,\mathrm{ML}$ and 2 ML. Despite a rather good accuracy of the d_{Cu} estimation in the experiment, which we roughly assessed to be $\pm 0.25\,\mathrm{ML}$, the studied case of $d_{\mathrm{Cu}} = 1.5\,\mathrm{ML}$ could be eventually closer to 2 ML and in this way agree with the theory. It is important to notice, that we were unable to reproduce experimentally the scenario for $d_{\mathrm{Cu}} = 1\,\mathrm{ML}$ due to the aforementioned Cu thickness inaccuracy and the risk of an incomplete coverage of the FM layer.

Now, we consider the variation of the exchange field H_{ex} which is related to an average molecular magnetic moment μ_{mol} as $\mu_{\mathrm{o}} H_{\mathrm{ex}} = \frac{-\Delta E}{2\mu_{\mathrm{mol}}}$ with $\Delta E = E_{\mathrm{AP}} - E_{\mathrm{P}}$. Unsurprisingly, the exchange field decreases rapidly with the Cu spacer thickness ($J_{\mathrm{IEC}} \sim 1/d_{\mathrm{Cu}}^2$ (see Eq. 5.1), such that the initial $\mu_{\mathrm{o}} H_{\mathrm{ex}} = +1480\,\mathrm{T}$ for MnPc directly on Co diminishes to $+12\,\mathrm{T}$ in the presence of a 3 ML Cu spacer. Such a small exchange field value for $d_{\mathrm{Cu}} = 3\,\mathrm{ML}$ would cause a negligible coupling strength and thus negligible spin polarization. This, however, is in contrast to the experimentally observed strongly spin-polarized Cu/MnPc interface. We therefore suggest that the calculations underestimate the exchange field amplitude.

Finally, we present the calculated spin-polarized spatial density maps of the Co/Cu/MnPc stack for $d_{\mathrm{Cu}} = 0$, 1, 2, and 3 ML (Fig. 5.17). Note how the charge density within the substrate evolves with d_{Cu}. The initial spin-up/spin-down channel imbalance for $d_{\mathrm{Cu}} = 0\,\mathrm{ML}$ naturally originates from the ferromagnetism of Co. The introduction of a Cu spacer leads to a dominant spin-down channel within Cu for $d_{\mathrm{Cu}} = 1\,\mathrm{ML}$, which then reverses to a spin-up prevailing for $d_{\mathrm{Cu}} = 2\,\mathrm{ML}$ and 3 ML. This results from an interplay between the weakening of a direct exchange with Co and the increasing contribution of IEC through spin-polarized QW states of Cu. We claim that the resulting charge imbalance at the interface provokes in turn a spin-dependent hybridization with the MnPc molecule. Note the prominent case for $d_{\mathrm{Cu}} = 3\,\mathrm{ML}$ where the distinct carbon sites are involved in hybridization for the spin-up and spin-down channels.

5.5.5 Discussion

Our experiment unambiguously leads to the conclusion that the interlayer exchange coupled Cu/MnPc interface is strongly spin-polarized for all the studied thicknesses of Cu spacer. The surprising prominence of this effect rises additional questions about the nature of the spinterface formation. Although the outcome of the measurement was predicted by theory, the amplitude of the effect and its robustness is nevertheless astonishing. All the main characteristics of the spin-polarized interface feature (amplitude, energy position, line width) within Cu/MnPc are quite similar to those of the previously studied systems where the organic molecules or amorphous carbon are in a direct contact with the ferromagnet. The systems Co/MnPc,[20] Co/H_2Pc,[20] and Co/C(amorphous)[26] consistently revealed the major role of the carbon sites in spinterface formation and the dominant mechanism of the C 2p-Co 3d hybridization[26] (see Sec. 1.3.2). Yet, in case of Cu/MnPc there are no available $3d$ states of Cu near the Fermi level for hybridization (see Fig. 5.14). The $3d$ band of Cu appears ~ 2.4eV away from E_{F}. This raises the question whether the Cu states can contribute to the spinterface formation and if the previously well-established mechanism is valid. One of the proposed scenario is a spin-dependent broadening and a downward shift in energy of the MnPc HOMO/LUMO such that a hybridization with a $3d$ band of Cu is possible. The other possibility is an interaction with the surface states of Cu. In the moment of writing of this manuscript the more theoretical calculations are performed along with additional ultraviolet photoelectron spectroscopy (UPS) experiment at IS2M at Mulhouse to address these issues.

Despite the lack of a full explanation for the formation mechanism of the Cu/MnPc spinterface we can certainly claim that the studied system exhibits a strong positive spin polarization at the Fermi level. This has a far going implications for the applications of the IEC interfaces as potential spin injectors. One can imagine a protected spinterface, as proposed in Sec. 5.4, to act as a spin-current generator in the transport devices with a possibility to tune the favorable conduction channel by selecting appropriate molecule-metal pairs.

5.6 Partial conclusions

In this chapter, we experimentally confirmed that the first ML of the MnPc molecules deposited on the Co surface is FM coupled to the substrate upon spinterface formation at RT. This interfacial effect is further responsible for the AFM ordering within the consecutive molecular layers. Such configuration, resembling an inorganic FM/AFM system, led to the first observation of exchange biasing of Co induced by the organic MnPc layer below $T_{\mathrm{B}} = 100\,\mathrm{K}$. This is a step forward to demonstrate a new realization within the scope of organic spintronics with the implications for device science. The latter may include an electrode magnetic pinning within a magnetoresistive device or sustainability of a spin-polarized current in magnetically ordered organic layers at RT.

We have shown that a spinterface can be equally formed indirectly, via interlayer exchange coupling, involving a noble metal spacer between Co and MnPc. This led to the notion of the protected spinterface in which the molecular layer is separated from the ferromagnetic substrate by a Cu spacer. In this way degradation of either the ferromagnetic substrate due to the deposition of molecules (for instance by wet chemistry) or of the molecules due to the ferromagnetic substrate can be avoided. In addition, it allows a tailoring of the magnetic coupling character and strength by controlling the noble metal spacer thickness.

Finally, we showed that the IEC Cu/MnPc interface is strongly spin-polarized ($P > 0$ at E_{F}) for all investigated Cu spacer thicknesses $d_{\mathrm{Cu}} = 1.5$, 2, and 3 ML. This rather unexpected result is of a notable importance for a charge transport through the protected spinterface. In that way, the structure can be efficiently used as a spin filter in magnetoresistive devices. Controversial remains the nature and the formation of the IEC mediated spinterface. Its characteristics resemble those of the molecules in direct contact with the ferromagnetic substrate. The hybridization cannot be explained in a straight forward manner by the widely accepted p_z-d mechanism due to a lack of the Cu $3d$ states at the Fermi level. The currently conducted calculations and UPS experiments should shine more light on this open question.

At the end we want to stress on the overall advantages arising from the demonstrated use of the organic MPcs (or similar molecules). A strong paramagnetic moment of the metal ion allowing a variety of magnetism related applications is protected in MPc by an organic cage from: (i) strong interactions between the ions reducing thus concurrent collective effects, (ii) interdiffusion to the inorganic layers. In that way, good quality contacts forming the spinterfaces and eminent diffusive spin coherence properties give a perspective for more efficient devices within the scope of organic spintronics.

6

Ferroelectric control over a metal/organic spinterface

In the previous section we focused on, what we called, the smallest building block of every organic spintronic device, namely ferromagnetic/organic interface. It revealed the unparalleled characteristics starting from the RT magnetism stabilization, to a strong spin polarization whether in direct (Co/MnPc) or indirect (Co/Cu/MnPc) system. In this chapter, we exploit that knowledge towards multifunctional applications. To do so, we use the ferroelectric (FE) ceramic substrate and construct a magnetoelectric-organic spintronic device (Pb(Zr,Ti)O_3//Co/FePc). It comprises doubly coupled magnetoelectric and ferromagnetic/organic interfaces and forms a prototypical system combining the multiferroicity and spinterface science. We start with a short description of the magnetoelectrically coupled systems, then we present the device's design, and discuss the results obtained during the *in operando* measurements at the DEIMOS beamline.

6.1 Multiferroicity and magnetoelectric coupling

The multiferroics by combining more than one ferroic order form, as such, a subclass of multifunctional materials.[351–353] From the spintronics point of view, these systems attracted considerable attention due to a perspective for an electrically-driven local control over the material's magnetisation.[354–357] That was recognized as possible by using the electric currents (via spin transfer torque), or applied voltages (magnetoelectric coupling process), and provided a low-power solution to much more expensive, and nowadays commonly used, method of magnetization reversal by current-generated magnetic fields.[356,358] Since the intrinsic multiferroics are rare and rather difficult to synthesize,[359] with perhaps the only $BiFeO_3$ (BFO)[360] or hexaferrites[361] exhibiting both magnetic order and ferroelectricity at RT, a strong interest was attracted by the so-called artificial multiferroics.[243,357,362]

The artificial multiferroics are composed of at least two materials which manifest ferromagnetism and ferroelectricity respectively with or without a coupling between them.[243,363] In addition to the RT multiferroicity, it has been shown that many of such systems may exhibit a magnetoelectric coupling (MEC) exceeding by several orders of magnitude the one measured in the archetypical single phase multiferroics. The converse MEC in these heterostructures, *i.e.*, the modulation of a magnetism by applying an electric field[354–356] can occur by two possible ways: (i) strain-mediated mechanism, or (ii) interface-related effects. The former results from the converse piezoelectric effect and magneto-elastic interactions, meanwhile the latter is a consequence of the electronic structure modification or exchange coupling.

In the following work we chose a ferroelectric Pb(Zr,Ti)O_3 (PZT) substrate (Fig. 6.1 (a)) and we will discuss now a particular case of MEC within the PZT/Co system. The PZT is a well known perovskite intensively studied because of its remarkable ferroelectric properties and commercial availability.[364] It was effectively employed in the magnetoresistive devices as a tunneling barrier (in Co/PZT/LSMO)[365] giving control over a spin polarization at the interface by ferroelectric switching. The theoretical studies of Borisov *et al.*[366] predicted a substantial variation of the Co magnetism upon a PZT polarization reversal. This was later highlighted by a recent work of our collaborators[28] who extensively studied the origin of the magnetoelectric coupling between the PZT and Co both in static and dynamic regime. In the following we discuss their results.

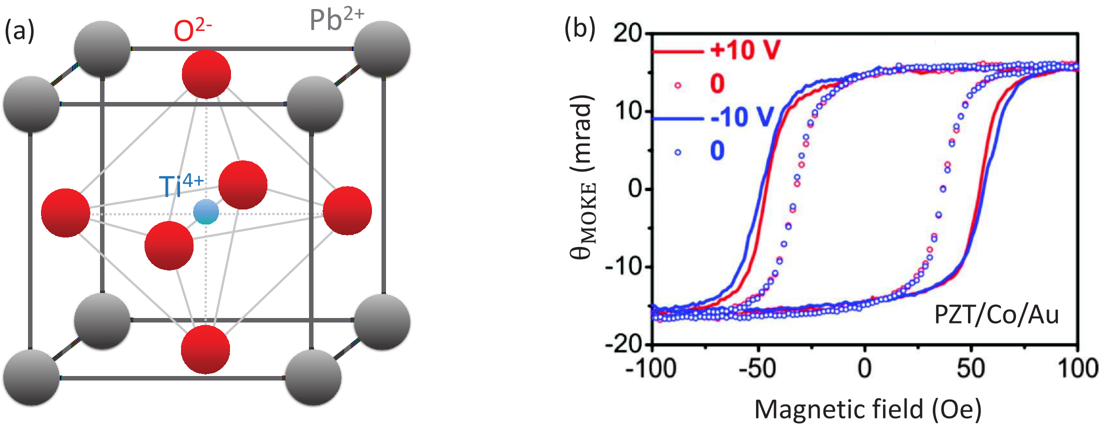

Figure 6.1: Magnetoelectric coupling (MEC) of the PZT/Co heterostructure. (a) The unit cell of Pb(Zr,Ti)O_3 (PZT). The ferroelectric polarization is induced by a relative displacement of the Ti^{4+} ions with respect to O^{2-}. In each second cell Ti is replaced by Zr^{4+}. (b) Hysteresis loops acquired in a magneto-optical Kerr effect measurement on PZT/Co(10 nm)/Au(5 nm) in presence and absence of a static bias voltage $V_{DC} = \pm 10\,\text{V}$. Figure taken from ref. 28.

By employing magneto-optical Kerr effect (MOKE) measurements performed on PZT/Co in presence of a static bias voltage $V_{\text{DC}} = \pm 10\,\text{V}$ (Fig. 6.1 (b)) they observed a clear and reversible coercivity variation from 25 Oe to 50 Oe of the Co hysteresis loop. It means that the magnetic anisotropy changes when the voltage is applied. The effect was shown to be vanishing when PZT and Co are separated by 8 nm thick Au layer. These measurements however, did not indicate the mechanism of the coupling. Later, the interface-related origin of this effect was experimentally evidenced by the detection of a magnetic ordering in the topmost PZT layer (non-zero XMCD signal at the Ti $L_{3,2}$-edges and O K-edge) (data not shown).

In order to understand the magnetoelectric coupling at the interface one has to consider an interatomic distance variation upon the substrate FE switching.[367] Roughly speaking, the ferroelectric polarization, which in case of PZT results mainly from the relative displacement of the Ti^{4+} ions with respect to its O^{2-} counterparts, is associated with particular interatomic distances between the atomic sites within PZT and also at the PZT/Co interface. The ferroelectric switching alters these distances, thus modifies the orbital overlaps, which govern, in turn, the electronic structure at the interface. To fully resolve the electronic configuration at the interface one has to follow an analogous procedure as discussed for the spinterface formation at the FM/organic contact, *i.e.*, by concerning the hybridization between all possible orbitals of the adjacent atomic sites. That was carried out by Borisov *et al.*[366] and extended by Vlašín *et al.*[28] for the case of PZT/Co.

Figure 6.2 presents a result of the *ab initio* calculations for the PZT/Co heterostructure and the two FE polarization states of PZT.[28] After the atomic positions relaxation one observes the bonds formation between Co and O sites within PZT. These bonds lengths appear as polarization dependent such that they vary in the range 1.914 Å – 2.022 Å (on Ti-O-Ti line) or 1.857 Å – 2.780 Å (on Ti-O-Zr line). Likewise, a lateral displacement of the Co atoms is observed. The hybridization occurs between Ti d and Co d states, and between O p and Co d states.[28, 366] This results in the induced magnetic moment on the otherwise non-magnetic O and Ti, such that the sign of Ti (O) moment is opposed to (consistent with) that of Co. The induced magnetic moments are polarization dependent. Finally, the magnetic properties of Co are altered upon the ferroelectric switching. The Co spin magnetic moment was established as $m_\mathrm{s} = 1.82\,\mu_\mathrm{B}$/atom for upward and $m_\mathrm{s} = 2.05\,\mu_\mathrm{B}$/atom for downward PZT polarization. This underscores the MEC originating from the interfacial effects and electronic structure modification due to the proximity of Ti, O, and Co atomic sites.

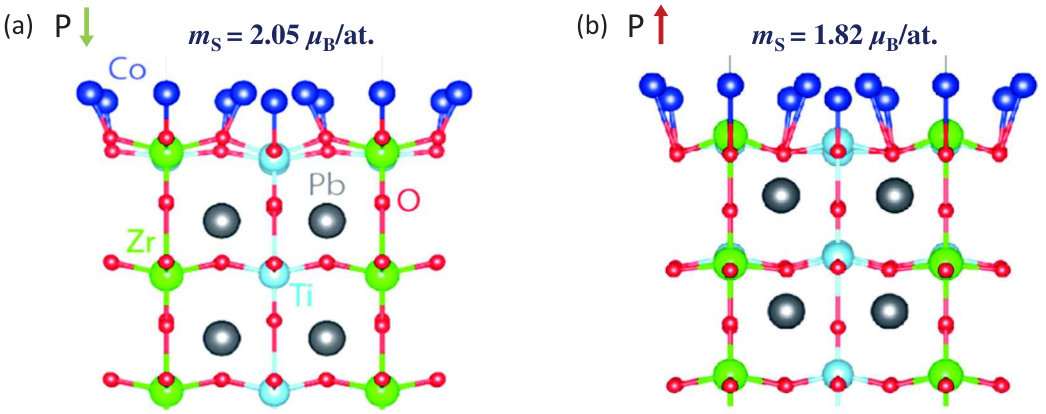

Figure 6.2: Magnetoelectric coupling at PZT/Co interface. The first principles calculations of 1 ML of Co atop PZT for two ferroelectric polarization states P↑ and P↓. Formation of the Co-O bonds at the interface and the interatomic distance variation upon the FE polarization reversal alters the Co spin magnetic moment from $2.05\,\mu_\mathrm{B}$/atom for upward to $1.82\,\mu_\mathrm{B}$/atom for downward polarization. Figure taken from ref. 28.

The MEC coupling strength, defined as induced surface magnetic moment ΔM for the coercive field E_c, *i.e.*, $\alpha_\mathrm{s} = \mu_\mathrm{o}\Delta M/E_\mathrm{c}$,[368] was estimated for PZT/Co($5-10\,\mathrm{nm}$) heterostructure as $\alpha_\mathrm{s} = 1-2\times10^{-10}\,\mathrm{G\,cm^2/V}$. In the following section we propose an architecture combining the MEC of PZT/Co with before studied ferromagnetic/organic spinterface encapsulated in a single device.

6.2 Magnetoelectric-organic spintronic device

The motivation behind designing a device that would combine multiferroicity and an organic spinterface arose from its potential multifunctionality. In Chapter 3, we showed that organic molecules can be strongly coupled to a ferromagnet at RT, what further opens the way towards unparalleled applications such as interlayer exchange coupled protected spinterfaces, or an organic spin injector in magnetoresistive device. Since they are strongly determined by the FM layer, one can imagine a bottom-up approach to control this FM properties. Resorting to a magnetoelectrically coupled system may allow this possibility via ferroelectric control. Therefore, we propose a concept of interconnecting two strongly coupled systems: (i) PZT/Co, and (ii) Co/FePc, to develop a magnetoelectric-organic spintronic device in a vertical architecture. We stress on its fully interfacially driven nature.[85]

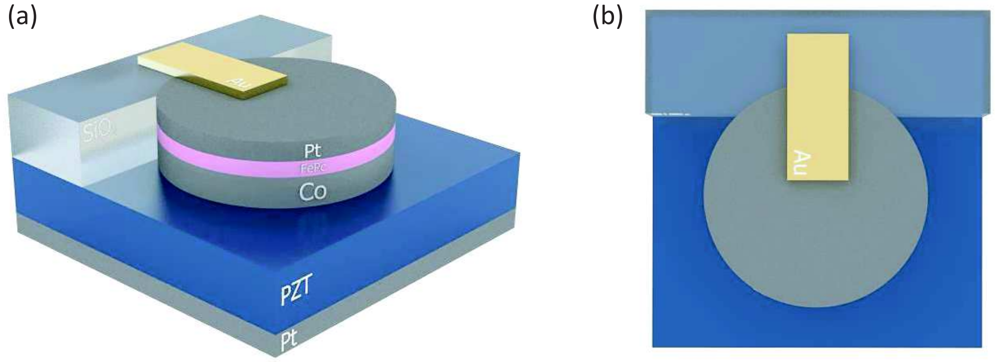

Figure 6.3: Magnetoelectric-organic spintronic device. 3d model of the vertical device combining the MEC interface PZT/Co, and ferromagnetic/organic spinterface Co/FePc in (a) isometric, and (b) top view. The pillar stack has composition: Pt($150\,\mathrm{nm}$)/PZT//Co($9\,\mathrm{ML}$)/FePc($1\,\mathrm{ML}$)/Pt($9\,\mathrm{ML}$). The $4\times4\,\mathrm{mm}^2$ sample contains a device of area $\sim 3\,\mathrm{mm}^2$. The picture is simplified, *i.e.*, in the real device the Co/FePc/Pt pillar is partially covering the SiO_2 insulating layer.

In the following section, we describe the design and fabrication of such a device followed by a post-processing characterization carried out in a collaboration with Salia Cherifi from the Département Surfaces–Interfaces (DSI) at the IPCMS.

6.2.1 Fabrication and processing

A commercially available substrate of 230 nm thick tetragonal $PbZr_{0.2}Ti_{0.8}O_3$ (textured with c-type domains) of size $4\times4\,\mathrm{mm}^2$ was partially covered with an insulating technological SiO_2. After annealing the substrate at 120 °C to desorb the contaminants, 9 ML of Co was thermally evaporated in UHV conditions through a shadow mask with a circular opening of 2 mm diameter. The magnetic properties of the FM layer were verified by the MOKE measurement performed on test PZT/Co(9 ML)/Pt(9 ML) stacks (Fig. 6.5 (a)). Then, 1 ML of FePc was deposited from a Knudsen cell heated up to 315 °C, and capped with 9 ML of Pt in order to protect the organic and FM materials from the atmosphere. After that, the sample was removed from vacuum and transferred for the thermal deposition of the gold top contact. The complete device architecture is presented in Fig. 6.3. We obtained a vertical device of area $\sim 3\,\mathrm{mm}^2$ containing the PZT/Co/FePc double interface of interest. Note that the large device area inevitably leads to a considerable leakage current ($\sim$ 20 mA) which eventually causes the PZT break down after a few poling sequences. Yet, such pillar size is necessary for a synchrotron studies to ascertain a satisfying signal to noise ratio (x-ray beam size: 400 µm × 600 µm). The future scaled-down device of the same architecture could be realized with microelectrodes increasing the endurance to nearly million cycles.[28]

In this configuration, the PZT substrate possesses an out-of-plane ferroelectric polarization which can be reversed upon applying a bias voltage between the electrodes. The FE polarization is coupled to the FM moment of Co (in-plane easy axis of magnetization), which in turn FM aligns the Fe centers of the FePc molecules. In our architecture the bottom electrode of the device is the 150 nm thick platinum layer below the PZT substrate, meanwhile the top one is formed by Pt/Au over the FePc. A technological SiO_2 prevents the accidental short-circuiting of the two electrodes while bonding.

The ferroelectric switching of the fabricated device was tested with an AixACCT TF 2000E probing station located at the IPCMS. It allows the measurement of the polarization loops $P(E)$ from the $I(V)$ characteristics by the time integration of a displacement current recorded in transverse geometry. We performed both the dynamic hysteresis and pulsed measurements which indicated the intense peaks in the $I(V)$ curves providing the evidence of the FE polarization existence and its switching. We relied on the pulsed measurements since recording the dynamic P-loops is known to

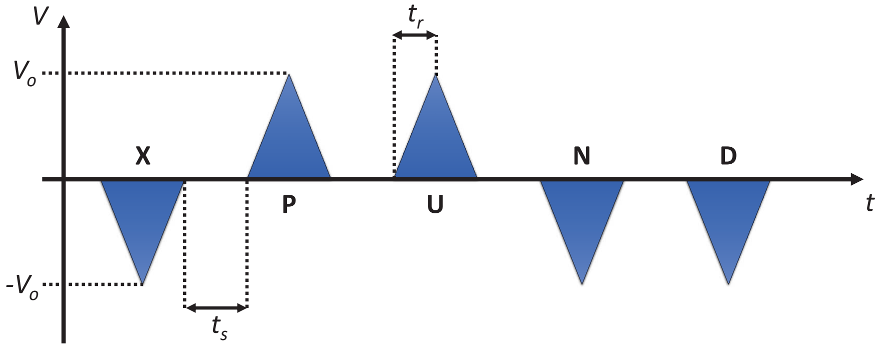

Figure 6.4: PUND measurement. Sequence of voltage pulses applied during PUND (P - positive, U - up, N - negative, D - down) measurement. We used pulses of maximum bias voltage $V_\mathrm{o} = \pm 10\,\mathrm{V}$, rise time $t_\mathrm{r} = 250\,\mu\mathrm{s}$ and separation between the pulses $t_\mathrm{s} = 1\,\mathrm{s}$. "X" denotes the pre-pulse applied to ensure the procedure to be always performed at the same conditions.

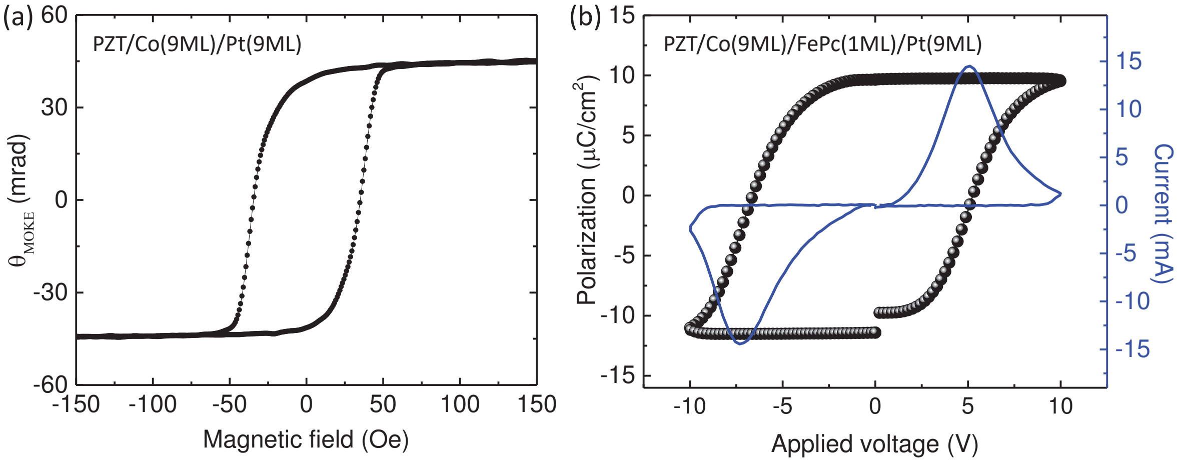

Figure 6.5: Ferromagnetic and ferroelectric testing of the magnetoelectric-organic device. (a) Result of MOKE measurement performed on PZT/Co(9 ML)/Pt(9 ML) test sample confirming proper ferromagnetic properties of Co layer. (b) Result of PUND measurement on complete PZT/Co(9 ML)/FePc(1 ML) device. The peaks in the $I(V)$ curves reveal two ferroelectric states of the device with polarization of $\sim \pm 12\,\mu\mathrm{C/cm^2}$.

overestimate the current value (strong contribution of the leakage current), which may lead to misleading results.[369]

The pulsed measurement mode records the current response of the device after the application of a sequence of pulse excitation signals. The method is commonly known as PUND what comes from the abbreviation of the applied pulses sequence: Positive, Up, Negative, Down.[370] The application of consecutive two positive and two negative voltage pulses allows the unambiguous distinction between a switching current and a leakage current. Let us assume the sample to be in initial, not defined state. By applying a P-pulse (Fig. 6.4) and measuring the response (*i.e.*, $I(V)$) we obtain the signal containing both switching and leakage current. Now, if we apply an additional positive pulse (U), the related current can only be attributed to the leakage. Therefore, by subtracting $[I(V)]_\mathrm{P}$ from $[I(V)]_\mathrm{U}$ one obtains a purely switching current that is directly related to the polarization. The same stands for the opposite pulses sequence, that is N and D. Eventually, the polarization is given by the integration of the current (positive and negative branches, *i.e.*, $[I(V)]_\mathrm{P-U} + [I(V)]_\mathrm{N-D}$) over time divided by the surface of the electrode.

The characteristics of the applied voltage sequence was fixed according to the previous experiments over the PZT-based systems. We used the triangular pulses of maximum bias voltage $V_\mathrm{o} = \pm 10\,\mathrm{V}$ with a rise time of $t_\mathrm{r} = 250\,\mu\mathrm{s}$ and separation between the consequent pulses in a sequence $t_\mathrm{s} = 1\,\mathrm{s}$. The result of PUND measurement performed on the complete device is presented in Fig. 6.5 (b). The $I(V)$ curves manifest the peaks reflecting two FE states associated with the polarization of $\sim \pm 12\,\mu\mathrm{C/cm^2}$. This proves a proper operation of the device after fabrication and processing.

6.2.2 *In situ* investigation with synchrotron radiation

An insight into particular electronic structure at buried PZT/Co and Co/FePc interface requires a sensitive and chemically selective method. This can be provided by soft x-ray spectroscopy. Therefore, in order to resolve the FE polarization dependent electronic alterations of the specific constituents of the device, we carried out x-ray absorption spectroscopy measurements at the DEIMOS beamline of the SOLEIL synchrotron. A new electrical insert of the beamline (V^2TI, see Sec. 4.7) was used to provide *in situ* electrical access for the FE polarization reversal. The sample was mounted on a dedicated chip such that the bottom Pt layer was connected with silver paste as a negative electrode and the Au top pad with a wire bonder as a positive one. In addition, a separate contact attached to the off-device region on the technological SiO_2 layer was used to measure the total electron yield signal.

In that way, we could monitor the electronic changes on a specific material component after each poling sequence. We cycled the FE polarization direction, denoted later as P↓ (P↑) for polarization vector pointing towards (away from) the bottom electrode, and monitored the modifications at the $L_{3,2}$-edges of Ti within the PZT substrate, Co, and Fe of FePc molecules in a remanent ferroelectric state. All the presented results were acquired in the center of the device's pillar at 45° incidence and at RT in total electron and fluorescence yield detection.

The reversal of the FE state was provoked by a sequence of voltage pulses provided by the Agilent 33512B function/arbitrary waveform generator programmed and triggered via a LabView-based software. Each sequence consisted of two pre-poling pulses $-10\,\mathrm{V}$ and $+10\,\mathrm{V}$ followed by one $+10\,\mathrm{V}$ pulse (two $-10\,\mathrm{V}$ pulses) for the desired up polarization P↑ (down polarization P↓) state. Schematically, by referring to Figure 6.4, the P↑ (P↓) state was obtained by the applied sequence X-P-U (X-P-N-D). The electrical connection between the V^2TI and the poling bench was established exclusively for a polarization reversal and removed during the XAS measurement so as to minimize electrical noise in the TEY signal.

Prior to the beamtime, the device was poled at the IPCMS as P↓. Therefore, after introducing the sample into the DEIMOS environment we started with the XAS data acquisition for the initial P↓ state. Then, the polarization was *in situ* reversed to P↑ and the procedure was repeated. Finally, we switched again to down polarization, which we will refer to as P_2↓ state, and after the data accumulation we explored the obtained spectra looking for a reversible pattern. Note that this strategy is more vulnerable to drift issues than the frequent polarization reversal followed by the data recording, yet the latter generates a high risk of the device breakdown due to the fatigue effects.[371] Thus, our experimental protocol ensured the maximum data yield obtained within the smallest number of poling procedures (including the post-processing ferroelectric testing). In the following section we discuss the obtained results.

6.2.2.1 PZT: Ti *L*-edge

It was demonstrated in *ex situ* experiments that the FE switching of the PZT state should be accompanied by the reversible alterations observed on the XAS spectra at Ti $L_{3,2}$-edges.[29] We employed this fact and used the XAS and x-ray linear dichroism (XLD) techniques to provide an evidence for the effective FE polarization reversal with our protocol.[29]

Figure 6.6 presents the XAS and XLD spectra acquired at the Ti $L_{3,2}$-edges for the device in the initial P↓ state. The absorption curves reflect a typical XAS of Ti^{4+}, *i.e.*, dipolar transitions from d^0 to $2p^5 3d^1$ configuration. The spin-orbit coupling of

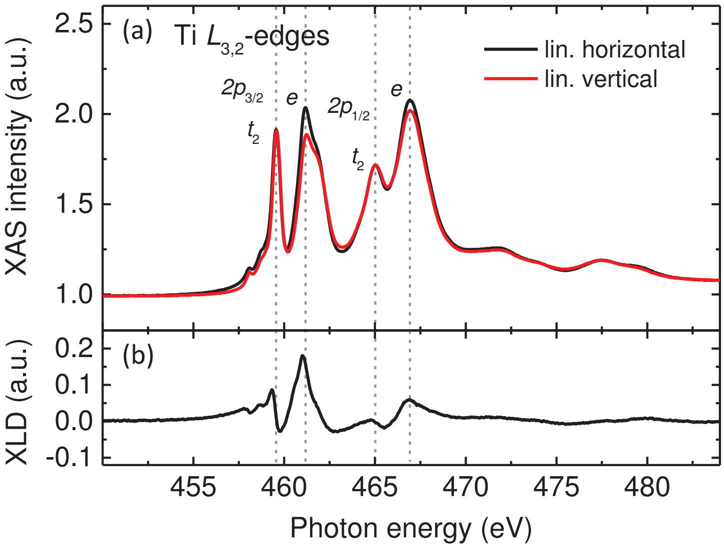

Figure 6.6: XAS at Ti $L_{3,2}$-edges of PZT. The absorption spectra acquired with linear horizontal and vertical x-ray polarization at the Ti $L_{3,2}$-edges (a), and the resulting linear dichroism (b) of PZT in initial P↓ state. The Ti $2p$ orbitals are split by the 5.45 eV spin-orbit coupling into $2p_{3/2}$ and $2p_{1/2}$ levels which are further subjected to 1.62 eV splitting by the octahedral crystal field into t_2 and e symmetry groups. This symmetry reduction leads to unequal absorption of the x-rays with linear vertical and horizontal polarization. The spectra were acquired in total fluorescence yield at applied magnetic field $H = 0.1\,\mathrm{T}$.

the initial Ti $2p$ states results in a 5.45 eV splitting[372] further subjected to a 1.62 eV octahedral crystal field split, which is FE polarization dependent, giving rise to e and t_2 symmetry groups.[373,374] The e orbitals are pointing towards the oxygen anions, meanwhile t_2 are oriented between them.[29,374] A stronger broadening of the transition peaks assigned to e states emerges from a distorted Ti octahedral environment. This, in turn, leads to a further splitting of $e(O)$ into $b_1 = d_{x^2-y^2}$ and $a_1 = d_{z^2}$, and of $t_2(O)$ into $b_2 = d_{xy}$ and $e = d_{xz}, d_{yz}$. This symmetry reduction is the reason of the unequal absorption of the x-rays with linear horizontal and vertical polarization (Fig. 6.7 (b)), reaching a maximum of $\sim 20\%$ at the $2p_{3/2}3d(e)$ peak. Note that the used PZT has textured structure, meaning a random orientation of the tetragonal unit cells in plane, yet still with a distinguishable c axis pointing out of the sample plane.

In the next step, we examined the alterations at the Ti $L_{3,2}$ absorption edges upon the ferroelectric polarization reversal. To do so, we compared the x-ray polarization averaged spectra acquired for the consequent FE states of PZT (Fig. 6.7). First, we discuss the difference between the curves corresponding to the P↓ initial and P↑ states (Fig. 6.7 (b)), thus after the first poling sequence. We observe the most prominent feature at $2p_{3/2}3d(t_2)$ peak (460 eV) reaching $\sim 3\%$ and resulting from the energetic shift of the orbital. That is followed by the features of smaller intensity for the states at higher energies. This can be explained by an interplay of an increased electrostatic potential within the PZT unit cell for P↑ with respect to P↓ due to a deformation along the c axis,[29] and the following modification of the octahedral crystal field strength.[374] By comparing the spectra corresponding to the second polarization reversal from P↑ to P_2↓ (Fig. 6.7 (d)) we observe the same set of the features as for the first poling, yet

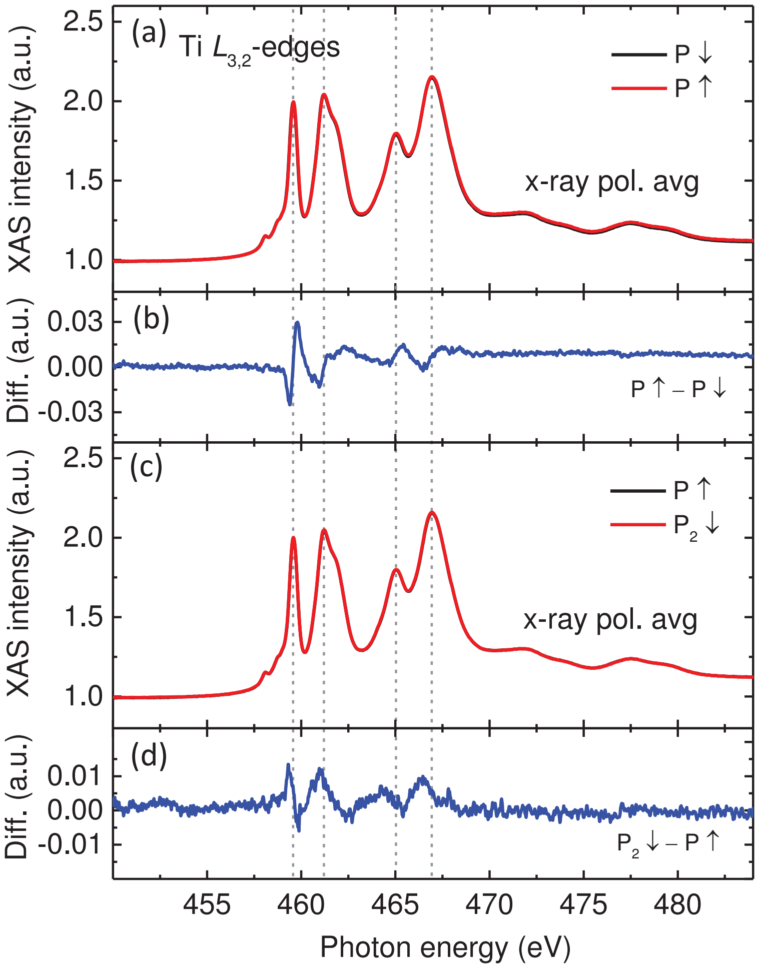

Figure 6.7: Modification of Ti electronic structure upon ferroelectric switching of the device. Linear polarization averaged XAS spectra at the Ti $L_{3,2}$-edges of PZT acquired successively for the ferroelectric polarization P ↓, P ↑, and P_2 ↓ states. Panels (a) and (c) show the averaged x-ray absorption used to calculate the differences (b) and (d). The features appearing in difference spectra as opposed in sign reflect the reversible changes of Ti electronic structure. The spectra were acquired in total fluorescence yield at applied magnetic field $H = 0.1\,\mathrm{T}$.

with an opposite sign. Since we consequently calculate the differences as a succeeding polarization state spectrum subtracted from the previous one, the features appearing as inverse in sign reflect a reversible effect. Knowing that the used PZT is textured, and thus there is no in-plane anisotropy, we infer that the observed alterations result from the Ti ions displacement along the *c* axis of the unit cell. This is in agreement with recently reported observation at Ti *K*-edge of the PZT.[375] Note however, that the amplitude of the effect after the second poling is almost threefold smaller than for the first one meaning that the switching is not completely reversible. This we suggest could be a consequence of the already arising fatigue effects, which at observed for the device large leakage currents, are expected to be significantly strong. The third polarization reversal resulted in the device remaining at P_2 ↓ state, hence loss of the switching abilities. We therefore claim to switch efficiently the FE polarization of PZT substrate 3 times (including the post-processing FE testing procedure).

In that way, we proved the FE polarization reversal of the PZT substrate. In the next sections we discuss the following alterations observed during the FE switching on the $L_{3,2}$-edges of Co and Fe in FePc.

6.2.2.2 Co *L*-edge

Since in the invoked study over the PZT/Co heterostructure by Vlašín *et al.*[28] the authors clearly infer the alteration of Co spin magnetic moment upon a ferroelectric polarization reversal, we focus now on the examination of the XMCD at the Co $L_{3,2}$-edges.

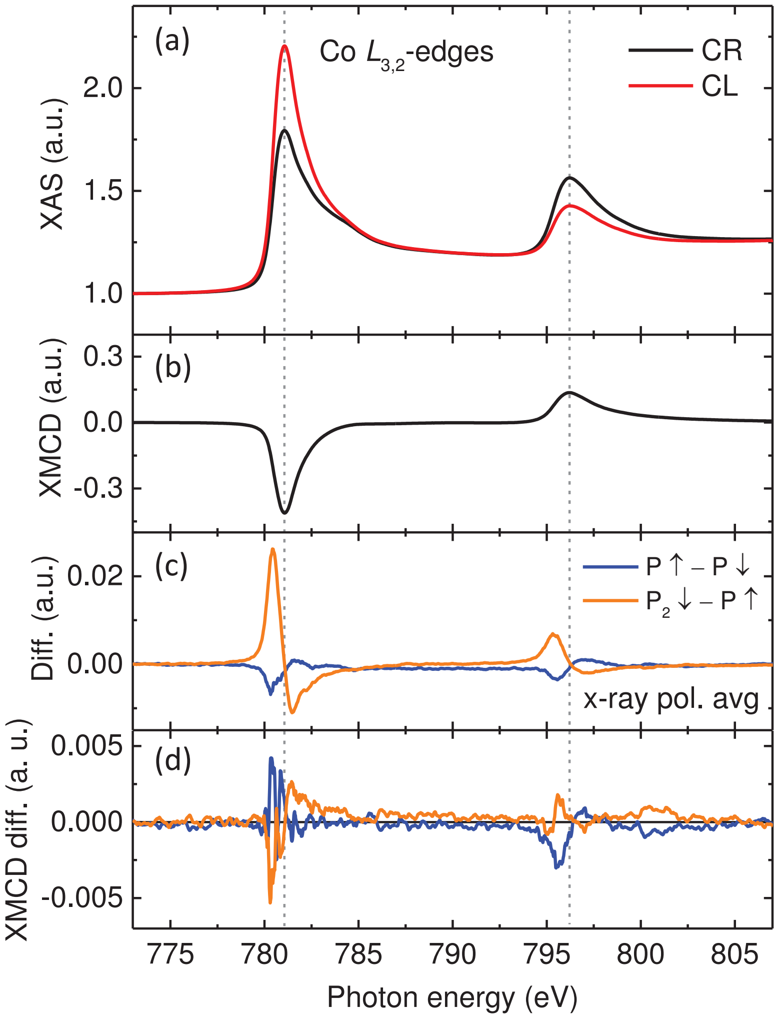

Figure 6.8: Modification of Co electronic/magnetic properties upon ferroelectric switching of the device. (a) Exemplary XAS spectra acquired at the $L_{3,2}$-edges of Co for the initial P ↓ state with (b) the resulting XMCD. The difference of (c) both circular x-ray polarization averaged XAS spectra, and (d) XMCD were calculated for the first (P ↑ − P ↓) and second (P_2 ↓ − P ↑) PZT polarization reversal. The spectra were acquired in total electron yield mode at both directions of the magnetic field $|H| = 0.1\,\mathrm{T}$.

First, we present the exemplary XAS at the Co $L_{3,2}$-edges corresponding to the device in the initial P$\downarrow$ state for both circular x-ray polarizations (Fig. 6.8 (a)) and the resulting XMCD (Fig. 6.8 (b)). Since 9 ML of Co give rise to a considerable signal amplitude it may overshadow the subtle alterations of the magnetization originating exclusively from the limited interfacial region. We isolate these small changes by examining how reversing the PZT polarization affects both x-ray polarization averaged XAS (Fig. 6.8 (c)) and XMCD spectra (Fig. 6.8 (d)). For polarization averaged XAS, we observe the asymmetric derivative-like features at both L_3- and L_2-edges of Co that appear as reversed in sign for two consecutive FE poling sequences. The same occurs when changes to XMCD are considered, reaching the maximum amplitude of $\sim 0.5\%$ at L_3-edge (Fig. 6.8 (d)). We suggest that the alterations illustrated in Fig. 6.8 (c) and (d) are originating from the ferroelectric polarization driven changes of the Co electronic and magnetic properties due to the aforementioned PZT/Co magnetoelectric coupling.[28] In this way, we validate the operation of the first PZT/Co interface within the device. Note that our considerations have rather qualitative character as uncertainty of the sum rules applied to such small amplitude variations at the Co $L_{3,2}$-edges would hinder a quantitative comparison.[214]

6.2.2.3 FePc: Fe *L*-edge

Finally, we focus on the second interface within the device, that is the hybrid Co/FePc spinterface. The FM coupling of the Fe centers in FePc to Co, resulting from spin-

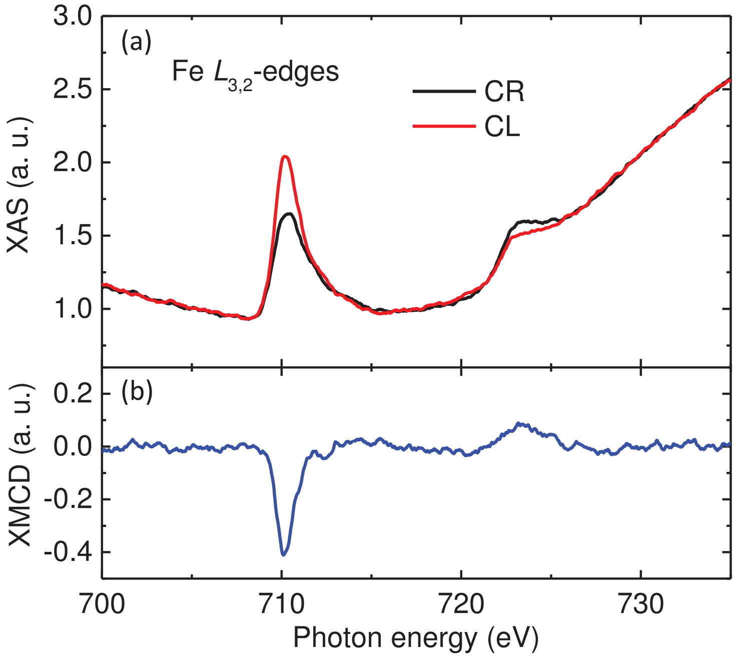

Figure 6.9: XAS and XMCD at the $L_{3,2}$-edges of Fe in FePc molecules. (a) X-ray absorption spectra acquired for both circular left (CL) and right (CR) x-ray polarization at the Fe $L_{3,2}$-edges of Fe in FePc, and (b) the resulting XMCD. A non-zero dichroic signal originates from the FM coupling of the Fe magnetic moments to the underlying Co. The spectra were acquired in total electron yield mode at both directions of the magnetic field $|H| = 0.1$ T.

dependent hybridization at the interface, was first confirmed by the RT XMCD at the Co and Fe $L_{3,2}$-edges (data not shown). Then, we investigated how the electronic structure of Fe is altered upon switching the PZT polarization.

Figure 6.9 presents the XAS and XMCD spectra at the Fe $L_{3,2}$-edges of FePc. The broad L_3-edge, devoid of clear multiplet peaks, is typical of spin hybridization induced by the spin-polarized charge transfer at the ferromagnet/molecule interface.[30] The XAS spectra exhibit a strong non-linear background, which originates from the absorption of the PZT substrate. We witnessed a notable evolution of the background upon ferroelectric polarization reversal, which is presumably arising from a charge distribution variation within the PZT upon poling. Due to the dilute number of Fe atoms in the 1 ML of FePc, which is buried under 9 ML of Pt, the XAS intensity at the Fe $L_{3,2}$-edges is very small, what makes the spectra especially vulnerable to these charge distribution variations. Since we nevertheless obtain, for all data, a flat, zero XMCD background before and after the Fe $L_{3,2}$-edges this allows us to directly compare the XMCD at the Fe L_3-edge for the consecutively switched PZT polarization states.

We witness the reversible alterations on the Fe L_3-edge XMCD driven by the FE polarization switching (Fig. 6.10). We focus on the features marked as A, B, and C, which are the most visible. (i) The pre-edge XMCD peak (feature A, marked with the red arrow) is present for P ↑ but not for P ↓ state. (ii) The L_3-edge XMCD maximum (feature B) is shifted by 0.1 eV upon flipping the PZT polarization. (iii) The feature C is a local maximum in the XCMD amplitude for P ↓ but not for P ↑ state. This underscores the strong similarities in the Fe L_3-edge XMCD according to the features A, B, and C between the P ↓ and P_2 ↓ states. In the same time, we did not observe reversible alterations at the L_2 edge of Fe (not shown).

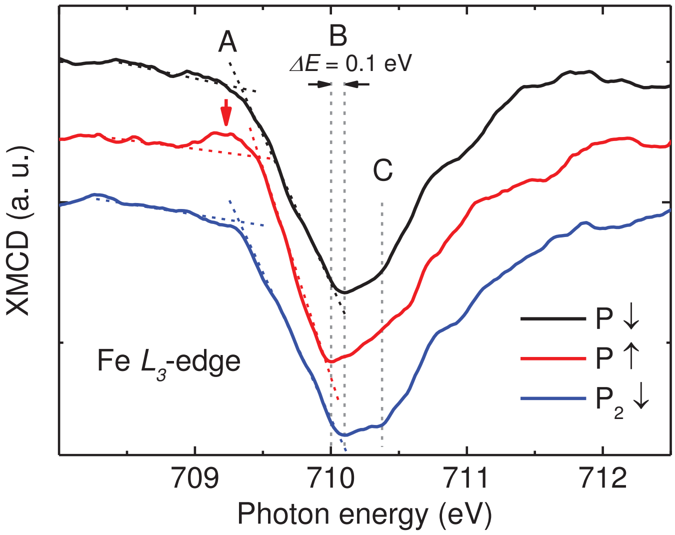

Figure 6.10: Modification of Fe L_3-edge XMCD upon ferroelectric switching of the device. XMCD at the Fe L_3-edge of FePc acquired for the consecutive PZT polarization P ↓, P ↑, and P_2 ↓ states. Note the features A, B, and C revealing the FE polarization driven changes and identical P ↓ and P_2 ↓ spectra. The spectra were acquired in total electron yield mode at both directions of the magnetic field $|H| = 0.1\,\mathrm{T}$.

These modest, yet fully reversible changes to the L_3-edge XMCD of Fe in FePc atop Co indicate that the FePc molecular layer's magnetic state, which is coupled to and results from the Co film's last monolayer, is being altered across the Co thin film due to switching of the ferroelectric polarization of PZT. This implies that the changes to the magnetoelectric properties of the PZT/Co interface, in turn, alter the ferromagnetic properties of the entire 9 ML thick Co film. In that way, we infer that alterations induced on the FE substrate are propagating through a doubly coupled structure, *i.e.*, the magnetoelectrically coupled PZT/Co and hybridized Co/FePc interface.

6.3 Partial conclusions

To conclude, we proposed a concept of a magnetoelectric-organic device combining the electric-field-control of the MEC interface with the virtues of the organic spinterface such as the long spin coherence time, spin filtering abilities, magnetism stabilization, etc. We emphasize on the device's entirely interfacially-driven operation. By means of the soft x-ray spectroscopy we demonstrated a chain of propagating reversible electronic changes starting from the $L_{3,2}$-edges of Ti, reflected at the FM Co layer, and eventually further observed on the Fe centers within the FePc molecules. Since the electronic modifications at the MEC PZT/Co interface are consistent with those previously predicted,[28] it was for the first time demonstrated as sensed by a remote organic spinterface. Although the evidenced changes are rather modest, they provide a state of the art, which if further developed may lead to memory or spin electronics devices exploiting these unique properties of both artificial multiferroics and organic spinterfaces. We anticipate an advancement in presented concept by improved interfaces quality and reduced FE and FM layer thicknesses leading to further enhancement of the interfacial effects. We are also looking forward to the results of theoretical study, carried out by our collaborators at the moment of this manuscript submission, which may provide the information about a charge transfer, hybridization and emergent electronic structure at the interfaces of PZT/Co/FePc system. We believe this would also shine more light on the explanation how the observed alterations provoked at PZT/Co contact may propagate through 3 nm thick Co layer.

7

Towards spin crossover based multifunctional device

In the previously discussed studies over the hybrid metal/organic spinterface or prototypical magnetoelectric-organic device the choice of organic material was limited, for sake of simplicity, to the archetypal metal-phthalocyanines. These, despite of their aforementioned excellent properties from the perspective of spintronic applications, create ”passive” layers whose properties are rather constant throughout a broad range of the external conditions, *e.g.*, temperature, pressure, magnetic field etc. In the next level of complexity we want to propose an ”active” layer made of organic spin crossover material. The fundamentals of the SCO phenomenon were introduced in Section 2. In this part, we briefly describe the properties of the particular Fe(II)-based SCO complexes and impose two requirements of desired material properties in our context of the spintronic applications.

To begin with, we report on a new sublimable complex $\mathrm{Fe\{[3{,}5\text{-}dMePy]_3BH_2\}_2}$ (Fe-pyrz) and characterize it from the point of view of its spin transition, LIESST effect, and surface morphology in sublimed film. Then, we propose a new direction in the field of SCO by exploring functionalization of the known molecules by chemical structure engineering so as to controllably exploit the desired material properties. Two parent complexes were used for this study: $\mathrm{Fe(bpz)_2(phen)}$ and $\mathrm{Fe(bpz)_2(bpy)}$ (bpz = dihydrobis(pyrazolyl)borate, bpy = 2,2’-bipyridine).

7.1 Fe(II)-based SCO complexes

7.1.1 General properties

Very soon after the discovery of the SCO, the scientific community focused particularly on studies over Fe(II)-based complexes what resulted in such mile stones in the field as, *e.g.*, thermodynamic study of Jung *et al.*[376] on the entropy driven SCO

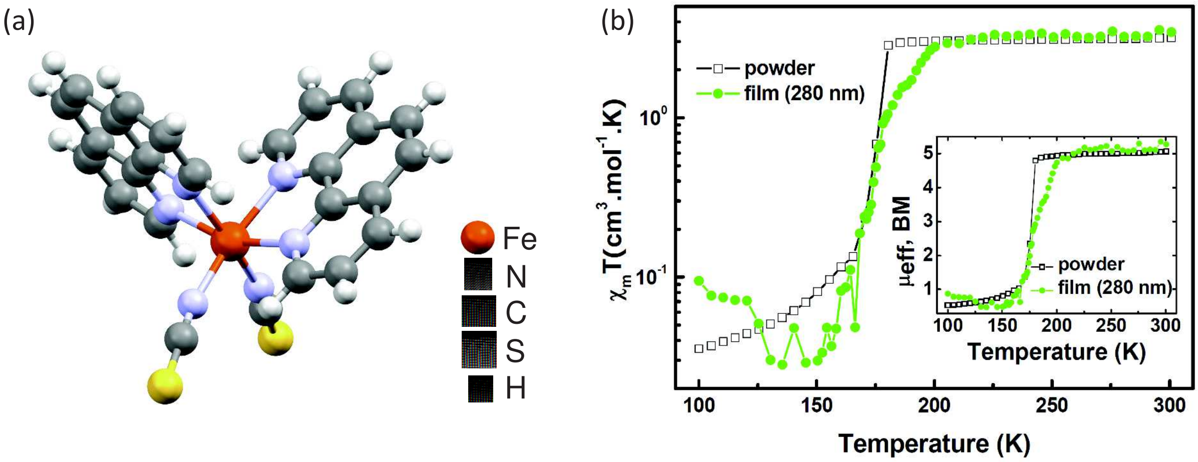

Figure 7.1: Fe(phen)$_2$(NCS)$_2$ (Fe-phen). (a) Model of the Fe-phen molecule. (b) Magnetic susceptibility as a function of temperature for the Fe-phen powder and a 280 nm thick UHV sublimed film. Measurement performed with SQUID. Figure taken from ref. 379.

in [Fe$_x$Zn$_{1-x}$(ptz)$_6$](BF$_4$)$_2$, discovery of a light induced excited spin state trapping in hexa-1-propyltetrazole-iron(II)tetrafluoroborate by Decurtins *et al.*,[160] or work on the cooperative effects by Kahn *et al.*[377]

The family of Fe(II)-based spin transition complexes does not significantly differ from the rest of the SCO compounds, nonetheless it is the most numerous and gives a general overview on trends in the field. The Fe(II) with d^6 configuration in octahedral environment adopts one of the two configurations: $^1A_1$ $((t_{2g})^6(e_g)^0)$ or $^5T_2$ $((t_{2g})^4(e_g)^2)$. The former with no unpaired electrons ($S = 0$, diamagnetic) is referred to as low spin (LS) state and the latter with 4 unbalanced electrons (S = 2, paramagnetic) as high spin (HS) state. A thermal activation or any other perturbation provoking a potential barrier crossing (see Fig. 2.6) triggers the $^1A_1 \longleftrightarrow {}^5T_2$ spin transition.

The vast majority of the Fe(II) SCO compounds is based on the Fe-N octahedral system where nitrogen atoms are part of bigger cyclic groups. Although chemical designing of a complex which would exhibit a spin transition is challenging, there are few general strategies to bring the material close to that bistability region: (i) by expanding the ligands with groups weakening the Fe-N interaction, thus destabilizing the singlet state and facilitating a SCO (*e.g.*, Fe(phen)$_3$ (no SCO) vs. Fe(mephen)$_3$, mephen = 2-methyl-1,10-phenanotroline); (ii) by substituting 6-membered ligands with 5-membered ones. That reduces the donor-acceptor character of the complex and imposes a strain promoting the quintet state (*e.g.*, Fe(bpy)$_3$ (no SCO) vs. Fe(pyim)$_3$, bpy = 2,2'-bipyridine, bpy = 2-(pyridin-2-yl)imidazole); (iii) by replacing heterocyclic ligands with aliphatic ones (*e.g.*, [Fe(pic)$_3$](anion)$_2$, pic = 2-picolyl-amine).[378] One has to keep in mind that the occurrence of SCO is in particular very sensitive and extremely easy to jeopardize by the slightest modification of the chemical structure or environment of the complex.

Historically, the first synthesized Fe(II)-based SCO complexes were derived from bis(phenanothroline) family (Fe(phen)$_2$X$_2$),[380,381] where the spin state of the Fe ion strongly depends on the X group. The magnetic moments and the Fe ground state configurations for complexes with several selected X groups are collected in Table 7.1.

Table 7.1: Effective magnetic moment and a ground state configuration of Fe(phen)$_2$X$_2$ complex for different X groups. Values taken from ref. 382, 383.

X group	Magnetic moment (μ_{B})	Ground state configuration at RT
Cl	5.27	$^5T_2$
Br	5.24	$^5T_2$
NCS	5.17	$^5T_2$
NCSe	4.98	$^5T_2$
NO$_2$	0.98	$^1A_1$
CN	0.61	$^1A_1$

One easily sees that the groups X = Cl, Br, and NCS lead to Fe paramagnetic character, meanwhile X = NO$_2$, and CN to its diamagnetism. One should therefore expect a spin transition for the groups exerting an intermediate field strength on the central atom between X = CN and Cl. Indeed, one of the first reported SCO were Fe(phen)$_2$(NCSe)$_2$ and Fe(phen)$_2$(NCS)$_2$. The latter drew notable attention of the scientific community and undoubtedly remains of interest to date. A single molecule of Fe(phen)$_2$(NCS)$_2$ (Fe-phen) contains two phenanthroline and two thiocyanate groups surrounding the Fe(II) ion in a quasi-octahedral symmetry (Fig. 7.1 (a)). The Fe-phen exhibits a robust SCO at a transition temperature $T_{1/2}$ =176.3 K.

The applicability of the SCO material in a spintronic device of vertical architecture, as discussed in this thesis, requires the fulfillment of two major conditions: (1) compatibility of the complex with thermal sublimation, and (2) possibility to grow the homogeneous flat films. In the following we comment on these two requirements.

7.1.2 Requirement I: sublimability

We mentioned that UHV sublimation is one of the most efficient methods to obtain the high purity nanometric films with a good control over their thickness. Furthermore, it is also highly desirable because of a growing interest on the nanoscale studies over the single monolayers or even isolated molecules (Fig. 7.2). These are rather precluded in wet deposition techniques.

There are numerous reports on successful SCO film fabrication by molecular self-assembly,[384] Langmuir-Blodgett deposition,[385] dip coating,[386] or drop casting. However, sublimability still remains rather challenging. Although a few hundreds of spin transition compounds were synthesized to date, only several of them were reported suitable for sublimation. Fe-phen was the first to be successfully sublimed with the conservation of SCO in a thin film form[379] (Fig. 7.1 (b)). In comparison with a powder reference it revealed the same level of a magnetization saturation and a moderate change of the transition slope thus decrease of the cooperativity.

This breakthrough was followed by submonolayer studies of Fe-phen on the surface focusing on the subtle effects occurring between the molecules and the substrate.[22] Figure 7.2 (a) presents the STM image of the single Fe-phen molecules on a Cu(100) surface revealing a coexistence of two distinct geometries corresponding to the HS (I) and the LS (II) states. The molecules were found to be chemisorbed on the surface

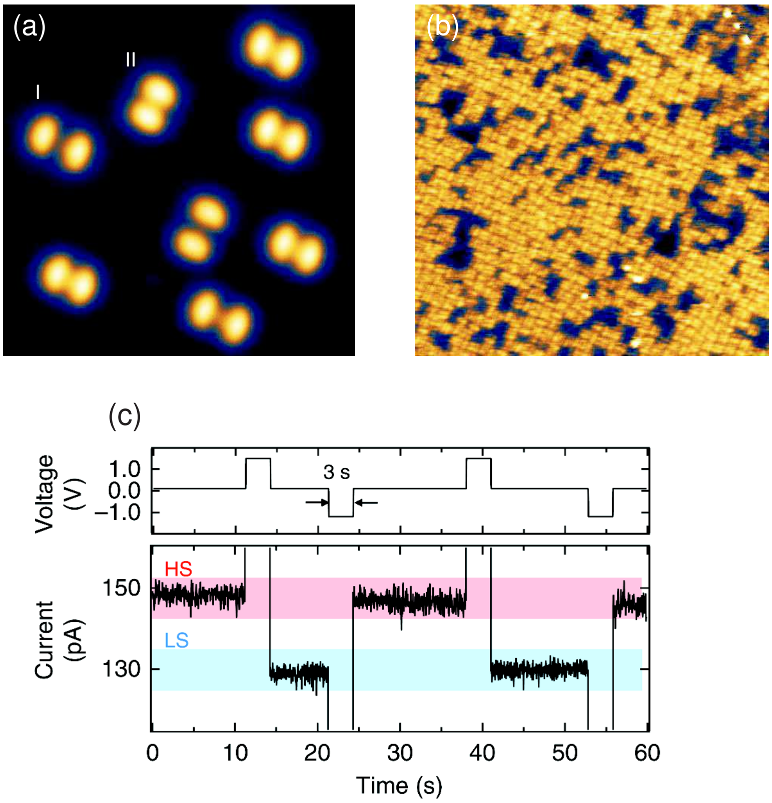

Figure 7.2: Spin crossover on the surface. (a) STM I-const. image of the Fe-phen isolated molecules sublimed on a Cu(100) surface ($13 \times 13\,\text{nm}^2$, $V = 30\,\text{mV}$, $I = 1\,\text{nA}$). Morphology I (II) corresponds to the molecular geometry in HS (LS) state. (b) STM I-const. image of the Cu(100)//Fe-phen(1.8 ML) surface revealing a short-range ordering of the molecules ($40 \times 40\,\text{nm}^2$, $V = 1.8\,\text{V}$, $I = 100\,\text{pA}$). (c) STM-tip-induced reversible HS ↔ LS switching of the Fe-phen single molecule on Cu(100)//CuN by applying +1.5 V pulse. The spin state is determined by measuring the tunneling current at $V = +0.1\,\text{V}$. Figures taken from ref. 22, 17.

by the thiocyanate groups. The studies revealed an important role of the molecule-substrate interaction on a spin transition. Meanwhile the chemisorption of Fe-phen on Cu(100) causes a quenching of SCO, addition of an intermediate layer of CuN restores a transition capability. Figure 7.2 (c) shows an effective switching of a single Fe-phen molecule on Cu(100)//CuN surface by applying +1.5 V via the STM tip. The invoked studies provided the evidence for SCO in sublimed isolated molecules on the surface observed by the STM.

This example highlights the possibilities given by UHV thermal sublimation. Nevertheless, it is rather difficult, from the chemical point of view, to synthesize a sublimable compound due to a delicate balance between the required SCO bistability and robustness of molecular structure at the same time. The most important requirements for sublimability include the thermal stability, low molecular weight, neutrality, and lack of solvent impurities in the lattice.[387] Undoubtedly, the most difficult to fulfill is the thermal stability, since the majority of known SCO compounds decomposes before the sublimation occurs, loosing thus irreversibly the spin transition properties. The rule of thumb, increasing the chance of obtaining a sublimable compound, is to select ligands which are sublimable in a free form.

7.1.3 Requirement II: continuity of thin film

Fabrication of the vertical device with SCO material as an active layer imposes a requirement on the material to form uniformly growing films upon deposition so as to effectively prevent two adjacent electrodes to be in contact. In general terms, the formation of a film follows the nucleation and growth stages. These include the adsorption, diffusion, and binding governed by the thermodynamics and growth kinetics. The most general classification of the growth modes distinguishes: (i) Volmer-Weber mode - when the molecule-molecule interactions are stronger than molecule-substrate, the deposited molecules nucleate in the clusters which then form the bigger islands by increasing their volume; (ii) Frank-van der Merwe mode - conversely, when intermolecular interactions are weaker than between a molecule and the substrate, a densely packed first layer is formed and then the second less bound atop of it; (iii) Stranski-Krastanov mode - an intermediate mode between (i) and (ii), starts with a creation of uniform layers up to a certain critical thickness, where the island formation becomes more favorable. The resulting structure consists of several complete monolayers with clusters atop. One has to keep in mind that a growth mode depends not only on the deposition conditions (temperature, pressure, rate, etc.) but is specific for a given pair molecule-substrate.

From the point of view of a vertical device fabrication the desired growth of SCO compound is following scenario (ii) or (iii). The Volmer-Weber mode, in turn, leads to formation of pinholes in the surface causing formation of the filaments between the adjacent electrodes. The discussed Fe-phen molecules on Cu(100) surface (Fig. 7.2 (b)) exhibit a typical Frank-van der Merwe growth. Despite an incomplete first monolayer the molecules tend to grow in a closed packed formation.

Those two requirements are crucial for the UHV fabrication of a multilayer device. The reader will see later that apart of these requisites, the field of spin crossover materials is essentially based on the compromises and until today a universal compound interconnecting all the desired characteristics has not being discovered.

7.2 Fe-pyrz: a new sublimable molecule

To begin with, we report on a new sublimable spin transition compound, namely Fe$\{[3,5\text{-dimethylopyrazolyl}]_3BH_2\}_2$, and study its properties from a perspective of vertical device fabrication. The section is organized in the following way. First, we introduce the general properties of the compound and provide a proof of a sublimation preserved SCO. Then, we compare the spin transition characteristic of a powder and a thick film. We employ the x-ray radiation to study the LIESST effect of Fe-pyrz films and finally, we focus on the morphology and growth mode of Fe-pyrz sublimed onto crystalline and amorphous surfaces.

7.2.1 Structure and general properties

Fe$\{[3,5\text{-dimethylopyrazolyl}]_3BH_2\}_2$, which we will refer to as Fe-pyrz, is a chelate encapsulating Fe(II) ion in an octahedral cage by six pyrazolyl groups (Fig. 7.3 (a)). The first

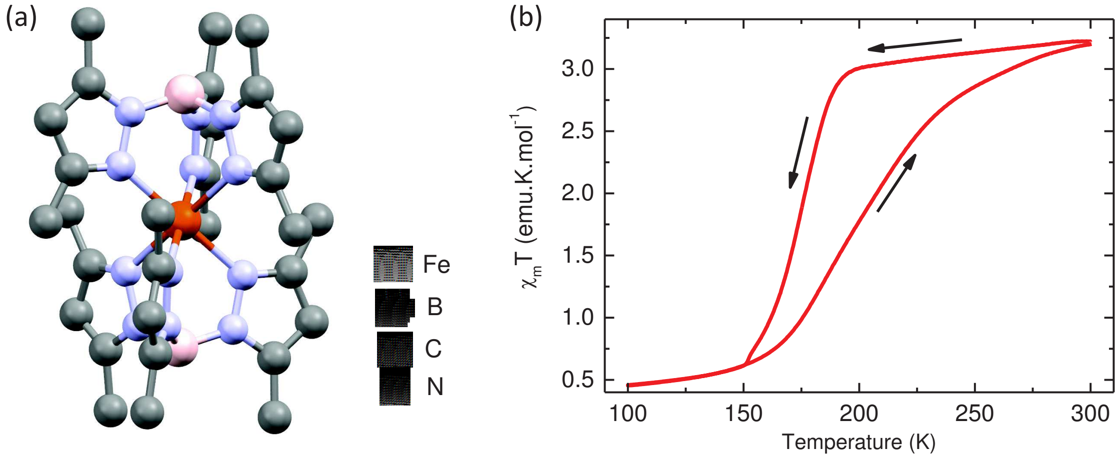

Figure 7.3: Fe{[3,5-dimethylopyrazolyl]$_3$BH$_2$}$_2$ (Fe-pyrz). (a) Molecular model of Fe-pyrz. The hydrogen atoms are omitted for clearance. (b) Magnetic susceptibility of the Fe-pyrz powder as a function of temperature measured by SQUID at $H = 0.5\,\mathrm{T}$.

poly(1-pyrazolyl)borates where synthesized in 1966 by Trofimenko *et al.*[388] These occurred to exhibit a strong chelating abilities of the divalent transition metals what led to intensification of the studies especially over its form with Fe(II) and dimethyl and trimethyl derivatives.[389] Particularly Fe-pyrz is known since 1967 when its synthesis was reported by Jesson *et al.*[131] along with a direct observation of ${}^5\mathrm{T}_2 \rightarrow {}^1\mathrm{A}_1$ transition by Mössbauer spectroscopy. Despite few publications on this compound[389, 390] it did not draw as much attention as Fe-phen and therefore its sublimability was presumably overlooked by the community.

Fe-pyrz manifests a spin transition hysteresis with $T^{\uparrow}_{1/2} = 199\,\mathrm{K}$ and $T^{\downarrow}_{1/2} = 174\,\mathrm{K}$ and more cooperative HS state ($\Gamma_{\mathrm{HS}} > \Gamma_{\mathrm{LS}}$) (Fig. 7.3 (b)). The asymmetry of the transition curve is attributed to a crystal phase transition. This is supported by the observation of a violent structural instability when the complex in a monocrystalline form is cooled down below 200 K. At room temperature Fe-pyrz has a triclinic form with $P-1$ space group. Interestingly, Fe-pyrz exhibits the biggest variation of the Fe-N bond lengths during the HS ↔ LS transition among all the Fe(II)-based complexes.[391] As a consequence, its spin transition is very vulnerable to external pressure change. Application of as little as 2 kbar at room temperature initiates the HS → LS conversion and at 4 kbar one finds already 50% of the low spin proportion. Similarly to Fe-phen, the low spin state of Fe-pyrz is diamagnetic meanwhile the HS is paramagnetic with a magnetic moment of $5.16 \pm 0.04\ \mu_{\mathrm{B}}$ per molecule (value for 297 K).[131]

The material for our studies was provided by Ana Gaspar from the group of José Antonio Real of the Institut de Ciencia Molecular Departament de Quimica Inorganica (Universitat de Valencia) who improved the synthesis reported by Jesson *et al.*[392] The K[HB(3,5-(CH$_3$)pz$_3$] salt dissolved in 15 mL of methanol was added in amount of 2 mmol to a methanolic solution of 1 mmol Fe(BF$_4$)$_2$·6H$_2$O. The process was performed in Ar atmosphere. After the complete addition of the salt the precipitation which appears is washed with the methanol and dried under vacuum. The synthesis yield was $\sim 60\%$.

7.2.2 SCO preserving sublimability of Fe-pyrz

The detailed study over the sublimability of Fe-pyrz was carried out by the predeceasing PhD student Vincent Davesne.[31] In this section we comment on this results. The films were prepared in high vacuum environment ($\sim 10^{-8}$ mbar) by thermal sublimation on Si/SiO$_x$ surface. Then, the magnetic moment as a function of temperature was measured by SQUID for two thick films (570 nm and 1200 nm) and compared to the powder reference. The result is presented in Fig. 7.4. It confirms that both thick films manifests the spin transition with a transition temperature $T_{1/2}$ shifted towards the lower temperatures. Such behavior was reported for some films of Fe(II)-based materials[32,393] and explained by a modification of the grains' surface tension, which can in turn affect both $T_{1/2}$ and the hysteresis shape.[394] We also observed a decrease in cooperativity resulting from the structural aspects, reflected by more gradual transition. This satisfies the requirement I of desired SCO preserving thermal sublimability. It is worth mentioning that this is the first report on a sublimable SCO complex that presents a spin transition with a hysteretic behavior.

One has to keep in mind that the SQUID measurements could be affected by such factors as the oxidation of the topmost layers of the films (witnessed by means of XPS) or diamagnetic background subtraction which is done by measuring the reference on the SiO$_x$ substrates after the molecules removal (cleaning with acetone and ethanol). These problems may hinder the measurements of very thin films by SQUID.

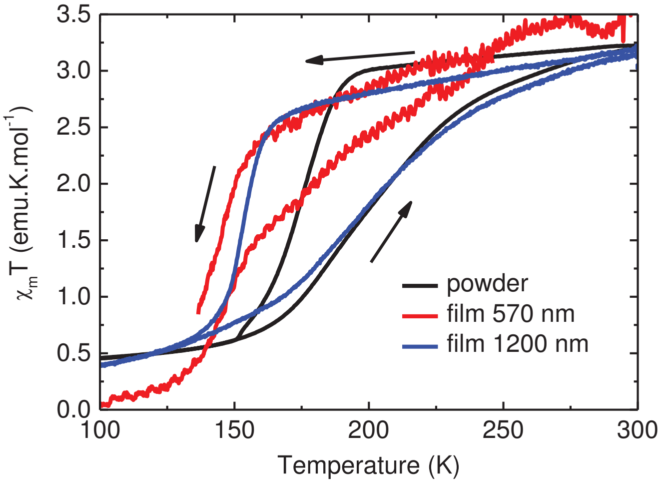

Figure 7.4: SCO of the Fe-pyrz powder and sublimed film. Magnetic susceptibility as a function of temperature for the Fe-pyrz powder and two thick films sublimed onto SiO$_x$. Note the preserved SCO and the shift in transition temperature for the thick film samples. The measurement was performed with SQUID at magnetic field $H = 4$ T. The arrows indicate a field sweep direction. Figure taken from ref. 31.

To have an insight into the spin transition of Fe-Pyrz in thinner layers we employed x-ray absorption spectroscopy. The 100 nm thick film of Fe-pyrz was sublimated onto SiO$_x$/Au(30 nm). The introduction of the gold layer played an important role for the subsequent LIESST studies and emerged from our previous experience with the Fe-phen molecules, which tend to decompose when overheated by, *e.g.*, laser radiation. The Au layer, having 3 − 4 times larger thermal conductivity then SiO_x efficiently dissipates the heat created by radiation, and therefore minimize the chance of local overheating. The samples were studied with synchrotron radiation at the TEMPO beamline of the SOLEIL synchrotron. In the following we demonstrate how x-ray absorption can be efficiently used to probe the spin crossover and discuss the obtained results.

Figure 7.5 presents the XAS spectra acquired at the Fe $L_{3,2}$-edges of Fe-pyrz powder and film at room temperature and at 80 K. First, we acknowledge a similar Fe $L_{3,2}$-edges absorption edges for the powder and the films at room temperature suggesting an unaltered molecular structure in the sublimed film sample. Any modification of the molecular bonds or Fe symmetry would result in easily distinguishable features in the edges. Then, we focus on the comparison of the high spin and low spin spectra acquired at $T = 300\,\mathrm{K}$ and 80 K respectively. One easily sees that the Fe L_3-edge of the powder exhibits two distinct subpeaks (marked with dashed lines in Fig. 7.5 as L_{3a} at 709.2 eV and L_{3b} at 710.4 eV) reflecting a different electronic structure of

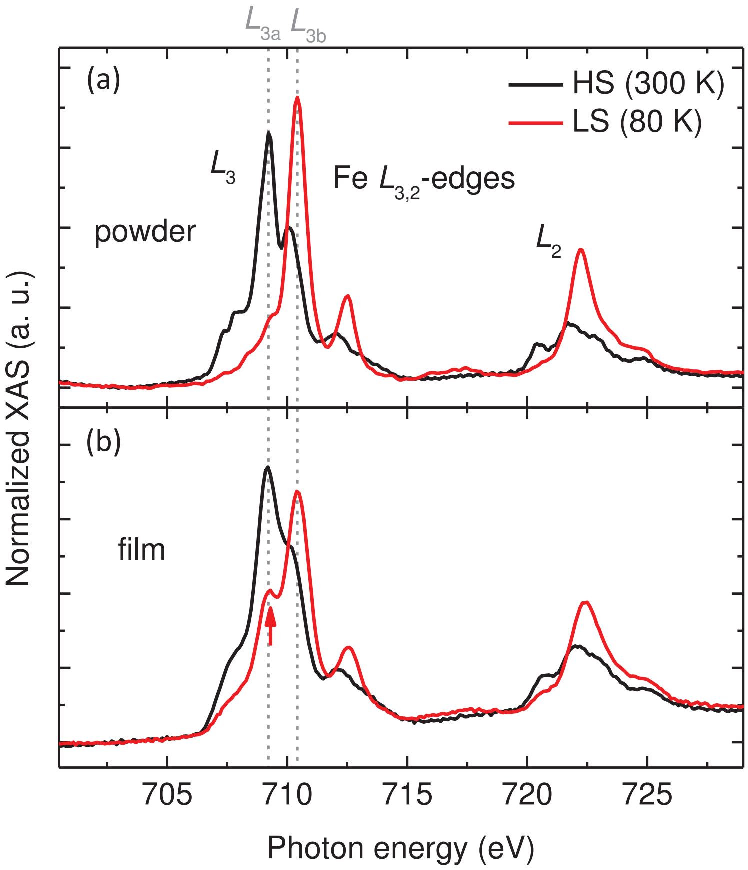

Figure 7.5: XAS at the Fe $L_{3,2}$-edges of the Fe-pyrz powder and sublimed film. The x-ray absorption spectra acquired at the Fe $L_{3,2}$-edges of Fe-pyrz in (a) powder, and (b) 100 nm thick film sublimed onto SiO_x/Au(30 nm). The distinct electronic structures of the Fe ion with dominant L_{3a} (L_{3b}) subpeak of L_3-edge reflect the molecules in the HS (LS) state. The comparison of the powder and film spectra proves a successful and SCO preserving sublimation. Note a residual HS fraction in the film LS spectrum (marked with the red arrow). The XAS for the HS (LS) state was recorded at $T = 300\,\mathrm{K}$ ($T = 80\,\mathrm{K}$) in total electron yield mode. The curves are normalized to its integral.

Fe in the HS and LS state, with a respective spectral intensity proportional to the amount of molecules in a given state. By decreasing the temperature from 300 K (HS) to 80 K (LS) we observe a diminishing L_{3a} and arising L_{3b} peak implying a HS → LS transition. Note that the Fe L_2-edge shape is also modified. Now, by comparing the powder referencial spectra to the one acquired on the thin film (Fig. 7.5 (a) to (b)) we infer that the spin transition within the latter is conserved. We identify a residual high spin fraction in the low spin spectrum (marked with the red arrow in Fig. 7.5 (b)) that may originate from the interfacial quenching of the SCO due to the interaction of the molecules with the substrate (well known case for the SCO in thin films[395,396]). By this brief demonstration, we confirmed a spin transition conservation in Fe-pyrz film and explained how the XAS can be employed to probe the spin state of the SCO compound.

Both the SQUID and XAS measurements by comparing the Fe-pyrz powder reference to sublimed film clearly evidenced the latter to preserve the spin transition, therefore proving a successful sublimation. In this way, we introduce a new sublimable SCO material exhibiting a transition with hysteresis, and thus we enrich this very narrow but desired subgroup of the spin transition compounds. In the next section, we provide the results of the LIESST effect investigations in Fe-pyrz sublimed film.

7.2.3 LIESST effect dynamics in Fe-pyrz film

We devoted a brief study to the investigation of the LIESST effect in the Fe-pyrz sublimed films. To do so, we employed an external light source to trigger the spin transition and simultaneously probed the Fe state by x-ray absorption. The experiment was carried out at the TEMPO beamline of the SOLEIL synchrotron. Note that the goal of the experiment was a validation of Fe-pyrz response to light and not a comprehensive study of the effect.

The samples were fabricated in the IPCMS prior to the beamtime and transported in a mobile desiccator preventing the organic layers from oxidation. The Fe-pyrz films

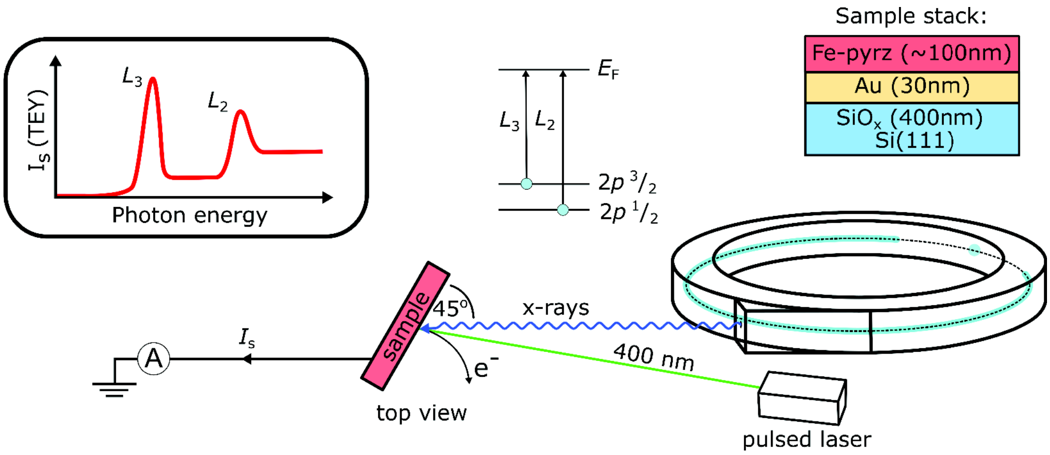

Figure 7.6: Studies of the LIESST effect in the Fe-pyrz film at the TEMPO beamline. Top view of the experimental set-up geometry with a pumping 400 nm pulsed laser (alternatively white LED). The spectra were recorded in total electron yield detection at 45° x-ray incidence.

were sublimed onto the Si/SiO$_x$/Au(30 nm) substrates. The sample stack along with the experimental geometry are depicted in Fig. 7.6. We used the photoemission end-station of the TEMPO beamline and recorded the x-ray absorption spectra in total electron yield mode. The x-rays impinged the sample at 45° relatively to the surface. To provoke the LIESST we use two sources of light: (i) the 400 nm RegA 9040 pulse laser with 300 kHz repetition rate and a pulse width $\sim$ 40 fs, and (ii) a white light emitting diode (LED).

7.2.3.1 HS/LS ratio determination

The further studies require a method for accurately establishing the HS/LS proportion ratio within the probed region based on the recorded XAS spectra. In general notion, any intermediate state between the pure HS or LS is a mixture of the two. This is why, by proper fitting of the referential spectra, recorded in conditions where nearly all the molecules are in pure HS or LS state, to any mixed state spectrum should reproduce the main features. In that way, the fitting coefficient yields the HS/LS ratio. We can thus write this linear combination as:

$$f(E)_x = \rho_{\mathrm{HS}} \cdot f(E)_{\mathrm{HS}} + (1 - \rho_{\mathrm{HS}}) \cdot f(E)_{\mathrm{LS}} \tag{7.1}$$

where $f(E)_x$ is the XAS spectrum of the mixed state, $f(E)_{\mathrm{HS(LS)}}$ stands for the referential spectrum acquired in purely HS (LS) state, and ρ_{HS} is the HS proportion. Note, that this approach requires a prior normalization of the curves to their integral. Equation 7.1 assumes that for constant number of probed molecules, the integral over the Fe $L_{3,2}$-edges is the same in the LS and HS state. One has to keep in mind that this is an approximation since the photoelectric absorption cross section may differ for the two spin states.

Figure 7.7 presents the exemplary result of a fit done with Eq. 7.1. The XAS at the Fe $L_{3,2}$-edges was recorded for the mixed state at $T = 165\,\mathrm{K}$. Then, the two referential spectra for the HS and LS state (see Fig. 7.5 (b)) were fitted. The procedure yielded a high spin proportion $\rho_{\mathrm{HS}} \sim 0.5$, *i.e.*, half of the sample in HS state. Note, that the fitted curve well reproduces the XAS spectrum near the maximum of the L_3 absorption edge meanwhile it starts to diverge at higher energies. This, arising from the accumulated background drift and not perfectly constant experimental conditions, may lead to obstacles during the fitting procedure. To avoid that, one can limit a considered region only to vicinity of the L_3-edge. Further, the method can be simplified to just calculating the particular peaks ratio after the curves renormalization. In this way, the high spin proportion can be evaluated from the expression:

$$\frac{f(L_{3\mathrm{a}})_x}{f(L_{3\mathrm{b}})_x} = \frac{\rho_{\mathrm{HS}} f(L_{3\mathrm{a}})_{\mathrm{HS}} + (1 - \rho_{\mathrm{HS}}) f(L_{3\mathrm{a}})_{\mathrm{LS}}}{\rho_{\mathrm{HS}} f(L_{3\mathrm{b}})_{\mathrm{HS}} + (1 - \rho_{\mathrm{HS}}) f(L_{3\mathrm{b}})_{\mathrm{LS}}} \tag{7.2}$$

where $f(L_{3\mathrm{a}})$ and $f(L_{3\mathrm{b}})$ stays for the spectral intensity of the two subpeaks of the Fe L_3-edge (see Fig. 7.5 dashed vertical lines), where the indices x, HS and LS correspond to a mixed state spectrum, high spin and low spin references respectively. Note, that the method is sensitive to the renormalization procedure. We apply this approach to estimate the high spin proportion for the LIESST effect studies presented from there on.

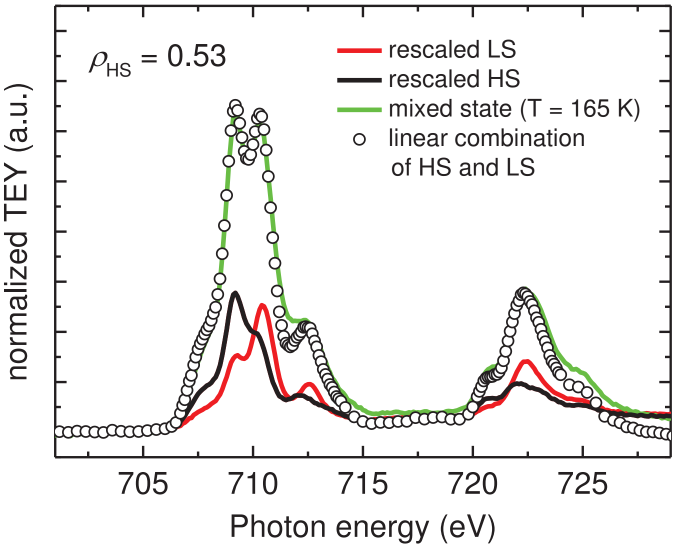

Figure 7.7: HS proportion determination by fitting the referential spectra. XAS at the Fe $L_{3,2}$-edges of Fe-pyrz film acquired for the mixed state at $T = 165\,\mathrm{K}$ fitted with two normalized LS and HS referential spectra recorded at 80 K and RT respectively. The fitting yields the high spin proportion $\rho_{\mathrm{HS}} \sim 0.5$.

7.2.3.2 Irradiating Fe-pyrz film with laser and white LED

The LIESST dynamics of the Fe-pyrz film was investigated for two external light sources: a 400 nm pulsed laser and a white LED. The former employed a second harmonic generated from the 800 nm fundamental wavelength with an average power of 50 mW. The pulsed mode was used to reduce the heating issue so as to to avoid the thermally provoked SCO. In Fig. 7.8 we present the evolution of the HS proportion under irradiation by the laser and the LED. Between the two measurements the sample was reset by increasing the temperature above 100 K. Time $t = 0$ corresponds to the opening of the laser (LED) shutter. The error bars correspond to the time needed to acquire one XAS spectrum. Note, that the HS proportion is calculated using the LS reference containing a residual HS fraction (see Fig. 7.5 (b)), therefore the absolute value of the HS/LS ratio is underestimated. One has to keep in mind that the observed effect is also in part provoked by the soft x-ray induced excited spin state trapping (SOXIESST, see Section 2.3.5).

Now, we analyze the dynamics of LIESST observed in Fig. 7.8. At first glance, one clearly sees that both time constant and the saturation level are substantially different when using either laser or LED. For a quantitative considerations one has to provide a dynamical model including the light induced excitation from the LS to metastable HS* state and the concurrent relaxation in the opposite direction with the corresponding rate constants as:

$$\mathrm{LS} \xrightarrow{k_1} \mathrm{HS}^*, \quad \mathrm{HS}^* \xrightarrow{k_2} \mathrm{LS} \tag{7.3}$$

In Section 2.3.4 we discussed the models for the excitation/relaxation process accompanying the LIESST effect[397–399] and stated that the proper approach should take into account the self-acceleration of the relaxation by inclusion of the cooperativity parameter. The latter is responsible for the non-exponential (sigmoidal) time dependence of

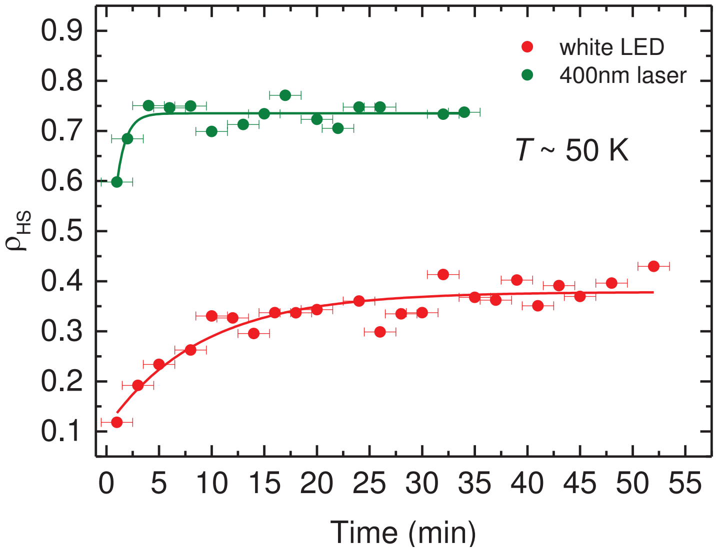

Figure 7.8: The LIESST effect in the Fe-pyrz sublimed film. The evolution of the high spin proportion ρ_{HS} within the 100 nm thick Fe-pyrz film when irradiated by the white LED or 400 nm pulsed laser (140 kHz repetition rate, 50 mW average power). The solid lines represent the fitting according to Eq. 7.4. The fitting parameters are collected in Table 7.2. Note the substantially faster effect with twice higher saturation level with use of the laser. Keep in mind the contributing SOXIESST effect.

the decaying HS proportion.[139] It was also reported to play a notable role in the photoexcitation by involving such intermediate states as incubation or phase separation.[400] To properly model all these contributions one needs to explicitly include them in the interaction Hamiltonian, what in turn is rather difficult due to often obscure nature of the intermolecular elastic interactions and sometimes the coexistence of more than one type of them.[141]

For sake of simplicity, we provide a reduced model including only two processes: light induced conversion from the LS to metastable HS* state, and relaxation from the metastable HS* to LS, both competing with the corresponding rate constants k_1 and k_2 respectively. This leads to a simplified HS proportion evolution expressed as:

$$\rho_{\mathrm{HS}} = \frac{-k_1}{k_1 + k_2} \mathrm{e}^{-(k_1+k_2)t} + \frac{k_1}{k_1 + k_2} \tag{7.4}$$

Now, way we can define the time constant as: $\tau = 1/(k_1 + k_2)$, and the saturation level as: τk_1. We used Eq. 7.4 to fit the experimental data from Fig. 7.8. The fitting parameters k_1, k_2 for the two cases of the laser and LED irradiation with the calculated values of time constant τ and saturation level τk_1 are collected in Table 7.2.

The obtained dynamical parameters imply that while irradiating the film with the laser one obtains an order of magnitude faster ρ_{HS} evolution (lower τ) than in case of a white LED. This results mainly from a larger value of k_1 for the laser, which is predicted to be arising from the photoexcitation rate dependence on the radiation intensity and increased probability of the LS → HS* conversion.[397] Obviously, the intensity of laser in our experiment surpasses drastically the one of the white LED. Moreover, by comparing the absorbance of Fe-pyrz with the emission spectra of the white LED and the used

Table 7.2: Dynamical parameters of the LIESST effect in Fe-pyrz film. The photoexcitation (k_1) and relaxation (k_2) rate constants, time constant $\tau = 1/(k_1 + k_2)$ and saturation level τk_1 resulting from the fitting of Eg. 7.4 to the experimental data from Fig. 7.8.

	k_1 (1/min)	k_2 (1/min)	Time constant τ (min)	Sat. level τk_1
white LED	0.042	0.069	9.0181	0.379
400 nm laser	0.843	0.304	0.872	0.735

monochromatic laser wavelength (Fig. 7.9), one easily sees that the absorption at 400 nm is about 30% greater than at the main emission peak of the white LED (at 450 nm). Therefore, the photoexcitation probability is superior in the case of our laser leading to more efficient build-up of the high spin population. The saturation level, in turn, is supposed to be governed mainly by the radiation intensity,[163] hence it is again unsurprising that the laser irradiation leads to nearly twice higher saturation level than while using the white LED. One has to keep in mind, that the slow LIESST dynamics (timescale of minutes) as well as incomplete transition, may originate from additional factors such as: (i) local heating (despite the taken precautions), (ii) pinned residual LS fraction due to the interaction with the substrate, and (iii) for a white LED the occurrence of a reverse-LIESST triggered by lower energy photons contained in the wide emission spectrum of the diode.

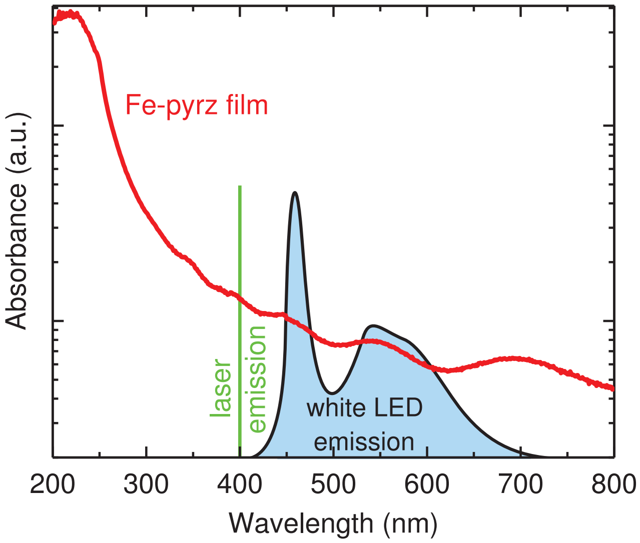

Figure 7.9: Absorbance of the Fe-pyrz film in the ultraviolet-visible region. Comparison of the Fe-pyrz film absorbance with the emission spectra of a white LED and a monochromatic 400 nm laser. Note that the absorption at the laser wavelength (400 nm) is ~ 30% greater than at the main emission peak of the white LED (450 nm). The laser and white LED emission spectra are schematic and their intensities are insignificant.

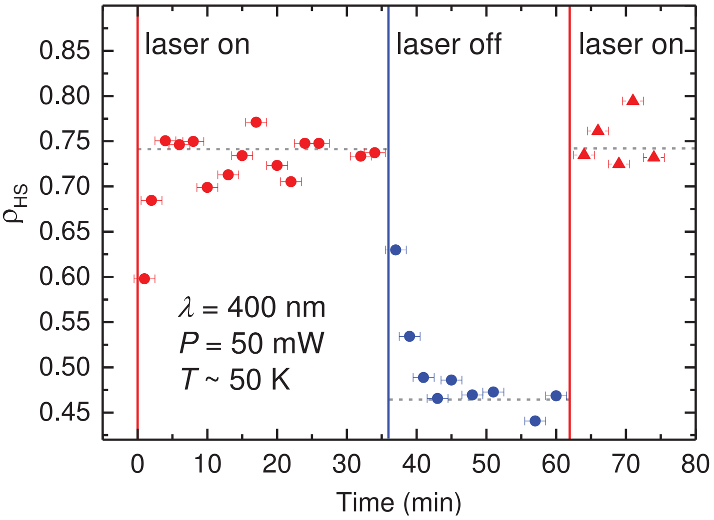

Figure 7.10: Reversible switching of the HS proportion in the Fe-pyrz film provoked by the laser. The high spin proportion ρ_{HS} evolution with time during the consecutive opening and closing of the 400 nm laser shutter. Note the non-zero ρ_{HS} level after relaxation (in absence of laser) resulting from the concurrent SOXIESST effect.

The calculated values of the LIESST dynamics parameters presented in Tab. 7.2 are of the same order of magnitude as those reported for other Fe(II)-based complexes.[163] Yet, a direct comparison with literature is rather difficult as it requires the conserved experimental conditions and well defined intensities of the pumping light and x-rays. These are often not provided and therefore the comparison may lead to deceptive conclusions.

Finally, in Fig. 7.10 we present a demonstration of the reversible ρ_{HS} switching provoked by the laser. We observe a build-up of the HS proportion when the shutter is opened (up to $\rho_{HS} \sim 0.75$), which is followed by the relaxation to $\rho_{HS} \sim 0.45$ when the laser shutter is closed. The system does not relax to the initial $\rho_{HS} \sim 0$ because of the concurrent SOXIESST effect. This brief demonstration illustrates how the LIESST effect in the Fe-pyrz film may be exploited for sensing purposes.

To sum up, we employed the soft x-ray spectroscopy to probe the spin state of the molecules within the Fe-pyrz sublimed film. The results confirmed the previously obtained by the SQUID measurements implying the preserved spin transition. We showed how the high spin proportion can be manipulated with visible light via the LIESST effect and witnessed the occurrence of the soft x-ray induced photoexcitation (SOXIESST). Unsurprisingly, the laser light appeared to be much more efficient in provoking the spin transition than the white LED. Finally, we showed that the observed effects may be exploited for light sensing purposes with the sublimed molecular film.

Till this moment we validated a successful sublimability of Fe-pyrz and witnessed its multifunctionality in a form of sensitivity to temperature and light. In the next step, we investigate the Fe-pyrz growth and its structural properties in thin film form.

7.2.4 Growth morphology and structural aspects

For the growth morphology studies of Fe-pyrz we moved to the ultra-high vacuum environment of the Multi-Probe system (described in Section 3.2). In the first step, we used a Cu(100) monocrystal as the substrate which was cleaned prior to deposition with the Ar^+-ions sputtering and annealing at 500 °C. The Fe-pyrz was sublimated from a Knudsen cell heated up to 115 °C. The sublimation rate was calibrated with a quartz microbalance. We used the Auger electron spectroscopy to *in situ* confirm the presence of the molecule constituting elements on the surface (Fig. 7.11).

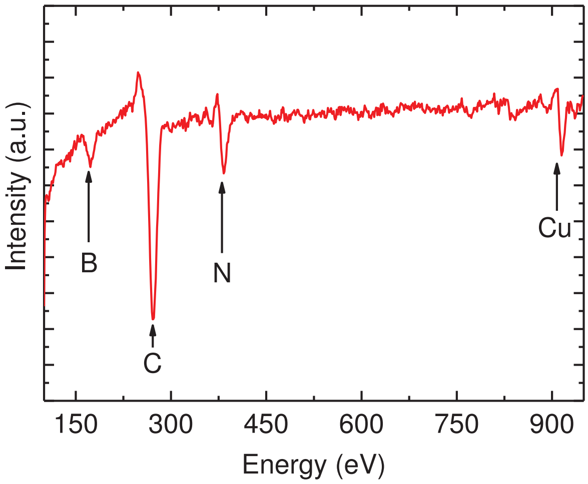

Figure 7.11: AES of Cu(100)//Fe-pyrz(2 nm). Result of Auger electron spectroscopy measurement performed on Cu(100)//Fe-pyrz(2 nm) proving the presence of the molecule constituting elements (boron, carbon and nitrogen) on the surface. Due to only one Fe site per molecule the signal arising from the Fe ions could not be resolved.

The sample was transferred to the Omicron VT SPM chamber and investigated with the STM in constant current mode. All the measurements were performed at room temperature. The exemplary images are presented in Fig. 7.12. The Cu(100) surface (prior to deposition) was confirmed to exhibit the large few hundred nanometers wide terraces with no sign of of significant contamination, and typical for Cu(100) crystal monoatomic steps of $\sim$ 180 pm height (Fig. 7.12 (a)). After the deposition of 1.5 ML of Fe-pyrz we observed two regions of distinct organization on the surface (Fig. 7.12 (b)), with the overall molecular growth uniformly mimicking the monoatomic steps of copper substrate. The closer image presented in Fig. 7.12 (c) suggests that the first monolayer of the molecules tends to organize in a lattice, meanwhile the second one is disordered. The organization of the first monolayer results from the relatively strong molecule-crystal interaction. The second layer is obviously less affected leading to an increased mobility of the molecules. It is reflected by the characteristic sharp lines between the 1st and the 2nd ML visible on the STM image in Fig. 7.12 (c), which indicate the STM-tip-induced molecular diffusion on the surface. In Fig. 7.12 (d) we present a zoom-in on the first layer of the molecules with the white rectangle marking a single Fe-pyrz molecule. The geometrical analysis suggests that the molecules are adsorbed on the substrate such that the longer axis is parallel to the surface plane.

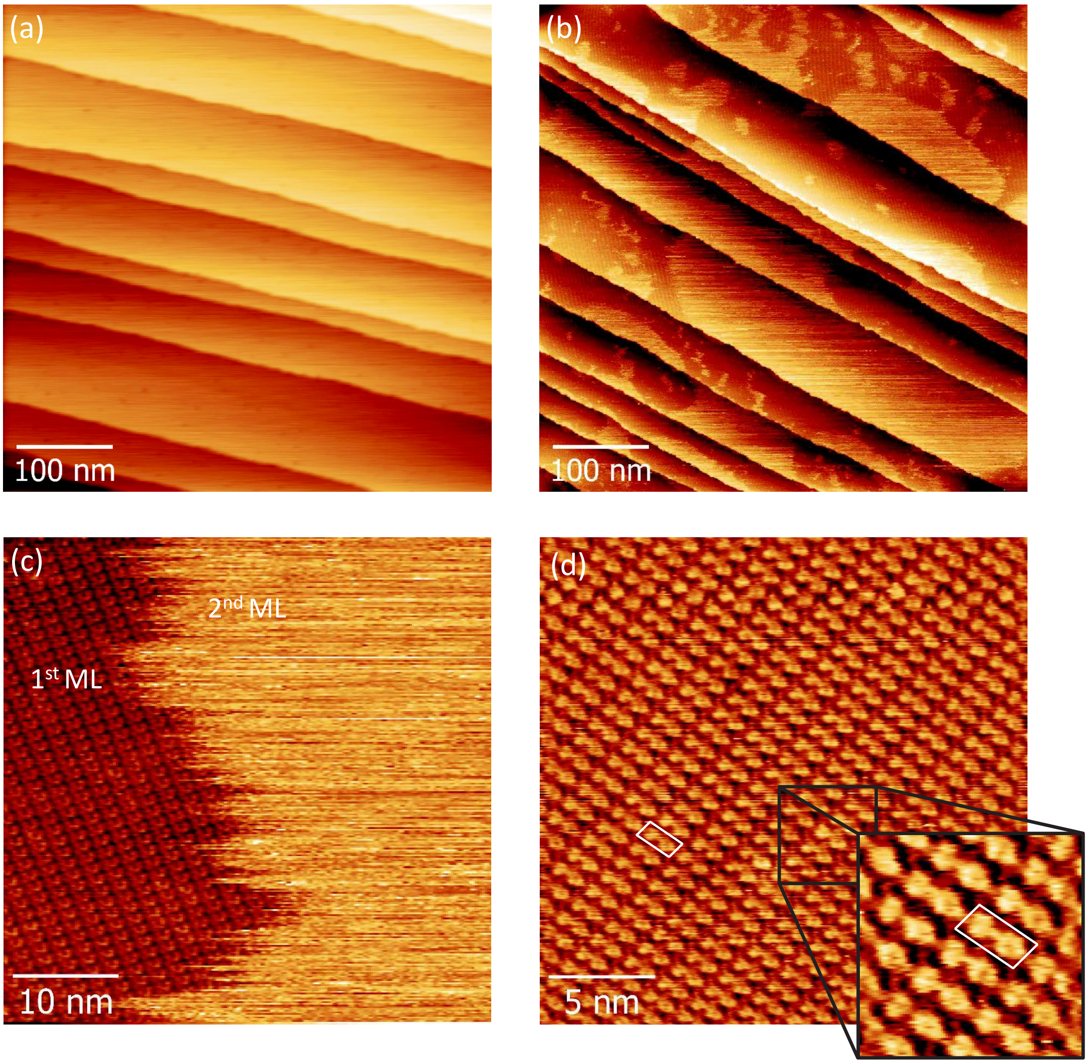

Figure 7.12: Growth morphology of Fe-pyrz on Cu(100) for 1 − 2 ML coverage. Surface topography images acquired in constant current STM mode at RT. (a) Cleaned Cu(100) surface with atomically flat terraces and the monoatomic ($\sim$ 180 pm height) steps of Cu. $I = 200$ pA, $V = 1$ V. (b) Large-scale image of the Cu(100)//Fe-pyrz(1.5 ML) surface. Note two distinct surface organization regions and overall flat coverage such that the molecular layers mimic the steps of Cu. $I = 300$ pA, $V = 0.65$ V. (c) Small-scale image highlighting a first well organized ML of the molecules and a second disordered one. $I = 170$ pA, $V = 1$ V. (d) Zoom-in on the 1st ML emphasizing the closed packed organization with a single Fe-pyrz molecule marked with a white rectangle. $I = 170$ pA, $V = 1$ V.

Consequently, we investigated the growth morphology at higher coverage. Onto Cu(100)//Fe-pyrz(1.5 ML) we deposited two additional ML of the molecules. The large-scale image is presented in Fig. 7.13. It is straightforward to see that at increased thickness the molecules tend to form grains rather than flat layers. This means the change in arrangement for thicker films which intuitively results from the reduced interaction with the substrate and increased contribution of the intermolecular adhesion. One can distinguish a particular stacking orientations with relative 60° and 120° angles. The roughness of the terraces remains relatively low (rms $\sim$ 0.3 nm). We did

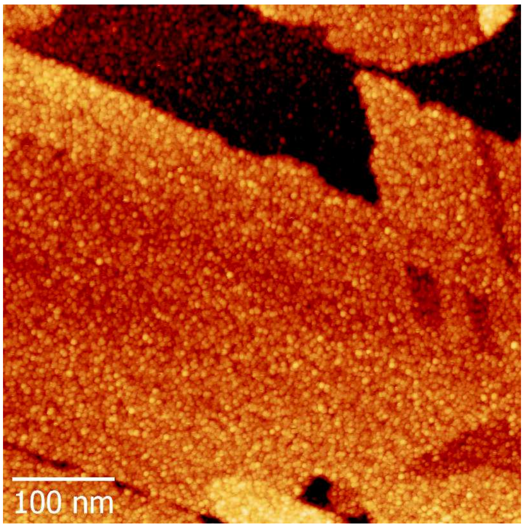

Figure 7.13: Growth morphology of Fe-pyrz on Cu(100) at higher coverage. Surface topography images of Cu(100)//Fe-pyrz(3.5 ML) acquired in constant current STM mode at RT. The reduced interaction of the topmost molecular layers with the substrate leads to the formation of grains. The terraces have surface roughness of rms $\sim 0.3\,\mathrm{nm}$. $I = 100\,\mathrm{pA}$, $V = 1\,\mathrm{V}$.

not observe any particular areas of material accumulation.

To summarize this part, we witnessed rather planar growth of the Fe-pyrz molecules sublimed onto crystalline surface. The observed molecular growth corresponds to the mechanism proposed by Frank-van der Merwe. The interaction of the molecules with the monocrystalline Cu surface surmounts the intermolecular adhesion imposing a layer-by-layer growth. At higher coverage, the topmost layers, experiencing a reduced influence from the substrate, stack into grains. The outcome of the experiment suggest that the material could be suitable for the fabrication of a multilayer device such that it may efficiently separate the two electrodes and effectively participate in electronic transport. However, the monocrystalline substrates are of limited use for applications, therefore we dedicated a brief experiment to morphological studies of Fe-pyrz film on oxide surface.

We prepared the Si/SiO$_\mathrm{x}$(400 nm) (silica) substrates by ultrasonic bath treatment in acetone and ethanol. Then, we used an oxygen plasma to remove the organic residues. In this way we obtained a surface roughness of rms $\sim 0.3\,\mathrm{nm}$. Such prepared substrates were mounted on an Omicron plate and introduced to the UHV environment of the Multi-Probe system. In analogous way as in the previous study we sublimed the molecules from the Knudsen cell onto the prepared surface. Since silica is non-conductive the STM could not be used for this study. Instead, we employed the AFM in taping mode available within the same Omicron VT SPM station. The acquired images of the surface morphology are presented in Fig. 7.14.

It is striking clear, that in contrary to the previously witnessed growth of Fe-pyrz on a Cu(100) surface, the molecules on silica form clusters. Note that in this form the thickness estimation in monolayers is rather meaningless. We found an average $\sim 20\,\mathrm{nm}$ height of the objects covering approximately $\sim 30\%$ of the surface. A closer image, presented in Fig. 7.14 (d), reveals the polycrystalline character of the clusters. In addition, one can identify smaller objects on the surface (Fig. 7.14 (b)), which are supposedly the seeds from which the further nucleation proceeds. To study how this growth evolves we sublimed an additional amount of molecules and witnessed that the average crystallites height increased to $\sim 35\,\mathrm{nm}$ and surface coverage to $\sim 60\%$ (Fig. 7.14 (c)). It is important to notice that even for such large amount of deposited material (equivalent of $\sim 50\,\mathrm{ML}$ in layer-by-layer growth) the molecules do not completely cover the surface. This leads to conclusion that Fe-pyrz on silica surface tends to follow the Volmer-Weber growth. We suggest that it is a consequence of relatively

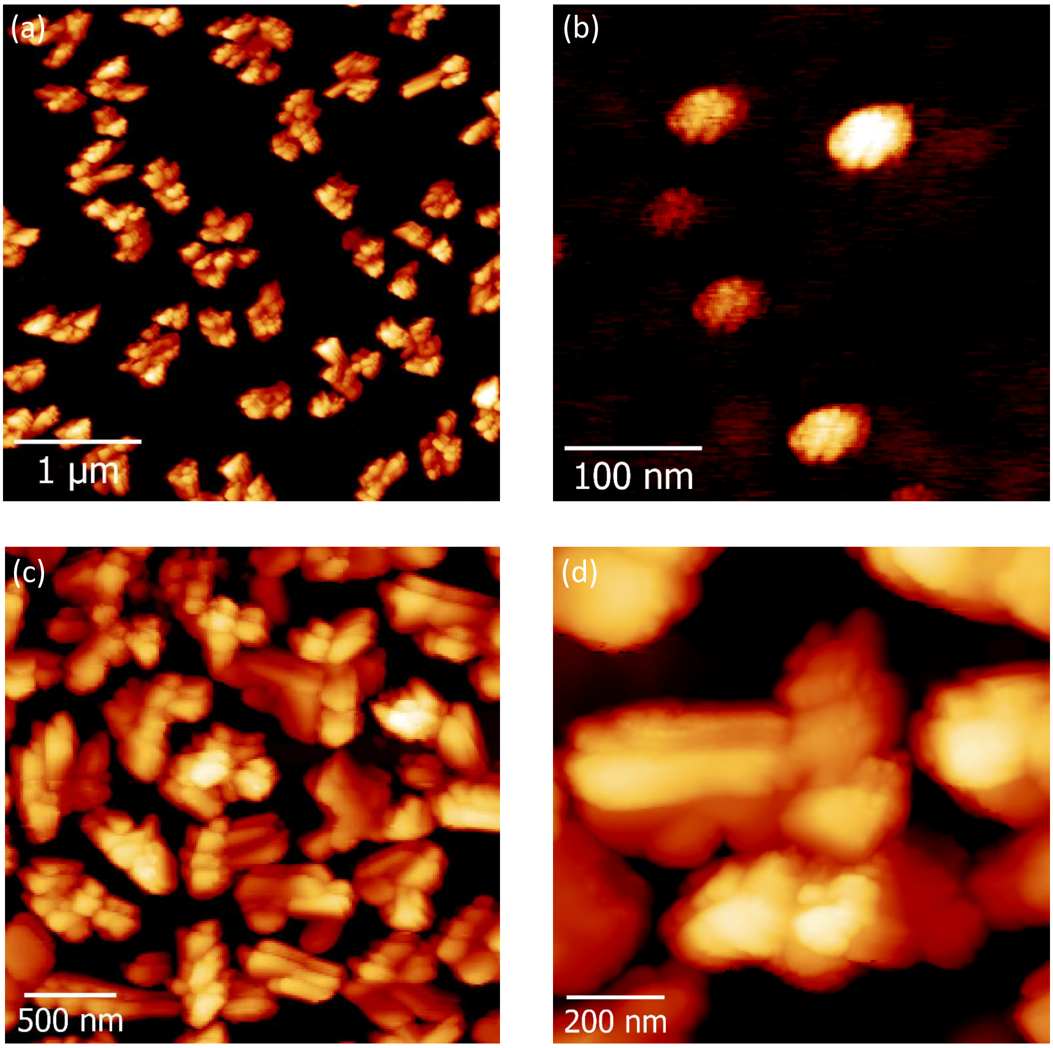

Figure 7.14: Growth morphology of Fe-pyrz on Si/SiO$_x$. Surface topography measurement of Si/SiO$_x$(400 nm)//Fe-pyrz by UHV RT AFM in tapping mode. (a) Large-scale image revealing Fe-pyrz crystallites. The surface coverage was estimated as $\sim 30\%$ with an average crystallites height of $\sim 20\,\mathrm{nm}$. (b) Small-scale image showing the seeds from which the nucleation proceeds. (c) Surface morphology after deposition of additional molecules. The coverage increased to $\sim 60\%$ with an average clusters size of $\sim 35\,\mathrm{nm}$ (equivalent of 50 ML in layer-by-layer growth) (d) Zoom-in on the clusters highlighting their polycrystalline character. The surface morphology evolution follows the Volmer-Weber growth mode.

less interactive SiO_x substrate and we expect this growth mechanism to be prevailing for Fe-pyrz on any oxide surface.

The presented morphology studies showed that Fe-pyrz can fulfil the requirement II (see 7.1.1) of desired homogeneous film formation when deposited on a crystalline surface. The interaction of the molecule with the substrate are is strong enough to overcome the intermolecular adhesion leading to formation of complete layers. This corresponds to Frank-van der Merwe growth. In contrary, replacing a crystalline substrate with an amorphous oxide changes the interacting environment and consequently the growth mechanism. Now, the strongly attracted to each other molecules form nanocrystallites with volumetric growth, reflecting in this way a typically Volmer-Weber mode. This behavior, which we believe would be the case also on other oxide substrates, may strongly impede the application of Fe-pyrz as an active layer in vertical device, which from technological reasons, rather exclude the use of the monocrystalline substrates. Despite the witnessed unfavorable growth of Fe-pyrz, a considerable effort was devoted to fabricate a simple Au/Fe-pyrz/Au vertical device, what resulted in notable difficulties.[31] It occurred to be exceptionally challenging to find an Fe-pyrz thickness ensuring a finite resistance of the layer devoid of the pinholes causing the short-circuiting of the device.

To conclude this part, we revealed a new SCO complex which can be thermally sublimed with preservation of the spin transition characteristics. To best of our knowledge, this is the only sublimable SCO material which exhibits transition with hysteretic behavior. We demonstrated that the Fe-pyrz molecular films manifest multifunctionality by being sensitive to temperature and light. We showed that the molecules can form smooth films when deposited on a crystalline metallic surface and rather strongly inhomogeneous clusters on amorphous oxide substrate. Note that this impedes the application of the material in device fabrication, but could employed for studies on the isolated SCO nanocrystals. One can imagine such objects to act as a memory cells where each can be separately addressed to write a spin state. In perspective, this could be investigated by the STM tip-induced SCO accompanied by morphological observation of the volumetric change of a cluster.

7.3 Functionalization of SCO materials

In this section we want to introduce a distinct approach in the field of spin transition materials, *i.e.*, the chemical functionalization of already known sublimable SCO compounds. This concept, being rather avoided due to the easiness of loosing the spin transition abilities by modifying the molecular structure, is based on one of the most prominent merits of organic spintronics, namely the perspective of chemical engineering. We demonstrate this approach on two parent complexes: $Fe(bpz)_2(phen)$ (bpz = dihydrobis(pyrazolyl)borate, phen = 1,10-phenanthroline) and $Fe(bpz)_2(bpy)$ (bpy = 2,2'-bipyridine), and report on the new functionalized derivatives which may shine a new light on the field. The work presented in the following section was done in a strong collaboration with the chemistry laboratory of Mario Ruben in Département des Matériaux Organiques (DMO) at the IPCMS. The synthesis of the materials was carried out by Senthil Kuppusamy.

7.3.1 Fe(bpz)$_2$(phen): general properties

To begin with, we introduce general information about Fe(bpz)$_2$(phen) which serves as a parent complex in the first part of this section. We invoke the studies highlighting the challenges arising when one intends to modify the chemical structure of the SCO compound. Then, we introduce the new functional Fe(bpz)$_2$(phen) derivatives.

In 2011, Naggert and coworkers[401] reported Fe(bpz)$_2$(phen) (Fig. 7.15 (a)) to be sublimable. Before that, only Fe-phen was known to undergo a thermal sublimation. The new material, whose spin transition properties have been thoroughly studied by the group of J. A. Real,[402,403] exhibits a robust transition at $T_{1/2} \sim 164\,\mathrm{K}$ with a narrow hysteresis loop (Fig. 7.15 (b)). The discovery of its sublimability attracted notable attention and led to such significant studies as the first demonstration of the LIESST effect in a UHV deposited thin film.[401] Ludwig *et al.*[404] employed the UV-photoemission spectroscopy to study the electronic structure and relaxation from the photoinduced spin transition in Fe(bpz)$_2$(phen).

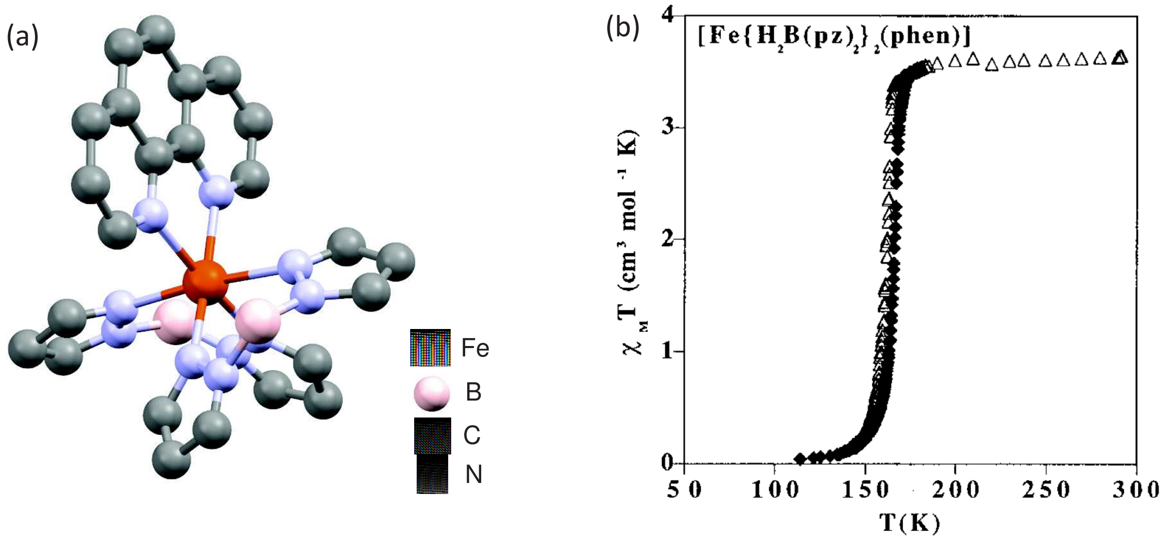

Figure 7.15: Fe(bpz)$_2$(phen). (a) Molecular model of Fe(bpz)$_2$(phen). The hydrogen atoms are omitted for clearance. (b) Thermal spin transition of the Fe(bpz)$_2$(phen) powder measured with pendulum-type susceptometer. Figure taken from ref. 402.

Gopakumar *et al.*[405] carried out the STM studies over the Fe(bpz)$_2$(phen) deposited onto the crystalline gold surface. They reveled a dissociation of the compound into a four-coordinate system upon adsorption, and restored spin transition of the intact second monolayer. The work also provided an evidence of the electron-induced spin state switching (ELIESST). The studies of Pronschinske *et al.*[406] pointed out the important role of the surface packing on the temperature independent coexistence of both spin states on Au(111) monocrystal. Recently, Fe(bpz)$_2$(phen) was a subject of an interesting XAS investigations of a single monolayer sublimed onto highly oriented pyrolytic graphite (HOPG) revealing a non-quenched spin transition and the LIESST effect allowed by a weakly interacting substrate.[407] This observation shed a new light on the spin crossover of ultrathin films on the surface.

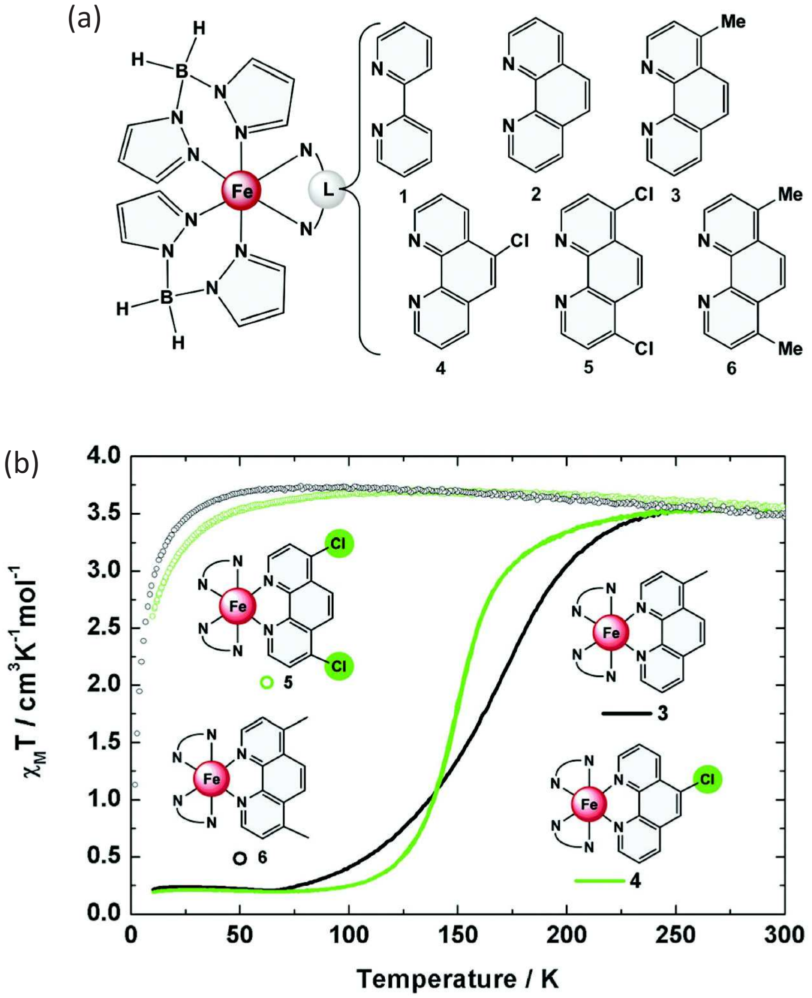

Figure 7.16: SCO of Fe(bpz)$_2$(phen) derivatives in crystalline form. (a) Structure of Fe(bpz)$_2$(L), with L = (1) 2,2'-bipyridine, (2) 1,10-phenanthroline, (3) 4-methyl-1,10-phenanthroline, (4) 5-chloro-1,10-phenanthroline, (5) 4,7-dichloro-1,10-phenanthroline, and (6) 4,7-dimethyl-1,10-phenanthroline. (b) Magnetic susceptibility measurement as a function of temperature for derivatives (3) – (6) in crystalline form. Note that the spin transition in compounds (5) and (6) is suppressed and its magnetic susceptibility drop at ~ 25 K results from zero-field splitting. Figure taken from ref. 127.

In 2015, Naggert *et al.*[127] carried out a notable study over the spin transition within Fe(bpz)$_2$(phen) (1) and its derivatives of structure Fe(bpz)$_2$(L) with L = (2) 1,10-phenanthroline, (3) 4-methyl-1,10-phenanthroline, (4) 5-chloro-1,10-phenanthroline, (5) 4,7-dichloro-1,10-phenanthroline, and (6) 4,7-dimethyl-1,10-phenanthroline. The motivation was to find ligands which would reduce the molecule interaction with a substrate and thus preserve the spin transition on the metallic surface. Figure 7.16 (b) shows the impact of this functionalization on the spin transition for the derivatives in crystalline form. The compounds (3) and (4) preserved the parent complex SCO, meanwhile (5) and (6) occurred to remain in HS state down to a very low temperature, *i.e.*, their spin crossover became largely suppressed. The abrupt susceptibility decrease at ~ 25 K results from zero-field splitting of the HS Fe(II) ion and should not be mis-

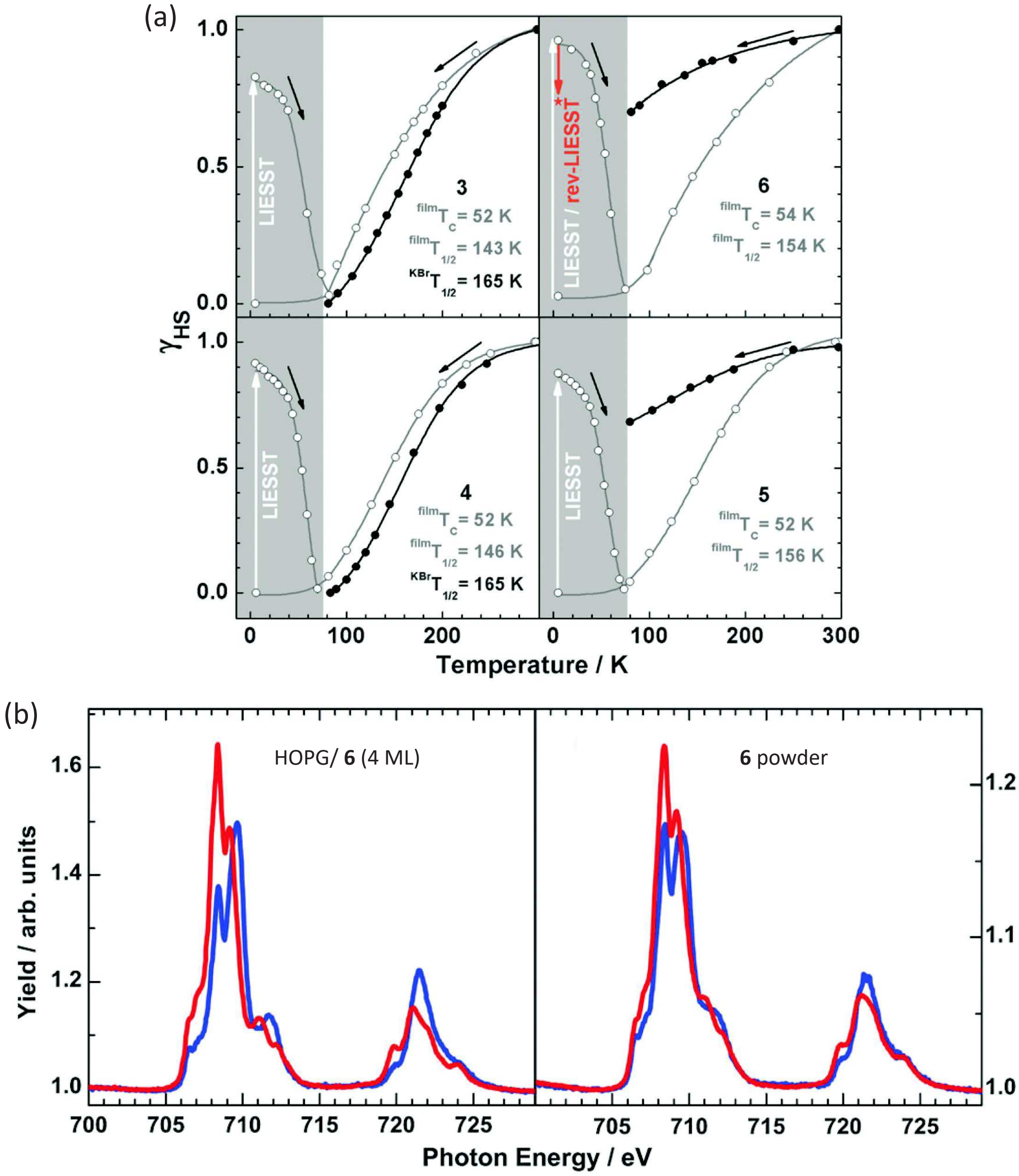

Figure 7.17: SCO of Fe(bpz)$_2$(phen) derivatives in UHV sublimed films. (a) High spin proportion (γ_{HS}) as a function of temperature as determined by UV/Vis spectroscopy for sublimed films of derivatives (3) – (6) (see Fig. 7.16 (a)). Black open circles represent the sublimed film and black full circles the powder reference dispersed in KBr. T_{c} denotes the critical LIESST temperature. (b) The XAS spectra at the Fe $L_{3,2}$-edges of 4 ML of complex (6) sublimed on HOPG (left), and bulk powder of the same complex on indium foil (right). Blue (red) curve corresponds to measurement in $T = 80\,\mathrm{K}$ ($T = 300\,\mathrm{K}$). Figures taken from ref. 127.

interpreted as the spin transition.[408] The electron-donating methane in (3) caused an increase of the transition temperature to $\sim 165\,\mathrm{K}$, and in contrast the electron withdrawing character of the chlorine group in (4) resulted in a slight decrease of $T_{1/2}$ to $\sim 151\,\mathrm{K}$.

Then, the authors verified the SCO performance for derivatives (3) – (6) in a form of UHV sublimed film (Fig. 7.17 (a)). Surprisingly, all four compounds exhibited a complete spin transition similar to that of the parent complex $Fe(bpz)_2$(phen). The restored SCO of derivatives (5) and (6), which was previously "blocked" in crystals, was attributed to reduced interaction between the ligands of adjacent molecules in the film (reduced formation of π-π dimers). Note that all four complexes occurred to be also LIESST-active.

The interesting outcomes were provided by the XAS measurement on 4 ML of derivative (6) deposited on HOPG and compared to bulk powder on indium foil (Fig. 7.17 (b)). One easily sees that in both cases the transition is incomplete. For the thin film on HOPG the authors recognized a decrease from $\sim$ 100% of HS at 300 K to merely $\sim$ 60% at 80 K. The reason of quenching was attributed to interaction with the substrate. Note, that it is in contradiction to before invoked study of $Fe(bpz)_2$(phen) on HOPG by Bernien *et al.*[407] who observed the non-quenched transition. Surprisingly, the powder reference occurred to exhibit even a stronger HS blocking (Fig. 7.17 (b), right) with $\sim$ 94% of HS state at 300 K and $\sim$ 75% at 80 K. This suggest that almost twice larger conversion of the high spin molecules is observed for the compound on HOPG than for the powder. The significant quenching of the bulk powder was explained by stronger intermolecular interactions in comparison to thin film, what is consistent with the data obtained on the compound in crystalline form (Fig. 7.16 (b) 6).

The invoked study can serve as an example underscoring the critical aspects of SCO functionalization. (i) The spin transition is very vulnerable to any structural changes within the molecular architecture (Fig. 7.16 (b)). The substitution of even a small group far from the central metal ion can shatter irreversibly the transition abilities. (ii) The functionalization can differently influence the spin transition in bulk powder, crystal, and thin film forms (compare Fig. 7.16 (b) and to 7.17 (a)). (iii) Functionalization of the SCO materials is a promising direction towards tailoring of intermolecular and molecule-substrate interactions, which are recognized as determining the SCO performance in various environments (Fig. 7.17 (b)).

We devoted an effort to further investigate the functionalization potential of the generic $Fe(bpz)_2$(L) family. We want to stress that in our approach we look for such materials which can be easily synthesized (max. 4 steps) with use of the easily accessible and relatively cheap precursors. In that way, we intend to develop the material which maximizes the degree of versatility and minimizes complexity and costs of production.

In the first step, we propose a functionalizing terminal NH_2 as a part of the phenanthroline group in $Fe(bpz)_2$(phen). In the next section we demonstrate the properties of this newly synthesized derivative.

7.3.2 $Fe(bpz)_2NH_2$-phen

The study of Naggert *et al.* presented in the previous section demonstrated how SCO performance may be affected by the addition of outermost groups to the molecular structure. Naggert *et al.* considered rather simple groups like chlorine or methane. We want to propose a broader approach of using a group which can serve as a terminal for the further functionalization and development of the chemical structure. This opens

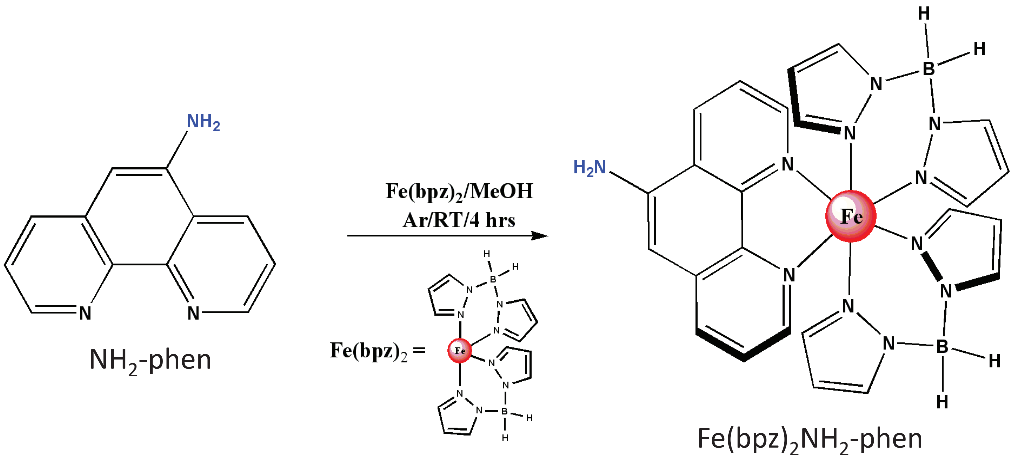

Figure 7.18: Synthesis of Fe(bpz)$_2$NH$_2$-phen. To obtain a terminating NH$_2$ group the commercially available 5-amino-1,10-phenanthroline (NH$_2$-phen) precursor was utilized.

the whole variety of possibilities such as the addition of the anchoring groups imposing self-organization on the surface or affinity to desired compounds.

To begin with, we introduce the NH$_2$ terminated Fe(bpz)$_2$(phen) along with its synthesis schematically depicted in Figure 7.18. The commercially available 5-amino-1,10-phenanthroline (NH$_2$-phen) precursor was utilized to synthesize a Fe(bpz)$_2$NH$_2$-phen. To a solution of Fe(II) perchlorate hydrate in 20 ml of dry methanol, potassium dihydro(bispyrazolyl)borate was added and the mixture was stirred for 15 min followed by a filtration to remove the precipitated KClO$_4$. The solution of NH$_2$-phen dissolved in 20 ml of dry methanol was added drop-wise to the pale yellow filtrate leading to the formation of pale pink precipitate which was then stirred for 4 h under the Ar protection. The precipitate was filtered, washed with methanol and dried in a vacuum oven for 6 h at 50 °C to yield the title complex as pale pink powder.

The molecular model of the synthesized Fe(bpz)$_2$NH$_2$-phen complex is presented in Fig. 7.19 (a). Note the position of the NH$_2$ group by comparing Fig. 7.19 (a) with the model of the parent complex in Fig. 7.15 (a).

7.3.2.1 Spin transition in bulk powder

To begin with, we investigate the spin transition of Fe(bpz)$_2$NH$_2$-phen in bulk powder. The result of magnetic moment measurement as a function of temperature recorded by SQUID is presented in Fig. 7.19. We confirm that the new complex exhibits a complete spin transition with $T_{1/2} \sim 154$ K, which is similar to that of the parent compound. It means that NH$_2$ group does not significantly modify the ligand field strength and therefore the Fe ion remains in the bistability region.

The material was crystallized and investigated with a variable temperature x-ray diffraction (XRD). Fe(bpz)$_2$NH$_2$-phen crystalizes in the triclinic P-1 space group with 4 molecules per unit cell. The Fe-N bonds length for two adjacent Fe(bpz)$_2$NH$_2$-phen molecules are collected in Table 7.3. By comparing the obtained result for $T = 300$ K (100 K) corresponding to purely HS (LS) state with values reported in the literature[402, 409, 410] we confirm that Fe(bpz)$_2$NH$_2$-phen exhibits SCO also in its crystalline form. The transition does not change the space group. This is in contrast with Fe-pyrz

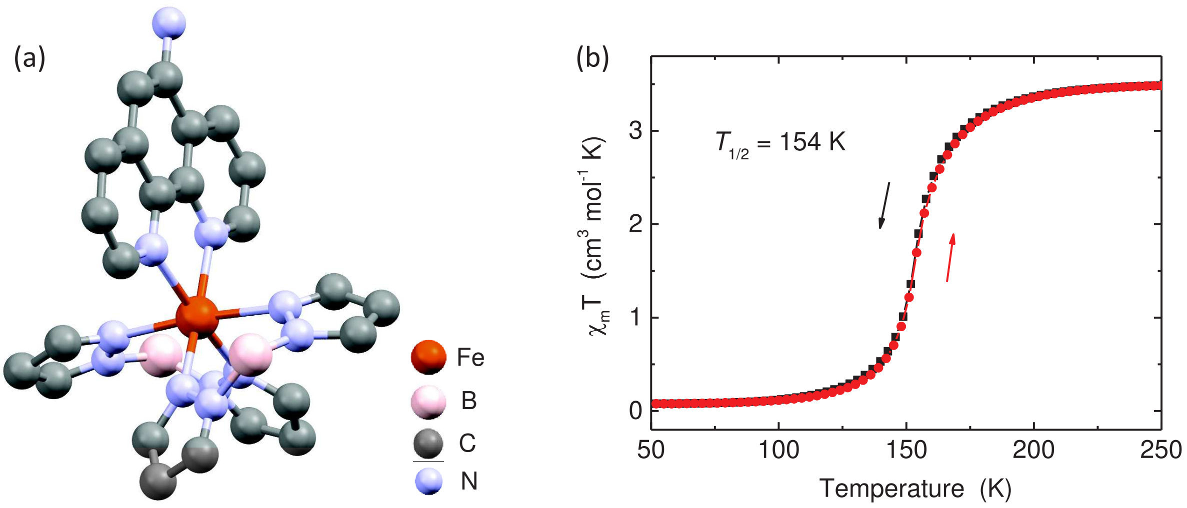

Figure 7.19: Fe(bpz)$_2$NH$_2$-phen. (a) Molecular model of Fe(bpz)$_2$NH$_2$-phen. Note the position of the NH$_2$ group by comparing with the model in Fig. 7.15 (a). (b) Magnetic moment measurement as a function of temperature for the Fe(bpz)$_2$NH$_2$-phen powder measured by SQUID.

which tends to change its crystal phase during the SCO leading to the internal stress and disintegration of the crystal while cooling down below 200 K.

Finally, we investigated the LIESST effect in Fe(bpz)$_2$NH$_2$-phen powder. The result is presented in Fig. 7.20 (a). The compound exhibits a photoexcitation which is typical for Fe(II)-based SCO materials below $\sim$ 41 K. The T_{LIESST} value was determined by calculating the derivative $d(\chi T)/dT$ and finding its minimum in the temperature dependence plot. In addition, the light induced thermal hysteresis (LITH) was observed by irradiating the powder with 637 nm light at $T = 10$ K, waiting until the magnetization saturation was reached, and cycling the temperature (Fig. 7.20 (b)). The resulting

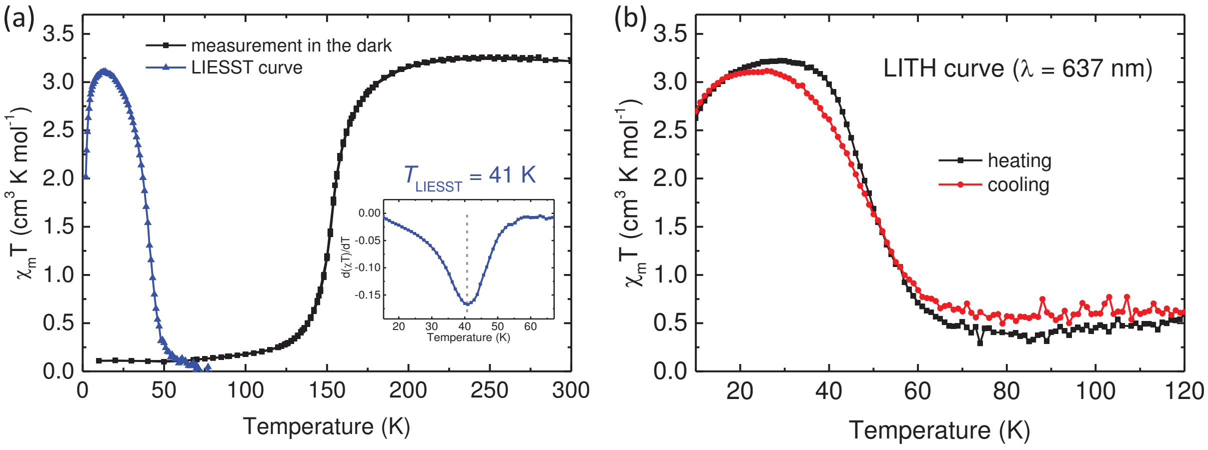

Figure 7.20: LIESST and LITH of Fe(bpz)$_2$NH$_2$-phen powder. (a) Thermal spin transition along with the LIESST curve measured on Fe(bpz)$_2$NH$_2$-phen powder. The derivative d(χT)/dT (inset) was used to determine T_{LIESST}. (b) Light induced thermal hysteresis (LITH) curve obtained by heating up and cooling down the sample with a permanent irradiation by a 637 nm laser.

Table 7.3: Variable temperature x-ray diffraction measurement on $Fe(bpz)_2NH_2$-phen monocrystal. Selected Fe-N bond lengths for two adjacent $Fe(bpz)_2NH_2$-phen molecules with metal ions denoted as Fe1 and Fe2, at $T = 300\,K$ and 100 K.

	Bond length (Å)	
	300 K (HS)	100 K (LS)
Fe1 - N1	2.2	1.99
Fe1 - N2	2.4	2.02
Fe2 - N1	2.27	2.05
Fe2 - N2	2.3	2.18

curve shows a small opening suggesting a rather small cooperativity of the molecules.

Summarizing the part dedicated to bulk studies, we demonstrated that the addition of the NH_2 group to the phenanthroline ring of $Fe(bpz)_2$(phen) conserves the SCO. In the next part we verify the sublimability of the new material and investigate its SCO performance in form of a thick film.

7.3.2.2 Sublimability and spin transition in film

We performed a thermogravimetric analysis of $Fe(bpz)_2NH_2$-phen powder at ambient Ar pressure (Fig. 7.21). At temperature $T \sim 175\,°C$ we observe a drop in the powder weight with a heat release. That implies that $Fe(bpz)_2NH_2$-phen undergoes a thermal sublimation at ambient pressure. In the next step, the molecular powder was put in a molybdenum crucible which was resistively heated by passing high current under high vacuum conditions. We sublimed a 230 nm thick molecular film on a quartz substrate and investigate its absorbance with UV-Vis spectroscopy. The result is pre-

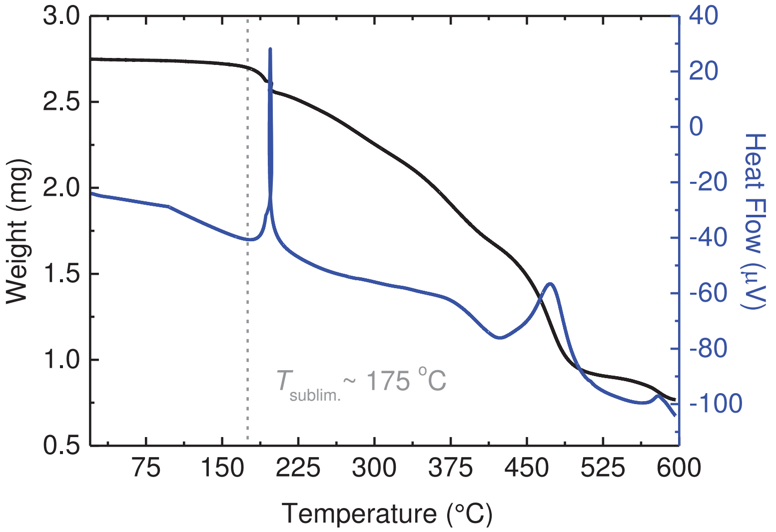

Figure 7.21: Thermogravimetric analysis of $Fe(bpz)_2NH_2$-phen powder at ambient Ar pressure. The powder weight loss and heat release at $T \sim 175\,°C$ proves that $Fe(bpz)_2NH_2$-phen undergoes thermal sublimation.

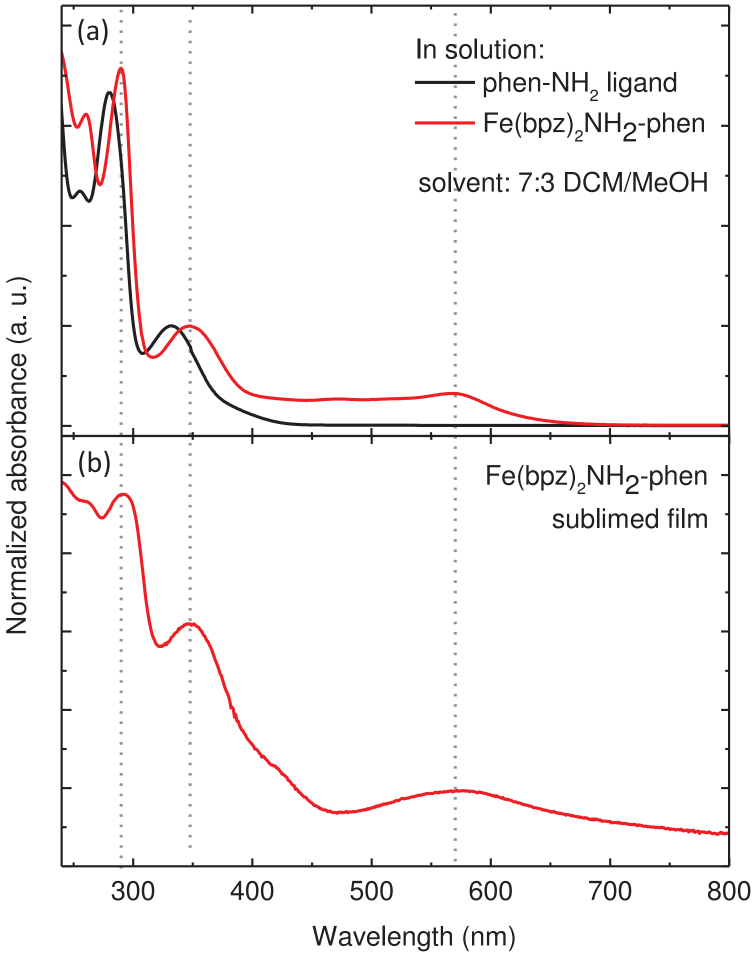

Figure 7.22: Absorbance of Fe(bpz)$_2$NH$_2$-phen in the ultraviolet-visible region. (a) Reference absorbance spectra of the phen-NH$_2$ ligand and Fe(bpz)$_2$NH$_2$-phen complex in DCM/MeOH solutions. Peaks at $\sim$ 290 nm and 350 nm correspond to the $^1(\pi \rightarrow \pi)$ absorption band of the ligand meanwhile the broad feature at $\sim$ 470 nm – 700 nm results from the transitions within distorted Fe(II) octahedral environment. (b) Absorbance of a quartz//Fe(bpz)$_2$NH$_2$-phen(200 nm) film sublimed in high vacuum. Dashed lines emphasize the preservation of the main referential features within the sublimed film spectrum. The absorbance spectra were corrected for the effect of the solvent and the quartz substrate.

sented in Figure 7.22. We acquired the reference spectra on the solutions of complete Fe(bpz)$_2$NH$_2$-phen complex and its phen-NH$_2$ ligand (Fig. 7.22 (a)). Both exhibit the absorption peaks at $\sim$ 290 nm and $\sim$ 350 nm which we attribute to the $^1(\pi \rightarrow \pi)$ absorption bands of ligand. In addition, the full complex manifests a broad feature at $\sim$ 470 nm – 700 nm resulting from the absorption of the Fe(II) ion in a disordered octahedral system. We assign it to a convolution of the $^1\mathrm{A} \rightarrow {}^1\mathrm{T}$ transitions and metal to ligand charge transfer band ^{1}MLCT. The overall shift between the spectrum of the ligand and the complete complex is a typical bathochromic shift observed also for others Fe(II)-based SCO systems.[145]

Now, we compare the absorbance of an Fe(bpz)$_2$NH$_2$-phen sublimed film to discussed references in solution (Fig.7.22(a)-(b)). The conservation of the absorption peaks at ∼ 290 nm and 350 nm as well as the convoluted 470 nm – 700 nm feature suggests that both ligands and octahedral Fe ion structure are well preserved within the sublimed film. Therefore, we claim that the molecules are intact on the quartz surface after sublimation. This confirms the sublimability of Fe(bpz)$_2$NH$_2$-phen.

In order to study the spin transition within the sublimed film we employed x-ray absorption at the DEIMOS beamline. We recorded the absorption spectra at the Fe $L_{3,2}$-edges of the reference power and sublimed film at RT to probe the purely HS state, and at T = 65 K (80 K) for the purely LS state of powder (thick film). The temperature for the LS state was chosen so as to avoid the SOXIESST influence. The results are presented in Figure 7.23. We found the HS spectra of thick film and powder to be identical. This, consistently with UV-Vis spectroscopy, suggests the preserved electronic structure of Fe ions, and thus the successful sublimation. At low temperature the powder spectrum exhibits a typical for Fe(II) SCO dominant L_{3b} peak at ∼ 711 eV and nearly no L_{3a} feature. This proves a complete spin transition of the powder, confirming therefore the SQUID results (Fig. 7.19 (b)). Yet, the SCO of thick film seems to be partially quenched such that at low temperature a notable fraction

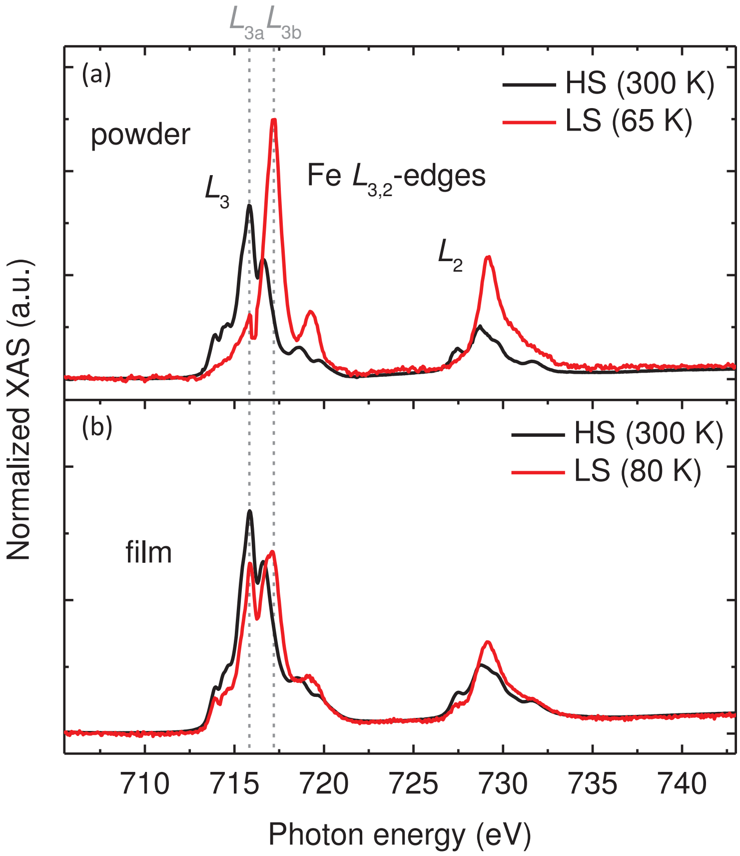

Figure 7.23: XAS at the Fe $L_{3,2}$-edges of Fe(bpz)$_2$NH$_2$-phen. XAS spectra acquired for (a) powder, and (b) sublimed film at RT for the molecules in the pure HS state and at 65 K and 80 K in the LS state for the powder and the thick film respectively. The dashed lines mark the position of two dominant L_{3a} and L_{3b} peaks characteristic for the HS and LS states. Note that the HS spectra of both powder and sublimed film are nearly identical. Comparison of the LS spectra reveals an incomplete transition of the thick film sample ($\rho_{\mathrm{HS}}(T = 80\,\mathrm{K}) \sim 75\%$).

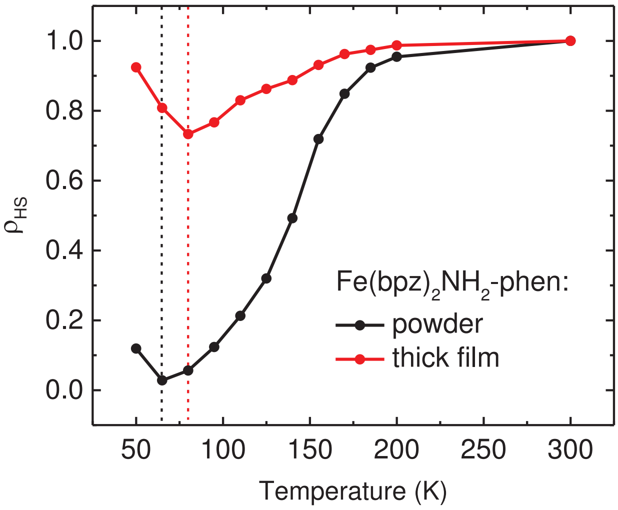

Figure 7.24: SCO in Fe(bpz)$_2$NH$_2$-phen powder and sublimed film as determined by variable temperature XAS. High spin proportion evolution with temperature as determined from the XAS spectra recorded at the Fe $L_{3,2}$-edges revealing a complete (incomplete) spin transition of the Fe(bpz)$_2$NH$_2$-phen powder (sublimed thick film). The ρ_{HS} values were estimated according to the method described in Section 7.2.3.1. Note the increase of ρ_{HS} at low temperature due to the SOXIESST effect and the different T_{SOXIESST} threshold for the powder and the film.

of HS molecules ($L_{3\mathrm{a}}$ peak) persists (Fig. 7.23 (b)). Note that the spectra resembles the case reported by Naggert *et al.*[127] and illustrated in Figure 7.17 (b). In our study, however, this is the film which becomes quenched and not the powder.

In the next step, we recorded the XAS spectra with varying temperature. To determine the ρ_{HS} value we employed the same method as described in Section 7.2.3.1. The result is presented in Figure 7.24. The evolution of the high spin proportion with temperature emphasizes the incomplete transition within the thick film sample. We observe only a $\sim 25\%$ decrease of the high spin proportion ρ_{HS} ($\rho_{\mathrm{HS}}(T = 300\,\mathrm{K}) \sim 1$, $\rho_{\mathrm{HS}}(T = 80\,\mathrm{K}) \sim 0.75$), meanwhile the reference powder undergoes a complete transition. The increase of ρ_{HS} at low temperatures is provoked by the SOXIESST effect. It is noteworthy that T_{SOXIESST} varies between the thick film and the powder. This is the reason why the LS referential spectra in Fig. 7.23 were recorded at different temperatures for the two samples.

The incomplete spin transition of the SCO complexes is an important and often reported issue. Based on the literature and our experience we will try now to find the answer on why the sublimed thick film of Fe(bpz)$_2$NH$_2$-phen do not exhibit a full transition. We list the reasons of this behavior and comment on them with respect to the case of Fe(bpz)$_2$NH$_2$-phen. The most often reported causes of the incomplete SCO include: (i) decomposition of the molecules during the sublimation, (ii) interaction of the molecules with the substrate,[395,396] (iii) change of the molecules chemical environment, *e.g.*, interaction with contaminant/dopant or defect sites,[411] (iv) increased intermolecular interactions or/and distortion of the Fe-N octahedral cage.[127] Regarding the studied Fe(bpz)$_2$NH$_2$-phen film we exclude the case (i) since the molecules were

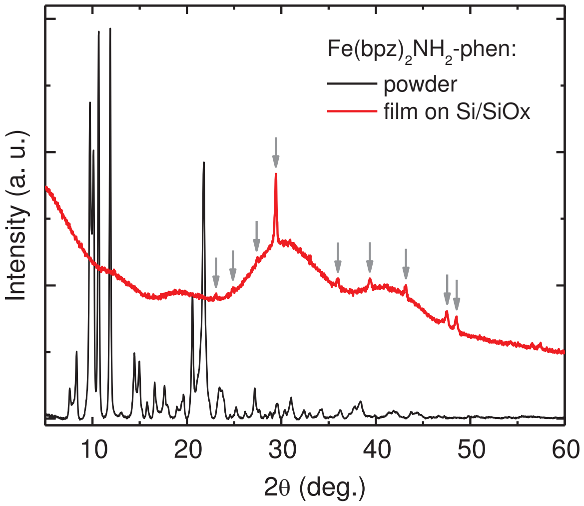

Figure 7.25: X-ray diffraction pattern of Fe(bpz)$_2$NH$_2$-phen powder and sublimed thick film. Diffractograms of powder and sublimed film on Si/SiO$_x$(400 nm) are compared. The arrows emphasize the peaks implying a crystallization of the molecules on the SiO$_x$ surface. The spectra were obtained at room temperature in the $\theta - 2\theta$ mode with monochromatic wavelength of $\lambda_{\text{CuK}\alpha_1} = 1.54056$ Å.

proved to be intact on the surface by means of the UV-Vis spectroscopy and the XAS at Fe $L_{3,2}$-edges. Moreover, we intentionally thermally decomposed the Fe(bpz)$_2$NH$_2$-phen powder and witnessed the resemblance of the molecular electronic structure to the ones in the LS state. Since in our film it is the HS which gets quenched we neglect the possible molecular decomposition. Concerning the case (ii) of increased interaction with the substrate it would be negligible in the case of a ~ 230 nm thick film where only the first monolayers could get quenched. We can also rule out the presence of a notable amount of contaminants (iii) as the films were sublimed in high vacuum conditions ensuring the cleanliness of the environment. In addition, the XAS did not reveal any presence of other elements than the ones constituting the Fe(bpz)$_2$NH$_2$-phen molecule. Therefore, we suggest the occurrence of the last possibility (iv) that is the modification of the intermolecular interactions and/or distortion of the Fe octahedral symmetry in a thick film form. Note that this explanation was invoked by Naggert *et al.*[127] for their quenched powder sample. In our case, we oppositely suggest that the intermolecular interactions are stronger within the sublimed film.

We employed the XRD measurement (at RT) to investigate the structural aspects of Fe(bpz)$_2$NH$_2$-phen powder and thick film. The results are presented in Fig. 7.25. First, we compared the diffractogram of a Fe(bpz)$_2$NH$_2$-phen monocrystal (not shown) to the acquired on powder and revealed that they do not coincide. We were not able to resolve the exact crystallographic system of the polycrystalline grains in powder but we claim that it does not exhibit the same triclinic form as the monocrystal. Then, we investigated the structure of the sublimed film. One can clearly see that a diffractogram exhibits the clear peaks (marked with the arrows) suggesting at least partial crystallization. The main feature at 29.3° does not correspond to any major peak neither of the powder nor of the monocrystal. This is opposite to what was observed on Fe-pyrz where the diffraction peaks of a thick film were reproducing the features

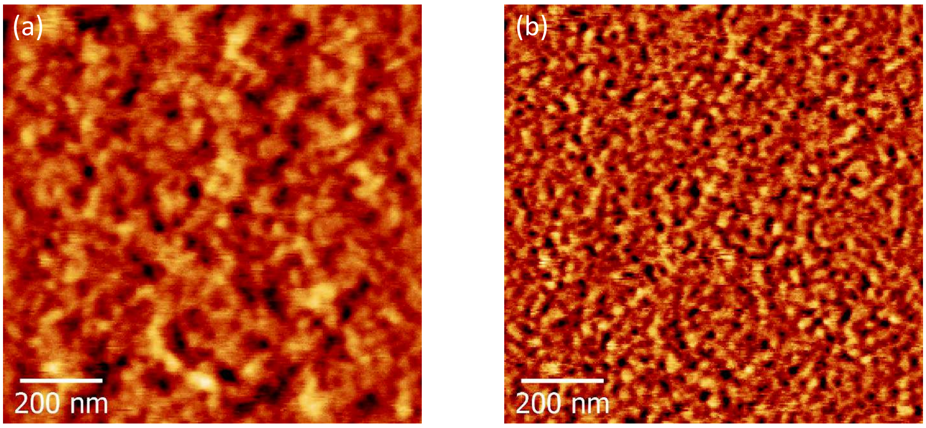

Figure 7.26: Morphology of Fe(bpz)$_2$NH$_2$-phen film on silica and platinum surface. Surface topography measurement by RT ambient pressure AFM in tapping mode of a 40 nm thick film of Fe(bpz)$_2$NH$_2$-phen sublimed onto (b) Si//SiO$_x$(400 nm), and (b) Si//SiO$_x$(400 nm)/Cr(2 nm)/Pt(13 nm).

of the powder suggesting therefore a preservation of the crystallographic structure.[31] In the case of Fe(bpz)$_2$NH$_2$-phen we observe rather the formation of a distinct phase or a mixture of phases what certainly must be accompanied with an alteration of the intermolecular interactions. Although we were not able to quantify these modifications we may suspect that the HS quenching within the film is caused by this formation of a new crystallographic structure upon sublimation.

Despite the reduced SCO performance of Fe(bpz)$_2$NH$_2$-phen in sublimed film we decided to validate its potential use for fabrication of vertical devices. First, we verified the surface morphology of the 40 nm Fe(bpz)$_2$NH$_2$-phen thick film on amorphous oxide and on sputtered platinum electrode by means of RT ambient pressure AFM in tapping mode. We limited our studies to a brief verification of the film morphology without focusing on details of its submonolayer growth mechanism. The result is presented in Figure 7.23. The film surface appears to be covering completely the substrate when deposited on silica and platinum. In case of the amorphous oxide the deposited molecular film forms a flat surface of rms $\sim$ 0.3 nm which approximately reproduces the roughness of a bare Si//SiO$_x$(400 nm) substrate. The surface of the film deposited on the platinum electrode has an rms roughness of $\sim$ 1.9 nm which can be still considered as sufficiently flat for our purposes. We can therefore conclude that Fe(bpz)$_2$NH$_2$-phen forms continuous films on amorphous oxide or partially crystallized (platinum) surfaces what satisfies our requirement II of desired SCO material characteristics. Because of that, we devoted some time for the investigations of the electronic transport through the Fe(bpz)$_2$NH$_2$-phen material encapsulated by two metallic electrodes.

7.3.2.3 Vertical SCO device

Since the SCO phenomenon involves both modification of electronic configuration and geometry of the molecule one can intuitively expect also the alteration of the charge transport properties. Baadji and coworkers[412] used the density functional theory and nonequilibrium Green's function method for quantum transport to model the conductance variation of FeL$_2$ (L = 2,2':6,2"-terpyridine) in the vicinity of a spin transition.

The spin crossover magnetoresistance (SCMR) defined as $R_{\mathrm{SCMR}} = (G_{\mathrm{HS}} - G_{\mathrm{LS}})/G_{\mathrm{LS}}$ was shown to be potentially as large as 3000% indicating $G_{\mathrm{HS}} > G_{\mathrm{LS}}$. In contrary, Meded *et al.*[413] pointed the opposite relation ($G_{\mathrm{HS}} < G_{\mathrm{LS}}$) for $\mathrm{FeL_2}$ (L = 4'-(4"-pyridyl)-1,2' : 6'1"-bis-(pyrazolyl)pyridine) and supported this statement by the density functional theory and first principles calculations combined with the experimental results on three-terminal device produced with the wet deposition methods. This discrepancy was later suggested to be presumably resulting from the involvement of two concurrent processes in the LS to HS transition: (i) the reduction of the HOMO-LUMO energy gap (G↗), and (ii) a decrease of the Fe(II) electronic coupling to the ligands (G↘).[414] The contribution of these processes can differ between the systems. Despite the intensive research, those concepts are still not well conceived.

The first who witnessed experimentally the synergy between the spin crossover and conductivity was Takahashi and coworkers[415] in 2006 who investigated the temperature dependent electronic transport through $\mathrm{Fe(qsal)_2[Ni(dmit)_2]_3{\cdot}CH_3CN{\cdot}H_2O}$ monocrystals. Since then, only a few SCO junctions have been demonstrated including the ones formed with an STM tip,[22, 405, 416] or nanogaps.[413, 417] These were focused on transport studies through a single molecule. To date, very little success was achieved in the field of SCO devices. In 2009, Shi *et al.*[379] presented a lateral junction comprising 100 nm of Fe-phen between two gold electrodes revealing the linear $I(V)$ characteristics with two transport regimes (Ohmic and space charge-limited), yet the authors did not demonstrate a spin state dependent transport. In 2015, Devid *et al.*[414] reported a study over the electronic transport of self-assembled SCO molecules on gold nanoparticles. Their work revealed the spin state dependent conductance, such that $G_{\mathrm{HS}} < G_{\mathrm{LS}}$, and proposed a percolation model to explain a current dependence on temperature. To the best of our knowledge, to date there is only one report on a SCO ensemble device fabricated by thermal evaporation. In this work by Mahfound *et al.*[418] $\mathrm{Fe(HB(pz)_3)_2}$ was sublimed under secondary vacuum ($\sim 10^{-5}$ mbar) on gold electrodes in a lateral architecture. The authors showed an irreversible device conductance variation upon thermal cycling and referred to the observed phenomenon as a non-volatile memory effect. Regardless of these demonstrations, the question on how the spin transition is reflected in the electric transport across the material seems to be open. The experimental results are rather inconsistent and further research is required.

For our studies we fabricated the crossed-wire junctions containing $\mathrm{Fe(bpz)_2NH_2}$-phen sandwiched between two metallic electrodes. We used a simple architecture to minimize the complexity of the junctions, and therefore reduce to minimum the alternative pathways for the current. The scheme of the device is presented in Figure 7.27. In Hybrid system (see Sec. 3.3) on cleaned and *in situ* annealed $\mathrm{Si/SiO_x}$(400 nm) substrates we sputtered 2 nm of chromium through a shadow mask as a wetting layer, and then 13 nm of Pt as the bottom electrode (BE) (Fig. 7.27 (b)-(c) (1)). The sample was transferred in atmosphere to the high vacuum environment of a Plassys system for molecular deposition. The $\mathrm{Fe(bpz)_2NH_2}$-phen was thermally sublimed over the entire sample area with rate of $\sim$ 0.1 nm/min. Then, the stack was introduced to a UHV evaporation chamber of the Hybrid set-up for the deposition of 10 nm thick gold top contacts (TC) with another motif of the shadow mask (Fig. 7.27 (b)-(c) (2)). This last step of the TC formation was technologically the most challenging. There are numerous reports on the critical impact of the top contacts fabrication method on the molecular layer structure.[419–421] In order to reduce the interdiffusion of gold atoms into the organic layer we cooled down the sample with liquid nitrogen to $T \sim 100\,\mathrm{K}$ during the evaporation and ensured a slow Au deposition rate ($\sim 0.2\,\mathrm{nm/min}$). During the BE or TC deposition the shadow mask was positioned few hundred micrometers above the sample surface so as to avoid the mechanical damage of the topmost layers. This precaution, in turn, led to more smeared motifs, yet it had no influence on the device performance. Note that during the TC deposition additional pads were formed (Fig. 7.27 (b)-(c) (3)) serving as an adhesion layer for the BE wiring. A single sample contained 4 identical junctions of area $\sim 0.03\,\mathrm{mm}^2$ (BE width $\sim 410\,\mu\mathrm{m}$, TC width $\sim 80\,\mu\mathrm{m}$). However, one has to keep in mind that the effective area across which the charge transport occurs may be different and rather difficult to estimate. The fabricated devices were tested by a probing station in 4-point measurement mode, which gives results correspond directly to the transport across the active junction region excluding the resistance of the electrical leads. We deduced, by trial and error, that to obtain the non-short-circuited junctions the molecular thickness has to be at least $\sim 40\,\mathrm{nm}$. We suggest that a thinner layer of the molecules is creating shorts at the edges of BE. On the other hand, a thickness exceeding 100 nm results in a too resistive layer such that the current is not detectable. We estimated the success rate of fabricated with this procedure junctions as $\sim 30\%$.

The electronic transport across Fe(bpz)$_2$NH$_2$-phen devices were investigated with the BMF set-up (abbrev. banc multifonctionnel, Eng. multifunctional bench) at the IPCMS. It is an electrical station equipped with a cryostat allowing to perform the measurements in a broad temperature range ($T = 15\,\mathrm{K} - 300\,\mathrm{K}$, $\mathrm{d}T = 2\,\mathrm{K}$) with possibility of multiplexing between numerous devices and with an optical access for the

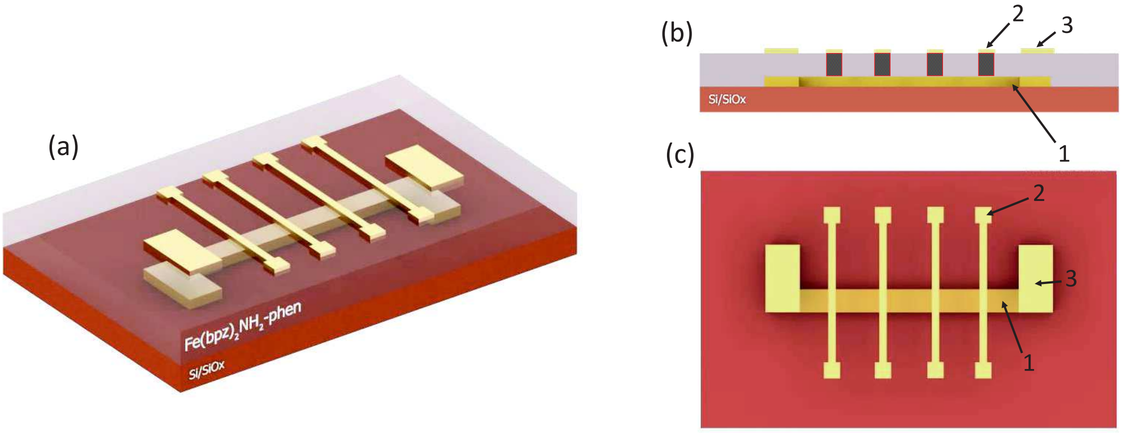

Figure 7.27: Vertical device for transport measurement through the SCO layer. 3d model of the crossed-wire architecture of the device in (a) isometric, (b) side, and (c) top view. The bottom electrode (BE) (1) was made of sputtered Cr(2 nm)/Pt(13 nm) layers. The Au(10 nm) top contacts (TC) (2) were thermally evaporated while cooling down the stack with liquid nitrogen to $T \sim 100\,\mathrm{K}$. The additional bonding pads (3) ensured a good adhesion of the BE wiring. The organic junctions (marked with red squares in panel (b)) are formed on the intersection of each TC with BE. A single sample contained 4 identical junctions of area $\sim 0.03\,\mathrm{mm}^2$.

photoexcitation. Prior to the measurement, the devices were mounted on a dedicated chips and wire bonded to allow the 4-point measurement of each junction. We investigated the sample containing a 40 nm thick Fe(bpz)$_2$NH$_2$-phen layer and recorded the junction resistance (current) as a function of temperature. After that, the measurement was repeated with simultaneous irradiation of the device area with a 405 nm laser. Consequently, we studied the $I(V)$ characteristics of the device as a function of temperature. The results are discussed below.

To begin with, we present the junction resistance evolution with temperature (Fig. 7.28 (a)) and discuss the result in absence and presence of light. We varied the temperature in the range 17 K – 300 K and used a low bias voltage of 50 mV. The latter was chosen so as to minimize the occurrence of electromigration of the electrodes' material into the barrier, which would cause an immediate short-circuiting of the device. At room temperature the junction resistance stayed in the mega ohm range, what is rather expected due to a poorly conducting organic layer. While decreasing temperature the resistance increases from 1.7 MΩ at RT to 100 GΩ (detection limit in our experiment) at 40 K in the dark and to 600 MΩ while irradiating the junction with a 405 nm laser. We did not observe any substantial change of the transport properties around the spin transition temperature $T_{1/2} = 154$ K. In the following, we first discuss the transport across the Fe(bpz)$_2$NH$_2$-phen layer.

By representing the acquired data in an Arrhenius plot (ln J vs. $1/T$ (Fig. 7.28 (b)) we can distinguish two transport regimes with a transition around 80 K. We expect the two conduction mechanisms to be (i) thermally activated hopping (at high T), and (ii) a tunneling (at low T). The occurrence of two regimes and the thermal activation of

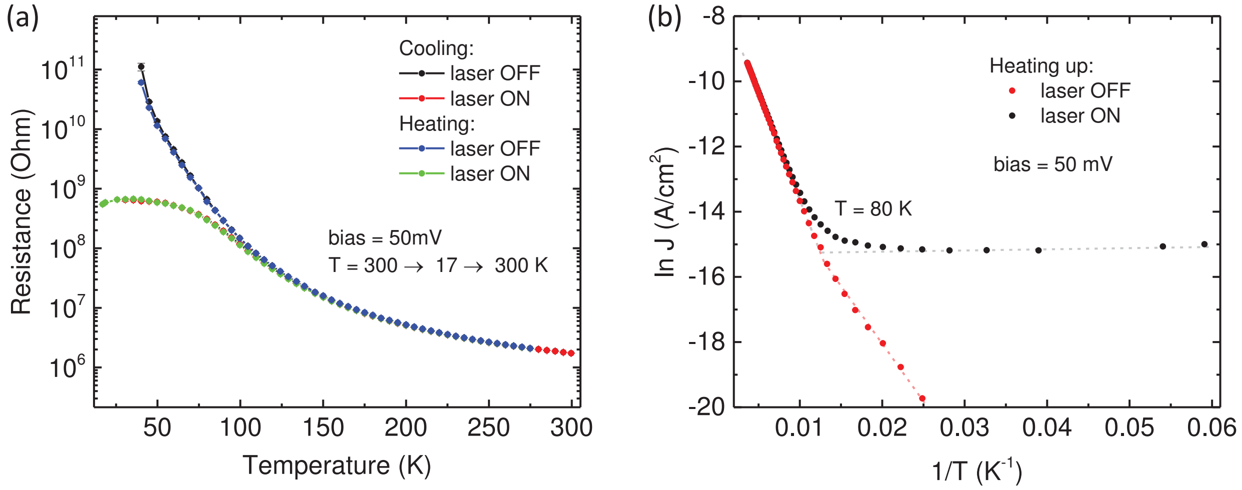

Figure 7.28: Electronic transport across Fe(bpz)$_2$NH$_2$-phen organic junction. Variable temperature measurement of a device containing 40 nm of Fe(bpz)$_2$NH$_2$-phen and fabricated in architecture presented in Fig. 7.27. (a) Resistance as a function of temperature measured in the dark (laser OFF) and with irradiating the junction with a 405 nm laser (laser ON). (b) Arrhenius plot of ln J vs. $1/T$ of the same data. The two linear evolutions reveal two transport regimes: high temperature hopping and low temperature tunneling. The dashed lines represent the linear regressions used to calculate the energy barrier heights collected in Table 7.4.

the transport has been reported for many molecular systems[422, 423] as well as described theoretically.[424] Regime (i) corresponds to the electrons' hopping which may involve one or more atomic sites of the molecule and is distinguished from incoherent tunneling by the involvement of the nuclear motion.[425] In other words, crossing of the electron over the barrier is possible only when the molecules rearrange in thermally activated motion so as to create a pathway for the charge to pass. Therefore, the process is strongly temperature dependent ($\ln R \sim 1/T$). This is not the case for the tunneling (ii) at low temperature where the electron can pass directly through the barrier. The previously activated hopping sites act now as the carrier traps and do not contribute to the current. Note that there are other transport mechanisms possible across the organic layers such as the thermionic emission, field ionization (Fowler-Nordheim tunneling), or Frenkel-Poole transport.[423] Since their occurrence requires larger values for the applied electric field, we claim that at $V = 50\,\mathrm{mV}$ the contribution of these effects is negligible.

The nature of the conduction mechanism can be deduced on the basis of the activation barrier height extracted from the Arrhenius representation of the current density versus the inverse temperature according to the relation:

$$J(T) = A \cdot V \cdot \exp\left(\frac{-E_\mathrm{a}}{k_\mathrm{B}T}\right) \tag{7.5}$$

where A is a pre-exponential factor related to the charge transfer rate, V bias voltage, and E_a the energy barrier height. Therefore, the slope of the linear region on $\ln J(1/T)$ plot is equal to $E_\mathrm{a}/\mathrm{k_B}$. The estimated values of the barrier height E_a for the transport regimes observed in Fig. 7.28 are collected in Tab. 7.4.

In high temperature regime, the barrier height stays at the similar level independently weather the laser is on or off. The calculated $E_\mathrm{a} \sim 56\,\mathrm{meV}$ suggests strongly temperature dependent process that is in agreement with presumed hopping regime. The obtained barrier energy value is similar to other reported molecular systems.[426] Below 80 K we observe that in absence of light the barrier height is reduced from 57 eV to 28.7 meV. The persisting temperature dependence of the process at low temperature suggests the coexistence of both conduction regimes hopping and tunneling with a strong contribution of thermally activated transport. A different situation is observed when the junction is irradiated with a 405 nm laser. We see that below 80 K the transport gradually changes to a nearly temperature independent transport associated with a barrier height of 0.5 meV. Such small value of the activation energy is in agreement with reports on similar systems[423, 426] and can be explained exclusively by tunneling. This clearly suggests an influence of the photons on transport across the molecular junction which we assign to photon-assisted tunneling.[427]

There are numerous light-driven mechanisms which can affect a transport across a molecular layer, *e.g.*, the internal photoemission, tunneling of excited electrons, or photon-assisted tunneling. In order to identify which is dominant, one can plot the current dependence on the radiation power in log-log scale.[428] Both the internal photoemission and tunneling of excited electrons follow a single exponential evolution, whereas the photon-assisted tunneling current for low light intensities is described by a linear dependence meanwhile for larger intensities by a double-logarithm.[428] We measured the current passing through the junction and varied the laser power as illustrated in Figure 7.29 (a). One clearly observes the logarithmic evolution (linear on log-log

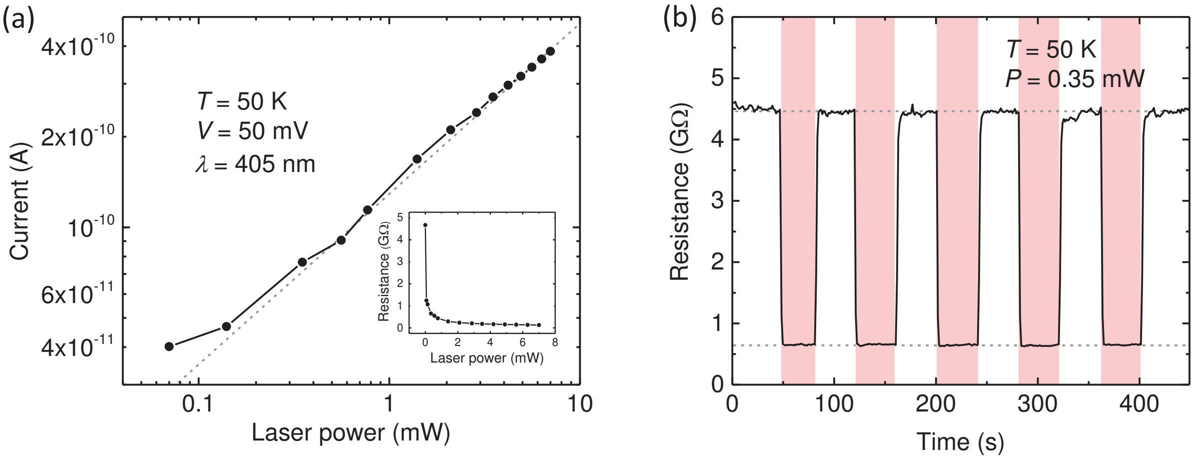

Figure 7.29: Photon-assisted tunneling across a Fe(bpz)$_2$NH$_2$-phen junction. (a) Dependence of current across the Fe(bpz)$_2$NH$_2$-phen junction on the laser power. The deviation from from linear regime at low power suggests that the photon-assisted tunneling is the dominant process for a power above $\sim 0.5\,\mathrm{mW}$.[428] (b) Influence of the 405 nm laser irradiation on the junction resistance at $T = 50\,\mathrm{K}$. The laser shutter was subsequently opened (red regions) and closed each $\sim 40\,\mathrm{s}$. The nearly immediate $\sim 400\%$ resistance change demonstrates the current control by photon-assisted tunneling across the molecular layer.

scale) down to $\sim 0.5\,\mathrm{mW}$ and then a deviation from the linear regime at lower power values. This, along with the observed temperature independence of the process, suggest that the 405 nm laser triggers photon-induced tunneling in a Fe(bpz)$_2$NH$_2$-phen junction below temperature $T = 80\,\mathrm{K}$. This mechanism can be roughly explained by the oscillatory light-driven barrier perturbation which leads to a tunneling probability enhancement. The effect is expected to be frequency and electric field dependent.[429] In Fig. 7.29 (b) we demonstrate the effect of switching between the two conduction mechanisms (hopping ↔ photon-assisted tunneling) at low temperature reflected by a variation of the junction resistance upon opening and closing the laser shutter. Note that the resistance change is as large as 400%. Therefore, we report on the current control by light irradiation of the Fe(bpz)$_2$NH$_2$-phen organic junction.

In the next step, we investigated $I(V)$ characteristics of the junction. We recorded $I(V)$ curves with a given temperature step in absence and presence of the light within

Table 7.4: Activation energy E_a of the electronic transport across a Fe(bpz)$_2$NH$_2$-phen junction. Energy barrier height values were established from the Arrhenius representation of $\ln J$ vs. $1/T$ (Fig. 7.28 (b)) according to Eq. 7.5 for bias voltage $V = 50\,\mathrm{mV}$.

	E_a (meV)	
	laser OFF	laser ON
high temperature ($T > 80\,\mathrm{K}$)	57	56
low temperature ($T < 80\,\mathrm{K}$)	28.7	0.5

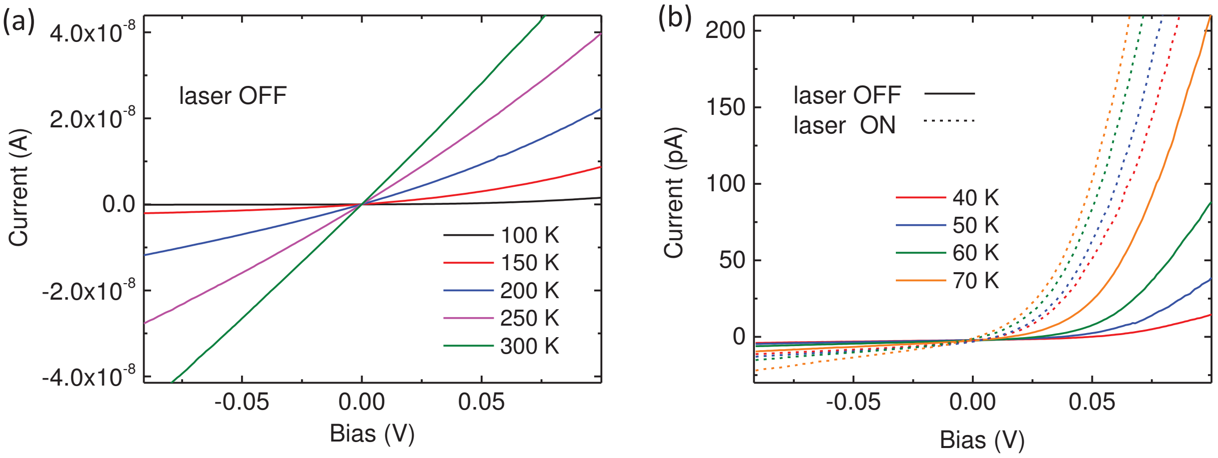

Figure 7.30: Current-voltage characteristics of Fe(bpz)$_2$NH$_2$-phen junction. (a) Selected $I(V)$ curves for a few temperatures revealing nearly linear evolution at RT and increasing non-linearity with decreasing temperature. (b) $I(V)$ curves highlighting the rectifying character of the junction at low temperatures. Note the impact of the laser radiation (dashed lines) strongly pronounced on the positive bias branch.

the ± 0.1 V region. We present some representative characteristics in Figure 7.30. At RT the $I(V)$s are nearly linear. With decreasing temperature we unsurprisingly observe a drop of the current (in accord with Fig. 7.28 (a)). At lower temperatures, the evolution begins to manifest non-linearity. To highlight this behavior we present the curves corresponding to $T = 40$ K, 50 K, 60 K, and 70 K in Fig 7.30 (b). In addition to non-linearity, they reveal also a strong current rectification at positive biases.

The rectifying behavior of molecular structures was envisaged long time ago in a famous work by Aviram and Ratner.[68] It was commonly accepted that this requires a donor-acceptor pair, yet later a study by Chabinyc *et al.*[430] revealed that neither this nor the dipolar moment are necessarily needed. It is essentially difficult to prove the particular molecular structure to be the cause of the rectification since there may be numerous other reasons of the asymmetry such as the metallic contacts and/or Schottky barrier formation at metal/molecule interfaces.[431] This is even further complicated because of the difficulty in conceiving the essential in this respect nature of the metal-molecule interaction/bonding which may strongly depending on the fabrication process.[432] Because of this, we state in general that our Fe(bpz)$_2$NH$_2$-phen junction exhibits a rectifying behavior as a whole device without distinguishing whether it originates from the molecular structure and/or asymmetric junction architecture.

Interestingly, we observe that the light influences the $I(V)$ curves predominantly on the positive bias branch (Fig. 7.30 (b) dashed lines) what can be rationalized by photon-assisted tunneling enhancement of rectification.[429] To have a better insight into this complex light impact on the junction $I(V)$ characteristics in bias and temperature space we represented the data on the contour 3d maps.

The maps presented in Fig. 7.31 were generated from the $I(V)$ characteristics recorded in ± 0.1 V bias range with $\Delta T = 10$ K temperature step. The maps are plotted in the absence of light (Fig. 7.31 (a), I_{OFF}), and for the difference $I_{\mathrm{ON}} - I_{\mathrm{OFF}}$ reflecting the impact of light on the current across the junction (Fig. 7.31 (b)). We

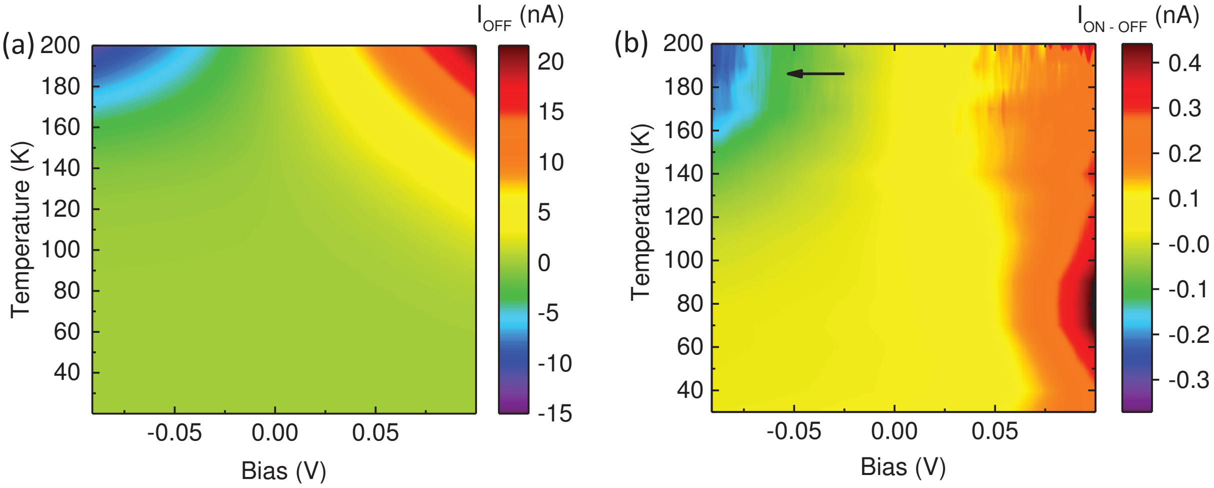

Figure 7.31: Contour maps of the current across a Fe(bpz)$_2$NH$_2$-phen junction. Intensity maps generated from the $I(V)$ curves acquired in a ±0.1 V bias range with $\Delta T = 10$ K temperature steps. (a) Data acquired in the dark. (b) Impact of light on the current, *i.e.*, the difference between the curves obtained in the dark and while irradiating the junction with a 405 nm laser. For sake of clarity only the data for $T < 200$ K are presented. Curves were interpolated.

present the interpolated data only for temperatures below 200 K to improve the visibility of the minor features. The influence of light is evidenced in Fig 7.31 (b). At positive bias, we see that the photon-assisted tunneling process goes with a rectification enhancement. It is manifested on the contour map as a positive $I_{\mathrm{ON}} - I_{\mathrm{OFF}}$ difference in the range 0.2 nA – 0.5 nA for the positive 0.05 V – 0.1 V bias region with an increasing the amplitude towards lower temperatures. To emphasize this light-assisted transport we present an extract of the low temperature region on the maps in Figure 7.32. Comparison of both panels illustrating the current in the dark and with a laser irradiation emphasizes the light-enhanced transport and the rectification at low temperatures.

We remark the appearance of an additional localized feature on the current intensity maps marked with the arrow in Fig. 7.31 (b). The light impact map reveals the light-induced current drop at negative bias at $T \sim 200$ K. Since it occurs at higher temperatures it obviously can not involve a tunneling and therefore we infer that it reflects a coupling of the 405 nm photons with the particular molecular energy levels.

The rather complex transport characteristics may be used towards multifunctional devices. One can imagine a temperature, bias, or light addressing used to involve a particular conduction mechanisms. Such approach was demonstrated for, *e.g.*, inorganic MgO-based tunnel junctions[10] and here we see that similarly it may also apply the organic device.

Since we did not observe directly the SCO accompanying transport modification in Fe(bpz)$_2$NH$_2$-phen junctions we took advantage of the synchrotron radiation to have an insight into the material structure within the complete device. To do so, we used the Versatile Variable Temperature Insert[33] (see Section 4.7). The sample containing the junctions was mounted on the dedicated chip (Fig. 7.33 (a)). After introducing the sample under the soft x-ray beam, we employed the XAS at the Fe $L_{3,2}$-edges to resolve the spin state of Fe ions while varying the temperature.

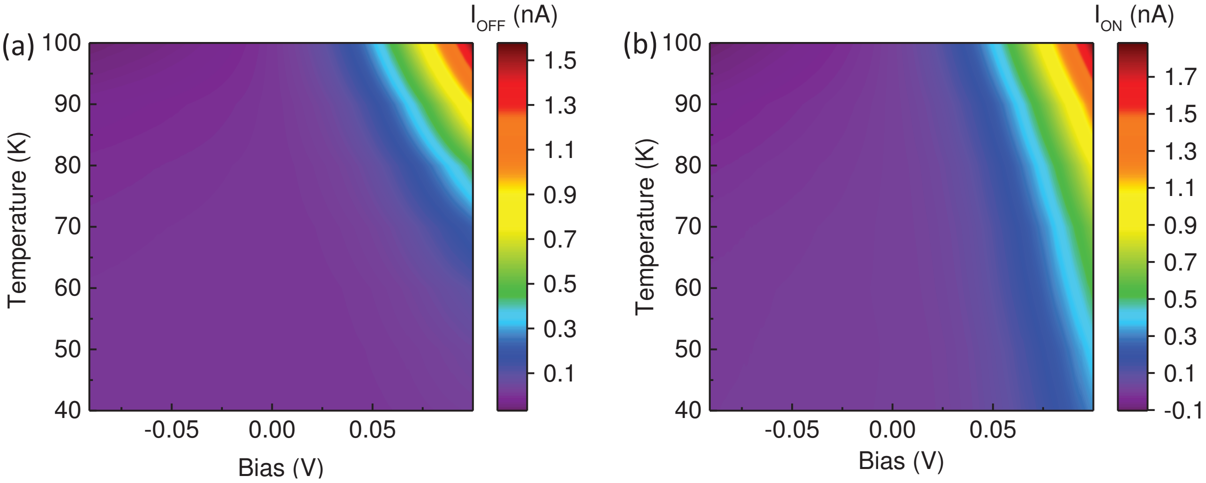

Figure 7.32: Contour maps of the current passing across a $\mathbf{Fe(bpz)_2NH_2}$-phen junction in the low temperature region. Intensity maps generated from the $I(V)$ curves acquired in $\pm 0.1\,\mathrm{V}$ bias range with temperature step $\Delta T = 10\,\mathrm{K}$. (a) Data acquired in the dark, and (b) while irradiating the junction with a 405 nm laser. By comparing the two maps one easily sees the current increase in the low temperature region upon laser irradiation which we attribute to the photon-assisted tunneling process. The maps are an extract from the data presented in Fig. 7.31.

After locating the junction we performed RT XAS scans at different positions along the junction's top contact (7.33). Then, the procedure was repeated at $T = 120\,\mathrm{K}$, *i.e.*, below $T_{1/2}$ of $Fe(bpz)_2NH_2$-phen. The acquired absorption edges are presented in Fig. 7.33 (c). The numbers correspond to the positions indicated in Fig. 7.33 (b) with the curves in red recorded exactly over a junction. Unsurprisingly, at RT all the spectra 1 – 4 are identical and of a typical HS shape. At 120 K the edges recorded away from the junction, *i.e.*, at positions 1 – 3, indicate a partial HS → LS transition what is in agreement with the previous studies over a thick film (see Fig. 7.23 (b)). However, the curve corresponding to the junction position (4 (red)) seems to be quenched. It is astonishing that upon cooling, exclusively the material localized at the BE and TC crossing does not undergo the transition. Further measurements revealed that this is the case always when $Fe(bpz)_2NH_2$-phen is directly deposited on a platinum electrode. Since these outcomes were consistent for a range of samples, we concluded that $Fe(bpz)_2NH_2$-phen within the device exhibits the SCO everywhere but in the junction's active region. On the other hand, this also suggest that our top contact fabrication procedure is non-destructive for the SCO layer. Therefore, excluding the Au top electrode influence and the other arguments considered, once again we suppose that the reason of the SCO blocking is the growth induced modification of intermolecular interactions.

To verify this point we performed XRD measurements on the Pt/$Fe(bpz)_2NH_2$-phen sample (Fig. 7.34). By comparing the obtained diffractogram with the one acquired on SiO_x/$Fe(bpz)_2NH_2$-phen we observed an increased peaks intensity especially prominent at the main 29.3° reflection. Therefore, we infer that the platinum surface enhances the $Fe(bpz)_2NH_2$-phen crystallization. Since we deduced previously that the observed distinct crystal phase formation is responsible for the SCO quenching in the thick film,

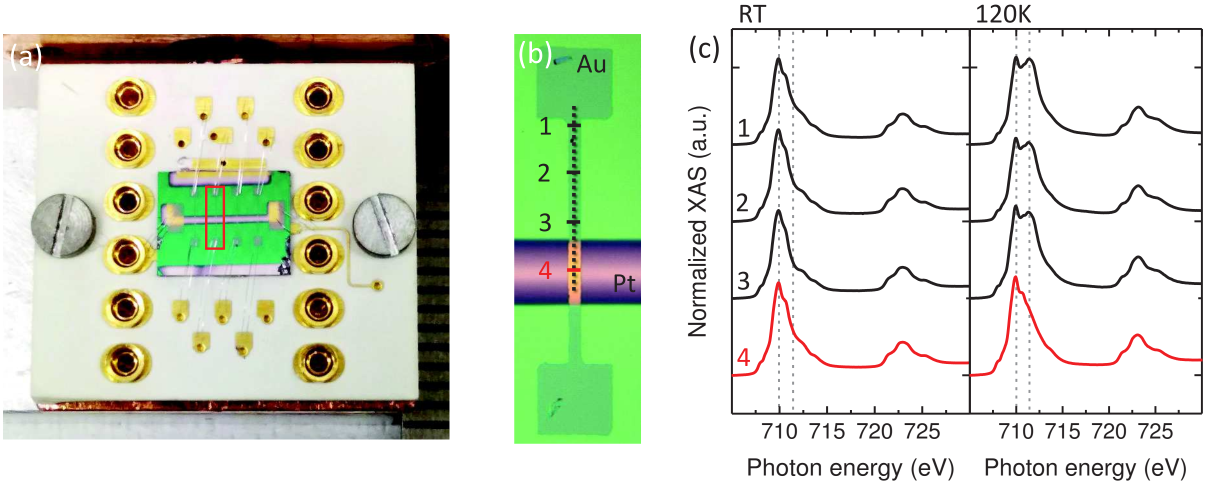

Figure 7.33: X-ray absorption study of the Fe(bpz)$_2$NH$_2$-phen junctions. (a) Sample containing Fe(bpz)$_2$NH$_2$-phen devices mounted on a V^{2}TI dedicated chip. The red square marks the top contact of the investigated junction. The scale on the right corresponds to millimeters. (b) Zoom-in on the top contact with numbers indicating positions where the x-ray absorption spectra were acquired. The red bar marks the exact junction position. (c) The Fe $L_{3,2}$-edges XAS spectra acquired in positions 1 – 4 at RT (left panel) and below the spin transition temperature (right panel) in total electron yield mode. The SCO at the exact junction position is quenched.

it is intuitively consistent that an even stronger crystallization on the platinum surface may explain a complete blocking of the HS state observed in the junction region. We can now attribute the studied electronic transport properties across the junction to the intrinsic, non-SCO-related, characteristics of Fe(bpz)$_2$NH$_2$-phen.

To sum up this part dedicated to Fe(bpz)$_2$NH$_2$-phen, we reported on a novel complex with the functional NH$_2$ terminal opening the way for the versatile functionalization of the molecular structure. The compound preserves the complete SCO in powder form and exhibits thermal sublimability. We fabricated the thick films of Fe(bpz)$_2$NH$_2$-phen and proved its integrity at a molecular level by UV-Vis spectroscopy and the x-ray absorption at the Fe $L_{3,2}$-edges. The partial crystallization, as observed by the XRD, inducing alteration of the intermolecular interactions led to the HS quenching of the thick film, such that only ~25% of the molecules undergo the spin state switching. The uniform growth of the material allowed us to fabricate the vertical transport devices in a crossed-wire architecture. We characterized the intrinsic charge transport properties across the Fe(bpz)$_2$NH$_2$-phen layer at low bias region and witnessed the photon-assisted tunneling at low temperatures. We demonstrated how the transport mechanism can be addressed and used for sake of multifunctionality by, *e.g.*, light-driven switching between conduction regimes. The enhancement of the material crystallization on a platinum electrode, resulting in a complete HS blocking of the molecules within the junction region, prevented us from observing the SCO-induced transport alterations.

The main virtue of this new material is the NH$_2$ group which gives an easily extendable molecular structure by addition of functional groups. We anticipate further research to involve the use of various groups so as to optimize the SCO performance by modifying the intermolecular interactions. Furthermore, we believe these findings may be followed by more exotic realizations such as employing the surface anchoring groups

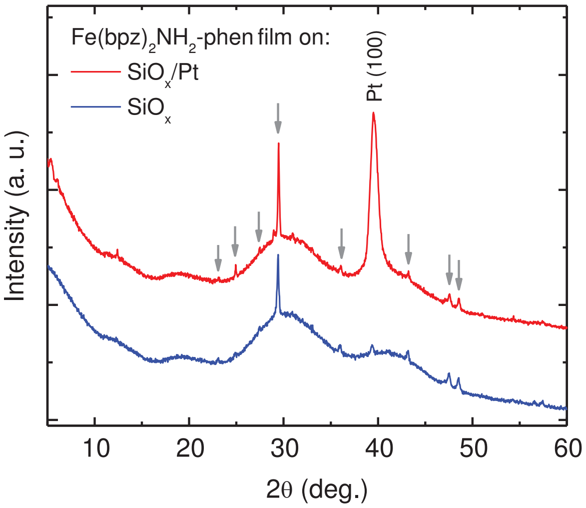

Figure 7.34: X-ray diffraction measurement of Fe(bpz)$_2$NH$_2$-phen films on silica and platinum surface. Diffractograms comparing the structure of the Fe(bpz)$_2$NH$_2$-phen film deposited on Si/SiO$_x$(400 nm) and Si/SiO$_x$(400 nm)/Cr(2 nm/Pt(13 nm). The increased intensity of the peaks with the dominant reflection at 29.3° suggests the enhancement of crystallization on a platinum surface. The spectra were obtained at room temperature in the $\theta - 2\theta$ mode with a monochromatic wavelength of $\lambda_{\mathrm{CuK}\alpha_1} = 1.54056$ Å.

and others available from myriads of possibilities limited mainly by the creativity of the organic chemists. Finally, still more research is required to address the important questions of the SCO-induced electronic transport alteration which to date remain open.

7.3.3 Fe(bpz)$_2$(bpy): general properties

Accordingly, we devoted an effort to investigate the functionalization potential of the other family of compounds, namely Fe(bpz)$_2$(bpy) (bpy = 2,2'-bipyridine) (Fig. 7.35 (a)). The synthesis of this parent complex was first time reported by the group of J. A. Real in 1997[402] along with the previously discussed Fe(bpz)$_2$(phen). The two materials are often studied together as it is easy to fabricate them in a similar procedure. The Fe(bpz)$_2$(bpy) crystallizes in a monoclinic $C2/c$ space group (room temperature structure) and exhibits the SCO transition temperature $T_{1/2} \sim 165\,\mathrm{K}$. It manifests less cooperativity thus more gradual transition than Fe(bpz)$_2$(phen) (Fig. 7.35 (b)).

Although the two Fe(bpz)$_2$(phen) and Fe(bpz)$_2$(bpy) were reported to be sublimable,[401] their growth on amorphous surfaces seems to be substantially different.[32] Fe(bpz)$_2$(phen) grows homogeneously, meanwhile Fe(bpz)$_2$(bpy) tends to form rather inhomogeneous microcrystallites on the surface. This non-uniform growth, which we witnessed also for Fe-pyrz on amorphous oxide, is undesirable characteristics being in opposition to our requirement II.

We suggest that this growth mode can be changed upon a proper functionalization of the complex. Therefore, in a first step we propose to extend the bipyridine in Fe(bpz)$_2$(bpy) with a -COOMe group, which then can be hydrolized to produce -COOH. This creates a versatile base complex and similarly as in case of Fe(bpz)$_2$NH$_2$-phen enables the further functionalization. After a brief verification of the SCO and sublimability conservation, we extended the compound structure by a long C$_{12}$ aliphatic

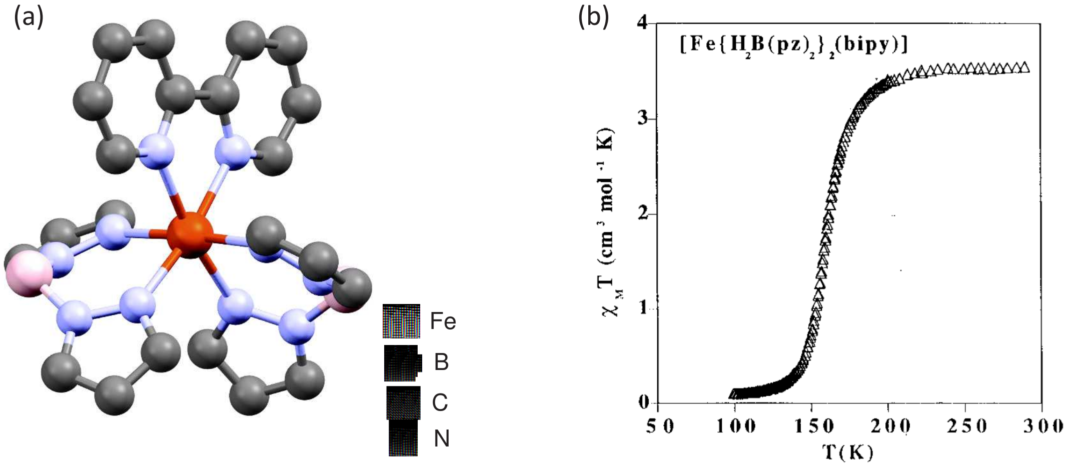

Figure 7.35: Fe(bpz)$_2$(bpy). (a) Molecular model of Fe(bpz)$_2$(bpy). The crystallographic data used for visualisation was taken from ref. 409. The hydrogen atoms were omitted for clearance. (b) Thermal spin transition of Fe(bpz)$_2$(bpy) measured with a pendulum-type susceptometer. Figure taken from ref. 402.

chain which was to impose a particular organization on the surface. In this way, we demonstrate an intentional modification of the growth mode on the surface.

We also propose a more exotic functionalization by extending the versatile Fe(bpy)$_2$C$_1$-bpy complex by a carbon chain connected pyrene group which is known to exhibit photoluminescence. As a result, we expect the complex to manifest a SCO accompanied photoluminescence alterations, such that a peculiar synergy between the spin transition and the properties of emitted light could be created. This has been already demonstrated for core-shell nanoparticles in solution,[433, 434] yet never for a sublimed film.

7.3.4 Fe(bpz)$_2$C$_1$-bpy

In order to open a way for Fe(bpz)$_2$(bpy) to be functionalized a carboxylic group -COOH was used. It played an analogous role as NH$_2$ in before discussed Fe(bpz)$_2$(phen). The synthesis is schematically presented in Fig. 7.36.

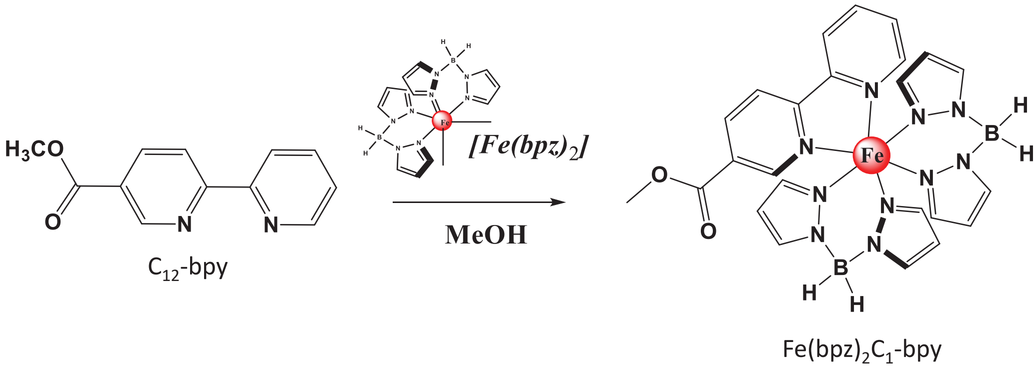

Figure 7.36: Synthesis of Fe(bpz)$_2$C$_1$-bpy. C$_1$-bpy is used as a precursor for the functionalizable Fe(bpz)$_2$C$_1$-bpy complex via a carboxylic group -COOH.

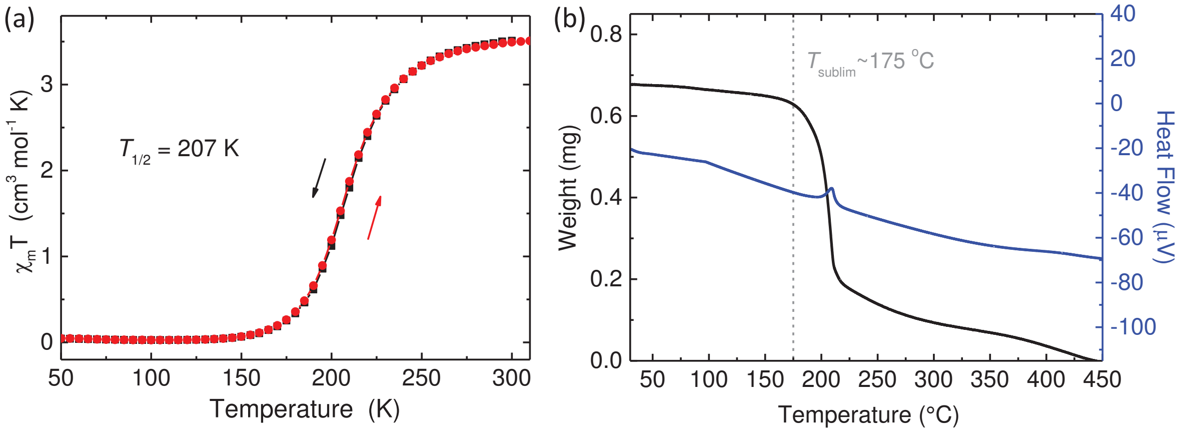

Figure 7.37: Spin transition and sublimability of Fe(bpz)$_2$C$_1$-bpy. (a) Magnetic moment measurement as a function of temperature acquired with SQUID on Fe(bpz)$_2$C$_1$-bpy powder. The new material preserves the complete spin transition of parent complex. (b) Thermogravimetric analysis of Fe(bpz)$_2$C$_1$-bpy proving the sublimability of the compound.

To a solution of Fe(II) perchlorate hydrate in 10 ml of methanol, potassium dihydro(bispyrazolyl)borate was added and the mixture was stirred for 15 min followed by filtration to remove the precipitated KClO$_4$. A solution of C$_1$-bpy dissolved in 25 ml of methanol was added drop-wise to the filtrate leading to the formation of a greenish precipitate upon continuous stirring for 4 h under Ar protection. The precipitate was filtered and dried in a vacuum oven for 6 h at 50 °C to yield a pale green powder.

The obtained functionalizable complex was first investigated by SQUID in a bulk powder form to prove the conservation of the SCO, and then subjected to TGA for the verification of sublimability. The results are presented in Fig. 7.37. The magnetic moment measurement as a function of temperature (Fig. 7.37 (a)) confirms the complete SCO of the new material. The transition is more gradual (decreased cooperativity) with respect to the parent complex, with a higher $T_{1/2}$ temperature ($\sim$ 207 K). The thermogravimetry (Fig. 7.37 (b)) provided an evidence for the compound sublimability. Therefore, we report on the successful substitution of -COOH group in bipyridine of Fe(bpz)$_2$(bpy) and thus the realization of the functionalizable Fe(bpz)$_2$C$_1$-bpy complex. In the next step, we extended the structure of Fe(bpz)$_2$C$_1$-bpy by a C$_{12}$ aliphatic chain in order to alter the molecular stacking on the surface.

7.3.5 Fe(bpz)$_2$C$_{12}$-bpy

We emphasized the critical role of the intermolecular interactions on both the SCO performance and the growth of the material. We demonstrated how the latter can disqualify the compound from the application in multilayer vertical devices. Here, we propose the approach of modifying the complex chemical structure so as to adjust the material properties towards the desired criteria. We demonstrate how the growth mode and molecular stacking can be modified by functionalization.

To do so, we start with the previously derived Fe(bpz)$_2$C$_1$-bpy and expand the structure by linear C$_{12}$ alkyl chain. Since the parent Fe(bpz)$_2$(bpy) complex was reported to grow on amorphous surfaces in a Volmer-Weber mode by crystallites formation,[32] we

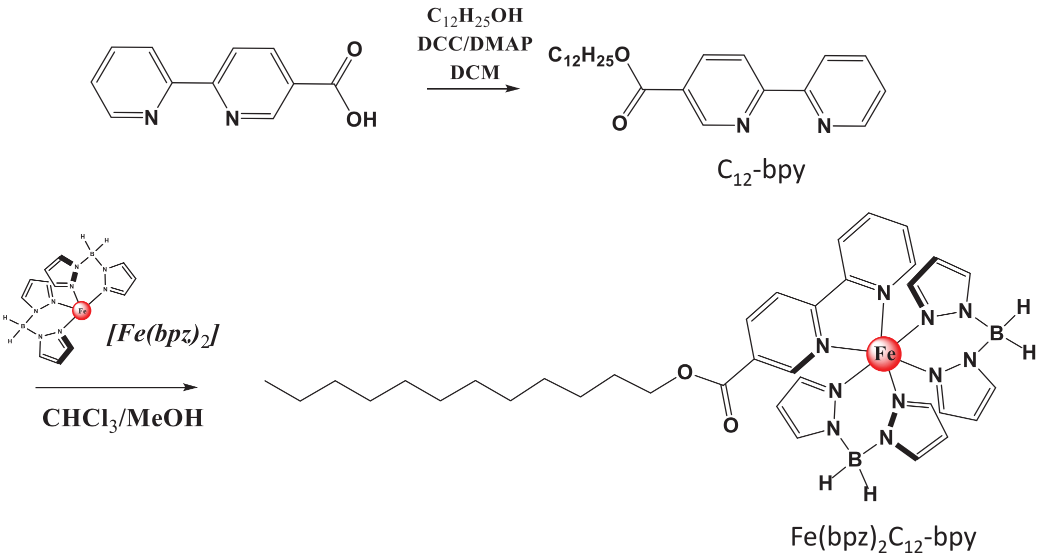

Figure 7.38: Synthesis of Fe(bpz)$_2$C$_{12}$-bpy. C$_1$-bpy is extended with a linear C$_{12}$ alkyl chain and used as a precursor to produce Fe(bpz)$_2$C$_{12}$-bpy complex.

expect the addition of a C$_{12}$ chain to impose a preferential stacking direction and make the material to grow in organized manner. In that way, we present an exploratory approach of intentional designing of a SCO architecture on the surface.

The synthesis of Fe(bpz)$_2$C$_{12}$-bpy is schematically illustrated in Fig. 7.38. To a solution of Fe(II) perchlorate hydrate in 5 ml of methanol, potassium dihydro(bispyrazolyl) borate was added and the mixture was stirred for 15 min followed by a filtration to remove the precipitated $KClO_4$. A solution of C$_{12}$-bpy dissolved in 1 ml of chloroform was added drop-wise to the filtrate leading to the formation of a greenish precipitate upon continuous stirring for 4 h under argon protection. The precipitate was filtered, washed with methanol and dried in a vacuum oven for 6 h at 50 °C to yield the as pale green powder.

Consequently, the new material was first investigated by SQUID followed by the confirmation of sublimability by means of TGA (Fig. 7.39). In comparison to Fe(bpz)$_2$C$_1$-bpy the new complex exhibits an even more gradual, yet still complete spin transition. The TGA revealed the material to be thermally sublimable. Therefore, we could deposit the material on a quartz substrate and verify the integrity of the molecular structure after sublimation by UV-Vis spectroscopy (data not shown). We confirmed the presence of the ligand and the MTLC absorption bands implying that the molecules in the thick film are intact. Due to the lack of access to synchrotron radiation at the moment of this study, we employed SQUID to investigate the SCO within the thick film on quartz (Fig. 7.40). The results revealed that nearly 75% of the molecules in the film undergo the thermal spin transition.

To investigate the structural aspects of the film we employed XRD measurement and compared the results with those obtained on the reference powder (Fig. 7.41 (a)). The diffractogram acquired on the thick film manifests a serie of 4 sharp peaks at small angles region and a broad feature centered around $2\theta \sim 22°$. This resembles a typical diffractogram of a smectic liquid crystal.[435] The equidistant small angle peaks, revealing the long-range lamellar organization, appear only for the smectic phase. The peaks

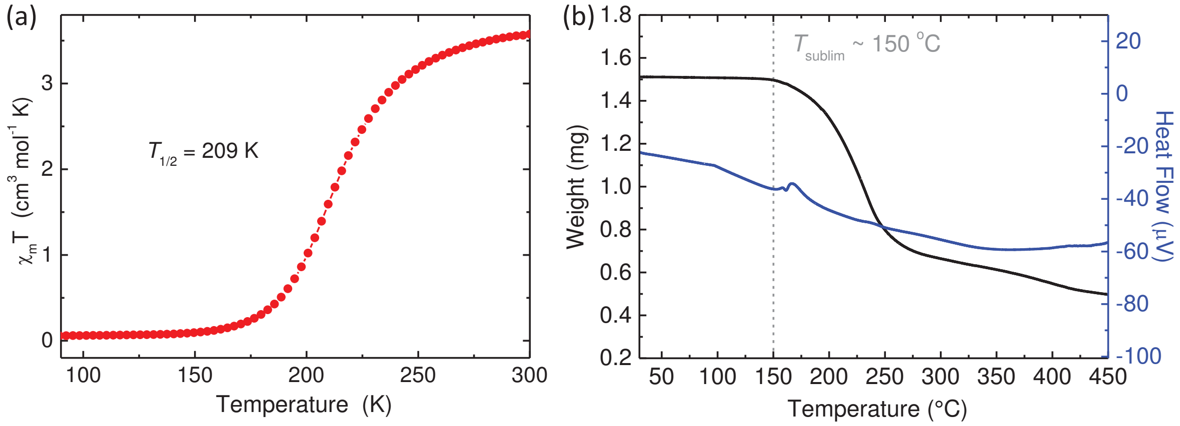

Figure 7.39: Spin transition and sublimability of Fe(bpz)$_2$C$_{12}$-bpy. (a) Magnetic moment measurement as a function of temperature acquired with SQUID on Fe(bpz)$_2$C$_{12}$-bpy powder. Note a more gradual transition than in Fe(bpz)$_2$C$_1$-bpy and Fe(bpz)$_2$(bpy). (b) Thermogravimetric analysis of Fe(bpz)$_2$C$_{12}$-bpy proving the sublimability of the complex.

positions are given by the Bragg's law: $2d\sin\theta = n\lambda$. Therefore, the distance between the peaks expressed in angstroms is directly related to the lamellar spacing. We collected the measured 2θ and d values for small angle reflections in Tab. 7.5. Good agreement of d_{mes} with the calculated values for ideally equidistant features unambiguously implies the formation of a smectic A-like mesophase within thick film of Fe(bpz)$_2$C$_{12}$-bpy. We found an average lamellar spacing $d = 2.43\,\mathrm{nm}$. Note that the periodic reflection pattern is present also in the powder reference, therefore we claim that the organization of the polycrystalline bulk and the film is similar. The broad wide angle feature at $2\theta = 17-25°$ arises from the lateral packing which we attribute to the presence of the linear alkyl chains and a small contribution from the Fe(bpz)$_2$(bpy) ligands. The broadening of the peak suggests a molten character of the chains, mean-

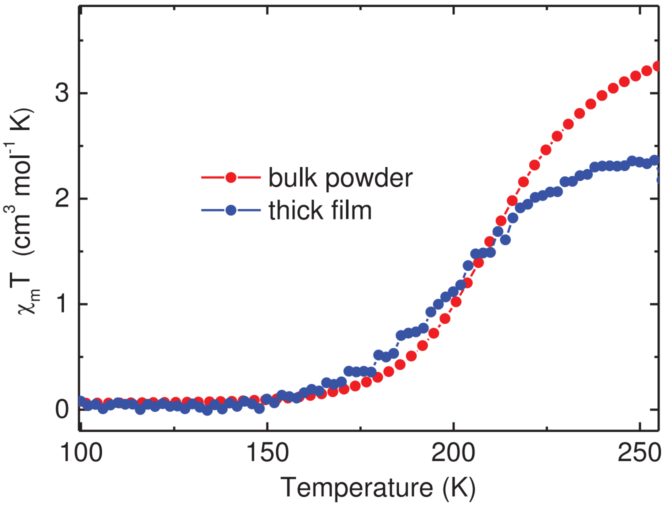

Figure 7.40: SCO of Fe(bpz)$_2$C$_{12}$-bpy thick film and powder. Results of the SQUID measurements comparing the spin transition of the bulk powder and the sublimed thick film. Approximately 73% of the molecules in thick film undergo the transition.

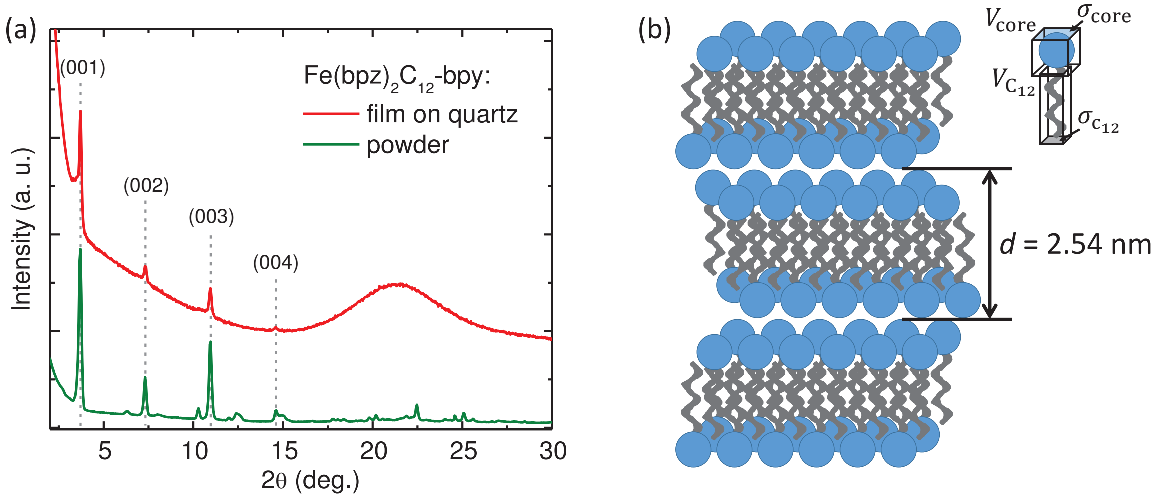

Figure 7.41: Organization in a Fe(bpz)$_2$C$_{12}$-bpy thick film. (a) X-ray diffraction pattern of a sublimed Fe(bpz)$_2$C$_{12}$-bpy film on a quartz substrate compared to the powder reference. The equidistant reflections (001) – (004) and a broad feature at $2\theta = 17° - 25°$ reveal a liquid crystal smectic A-like mesophase in the thick film. The diffractograms were acquired at room temperature in the $\theta - 2\theta$ mode with a monochromatic wavelength of $\lambda_{\mathrm{CuK}\alpha 1} = 1.54056$ Å. (b) Geometrically deduced bilayer arrangement of the Fe(bpz)$_2$C$_{12}$-bpy film with interdigitating C$_{12}$ alkyl chains.

while the absence of this feature for the powder implies a crystallization of the cores and the chains of the molecules.

In order to deduce the molecular arrangement, we used a geometrical reasoning. We calculated a theoretical volume of a single molecule as a sum of the Fe(bpz)$_2$bpy core volume (taken from the crystallographic data as $V_{\mathrm{core}} = 645\,\text{Å}^3$ for 20 °C), and volume of the molten chain as twelve volumes of a methylene group ($V_{\mathrm{C}_{12}} = 12 \cdot V_{\mathrm{CH}_2} = 324\,\text{Å}^3$). Eventually, we obtained $V_{\mathrm{mol}} = V_{\mathrm{core}} + V_{\mathrm{C}_{12}} = 970 \pm 30\,\text{Å}^3$ with the tolerance approximated as 3% of the volume resulting from the thermal motion of the molecule (Fig. 7.41 (b)). Then, we approximated the molecular cores (Fe(bpz)$_2$(bpy)) to rigid spheres connected to C$_{12}$ molten chains. The transverse section of the core was estimated as $\sigma_{\mathrm{core}} \sim 80\,\text{Å}^2$, meanwhile for C_{12} we took value $\sigma_{\mathrm{C}_{12}} \sim 21.3\,\text{Å}^2$ as the natural section of the aliphatic chain at 20 °C. By using the lamellar spacing d resulting from XRD measurement we calculated the theoretical molecular area $s = V_{\mathrm{mol}}/d = 40 \pm 1\,\text{Å}^2$

Table 7.5: Small angle x-ray scattering of a Fe(bpz)$_2$C$_{12}$-bpy thick film. Measured and calculated values of 2θ positions on the diffractogram and the spacing between the peaks d revealing the presence of a smectic phase within the sublimated Fe(bpz)$_2$C$_{12}$-bpy thick film with an average lamellar spacing $d = 2.54$ Å.

hkl	$2\theta_{\mathrm{mes}}(°)$	$\mathrm{d}_{\mathrm{mes}}$(Å)	$2\theta_{\mathrm{calc}}(°)$	$\mathrm{d}_{\mathrm{calc}}$(Å)
001	3.61	24.45	3.63	24.30
002	7.26	12.17	7.26	12.15
003	10.91	8.10	10.90	8.10
004	14.59	6.07	14.53	6.0

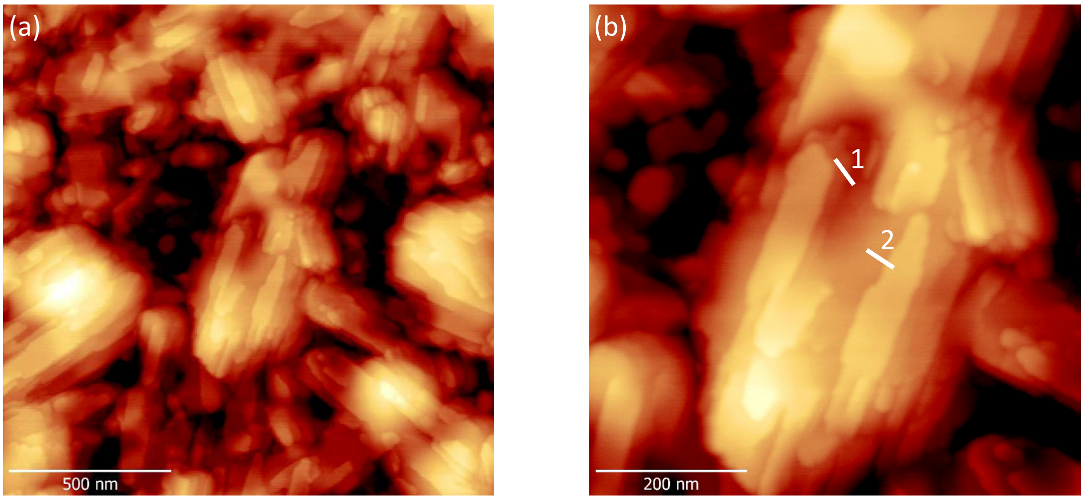

Figure 7.42: Surface morphology of a sublimated Fe(bpz)$_2$C$_{12}$-bpy film. Surface topography measurement performed by RT AFM in tapping mode of Si/SiO$_x$(400 nm)/Fe(bpz)$_2$C$_{12}$-bpy(10 nm). (a) Large-scale image revealing the flat terraces. (b) Detail of image (a) highlighting the consecutive layers with a step height of $d = 1.26$ nm and $d = 2.44$ nm along the profiles 1 and 2 respectively, which we identify as the single and bilayers of the lamellar molecular stacking.

and compared it with the cross sections σ_{core} and $\sigma_{C_{12}}$. The obtained relation $\sigma_{\text{core}} \sim 2s$ implies the bilayer organization and $\sigma_{C_{12}} \sim 0.5s$ points to interdigitated and strongly refolded alkyl chains. Therefore, we claim that the only possible molecular stacking arrangement in this case is the one presented in Figure 7.41 (b).

To confirm this hypothesis we fabricated a 10 nm thick film on silica and performed the RT AFM measurement in tapping mode. The results are presented in Figure 7.42. In the large-scale image one easily sees that the molecules form the stacks of the flat terraces. By measuring the observed steps profiles (Fig. 7.42 (b)) we witnessed the relative height of either $d \sim 1.1 - 1.3$ nm or $d \sim 2.2 - 2.6$ nm. These are compatible with the spacing deduced from XRD and correspond to the single or bilayers spacing. Based on the AFM measurement we could therefore confirm the presence of a smectic mesophase within the sublimed film.

To summarize, we demonstrated the SCO complex functionalization which alters the material properties by modifying the molecular stacking arrangement, meanwhile preserving its spin transition and sublimability. We used the parent complex Fe(bpz)$_2$(bpy) and by adding a linear alkyl chain imposed the bilayer growth on the surface in the smectic-A mesophase order. To the best of our knowledge, this is the first successful attempt of such modification of the material properties in a spin transition compound. We believe it may open a way for a more engineering-oriented approach in the field of spin crossover materials and enable the tuning of physical and chemical properties of the compounds towards applications.

7.3.6 Fe(bpz)$_2$Py-bpy: perspective

In this last section, we propose the most exotic case of the SCO functionalization carried out in this thesis, which is still in a development phase, yet already with a notable success.

Our concept was to combine the spin crossover phenomenon of the parent Fe(bpz)$_2$(bpy) complex with the photo-physical properties of a polyaromatic fluorophore, namely a pyrene. In this way we intend to fabricate a complex which would create a specific synergy between the central metal ion spin state and the photoluminescent behavior of pyrene. This would enrich an already multifunctional material with a new response signal in a form of the characteristics of the emitted light.

This is potentially possible because the monomer and excimer spectra of pyrene have a different emission spectrum (Fig. 7.43 (a)).[433] In general, the excimer (excited dimer) is formed when a pyrene in excited and ground state are in closed proximity (~ 10 Å). If pyrene is incorporated into a spin crossover complex the inter-pyrene distance, and

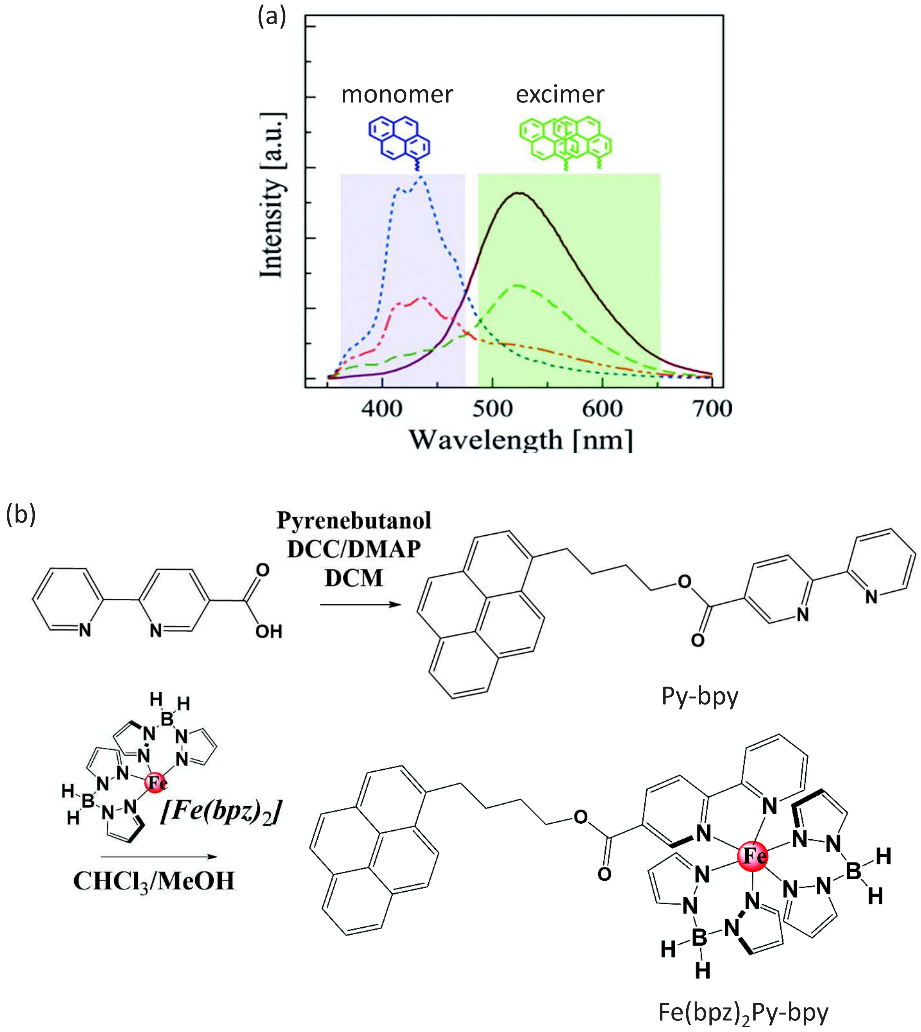

Figure 7.43: Fe(bpz)$_2$Py-bpy: synergy between the SCO and photoluminescence. (a) The photoluminescence dependence on the monomer/excimer formation in pyrene. Figure taken from ref. 433. (b) Synthesis of Fe(bpz)$_2$Py-bpy.

thus the ratio of the pyrene monomers/excimers, should vary when the volume of the molecules changes upon the spin transition. In that way, one should be able to detect the spin state dependent photoluminescence from the pyrene groups. This has been already demonstrated in core-shell structures as an increase of the excimer lifetime and luminescence intensity, as well as a redshift of the pyrene emission spectra during the LS → HS transition.[433] We intend to demonstrate it for the first time in a film made by sublimation.

Fe(bpz)$_2$Py-bpy was synthesized according to the procedure as illustrated in Fig. 7.43 (b). To a solution of Fe(II) perchlorate hydrate in 10 ml of methanol, potassium dihydro(bispyrazolyl)borate was added and the mixture was stirred for 15 mins followed by filtration to remove the precipitated KClO$_4$. A solution of Py-bpy dissolved in 5 ml of 4:1 chloroform/methanol solvent mixture was added drop-wise to the filtrate leading to the formation of a greenish precipitate upon continuous stirring for 4 h under Argon protection. The precipitate was filtered, washed with methanol and dried in a vacuum oven for 6 h at 50 °C to yield a pale green powder.

Till the moment of this manuscript submission, we confirmed the preservation of a spin transition within the Fe(bpz)$_2$Py-bpy bulk powder, with occurrence of a residual fraction of the HS state remaining at low temperature (Fig. 7.44 (a)). We also positively verified the material sublimability. By means of the UV-Vis spectroscopy we evidenced a conservation of the bipyridine absorption spectra and a proper band shape revealing the Fe(II) octahedral environment. The thick films of the Fe(bpz)$_2$Py-bpy are presently under investigation from the point of view of its SCO performance and photoluminescent properties.

We believe this case may open new perspectives in optically active SCO films underscoring the functionalized approach towards the multifunctional materials.

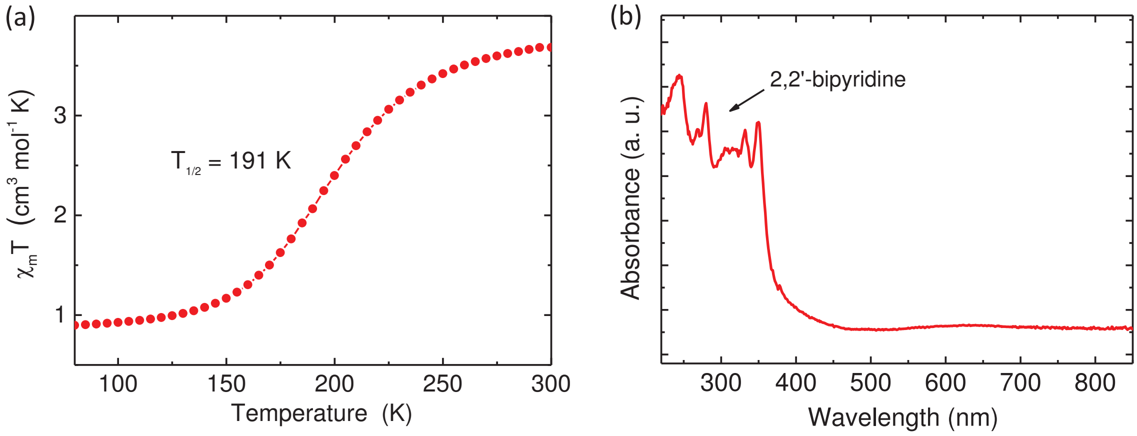

Figure 7.44: SCO and sublimability of Fe(bpz)$_2$Py-bpy. (a) Magnetic susceptibility measurement as a function of temperature measured with SQUID on Fe(bpz)$_2$Py-bpy powder confirming the preserved SCO with a gradual transition and $T_{1/2} = 191\,\mathrm{K}$. (b) Absorbance of a sublimed Fe(bpz)$_2$Py-bpy thick film exhibiting a proper spectra of the bipyridine ligands and the preservation of the octahedral Fe(II) environment.

At the very end of this chapter we want to emphasize on the impact of the discussed functional groups on the spin crossover performance of the parent compounds. We collected the results of the SQUID measurements performed on all the presented functionalized derivatives along with their parent references in powder form in Figure 7.45. It is striking clear that the addition of the peripheral groups to the chemical structure of the complex modifies its spin transition temperature. Interestingly, functionalization of Fe(bpz)$_2$(phen) with NH$_2$ causes a decrease of $T_{1/2}$ by 10 K (Fig. 7.45 (a)), meanwhile addition of C$_1$, C$_{12}$, or pyrene to Fe(bpz)$_2$(bpy) results in an increase of transition temperature by 42 K, 44 K, or 26 K respectively (Fig. 7.45 (b)). We therefore immediately notice, that except of the emergent novel material functionalities in this approach one can also tailor the transition temperature by chemical structure engineering. In addition, for both cases of Fe(bpz)$_2$(phen) and Fe(bpz)$_2$(bpy) functionalization is accompanied by an increase of the gradual transition character. This may be rationalized by the decrease of the cooperativity due to the reduction of the intermolecular interactions. This, in turn, results from the new peripheral groups which act as the molecular separators. We believe that in this way we demonstrated a great potential and versatility behind this functionalization approach.

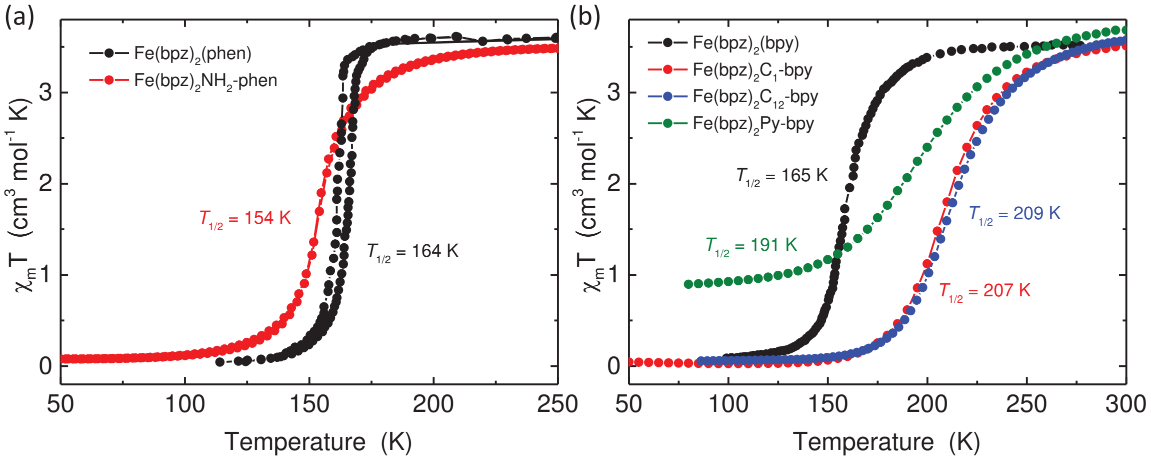

Figure 7.45: Impact of functionalization on SCO performance. Collected results of the magnetic moment measurements as a function of temperature by SQUID of (a) Fe(bpz)$_2$(phen), and (b) Fe(bpz)$_\mathbf{2}$(bpy) and their derivatives in the powder form discussed before in this chapter. Note a transition temperature modification upon compound functionalization and increase of the gradual transition character (reduced cooperativity). The data for Fe(bpz)$_2$(phen) and Fe(bpz)$_2$(bpy) parent compounds were taken from ref. 402.

7.4 Partial conclusions

Within the framework of this thesis we dedicated a considerable effort to investigate the multifunctional character of novel spin crossover complexes. This was motivated by a particular suitability of these materials for an active layer of a spintronic device. We formulated two requirements for the desired material characteristics: (i) sublimability, and (ii) homogeneous growth of the sublimated films.

In the first part, we reported on a new sublimable complex, namely Fe-pyrz, along with its properties. A multifunctionality in a form of sensitivity to temperature (thermal SCO) and light (LIESST) was demonstrated. The time resolved x-ray absorption was used to study the LIESST dynamics and proved the applicability of the material for optical sensing purposes. The AFM/STM studies revealed a strongly substrate dependent growth of Fe-pyrz such that it fulfills the requirement (ii) when sublimed on a crystalline substrate and a contrary result on the amorphous oxide surface. The study over Fe-pyrz was published in ref. 126.

In the second part, we proposed a novel pathway in the field of SCO, *i.e.*, the functionalization of the spin transition compounds. It was motivated by an attractive possibility of appending various functional groups so as to either tune the existing properties of a parent complex or enrich its capabilities with the new exotic features such as the photoluminescence or surface anchoring. We emphasized on the strong synergy required between organic chemistry and material science required to develop this SCO engineering approach. We introduced two versatile complexes: Fe(bpz)$_2$C$_1$-bpy and Fe(bpz)$_2$NH$_2$-phen which thanks to the functionalizability via NH$_2$ and C$_1$ terminals respectively can be further developed with a myriads of additional groups. We proved that the two materials can be sublimed. The Fe(bpz)$_2$NH$_2$-phen was thoroughly studied from the point of view of SCO performance and electronic transport within a vertical device in a crossed-wire architecture. The low temperature photon-induced tunneling revealed the additional dimension in the material multifunctionality. The x-ray absorption studies combined with the x-ray diffraction implied a distinct crystal phase formation within the thick sublimed film causing the partial HS quenching when deposited on the oxide surface and a complete blocking of SCO on the platinum electrode of the device. We expect this finding to be followed by further studies focusing on the adjusting of the SCO performance by further functionalization of the compound.

We demonstrated the structural modification of Fe(bpz)$_2$C$_1$-bpy with use of a linear C$_{12}$ alkyl chain. Since the parent complex was reported to exhibit a microcrystalline growth, the goal of the functionalization was to impose a particular stacking mechanism which enforces a more homogeneous organization. The obtained Fe(bpz)$_2$C$_{12}$-bpy material was proved to be sublimable while preserving the spin transition. The x-ray diffraction analysis revealed that the molecules form a lamellar smectic A-like mesophase in the sublimed the film, such that they organize in bilayers with interdigitating molten C$_{12}$ chains. This was confirmed by the AFM studies. This is the first report on engineering an SCO complex to adopt a particular stacking organization while preserving its sublimability and spin transition.

In a perspective, we devoted an effort to functionalize a sublimable SCO with the photo-active pyrene group in order to fabricate a synergetic spin transition - photoluminescent material. The preliminary results revealed the conservation of the SCO and sublimability of the new Fe(bpz)$_2$Py-bpy complex. We believe the photoluminescence studies, carried out at the moment of this manuscript submission, would lead to the first sublimable SCO material with a spin state dependent light-response.

The studies presented in this chapter reported on 5 new sublimable SCO compounds and therefore enriched the desired, yet not numerous, family of the SCO materials compatible with a thermal sublimation (only 7 species known before). We believe this opens the new possibilities in the field of multifunctional materials not only because of novel interesting complexes but also due to a new approach of the SCO engineering by functionalization. The latter is a first step towards the countless applications limited only by the creativity of chemists.

8

Conclusions and perspectives

In the introduction to this manuscript we explained a strong need for the exploratory research towards the new technologies in the field of *electronics*. We pointed out how the *spin electronics* exploiting organic materials gives promises for the new development direction, yet equally rises some fundamental questions about the nature of the interfaces or new materials' electronic and magnetic properties. This thesis was dedicated to deeper understanding of these issues with a special emphasis on the emerging *multifunctionality* when interconnecting the organics with inorganic counterparts. The work presented in this manuscript was carried out in the collaboration between the IPCMS and the DEIMOS beamline of the SOLEIL synchrotron.

On the beginning, we investigated a prototypical hybrid interface between the MnPc molecules and the ferromagnetic Co substrate. The previous studies of our group suggested that such FM/organic contact region can be strongly spin-polarized due to the adsoprtion induced spin dependent hybridization.[20,26] By means of the XAS and XMCD techniques we revealed that this hybridization and formation of the Co/MnPc spinterface results in the magnetic moment stabilization of the Mn paramagnetic centers at RT. The studies of the *in situ* fabricated wedge-shaped samples, which varied the MnPc layer thickness, provided the evidence that the Mn magnetic centers within the first ML of the molecules couple ferromagnetically to the underlying Co. This in turn is followed by the antiferromagnetic coupling of the Mn moments in consecutive second and further layers of MnPcs. Therefore, we inferred that the spinterface formation between the MnPc and Co at room temperature leads to magnetic moment coupling at the interface, what is further responsible for the AFM order stabilization between the Mn, otherwise paramagnetic, centers away from the interface. The *ab initio* calculations supported the experiment and pointed out the strong hybridization of the first ML molecules with the substrate, associated with the Mn magnetic moment of $+2.51\,\mu_\mathrm{B}$ ($\sim 3.1\,\mu_\mathrm{B}$ for the free molecule) consistent in direction to that of Co. The magnetic moment of Mn within the successive layers was calculated as $-3.04\,\mu_\mathrm{B}$ (2nd ML) and $+3.09\,\mu_\mathrm{B}$ (3rd ML) supporting thus the observed AFM coupling.

The evidenced magnetic correlations in the system led to observation of the unidirectional anisotropy of recorded by the MOKE measurement hysteresis loops of Co. It revealed that the FM layer is exchange biased by the organic MnPc molecules up to blocking temperature $T_{\mathrm{B}} = 100\,\mathrm{K}$.[349] That provided a perspective for the EB applications, which are commonly realized by the inorganic pinning layers (in, *e.g.*, MTJs), to be equally feasible in the organic spintronic devices as provoked by the organic molecules.

Since fabrication of a direct Co/MnPc interface requires an utterly clean FM surface, such that one needs to resort to the UHV environment, we proposed a concept on an indirect spinterface mediated by the interlayer exchange coupling. We studied the magnetic ordering by the XAS/XMCD within the system Co/Cu/MnPc with varying the noble metal spacer thickness. We compared the results to the referential Co/Cu/Co stack fabricated on the same sample. We witnessed the RT magnetic coupling of the Mn centers of MnPc to Co through the spin-polarized quantum well states of Cu. By tracking the changes along the wedge of a noble metal we evidenced the oscillatory FM/AFM ordering as predicted by the IEC theory and resulting from the Fermi surface of the spacer. In that way, we provided a first demonstration of the interlayer coupling of the paramagnetic centers in organic molecule to a strong ferromagnet and suggested a conservation of the spin-dependent hybridization in such system. We proposed a concept of a protected spinterface, *i.e.*, an FM substrate covered with a noble metal allowing deposition of various molecular materials, including the ones which are incompatible with the UHV sublimation. In that way, the system offers all the merits of the hybrid spinterface, such as the magnetic moment stabilization or spin-polarization at the interface, and allows tuning of the coupling strength and its character (FM/AFM) by controlling the spacer thickness. In addition, the noble metal spacer may reduce a direct molecule-substrate interaction, what can be of a notable importance for some sensitive molecular effects, *e.g.*, spin crossover.

The naturally emerging question was whether the Cu/MnPc interface in the IEC system Co/Cu/MnPc is spin-polarized. We addressed this issue by the SR-PES experiment at the CASSIOPÉE beamline of the SOLEIL synchrotron. We fabricated a set of the samples of composition Co/Cu(d_{Cu})/MnPc(1 ML) with $d_{\mathrm{Cu}} = 1.5$ ML, 2 ML, and 3 ML. By recording the asymmetry in the spin-resolved measurement and applying a subtraction procedure we could resolve the electron distribution curves arising from the electronic structure at the exact Cu/MnPc interface. Independently of the Cu thickness we found a strong spin polarization near the Fermi level, with a dominant spin-up channel, that is $P > 0$. Surprisingly, the obtained result resembled the one from a direct Co/MnPc,[20] or Co/C[26] interfaces. We excluded the possibility of a direct contact between MnPc and Co in studied Co/Cu/MnPc system by performing the ion scattering spectroscopy measurement. It proved that already 1 ML of Cu covers nearly 90% of Co substrate and at 1.5 ML the Cu coverage is complete. This all together implies that the Cu/MnPc interface in the studied interlayer coupled system is strongly spin-polarized. This was further supported by DFT calculations showing a distinct hybridizing spin-up and spin-down channels depending on d_{Cu}. In that way we confirmed that the protected spinterface not only offers the magnetic moment stabilization but also a spin-polarization at E_{F}. However, the question about the formation mechanism of this spinterface at the Cu/MnPc contact remains open. Since in a direct interface with a ferromagnet the dominating hybridization pathway was recognized as of p_z-d exchange,[89] the $3d$ states of Cu are lying relatively far from E_F, therefore it is rather questionable if they contribute in the spinterface formation. In the perspective, we anticipate the DFT calculations which would resolve the site and orbital projected DOS of the MnPc molecule atop Co/Cu substrate as a function of molecule-substrate distance. This would allow to identify the contributing orbitals of the molecule and bands of Cu. In addition, we are looking forward to the UPS study which may shine a light on a potential involvement of the Cu surface states on the spinterface formation. To summarize, we demonstrated how a hybrid inorganic/organic interface whether direct or mediated by the interlayer exchange may reveal exotic properties giving perspective for the magnetic pinning layers or spin-current injectors in organic spintronic devices.

In the next step, we proposed a concept of extending a hybrid spinterface by an artificial multiferroic substrate, adding thus a multifunctional character in a form of a ferroelectric control over the FM magnetism. We designed a device comprising the magnetoelectrically coupled system Pb(Zr,Ti)O_3/Co and a spinterface Co/FePc in a vertical architecture. The device was tested with a PUND measurement which confirmed the conservation of an FE switching properties and polarization of $\sim 12\,\mu C/cm^2$. We performed the XAS/XMCD studies at the DEIMOS beamline with an *in situ* electrical access to reverse the FE polarization, and explored for the reversible electronic structure alterations of the device constituent materials. We provided an evidence of a proper PZT FE switching by observing a reversible changes to XAS at Ti $L_{3,2}$-edges. This was further followed by the alterations observed at Co $L_{3,2}$-edges attributed to the magnetoelectric coupling at PZT/Co interface, as suggested by previous studies.[28,366] Eventually, we witnessed a reversible pattern at the $L_{3,2}$-edges of Fe in FePc suggesting that a remote spinterface may sense the FE/FM changes away from the interface. In that way we demonstrated a prototypical device combining the artificial multiferroic with concept of a hybrid FM/organic spinterface. We stress on the purely interfacially driven operation of the device and its multifunctionality in a form of sensitivity to bias voltage and magnetic field. As a perspective, we look forward to improved interfaces quality at PZT/Co and Co/FePc contact regions which would allow a further FM layer thickness reduction and enhancement of the interfacial effects. In addition, the theoretical calculations could provide the details about the coupling mechanism in such system including the charge transfer at both interfaces.

Finally, we investigated a distinct subclass of organic compounds which are intrinsically multifunctional, namely the spin crossover materials. We formulated two requirements of desired material characteristics: sublimability, and uniform growth of a thin films, which we found crucial for potential substitution of the previously demonstrated archetypal metal-phthalocyanine complexes. To begin with, we presented the new sublimable material, Fe-pyrz, and demonstrated its sublimability and preservation of the spin transition in a thick film form.[126] By using the XAS we proved the compound to be LIESST-active. Finally, by carrying out the STM/AFM morphology studies we witnessed a strongly substrate dependent growth mode of the complex, such that on crystalline surfaces it forms uniform flat film, meanwhile on amorphous oxides it tends to grow in microcrystalline form.

We proposed a new direction in the field, based on the functionalization of spin crossover compounds. The aim of the study was to demonstrate that by a specific modification of the chemical structure of the SCO material one can tune the desired material properties while conserving the sublimability and the spin transition in a film. We focused on two well-known parent complexes: $Fe(bpz)_2(phen)$ and $Fe(bpz)_2(bpy)$ (bpz = dihydrobis(pyrazolyl)borate), phen = 1,10-phenanthroline, bpy = 2,2-bipyridine). We employed such functional groups (NH_2, -COOH) which allows a further unrestricted structure expansion. In that way, we reported on two versatile complexes: $Fe(bpz)_2NH_2$-phen and $Fe(bpz)_2C_1$-bpy, which once announced to community can be further developed in the countless ways. Both conserve the sublimability of a parent complex and a partial SCO. The reason of the incomplete spin transition was identified as arising from the modification of the intermolecular interactions in a sublimed film. We further functionalized a $Fe(bpz)_2C_1$-bpy complex by C_{12} linear alkyl chain in order to intentionally modify the growth mode of the parent complex which was known to be creating the nonuniform microcrystallites on the surface upon sublimation. The newly synthesized material occurred to exhibit a bilayer growth with a high degree of self-organization in film on amorphous surface, what we evidenced by the XRD and AFM studies. We demonstrated that a functionalization of the SCO material may be used for crafting of desired material properties. As a perspective we proposed a functional compound which in synergetic way combines the virtues of the spin transition and photoluminescent properties. The synthesized $Fe(bpz)_2$Py-bpy complex is expected to manifest a dependence of the light emitted in a photoluminescence process by the bipyridine group on the spin state of the molecular core. We confirmed the conservation of the sublimability of the material and we look forward to the result of the SQUID and the luminescent measurements. We believe that the demonstrated approach may ignite the interest on the molecular structure modifications of already known sublimable SCO materials.

It is important to mention that the part of this PhD studies was also devoted to development of the new electrical insert at the DEIMOS beamline called the Versatile Variable Temperature Insert.[33] Fabricated in a strong collaboration between the IPCMS engineering team and the DEIMOS scientists, provided a powerful tool for the combined electrical and spectroscopic studies with use of the synchrotron radiation. We employed the insert to perform a first scientific project dedicated to studies of the MgO-based MTJs. The joint XAS and magnetoresistance measurements allowed us to develop the methodology to resolve how the subset of the active atomic sites constituting the device impact its operation. This, we infer may provide a new method towards the understanding of numerous microelectronic devices' operation which in many cases remains only phenomenological.

We believe that the studies presented in this manuscript may contribute to better understanding and the overall progress of the rapidly developing *inorganic/organic spintronics*. The large variety of employed materials and involved concepts which we demonstrated, highlights the great potential hidden behind interconnecting these usually separately studied systems, such as the ferromagnetic substrates, magnetoelectrics, organometallic, or spin crossover compounds. We anticipate an enduring intensive research towards these hybrid systems for further and deeper exploration of their emerging *multifunctional applications*.

Acronyms and abbreviations

6T	sexithienyl
AES	Auger electron spectroscopy
AFM	atomic force microscopy
Alq$_3$	8-hydroxy-quinoline aluminum
AP	antiparallel
BE	bottom electrode
bpy	2,2'-bipyridine
bpz	dihydrobis(pyrazolyl)borate
BW	bandwidth
CASSIOPÉE	Combined Angular- and Spin-resolved SpectroscopIes Of PhotoEmitted Electrons
CBS	complex band structure
CL	circular left
CR	circular right
DEIMOS	Dichroism Experimental Installation for Magneto-Optical Spectroscopy
DFT	density functional theory
DMO	Département des Matériaux Organiques
DOS	density of states
DSI	Département Surfaces et Interfaces
EB	exchange bias
ELIESST	electron-induced excited spin state trapping
ESP	electron spin polarization
EXAFS	extended x-ray absorption fine structure
F, F$^+$, F*	ground state, charged, and excited single oxygen vacancy in MgO crystal
FC	field cooling
FE	ferroelectric
FePc	iron-phthalocyanine
Fe-phen	Fe(phen)$_2$(NCS)$_2$
Fe-pyrz	Fe$\{$[3,5-dMePy]$_3$BH$_2\}_2$
FM	ferromagnet(ic)
FOM	figure of merit
GMR	giant magnetoresistance
HAXIESST	hard x-ray induced excited spin state trapping
HOMO	highest occupied molecular orbital
HOPG	highly oriented pyrolytic graphite
HS	high spin
IEC	interlayer exchange coupling
IPCMS	Institut de Physique et Chimie des Matériaux de Strasbourg
ISS	ion scattering spectroscopy
ITRS	International Technology Roadmap for Semiconductors
KPFM	Kelvin probe force microscopy

LD-LISC	ligand-driven light-induced spin change
l-DOS	local density of states
LEED	low-energy electron diffraction
LFT	ligand field theory
LH	linear horizontal
LIESST	light induced excited spin state trapping
LIPTH	light induced perturbation of a thermal hysteresis
LITH	light induced thermal hysteresis
LS	low spin
LSMO	lanthanum strontium manganite ($La_{1-x}Sr_xMnO_3$)
LT	low temperature
LUMO	lowest unoccupied molecular orbital
LV	linear vertical
MBE	molecular beam epitaxy
MCA	magnetocrystalline anisotropy
MEC	magnetoelectric coupling
ML	monolayer
MLCT	metal to ligand charge transfer
MnPc	manganese-phthalocyanine
MOKE	magneto-optical Kerr effect
MP	Multi-Probe
MPc	metal-phthalocyanine
MRAM	magnetoresistive random access memory
MTJ	magnetic tunnel junction
NEXAFS	near edge x-ray absorption fine structure
OCS	organic semiconductor
OMAR	organic magnetoresistance
OMBE	organic molecular beam epitaxy
P	parallel
Pc	phthalocyanine
PC	photocurrent
PCB	printed circuit board
PES	photoemission spectroscopy
PFM	piezoresponse force microscopy
phen	1,10-phenanthroline
PUND	positive up negative down
PZT	Lead zirconate titanate ($Pb(Ti,Zr)O_3$)
QW	quantum well
RHEED	reflection high-energy electron diffraction
RKKY	Ruderman–Kittel–Kasuya–Yosida
RT	room temperature
SCO	spin crossover
SDT	spin-dependent tunneling
SMM	single-molecule magnet
SOLEIL	Source Optimisée de Lumière d'Énergie Intermédiaire du LURE
SOXIESST	soft x-ray induced excited spin state trapping
SOXPC	soft x-ray photochemistry
SPM	scanning probe microscopy
SQUID	superconducting quantum interference device

SR-PES	spin-resolved photoemission spectroscopy
STM	scanning tunneling microscopy
STT	spin transfer torque
TC	top contact
TEMPO	Time resolved Experiments on Materials with PhOtoelectron spectroscopy
TEY	total electron yield
TFY	total fluorescence yield
TGA	thermogravimetric analysis
TMP	turbo molecular pump
TMR	tunneling magnetoresistance
UHV	ultra high vacuum
UPS	ultraviolet photoemission spectroscopy
UV	ultraviolet
V^{2}TI	Versatile Variable Temperature Insert
VGD	variable groove depth
XAS	x-ray absorption spectroscopy
XMCD	x-ray magnetic circular dichroism
XMD	x-ray magnetic dichroism
XMLD	x-ray magnetic linear dichroism
XNLD	x-ray natural linear dichroism
XLD	x-ray linear dichroism
XRD	x-ray diffraction

Mathematical symbols and constants

Constants:

α	fine structure constant (0.0072973526)
c	speed of light ($299792458\,\mathrm{m/s^2}$)
e	electron charge ($1.60217662 \times 10^{-19}\,\mathrm{C}$)
$\hbar$	reduced Planck constant ($1.054571800 \times 10^{-34}\,\mathrm{J\,s}$)
k_B	Boltzmann constant ($1.38064853 \times 10^{-23}\,\mathrm{J\,K^{-1}}$)
m_e	electron mass ($9.10938356 \times 10^{-31}\,\mathrm{kg}$)
μ_o	permeability of vacuum ($1.25663706 \times 10^{-6}\,\mathrm{H\,m^{-1}}$)
N_A	Avogadro's number ($6.0221409 \times 10^{23}\,\mathrm{mol^{-1}}$)
R	gas constant ($8.3144599\,\mathrm{J\,mol^{-1}\,K^{-1}}$)

Introduction and background:

E	energy
E_F	Fermi energy
$\Delta E^\mathrm{o}_\mathrm{HL}$	zero-point energy separation
$\Delta E^\mathrm{o}_\mathrm{HS(LS)}$	bottom of the HS (LS) state potential well
ΔE_p	electron pairing energy
$F(T)$	Franck-Condon factor
Γ	cooperativity
$G_\mathrm{HS(LS)}$	free Gibbs energy per molecule in a high (low) spin state
G_P	conductance of a magnetoresistive device for parallel (antiparallel) configuration of the electrodes' magnetization
GMR	giant magnetoresistance ratio
$\hbar\omega$	vibrational energy
H	magnetic field
ΔH	molar enthalpy variation
k_HL	LIESST relaxation rate constant
μ_B	Bohr magneton
$n = \frac{\Delta E^\mathrm{o}_\mathrm{HL}}{\hbar\omega}$	reduced energy gap (zero-point energy separation in vibrational quanta units)
N	number of molecules in an ensemble
$N_{\uparrow(\downarrow)}$	density of states for majority (minority) electrons at the Fermi level
p	pressure

P	spin polarization
ΔQ_{HL}	horizontal separation of HS and LS potential wells
$\rho_{\mathrm{HS(LS)}}, \gamma_{\mathrm{HS(LS)}}$	high (low) spin proportion
r_{HL}	metal-ligand distance
$R_{\mathrm{P(AP)}}$	resistance of a magnetoresistive device for parallel (antiparallel) configuration of the electrodes' magnetization
S	spin
S_{mix}	mixing entropy
$\Delta S = S_{\mathrm{HS}} - S_{\mathrm{LS}}$	variation of molar entropy
T	temperature
$T_{1/2}$	spin transition temperature
T_{LIESST}	LIESST effect temperature
TMR	tunnel magnetoresistance ratio
ΔU	change of internal energy
$v_{\uparrow(\downarrow)}$	Fermi velocity of majority (minority) electrons
ΔV	variation of a unit cell volume
Δv	volume change of the crystal per one molecule
Δ_{o} $(10Dq)$	ligand/crystal field splitting
$\chi_{\mathrm{(m)}}$	(molar) susceptibility
Z	atomic number

Experimental methods:

A	atomic mass number (mass/mol)
$\boldsymbol{A}$	vector potential of electric field
$A(\theta)$	scattering asymmetry
d	distance
$\mathrm{d}\boldsymbol{q}$	volume element in reciprocal space
$\boldsymbol{e_\lambda}$	photon polarization vector
E	energy
E_{b}	binding energy
E_{pe}	kinetic energy of photoelectron
E_{ro}	electron rest energy
E_{vac}	vacuum level
E_{vb}	electron energy at top of a valence band
$FOM(\epsilon)$	figure of merit (polarimeter efficiency)
g	gyromagnetic factor
$\boldsymbol{G}$	reciprocal lattice vector
$\hbar\omega$	photon energy
$I(\theta)$	isotropic spin-averaged scattered intensity of photoelectrons
$I(E)$	current as a function of incident photon energy
I_{o}	x-ray beam initial intensity
j	total angular momentum quantum number
$\boldsymbol{k}$	photon propagation direction vector
$\boldsymbol{k}^{\mathrm{vac(solid)}}$	electron wave vector in vacuum (solid)

$\kappa_{1(5)}$	tunneling current attenuation coefficient for Δ_1 (Δ_5) symmetry electrons
l	orbital quantum number
$\boldsymbol{L}$	orbital angular momentum
$\lambda(E)$	inelastic mean free path
λ_u	undulator period
λ_x	x-ray attenuation length
m_o	electron rest mass
m_orb	orbital magnetic moment
m_spin	spin magnetic moment
m_j	secondary total angular momentum quantum number
m_s	secondary spin quantum number
μ	mass attenuation coefficient
μ^o	absorption coefficient for x-ray photons with linear polarization
$\mu^{+(-)}$	absorption coefficient for x-ray photons with circular left (right) polarization
μ_x	linear x-ray absorption coefficient
n	principal quantum number
$\hat{\boldsymbol{n}}$	unit vector normal to the surface
n_{3d}	number of electrons in the $3d$ shells
p	pressure
$\boldsymbol{p}$	electron momentum operator
$\boldsymbol{P}$	polarization of scattered photoelectrons
P_circ	degree of circular polarization of photons
Φ	work function
Φ_o	photon flux
$\boldsymbol{r}$	position operator
ρ	density
ρ_a	atomic number density (atoms/volume)
ρ_m	atomic mass density (mass/volume)
$R(E)$	resistance as a function of incident photon energy
$R_{n,l}$	radial part of a spherical harmonic
s	spin quantum number
$S(\theta)$	asymmetry Sherman function
S_eff	effective Sherman function
$\langle S_z \rangle$	expectation value of the z-component of spin
σ_a	absorption cross section
σ_s	scattering cross section
$\gamma(v)$	Lorentz factor
$\langle T_z \rangle$	expectation value of the magnetic dipole operator
V	bias voltage
V_SO	spin-orbit potential
W	number of absorption events per second
Z	atomic number

Metal/organic interface: magnetic ordering and spin polarization:

A_1, A_2	amplitude of IEC oscillations
d_{Cu}	thickness of Cu spacer
E_{MCA}	magnetocrystalline anisotropy energy
$\Delta E = E_{\mathrm{P}} - E_{\mathrm{AP}}$	exchange energy, *i.e.*, the difference of IEC system energy for parallel and antiparallel configuration of the FM layers
H	magnetic field
H_{eff}	effective magnetic field
H_{ex}	exchange field
H_{ext}	external magnetic field
H_{IEC}	IEC related exchange field
J	exchange energy
J_{IEC}	interlayer exchange coupling strength
Λ_1, Λ_2	long and short IEC oscillations periodicity
μ_{mol}	average molecular magnetic moment
P	spin polarization
Φ	phase shift
T	temperature
T_{B}	blocking temperature
T_{c}	Curie temperature

Ferroelectric control over metal/organic spinterface:

α_{s}	magnetoelectric coupling strength
E_{c}	coercive field
H	magnetic field
I	current
ΔM	induced surface magnetic moment
P	electric polarization
T	temperature
t_{r}	rise time
t_{s}	separation time
V	bias voltage

Towards spin crossover based multifunctional device:

A	pre-exponential factor related to charge transfer rate
$\mathrm{d}T$	temperature step
d	distance
E_{a}	energy barrier height
$G_{\mathrm{HS(LS)}}$	conductance of high (low) spin state molecule
$I_{\mathrm{ON(OFF)}}$	current across the junction in presence (absence) of light
J	current density
k_1, k_2	photoexcitation and relaxation rate constants

λ	wavelength
$Q = 2\pi l/d$	peak position in diffracted vector notation
R	resistance
R_{SCMR}	spin crossover magnetoresistance
$s = V_{\mathrm{mol}}/d$	transverse area of a molecule
$\sigma_{\mathrm{C}_{12}}$	transverse section of an alkyl chain
σ_{core}	transverse section of a molecular core
T	temperature
$T_{1/2}$	spin transition temperature
T_{sublim}	sublimation temperature
τ	time constant
τk_1	saturation level
V_{mol}	volume of a single molecule
χ_m	molar magnetic susceptibility

Bibliography

[1] G. E. Moore. Cramming more components onto integrated circuits. *IEEE Solid-State Circuits Newsletter*, 20(3): 33–35, 2006.

[2] C. A. Mack. Fifty Years of Moore's Law. *IEEE Transactions on Semiconductor Manufacturing*, 24(2): 202–207, 2011.

[3] E. Mollick. Establishing Moore's Law. *IEEE Annals of the History of Computing*, 28(3): 62–75, 2006.

[4] R. W. Keyes. Fundamental Limits of Silicon Technology. *Proceedings of the IEEE*, 89(3): 227–239, 2001.

[5] K. J. Kuhn. Moore's law past 32nm: Future challenges in device scaling. *Proceedings to 13th International Workshop on Computational Electronics*, pp. 1–4, 2009.

[6] I. Žutić, J. Fabian, and S. Das Sarma. Spintronics: Fundamentals and applications. *Reviews of Modern Physics*, 76(2): 323–410, 2004.

[7] G.-X. Miao, M. Münzenberg, and J. S. Moodera. Tunneling path toward spintronics. *Reports on Progress in Physics*, 74(3): 036501, 2011.

[8] S. Sanvito. Organic electronics: Spintronics goes plastic. *Nature Materials*, 6(11): 803–804, 2007.

[9] J. Camarero and E. Coronado. Molecular vs. inorganic spintronics: the role of molecular materials and single molecules. *Journal of Materials Chemistry*, 19: 1678, 2009.

[10] F. Schleicher, U. Halisdemir, D. Lacour, M. Gallart, S. Boukari, G. Schmerber, V. Davesne, P. Panissod, D. Halley, H. Majjad, Y. Henry, B. Leconte, A. Boulard, D. Spor, N. Beyer, C. Kieber, E. Sternitzky, O. Cregut, M. Ziegler, F. Montaigne, E. Beaurepaire, P. Gilliot, M. Hehn, and M. Bowen. Localized states in advanced dielectrics from the vantage of spin- and symmetry-polarized tunnelling across MgO. *Nature Communications*, 5: 4547, 2014.

[11] F. Schleicher. *Impact of structural defects on spin-polarized transport across magnetic tunnel junctions*. Ph.D. thesis, University of Strasbourg, 2012.

[12] C. H. Shang, J. Nowak, R. Jansen, and J. S. Moodera. Temperature dependence of magnetoresistance and surface magnetization in ferromagnetic tunnel junctions. *Physical Review B*, 58(6): R2917–R2920, 1998.

[13] E. Coronado and P. Day. Magnetic Molecular Conductors. *Chemical Reviews*, 104(11): 5419–5448, 2004.

[14] M. M. Matsushita, H. Kawakami, T. Sugawara, and M. Ogata. Molecule-based system with coexisting conductivity and magnetism and without magnetic inorganic ions. *Physical Review B*, 77(19): 1–6, 2008.

[15] M. Castellano, R. Ruiz-García, J. Cano, J. Ferrando-Soria, E. Pardo, F. R. Fortea-Pérez, S.-E. Stiriba, W. P. Barros, H. O. Stumpf, L. Cañadillas-Delgado, J. Pasán, C. Ruiz-Pérez, G. de Munno, D. Armentano, Y. Journaux, F. Lloret, and M. Julve. Metallosupramolecular approach toward multifunctional magnetic devices for molecular spintronics. *Coordination Chemistry Reviews*, 303: 110–138, 2015.

[16] A. B. Gaspar, V. Ksenofontov, M. Seredyuk, and P. Gütlich. Multifunctionality in spin crossover materials. *Coordination Chemistry Reviews*, 249(23): 2661–2676, 2005.

[17] M. Gruber. *Electronic and magnetic properties of hybrid interfaces. From single molecules to ultra-thin molecular films on metallic substrates.* Ph.D. thesis, Université de Strasbourg, 2014.

[18] K. W. Hipps. It's All About Contacts. *Science*, 294(5542): 536–537, 2001.

[19] S. Sanvito. Organic electronics: Spintronics goes plastic. *Nature Materials*, 6: 803–804, 2007.

[20] F. Djeghloul, F. Ibrahim, M. Cantoni, and M. Bowen. Direct observation of a highly spin-polarized organic spinterface at room temperature. *Scientific Reports*, 3: 1272, 2013.

[21] M. Gruber, F. Ibrahim, S. Boukari, H. Isshiki, L. Joly, M. Peter, M. Studniarek, V. Da Costa, H. Jabbar, V. Davesne, U. Halisdemir, J. Chen, J. Arabski, E. Otero, F. Choueikani, K. Chen, P. Ohresser, W. Wulfhekel, F. Scheurer, W. Weber, M. Alouani, E. Beaurepaire, and M. Bowen. Exchange bias and room-temperature magnetic order in molecular layers. *Nature Materials*, 14(10): 981–984, 2015.

[22] T. Miyamachi, M. Gruber, V. Davesne, M. Bowen, S. Boukari, L. Joly, F. Scheurer, G. Rogez, T. K. Yamada, P. Ohresser, E. Beaurepaire, and W. Wulfhekel. Robust spin crossover and memristance across a single molecule. *Nature Communications*, 3(938), 2012.

[23] W. Weber, R. Allenspach, and A. Bischof. Exchange Coupling Across Cu(100): a High-Precision Study. *Europhysics Letters*, 32(4): 379–379, 1995.

[24] Z. Q. Qiu and N. V. Smith. Quantum well states and oscillatory magnetic interlayer coupling. *Journal of Physics: Condensed Matter*, 14(8): R169–R193, 2002.

[25] C. Würsch, C. Stamm, and S. Egger. Quantum oscillations in a confined electron gas. *Nature*, 389: 937–939, 1997.

[26] F. Djeghloul, G. Garreau, M. Gruber, L. Joly, S. Boukari, J. Arabski, H. Bulou, F. Scheurer, A. Hallal, F. Bertran, P. Le Fèvre, A. Taleb-Ibrahimi, W. Wulfhekel, E. Beaurepaire, S. Hajjar-Garreau, P. Wetzel, M. Bowen, and W. Weber. Highly spin-polarized carbon-based spinterfaces. *Carbon*, 87: 269–274, 2015.

[27] T. Schwieger, H. Peisert, M. S. Golden, M. Knupfer, and J. Fink. Electronic structure of the organic semiconductor copper phthalocyanine and K-CuPc studied using photoemission spectroscopy. *Physical Review B*, 66(15): 155207, 2002.

[28] O. Vlašín, R. Jarrier, R. Arras, L. Calmels, B. Warot-Fonrose, C. Marcelot, M. Jamet, P. Ohresser, F. Scheurer, R. Hertel, G. Herranz, and S. Cherifi Hertel. Interface Magnetoelectric Coupling in Co/Pb(Zr,Ti)O_3. *ACS Applied Materials & Interfaces*, 11(8): 7553–7563, 2016.

[29] E. Arenholz, G. van der Laan, a. Fraile-Rodríguez, P. Yu, Q. He, and R. Ramesh. Probing ferroelectricity in $PbZr_{0.2}Ti_{0.8}O_3$ with polarized soft x rays. *Physical Review B*, (14): 140103.

[30] S. Javaid, M. Bowen, S. Boukari, L. Joly, J.-B. Beaufrand, X. Chen, Y. J. Dappe, F. Scheurer, J.-P. Kappler, J. Arabski, W. Wulfhekel, M. Alouani, and E. Beaurepaire. Impact on interface spin polarization of molecular bonding to metallic surfaces. *Physical Review Letters*, 105(7): 077201, 2010.

[31] V. Davesne. *Organic Spintronics: An Investigation on Spin-Crossover Complexes from Isolated Molecules to the Device.* Ph.D. thesis, Université de Strasbourg, 2013.

[32] T. Palamarciuc, J. C. Oberg, F. El Hallak, C. F. Hirjibehedin, M. Serri, S. Heutz, J.-F. Létard, and P. Rosa. Spin crossover materials evaporated under clean high vacuum and ultra-high vacuum conditions: from thin films to single molecules. *Journal of Materials Chemistry*, 22(19): 9690, 2012.

[33] L. Joly, B. Muller, E. Sternitzky, J.-G. Faullumel, A. Boulard, E. Otero, F. Choueikani, J.-P. Kappler, M. Studniarek, M. Bowen, and P. Ohresser. Versatile variable temperature insert at the DEIMOS beamline for in situ electrical transport measurements. *Journal of Synchrotron Radiation*, 23(3): 652–657, 2016.

[34] M. Bowen, J.-L. Maurice, A. Barthélémy, P. Prod'homme, E. Jacquet, J.-P. Contour, D. Imhoff, and C. Colliex. Bias-crafted magnetic tunnel junctions with bistable spin-dependent states. *Applied Physics Letters*, 89(10): 103517, 2006.

[35] F. M. F. de Groot, M. Grioni, J. C. Fuggle, J. Ghijsen, G. A. Sawatzky, and H. Petersen. Oxygen 1s x-ray-absorption edges of transition-metal osxides. *Physical Review B*, 40(8): 5715–5723, 1989.

[36] C. Martinez-Boubeta, L. Balcells, and B. Martínez. On the changes at the Fe/MgO interface upon annealing. *Journal of Applied Physics*, 113(12): 123908, 2013.

[37] D. Telesca, B. Sinkovic, S.-H. Yang, and S. S. P. Parkin. X-ray studies of interface Fe-oxide in annealed MgO based magnetic tunneling junctions. *Journal of Electron Spectroscopy and Related Phenomena*, 185(5–7): 133–139, 2012.

[38] D. S. Urch. Soft X-ray spectroscopy. *Journal de Physique III*, 4(9): 1613–1623, 1994.

[39] International Technology Roadmap for Semiconductors 2.0: Executive Report. *Tech. rep.*, 2015.

[40] S. T. S. Portal. Consumer Electronics Worldwide. `https://www.statista.com/outlook/251/100/consumer-electronics/worldwide#market-revenue`. [Accessed 9 August 2016].

[41] D. A. Thompson and J. S. Best. The future of magnetic data storage techology. *IBM Journal of Research and Development*, 44(3): 311–322, 2000.

[42] S. A. Wolf, D. D. Awschalom, R. A. Buhrman, J. M. Daughton, S. von Molnár, M. L. Roukes, A. Y. Chtchelkanova, and D. M. Treger. Spintronics: a spin-based electronics vision for the future. *Science*, 294(5546): 1488–95, 2001.

[43] M. N. Baibich, J. M. Broto, A. Fert, F. N. Van Dau, F. Petroff, P. Etienne, G. Creuzet, A. Friederich, and J. Chazelas. Giant Magnetoresistance of (001)Fe/(001)Cr Magnetic Superlattices. *Physical Review Letters*, 61(21): 2472–2475, 1988.

[44] G. Binasch, P. Grünberg, F. Saurenbach, and W. Zinn. Enhanced magnetoresistance in layered magnetic structures with antiferromagnetic interlayer exchange. *Physical Review B*, 39(7): 4828–4830, 1989.

[45] N. F. Mott. The Electrical Conductivity of Transition Metals. *Proceedings of the Royal Society A: Mathematical, Physical and Engineering Sciences*, 153(880): 699–717, 1936.

[46] A. Fert. The present and the future of spintronics. *Thin Solid Films*, 517(1): 2–5, 2008.

[47] A. Fert. Origin, Development, and Future of Spintronics (Nobel Lecture). *Angewandte Chemie International Edition*, 47(32): 5956–5967, 2008.

[48] M. Julliere. Tunneling between ferromagnetic films. *Physics Letters A*, 54(3): 225–226, 1975.

[49] J. S. Moodera, L. R. Kinder, T. M. Wong, and R. Meservey. Large Magnetoresistance at Room Temperature in Ferromagnetic Thin Film Tunnel Junctions. *Physical Review Letters*, 74(16): 3273–3276, 1995.

[50] T. Miyazaki and N. Tezuka. Giant magnetic tunneling effect in Fe/Al_2O_3/Fe junction. *Journal of Magnetism and Magnetic Materials*, 139(3): L231–L234, 1995.

[51] D. Wang, C. Nordman, J. Daughton, Z. Qian, J. Fink, D. Wang, C. Nordman, J. Daughton, Z. Qian, and J. Fink. 70% TMR at Room Temperature for SDT Sandwich Junctions With CoFeB as Free and Reference Layers. *IEEE Transactions on Magnetics*, 40(4): 2269–2271, 2004.

[52] J. Mathon and A. Umerski. Theory of tunneling magnetoresistance of an epitaxial Fe/MgO/Fe(001) junction. *Physical Review B*, 63(22): 220403, 2001.

[53] S. Yuasa, T. Nagahama, A. Fukushima, Y. Suzuki, and K. Ando. Giant room-temperature magnetoresistance in single-crystal Fe/MgO/Fe magnetic tunnel junctions. *Nature Materials*, 3(12): 868–871, 2004.

[54] S. S. P. Parkin, C. Kaiser, A. Panchula, P. M. Rice, B. Hughes, M. Samant, and S.-H. Yang. Giant tunnelling magnetoresistance at room temperature with MgO (100) tunnel barriers. *Nature Materials*, 3(12): 862–867, 2004.

[55] P. M. Tedrow and R. Meservey. Spin-Dependent Tunneling into Ferromagnetic Nickel. *Physical Review Letters*, 26(4): 192–195, 1971.

[56] J. M. D. Coey and S. Sanvito. Magnetic semiconductors and half-metals. *Journal of Physics D: Applied Physics*, 37(7): 988–993, 2004.

[57] R. A. de Groot, F. M. Mueller, P. G. van Engen, and K. H. J. Buschow. New Class of Materials: Half-Metallic Ferromagnets. *Physical Review Letters*, 50(25): 2024–2027, 1983.

[58] J. M. D. Coey and M. Venkatesan. Half-metallic ferromagnetism: Example of CrO_2. *Journal of Applied Physics*, 91(10): 8345, 2002.

[59] D. J. Monsma and S. S. P. Parkin. Temporal evolution of spin polarization in ferromagnetic tunnel junctions. *Applied Physics Letters*, 77(6): 883, 2000.

[60] J. S. Moodera and G. Mathon. Spin polarized tunneling in ferromagnetic junctions. *Journal of Magnetism and Magnetic Materials*, 200(1-3): 248–273, 1999.

[61] I. I. Mazin. How to Define and Calculate the Degree of Spin Polarization in Ferromagnets. *Physical Review Letters*, 83(7): 1427–1430, 1999.

[62] E. Y. Tsymbal and D. G. Pettifor. Modelling of spin-polarized electron tunnelling from 3d ferromagnets. *Journal of Physics: Condensed Matter*, 9(30): L411–L417, 1999.

[63] I. I. Oleinik, E. Y. Tsymbal, and D. G. Pettifor. Structural and electronic properties of Co/Al_2O_3/Co magnetic tunnel junction from first principles. *Physical Review B*, 62(6): 3952–3959, 2000.

[64] J. M. De Teresa. Role of Metal-Oxide Interface in Determining the Spin Polarization of Magnetic Tunnel Junctions. *Science*, 286(5439): 507–509, 1999.

[65] W. H. Butler, X.-G. Zhang, T. C. Schulthess, and J. M. MacLaren. Spin-dependent tunneling conductance of Fe|MgO|Fe sandwiches. *Phys. Rev. B*, 63: 054416, 2001.

[66] J.-G. J. Zhu and C. Park. Magnetic tunnel junctions. *Materials Today*, 9(11): 36–45, 2006.

[67] W. Digital. 2008 Annual Report and Form 10-K. *Tech. rep.*, 2008.

[68] A. Aviram and M. A. Ratner. Molecular rectifiers. *Chemical Physics Letters*, 29(2): 277–283, 1974.

[69] R. H. Friend, R. W. Gymer, A. B. Holmes, J. H. Burroughes, R. Marks, C. Taliani, D. D. C. Bradley, D. A. Dos Santos, J. L. Bredas, M. Logdlund, and W. R. Salaneck. Electroluminescence in conjugated polymers. *Nature*, 397: 121–128, 1999.

[70] V. I. Krinichnyi, S. D. Chemerisov, and Y. S. Lebedev. EPR and charge-transport studies of polyaniline. *Physical Review B*, 55(24): 16233–16244, 1997.

[71] S. Pramanik, C.-G. Stefanita, S. Patibandla, S. Bandyopadhyay, K. Garre, N. Harth, and M. Cahay. Observation of extremely long spin relaxation times in an organic nanowire spin valve. *Nature Nanotechnology*, 2(4): 216–219, 2007.

[72] V. Dediu, M. Murgia, F. Matacotta, C. Taliani, and S. Barbanera. Room temperature spin polarized injection in organic semiconductor. *Solid State Communications*, 122(3): 181–184, 2002.

[73] K. Tsukagoshi, B. W. Alphenaar, and H. Ago. Coherent transport of electron spin in a ferromagnetically contacted carbon nanotube. *Nature*, 401(6753): 572–574, 1999.

[74] S. Majumdar, H. S. Majumdar, R. Laiho, and R. Österbacka. Organic spin valves: effect of magnetic impurities on the spin transport properties of polymer spacers. *New Journal of Physics*, 11(1): 013022, 2009.

[75] V. A. Dediu, L. E. Hueso, I. Bergenti, and C. Taliani. Spin routes in organic semiconductors. *Nature Materials*, 8(10): 707–716, 2009.

[76] G. Szulczewski, S. Sanvito, and M. Coey. A spin of their own. *Nature Materials*, 8(9): 693–695, 2009.

[77] D. Sun, E. Ehrenfreund, and Z. Valy Vardeny. The first decade of organic spintronics research. *Chemical Communications*, 50(15): 1781, 2014.

[78] S. Sanvito and V. A. Dediu. Spintronics: News from the organic arena. *Nature Nanotechnology*, 7(11): 696–697, 2012.

[79] Z. H. Xiong, D. Wu, Z. V. Vardeny, and J. Shi. Giant magnetoresistance in organic spin-valves. *Nature*, 427(6977): 821–824, 2004.

[80] C. Barraud, P. Seneor, R. Mattana, S. Fusil, K. Bouzehouane, C. Deranlot, P. Graziosi, L. Hueso, I. Bergenti, V. Dediu, F. Petroff, and A. Fert. Unravelling the role of the interface for spin injection into organic semiconductors. *Nature Physics*, 6(8): 615–620, 2010.

[81] A. Riminucci, I. Bergenti, L. E. Hueso, M. Murgia, C. Taliani, Y. Zhan, F. Casoli, M. P. de Jong, and V. Dediu. Negative Spin Valve effects in manganite/organic based devices. *eprint arXiv:cond-mat/0701603*, 2007.

[82] V. Dediu, L. E. Hueso, I. Bergenti, A. Riminucci, F. Borgatti, P. Graziosi, C. Newby, F. Casoli, M. P. De Jong, C. Taliani, and Y. Zhan. Room-temperature spintronic effects in Alq3-based hybrid devices. *Physical Review B*, 78(11): 115203, 2008.

[83] T. S. Santos, J. S. Lee, P. Migdal, I. C. Lekshmi, B. Satpati, and J. S. Moodera. Room-Temperature Tunnel Magnetoresistance and Spin-Polarized Tunneling through an Organic Semiconductor Barrier. *Physical Review Letters*, 98(1): 016601, 2007.

[84] A. R. Rocha, V. M. García-suárez, S. W. Bailey, C. J. Lambert, J. Ferrer, and S. Sanvito. Towards molecular spintronics. *Nature Materials*, 4(4): 335–339, 2005.

[85] S. Sanvito. Molecular spintronics: The rise of spinterface science. *Nature Physics*, 6(8): 562–564, 2010.

[86] Y. Q. Zhan, M. P. De Jong, F. H. Li, V. Dediu, M. Fahlman, and W. R. Salaneck. Energy level alignment and chemical interaction at $\mathrm{Alq_3}$/Co interfaces for organic spintronic devices. *Physical Review B*, 78(4): 045208, 2008.

[87] Y. Q. Zhan, I. Bergenti, L. E. Hueso, V. Dediu, M. P. de Jong, and Z. S. Li. Alignment of energy levels at the $\mathrm{Alq_3/La_{0.7}Sr_{0.3}MnO_3}$ interface for organic spintronic devices. *Physical Review B*, 76(4): 045406, 2007.

[88] S. Schmaus, A. Bagrets, Y. Nahas, T. K. Yamada, A. Bork, M. Bowen, E. Beaurepaire, F. Evers, and W. Wulfhekel. Giant magnetoresistance through a single molecule. *Nature Nanotechnology*, 6(3): 185–9, 2011.

[89] N. Atodiresei, J. Brede, P. Lazić, V. Caciuc, G. Hoffmann, R. Wiesendanger, and S. Blügel. Design of the Local Spin Polarization at the Organic-Ferromagnetic Interface. *Physical Review Letters*, 105(6): 066601, 2010.

[90] T. Dietl. Ferromagnetic semiconductors. *Semiconductor Science and Technology*, 17(4): 377–392, 2002.

[91] K. V. Raman, A. M. Kamerbeek, A. Mukherjee, N. Atodiresei, T. K. Sen, P. Lazić, V. Caciuc, R. Michel, D. Stalke, S. K. Mandal, S. Blügel,

M. Münzenberg, and J. S. Moodera. Interface-engineered templates for molecular spin memory devices. *Nature*, 493(7433): 509–513, 2013.

[92] H. Ma, H.-L. Yip, F. Huang, and A. K.-Y. Jen. Interface Engineering for Organic Electronics. *Advanced Functional Materials*, 20(9): 1371–1388, 2010.

[93] R. Pang, X. Shi, and M. A. Van Hove. Manipulating Magnetism at Organic/Ferromagnetic Interfaces by Molecule-Induced Surface Reconstruction. *Journal of the American Chemical Society*, 138(12): 4029–4035, 2016.

[94] M. Galbiati, S. Tatay, C. Barraud, A. V. Dediu, F. Petroff, R. Mattana, and P. Seneor. Spinterface: Crafting spintronics at the molecular scale. *MRS Bulletin*, 39(07): 602–607, 2014.

[95] M. Cinchetti, K. Heimer, J.-P. Wüstenberg, O. Andreyev, M. Bauer, S. Lach, C. Ziegler, Y. Gao, and M. Aeschlimann. Determination of spin injection and transport in a ferromagnet/organic semiconductor heterojunction by two-photon photoemission. *Nature Materials*, 8(2): 115–119, 2009.

[96] P. K. J. Wong, W. Zhang, G. Van Der Laan, and M. P. De Jong. Hybridization-induced charge rebalancing at the weakly interactive $C_{60}/Fe_3O_4(001)$ spinterface. *Organic Electronics*, 29: 39–43, 2016.

[97] A. J. Drew, J. Hoppler, L. Schulz, F. L. Pratt, P. Desai, P. Shakya, T. Kreouzis, W. P. Gillin, A. Suter, N. A. Morley, V. K. Malik, A. Dubroka, K. W. Kim, H. Bouyanfif, F. Bourqui, C. Bernhard, R. Scheuermann, G. J. Nieuwenhuys, T. Prokscha, and E. Morenzoni. Direct measurement of the electronic spin diffusion length in a fully functional organic spin valve by low-energy muon spin rotation. *Nature Materials*, 8(2): 109–114, 2009.

[98] F. Djeghloul, M. Gruber, E. Urbain, D. Xenioti, L. Joly, S. Boukari, J. Arabski, H. Bulou, F. Scheurer, F. Bertran, P. Le Fèvre, A. Taleb-Ibrahimi, W. Wulfhekel, G. Garreau, S. Hajjar-Garreau, P. Wetzel, M. Alouani, E. Beaurepaire, M. Bowen, and W. Weber. High Spin Polarization at Ferromagnetic Metal–Organic Interfaces: A Generic Property. *The Journal of Physical Chemistry Letters*, 7(13): 2310–2315, 2016.

[99] Y. Huai, F. Albert, P. Nguyen, M. Pakala, and T. Valet. Observation of spin-transfer switching in deep submicron-sized and low-resistance magnetic tunnel junctions. *Applied Physics Letters*, 84(16): 3118, 2004.

[100] P. Němec, E. Rozkotová, N. Tesařová, F. Trojánek, E. De Ranieri, K. Olejník, J. Zemen, V. Novák, M. Cukr, P. Malý, and T. Jungwirth. Experimental observation of the optical spin transfer torque. *Nature Physics*, 8(5): 411–415, 2012.

[101] J. C. Slonczewski. Initiation of spin-transfer torque by thermal transport from magnons. *Physical Review B*, 82(5): 054403, 2010.

[102] H. Yu, S. Granville, D. P. Yu, and J.-P. Ansermet. Evidence for Thermal Spin-Transfer Torque. *Physical Review Letters*, 104(14): 146601, 2010.

[103] A. M. Deac, A. Fukushima, H. Kubota, H. Maehara, Y. Suzuki, S. Yuasa, Y. Nagamine, K. Tsunekawa, D. D. Djayaprawira, and N. Watanabe. Bias-driven high-power microwave emission from MgO-based tunnel magnetoresistance devices. *Nature Physics*, 4(10): 803–809, 2008.

[104] Y. Huai. Spin-Transfer Torque MRAM (STT-MRAM): Challenges and Prospects. *AAPPS bulletin*, 18(6): 33–40, 2008.

[105] J. M. Lee, Y. B. Pyun, J. Yi, J. W. Choung, and W. I. Park. ZnO Nanorod-Graphene Hybrid Architectures for Multifunctional Conductors. *The Journal of Physical Chemistry C*, 113(44): 19134–19138, 2009.

[106] G. Xing, D. Wang, J. Yi, L. Yang, M. Gao, M. He, J. Yang, J. Ding, T. C. Sum, and T. Wu. Correlated d_0 ferromagnetism and photoluminescence in undoped ZnO nanowires. *Applied Physics Letters*, 96(11): 112511, 2010.

[107] M. Bibes and A. Barthelemy. Oxide Spintronics. *IEEE Transactions on Electron Devices*, 54(5): 1003–1023, 2007.

[108] K.-j. Jin, H.-b. Lu, K. Zhao, C. Ge, M. He, and G.-z. Yang. Novel Multifunctional Properties Induced by Interface Effects in Perovskite Oxide Heterostructures. *Advanced Materials*, 21(45): 4636–4640, 2009.

[109] M. Gajek, M. Bibes, S. Fusil, K. Bouzehouane, J. Fontcuberta, A. Barthélémy, and A. Fert. Tunnel junctions with multiferroic barriers. *Nature Materials*, 6(4): 296–302, 2007.

[110] A. Crha, R. Růžička, and V. Šimek. Novel Approach To Synthesis of Logic Circuits Based on Multifunctional Components. *Journal of Electrical Engineering*, 67(1): 29–35, 2016.

[111] M. Prezioso, A. Riminucci, I. Bergenti, P. Graziosi, D. Brunel, and V. A. Dediu. Electrically Programmable Magnetoresistance in Multifunctional Organic-Based Spin Valve Devices. *Advanced Materials*, 23(11): 1371–1375, 2011.

[112] B. Averill and P. Eldredge. *General chemistry: principles, patterns, and applications*. 2011.

[113] H. A. Bethe. Splitting of Terms in Crystals. *Annalen der Physik*, 3: 133–206, 1929.

[114] H. A. Jahn and E. Teller. Stability of Polyatomic Molecules in Degenerate Electronic States. I. Orbital Degeneracy. *Proceedings of the Royal Society of London A*, 161(905): 220–235, 1937.

[115] Y. Tanabe and S. Sugano. On the Absorption Spectra of Complex Ions. I. *Journal of the Physical Society of Japan*, 9(5): 753–766, 1954.

[116] M. Womes, J.-C. Jumas, J. Olivier-Fourcade, F. Aubertin, U. Gonser. High spin ($^5T_2$)- low spin ($^1A_1$) equilibrium of iron(II) in $M_2FeSn_3S_8$ thiospinels (M = Cu, Ag). *Chemical Physics Letters*, 201(January): 555–558, 1993.

[117] W. R. Scheidt and C. A. Reed. Spin-state/stereochemical relationships in iron porphyrins: implications for the hemoproteins. *Chemical Reviews*, 81(6): 543–555, 1981.

[118] L. Cambi and L. Szegö. Über die magnetische Susceptibilität der komplexen Verbindungen. *Berichte der deutschen chemischen Gesellschaft (A and B Series)*, 64(10): 2591–2598, 1931.

[119] M. A. Halcrow. *Spin-crossover materials: properties and applications.* John Wiley & Sons, 2013.

[120] P. Gütlich and H. Goodwin. *Spin Crossover in Transition Metal Compounds II.* Springer-Verlag, 2004.

[121] P. J. van Koningsbruggen, H. Oshio, Y. Maeda, P. J. Koningsbruggen, Y. Maeda, and H. Oshio. Iron(III) Spin Crossover Compounds. In: *Spin Crossover in Transition Metal Compounds I*, pp. 259–324. Springer-Verlag, 2004.

[122] P. Gütlich and H. Goodwin. Spin Crossover—An Overall Perspective. In: *Spin Crossover in Transition Metal Compounds I*, pp. 1–47. Springer Berlin Heidelberg, Berlin, Heidelberg, 2004.

[123] A. Bousseksou, G. Molnár, L. Salmon, and W. Nicolazzi. Molecular spin crossover phenomenon: recent achievements and prospects. *Chemical Society Reviews*, 40(6): 3313, 2011.

[124] A. Hauser. Light-Induced Spin Crossover and the High-Spin → Low-Spin Relaxation. In: *Spin Crossover in Transition Metal Compounds II*, pp. 155–198. Springer-Verlag, 2004.

[125] N. Moliner, M. Muñoz, S. Létard, J.-F. Létard, X. Solans, R. Burriel, M. Castro, O. Kahn, and J. A. Real. Spin-crossover in the $[Fe(abpt)_2(NCX)_2]$ (X=S, Se) system: structural, magnetic, calorimetric and photomagnetic studies. *Inorganica Chimica Acta*, 291(1-2): 279–288, 1999.

[126] V. Davesne, M. Gruber, M. Studniarek, W. H. Doh, S. Zafeiratos, L. Joly, F. Sirotti, M. G. Silly, a. B. Gaspar, J. a. Real, G. Schmerber, M. Bowen, W. Weber, S. Boukari, V. Da Costa, J. Arabski, W. Wulfhekel, and E. Beaurepaire. Hysteresis and change of transition temperature in thin films of $Fe[Me_2Pyrz]_3BH_2$, a new sublimable spin-crossover molecule. *The Journal of Chemical Physics*, 142(19): 194702, 2015.

[127] H. Naggert, J. Rudnik, L. Kipgen, M. Bernien, F. Nickel, L. M. Arruda, W. Kuch, C. Näther, and F. Tuczek. Vacuum-evaporable spin-crossover complexes: physicochemical properties in the crystalline bulk and in thin films deposited from the gas phase. *Journal of Materials Chemistry C*, 3(30): 7870–7877, 2015.

[128] W. Morscheidt, J. Jeftic, E. Codjovi, J. Linares, A. Bousseksou, H. Constant-Machado, and F. Varret. Optical detection of the spin transition by reflectivity. *Measurement Science and Technology*, 9(8): 1311–1315, 1998.

[129] B. Warner, J. C. Oberg, T. G. Gill, F. El Hallak, C. F. Hirjibehedin, M. Serri, S. Heutz, M.-A. Arrio, P. Sainctavit, M. Mannini, G. Poneti, R. Sessoli, and P. Rosa. Temperature- and Light-Induced Spin Crossover Observed by X-ray Spectroscopy on Isolated Fe(II) Complexes on Gold. *The Journal of Physical Chemistry Letters*, 4(9): 1546–1552, 2013.

[130] M. Bernien, D. Wiedemann, C. F. Hermanns, A. Krüger, D. Rolf, W. Kroener, P. Müller, A. Grohmann, and W. Kuch. Spin Crossover in a Vacuum-Deposited Submonolayer of a Molecular Iron(II) Complex. *The Journal of Physical Chemistry Letters*, 3(23): 3431–3434, 2012.

[131] J. P. Jesson. Direct Mössbauer Observation of the $^5T_2$—$^1A_1$ Crossover in an Octahedral Ferrous System. *The Journal of Chemical Physics*, 46(5): 1995, 1967.

[132] T. Granier, B. Gallois, J. Gaultier, J. A. Real, and J. Zarembowitch. High-pressure single-crystal x-ray diffraction study of two spin-crossover iron (II) complexes: $Fe(Phen)_2(NCS)_2$ and $Fe(Btz)_2(NCS)_2$. *Inorganic Chemistry*, 32(23): 5305–5312, 1993.

[133] K. Bairagi, O. Iasco, A. Bellec, A. Kartsev, D. Li, J. Lagoute, C. Chacon, Y. Girard, S. Rousset, F. Miserque, Y. J. Dappe, A. Smogunov, C. Barreteau, M.-L. Boillot, T. Mallah, and V. Repain. Molecular-scale dynamics of light-induced spin cross-over in a two-dimensional layer. *Nature Communications*, 7(12212), 2016.

[134] J.-P. Martin, J. Zarembowitch, A. Bousseksou, A. Dworkin, J. G. Haasnoot, and F. Varret. Solid State Effects on Spin Transitions: Magnetic, Calorimetric, and Moessbauer-Effect Properties of $[Fe_xCo_{1-x}(4,4'\text{-bis-}1,2,4\text{-triazole})_2(NCS)_2]\cdot H_2O$ Mixed-Crystal Compounds. *Inorganic Chemistry*, 33(26): 6325–6333, 1994.

[135] E. König. Nature and dynamics of the spin-state interconversion in metal complexes. In: *Structure and Bonding*, pp. 51–152. Springer-Verlag, 1991.

[136] M. Sorai and S. Seki. Phonon coupled cooperative low-spin $^1A_1 \rightleftharpoons$ high-spin $^5T_2$ transition in $[Fe(phen)_2(NCS)_2]$ and $[Fe(phen)_2(NCSe)_2]$ crystals. *Journal of Physics and Chemistry of Solids*, 35(4): 555–570, 1974.

[137] P. Gütlich, A. Hauser, and H. Spiering. Thermal and Optical Switching of Iron(II) Complexes. *Angewandte Chemie International Edition in English*, 33(20): 2024–2054, 1994.

[138] M. Sorai. *Heat Capacity Studies of Spin Crossover Systems*. Springer-Verlag, 2004.

[139] H. Spiering, E. Meissner, H. Köppen, E. Müller, and P. Gütlich. The effect of the lattice expansion on high spin ↔ low spin transitions. *Chemical Physics*, 68(1-2): 65–71, 1982.

[140] C. P. Slichter and H. G. Drickamer. Pressure-Induced Electronic Changes in Compounds of Iron. *The Journal of Chemical Physics*, 56(5): 2142–2160, 1972.

[141] H. Banerjee, M. Kumar, and T. Saha-Dasgupta. Cooperativity in spin-crossover transition in metalorganic complexes: Interplay of magnetic and elastic interactions. *Physical Review B*, 90(17): 174433, 2014.

[142] M. Kepenekian, B. L. Guennic, and V. Robert. Primary Role of the Electrostatic Contributions in a Rational Growth of Hysteresis Loop in Spin-Crossover Fe(II) Complexes. *Journal of the American Chemical Society*, 131(32): 11498–11502, 2009.

[143] F. Renz, H. Spiering, H. A. Goodwin, and P. Gütlich. Light-perturbed hysteresis in an iron(II) spin-crossover compound observed by the Mössbauer effect. *Hyperfine Interactions*, 126(1-4): 155–158, 2000.

[144] P. Gütlich, Y. Garcia, and H. Goodwin. Spin crossover phenomena in Fe(II) complexes. *Chemical Society Reviews*, 29(6): 419–427, 2000.

[145] K. Senthil Kumar, I. Šalitroš, B. Heinrich, O. Fuhr, and M. Ruben. A charge neutral iron(II) complex with an above room temperature spin crossover (SCO) and hysteresis loop. *Journal of Materials Chemistry C*, 3(44): 11635–11644, 2015.

[146] S. Cobo, G. Molnár, J. A. Real, and A. Bousseksou. Multilayer Sequential Assembly of Thin Films That Display Room-Temperature Spin Crossover with Hysteresis. *Angewandte Chemie International Edition*, 45(35): 5786–5789, 2006.

[147] Y. Garcia, P. J. van Koningsbruggen, E. Codjovi, R. Lapouyade, O. Kahn, and L. Rabardel. Non-classical Fe^{II} spin-crossover behaviour leading to an unprecedented extremely large apparent thermal hysteresis of 270 K: application for displays. *Journal of Materials Chemistry*, 7(6): 857–858, 1997.

[148] H. G. Drickamer. Elektronische Umwandlungen in Übergangsmetallverbindungen bei hohem Druck. *Angewandte Chemie*, 86(2): 61–70, 1974.

[149] S. Usha, R. Srinivasan, and C. Rao. High-pressure magnetic susceptibility studies of spin-state transition in Fe(II) complexes. *Chemical Physics*, 100(3): 447–455, 1985.

[150] V. Ksenofontov, H. Spiering, A. Schreiner, G. Levchenko, H. Goodwin, and P. Gütlich. The influence of hydrostatic pressure on hysteresis phase transition in spin crossover compounds. *Journal of Physics and Chemistry of Solids*, 60(3): 393–399, 1999.

[151] J. Jeftić, R. Hinek, S. C. Capelli, and A. Hauser. Cooperativity in the Iron(II) Spin-Crossover Compound $[Fe(ptz)_6](PF_6)_2$ under the Influence of External Pressure (ptz = 1-n-Propyltetrazole). *Inorganic Chemistry*, 36(14): 3080–3087, 1997.

[152] D. C. Fisher. Effect of Pressure on the Spin State of Iron in Ferrous Phenanthroline Compounds. *The Journal of Chemical Physics*, 54(11): 4825, 1971.

[153] V. Ksenofontov, G. Levchenko, H. Spiering, P. Gütlich, J.-F. Létard, Y. Bouhedja, and O. Kahn. Spin crossover behavior under pressure of Fe(PM-L)$_2$(NCS)$_2$ compounds with substituted 2'-pyridylmethylene 4-anilino ligands. *Chemical Physics Letters*, 294(6): 545–553, 1998.

[154] Y. Garcia, O. Kahn, J.-P. Ader, A. Buzdin, Y. Meurdesoif, and M. Guillot. The effect of a magnetic field on the inversion temperature of a spin crossover compound revisited. *Physics Letters A*, 271(1-2): 145–154, 2000.

[155] Y. Qi, E. Müller, H. Spiering, and P. Gütlich. The effect of a magnetic field on the high-spin $\rightleftharpoons$ low-spin transition in [Fe(phen)$_2$(NCS)$_2$]. *Chemical Physics Letters*, 101(4-5): 503–505, 1983.

[156] J. Lejay, A. G. M. Jansen, P. Wyder, W. Bronger, and W. Kläui. Spin equilibrium of Co^{3+} complexes infiuenced by a magnetic field. *Physical Review B*, 43(10): 8196–8198, 1991.

[157] N. Negre, M. Goiran, A. Bousseksou, J. Haasnoot, K. Boukheddaden, S. Askenazy, and F. Varret. High magnetic field induced spin transition, H.M.F.I.S.T. effect, in [Fe$_{0.52}$Ni$_{0.48}$(btr)$_2$(NCS)$_2$]H$_2$O. *Synthetic Metals*, 115(1-3): 289–292, 2000.

[158] A. Bousseksou, N. Negre, M. Goiran, L. Salmon, J.-P. Tuchagues, M.-L. Boillot, K. Boukheddaden, and F. Varret. Dynamic triggering of a spin-transition by a pulsed magnetic field. *The European Physical Journal B*, 13(3): 451–456, 1999.

[159] J. J. McGravey and I. Lawthers. Photochemically-induced perturbation of the ^{1}A $\rightleftharpoons$ ^{5}T equilibrium in Fe$^{\mathrm{II}}$ complexes by pulsed laser irradiation in the metal-to-ligand charge-transfer absorption band. *Journal of the Chemical Society, Chemical Communications*, (16): 906–907, 1982.

[160] S. Decurtins, P. Gütlich, C. Köhler, H. Spiering, and A. Hauser. Light-induced excited spin state trapping in a transition-metal complex: The hexa-1-propyltetrazole-iron (II) tetrafluoroborate spin-crossover system. *Chemical Physics Letters*, 105(1): 1–4, 1984.

[161] A. Hauser. Reversibility of light-induced excited spin state trapping in the Fe(ptz)$_6$(BF$_4$)$_2$, and the Zn$_{1-\mathrm{x}}$Fe$_{\mathrm{x}}$(ptz)$_6$(BF$_4$)$_4$ spin-crossover systems. *Chemical Physics Letters*, 124(6): 543–548, 1986.

[162] P. Poganiuch, S. Decurtins, and P. Guetlich. Thermal- and light-induced spin transition in [Fe(mtz)$_6$](BF$_4$)$_2$: first successful formation of a metastable low-spin state by irradiation with light at low temperatures. *Journal of the American Chemical Society*, 112(9): 3270–3278, 1990.

[163] V. Davesne, M. Gruber, T. Miyamachi, V. Da Costa, S. Boukari, F. Scheurer, L. Joly, P. Ohresser, E. Otero, F. Choueikani, a. B. Gaspar, J. a. Real, W. Wulfhekel, M. Bowen, and E. Beaurepaire. First glimpse of the soft x-ray induced excited spin-state trapping effect dynamics on spin cross-over molecules. *The Journal of Chemical Physics*, 139(7): 074708, 2013.

[164] J.-F. Létard, L. Capes, G. Chastanet, N. Moliner, S. Létard, J.-A. Real, and O. Kahn. Critical temperature of the LIESST effect in iron(II) spin crossover compounds. *Chemical Physics Letters*, 313(1-2): 115–120, 1999.

[165] S. Hayami, Z.-z. Gu, Y. Einaga, Y. Kobayasi, Y. Ishikawa, Y. Yamada, A. Fujishima, and O. Sato. A Novel LIESST Iron(II) Complex Exhibiting a High Relaxation Temperature. *Inorganic Chemistry*, 40(13): 3240–3242, 2001.

[166] a. Desaix, O. Roubeau, J. Jeftic, J. G. Haasnoot, K. Boukheddaden, E. Codjovi, J. Linares, M. Nogues, F. o. Varret, J. Linarès, and M. Noguès. Light-induced bistability in spin transition solids leading to thermal and optical hysteresis. *The European Physical Journal B*, 6(2): 183–193, 1998.

[167] C. Roux, J. Zarembowitch, B. Gallois, T. Granier, and R. Claude. Toward Ligand-Driven Light-Induced Spin Changing. Influence of the Configuration of 4-Styrylpyridine (stpy) on the Magnetic Properties of $Fe^{II}(stpy)_4(NCS)_2$ Complexes. Crystal Structures of the Spin-Crossover Species $Fe(trans\text{-}stpy)_4(NCS)_2$ and of the High-Spin Species $Fe(cis\text{-}stpy)_4(NCS)_2$. *Inorganic Chemistry*, 33(10): 2273–2279, 1994.

[168] M. Marchivie, P. Guionneau, J. a. K. Howard, G. Chastanet, J.-F. Létard, A. E. Goeta, and D. Chasseau. Structural Characterization of a Photoinduced Molecular Switch. *Journal of the American Chemical Society*, 124(2): 194–195, 2002.

[169] E. Buhks, G. Navon, M. Bixon, and J. Jortner. Spin conversion processes in solutions. *Journal of the American Chemical Society*, 102(9): 2918–2923, 1980.

[170] C. L. Xie and D. N. Hendrickson. Mechanism of spin-state interconversion in ferrous spin-crossover complexes: direct evidence for quantum mechanical tunneling. *Journal of the American Chemical Society*, 109(23): 6981–6988, 1987.

[171] A. Hauser. Cooperative effects on the HS → LS relaxation in the $[Fe(ptz)_6](BF_4)_2$ spin-crossover system. *Chemical Physics Letters*, 192(1): 65–70, 1992.

[172] J. Jeftić and A. Hauser. The HS → LS relaxation under external pressure in the Fe(II) spin-crossover system $[Zn_{1-x}Fe_x(ptz)_6](BF_4)_2$(ptz = 1-propyltetrazole, x = 0.1). *Chemical Physics Letters*, 248(5-6): 458–463, 1996.

[173] D. Collison, C. D. Garner, C. M. McGrath, J. F. W. Mosselmans, M. D. Roper, J. M. W. Seddon, E. Sinn, and N. A. Young. Soft X-ray induced excited spin state trapping and soft X-ray photochemistry at the iron $L_{2,3}$ edge in $[Fe(phen)_2(NCS)_2]$ and $[Fe(phen)_2(NCSe)_2]$ (phen = 1,10-phenanthroline). *Journal of the Chemical Society, Dalton Transactions*, 2(22): 4371–4376, 1997.

[174] G. Vankó, F. Renz, G. Molnár, T. Neisius, and S. Kárpáti. Hard-X-ray-Induced Excited-Spin-State Trapping. *Angewandte Chemie International Edition*, 46(28): 5306–5309, 2007.

[175] Chambers, A., Fitch, R. K., Halliday , B.S. *Basic Vacuum Concepts.* Institute of Physics Publishing, Briston and Philadelphia, 1998.

[176] W. Umrath. *Fundamentals of Vacuum Technology.* Leybold Vacuum Products and Reference Book, 1998.

[177] S. M. Hubbell, J H ; Seltzer. Tables of X-ray mass attenuation coefficients and mass energy-absorption coefficients 1 keV to 20 MeV for elements Z=1 to 92 and 48 additional substances of dosimetric interest. *Tech. rep.*, The National Institute of Standards and Technology (NIST), 1995.

[178] J. Maddox. The sensational discovery of X-rays. *Nature*, 375(6528): 183–183, 1995.

[179] D. Iwanenko and I. Pomeranchuk. On the Maximal Energy Attainable in a Betatron. *Physical Review*, 65(11-12): 343–343, 1944.

[180] D. H. Tomboulian and P. L. Hartman. Spectral and Angular Distribution of Ultraviolet Radiation from the 300-Mev Cornell Synchrotron. *Physical Review*, 102(6): 1423–1447, 1956.

[181] P. Willmott. *An Introduction to Synchrotron Radiation: Techniques and Applications.* A John Wiley & Sons, Ltd., Publication, 2011.

[182] Lightsources.org. Lightsources of the World. `http://www.lightsources.org/regions`. [Accessed 22 September 2016].

[183] Copyright © EPSIM 3D/JF Santarelli, Synchrotron Soleil.

[184] N. Dyson. *X-Rays in atomic and nuclear physics.* Cambridge University Press, Cambridge, 1990.

[185] J. Als-Nielsen and D. McMorrow. *Elements of modern X-ray physics.* A John Wiley & Sons, Ltd Publication, 2011.

[186] P. A. M. Dirac. The Quantum Theory of the Emission and Absorption of Radiation. *Proceedings of the Royal Society A*, 114(767): 243–265, 1927.

[187] Nuclear physics: A course given by Enrico Fermi at the University of Chicago, University of Chicago Press, 1950, Rev. ed.

[188] H. Hirayama. Lecture note on photon interactions and cross sections, Tutorials for Electron/Gamma Monte Carlo building blocks and applications, International Conference on the Monte Carlo, Lisbon, Portugal. 2000.

[189] J. Chen. NEXAFS investigations of transition metal oxides, nitrides, carbides, sulfides and other interstitial compounds. *Surface Science Reports*, 30(1-3): 1–152, 1997.

[190] J. Stöhr. *NEXAFS Spectroscopy.* Springer-Verlag, 1996.

[191] B. Teo and D. Joy. *EXAFS Spectroscopy: Techniques and Applications.* Springer US, Boston, MA, 1981.

[192] J. Leroux. *Revised tables of X-ray mass attenuation coefficients.* Corporation scientifique claisse, 1977.

[193] R. H. Millar and J. R. Greening. Experimental x ray mass attenuation coefficients for materials of low atomic number in the energy range 4 to 25 keV. *Journal of Physics B: Atomic and Molecular Physics*, 7(17): 2232–2344, 1974.

[194] J. Stöhr and H. C. Siegmann. *Magnetism: From fundamentals to nanoscale dynamics*. Springer-Verlag, 2006.

[195] National Institute of Standards and Technology: Physical Measurement Laboratory. X-ray Form Factor, Attenuation, and Scattering Tables. `http://physics.nist.gov/PhysRefData/FFast/html/form.html`. [Accessed 9 August 2016].

[196] CXRO: The Center for X-ray Optics. X-ray Attenuation Length. `http://henke.lbl.gov/optical_constants/atten2.html`. [Accessed 9 August 2016].

[197] C. Chen, Y. Idzerda, H. Lin, and N. Smith. Experimental confirmation of the X-ray magnetic circular dichroism sum rules for iron and cobalt. *Physical Review Letters*, 75(1): 152–155, 1995.

[198] D. Attwood. *Soft X-Rays and Extreme Ultraviolet Radiation: Principles and Applications*. Cambridge University Press, 2013.

[199] R. Nakajima, J. Stöhr, and Y. Idzerda. Electron-yield saturation effects in L-edge x-ray magnetic circular dichroism spectra of Fe, Co, and Ni. *Physical Review B*, 59(9): 6421–6429, 1999.

[200] V. Chakarian and Y. U. Idzerda. Total electron yield method in x-ray absorption spectroscopy: A closer look at the saturation/self-absorption effects. *Journal of Applied Physics*, 81(8): 4709, 1997.

[201] P. Pfalzer, J.-P. Urbach, M. Klemm, S. Horn, M. L. DenBoer, A. I. Frenkel, and J. P. Kirkland. Elimination of self-absorption in fluorescence hard-x-ray absorption spectra. *Physical Review B*, 60(13): 9335–9339, 1999.

[202] C. H. Booth and F. Bridges. Improved SelfAbsorption Correction for Fluorescence Measurements of Extended XRay Absorption FineStructure. *Physica Scripta*, 2005(T115): 202, 2005.

[203] L. Tröger, D. Arvanitis, K. Baberschke, H. Michaelis, U. Grimm, and E. Zschech. Full correction of the self-absorption in soft-fluorescence extended x-ray-absorption fine structure. *Physical Review B*, 46(6): 3283–3289, 1992.

[204] M. O. Krause. Atomic radiative and radiationless yields for K and L shells. *Journal of Physical and Chemical Reference Data*, 8(2): 307, 1979.

[205] E. D. Palik. *Handbook of Optical Constants of Solids II.* Elsevier Science (USA), 1991.

[206] F. C. Hermanns. *X-ray absorption studies of metalloporphyrin molecules on surfaces: Electronic interactions, magnetic coupling, and chemical switches.* Ph.D. thesis, Freien Universitat at Berlin, 2013.

[207] P. Carra, B. T. Thole, M. Altarelli, and X. Wang. X-ray circular dichroism and local magnetic fields. *Physical Review Letters*, 70(5): 694–697, 1993.

[208] B. T. Thole, P. Carra, F. Sette, and G. van der Laan. X-ray circular dichroism as a probe of orbital magnetization. *Physical Review Letters*, 68(12): 1943–1946, 1992.

[209] R. Wu and A. J. Freeman. Limitation of the magnetic-circular-dichroism spin sum rule for transition metals and importance of the magnetic dipole term. *Physical Review Letters*, 73(14): 1994–1997, 1994.

[210] R. Wu, D. Wang, and A. J. Freeman. First principles investigation of the validity and range of applicability of the x-ray magnetic circular dichroism sum rule. *Physical Review Letters*, 71(21): 3581–3584, 1993.

[211] M. Altarelli. Sum rules for X-ray magnetic circular dichroism. *Il Nuovo Cimento*, 20 D(7-8): 1067–1073, 1998.

[212] J. Stöhr and H. König. Determination of spin- and orbital-moment anisotropies in transition metals by angle-dependent X-ray magnetic circular dichroism. *Physical Review Letters*, 75(20): 3748–3751, 1995.

[213] P. Ohresser, E. Otero, F. Choueikani, K. Chen, S. Stanescu, F. Deschamps, T. Moreno, F. Polack, B. Lagarde, J.-P. Daguerre, F. Marteau, F. Scheurer, L. Joly, J.-P. Kappler, B. Muller, O. Bunau, and P. Sainctavit. DEIMOS: A beamline dedicated to dichroism measurements in the 350–2500 eV energy range. *Review of Scientific Instruments*, 85(1): 013106, 2014.

[214] C. Piamonteze, P. Miedema, and F. M. F. de Groot. Accuracy of the spin sum rule in XMCD for the transition-metal L edges from manganese to copper. *Physical Review B*, 80(18): 184410, 2009.

[215] W. L. O'Brien and B. P. Tonner. Orbital and spin sum rules in x-ray magnetic circular dichroism. *Physical Review B*, 50(17): 12672–12681, 1994.

[216] J. Goedkoop, N. Brookes, M. van Veenendaal, and B. Thole. Soft X-ray fluorescence yield XMCD sum rules. *Journal of Electron Spectroscopy and Related Phenomena*, 86(1-3): 143–150, 1997.

[217] S. Hüfner. *Photoelectron Spectroscopy.* Springer Series in Solid-State Sciences. Springer, Berlin, Heidelberg, 1996.

[218] C. N. Berglund and W. E. Spicer. Photoemission Studies of Copper and Silver: Theory. *Physical Review*, 136(4A): A1030–A1044, 1964.

[219] G. D. Mahan. Theory of Photoemission in Simple Metals. *Physical Review B*, 2(11): 4334–4350, 1970.

[220] A. Damascelli. Probing the Electronic Structure of Complex Systems by ARPES. *Physica Scripta*, T109: 61–74, 2004.

[221] U. Müller, H. Burtscher, and A. Schmidt-Ott. Photoemission from small metal spheres: A model calculation using an enhanced three-step model. *Physical Review B*, 38(11): 7814–7816, 1988.

[222] E. Tamura, W. Piepke, and R. Feder. New spin-polarization effect in photoemission from nonmagnetic surfaces. *Physical Review Letters*, 59(8): 934–937, 1987.

[223] J. A. Knapp, F. J. Himpsel, and D. E. Eastman. Experimental energy band dispersions and lifetimes for valence and conduction bands of copper using angle-resolved photoemission. *Physical Review B*, 19(10): 4952–4964, 1979.

[224] T. Miller, W. E. McMahon, and T.-C. Chiang. Interference between Bulk and Surface Photoemission Transitions in Ag(111). *Physical Review Letters*, 77(6): 1167–1170, 1996.

[225] P. D. Johnson. Spin-polarized photoemission. *Reports on Progress in Physics*, 60(11): 1217, 1997.

[226] T. Feuchtwang, P. Cutler, and D. Nagy. A review of the theoretical and experimental analyses of electron spin polarization in ferromagnetic transition metals. *Surface Science*, 75(3): 490–528, 1978.

[227] T. Feuchtwang, P. Cutler, and J. Schmit. A review of the theoretical and experimental analyses of electron spin polarization in ferromagnetic transition metals. *Surface Science*, 75(3): 401–489, 1978.

[228] N. F. Mott. The Scattering of Fast Electrons by Atomic Nuclei. *Proceedings of the Royal Society of London*, 124(794): 425–442, 1929.

[229] T. J. Gay and F. B. Dunning. Mott electron polarimetry. *Review of Scientific Instruments*, 63(2): 1635, 1992.

[230] J. Kessler. *Polarized Electrons*. Springer-Verlag, 1985.

[231] S. Qiao and A. Kakizaki. Monte Carlo calculations for the design of Mott scattering spin polarimeters. *Review of Scientific Instruments*, 68(11): 4017, 1997.

[232] N. Sherman. Coulomb Scattering of Relativistic Electrons by Point Nuclei. *Physical Review*, 103(6): 1601–1607, 1956.

[233] D. J. Huang, W. P. Wu, J. Chen, C. F. Chang, S. C. Chung, M. Yuri, H.-J. Lin, P. D. Johnson, and C. T. Chen. Performance of a Mott detector for undulator-based spin-resolved spectroscopy. *Review of Scientific Instruments*, 73(11): 3778, 2002.

[234] S. Souma, A. Takayama, K. Sugawara, T. Sato, and T. Takahashi. Ultrahigh-resolution spin-resolved photoemission spectrometer with a mini Mott detector. *Review of Scientific Instruments*, 81(9): 095101, 2010.

[235] CASIOPÉE beamline. Detailed beamline desciprtion, spin-resolved endstation. http://www.synchrotron-soleil.fr/Recherche/LignesLumiere/CASSIOPEE/detailed_beamline_description/endstations#spin_resolved. [Accessed 15 August 2016].

[236] CASIOPÉE beamline poster.

[237] DEIMOS beamline poster 2013. Reprinted with permission of the author.

[238] J. Chavanne, P. Elleaume, P. V. Vaerenbergh, and F.-G. C. France. A novel fast switching linear/helical undulator. In: *Proceedings of EPAC98*, pp. 317–319. Stockholm, Sweden, 1988.

[239] L. Joly, E. Otero, F. Choueikani, F. Marteau, L. Chapuis, and P. Ohresser. Fast continuous energy scan with dynamic coupling of the monochromator and undulator at the DEIMOS beamline. *Journal of Synchrotron Radiation*, 21(3): 502–506, 2014.

[240] A. Gurlo and R. Riedel. In Situ and Operando Spectroscopy for Assessing Mechanisms of Gas Sensing. *Angewandte Chemie International Edition*, 46(21): 3826–3848, 2007.

[241] N. Barrett, D. M. Gottlob, C. Mathieu, C. Lubin, J. Passicousset, O. Renault, and E. Martinez. Operando x-ray photoelectron emission microscopy for studying forward and reverse biased silicon p-n junctions. *Review of Scientific Instruments*, 87(5), 2016.

[242] S.-W. Cheong and M. Mostovoy. Multiferroics: a magnetic twist for ferroelectricity. *Nature Materials*, 6(1): 13–20, 2007.

[243] C. A. Fernandes Vaz and U. Staub. Artificial multiferroic heterostructures. *Journal of Materials Chemistry C*, 1(41): 6731, 2013.

[244] T. Bertaud, M. Sowinska, D. Walczyk, S. Thiess, A. Gloskovskii, C. Walczyk, and T. Schroeder. In-operando and non-destructive analysis of the resistive switching in the Ti/HfO_2/TiN-based system by hard x-ray photoelectron spectroscopy. *Applied Physics Letters*, 101(14): 1–6, 2012.

[245] X. Liu, W. Yang, and Z. Liu. Recent progress on synchrotron-based in-situ soft X-ray spectroscopy for energy materials. *Advanced Materials*, 26(46): 7710–7729, 2014.

[246] W. Wang, C. J. Schaffer, L. Song, V. Körstgens, S. Pröller, E. D. Indari, T. Wang, A. Abdelsamie, S. Bernstorff, and P. Müller-Buschbaum. In operando morphology investigation of inverted bulk heterojunction organic solar cells by GISAXS. *Journal of Materials Chemistry A*, 3(16): 8324–8331, 2015.

[247] Y. Gorlin, M. U. M. Patel, A. Freiberg, Q. He, M. Piana, M. Tromp, and H. A. Gasteiger. Understanding the Charging Mechanism of Lithium-Sulfur Batteries Using Spatially Resolved Operando X-Ray Absorption Spectroscopy. *Journal of The Electrochemical Society*, 163(6): A930–A939, 2016.

[248] M. Studniarek, U. Halisdemir, F. Schleicher, B. Taudul, E. Urbain, M. Herve, C.-H. Lambert, A. Hamadeh, S. Petit-Watelot, O. Zill, D. Lacour, S. Boukari, L. Joly, F. Scheurer, G. Schmerber, V. Da Costa, A. Dixit, P.-A. Guitard, M. Acosta, F. Leduc, F. Chouekani, E. Otero, W. Wulfhekel, F. Montaigne, E. Monteblanco, J. Arabski, P. Ohresser, E. Beaurepaire, W. Weber, M. Alouani, M. Hehn, and M. Bowen. Probing a device's active atoms using synchrotron radiation. Submitted.

[249] J. Bernos, M. Hehn, F. Montaigne, C. Tiusan, D. Lacour, M. Alnot, B. Negulescu, G. Lengaigne, E. Snoeck, and F. G. Aliev. Impact of electron-electron interactions induced by disorder at interfaces on spin-dependent tunneling in Co-Fe-B/MgO/Co-Fe-B magnetic tunnel junctions. *Physical Review B*, 82(6): 060405, 2010.

[250] D. Halley, H. Majjad, M. Bowen, N. Najjari, Y. Henry, C. Ulhaq-Bouillet, W. Weber, G. Bertoni, J. Verbeeck, and G. Van Tendeloo. Electrical switching in Fe/Cr/MgO/Fe magnetic tunnel junctions. *Applied Physics Letters*, 92(21): 212115, 2008.

[251] U. Halisdemir. Sensing light with solid-state tunneling. Submitted.

[252] A. K. Rumaiz, J. C. Woicik, W. G. Wang, J. Jordan-Sweet, G. H. Jaffari, C. Ni, J. Q. Xiao, and C. L. Chien. Effects of annealing on the local structure of Fe and Co in CoFeB/MgO/CoFeB tunnel junctions: An extended x-ray-absorption fine structure study. *Applied Physics Letters*, 96(11), 2010.

[253] E. Negusse, A. Lussier, J. Dvorak, Y. U. Idzerda, S. R. Shinde, Y. Nagamine, S. Furukawa, K. Tsunekawa, and D. D. Djayaprawira. Magnetic characterization of CoFeB/MgO and CoFe/MgO interfaces. *Applied Physics Letters*, 90(9), 2007.

[254] J. C. Read, P. G. Mather, and R. A. Buhrman. X-ray photoemission study of CoFeB/MgO thin film bilayers. *Applied Physics Letters*, 90(13): 132503, 2007.

[255] A. N. Chiaramonti, D. K. Schreiber, W. F. Egelhoff, D. N. Seidman, and A. K. Petford-Long. Effects of annealing on local composition and electrical transport correlations in MgO-based magnetic tunnel junctions. *Applied Physics Letters*, 93(10): 103113, 2008.

[256] V. Serin, S. Andrieu, R. Serra, F. Bonell, C. Tiusan, L. Calmels, M. Varela, S. J. Pennycook, E. Snoeck, M. Walls, and C. Colliex. TEM and EELS measurements of interface roughness in epitaxial Fe/MgO/Fe magnetic tunnel junctions. *Physical Review B*, 79(14): 144413, 2009.

[257] A. T. Hindmarch, K. J. Dempsey, D. Ciudad, E. Negusse, D. A. Arena, and C. H. Marrows. Fe diffusion, oxidation, and reduction at the CoFeB/MgO interface studied by soft x-ray absorption spectroscopy and magnetic circular dichroism. *Applied Physics Letters*, 96(9): 092501, 2010.

[258] S.-H. Yang, B. Balke, C. Papp, S. Döring, U. Berges, L. Plucinski, C. Westphal, C. M. Schneider, S. S. P. Parkin, and C. S. Fadley. Determination of layer-resolved composition, magnetization, and electronic structure of an Fe/MgO tunnel junction by standing-wave core and valence photoemission. *Physical Review B*, 84(18): 184410, 2011.

[259] M. Kapilashrami, H. Zhang, M. Fang, X. Li, X. Sun, K. V. Rao, L. Belova, Y. Luo, and J. Guo. Electronic structure of room-temperature ferromagnetic $\mathrm{Mg_{1-x}Fe_xO_y}$ thin films. *Applied Physics Letters*, 101(8): 082411, 2012.

[260] X.-G. Zhang, W. H. Butler, and A. Bandyopadhyay. Effects of the iron-oxide layer in Fe-FeO-MgO-Fe tunneling junctions. *Physical Review B*, 68(9): 092402, 2003.

[261] G. Miao, Y. Park, J. Moodera, M. Seibt, G. Eilers, and M. Münzenberg. Disturbance of Tunneling Coherence by Oxygen Vacancy in Epitaxial Fe/MgO/Fe Magnetic Tunnel Junctions. *Physical Review Letters*, 100(24), 2008.

[262] D. J. Kim, W. S. Choi, F. Schleicher, R. H. Shin, S. Boukari, V. Davesne, C. Kieber, J. Arabski, G. Schmerber, E. Beaurepaire, W. Jo, and M. Bowen. Control of defect-mediated tunneling barrier heights in ultrathin MgO films. *Applied Physics Letters*, 97(26): 263502, 2010.

[263] J. M. Teixeira, J. Ventura, J. P. Araujo, J. B. Sousa, P. Wisniowski, S. Cardoso, and P. P. Freitas. Resonant Tunneling through Electronic Trapping States in Thin MgO Magnetic Junctions. *Physical Review Letters*, 106(19), 2011.

[264] B. Taudul, E. N. Monteblanco, U. Halisdemir, D. Lacour, F. Schleicher, F. Montaigne, E. Beaurepaire, S. Boukari, M. Hehn, M. Alouani, and M. Bowen. Tunnelling spintronics across MgO driven by double oxygen vacancies. Submitted.

[265] V. Da Costa, C. Tiusan, T. Dimopoulos, and K. Ounadjela. Tunneling Phenomena as a Probe to Investigate Atomic Scale Fluctuations in Metal/Oxide/Metal Magnetic Tunnel Junctions. *Physical Review Letters*, 85(4): 876–879, 2000.

[266] B.-K. Teo and P. A. Lee. Ab initio calculations of amplitude and phase functions for extended x-ray absorption fine structure spectroscopy. *Journal of the American Chemical Society*, 101(11): 2815–2832, 1979.

[267] P. A. Lee and G. Beni. New method for the calculation of atomic phase shifts: Application to extended x-ray absorption fine structure (EXAFS) in molecules and crystals. *Physical Review B*, 15(6): 2862–2883, 1977.

[268] J. Mustre de Leon, J. J. Rehr, S. I. Zabinsky, and R. C. Albers. Ab initio curved-wave x-ray-absorption fine structure. *Physical Review B*, 44(9): 4146–4156, 1991.

[269] G. Kresse and J. Furthmüller. Efficient iterative schemes for ab initio total-energy calculations using a plane-wave basis set. *Physical Review B*, 54(16): 11169–11186, 1996.

[270] A. Dixit. *Relativistic Effects: Applications to Multiferroic Materials.* Ph.D. thesis, Universty of Strasbourg, 2015.

[271] J. P. Perdew, K. Burke, and M. Ernzerhof. Generalized Gradient Approximation Made Simple. *Physical Review Letters*, 77(18): 3865–3868, 1996.

[272] G. Kresse and D. Joubert. From ultrasoft pseudopotentials to the projector augmented-wave method. *Physical Review B*, 59(3): 1758–1775, 1999.

[273] P. Giannozzi, S. Baroni, N. Bonini, M. Calandra, R. Car, C. Cavazzoni, D. Ceresoli, G. L. Chiarotti, M. Cococcioni, I. Dabo, A. Dal Corso, S. de Gironcoli, S. Fabris, G. Fratesi, R. Gebauer, U. Gerstmann, C. Gougoussis, A. Kokalj, M. Lazzeri, L. Martin-Samos, N. Marzari, F. Mauri, R. Mazzarello, S. Paolini, A. Pasquarello, L. Paulatto, C. Sbraccia, S. Scandolo, G. Sclauzero, A. P. Seitsonen, A. Smogunov, P. Umari, and R. M. Wentzcovitch. QUANTUM ESPRESSO: a modular and open-source software project for quantum simulations of materials. *Journal of Physics: Condensed Matter*, 21(39): 395502, 2009.

[274] H. Joon Choi and J. Ihm. Ab initio pseudopotential method for the calculation of conductance in quantum wires. *Physical Review B*, 59(3): 2267–2275, 1999.

[275] A. Smogunov, A. Dal Corso, and E. Tosatti. Ballistic conductance of magnetic Co and Ni nanowires with ultrasoft pseudopotentials. *Physical Review B*, 70(4): 045417, 2004.

[276] V. Garcia, M. Bibes, L. Bocher, S. Valencia, F. Kronast, A. Crassous, X. Moya, S. Enouz-Vedrenne, A. Gloter, D. Imhoff, C. Deranlot, N. D. Mathur, S. Fusil, K. Bouzehouane, and A. Barthelemy. Ferroelectric Control of Spin Polarization. *Science*, 327(5969): 1106–1110, 2010.

[277] A. Chanthbouala, V. Garcia, R. O. Cherifi, K. Bouzehouane, S. Fusil, X. Moya, S. Xavier, H. Yamada, C. Deranlot, N. D. Mathur, M. Bibes, A. Barthélémy, and J. Grollier. A ferroelectric memristor. *Nature Materials*, 11(10): 860–864, 2012.

[278] M. A. Green, A. Ho-Baillie, and H. J. Snaith. The emergence of perovskite solar cells. *Nature Photonics*, 8(7): 506–514, 2014.

[279] J. Yan and B. R. Saunders. Third-generation solar cells: a review and comparison of polymer:fullerene, hybrid polymer and perovskite solar cells. *RSC Advances*, 4(82): 43286–43314, 2014.

[280] T. C. Sum and N. Mathews. Advancements in perovskite solar cells: photophysics behind the photovoltaics. *Energy & Environmental Science*, 7(8): 2518–2534, 2014.

[281] A. Braun and J. Tcherniac. Über die Produkte der Einwirkung von Acetanhydrid auf Phthalamid. *Berichte der deutschen chemischen Gesellschaft*, 40(2): 2709–2714, 1907.

[282] R. P. Linstead. Phthalocyanines. Part I. A New Type of Synthetic Coburing Matters. *Journal of the Chemical Society*, (1016): 1016–1017, 1933.

[283] H. de Diesbach and E. von der Weid. Quelques sels complexes des o-dinitriles avec le cuivre et la pyridine. *Helvetica Chimica Acta*, 10(1): 886–888, 1927.

[284] F. Moser and A. Thomas. *Phthalocyanine compounds*. Reinhold Publishing Corporation, New York, 1963.

[285] P. Peumans and S. R. Forrest. Very-high-efficiency double-heterostructure copper phthalocyanine/C_{60} photovoltaic cells. *Applied Physics Letters*, 79(1): 126–128, 2001.

[286] M. G. Walter, A. B. Rudine, and C. C. Wamser. Porphyrins and phthalocyanines in solar photovoltaic cells. *Journal of Porphyrins and Phthalocyanines*, 14(09): 759–792, 2010.

[287] S. A. Van Slyke, C. H. Chen, and C. W. Tang. Organic electroluminescent devices with improved stability. *Applied Physics Letters*, 69(15): 2160–2162, 1996.

[288] D. Hohnholz, S. Steinbrecher, and M. Hanack. Applications of phthalocyanines in organic light emitting devices. *Journal of Molecular Structure*, 521(1-3): 231–237, 2000.

[289] G. Guillaud, J. Simon, and J. P. Germain. Metallophthalocyanines: Gas sensors, resistors and field effect transistors. *Coordination Chemistry Reviews*, 178-180: 1433–1484, 1998.

[290] M. Bouvet, G. Guillaud, A. Leroy, A. Maillard, S. Spirkovitch, and F. G. Tournilhac. Phthalocyanine-based field-effect transistor as ozone sensor. *Sensors and Actuators B*, 73(1): 63–70, 2001.

[291] H. S. Majumdar, A. Bandyopadhyay, and A. J. Pal. Data-storage devices based on layer-by-layer self-assembled films of a phthalocyanine derivative. *Organic Electronics*, 4(1): 39–44, 2003.

[292] J. Mack and M. J. Stillman. Assignment of the optical spectra of metal phthalocyanines through spectral band deconvolution analysis and ZINDO calculations. *Coordination Chemistry Reviews*, 219-221: 993–1032, 2001.

[293] D. D. R. Tackley, G. Dent, W. Ewen Smith, and W. Smith. Phthalocyanines: structure and vibrations. *Physical Chemistry Chemical Physics*, 3(8): 1419–1426, 2001.

[294] M. Ashida, N. Uyeda, and E. Suito. Thermal transformation of vacuum-condensed thin films of copper-phthalocyanine. *Journal of Crystal Growth*, 8(1): 45–56, 1971.

[295] R. Gould. Structure and electrical conduction properties of phthalocyanine thin films. *Coordination Chemistry Reviews*, 156: 237–274, 1996.

[296] S. Heutz, S. M. Bayliss, R. L. Middleton, G. Rumbles, and T. S. Jones. Polymorphism in Phthalocyanine Thin Films: Mechanism of the $\alpha \to \beta$ Transition. *The Journal of Physical Chemistry B*, 104(30): 7124–7129, 2000.

[297] S. Nešpůrek, H. Podlesak, and C. Hamann. Structure and photoelectrical behaviour of vacuum-evaporated metal-free phthalocyanine films. *Thin Solid Films*, 249(2): 230–235, 1994.

[298] M. Evangelisti, J. Bartolomé, L. J. de Jongh, and G. Filoti. Magnetic properties of α-iron(II) phthalocyanine. *Physical Review B*, 66(14): 144410, 2002.

[299] M. S. Liao and S. Scheiner. Electronic structure and bonding in metal phthalocyanines, metal=Fe, Co, Ni, Cu, Zn, Mg. *Journal of Chemical Physics*, 114(22): 9780–9791, 2001.

[300] L. Lozzi, S. Santucci, S. La Rosa, B. Delley, and S. Picozzi. Electronic structure of crystalline copper phthalocyanine. *Journal of Chemical Physics*, 121(4): 1883–1889, 2004.

[301] I. E. Brumboiu, R. Totani, M. De Simone, M. Coreno, C. Grazioli, L. Lozzi, H. C. Herper, B. Sanyal, O. Eriksson, C. Puglia, and B. Brena. Elucidating the 3d electronic configuration in manganese phthalocyanine. *Journal of Physical Chemistry A*, 118(5): 927–932, 2014.

[302] B. E. Williamson, T. C. VanCott, M. E. Boyle, G. C. Misener, M. J. Stillman, and P. N. Schatz. Determination of the ground state of manganese phthalocyanine in an argon matrix using magnetic circular dichroism and absorption spectroscopy. *Journal of the American Chemical Society*, 114(7): 2412–2419, 1992.

[303] B. Białek, I. G. Kim, and J. I. Lee. First-principles study on the electronic structures of iron phthalocyanine monolayer. *Surface Science*, 526(3): 367–374, 2003.

[304] B. W. Dale, R. J. P. Williams, C. E. Johnson, and T. L. Thorp. S = 1 Spin State of Divalent Iron. I. Magnetic Properties of Phthalocyanine Iron (II). *The Journal of Chemical Physics*, 49(8): 3441–3444, 1968.

[305] S. Lach, A. Altenhof, K. Tarafder, F. Schmitt, M. E. Ali, M. Vogel, J. Sauther, P. M. Oppeneer, and C. Ziegler. Metal-organic hybrid interface states of a ferromagnet/organic semiconductor hybrid junction as basis for engineering spin injection in organic spintronics. *Advanced Functional Materials*, 22(5): 989–997, 2012.

[306] A. Calzolari, A. Ferretti, and M. B. Nardelli. Ab initio correlation effects on the electronic and transport properties of metal(II)-phthalocyanine-based devices. *Nanotechnology*, 18(42): 424013, 2007.

[307] J. Wang, Y. Shi, J. Cao, and R. Wu. Magnetization and magnetic anisotropy of metallophthalocyanine molecules from the first principles calculations. *Applied Physics Letters*, 94(12), 2009.

[308] C. G. Barraclough, R. L. Martin, S. Mitra, and R. C. Sherwood. Paramagnetic Anisotropy, Electronic Structure, and Ferromagnetism in Spin S = 3/2 Manganese(II) Phthalocyanine. *The Journal of Chemical Physics*, 53(5): 1638, 1970.

[309] G. de la Torre, G. Bottari, U. Hahn, and T. Torres. *Functional Phthalocyanine Molecular Materials*. Springer, Heidelberg, 2010.

[310] A. Lodi Rizzini, C. Krull, A. Mugarza, T. Balashov, C. Nistor, R. Piquerel, S. Klyatskaya, M. Ruben, P. M. Sheverdyaeva, P. Moras, C. Carbone, C. Stamm, P. S. Miedema, P. K. Thakur, V. Sessi, M. Soares, F. Yakhou-Harris, J. C. Cezar, S. Stepanow, and P. Gambardella. Coupling of single, double, and triple-decker metal-phthalocyanine complexes to ferromagnetic and antiferromagnetic substrates. *Surface Science*, 630: 361–374, 2014.

[311] E. Annese, J. Fujii, I. Vobornik, G. Panaccione, and G. Rossi. Control of the magnetism of cobalt phthalocyanine by a ferromagnetic substrate. *Physical Review B*, 84(17): 174443, 2011.

[312] E. Annese, F. Casolari, J. Fujii, and G. Rossi. Interface magnetic coupling of Fe-phthalocyanine layers on a ferromagnetic surface. *Physical Review B*, 87(5): 054420, 2013.

[313] X. Chen, Y.-S. Fu, S.-H. Ji, T. Zhang, P. Cheng, X.-C. Ma, X.-L. Zou, W.-H. Duan, J.-F. Jia, and Q.-K. Xue. Probing Superexchange Interaction in Molecular Magnets by Spin-Flip Spectroscopy and Microscopy. *Physical Review Letters*, 101(19): 197208, 2008.

[314] V. Skumryev, S. Stoyanov, Y. Zhang, G. Hadjipanayis, D. Givord, and J. Nogués. Beating the superparamagnetic limit with exchange bias. *Nature*, 423(6942): 850–853, 2003.

[315] A. Berkowitz and K. Takano. Exchange anisotropy — a review. *Journal of Magnetism and Magnetic Materials*, 200(1-3): 552–570, 1999.

[316] B. Dieny, V. S. Speriosu, S. S. P. Parkin, B. A. Gurney, D. R. Wilhoit, and D. Mauri. Giant magnetoresistive in soft ferromagnetic multilayers. *Physical Review B*, 43(1): 1297–1300, 1991.

[317] M. Kiwi. Exchange bias theory. *Journal of Magnetism and Magnetic Materials*, 234(3): R247–R268, 2001.

[318] J. Nogués and I. K. Schuller. Exchange bias. *Journal of Magnetism and Magnetic Materials*, 192(2): 203–232, 1999.

[319] R. L. Stamps. Mechanisms for exchange bias. *Journal of Physics D: Applied Physics*, 34(3): 444–444, 2001.

[320] J. Nogués, J. Sort, V. Langlais, V. Skumryev, S. Suriñach, J. S. Muñoz, and M. D. Baró. Exchange bias in nanostructures. *Physics Reports*, 422(3): 65–117, 2005.

[321] W. H. Meiklejohn and C. P. Bean. New Magnetic Anisotropy. *Physical Review*, 105(3): 904–913, 1957.

[322] A. Punnoose, H. Magnone, M. S. Seehra, and J. Bonevich. Bulk to nanoscale magnetism and exchange bias in CuO nanoparticles. *Physical Review B*, 64(17): 174420, 2001.

[323] H. Moradi. Field-dependent spin-wave damping in ferromagnet/antiferromagnet bilayers. *Journal of Magnetism and Magnetic Materials*, 299(1): 240–246, 2006.

[324] M. Husain, A. Adeyeye, C. Wang, V. Ng, and T. Low. Exchange bias effects in ferromagnetic wires. *Journal of Magnetism and Magnetic Materials*, 267(2): 191–196, 2003.

[325] J. Yu, A. D. Kent, and S. S. P. Parkin. Exchange biasing in polycrystalline thin film microstructures. *Journal of Applied Physics*, 87(9): 5049, 2000.

[326] J. Nogues, J. Sort, V. Langlais, S. Doppiu, B. Dieny, J. S. Munoz, S. Surinach, M. D. Baro, S. Stoyanov, and Y. Zhang. Exchange Bias in Ferromagnetic Nanoparticles Embedded in an Antiferromagnetic Matrix. *International Journal of Nanotechnology*, 2(1-2): 23–42, 2005.

[327] D. Geoghegan, P. G. McCormick, and R. Street. Mechanically Alloyed Antiferromagnetic-Ferromagnetic Exchange Coupled Nano-Composites. *Materials Science Forum*, 179-181: 629–634, 1995.

[328] X. Liu, B. Gu, W. Zhong, H. Jiang, and Y. Du. Ferromagnetic/antiferromagnetic exchange coupling in $SrFe_{12}O_{19}$/CoO composites. *Applied Physics A*, 77(5): 673–676, 2003.

[329] A. Lodi Rizzini, C. Krull, T. Balashov, A. Mugarza, C. Nistor, F. Yakhou, V. Sessi, S. Klyatskaya, M. Ruben, S. Stepanow, and P. Gambardella. Exchange Biasing Single Molecule Magnets: Coupling of TbPc 2 to Antiferromagnetic Layers. *Nano Letters*, 12(11): 5703–5707, 2012.

[330] P. Grünberg, R. Schreiber, Y. Pang, U. Walz, M. B. Brodsky, and H. Sowers. Layered magnetic structures: Evidence for antiferromagnetic coupling of Fe layers across Cr interlayers. *Journal of Applied Physics*, 61(8): 3750, 1987.

[331] G. Binasch, P. Grünberg, F. Saurenbach, and W. Zinn. Enhanced magnetoresistance in layered magnetic structures with antiferromagnetic interlayer exchange. *Physical Review B*, 39(7): 4828–4830, 1989.

[332] P. Bruno and C. Chappert. Oscillatory coupling between ferromagnetic layers separated by a nonmagnetic metal spacer. *Physical Review Letters*, 67(12): 1602–1605, 1991.

[333] M. Ruderman and C. Kittel. Indirect exchange coupling of nuclear magnetic moments by conduction electrons. *Physical Review*, 96(3): 72–75, 1954.

[334] T. Kasuya. A Theory of Metallic Ferro- and Antiferromagnetism on Zener's Model. *Progress of Theoretical Physics*, 16(1): 45–57, 1956.

[335] K. Yosida. Magnetic Properties of Cu-Mn Alloys. *Physical Review*, 106(5): 893–898, 1957.

[336] J. Friedel. Metallic alloys. *Il Nuovo Cimento*, 7(S2): 287–311, 1958.

[337] M. Stiles. Interlayer Exchange Coupling. In: *Ultrathin Magnetic Structures III*, pp. 99–142. Springer-Verlag, Berlin Heidelberg, 2005.

[338] R. K. Kawakami, E. Rotenberg, E. J. Escorcia-Aparicio, H. J. Choi, J. H. Wolfe, N. V. Smith, and Z. Q. Qiu. Determination of the Magnetic Coupling in the Co/Cu/Co(100) System with Momentum-Resolved Quantum Well States. *Physical Review Letters*, 82(20): 4098–4101, 1999.

[339] R. K. Kawakami, E. Rotenberg, H. J. Choi, E. J. Escorcia-Aparicio, M. O. Bowen, J. H. Wolfe, E. Arenholz, Z. D. Zhang, N. V. Smith, and Z. Q. Qiu. Quantum-well states in copper thin films. *Nature*, 398(6723): 132–134, 1999.

[340] J. E. Ortega and F. J. Himpsel. Quantum well states as mediators of magnetic coupling in superlattices. *Physical Review Letters*, 69(5): 844–847, 1992.

[341] K. Garrison, Y. Chang, and P. D. Johnson. Spin polarization of quantum well states in copper thin films deposited on a Co(001) substrate. *Physical Review Letters*, 71(17): 2801–2804, 1993.

[342] P. Bruno and C. Chappert. Ruderman-Kittel theory of oscillatory interlayer exchange coupling. *Physical Review B*, 46(1): 261–270, 1992.

[343] F. Herman, J. Sticht, and M. Van Schilfgaarde. Spin-polarized band structure of magnetically coupled multilayers. *Journal of Applied Physics*, 69(8): 4783, 1991.

[344] D. Stoeffler and F. Gautier. Electronic Structure, Magnetic Order and Interlayer Magnetic Couplings in Metallic Superlattices. *Progress of Theoretical Physics Supplement*, 101(101): 139–157, 1990.

[345] P. Bruno. Theory of interlayer magnetic coupling. *Physical Review B*, 52(1): 411–439, 1995.

[346] J. Slonczewski. Overview of interlayer exchange theory. *Journal of Magnetism and Magnetic Materials*, 150(1): 13–24, 1995.

[347] R. K. Kawakami, E. Rotenberg, E. J. Escorcia-Aparicio, H. J. Choi, T. R. Cummins, J. G. Tobin, N. V. Smith, and Z. Q. Qiu. Observation of the Quantum Well Interference in Magnetic Nanostructures by Photoemission. *Physical Review Letters*, 80(8): 1754–1757, 1998.

[348] F. L. Battye, A. Goldmann, and L. Kasper. Ultraviolet Photoelectron Valence Band Studies on Phthalocyanine Compounds. *Physica Status Solidi (b)*, 80(2): 425–432, 1977.

[349] M. Gruber, F. Ibrahim, S. Boukari, L. Joly, V. Da Costa, M. Studniarek, M. Peter, H. Isshiki, H. Jabbar, V. Davesne, J. Arabski, E. Otero, F. Choueikani, K. Chen, P. Ohresser, W. Wulfhekel, F. Scheurer, E. Beaurepaire, M. Alouani, W. Weber, and M. Bowen. Spin-Dependent Hybridization between Molecule and Metal at Room Temperature through Interlayer Exchange Coupling. *Nano Letters*, 15(12): 7921–7926, 2015.

[350] S. Javaid, S. Lebègue, B. Detlefs, F. Ibrahim, F. Djeghloul, M. Bowen, S. Boukari, T. Miyamachi, J. Arabski, D. Spor, J. Zegenhagen, W. Wulfhekel, W. Weber, E. Beaurepaire, and M. Alouani. Chemisorption of manganese phthalocyanine on Cu(001) surface promoted by van der Waals interactions. *Physical Review B*, 87(15): 155418, 2013.

[351] N. a. Spaldin, S.-w. Cheong, and R. Ramesh. Multiferroics: Past, present, and future. *Physics Today*, 63(10): 38–43, 2010.

[352] L. W. Martin, S. P. Crane, Y.-H. Chu, M. B. Holcomb, M. Gajek, M. Huijben, C.-H. Yang, N. Balke, and R. Ramesh. Multiferroics and magnetoelectrics: thin films and nanostructures. *Journal of Physics: Condensed Matter*, 20(43): 434220, 2008.

[353] H. Schmid. Multi-ferroic magnetoelectrics. *Ferroelectrics*, 162(1): 317–338, 1994.

[354] S. Fusil, V. Garcia, A. Barthélémy, and M. Bibes. Magnetoelectric Devices for Spintronics. *Annual Review of Materials Research*, 44(1): 91–116, 2014.

[355] E. Y. Tsymbal. Spintronics: Electric toggling of magnets. *Nature Materials*, 11(1): 12–13, 2011.

[356] M. Trassin. Low energy consumption spintronics using multiferroic heterostructures. *Journal of Physics: Condensed Matter*, 28(3): 033001, 2016.

[357] V. Garcia, M. Bibes, and A. Barthélémy. Artificial multiferroic heterostructures for an electric control of magnetic properties. *Comptes Rendus Physique*, 16(2): 168–181, 2015.

[358] F. Matsukura, Y. Tokura, and H. Ohno. Control of magnetism by electric fields. *Nature Nanotechnology*, 10(3): 209–220, 2015.

[359] N. A. Hill. Why Are There so Few Magnetic Ferroelectrics? *The Journal of Physical Chemistry B*, 104(29): 6694–6709, 2000.

[360] J. Kreisel and M. Kenzelmann. Multiferroics - the challenge of coupling magnetism and ferroelectricity. *Europhysics News*, 40(5): 17–20, 2009.

[361] T. Kimura. Magnetoelectric Hexaferrites. *Annual Review of Condensed Matter Physics*, 3(1): 93–110, 2012.

[362] R. Ramesh and N. A. Spaldin. Multiferroics: progress and prospects in thin films. *Nature Materials*, 6: 21–29, 2007.

[363] J. Ma, J. Hu, Z. Li, and C.-W. Nan. Recent Progress in Multiferroic Magnetoelectric Composites: from Bulk to Thin Films. *Advanced Materials*, 23(9): 1062–1087, 2011.

[364] M. Fiebig. Revival of the magnetoelectric effect. *Journal of Physics D: Applied Physics*, 38(8): R123–R152, 2005.

[365] D. Pantel, S. Goetze, D. Hesse, and M. Alexe. Reversible electrical switching of spin polarization in multiferroic tunnel junctions. *Nature Materials*, 11(4): 289–293, 2012.

[366] V. S. Borisov, S. Ostanin, I. V. Maznichenko, A. Ernst, and I. Mertig. Magnetoelectric properties of the Co/$\mathrm{PbZr_xTi_{1-x}O_3}$ (001) interface studied from first principles. *Physical Review B*, 89(5): 1–8, 2014.

[367] K. Yamauchi, B. Sanyal, and S. Picozzi. Interface effects at a half-metal/ferroelectric junction. *Applied Physics Letters*, 91(6): 062506, 2007.

[368] V. Dugaev, A. Wal, and J. Barnaś. *Symmetry, Spin Dynamics and the Properties of Nanostructures: Lecture Notes of the 11th International School on Theoretical Physics*. World Scientific Publishing Co. Pte. Ltd., Singapore, 2016.

[369] J. F. Scott. Ferroelectrics go bananas. *Journal of Physics: Condensed Matter*, 20(2): 021001, 2008.

[370] K. M. Rabe, C. Ahn, and J.-M. Triscone. *Physics of Ferroelectrics: A Modern Perspective*, vol. 105. Springer-Verlag, Berlin, 2007.

[371] Y. A. Genenko, J. Glaum, M. J. Hoffmann, and K. Albe. Mechanisms of aging and fatigue in ferroelectrics. *Materials Science and Engineering B*, 192: 52–82, 2015.

[372] J. C. Jan, H. M. Tsai, C. W. Pao, J. W. Chiou, K. Asokan, K. P. K. Kumar, W. F. Pong, Y. H. Tang, M.-H. Tsai, S. Y. Kuo, and W. F. Hsieh. Direct experimental evidence of hybridization of Pb states with O 2p states in ferroelectric perovskite oxides. *Applied Physics Letters*, 87(1): 012103, 2005.

[373] G. van der Laan and I. W. Kirkman. The 2p absorption spectra of 3d transition metal compounds in tetrahedral and octahedral symmetry. *Journal of Physics: Condensed Matter*, 4(16): 4189–4204, 1992.

[374] S. C. Ray, H. C. Hsueh, C. H. Wu, C. W. Pao, K. Asokan, M. T. Liu, H. M. Tsai, C. H. Chuang, W. F. Pong, J. W. Chiou, M.-H. Tsai, J. M. Lee, L. Y. Jang, J. M. Chen, and J. F. Lee. Local atomic and electronic structures and ferroelectric properties of $\mathrm{PbZr_{0.52}Ti_{0.48}O_3}$: An x-ray absorption study. *Applied Physics Letters*, 99(4): 042909, 2011.

[375] W. Kempet, B. Marungsri, R. Yimnirun, W. Klysubun, T. Fangsuwannarak, S. Rattanachan, N. Pisitpipathsin, M. Promsawat, and S. Pojprapai. Polarization Switching of PZT under Electrical Field via in-situ Synchrotron X-ray Absorption Spectroscopy. *Ferroelectrics*, 492(1): 35–42, 2016.

[376] J. Jung, H. Spiering, Z. Yu, and P. Gütlich. The debye-waller factor in spin-crossover molecular crystals: a mössbauer study on $[Fe_xZn_{1-x}(ptz)_6](BF_4)_2$. *Hyperfine Interactions*, 95(1): 107–128, 1995.

[377] O. Kahn and J. Launay. Molecular bistability: An overview. *Chemtronics*, 3: 140–151, 1988.

[378] R. J. Dosser, W. J. Eilbeck, A. E. Underhill, P. R. Edwards, and C. E. Johnson. Magnetic and Mössbauer studies of a ^5T–^1A equilibrium in some iron(II)–2-(2-pyridyl)imidazole complexes. *Journal of the Chemical Society A*, (810): 810–816, 1969.

[379] S. Shi, G. Schmerber, J. Arabski, J.-B. Beaufrand, D. J. Kim, S. Boukari, M. Bowen, N. T. Kemp, N. Viart, G. Rogez, E. Beaurepaire, H. Aubriet, J. Petersen, C. Becker, and D. Ruch. Study of molecular spin-crossover complex $Fe(phen)_2(NCS)_2$ thin films. *Applied Physics Letters*, 95(4): 043303, 2009.

[380] K. Madeja and E. König. Zur Frage der bindungsverhältnisse in komplexverbindungen des eisen(II) mit 1,10- phenanthrolin. *Journal of Inorganic and Nuclear Chemistry*, 25(1963): 377–385, 1963.

[381] E. König and K. Madeja. $^5T_2$-$^1A_1$ Equilibriums in some iron(II)-bis(1,10-phenanthroline) complexes. *Inorganic Chemistry*, 6(1): 48–55, 1967.

[382] E. König. Some aspects of the chemistry of bis(2,2'-dipyridyl) and bis(1,10-phenanthroline) complexes of iron(II). *Coordination Chemistry Reviews*, 3(4): 471–495, 1968.

[383] W. A. Baker Jr, H. M. Bobonich, W. Baker, and W. A. B. Jr. Magnetic properties of some high-spin complexes of iron (II). *Inorganic Chemistry*, 3(8): 1184–1188, 1964.

[384] M. Ruben, J. Rojo, F. J. Romero-Salguero, L. H. Uppadine, and J. M. Lehn. Grid-type metal ion architectures: Functional metallosupramolecular arrays. *Angewandte Chemie - International Edition*, 43(28): 3644–3662, 2004.

[385] H. Soyer, C. Mingotaud, M.-L. Boillot, and P. Delhaes. Spin Crossover of a Langmuir-Blodgett Film Based on an Amphiphilic Iron(II) Complex. *Langmuir*, 14(20): 5890–5895, 1998.

[386] A. Lapresta-Fernández, S. Titos-Padilla, J. M. Herrera, A. Salinas-Castillo, E. Colacio, and L. F. Capitán Vallvey. Photographing the synergy between magnetic and colour properties in spin crossover material $[Fe(NH_2trz)_3](BF_4)_2$: a temperature sensor perspective. *Chemical Communications*, 49(3): 288–290, 2013.

[387] H. J. Shepherd, G. Molnár, W. Nicolazzi, L. Salmon, and A. Bousseksou. Spin Crossover at the Nanometre Scale. *European Journal of Inorgadnic Chemistry*, 2013(5-6): 653–661, 2013.

[388] S. Trofimenko. Boron-Pyrazole Chemistry. *Journal of the American Chemical Society*, 88(8): 1842–1844, 1966.

[389] G. J. Long and B. B. Hutchinson. Spin equilibrium in iron(II) poly(1-pyrazolyl)borate complexes: low-temperature and high-pressure Mössbauer spectral studies. *Inorganic Chemistry*, 26(4): 608–613, 1987.

[390] G. J. Long, F. Grandjean, and D. L. Reger. Spin Crossover in Pyrazolylborate and Pyrazolylmethane Complexes. In: *Spin Crossover in Transition Metal Compounds I*, vol. 233, pp. 91–122. Springer Berlin Heidelberg, 2004.

[391] J. D. Oliver, D. F. Mullica, B. B. Hutchinson, and W. O. Milligan. Iron-nitrogen bond lengths in low-spin and high-spin iron(II) complexes with poly(pyrazolyl)borate ligands. *Inorganic Chemistry*, 19(1): 165–169, 1980.

[392] J. P. Jesson. Mössbauer and Magnetic Susceptibility Investigation of the $^5T_2$-$^1A_1$ Crossover in Some Octahedral Ferrous Complexes in the Solid State. *The Journal of Chemical Physics*, 48(5): 2058, 1968.

[393] M. Mikolasek, G. Félix, W. Nicolazzi, G. Molnár, L. Salmon, and A. Bousseksou. Finite size effects in molecular spin crossover materials. *New Journal of Chemistry*, 38(5): 1834, 2014.

[394] G. Félix, W. Nicolazzi, L. Salmon, G. Molnár, M. Perrier, G. Maurin, J. Larionova, J. Long, Y. Guari, and A. Bousseksou. Enhanced Cooperative Interactions at the Nanoscale in Spin-Crossover Materials with a First-Order Phase Transition. *Physical Review Letters*, 110(23): 235701, 2013.

[395] M. Gruber, V. Davesne, M. Bowen, S. Boukari, E. Beaurepaire, W. Wulfhekel, and T. Miyamachi. Spin state of spin-crossover complexes: From single molecules to ultrathin films. *Physical Review B*, 89(19): 195415, 2014.

[396] S. Gueddida and M. Alouani. Spin crossover in a single Fe(phen)$_2$(NCS)$_2$ molecule adsorbed onto metallic substrates: An ab initio calculation. *Physical Review B*, 87(14): 144413, 2013.

[397] C. Enachescu, H. Constant-Machado, E. Codjovi, J. Linares, K. Boukheddaden, and F. Varret. Direct access to the photo-excitation and relaxation terms in photo-switchable solids: non-linear aspects. *Journal of Physics and Chemistry of Solids*, 62(8): 1409–1422, 2001.

[398] A. Gindulescu, A. Rotaru, J. Linares, M. Dimian, and J. Nasser. Excited metastables electronic spin states in spin crossover compounds studies by atom-phonon coupling model: Gradual and two-step transition cases. *Journal of Applied Physics*, 107(9): 09A959, 2010.

[399] K. Boukheddaden, I. Shteto, B. Hôo, and F. Varret. Dynamical model for spin-crossover solids. II. Static and dynamic effects of light in the mean-field approach. *Physical Review B*, 62(22): 14806–14817, 2000.

[400] Y. Ogawa, S. Koshihara, K. Koshino, T. Ogawa, C. Urano, and H. Takagi. Dynamical Aspects of the Photoinduced Phase Transition in Spin-Crossover Complexes. *Physical Review Letters*, 84(14): 3181–3184, 2000.

[401] H. Naggert, A. Bannwarth, S. Chemnitz, T. von Hofe, E. Quandt, and F. Tuczek. First observation of light-induced spin change in vacuum deposited thin films of iron spin crossover complexes. *Dalton Transactions*, 40(24): 6364, 2011.

[402] J. A. Real, M. C. Muñoz, J. Faus, and X. Solans. Spin Crossover in Novel Dihydrobis(1-pyrazolyl)borate $[H_2B(pz)_2]$-Containing Iron(II) Complexes. Synthesis, X-ray Structure, and Magnetic Properties of $[FeL\{H_2B(pz)_2\}_2]$ (L = 1,10-Phenanthroline and 2,2‘-Bipyridine). *Inorganic Chemistry*, 36(14): 3008–3013, 1997.

[403] N. Moliner, L. Salmon, L. Capes, M. C. Muñoz, J.-F. Létard, A. Bousseksou, J.-p. Tuchagues, J. J. McGarvey, A. C. Dennis, M. Castro, R. Burriel, and J. A. Real. Thermal and Optical Switching of Molecular Spin States in the $\{[FeL[H_2B(pz)_2]_2\}$ Spin-Crossover System (L = bpy, phen). *The Journal of Physical Chemistry B*, 106(16): 4276–4283, 2002.

[404] E. Ludwig, H. Naggert, M. Kalläne, S. Rohlf, E. Kröger, A. Bannwarth, A. Quer, K. Rossnagel, L. Kipp, and F. Tuczek. Iron(II) Spin-Crossover Complexes in Ultrathin Films: Electronic Structure and Spin-State Switching by Visible and Vacuum-UV Light. *Angewandte Chemie International Edition*, 53(11): 3019–3023, 2014.

[405] T. G. Gopakumar, F. Matino, H. Naggert, A. Bannwarth, F. Tuczek, and R. Berndt. Electron-Induced Spin Crossover of Single Molecules in a Bilayer on Gold. *Angewandte Chemie International Edition*, 51(25): 6262–6266, 2012.

[406] A. Pronschinske, Y. Chen, G. F. Lewis, D. A. Shultz, A. Calzolari, M. Buongiorno Nardelli, and D. B. Dougherty. Modification of Molecular Spin Crossover in Ultrathin Films. *Nano Letters*, 13(4): 1429—-1434, 2013.

[407] M. Bernien, H. Naggert, L. M. Arruda, L. Kipgen, F. Nickel, J. Miguel, C. F. Hermanns, A. Krüger, D. Krüger, E. Schierle, E. Weschke, F. Tuczek, and W. Kuch. Highly Efficient Thermal and Light-Induced Spin-State Switching of an Fe(II) Complex in Direct Contact with a Solid Surface. *ACS Nano*, 9(9): 8960–8966, 2015.

[408] A. Arroyave, A. Lennartson, A. Dragulescu-Andrasi, K. S. Pedersen, S. Piligkos, S. A. Stoian, S. M. Greer, C. Pak, O. Hietsoi, H. Phan, S. Hill, C. J. McKenzie, and M. Shatruk. Spin Crossover in Fe(II) Complexes with N$_{4}$ S$_{2}$ Coordination. *Inorganic Chemistry*, 55(12): 5904–5913, 2016.

[409] A. L. Thompson, A. E. Goeta, J. A. Real, A. Galet, and M. Carmen Muñoz. Thermal and light induced polymorphism in iron(II) spin crossover compounds. *Chemical Communications*, (12): 1390–1391, 2004.

[410] E. König. Structural Changes Accompanying Continuous and Discontinuous Spin-State Transitions. In: *Progress in Inorganic Chemistry*, vol. 35, pp. 527–622. 1987.

[411] M. S. Haddad, W. D. Federer, M. W. Lynch, and D. N. Hendrickson. Spin-crossover ferric complexes: unusual effects of grinding and doping solids. *Inorganic Chemistry*, 20(1): 131–139, 1981.

[412] N. Baadji and S. Sanvito. Giant Resistance Change across the Phase Transition in Spin-Crossover Molecules. *Physical Review Letters*, 108(21): 217201, 2012.

[413] V. Meded, A. Bagrets, K. Fink, R. Chandrasekar, M. Ruben, F. Evers, A. Bernand-Mantel, J. S. Seldenthuis, A. Beukman, and H. S. J. van der Zant. Electrical control over the Fe(II) spin crossover in a single molecule: Theory and experiment. *Physical Review B*, 83(24): 245415, 2011.

[414] E. J. Devid, P. N. Martinho, M. V. Kamalakar, I. Šalitroš, Ú. Prendergast, J.-F. Dayen, V. Meded, T. Lemma, R. González-Prieto, F. Evers, T. E. Keyes, M. Ruben, B. Doudin, and S. J. van der Molen. Spin Transition in Arrays of Gold Nanoparticles and Spin Crossover Molecules. *ACS Nano*, 9(4): 4496–4507, 2015.

[415] K. Takahashi, H.-B. Cui, Y. Okano, H. Kobayashi, Y. Einaga, and O. Sato. Electrical Conductivity Modulation Coupled to a High-Spin-Low-Spin Conversion in the Molecular System $[\mathrm{Fe^{III}(qsal)_2}][\mathrm{Ni(dmit)_2}]_3 \cdot \mathrm{CH_3CN{\cdot}H_2O}$. *Inorganic Chemistry*, 45(15): 5739–5741, 2006.

[416] M. S. Alam, M. Stocker, K. Gieb, P. Müller, M. Haryono, K. Student, and A. Grohmann. Spin-State Patterns in Surface-Grafted Beads of Iron(II) Complexes. *Angewandte Chemie International Edition*, 49(6): 1159–1163, 2010.

[417] F. Prins, M. Monrabal-Capilla, E. A. Osorio, E. Coronado, and H. S. J. van der Zant. Room-Temperature Electrical Addressing of a Bistable Spin-Crossover Molecular System. *Advanced Materials*, 23(13): 1545–1549, 2011.

[418] T. Mahfoud, G. Molnár, S. Cobo, L. Salmon, C. Thibault, C. Vieu, P. Demont, and A. Bousseksou. Electrical properties and non-volatile memory effect of the $[\mathrm{Fe(HB(pz)_3)_2}]$ spin crossover complex integrated in a microelectrode device. *Applied Physics Letters*, 99(5): 053307, 2011.

[419] B. Haynie, A. Walker, T. Tighe, D. Allara, and N. Winograd. Adventures in molecular electronics: how to attach wires to molecules. *Applied Surface Science*, 203-204: 433–436, 2003.

[420] C. A. Hacker, C. A. Richter, N. Gergel-Hackett, and L. J. Richter. Origin of Differing Reactivities of Aliphatic Chains on H-Si(111) and Oxide Surfaces with Metal. *The Journal of Physical Chemistry C*, 111(26): 9384–9392, 2007.

[421] C. A. Richter, C. A. Hacker, and L. J. Richter. Electrical and Spectroscopic Characterization of Metal/Monolayer/Si Devices. *The Journal of Physical Chemistry B*, 109(46): 21836–21841, 2005.

[422] Y. Selzer, M. A. Cabassi, T. S. Mayer, and D. L. Allara. Thermally Activated Conduction in Molecular Junctions. *Journal of the American Chemical Society*, 126(13): 4052–4053, 2004.

[423] C. C. Bof Bufon, C. Vervacke, D. J. Thurmer, M. Fronk, G. Salvan, S. Lindner, M. Knupfer, D. R. T. Zahn, and O. G. Schmidt. Determination of the charge transport mechanisms in ultrathin copper phthalocyanine vertical heterojunctions. *Journal of Physical Chemistry C*, 118(14): 7272–7279, 2014.

[424] E. G. Petrov and V. May. A Unified Description of Superexchange and Sequential Donor-Acceptor Electron Transfer Mediated by a Molecular Bridge. *The Journal of Physical Chemistry A*, 105(45): 10176–10186, 2001.

[425] R. L. McCreery. Molecular Electronic Junctions. *Chemistry of Materials*, 16(23): 4477–4496, 2004.

[426] H. Yan, A. J. Bergren, R. McCreery, M. L. Della Rocca, P. Martin, P. Lafarge, and J. C. Lacroix. Activationless charge transport across 4.5 to 22 nm in molecular electronic junctions. *Proceedings of the National Academy of Sciences of the United States of America*, 110(14): 5326–30, 2013.

[427] S. W. Wu, N. Ogawa, and W. Ho. Atomic-scale coupling of photons to single-molecule junctions. *Science*, 312(5778): 1362–5, 2006.

[428] A. Thon, M. Merschdorf, W. Pfeiffer, T. Klamroth, P. Saalfrank, and D. Diesing. Photon-assisted tunneling versus tunneling of excited electrons in metal-insulator-metal junctions. *Applied Physics A*, 78(2): 189–199, 2004.

[429] J. Lehmann, S. Kohler, P. Hänggi, and A. Nitzan. Molecular Wires Acting as Coherent Quantum Ratchets. *Physical Review Letters*, 88(22): 228305, 2002.

[430] M. L. Chabinyc, X. Chen, R. E. Holmlin, H. Jacobs, H. Skulason, C. D. Frisbie, V. Mujica, M. A. Ratner, M. A. Rampi, and G. M. Whitesides. Molecular Rectification in a Metal-Insulator-Metal Junction Based on Self-Assembled Monolayers. *Journal of the American Chemical Society*, 124(39): 11730–11736, 2002.

[431] C. Zhou, M. R. Deshpande, M. A. Reed, L. Jones, and J. M. Tour. Nanoscale metal/self-assembled monolayer/metal heterostructures. *Applied Physics Letters*, 71(5): 611, 1997.

[432] K. Konstadinidis, P. Zhang, R. Opila, and D. Allara. An in-situ X-ray photoelectron study of the interaction between vapor-deposited Ti atoms and functional groups at the surfaces of self-assembled monolayers. *Surface Science*, 338(1-3): 300–312, 1995.

[433] I. Suleimanov, O. Kraieva, J. Sánchez Costa, I. O. Fritsky, G. Molnár, L. Salmon, and A. Bousseksou. Electronic communication between fluorescent pyrene excimers and spin crossover complexes in nanocomposite particles. *Journal of Materials Chemistry C*, 3(19): 5026–5032, 2015.

[434] S. Titos-Padilla, J. M. Herrera, X.-W. Chen, J. J. Delgado, and E. Colacio. Bifunctional Hybrid SiO_2 Nanoparticles Showing Synergy between Core Spin Crossover and Shell Luminescence Properties. *Angewandte Chemie International Edition*, 50(14): 3290–3293, 2011.

[435] J. M. Seddon. *Handbook of Liquid Crystals Set.* Wiley-VCH Verlag GmbH, Weinheim, Germany, 1998.

Michał STUDNIAREK

Interface and Multifunctional Device Spintronics. Studies with Synchrotron Radiation.

Résumé

La spintronique multifonctionnelle est une nouvelle direction d'avancement pour aller au-delà des limites de l'électronique moderne. Il vise à développer des dispositifs qui seraient sensibles à plus d’un stimulus et/ou ont un signal multi-réponse. Dans cette thèse, nous explorons cette voie multifonctionnelle émergente en combinant l’électronique de spin et les systèmes organique pour ouvrir la voie vers des dispositifs polyvalents. Nous étudions la formation d'une spinterface dans le système Co/manganèse-phthalocyanine. Nous proposons l'introduction de multifonctionnalités intrinsèques en utilisant des matériaux à transition de spin. Nous développons une nouvelle approche de fonctionnalisation pour ajuster leurs propriétés vers des applications. Nous proposons un contrôle fonctionnel externe sur une spinterface en utilisant un substrat multiferroïque. Dans le cadre de cette thèse, un insert polyvalent à température variable a été développé à la ligne de lumière DEIMOS du synchrotron SOLEIL. Nous démontrons comment il peut être utilisé pour sonder des atomes actifs dans n'importe quel dispositif électronique.

Mots-clés : spintronique multifonctionnelle, spinterface, transition de spin, rayonnement synchrotron.

Summary

Multifunctional spintronics is a new direction of advancement beyond the limits of modern electronics. By combining elementary charge of an electron and its spin, it aims to develop devices which would be sensitive to more than one stimuli and/or have multiresponse signal. In this thesis, we explore the multifunctional potential emerging while combining spin electronic and organic systems to pave the way towards multipurpose devices. First, we study formation of a ferromagnetic/organic spinterface in Co/manganese-phthalocyanine system. We propose introduction of intrinsic multifunctionality by using spin crossover materials. We develop a novel functionalization approach for tuning their properties towards device applications. We propose an external functional control over any hybrid spinterface by using multiferroic substrate. In the framework of this thesis, a Versatile Variable Temperature Insert was developed at the DEIMOS beamline of the SOLEIL synchrotron. We demonstrate how it can be used to probe active atoms in any microelectronic device.

Keywords: multifunctional spintronics, spinterface, spin crossover, synchrotron radiation.